

AD-A283 926



WL-TR-94- 4084

Volume II

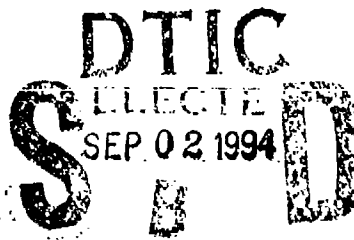
CONFERENCE ON AEROSPACE TRANSPARENT MATERIALS AND ENCLOSURES  
VOLUME II - SESSIONS V-IX

Compiled by Samuel A. Marolo

March 1994

Conference Report for Period 9-13 August 1993

Approved for Public Release; Distribution Unlimited



563

94-28511



MATERIALS DIRECTORATE  
WRIGHT LABORATORY  
MATERIAL COMMAND  
WRIGHT-PATTERSON AIR FORCE BASE, OHIO 45433-6533

DTIC QUALITY INSPECTED 1

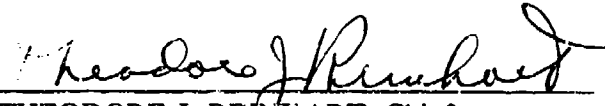
94 9 01 104

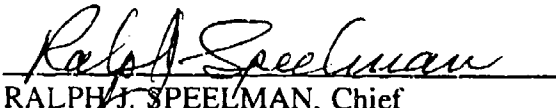
## NOTICE

When Government drawings, specifications, or other data are used for any purpose other than in connection with a definitely Government-related procurement, the United States Government incurs no responsibility or any obligation whatsoever. The fact that the government may have formulated or in any way supplied the said drawings, specifications, or other data, is not to be regarded by implication, or otherwise in any manner construed, as licensing the holder, or any other person or corporation; or as conveying any rights or permission to manufacture, use, or sell any patented invention that may in any way be related thereto.

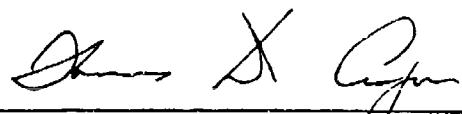
This report is releasable to the National Technical Information Service (NTIS). At NTIS, it will be available to the general public, including foreign nations.

This technical report has been reviewed and is approved for publication.

  
THEODORE J. REIMHART, Chief  
Materials Engineering Branch  
Systems Support Division  
Wright Laboratory

  
RALPH J. SPEELMAN, Chief  
Aircrew Protection Branch  
Vehicle Subsystems Division  
Wright Laboratory

FOR THE COMMANDER

  
THOMAS D. COOPER, Chief  
System Support Division  
Materials Laboratory

If your address has changed, if you wish to be removed from our mailing list, or if the addressee is no longer employed by your organization please notify WL/FIVR, WPAFB, OH 45433-6553 to help us maintain a current mailing list.

Copies of this report should not be returned unless return is required by security considerations, contractual obligations, or notice on a specific document.

REPORT DOCUMENTATION PAGE			Form Approved OMB No. 0704-0188	
Public reporting burden for this collection of information is estimated to average 1 hour per response, including the time for reviewing instructions, searching existing data sources, gathering and maintaining the data needed, and completing and reviewing the collection of information. Send comments regarding this burden estimate or any other aspect of this collection of information, including suggestions for reducing this burden, to Washington Headquarters Services, Directorate for Information Operations and Reports, 1215 Jefferson Davis Highway, Suite 1204, Arlington, VA 22202-4302, and to the Office of Management and Budget, Paperwork Reduction Project (0704-0188), Washington, DC 20503.				
1. AGENCY USE ONLY (Leave blank)	2. REPORT DATE March 1994	3. REPORT TYPE AND DATES COVERED Interim 9AUG to 13 AUG 1993		
4. TITLE AND SUBTITLE Conference on Aerospace Transparent Materials and Enclosures, Volume II: Sessions V-IX		5. FUNDING NUMBERS F33615-92-C-3400		
6. AUTHOR(S) Compiled by Samuel A. Marolo				
7. PERFORMING ORGANIZATION NAME(S) AND ADDRESS(ES) University of Dayton Research Institute 300 College Park Avenue Dayton, Ohio 45469-0110		8. PERFORMING ORGANIZATION REPORT NUMBER		
9. SPONSORING/MONITORING AGENCY NAME(S) AND ADDRESS(ES) Flight Dynamics Directorate (WL/FIVR) Wright Laboratory, Materiel Command Wright-Patterson Air Force Base, OH 45433-6533		10. SPONSORING/MONITORING AGENCY REPORT NUMBER WL-TR-94-4084		
11. SUPPLEMENTARY NOTES				
12a. DISTRIBUTION/AVAILABILITY STATEMENT APPROVED FOR PUBLIC RELEASE; DISTRIBUTION UNLIMITED		12b. DISTRIBUTION CODE		
13. ABSTRACT (Maximum 200 words) The purpose of this report is to make available the technical papers presented at the Sixteenth Conference on Aerospace Transparent Materials and Enclosures. Sixty-seven technical papers are presented in nine sessions that address transparent material for enclosures, coatings for transparencies, transparency design; bird impact resistance; human factors and optics; operational problems; design criteria on transparent plastics, glasses and elastomers; aircraft-structural integration of windshields and canopies; computed design; testing techniques; and cost of ownership reduction. The papers contained herein have been reproduced directly from the original manuscripts.				
14. SUBJECT TERMS injection molding, optics, photochromics, polycarbonate, acrylic, interlayers, windshields, canopies, coatings, transparent materials, environmental resistance, computed design, design criteria, cost of ownership reduction, frameless transparency, new transparent materials		15. NUMBER OF PAGES 585		16. PRICE CODE
17. SECURITY CLASSIFICATION OF REPORT UNCLASSIFIED	18. SECURITY CLASSIFICATION OF THIS PAGE UNCLASSIFIED	19. SECURITY CLASSIFICATION OF ABSTRACT UNCLASSIFIED	20. LIMITATION OF ABSTRACT SAR	

## PREFACE

This report was prepared by the Materials Engineering Branch under Project 1926, "Aircraft Windshield Development." It was administered under the direction of the Wright Laboratory, Materials Directorate and Flight Dynamics Directorate, Air Force Material Command.

The technical papers enclosed in this report were presented at the Flight Dynamics/Materials Directorate "Conference on Aerospace Transparent Materials and Enclosures," held at the Sheraton Harbor Island Hotel, San Diego, California, on 9-13 August 1993. Mr. Samuel A. Marolo served as Conference Chairperson.

There were many who contributed to this very successful and timely conference which covered enhanced enclosure materials and advanced design technology. Special thanks are expressed to Mr. Russell E. Urzi, WL/FIVR, for providing a superior performance as Conference Technical Chairperson and as Conference Chairperson for Systems Technology. Gratitude and appreciation are expressed to Mr. Theodore J. Reinhart, WL/MLSE; Mrs. Louise Farren, Mrs. Mary Wright, and Ms. Evie Beyers, all of the University of Dayton; and Mrs. Nancy Holland and Mrs. Christine Kindle, Wright Laboratory, for the outstanding job accomplished as Chairperson for Materials Technology, Conference Administration, Conference Secretary, Administrative Assistant, and Conference Aides, respectively. Gratitude is also expressed to Lt. David Hammershock, WL/FIVR, who served as Conference Display/Exhibit Chairperson.

Special appreciation and thanks are expressed to Mr. Ralph J. Speelman, WL/FIVR, for his timely help and contribution to the success of the Conference.

Appreciation and thanks are expressed to Col Robert L. Herklotz, Director, Flight Dynamics Directorate, and Dr. Vincent J. Russo, Director, Materials Directorate, for their support of the Conference and their expressed support of this technical area. Gratitude is also expressed to Col Herklotz and Lt Col Bruce Thompson, Deputy Chief of Fighter Requirements for Power Projection at HQ Air Combat Command, for their warm welcoming addresses and their expressions of importance of this technical area to the Air Force. Heartfelt appreciation is expressed to Mr. Eric E. Abell, Chief of All Technical and Engineering Operations for the F-22 System Program Office, for taking time from an overloaded schedule to deliver a timely, challenging, informative keynote address which set the tone for the technical papers which followed.

This report was submitted for publication in March 1994.

Publication of this report does not constitute Air Force approval of the findings or conclusions presented. It is published only for the exchange and stimulation of ideas.

Accession For	
NTIS GRA&I	<input checked="checked" type="checkbox"/>
DTIC TAB	<input type="checkbox"/>
Unannounced	<input type="checkbox"/>
Justification	
By	
Distribution/	
Availability Codes	
and/or	
Special	
D1-1	



## TABLE OF CONTENTS

<u>SESSION I: SYSTEMS OVERVIEW - PART A</u>	<u>PAGE</u>
ACQUISITION MANAGEMENT OF CONSUMABLE TECHNOLOGY UTILIZING A NOVEL TECHNOLOGY TRANSITION PROCESS Russell E. Urzi, Flight Dynamics Directorate, Wright Laboratory	2
TECHNIQUES TO CREATE A SUPPORTABLE TECHNOLOGY PROGRAM T. R. Bennett, Flight Dynamics Directorate, Wright Laboratory	8
<u>SESSION I: SYSTEMS OVERVIEW - PART B</u>	17
TRANSPARENCY SYSTEM (CANOPY) TECHNOLOGY CHALLENGES G. C. Stone, Lockheed Fort Worth Co.	18
AIRCRAFT TRANSPARENCY TECHNOLOGY DEVELOPMENT AND VALIDATION FOR TRANSITION TO DoD FLIGHT VEHICLE SYSTEMS Robert E. McCarty, Flight Dynamics Directorate, Wright Laboratory	32
<u>SESSION II: CURRENT SYSTEMS - PART A</u>	50
ADVANCED TRANSPARENCY DEVELOPMENT FOR USAF AIRCRAFT Michael P. Cuchard, University of Dayton, and 1Lt Joseph C. Davisson, Flight Dynamics Directorate, Wright Laboratory	51
INTEGRATED SYSTEMS APPROACH TO STRATEGIC TRANSPARENCIES 1Lt Joe Coogan, Flight Dynamics Directorate, Wright Laboratory	62
RAIN EROSION TESTING REQUIREMENTS - THE F-16 TRANSPARENCY SPECIFICATION REVISITED Clifton A. Webster, Lockheed Fort Worth Company	78
EVALUATION OF HARDENED B-1B WINDSHIELD MATERIALS 1Lt Joe Coogan, WL/FIVR, and K. I. Clayton, University of Dayton	93
ABRASION RESISTANT CANOPY (ARC) MATERIALS EVALUATION PROJECT Steven D. Webster, Bell Helicopter Textron, Inc.; Peter G. Dehmer, ARL - Materials Directorate; and Kristen Alexander, WL/FIVR	104
<u>SESSION II: CURRENT SYSTEMS - PART B</u>	124
F-16 CANOPY TECHNOLOGIES: ACCOMPLISHMENTS, CHALLENGES, AND OPPORTUNITIES Lt Joseph Davisson, Jr., WL/FIVR and D. Reed Nelson, OO-ALC/LAAEA	125
MISSION INTEGRATED TRANSPARENCY SYSTEM (MITS) ACCOMPLISHMENTS AND STATUS Gordon C. Stone, Lockheed Fort Worth Company	135
F-15 ADVANCED TRANSPARENCY DEVELOPMENT: A TEAM APPROACH 1Lt Guy Graening, Flight Dynamics Directorate	188

T-38 BIRD IMPACT RESISTANT COMPOSITE WINDSHIELD FRAME DEVELOPMENT S. Hargis, SM-ALC/TiEC, and G. J. Stenger, University of Dayton	198
<u>SESSION III: UNDERSTANDING CURRENT MATERIALS - PART A</u>	237
INTERLAYER DESIGN FOR GLASS/PLASTIC TRANSPARENCIES Thomas G. Rukavina, PPG Industries	238
USE OF PHOTOCHROMIC MATERIALS IN AIRCRAFT TRANSPARENCIES J. A. Andrechak and M. V. Moncur, Pilkington Aerospace	271
HIGH TEMPERATURE URETHANE (S-240) Khushroo H. Lakdawala and John A. Raffo, Sierracin/Sylmar Corp.	288
<u>SESSION III: UNDERSTANDING CURRENT MATERIALS - PART B</u>	315
SOLID PARTICLE IMPACT EFFECTS ON AIRCRAFT TRANSPARENCIES Robert G. Oeding, PDA Engineering	316
HYPERVELOCITY IMPACT DAMAGE TOLERANCE OF FUSED SILICA GLASS K. S. Edelstein, NASA/Johnson Space Center	343
FATIGUE ANALYSIS OF POLYCARBONATE TRANSPARENCIES L. Garrett, A. Mayer, and R. McCarty, Flight Dynamics Directorate, and Y. Kin, Purdue University Calumet	364
PHYSICAL AGING OF POLYCARBONATE BY FREE VOLUME CONSIDERATIONS D. M. Bigg and K. J. Heater, Battelle Memorial Institute	382
RELIABILITY ANALYSIS AND CRACK INITIATION STUDY IN CANOPY GRADE POLYCARBONATE A. Chudnovsky, T.-J. Chen, and S. Wu, University of Illinois at Chicago; L. V. Garrett and M. Gran, Flight Dynamics Directorate; and C. P. Bosnyak, Dow Chemical	399
EVALUATION OF CRAZE INITIATION CRITERIA FOR CAST ACRYLIC Daniel R. Bowman and Thomas J. Whitney, University of Dayton	420
STRESS MEASUREMENT IN STRUCTURAL PLASTICS BY L-cr WAVES Nisar Shaikh, Analytic Engineering Company	450
AIRCRAFT WINDOW PROBLEMS - AIRCRAFT MANUFACTURER'S ASSISTANT - HELP OR OBSTRUCTION? Klaus W. Ewald, Lufthansa German Airlines	460
<u>SESSION IV: EMERGING CAPABILITIES - PART A</u>	481
SURFACE SEAL™ COATED GLASS G. B. Goodwin and William E. Heidish, PPG Industries, Inc.	482

SCRATCH RESISTANT COATINGS FOR AIRCRAFT TRANSPARENCIES PREPARED BY PLASMA POLYMERIZATION A. Baalmann, H. Stuke, and K. D. Vissing, Fraunhofer-Institut IFAM	492
VERSATILE APPLICATIONS OF s-243 PROTECTIVE COATING SYSTEM ON AIRCRAFT TRANSPARENCIES A. Z. Bimanand and J. A. Raffo, Sierracin/Sylmar Corp.	509
BATTLE DAMAGE REPAIR OF AIRCRAFT TRANSPARENCIES D. W. Carter, Flight Dynamics Directorate	546
TRANSPARENCY RECORDER FOR OBTAINING IN-FLIGHT ENVIRONMENTAL LIFE HISTORY R. Sinclair, Nonvolatile Electronics Inc.	564
<u>SESSION IV: EMERGING CAPABILITIES - PART B</u>	574
TEXSTAR DESIGNED QUICK SEAL PROGRAM FOR AIRCRAFT TRANSPARENCIES J. V. Irion and R. M. Webb, Texstar, Inc.	575
QUICK FIX AND QUICK CHANGE OF TRANSPARENCIES M. E. Kelley, Flight Dynamics Laboratory	590
COCKPIT SOLAR SHIELDS FOR DOD AIRCRAFT M. E. Kelley, Flight Dynamics Laboratory	600
EXTERIOR TRANSPARENCY COVERS & HAIL TESTING M. E. Kelley, Flight Dynamics Laboratory	616
<u>SESSION V: TESTING TECHNOLOGY - PART A</u>	643
AN EXPERIMENTAL EVALUATION OF THE EFFECT OF HOLE FABRICATION/TREATMENT TECHNIQUES ON RESIDUAL STRENGTH AND FATIGUE LIFE OF POLYCARBONATE SPECIMENS WITH HOLES D. R. Bowman, University of Dayton	644
PENETRATION AND SURFACE SPALLING DUE TO HYPERVELOCITY IMPACT INTO FUSED SILICA GLASS K. Edelstein, NASA/Johnson Space Center and M. L. Fudge, Kaman Sciences Corp.	675
DEVELOPMENT OF A TRANSPARENCY DURABILITY TEST CRITERIA: COUPON SCALE TESTING, FIELD SERVICE DATA ANALYSIS, AND FULL SCALE TESTING T. Whitney and D. R. Bowman, University of Dayton, and R. A. Smith, Flight Dynamics Laboratory	689
<u>SESSION V: TESTING TECHNOLOGY - PART B</u>	726
ASSESSMENT OF DURABILITY OF FULL-SCALE TRANSPARENCY SYSTEMS S. Hamilton and G. Brockfeld, Flight Dynamics Directorate	727

PRESSURE BURST TESTING OF KC-135 CELESTIAL NAVIGATION WINDOWS T. J. Whitney and D. R. Bowman, University of Dayton, and R. Urzi, Flight Dynamics Directorate	745
<u>SESSION VI: BIRDSTRIKE HAZARDS AND OPTICS - PART A</u>	764
BIOLOGICAL VALIDATION AND STANDARDIZATION OF INTERNATIONAL BIRDSTRIKE TESTING TECHNIQUES J. Allan, Central Science Laboratory (MAFF), and D. M. Hamershock, Flight Dynamics Directorate	765
INTEGRATION OF BIOLOGICAL AND ENGINEERING TECHNOLOGIES: X3D ANALYSIS OF SIX BIRD SPECIES IMPACTING AIRCRAFT TRANSPARENCIES D. M. Hamershock, Flight Dynamics Directorate, and Steven E. Olson and Michael P. Bouchard, University of Dayton	785
ASSESSMENT OF MATHEMATICAL BIRD MODELS FOR BIRD IMPACT ANALYSIS WITH AN EXPLICIT FINITE ELEMENT CODE F. Stoll and R. A. Brockman, University of Dayton	801
<u>SESSION VI: BIRDSTRIKE HAZARDS AND OPTICS - PART B</u>	823
BIRD STRIKE HAZARDS: SUPPORT FOR A 4.5 POUND BIRD TEST CRITERIA R. L. Merritt, Bird Aircraft Strike Hazard and J. J. Short, Flight Dynamics Directorate	824
TURKEY VULTURE BIRD STRIKE HAZARD AND USING SATELLITE TELEMETRY FOR BIRD AVOIDANCE D. J. Rubin, Spectrum Sciences and Software	832
ROUND ROBIN TESTING TO DETERMINE THE PRECISION AND ACCURACY IN MEASURING MULTIPLE IMAGES IN AIRCRAFT TRANSPARENCIES W. N. Kama, Armstrong Laboratory	835
<u>SESSION VII: NEW MATERIALS AND PROCESSES - PART A</u>	853
A SURVEY OF NEW HIGH USE TEMPERATURE THERMOPLASTICS FOR STRUCTURAL TRANSPARENCY APPLICATIONS M. R. Unroe, Materials Directorate	854
LASER-PROTECTIVE AIRCRAFT TRANSPARENCIES J. A. Brown, John Brown Associates, Inc.	866
FAILURE ANALYSIS OF DIAMOND-LIKE CARBON (DLC) COATED POLYCARBONATES: MECHANICAL CHARACTERIZATION A. J. Hsieh, Army Research Laboratory	873
NEW HIGH TEMPERATURE HEXAFLUORINATED POLYBENZOXAZOLES FOR CANOPY APPLICATIONS R. K. Gupta and P. J. King, Daychem Laboratories, and M. R. Unroe, Materials Directorate	874

<u>SESSION VII: NEW MATERIALS AND PROCESSES - PART B</u>	888
ADVANCED CANOPY COATINGS	889
K. Alexander, Flight Dynamics Directorate, and G. C. Stone, Lockheed Fort Worth Company	
SULLINER (UE-100) ANTI-CRAZING COATING FOR ACRYLICS	912
J. J. Demeester, Sully Produits Speciaux	
P-STATIC CONTROL	919
E. Joy, Flight Dynamics Directorate; J. Anderson, Bell Helicopter Textron; N. Wild, Jaycor, and J. Short, Texstar	
TRANSPARENCY REPAIR - TIME - TRAINING - QUALITY	935
J. Archer, Micro-Surface Finishing Products, Inc.	
EXTERIOR SURFACE COATING SYSTEM FOR ELECTROSTATIC DISCHARGE DAMAGE PREVENTION FOR THE F-16 CANOPY	942
S. Sandlin, R. L. Fogarty, and M. V. Moncur, Pilkington Aerospace	
<u>SESSION VIII: COMPUTER AIDED ANALYSIS - PART A</u>	963
TRANSPARENCY IMPACT SIMULATION: STATUS AND RESEARCH	964
R. A. Brockman and T. W. Held, University of Dayton	
CONSTITUTIVE MODELS FOR RATE-SENSITIVE TRANSPARENCY MATERIALS	974
G. J. Frank and R. A. Brockman, University of Dayton	
ANALYTICAL SIMULATION OF LOW PRESSURE, THICK WALLED INJECTION MOLDING FOR AIRCRAFT TRANSPARENCIES	989
W. R. Pinnell, Flight Dynamics Directorate	
<u>SESSION VIII: COMPUTER AIDED ANALYSIS - PART B</u>	1011
ANALYTICAL DESIGN PACKAGE - ADP2 A COMPUTER AIDED ENGINEERING TOOL FOR AIRCRAFT TRANSPARENCY DESIGN	1012
J. Wuerer, PDA Engineering; M. Gran, Flight Dynamics Directorate; and T. W. Held, University of Dayton	
THE USE OF COMPUTERIZED MATERIALS DATA IN ADP2	1042
T. E. Mack and T. E. Kipp, PDA Engineering; T. J. Whitney, University of Dayton; and M. Gran, Flight Dynamics Directorate	
VALIDATION OF BIRD IMPACT DESIGN TOOLS FOR THE F-22 CANOPY SYSTEM	1069
M. P. Bouchard, University of Dayton and J. C. Davisson, Flight Dynamics Directorate	
ESTIMATING LIFE-CYCLE COSTS OF HAZARDOUS MATERIALS	1085
J. J. Short, Flight Dynamics Directorate	

<u>SESSION IX. INJECTION MOLDING - PART A</u>	1097
DEVELOPMENT OF DIRECTLY FORMED AND FRAMELESS AIRCRAFT TRANSPARENCY TECHNOLOGY	1098
W. R. Pinnell, Flight Dynamics Directorate	
INJECTION MOLDING AS A DIRECT FORMING METHOD FOR AIRCRAFT TRANSPARENCIES	1121
C. Mills, Enviretech Molded Products and W. R. Pinnell, Flight Dynamics Directorate	
OPTICAL EVALUATION OF TRANSPARENCIES UTILIZING NEW TEST APPARATUS	1129
T. L. Robson and W. R. Pinnell, Flight Dynamics Directorate	
EFFECTS OF THICKNESS TAILORING ON THE IMPACT RESISTANCE OF DIRECTLY FORMED TRANSPARENCIES	1140
W. R. Braisted and M. A. Huelsman, University of Dayton, and W. R. Pinnell, Flight Dynamics Directorate	
<u>SESSION IX: INJECTION MOLDING - PART B</u>	1159
MECHANICAL PROPERTIES EVALUATION OF DIRECTLY FORMED TRANSPARENCY MATERIALS	1160
G. J. Frank, University of Dayton, and W. R. Pinnell, Flight Dynamics Directorate	
DIMENSIONAL MAPPING AND SHRINKAGE CHARACTERIZATION OF LARGE, THICK-WALLED, DIRECTLY-FORMED TRANSPARENT PANELS	1172
K. Roach, University of Dayton, and J. G. Chow, Florida International University	
ANALYSIS OF TRANSPARENCY PANEL SHRINKAGE CHARACTERISTICS AND THEIR APPLICATION TO TRANSPARENCY MOLD DESIGN	1207
J. G. Chow, Florida International University, and K. Roach, University of Dayton	

SESSION V

TESTING TECHNOLOGY - PART A

Chairman: K. Clayton  
University of Dayton

Co-Chairman: S. Wortman  
McClellan Air Force Base

Coordinator: G. Brockfeld  
Flight Dynamics Directorate  
Wright Laboratory

AN EXPERIMENTAL EVALUATION OF THE EFFECT OF  
HOLE FABRICATION/TREATMENT TECHNIQUES ON RESIDUAL STRENGTH  
AND FATIGUE LIFE OF POLYCARBONATE SPECIMENS WITH HOLES

D. R. Bowman  
University of Dayton



# AN EXPERIMENTAL EVALUATION OF THE EFFECT OF HOLE FABRICATION/TREATMENT TECHNIQUES ON RESIDUAL STRENGTH AND FATIGUE LIFE OF POLYCARBONATE SPECIMENS WITH HOLES\*

Daniel R. Bowman, UDRI  
University of Dayton Research Institute  
Dayton, Ohio 45469-0110  
(513) 229-3018

## ABSTRACT

An experimental test program was conducted to evaluate different techniques of fabricating/treating holes in extruded polycarbonate. This program included surface finish evaluation and tension-tension fatigue and tensile residual strength testing of polycarbonate specimens with open holes. Eight different hole fabrication/treatment techniques were developed, including drilling (several variations), step drilling, entry and exit radiusing, solvent polishing, shot peening, and cold working. The differences in tensile residual strength for the specimens with holes was minimal; however, fatigue life varied by as much as a factor of ten between the best technique, cold working, and the worst, chemical polishing. In addition, limited testing indicated that annealing extruded polycarbonate decreases fatigue life by eliminating favorable residual surface compressive stresses.

## SECTION 1 INTRODUCTION/BACKGROUND

As the usage of engineering plastics increases, the desire for better understanding of the plastic material behavior increases. In addition to basic material mechanical properties such as tensile strength, tensile modulus, etc., it is desirable to understand the effect of flaws on material behavior, and to understand joining techniques such as welding, bonding, and fastening with bolts or rivets. Flaws include inclusions, scratches, machined surfaces, rough surfaces etc. Fasteners are often used to join plastics to plastics or other materials. Fasteners require that holes be made in the plastic. These holes and holes made in the plastic for other reasons are potential failure locations as they can be thought of as flaws in the material which result in stress concentrations. One of the uses of plastics for the USAF is aircraft transparencies, which are typically bolted to the aircraft. These transparencies are subject to flight, thermal, and aerodynamic loadings, which independently or in conjunction with chemicals can cause fatigue cracking at the fastener locations<sup>1,2</sup>.

In this effort, testing was conducted to evaluate different techniques of hole fabrication/treatment for polycarbonate. While much work in this area has been conducted for metals, essentially no published work exists for plastics.

## SECTION 2 PROGRAM OBJECTIVE/SCOPE

The objective of this effort was to identify hole fabrication/treatment techniques which had potential for improving fatigue life, static strength, fracture toughness, and fatigue crack growth properties for polycarbonate. As part of this effort, a number of different hole fabrication/treatment techniques for polycarbonate which had potential for improving the properties listed above were identified and eight of these identified techniques were evaluated. This evaluation consisted of tensile testing and tension-tension fatigue testing of unflawed dogbone polycarbonate specimens as well as tensile residual strength testing and tension-tension fatigue testing of rectangular specimens with a hole at the center of the specimen.

\* Performed under Air Force Contract F33615-92-C-3402 for the Wright Laboratory, Flight Dynamics Directorate, Wright-Patterson Air Force Base, Ohio.

### SECTION 3

#### LITERATURE SEARCH AND INVESTIGATION OF HOLE DRILLING

A literature search was made using the NASA, COMPENDEX, and Chemical Abstracts data bases. Subject areas included hole drilling/fabrication techniques and fatigue, fracture, and tensile testing of specimens with flaws or holes. The majority of the information in the data bases was for metals. Information on fabricating/treating holes to improve engineering properties for plastics was virtually non-existent. Many of the concepts which have been used to improve fatigue life, static strength, fracture toughness, and fatigue crack growth for metals are applicable to plastics.

There are a number of good reviews of fatigue testing of polymers<sup>3-6</sup>, and there are a number of papers specifically dealing with fatigue of polycarbonate<sup>7-17</sup>. Tayebi and Agrawal studied the effects of stress concentrations around holes in polycarbonate<sup>18</sup>. They reported significant reductions in effective breaking stress for rectangular bar tensile specimens with a hole drilled in the center. There is a very large body of data in the literature for fatigue testing of metals and other materials. A number of techniques have been investigated and reported on for increasing fatigue life and improving fatigue crack initiation and growth properties for both specimens and engineering systems which have open holes (not loaded by a lug or fastener) or loaded holes (loaded by a lug or fastener).

There are basically four areas in which efforts to increase service life and strength around holes in engineering materials can be focused. These four areas are surface finish of the hole, residual stress in hole vicinity, heat or chemical affected zone in hole vicinity, and mechanical additions to the hole surface or vicinity such as bonded patches and washers or bushings. It should be noted that there can be synergistic effects between these four areas. Surface finish is a function of the hole fabrication/treatment technique and determines flaw size and the effective stress concentration factor associated with the hole. Typically fatigue life and residual strength are believed to increase with increased surface smoothness, both for holes and free edges of structural components (see Figure 1 for a conceptual example); however, some materials are somewhat insensitive to surface smoothness, and it is expected that there is a limit beyond which increases in smoothness do not result in great improvements in fatigue life. An example of the effect of crack length (flaw size) on residual strength, taken from testing of metal specimens, is shown in Figure 2. It should be noted that surface roughness can be thought of as a crack (or flaw) of some finite length, such that specimens with different surface roughnesses can be thought of as specimens with different "crack" lengths. Residual stress may be present in the material prior to fabrication of the hole, or it may be caused by the hole fabrication/treatment technique. The heat affected zone is a function of cutting tool speed, feed, and sharpness, as well as post fabrication treatments. The chemical affected zone is a function of the cutting lubricant or post fabrication polishing or chemical treatment. Mechanical additions to the hole surface or interior change the load path through the hole, possibly resulting in a lower stress concentration factor. Table 1 lists the specific potential hole fabrication/treatment techniques identified.

Both surface finish and the disturbed or worked state of the hole surface layer are discussed by Forsyth for metallic specimens with an open hole<sup>19</sup>. For open hole specimens, Jarfall and Magnusson found no correlation between surface roughness and fatigue performance for holes made with the same machining technique<sup>20</sup>. Others have shown that hole surface roughness features such as rifling (spiral) marks, drill chatter, etc. do not adversely affect fatigue performance, while axial surface roughness features such as axial scratches and score marks along the bore of the hole cause early initiation of cracks and reduced fatigue lives, and that surface roughness below a certain value does not increase fatigue performance<sup>21-23</sup>. Similar findings were reported by Noronha et al.; in addition, they reported significant improvement in fatigue performance of open hole specimens and low load transfer specimens with improved drilling techniques which included rotation of the drill upon retraction from the hole to reduce axial scratches; they reported that drilled holes may be slightly better than reamed holes as removal of the reamer can contribute to axial scratches; and, they reported that open holes drilled using non-standard production techniques behaved only slightly worse than properly drilled holes when tested in fatigue<sup>24</sup>. Findings summarized by Coombe were that for open hole specimens and for interference fit fastener loaded holes, hole quality does not

affect fatigue life, but for interference fit, interference is critical<sup>25</sup>. Mann et al., found no difference in fatigue life for clearance fit lug loaded holes as a function of surface finish<sup>26</sup>.

Fjelstad reported that electrochemical deburring of printed wiring boards can result in rounding of sharp corners of holes in the board, in turn resulting in lower stress concentrations and increased fatigue life<sup>27</sup>.

Adhesive bonding of fasteners or sleeves into holes has been shown to decrease stress concentration and stress intensity factors and increase fatigue life of lug loaded holes in aluminum specimens, including those which have all ready cracked<sup>28-30</sup>.

A transverse normal pressure in the vicinity of a hole in sheet molding compound, induced by using a bolt with washers on each end to create a clamping force, was shown to increase tensile static strength and fatigue life of an open hole (no load applied to the hole surfaces) specimen<sup>31</sup>.

Sniewchuk and others reported on a dimpling technique used for sheet metals which cold works the material in the vicinity of the hole and results in increased fatigue life for fastener joined sheet metal specimens<sup>32,33</sup>.

There is a significant body of literature dealing with cold working of holes to improve fatigue life and fatigue crack growth performance. Stress coining techniques were reported by Speakman<sup>34</sup>. Other cold working techniques are summarized by Phillips and Champoux<sup>35-37</sup>. A large number of papers deal with specific applications of coldworking, a sampling of which are referenced herein<sup>23,38-45</sup>. In addition, significant theoretical treatment of coldworking has been conducted along with measurement of induced stresses, a sampling of which are referenced herein<sup>46-56</sup>.

Shot peening has been used extensively for automotive and aerospace applications. General summaries of shot peening with many references have been published by the Society of Automotive Engineers<sup>57</sup>, and by the Metal Improvement Company in a trade publication<sup>58</sup>. A brief summary of theory and application is included in a company brochure by Pangborn<sup>59</sup>. Shot peening of metal parts is covered by a Military Specification, MIL-S-13165C<sup>60</sup>.

The most common, basic, and inexpensive technique of fabricating holes in engineering materials is drilling. As this technique was considered to be the baseline against which other fabrication/treatment techniques would be measured, a limited investigation of hole drilling as a stand-alone topic was conducted. Based on an evaluation of hole drilling and machining techniques for polycarbonate by UDRI<sup>61</sup> and on work conducted at UDRI in the development of a technique for measuring residual strain in plastics using the strain gage hole drilling technique<sup>62</sup>, the standard twist drill was chosen as the technique for producing all holes in the test specimens. Figure 3, reproduced from Reference 62, shows induced machining strain in cast acrylic for a standard twist drill, a carbide cutter, a lubricated carbide cutter, a relieved end mill, and a high speed carbide cutter. The induced strain caused by drilling a hole with a standard drill was 4 to 200 times smaller for the standard twist drill than for the other types of tools. While multiple drill tools and machining tools exist, evaluation of these was beyond the scope of this program.

Prior to drilling holes in each of the specimens, a brief evaluation of the effect of hole drilling parameters on induced residual stress was conducted. A matrix of holes were drilled in a ten inch square blank of polycarbonate, with feed rate/RPM combinations including feed rates of 0.0015, 0.003, and 0.006 inches per revolution and tool speeds between 50 and 2500 RPM. The holes were drilled in a Bridgeport vertical milling machine. The procedure was as follows: the holes were initiated with a No. 3 centering drill and then a new 0.250-inch high speed drill, general purpose, manufactured by Cleveland Drill Company was used in the machine with constant RPM and constant automatic feed. After allowing the blank of material to relax for 24 hours, stress in the vicinity of the holes was estimated by viewing the vicinity of the hole using polarized sheets on the front and back of the specimen. Fringe orders were counted and stress was calculated using a fringe order constant of 150 psi. The lowest induced stress was for specimens drilled at the lowest tool speed; no gross differences in residual stress

were discernable between the different feed rates. The effect of tool speed on residual stress is shown in Figure 4 and Table 2.

#### SECTION 4 CHOICE AND DESCRIPTION OF HOLE FABRICATION/TREATMENT TECHNIQUES

The techniques chosen for evaluation are discussed below. These techniques cover a broad spectrum of the potential techniques from Table 1. Many of the techniques shown in Table 1 were considered to be too exotic and expensive for this program, or not suited for plastics.

Hole fabrication/treatment techniques chosen for evaluation in this program are as follows:

[Notes: All holes were started with a centering drill except those drilled by PPG, and a new drill bit was used for each different group of holes except as noted.]

Group 1. Holes were drilled in a Bridgeport vertical milling machine with a constant speed of 60 RPM and a constant feed rate of 0.0015 inches/revolution, using a new 0.250 inch general purpose high speed steel standard twist drill from Cleveland Drill Company. This technique represented the highest quality most controlled single step production of holes. The shape of the standard twist drill evolved over the early history of machining of materials, and has remained essentially unchanged for many years.

Group 2. Holes were step drilled with technique 1 using a new 0.242 inch drill first and then a new 0.250 inch drill. Step drilling decreases the amount of material which must be removed with each cut, which, in turn, reduces the heat affected zone surrounding the hole.

Group 3. Holes were drilled using technique 1, then the entry and exit corners of the hole were radiused with a modified counter sink which had a 1/32 inch radius and a 0.250 inch pilot mounted in a drill press with a stop counter sink to control depth of cut and run at approximately 200 rpm with manual feed. The surfaces of the holes were shot peened by Metal Improvement Inc. with various shot sizes and intensities as shown in Table 3. Shot peening can be used to relieve residual stresses, or to impart compressive residual stresses which tend to retard crack initiation and crack growth. The entry and exit corners of the hole were radiused to allow shot peening of the hole corners.

Group 4. Holes were drilled by PPG Industries, using a new 0.250 inch general purpose high speed steel standard twist drill and a proprietary hole drilling technique which they have developed specifically for drilling polycarbonate aircraft transparencies. They have reported a substantial increase in birdstrike resistance of F-111 ADBIRT windshield transparencies with this technique over standard hole drilling techniques.

Group 5. Holes were drilled using technique 1, and were then polished by inserting a cotton swab soaked in toluene into the hole and rotating the swab five times, and then inserting the swab into the hole from the other side and rotating the swab five times. Chemical polishing techniques potentially could be used to reduce burrs and minor surface irregularities at minimal cost. Solvents can be used to polish the surface by dissolving burrs and softening the surface material, allowing irregularities to be smoothed out. Care must be taken not to contaminate the specimens and not to apply the chemicals to specimens with high residual stresses, as crazing would result. A number of candidate chemicals were identified as possible choices for polishing the holes. These candidates included THF, MEK, acetone, methylene chloride, and toluene. Dichloro-Methane was used to solvent polish machined edges in Reference 61 in an attempt to increase craze resistance of the machined edge. No noticeable improvement in solvent resistance was detected, however the edges did become glassy smooth. Polycarbonate is at least partially soluble in all of these chemicals.

Group 6. Holes were drilled using technique 1, then cold worked using the setup shown in Figure 5 by pushing a vaseline lubricated 0.2812 inch diameter tapered pin through the hole. Some developmental work was

conducted to choose an appropriate amount of interference (12.5 % was chosen), but no effort was made to optimize the interference. Interferences of 2 to 4 % are common for aircraft grade aluminums, where the yield strain is on the order of 0.5 %. For polycarbonate the actual yield strain is defined in different ways by different people. Herein it is defined as the strain which corresponds to the yield stress, where the yield stress is the first stress peak in the stress strain curve. For static strain rates, the nominal yield stress for polycarbonate is 9500 psi and the corresponding yield strain is 8 %. Cold working is one of the most promising techniques and has been studied extensively for metals. Cold working results in compressive stresses at the surfaces of the hole, which tend to retard crack initiation and crack growth.

Group 7. Holes were drilled using technique 1, then the entry and exit corners of the hole were radiused with a modified counter sink which had a 1/32 inch radius and a 0.250 inch pilot mounted in a drill press with a stop counter sink to control depth of cut and run at approximately 200 rpm with manual feed. Sharp corners are generally associated with high stress concentrations. Removing the sharp corners by radiusing the hole entry and exit reduces the stress concentration at these locations.

Group 8. Holes were drilled manually using a 0.250 inch general purpose high speed steel standard twist drill from the machinist's tool box with a high speed air drill at a nominal speed of 3640 RPM. This technique was considered representative of typical field or shop drilling of holes by hand. Hand drilling with the standard twist drill is the most basic and inexpensive technique for producing holes in plastics.

Extruded polycarbonate sheet has residual compressive stresses at the surface which may result in an increase in various engineering properties such as fatigue, fatigue crack growth, fracture toughness, and toughness during tensile testing. These residual stresses can be removed by annealing the polycarbonate. It is well established that thermal history affects many properties of polycarbonate<sup>63-78</sup>; yield strength increases with annealing, and toughness (or elongation) decreases. The majority of the test specimens from this program were fabricated directly from the extruded sheet with no additional thermal treatment; however, a number of tensile dogbone specimens and several specimens with holes were annealed as per the thermal profile shown in Figure 6, to evaluate the effect of annealing on tensile fatigue properties.

## SECTION 5

### TEST ARTICLE, SPECIMEN FABRICATION DESCRIPTION, AND TEST MATRIX

The material used for all testing conducted in this program was removed from a single 86 inch x 86 inch x 0.25 inch sheet of aircraft grade polycarbonate Tuffak sheet manufactured by Rohm and Haas to meet Mil-P-83310. The polycarbonate molecular weight of two samples from the sheet were characterized by UDRI; sample 1:  $M_n = 15166$ ,  $M_w = 31008$ ,  $M_z = 48908$ ; sample 2:  $M_n = 16132$ ,  $M_w = 31299$ ,  $M_z = 48184$ . The material was subjected to no special conditioning except as noted in Section 4 for annealed specimens. The tensile dogbone specimen designs used are shown in Figures 7-10. At certain stress levels, the tensile dogbone specimens consistently failed outside of the gage length during fatigue testing. Initially specimen design was thought to play a role in the failure outside the gage section, and several designs were tested with no change in the failure mode (failure was still consistently outside the gage section at certain stress levels). A more complete discussion of this phenomenon is included in Section 8. The specimen design for the rectangular specimens with holes is shown in Figure 11. The specimens were fabricated in the UDRI experimental fabrication shop. The specimens were blanked out using a bandsaw. The dogbone specimens were fabricated one at a time sidecutting with an 1/2 to 3/4 inch end mill at 800-1000 rpm with hand feed. For the specimens with holes, stacks of four were cut with a 1 and 1/4 inch diameter fly cutter at 1200 rpm, with a table speed of 2-4 inches/minute. The holes were produced as described in Section 4. The test matrix is shown in Table 4.

## SECTION 6

### DOCUMENTATION OF HOLE SURFACE FINISH

Surface roughness measurements were made using one specimen from each group (typically the 21st

specimen produced). For the shot peened specimens, the surface roughness was characterized for only the Group 3.1 specimens, as sufficient specimens were not available for the other specimens shot peened using different conditions. Circumferential surface roughness measurements were made circumferentially around the hole surface at approximately half the depth of the hole, and axial surface roughness measurements were made along four lines separated by 90 degrees parallel to the axis of the hole. Measurements were made at the Giddings and Lewis Company Eli Whitney Metrology Laboratory using a Sheffield Indicorder Spectre. The hole surface roughnesses are summarized in Tables 5 and 6. For a more complete discussion of the parameters measured, see Reference 79. It should be noted that the circumferential surface roughness (which detects axial surface features) is probably the most important measurement, since axial features (such as scratches caused by removing the drilling tool) reportedly influence crack initiation and fatigue life. This agrees with intuition as cracks tend to be purely axial; that is, they are parallel to the thickness dimension of the material. Axial surface roughness (which detects circumferential features) has less of an effect on fatigue life and crack initiation, as these features are perpendicular to the axis of the cracks.

In terms of circumferential surface roughness, Groups 6, 2, and 1 have the lowest roughness averages,  $R_a$ , of 10, 12, and 12 microinches respectively; followed by groups 4, 5, and 7 for which  $R_a$  is 35, 40, and 58 microinches respectively; the roughest holes are from Group 8 with  $R_a = 110$  microinches, and Group 3 with  $R_a = 142$  microinches. Group 6 holes were cold worked by pushing a vaseline lubricated tapered oversize pin through the hole. This apparently provides a polishing effect resulting in a slightly better surface finish than the drilled hole alone. Group 2 holes were the step drilled holes. The surface finish of these holes is nearly indistinguishable from the surface finish of the Group 1 holes which were drilled in one step. Group 4 holes were drilled by PPG Industries. Group 5 holes were the same as group 1 except they were polished with toluene. This polishing did not result in better surface finish; in fact the surface finish of the toluene polished holes was worse than the surface finish of the unpolished holes. Group 7 holes were the same as Group 1 holes except that the entry and exit of the holes was radiused. For reasons unknown, the surface finish of the Group 7 holes is not nearly as good as that of the Group 1 holes. They should have been very similar. Group 8 holes were hand drilled with a used drill bit which explains the higher surface roughness. Group 3 holes were the same as Group 7 except they were also shot peened, resulting in the highest surface roughness of any of the holes.

## SECTION 7 TEST SETUP AND METHODS

Special grips were made for this testing and are shown in Figure 12. The shoulder bolts used in the specimens grips were torqued to 40 foot pounds. A special fixture was used to align the specimens in the grips. The grip design was marginal in terms of grip area for the tensile residual strength specimens with holes, as a number of those specimens failed in the grip. No problems with the grips were experienced with the fatigue testing. The testing was conducted with MTS test machines. A displacement rate of 2 inches/minute was used for the tensile testing, and the tensile fatigue tests were conducted at 2 Hz. The ratio of the minimum load to the maximum load was 0.10 (no compression).

## SECTION 8 TEST RESULTS/DISCUSSION

The results of the residual strength testing of the tensile dogbone specimens and the rectangular specimens with holes are shown in Table 7. Typical stress-strain curves for the dogbone specimens are shown in Figure 13. Typical load displacement curves for the rectangular specimens are shown in Figure 14. In contrast with Tayebi and Agrawal<sup>18</sup>, the reduction in effective breaking stress was minimal for the tensile/residual strength specimens. Elongation was markedly reduced for specimens with holes. There was minimal variation in tensile residual strength between the hole designs. No tensile residual strength testing was conducted for Group 3 and 8 specimens. Group 3 specimens were not tested as there were only a limited number available, and those were dedicated to fatigue testing. Hand drilling (Group 8) was chosen late in the program and there was not sufficient time to conduct tensile residual strength testing of these specimens.

The results of the fatigue testing are summarized in Tables 8, 9, and 10. A composite plot of all of the fatigue data is shown in Figure 15. Plots for each of the individual specimen designs are shown in Figures 16-24. The maximum stress reported on the tables and graphs is gross stress, not net stress.

Fatigue testing of the dogbone specimens produced some unusual results in the 8.5 ksi down to the 5.5 ksi region. In this region, the life (cycles to failure) is nearly constant and may even be slightly shorter for some of the lower stresses. In addition, the majority of the specimens in this region did not fail in the gage length. The shape of the S-N curve for the dogbone specimens is similar to those reported for polycarbonate from References 14 and 16. It was suspected that the cause of the unusual shape of the S-N curve and the failures outside of the gage length for the dogbone specimens was residual surface compressive stresses which were caused by the extrusion process. Cracks tended to initiate at the specimen edges and propagate within the specimen. Cracks which initiated at a corner also tended to propagate within the specimen and were retarded at the surface (indicating significant residual surface compressive stresses). A limited number of specimens were annealed and tested. As was expected, annealing resulted in shorter fatigue lives, the vertical portion of the S-N curve disappeared, and the specimens all failed within the gage length.

The hole fabrication/treatment techniques evaluated in this program are listed below in order of fatigue performance, with the high cycle fatigue at 1.25 ksi maximum stress as the criteria, and the best technique listed first.

- (1) Group 6 - Cold working
- (2) Group 2 - Step drilling
- (3) Group 1 - Drilling with new drill, one step
- (4) Group 4 - PPG Hole Drilling
- (5) Group 8 - Hand drilling
- (6) Group 7 - Radiused entry and exit
- (7) Group 5 - Polishing with toluene

Group 3, the shot peened holes, are not included as no specimens were tested at 1.25 ksi. Group 3 would most likely perform similarly to Groups 1, 4, and 8. Examination of the shot peened results in Table 10 indicates that higher intensities and pressures may result in better fatigue performance. Higher intensities and pressures would be expected to result in higher and/or deeper induced residual stress in the vicinity of the hole. The results of the fatigue testing of shot peened specimens seems to indicate that at low pressures and intensities, shot peening results in some degradation due to roughening of the hole surface. With increased pressure and intensities, this roughening increases with minimal cold working, resulting in continued decrease of fatigue properties. Eventually, this trend changes and fatigue life starts to improve with increased pressure and intensity as the induced favorable residual compressive stresses start to overcome the degradation induced by increased surface roughness. In addition, surface roughness most likely peaks out at some point, and does not increase with additional shot peening (this is a hypothesis based on the author's experiences with salt blasting of plastics and no testing was conducted in this program to confirm this). Group 7, with radiused hole entry and exit, did not perform well, it appears that removal of the extra material to create the radius decreases fatigue life. Polishing with toluene, as with group 5, did not perform well. Careful hole drilling appears to be a much safer way of obtaining good surface finish than chemical polishing after drilling. Based on these test results, a carefully machined hole which is cold worked, Group 6, has a fatigue life of 2 to as much as 6 times the fatigue life of a hand drilled hole. This represents a considerable improvement.

It is important to note that depending on the stress level chosen to evaluate the different techniques, the ranking would change. None of the techniques chosen were optimized, and optimization could easily change the ranking. Also, testing more specimens at each stress level would result in improved definition of individual S-N curves, resulting in more exact discrimination between different hole fabrication/treatment techniques.

The effects of surface finish on fatigue life can not easily be discerned from this testing. As noted in

Section 3, surface finish is only one factor influencing fatigue, residual strength, etc. The hole fabrication/treatment techniques evaluated in this report did not concentrate on surface finish alone. Comparing specimen groups with drilled holes (and no other post-fabrication treatment), Groups 2, 1, 4, and 8 have increasing surface roughness, with Group 2 holes being the smoothest and Group 8 the roughest, and Groups 2, 1, 4, and 8 have decreasing fatigue life, with Group 2 having the longest lives, and Group 8 the shortest. There does appear to be a correlation between surface roughness and fatigue life for specimens which were drilled (with no other post-fabrication treatment), with the smoother holes having the longest lives.

## SECTION 9 CONCLUSIONS/SUMMARY

A number of different potential hole fabrication/treatment techniques were identified. Eight of these were chosen for tensile residual strength and tensile-tensile fatigue evaluation in this program. The differences in tensile residual strength for the specimens with holes were minimal. While no attempt was made to optimize the hole fabrication/treatment techniques, there was a fair amount of spread in fatigue performance for the techniques chosen for evaluation. Fatigue life varied by as much as a factor of 10 between the best technique, cold working, and the worst, chemical polishing. In addition to cold working, optimized hole drilling and shot peening also show promise for improvements in fatigue life. Based on limited testing, there is a correlation between surface roughness and fatigue life for specimens which were drilled (with no other post-fabrication treatment), with smoother holes having longer lives.

It should be noted that the results of this program apply to extruded polycarbonate and open (unloaded) holes. Indications are, from the limited number of annealed specimens which were tested, that annealing decreases fatigue life by eliminating favorable residual surface compressive stresses. The effect of annealing on tensile residual strength was not evaluated in this program; annealing might result in greater differences in residual strength between the different hole fabrication/treatments. Also, specimens with lug-loaded holes may show marked differences from the results reported herein. Evaluation of some of the parameters affecting hole performance, evaluation of the hole fabrication/treatment techniques identified herein for lug-loaded holes, optimization of some of the techniques identified herein for open holes, and evaluation of some of the identified candidate techniques for improving hole performance (which were not chosen for evaluation in this program) are areas for additional research.

## REFERENCES

1. Bowman, Daniel R. and Blaine S. West, "An Investigation Into the Structural Degradation of In-Service Aged F-111 ADBIRT Windshield Transparencies," UDR-TR-90-34, University of Dayton Research Institute, Dayton, Ohio, June 1990.
2. Hinds, B. G. and J. A. Raffo, "In-Service Cracking of F-16 Windshield/Canopies," Conference on Aerospace Transparent Materials and Enclosures, January 16-20, 1989, WRDC-TR-89-4044, Air Force Wright Aeronautical Laboratories, Wright-Patterson Air Force Base, Ohio, April 1989.
3. Hertzberg, R. W. and J. A. Manson, "Fatigue in Engineering Plastics," Academic Press, New York, 1980.
4. Sauer, J. A. and G. C. Richardson, "Fatigue of Polymers," International Journal of Fracture, 16, 1980, 499.
5. Radon, J. C., "Fatigue Crack Growth in Polymers," International Journal of Fracture, 16, 1980, 533.
6. "Fatigue in Polymers," International Conference, The Plastic and Rubber Institute, London, June 29 & 30, 1983.
7. Rabinowitz, S. and P. Beardmore, "Cyclic Deformation and Fracture of Polymers," Journal of Materials Science, 9, 1974, 81-99.
8. Crawford, R. J. and P. P. Benham, "Some Fatigue Characteristics of Thermoplastics," Polymer, 16, December, 1975, 908-914.



9. Skibo, M. D., R. W. Hertzberg, J. A. Manson, and S. L. Kim, "On the Generality of Discontinuous Fatigue Crack Growth in Glassy Polymers," *Journal of Materials Science*, 12, 1977, 531-542.
10. Mackay, M. E., T. G. Teng, and J. M. Schultz, "Craze Roles in the Fatigue of Polycarbonate," *Journal of Materials Science*, 14, 1979, 221-227.
11. Sikka, S., "Some Observations on Fatigue and Crazing of Polycarbonate (Bisphenol A)," *Polymer Bulletin*, 3, 1980, 61-68.
12. Mills, N. J. and N. Walker, "Fatigue Crack Initiation in Glassy Plastics in High Strain Fatigue Tests," *Journal of Materials Science*, 15, 1980, 1832-1840.
13. Takemori, M. T. and R. P. Kambour, "Discontinuous Fatigue Crack Growth in Polycarbonate," *Journal of Materials Science*, 16, 1981, 1108-1110.
14. Gotham, K. V., "Fatigue in Polycarbonate," *Plastics and Rubber Processing and Applications* Vol. 4, No. 1, 1984.
15. Takemori, Michael T., "Fatigue Fracture of Polycarbonate," *Polymer Engineering and Science*, Vol. 22, No. 15, October 1982, 937-945.
16. Liu, Liang B., Albert F. Yee, and David W. Gidley, "Effect of Cyclic Stress on Enthalpy Relaxation in Polycarbonate," *Journal of Polymer Science: Part B: Polymer Physics*, Vol. 30, 1992, 221-230.
17. Liu, Liang B., David W. Gidley, and Albert F. Yee, "Effect of Cyclic Stress on Structural Changes in Polycarbonate as Probed by Positron Annihilation Lifetime Spectroscopy," *Journal of Polymer Science: Part B: Polymer Physics*, Vol. 30, 1992, 231-238.
18. Tayebi, A. and A. Agrawal, "Effects of Stress Concentrations Around Holes in Polycarbonate," *Am Chem Soc, Div Org Coat and Plast Chem Prepr* v 41, Paper presented at Natl Meet of the Am Chem Soc, 178th, Washington, DC, Sep 9-14, 1979, 411-417.
19. Forsyth, P. J. E., "Microstructural Changes that Drilling and Reaming Can Cause in the Bore Holes in DTD 5015 (RR58 Extrusions)," *Aircraft Engineering*, Vol. 44, No. 11, November 1972, 20-23.
20. Jarfall, L. and A. Magnusson, "Fatigue Performance of 5 mm Sheet AA7050-T76, When Notched by Three Qualities of Open Holes and by Four Different Fastener Installations," *Flygtekn. Forsöksanst. Tech. Note* No. 678, November 1980.
21. Noronha, P. J. et al., "Fastener Hole Quality," AFFDL-TR-78-206, Vol. 1, US Air Force Systems Command, Air Force Flight Dynamics Laboratory, December 1978.
22. Perrett, B. H. E., "The United Kingdom Contribution to the AGARD Critically Loaded Hole Study on the Effect of Fastener Hole Preparation and Fit on Fatigue Performance - Fatigue Tests," TR-80109, Royal Aircraft Establishment, September 1980.
23. Magnusson, Ake, "Fatigue Life Reduction Caused by Surface Roughness Inside Bolt Holes," FFA TN 1982-13, Flygtekniska Forsöksanstalten, The Aeronautical Research Institute of Sweden, 1982.
24. Noronha, P. J., S. P. Henslee, D. E. Gordon, Z. R. Woianski, and B. G. W. Yee, "Fastener Hole Quality," AFFDL-TR-78-206, Volume 1, Air Force Flight Dynamics Laboratory, Air Force Wright Aeronautical Laboratories, Wright-Patterson Air Force Base, Ohio, December 1978.
25. Coombe, T. and R. B. Urzi, "Critically Loaded Hole Technology Pilot Collaborative Test Program - Final Technical Report," AGARD Rep. No. 678, NATO Advisory Group for Aerospace Research and Development, November 1980.
26. Mann, J. Y., G. W. Revill, and R. A. Peil, "Influence of Hole Surface Finish, Cyclic Frequency and Spectrum Severity on the Fatigue Behavior of Thick Section Aluminum Alloy Pin Joints," ARL-STRUC-R-430, Department of Defence, Defence Science and Technology Organisation Aeronautical Research Laboratory, Melbourne, Victoria, Australia, December 1987.

27. Fjelstad, J. C., "Electrochemical Deburring of Printed Wiring Boards," Proceedings of the Twelfth National SAMPE Technical Conference, Seattle, WA, October 7-9, 1980, 182-185.
28. Mann, J. Y., R. A. Pell, R. Jones, and M. Heller, "Reducing the Effects of Rivet Holes on Fatigue Life by Adhesive Bonding," Theoretical and Applied Fracture Mechanics, Vol. 3, May 1985, 113-124.
29. Heller, M., R. Jones, and J. F. Williams, "Analysis of Bonded Inserts for the Repair of Fastener Holes," Engineering Fracture Mechanics, Vol. 24, No. 4, 1986, 523-532.
30. Heller, M., T. G. Hill, J. F. Williams, and R. Jones, "Increasing the Fatigue Life of Cracked Fastener Holes Using Bonded Repairs," Theoretical and Applied Fracture Mechanics, 11, 1989, 1-8.
31. Mallick, P. K., "Effects of Hole Stress Concentration and its Mitigation on the Tensile Strength of Sheet Moulding Compound (SMC-R50) Composites," Composites, Vol. 19, No. 4, July 1988, 283-287.
32. Shewchuk, J. and F. A. Roberts, "Increasing the Fatigue Strength of Loaded Holes by Dimpling," Journal of Engineering Materials and Technology, 96 (3), July 1974, 222-226.
33. Shewchuk, J. and A. Lohse, "The Effect of Dimpling on the Fatigue Strength of Loaded Holes in a Corrosive Environment," Experimental Techniques, Vol. 9, September 1985, 33-36.
34. Speakman, E. R., "Fatigue Life Improvement Through Stress Coining Methods," Symposium on Achievement of High Fatigue Resistance in Metals and Alloys, ASTM STP 467, American Society for Testing and Materials, Atlantic City, New Jersey, June 22-27, 1969, 209-227.
35. Phillips, Joseph L., "Fatigue Improvement by Sleeve Coldworking," Society of Automotive Engineers National Aerospace Engineering and Manufacturing Meeting, Los Angeles, California, October 16-18, 1973.
36. Phillips, Joseph L., "Sleeve Coldworking Fastener Holes, Volume I, Discussion and Summary," AFML-TR-74-10, Volume I, Air Force Materials Laboratory, Wright-Patterson Air Force Base, Ohio, February 1974.
37. Champoux, R. L., "An Overview of Cold Expansion Methods," Fatigue Prevention and Design, Chamelon Press, London, 1986, 35-52.
38. de Graf, E. A. B., R. J. H. Wanhill, and A. U. de Koning, "The Effects of Peening and Hole Expansion on the Fatigue Behavior of 7079-T652 Aluminium [sic] Alloy," NLR TR 74016 U, National Aerospace Laboratory (NLR), Amsterdam, The Netherlands, January 1974.
39. Buch, A. and A. Berkovits, "Effect of Cold-Working by Hole Expansion on Fatigue Life of 7075-T7351 and 7475-T761 Aluminum Lugs with and without Initial Flaws under Maneuver Loading Spectrum," TAE No.561, Technion - Israel Institute of Technology, January 1985.
40. Ozelton, Malcolm W. and Timothy G. Coyle, "Fatigue Life Improvement by Cold Working Fastener Holes in 7050 Aluminum," Proceedings of the Symposium on Fatigue in Mechanically Fastened Composite and Metallic Joints, ASTM STP 927, American Society for Testing and Materials, Charleston, SC, March 18 and 19, 1985, 53-71.
41. Brot, A. and A. Nathan, "Increasing Fatigue and Crack Growth Lives of Short Edge-Margin Holes," Proceedings from the 13th Symposium on Durability and Damage Tolerance in Aircraft Design, Pisa, Italy, May 22-24, 1985, Warley, England, Engineering Materials Advisory Services, Ltd., 229-245.
42. Gong-Fan, She, Chen Yong, and Chen Yan, "Cold Expanding of Holes Improves Fatigue-Life of Aluminium [sic] Alloy Components," Proceedings of the International Conference on Fatigue Prevention and Design, Amsterdam, Netherlands, April 21-24, 1986, Warley, England, Engineering Materials Advisory Services, Ltd., 1986, 99-121.
43. Beaver, P. W., J. Y. Mann, and J. G. Sparrow, "Fatigue Life Enhancement by the Cold-Expansion of Holes - Research and Case Study," Proceedings of the International Conference on Fatigue Prevention and Design, Amsterdam, Netherlands, April 21-24, 1986, Warley, England, Engineering Materials Advisory Services, Ltd., 1986, 123-136.

44. Cannon, D. F., J. Sinclair, and K. A. Sharpe, "Improved Fatigue Performance of Railway Rail Bolt Holes by Cold Expansion," Proceedings of the International Conference on Fatigue Prevention and Design, Amsterdam, Netherlands, April 21-24, 1986, Warley, England, Engineering Materials Advisory Services, Ltd., 1986, 137-157.
45. Hermann, R. and C. N. Reid, "Enhancing the Fatigue Life of Fastener Holes in Aluminium[sic]-Lithium Alloy 8090," Volume 3 of Proceedings of 5th International Aluminum-Lithium Conference, Williamsburg, Virginia, March 27-31, 1989, Materials and Components Engineering Publishers, Ltd. Birmingham, England, 1607-1614.
46. Sharpe, William N., Jr., "Measurement of Residual Strains Around Coldworked Fastener Holes," AFOSR-TR-77-0020, Air Force Office of Scientific Research, Bolling Air Force Base, D. C., April 1976.
47. Poolsuk, Saravut, "Measurement of the Elastic-Plastic Boundary Around Coldworked Fastener Holes," Ph. D. Thesis, Applied Mechanics, Michigan State University, 1977.
48. Chandawanich, Nopporn, "An Experimental Study of Crack Initiation and Growth from Coldworked Holes," Doctor of Philosophy Thesis, Department of Metallurgy, Mechanics, and Materials Science, Michigan State University, 1977.
49. Sharpe, William N., Jr., Experimental Studies of Coldworked Fastener Holes, AFOSR-TR-78-0421, Air Force Office of Scientific Research, Bolling Air Force Base, D. C., February 1978.
50. Poolsuk, S. and W. N. Sharpe, Jr., "Measurement of the Elastic-Plastic Boundary Around Coldworked Fastener Holes," Journal of Applied Mechanics, Vol. 45, September 1978, 515-520.
51. Grandt, A. F. and R. M. Potter, "An Analysis of Residual Stresses and Displacements Due to Radial Expansion of Fastener Holes," AFML-TR-79-4048, Air Force Materials Laboratory, Wright-Patterson Air Force Base, Ohio, July 1979.
52. Armen, H. and Alvin Levy, "Elastic-Plastic Behavior of Coldworked Holes," Proceedings from the 24th Structures, Structural Dynamics, Material Conference, Part I, Lake Tahoe, Nevada, May 2-4, 1983, 252-262.
53. Beaver, P. W., J. Y. Mann, and J. G. Sparrow, "Grid Technique for the Measurement of Strains Close to Cold-expanded Holes," Proceedings from the Conference Measurement and Fatigue - EIS '86, Engineering Integrity Society, Bournemouth, England, March 17-20, 1986, Engineering Materials Advisory Services, Ltd., Warley, England, 491-505.
54. Su, X., M. Gu, and M. Yan, "A Simplified Residual Stress Model for Predicting Fatigue Crack Growth Behavior at Coldworked Fastener Holes," Fatigue and Fracture of Engineering Materials and Structures, Vol. 9, No. 1, 1986, 57-64.
55. Heller, M., R. Jones, and J. F. Williams, "Analysis of Cold-expansion for Cracked and Uncracked Fastener Holes," Engineering Fracture Mechanics, Vol. 39, No. 2, 1992, 195-212.
56. Clark, G., "Modelling Residual Stresses and Fatigue Crack Growth at Cold-expanded Fastener Holes," Fatigue and Fracture of Engineering Materials and Structures, Vol. 14, No. 5, 1991, 579-589.
57. "SAE Manual on Shot Peening, Third Edition," SAE HS-84, Society of Automotive Engineers, Inc., Warrendale, Pennsylvania, September 1991.
58. "Shot Peening Applications, 7th Edition," Metal Improvement Company, Inc. Brochure, Paramus, New Jersey.
59. "Shot Peening Theory and Application," Pangborn Brochure, Hagerstown, Maryland.
60. "Military Specification - Shot Peening of Metal Parts," MIL-S-13165C, June 7, 1989.
61. Husman, George E. and Ronald J. Kuhbender, "Environmental Data and Machining Techniques of Polycarbonates," Conference on Transparent Aircraft Enclosures, Las Vegas, Nevada, AFML-TR-73-126, Air Force Materials Laboratory, Wright-Patterson Air Force Base, Ohio, June 1973.
62. Flaman, M. T. and J. A. Herring, "Comparison of Four Hole-Producing Techniques for the Center-Hole Residual-Stress Measurement Method," Experimental Techniques, Vol. 9, No. 8, August 1985, 30-32.

63. Pielstocker, G., *Kunststoffe*, Vol. 51, 1961, 509.
64. Pielstocker, G., *Brit. Plastics*, Vol. 35, 1962, 365.
65. Golden, J. H., B. L. Hammant, and E. A. Hazell, "The Effect of Thermal Pretreatment on the Strength of Polycarbonate," *Journal of Applied Polymer Science*, Vol. 11, January 1967, 1571-1579.
66. Neki, K. and P. H. Geil, "Morphology-Property Studies of Amorphous Polycarbonate," *J. Macromol. Sci-Phys.*, B8(1-2), 1973, 295-341.
67. Morgan, R. J. and J. E. O'Neal, "The Effect of Thermal History on the Mechanical Properties and Crystallinity of Polycarbonate," MDRL 75-37, November 1975.
68. Ryan, J. T., "Impact and Yield Properties of Polycarbonate as a Function of Strain Rate, Molecular Weight, Thermal History, and Temperature," *Polymer Engineering and Science*, Vol. 18, No. 4, March 1978, 264-267.
69. Pitman, G. L., I. M. Ward, and R. A. Duckett, "The Effect of Thermal Pre-Treatment and Molecular Weight on the Impact Behaviour of Polycarbonate," *Journal of Materials Science*, Vol. 13, No. 10, October 1978, 2092-2104.
70. Yakouchi, M. and Y. Kobayashi, "Effect of Heat Pretreatment and Strain Rate on Tensile Properties of Polycarbonate Sheet," *Journal of Applied Polymer Science*, Vol. 26, No. 2, February 1981, 431-440.
71. Parvin, M., "The Effect of Annealing on Fracture Behaviour of Polycarbonate," *Journal of Materials Science*, Vol. 16, No. 7, 1981, 1796-1800.
72. Heath, J. B. R. and R. W. Gould, "Degradation of the Bird Impact Resistance of Polycarbonate," *SAMPE Quarterly*, October 1982, 20-29.
73. Varadarajan, K. and R. F. Boyer, "Effects of Thermal History, Crystallinity, and Solvent on the Transitions and Relaxations in poly(bisphenol-A carbonate)," *Journal of Polymer Science: Polymer Physics Edition*, Vol. 20, No. 1, January 1982, 141-154.
74. Bauwens-Crowet, C. and J. -C. Bauwens, "The Relationship Between the Effect of Thermal Pre-treatment and the Viscoelastic Behaviour of Polycarbonate in the Glassy State," *Journal of Materials Science*, Vol. 14, No. 8, 1979, 1817-1826.
75. Bauwens-Crowet, C. and J. -C. Bauwens, "Annealing of Polycarbonate Below the Glass Transition: Quantitative Interpretation of the Effect of Yield Stress and Differential Scanning Calorimetry Measurements," *Polymer*, Vol. 23, October 1982, 1599-1604.
76. Bauwens, J. -C., "Attempt to Correlate the Yield Processes Above and Below the Glass Transition in Glassy Polymers," *Polymer*, Vol. 25, No. 10, October 1984, 1523-1526.
77. Bubeck, R. A. and S. E. Bales, "Changes in Yield and Deformation of Polycarbonates Caused by Physical Aging," *Polymer Engineering and Science*, Vol. 24, No. 10, October 1984, 1142-1148.
78. Zurimendi, J. A., F. Biddlestone, J. N. Hay, and R. N. Haward, "Physical Factors Affecting the Impact Strength of Polycarbonate," *Journal of Materials Science*, Vol. 17, No. 1, January 1982, 199-203.
79. Amstutz, Hu, "Surface Texture, The Parameters," Sheffield Measurement Division Corporate Publication, Copyright 1981 and 1985.

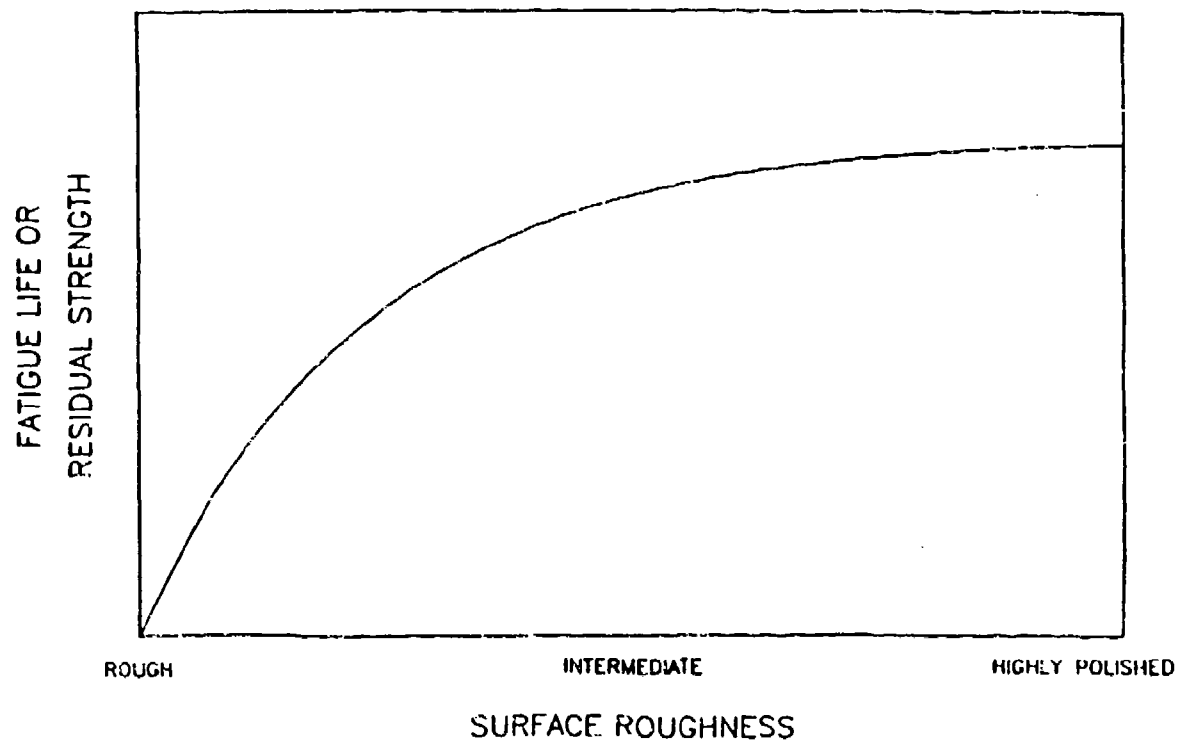


Figure 1. Hypothetical Effect of Surface Roughness on Fatigue Life and Residual Strength

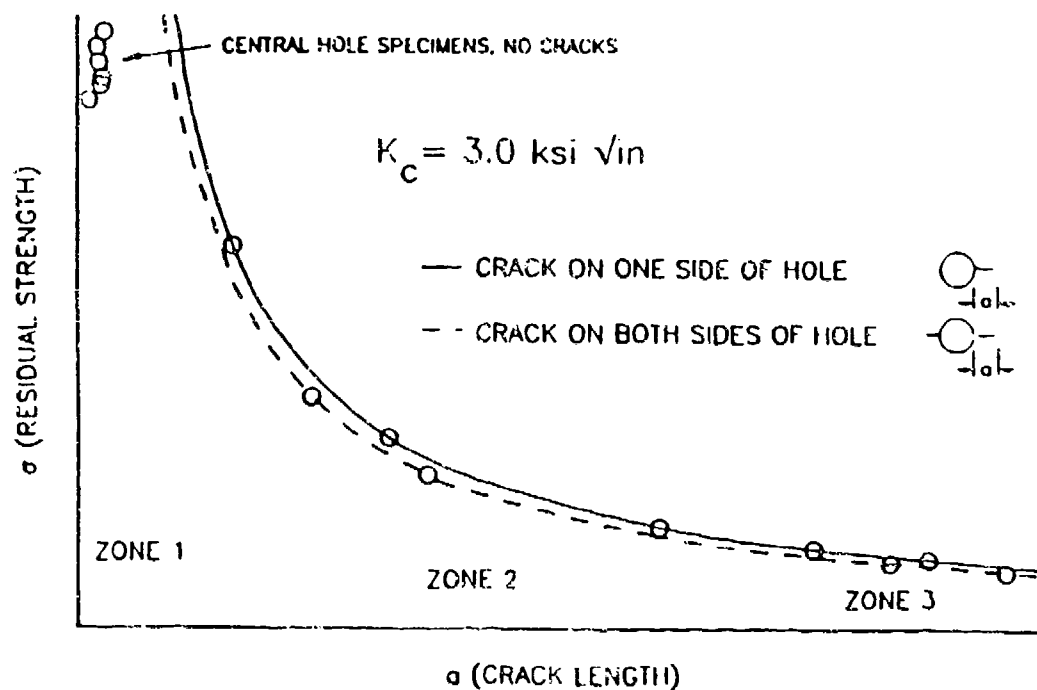


Figure 2. Influence of Crack Length on Residual Strength, from Testing of Metals.

# Machining Induced Microstrain

Averaged Absolute Values

FROM WL-TR-92-3025

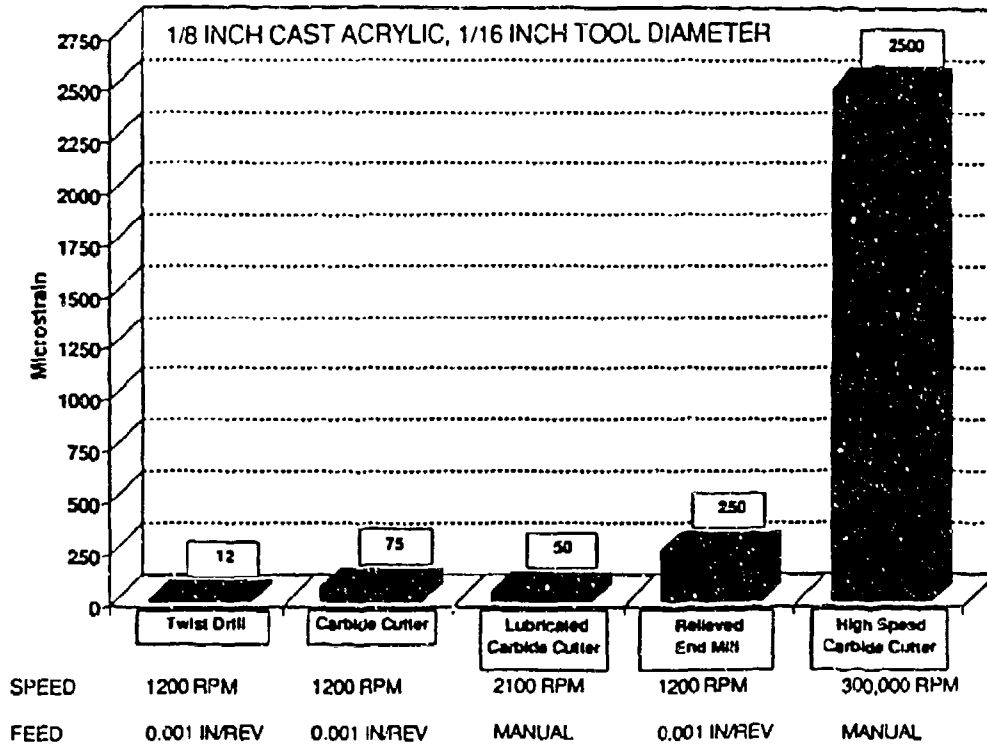


Figure 3. Machining Induced Strain for Cast Acrylic.

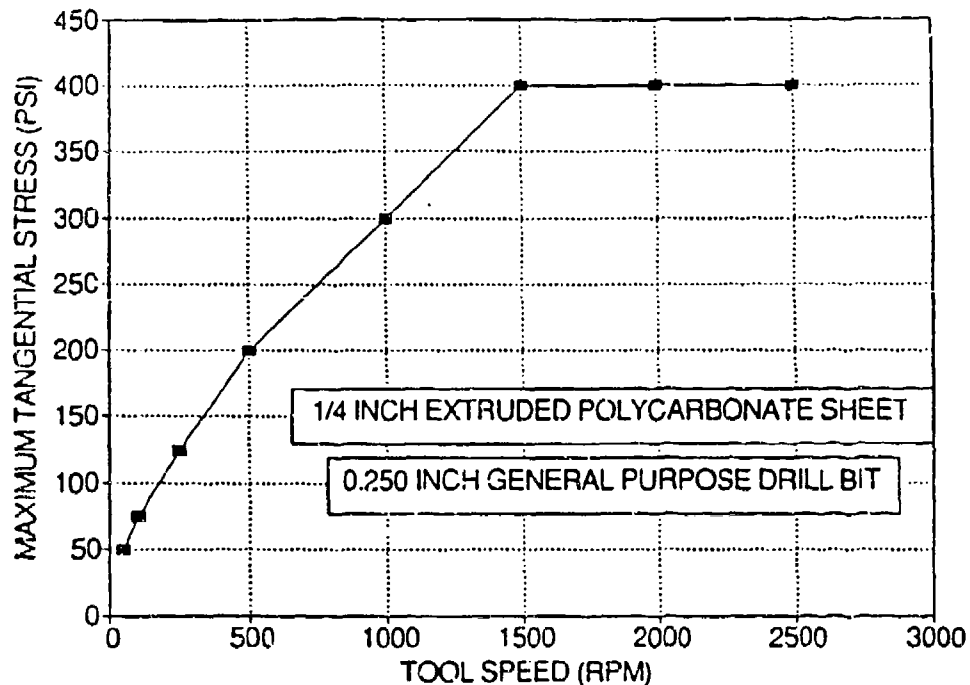


Figure 4. Approximate Maximum Tangential Stress Induced in Extruded Polycarbonate as a Function of Drilling Parameters.

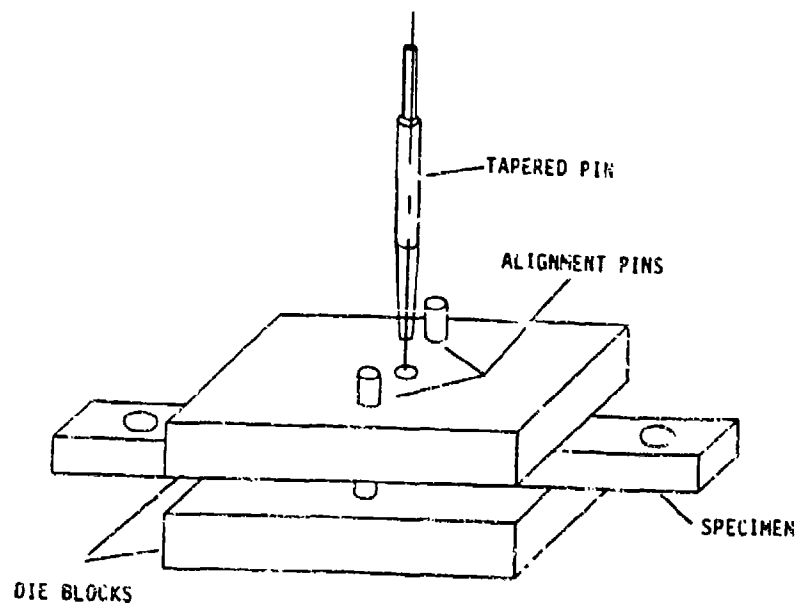
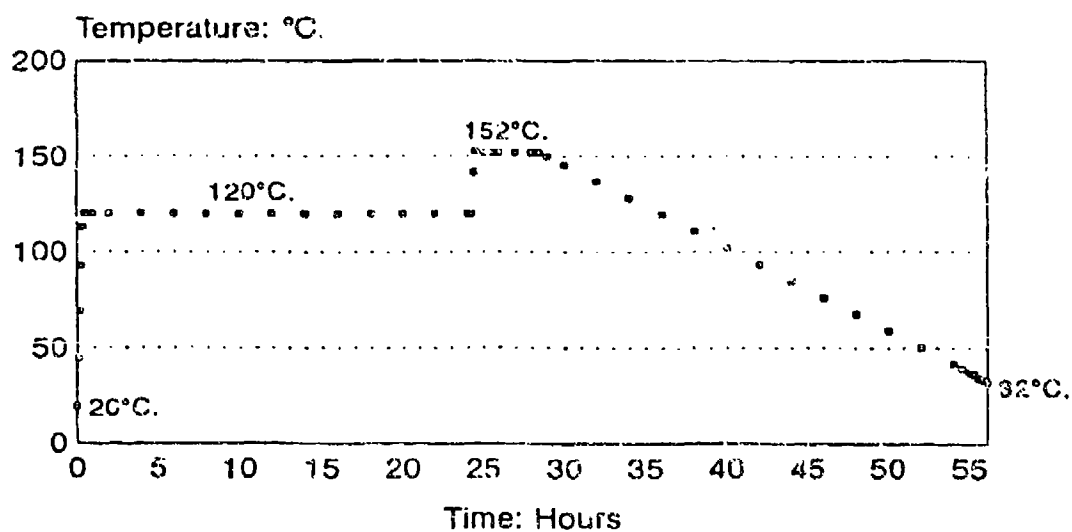


Figure 5. Cold Working Setup.



Turned chamber off at 37.6°C. allowed specimens to cool to 33.8°C. Switched specimens to a 32°C. preheated chamber and allowed to cool to ambient temperature.

Figure 6. Temperature Profile to Anneal Specimens.

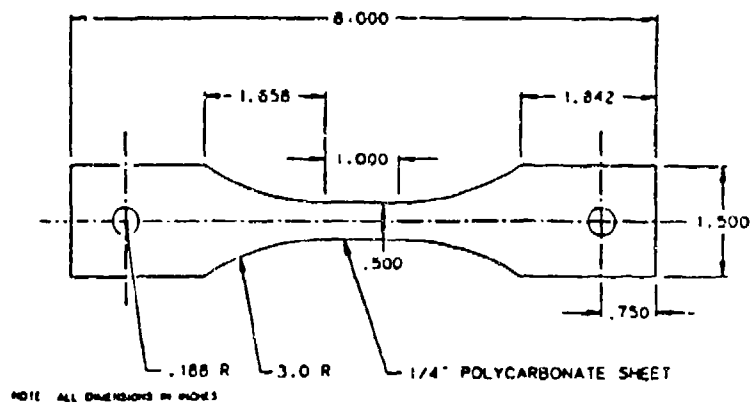


Figure 7. Test Specimens Without Holes, Group A.

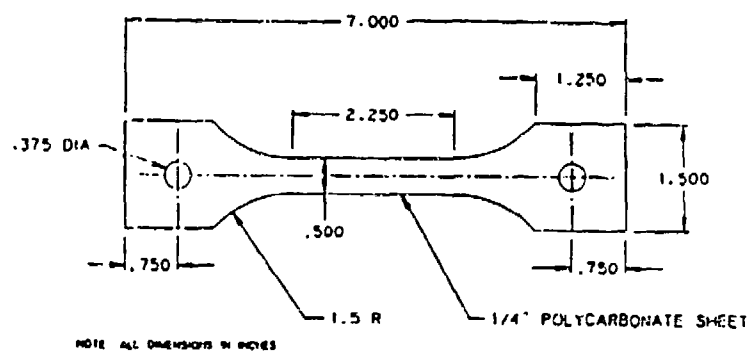


Figure 8. Test Specimens Without Holes, Group B.

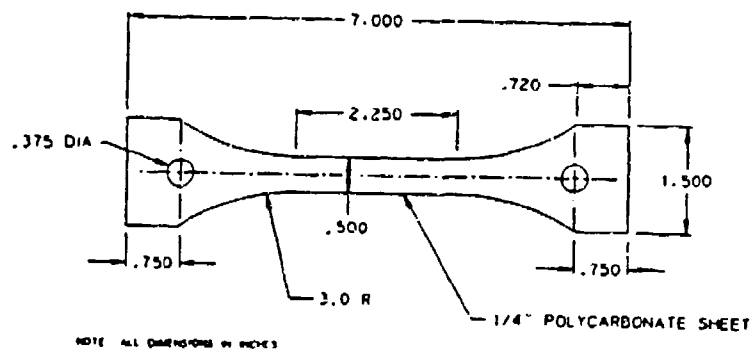
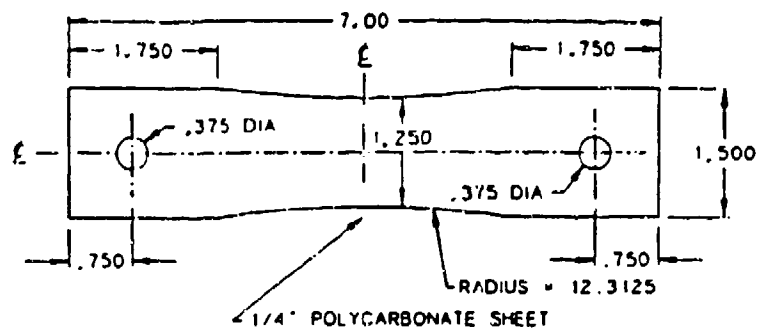


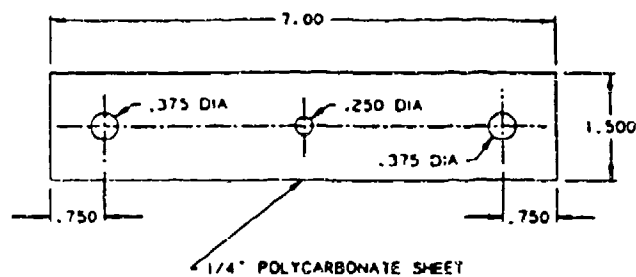
Figure 9. Test Specimens Without Holes, Group O.





NOTE: ALL DIMENSIONS IN INCHES

Figure 10. Test Specimens Without Holes, Group 9.



NOTE: ALL DIMENSIONS IN INCHES

Figure 11. Test Specimens With Holes.

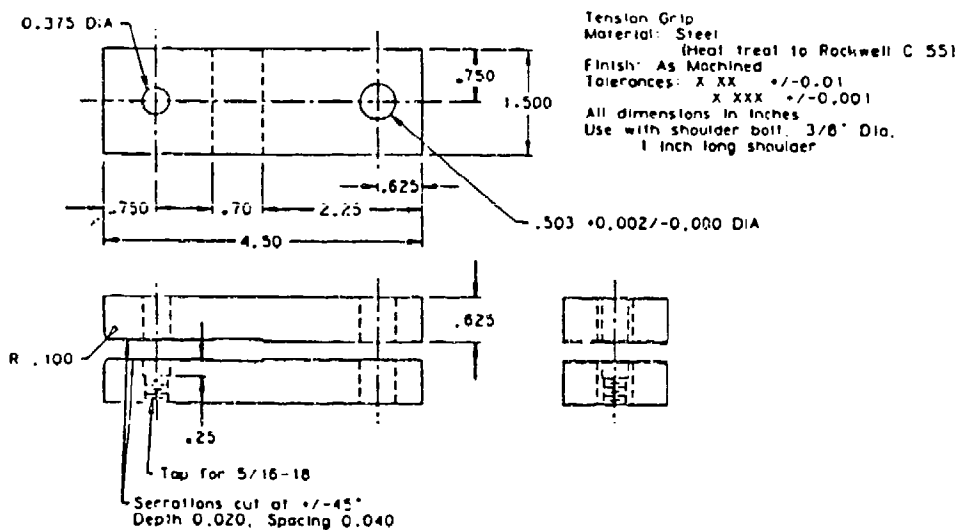


Figure 12. Test Grip.

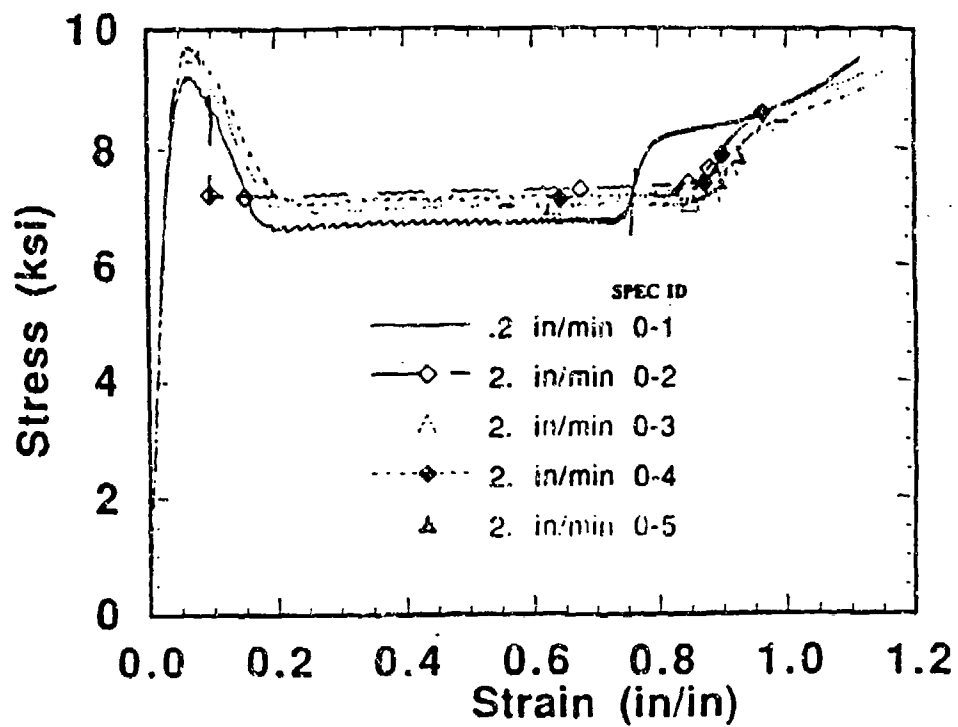


Figure 13. Typical Stress Strain Curves for Tensile Dogbone Specimens.

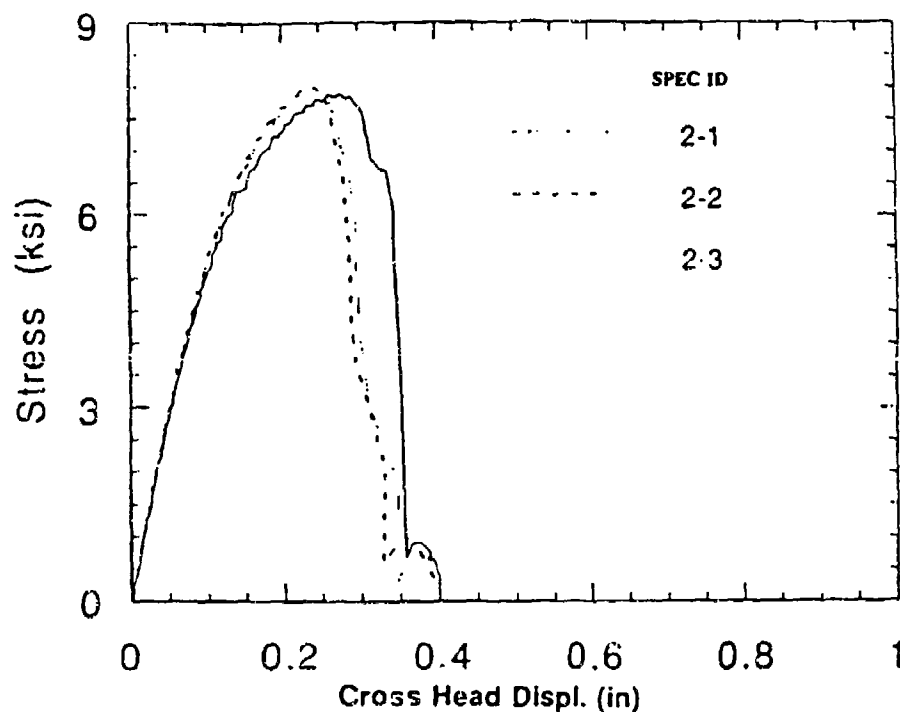


Figure 14. Typical Load Displacement Curves for Tensile Residual Strength Specimens with Holes.

# FATIGUE OF AS-RECEIVED PC: WITH & WITHOUT HOLES

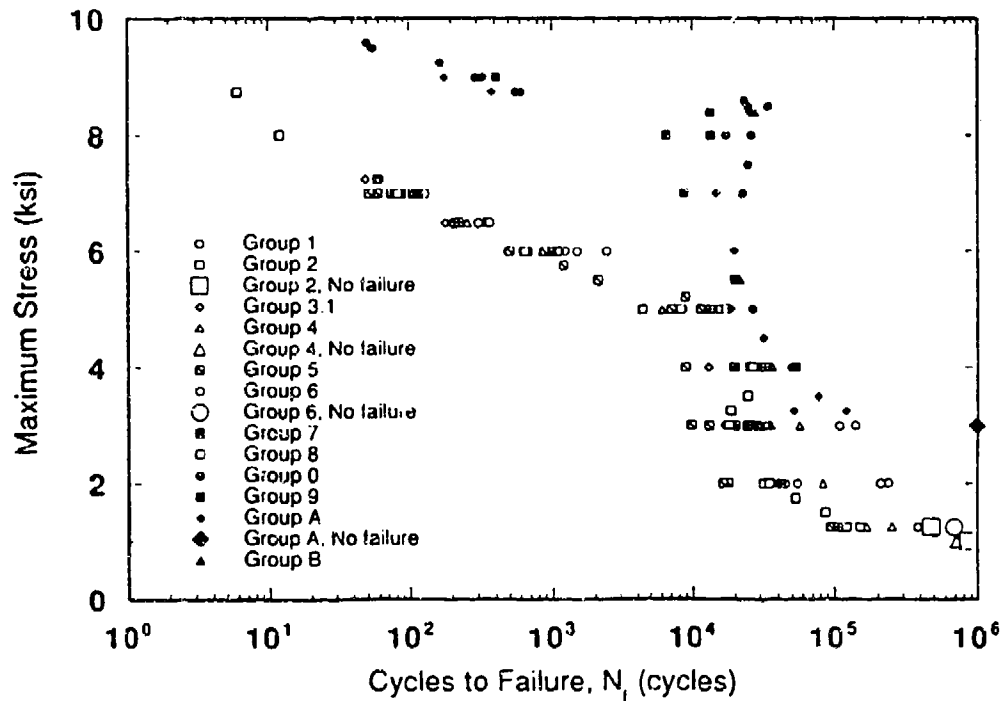


Figure 15. Fatigue of As-Received PC: With and Without Holes.

## TENSILE FATIGUE OF PC WITH NO HOLE

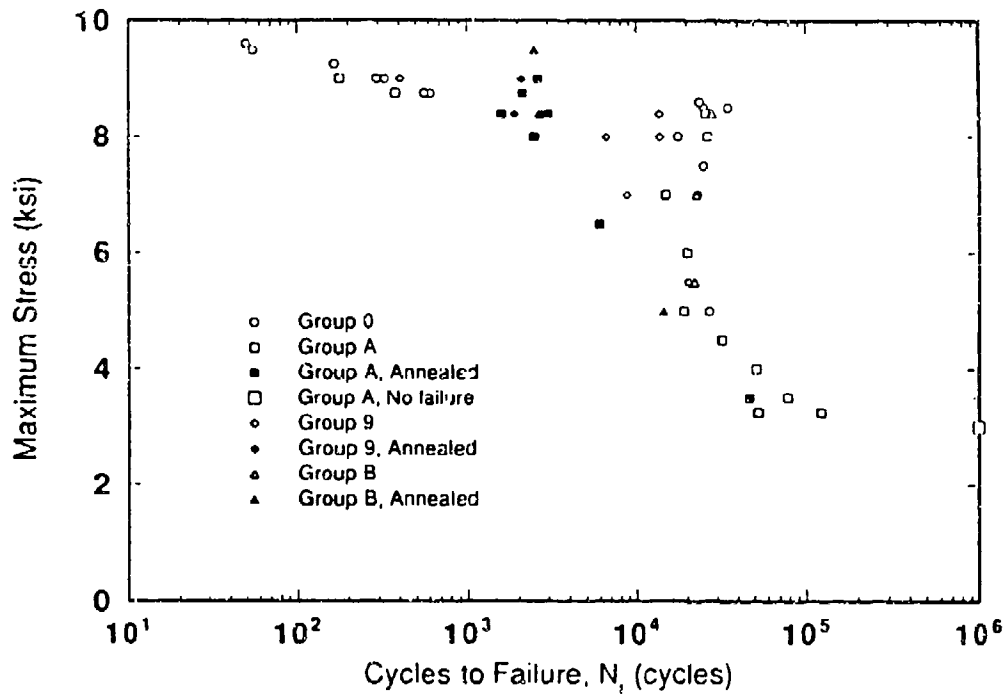
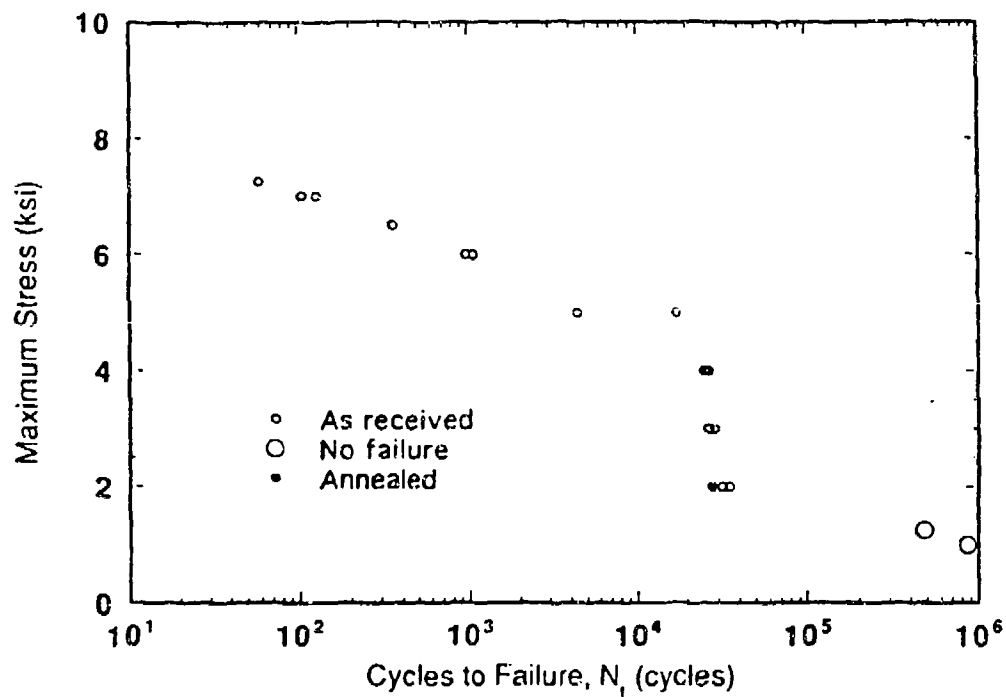


Figure 16. Tensile Fatigue of PC with No Hole.

Figure 1 is a log-log plot showing the relationship between Maximum Stress (ksi) on the y-axis and Cycles to Failure,  $N_f$  (cycles) on the x-axis. The y-axis ranges from 0 to 10 ksi, and the x-axis ranges from  $10^1$  to  $10^6$  cycles. The plot compares two conditions: 'As received' (represented by open circles) and 'Annealed' (represented by filled circles). The 'As received' data points generally show higher maximum stress for a given number of cycles compared to the 'Annealed' data points.

Condition	Cycles to Failure, $N_f$ (cycles)	Maximum Stress (ksi)
As received	~60	~7.3
As received	~100	~7.1
As received	~250	~6.6
As received	~1000	~6.1
As received	~10000	~5.1
As received	~20000	~4.1
As received	~30000	~3.1
As received	~40000	~2.1
As received	~50000	~2.1
As received	~100000	~2.1
As received	~400000	~1.3
Annealed	~1000	~0.8

## TENSILE FATIGUE OF GROUP 2



664

### TENSILE FATIGUE OF GROUP 3

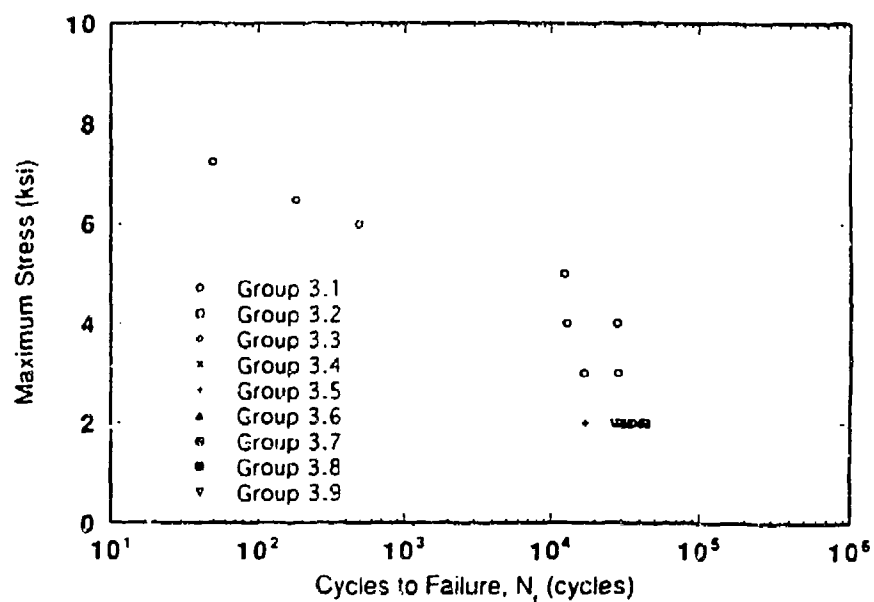


Figure 19. Tensile Fatigue of Group 3 Specimens With Holes.

### TENSILE FATIGUE OF GROUP 4

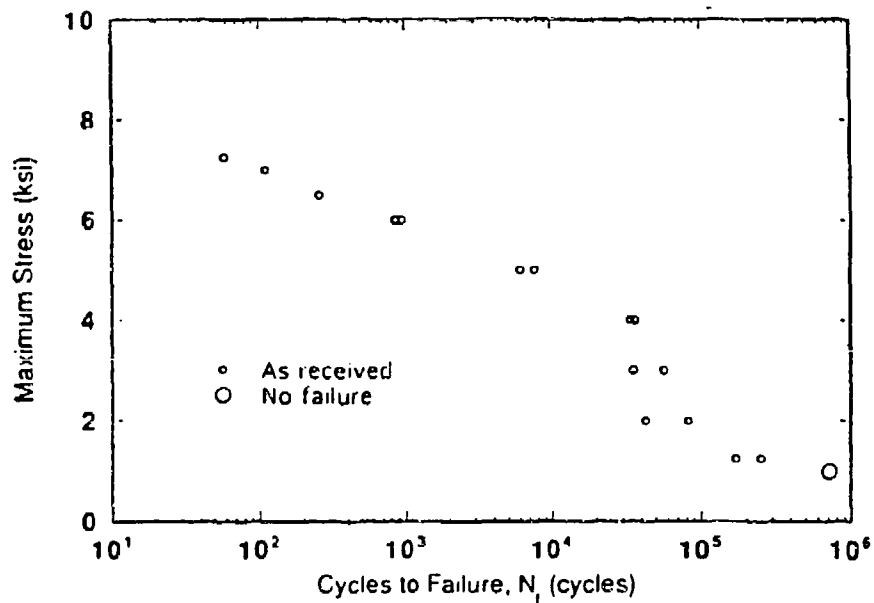


Figure 20. Tensile Fatigue of Group 4 Specimens With Holes.

### TENSILE FATIGUE OF GROUP 5

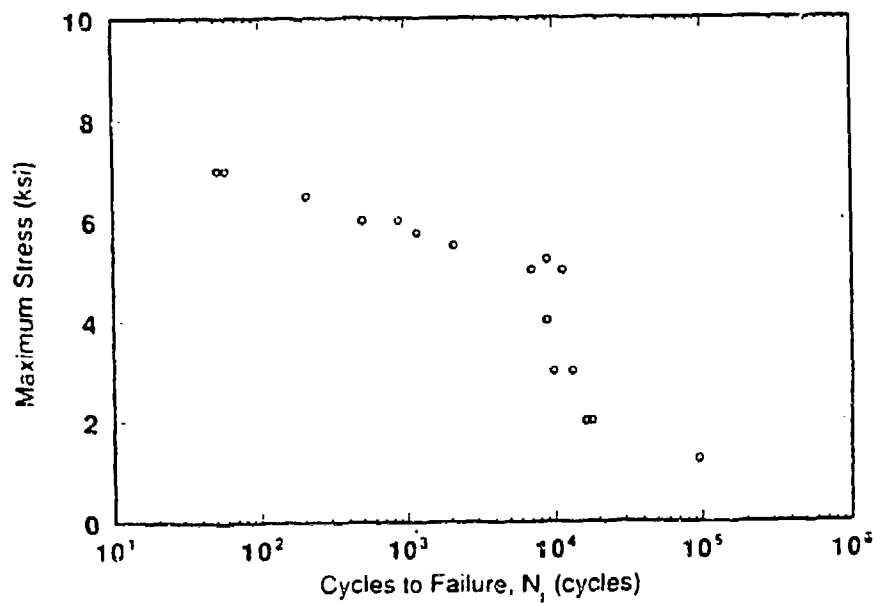


Figure 21. Tensile Fatigue of Group 5 Specimens With Holes.

### TENSILE FATIGUE OF GROUP 6

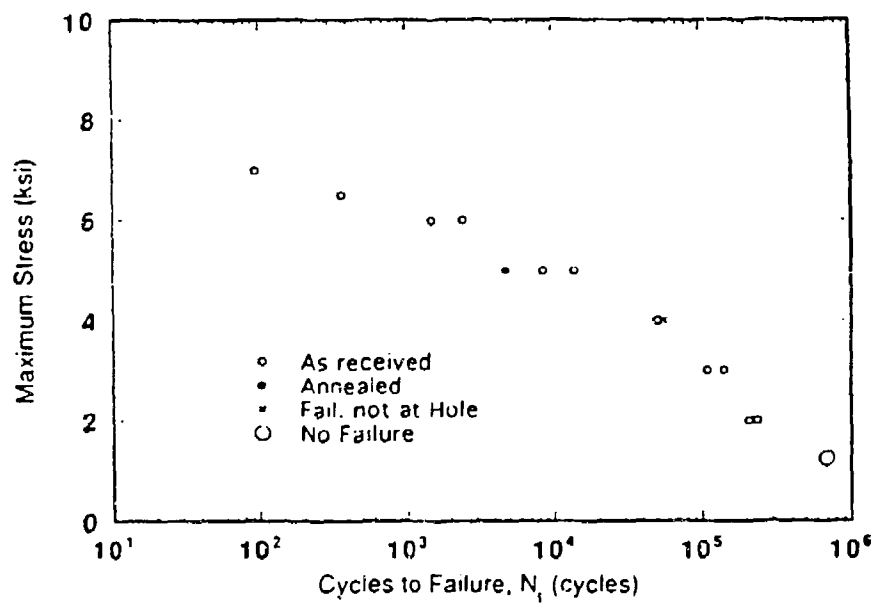


Figure 22. Tensile Fatigue of Group 6 Specimens With Holes.

### TENSILE FATIGUE OF GROUP 7

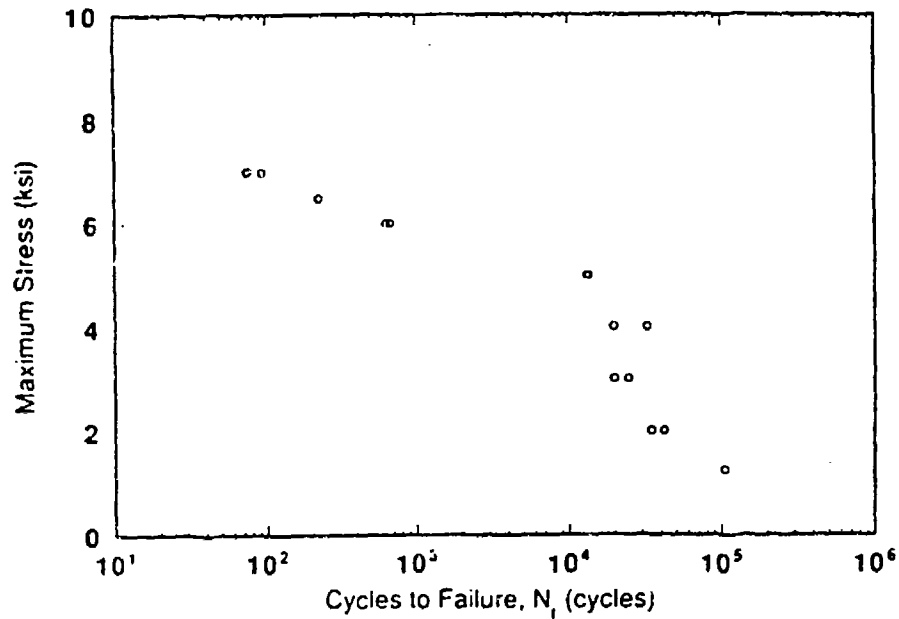


Figure 23. Tensile Fatigue of Group 7 Specimens With Holes.

### TENSILE FATIGUE OF GROUP 8

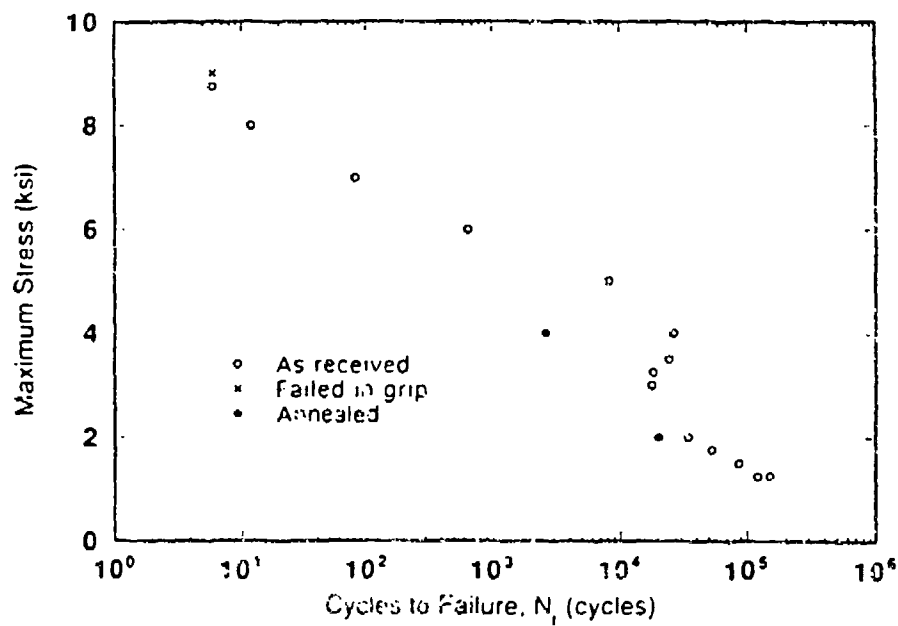


Figure 24. Tensile Fatigue of Group 8 Specimens With Holes.

**Table 1. Potential Hole Fabrication and Treatment Techniques.**

**HOLE FABRICATION TECHNIQUES:**

1. Standard Twist Drill
2. End Mill
3. Boring Bar
4. Drills, Mills, and Boring Bars with Various Geometries and Materials
5. Step Drill with (1) through (4)
6. Methods (1) through (5) with Coolants
7. Standard Drill, then Ream
8. Ultrasonic Hole Drilling
9. Water Jet Cutter
10. Laser Cutter
11. Electric Discharge Machining (EDM)
12. Methods (1) through (11) with Radiused Entry and Exit
13. PPG Hole Drilling Technique

**HOLE TREATMENT TECHNIQUES:**

1. Mechanical Polish
2. Chemical Polish
3. Anneal Specimen
4. Quench Specimen
5. Cold Work
  - Tapered Pin with or without Bushing
  - Ballizing
6. Stress Coining
7. Shot Peening
8. Dimpling
9. Interference Fit Bushing
10. Polymer Coating

**Table 2. Approximate Maximum Tangential Stress (PSI) Induced by Drilling 1/4 Inch Polycarbonate Sheet With a 0.250 Inch Drill Bit as a Function of Drilling Parameters.**

RPM SPEED (FPM)	50 3.3	100 6.3	250 15.8	500 31.5	1000 63	1500 95	2000 130	2500 160
FEED (IN/REV)								
0.006	50	75	125	200	300	400	400	400
0.003	50	75	125	200	300	400	400	400
0.0015	50	75	125	200	300	400	400	400

**Table 3. Shot Peening Data.**

SHOT SIZE	MI-70-H	MI-70-H	MI-70-H	MI-170-H	MI-170-H	MI-170-H	MI-170-H	MI-170-H	MI-170-H
AIR PRESSURE (PSI)	10	20	70	5	10	20	30	40	80
ALMEN INTENSITY	4.4N	7.4N	7.4A*	2.0N	4.6N	8.7N	4.3A	5.2A	7.5A
GFOUP NUMBER	3.6	3.8	3.1	3.5	3.3	3.2	3.9	3.4	3.7

\*MEASUREMENT UNCERTAIN

SHOT PEENING CONDUCTED BY METAL IMPROVEMENT COMPANY, CINCINNATI DIVISION



TABLE 4  
TEST MATRIX

TEST	WITHOUT HOLE	HOLE DESIGN GROUP NUMBER							
		#1	#2	#3	#4	#5	#6	#7	#8
FATIGUE	45	16	17	25	17	17	14	14	18
TENSILE/ RESIDUAL STRENGTH	13	3	3	0	3	3	3	3	4
SURFACE FEATURES/ ROUGHNESS		1	1	1	1	1	1	1	1
	TOTAL								226

Table 5. Summary of Hole Circumferential Surface Roughness Measurements.

MEASUREMENT	GROUP 1	GROUP 2	GROUP 3	GROUP 4	GROUP 5	GROUP 6	GROUP 7	GROUP 8
Ra	12	12	142	35	40	10	58	110
Ri	118	115	963	292	345	90	503	840
Rz	58	55	257	82	90	48	330	312
Rtm	75	78	702	185	205	62	413	555
Rq	15	15	185	50	52	12	80	142
Rp	70	60	510	138	170	38	305	430
Rv	-48	-55	-453	-155	-175	-52	-197	-410
Rsm	600	600	5100	900	1600	600	1700	2900
Rlq	500	500	4400	1700	1600	500	1900	3700

NOTES:

ALL MEASUREMENTS REPORTED IN MICROINCHES  
CIRCUMFERENTIAL MEASUREMENTS MADE AT HALF THE HOLE DEPTH

KEY:

Ra = ARITHMETIC AVERAGE ROUGHNESS HEIGHT  
Ri = MAXIMUM ROUGHNESS HEIGHT IN FIVE CUTOFFS  
Rz = MAXIMUM ROUGHNESS HEIGHT IN ONE CUTOFF  
Rtm = MEAN "Ri"  
Rq = RMS (ROOT MEAN SQUARE) AVERAGE ROUGHNESS HEIGHT  
Rp = MAXIMUM PEAK HEIGHT IN ONE CUTOFF  
Rv = MAXIMUM VALLEY HEIGHT IN ONE CUTOFF  
Rsm AND Rlq ARE ROUGHNESS SPACING PARAMETERS FOR KEY FEATURES

Table 6. Summary of Hole Axial Surface Roughness Measurements.

MEASUREMENT	GROUP 1					GROUP 2					GROUP 3.1					GROUP 4				
	20	20	15	20	20	15	20	15	20	15	150	265	255	215	50	55	125	130	130	130
Pa	230	275	300	510	240	140	520	145	1250	1780	2430	1290	425	530	1200	650	650	650	650	650
Pt	85	75	150	65	70	70	100	80	350	505	595	425	55	80	130	110	110	110	110	110
Pm	150	130	130	180	135	100	205	100	705	1310	1390	1065	200	310	525	470	470	470	470	470
Pq	25	25	20	35	25	20	40	20	185	335	345	260	70	85	200	155	155	155	155	155
Pp	150	120	100	390	95	80	160	95	740	1085	830	630	145	170	475	280	280	280	280	280
Pv	80	155	220	120	145	60	360	50	510	695	1610	460	280	360	725	370	370	370	370	370
Psm	2300	2000	1900	2100	2700	1700	2100	2100	6700	7500	7800	8100	5000	5200	5400	8400	8400	8400	8400	8400
Pdq	1400	1500	1100	1400	1700	1100	1100	1200	5500	6900	7000	7000	3400	4000	7900	7900	7900	7900	7900	7900

MEASUREMENT	GROUP 5					GROUP 6					GROUP 7					GROUP 8				
	110	58	140	70	25	35	30	35	70	75	70	75	70	50	220	325	215	130	130	130
Pa	935	427	335	505	195	230	255	385	625	700	825	575	2065	3315	2060	1480	1480	1480	1480	1480
Pt	190	95	145	135	95	115	75	135	300	370	355	290	310	585	915	290	290	290	290	290
Pm	485	283	240	340	155	185	175	230	455	505	545	420	1240	1795	1430	715	715	715	715	715
Pq	155	75	60	90	30	40	40	45	90	105	100	75	290	490	290	185	185	185	185	185
Pp	890	235	190	265	85	110	175	250	265	245	335	250	965	1755	1015	825	825	825	825	825
Pv	245	192	165	240	110	120	120	135	360	455	490	325	1100	1560	1045	655	655	655	655	655
Psm	8400	5500	5100	6100	3700	3600	3700	4800	3900	4300	2900	2500	6500	5300	4500	6400	6400	6400	6400	6400
Pdq	6100	5600	3600	5000	2100	2500	2600	2700	2800	3500	2700	2800	5400	7500	4400	4500	4500	4500	4500	4500

NOTES:

ALL MEASUREMENTS REPORTED IN MICROINCHES

FOUR AXIAL MEASUREMENTS MADE PER HOLE AT INTERVALS OF 90 DEGREES AROUND THE PERIMETER OF THE HOLE

TABLE 7  
TENSILE RESIDUAL STRENGTH TEST RESULTS

HOLE DESIGN	AVERAGE NET FAILURE STRESS (KSI)	STANDARD DEVIATION	AVERAGE GROSS FAILURE STRESS (KSI)	STANDARD DEVIATION
NO HOLE*	9.68	0.12	9.68	0.12
ANNEALED	10.7		10.7	
#1	9.57	0.06	7.98	0.05
#2	9.57	0.07	7.98	0.06
#3	NO SPECIMENS TESTED			
#4	9.46	0.07	7.89	0.06
#5	9.48	0.09	7.9	0.07
#6	9.48	0.04	7.9	0.03
#7	9.5	0.05	7.92	0.05
#8	9.59	0.02	7.99	0.02
ANNEALED	10.28		8.57	

\* YIELD STRESS REPORTED FOR SPECIMENS WITHOUT HOLES

**TABLE 8**  
**FATIGUE LIFE (CYCLES TO FAILURE) FOR DOGBONE SPECIMENS**

MAXIMUM STRESS (KSI)	GROUP A	GROUP B	GROUP 0	GROUP 9
9.60			50	
9.50			55	
9.50 ANNEALED		2492		
9.25			167	
9.00	179		294 328	406
9.00 ANNEALED	2599			2092
8.75	381		562 613	
8.75 ANNEALED	2126			
8.60			23519	
8.50			34497 24955	
8.40 ANNEALED	2989 1592	2620 2723		1896
8.40	25680	27471 27948		13576
8.00 ANNEALED	2450			2512
8.00	26229		26357 17462	6559 13632
7.50		22650	24984	
7.00	14788		22943	8745
6.50 ANNEALED	5972			
6.00	19909			
5.50		21948		20035
5.00	18877		36885	
5.00 ANNEALED		14352		
4.50	31784			
4.00	50749			53979
3.50	77559			
3.50 ANNEALED	46441			
3.25	52052 121811			
3.00	1029773*			

\* DID NOT FAIL

**TABLE 9**  
**FATIGUE LIFE (CYCLES TO FAILURE) FOR SPECIMENS WITH HOLES**

MAXIMUM STRESS (KSI)	GROUP 1	GROUP 2	GROUP 3	GROUP 4	GROUP 5	GROUP 6	GROUP 7	GROUP 8
9.00								6
8.75								6
8.60								12
7.25	61	59	49	59				
7.00	110	105		109	50		74	82
	117	127		111	52	91	93	
6.50	305	355	121	256	210	366	224	
6.00	1243	973	489	944	509	1518	627	646
	1128	1081		854	869	2454	678	
5.75					1205			
5.50					2127			
5.20					8985			
5.00	12799	4405	12495	7640	11418	8559	13558	8242
	15401	17378		6064	7033	13928	13258	
5.00 ANNEALED						4791		
4.00	28497	26597	26253	36524	8981	50223	19665	26588
	26379	25416	12999	34167	8846	55530*	32448	
4.00 ANNEALED								2616
3.50								24584
3.25								18602
3.00	32754	26707	17003	35063	9843	141096	24458	18019
	33302	28899	28690	56994	13097	108904	19940	
2.00	44695	35347	35917	83374	17901	237339	41913	34749
	55041	31842		42919	16317	209995	34949	
2.00 ANNEALED	35140	27869						20706
								20294
1.75								53007
1.50								87199
1.25	385392	490254**		170132	95522	691669**	106074	152297
				251978				122455
1.00		858350**		713271**				

\* DID NOT FAIL THROUGH HOLE

\*\* DID NOT FAIL

TABLE 10  
FATIGUE LIFE (CYCLES TO FAILURE) FOR SHOT PEENED SPECIMENS

SHOT SIZE	MI-70-H	MI-70-H	MI-70-H	MI-70-H	MI-170-H	MI-170-H	MI-170-H	MI-170-H	MI-170-H	MI-170-H
AIR PRESSURE (PSI)	10	20	70	5	10	20	30	40	80	
ALMEN INTENSITY	4.4N	7.4N	7.4A*	2.0N	4.6N	8.7N	4.3A	5.2A	7.5A	
GROUP NUMBER	3.6	3.8	3.1	3.5	3.3	3.2	3.9	3.4	3.7	
MAXIMUM STRESS (PSI)										
7.25			49							
6.50			181							
6.00			488							
5.00			12495							
4.00			28253							
3.00			12999							
			17003							
			28690							
2.00	28369	31604	35917	28843	36273	32595	29386	29288	43879	
	41094	30120		17420	36632	31840	27227	32891	42574	

\*MEASUREMENT UNCERTAIN

PENETRATION AND SURFACE SPALLING DUE TO HYPERVELOCITY  
IMPACT INTO FUSED SILICA GLASS

K. Edelstein  
NASA/Johnson Space Center

M. L. Fudge  
Kaman Sciences Corporation

# **Penetration and Surface Spalling due to Hypervelocity Impact into Fused Silica Glass**

Karen S. Edelstein  
NASA/JSC

Michael L. Fudge  
Kaman Sciences Corporation

## **Abstract**

The principal author has conducted research at the Johnson Space Center concerning the response of fused silica glass to hypervelocity impact damage. The data collected in this research was compared to previously published penetration equations for fused silica and theoretical penetration equations for general materials. Also, the co-author along with the principal author has developed a new relationship between the diameter of the front surface spall and the momentum of the impact. These data and equations are being used in an effort to further understand the effect of such impacts on the residual strength of the fused silica target.

Of the penetration equations used for comparison in this research, one was consistently at the mean of the data collected. The generic equations were somewhat useful in bracketing the test data. The spall-momentum relationship, when compared to the available penetration equations, provides the best predictor of impact parameters given the dimensions of the crater and spall.

The presentation will show examples of the penetration equations and the test data. The spall-momentum relationship will be shown also. Examples of how these relationships might be used to examine Shuttle window damage will be given.

## **Nomenclature**

$P_c$	Crater depth, penetration depth; also $P$
$D_p$	Projectile diameter
$V_p$	Projectile velocity
$\rho_p$	Projectile density
$C_v$	Specific heat at constant volume
$K$	Bulk modulus

## **Background**

Since the beginning of the manned space program in this country, space craft have included windows. Beginning with the Apollo program, researchers investigated a windows' ability to withstand orbital impact from micrometeoroids. This ability has been a requirement from the start of the Space Shuttle Orbiter design.

In 1984, a window from STS-7 was removed and replaced because of damage from such an impact. When the glass was cored and examined under a scanning electron microscope (SEM), the source of the damage was identified not as a micrometeoroid, but as a very small piece of white paint -- space de-



bris, in orbit not by natural means but as the detritus of global space programs. The problem of man-made debris in low-earth orbit has since become an important topic of discussion in the space business, triggering international treaties, Shuttle avoidance maneuvers, and possibly some satellite failures.

Although window replacement was an expected part of the Shuttle's reusability, and has been done many times over the life of the Shuttle program for impact damage and for other reasons, the original design only considered the natural environment. Of course, our experience includes both the meteoroids and man-made debris. The attrition rate of windows is not a safety concern, but considering that NASA plans to fly this vehicle into at least the near future, there is a renewed effort to understand the orbital environment and its effect on Shuttle components like the windows. Cost saving are a major motivation for this effort.

The current research was undertaken in an attempt to reduce the replacement rate for Shuttle windows. In the whole Shuttle program, through STS-57, 36 windows have been replaced at a rate of about one window for every ten mission days. Figure 1 shows how the replacement rate has varied since STS-1. The decision to replace or retain a damaged window is based on an analysis that considers the depth of the damage, the stress environment the window pane must endure, and the life required of that window. This analysis technique was developed along with the design of the windows and is extremely conservative.

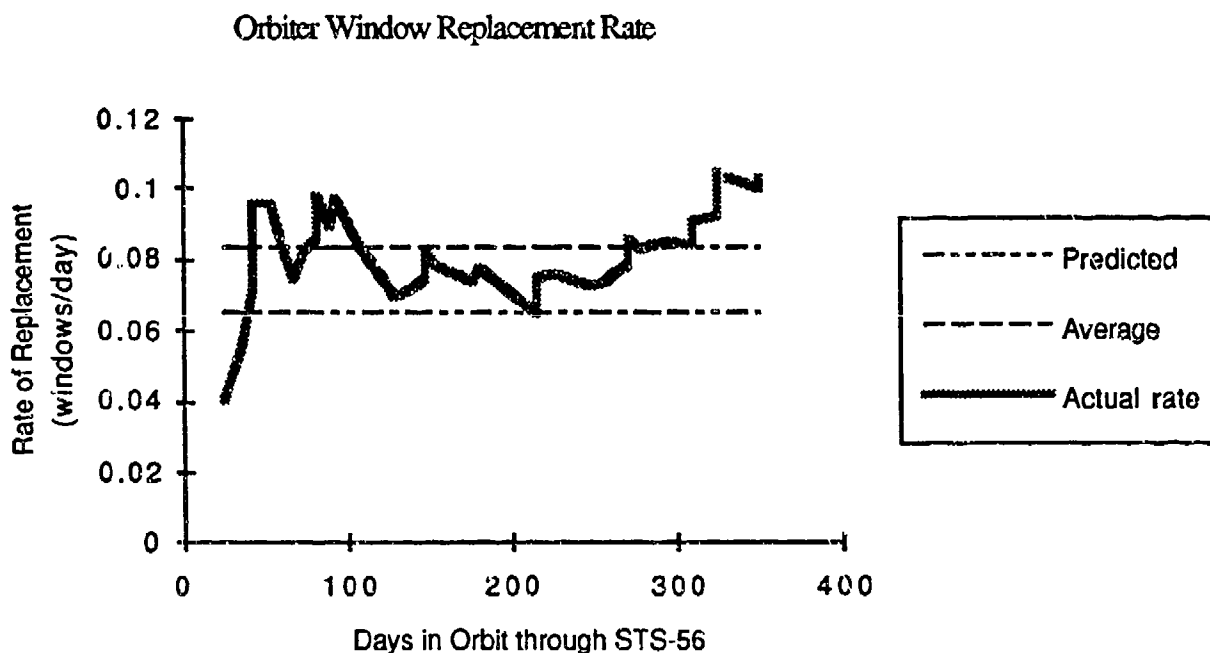


Figure 1

The objectives of this research are to define a new technique for determining when a window should be replaced, and to improve the existing

penetration equations by broadening the database for hypervelocity impact into glass targets. The current paper will address only the penetration equation part of this research effort.

The literature concerning hypervelocity impact penetration of fused silica targets contains two penetration equations. Burton Cour-Palais, formerly of the NASA Johnson Space Center, developed a penetration equation for fused silica glass during the Apollo program. The data he used were from hypervelocity impact testing done from 6 to 7.5 km/s.<sup>1</sup>

$$P = .53 \rho_p^5 d_p^{1.06} V_p^{3/2}, \text{ g-cm-s, except } V \text{ is km/s} \quad (1)$$

To support their preliminary design effort on the Space Shuttle program, Rockwell (North American Aviation) engineers McHugh and Richardson<sup>2</sup> compiled Cour-Palais' data with their company's test data and derived their own penetration equation:

$$P = .64 \rho_p^5 d_p^{1.2} V_p^{3/2}, \text{ g-cm-s, except } V \text{ is km/s} \quad (2)$$

Figure 2 demonstrates how equations (1) and (2) typically related to the test data.

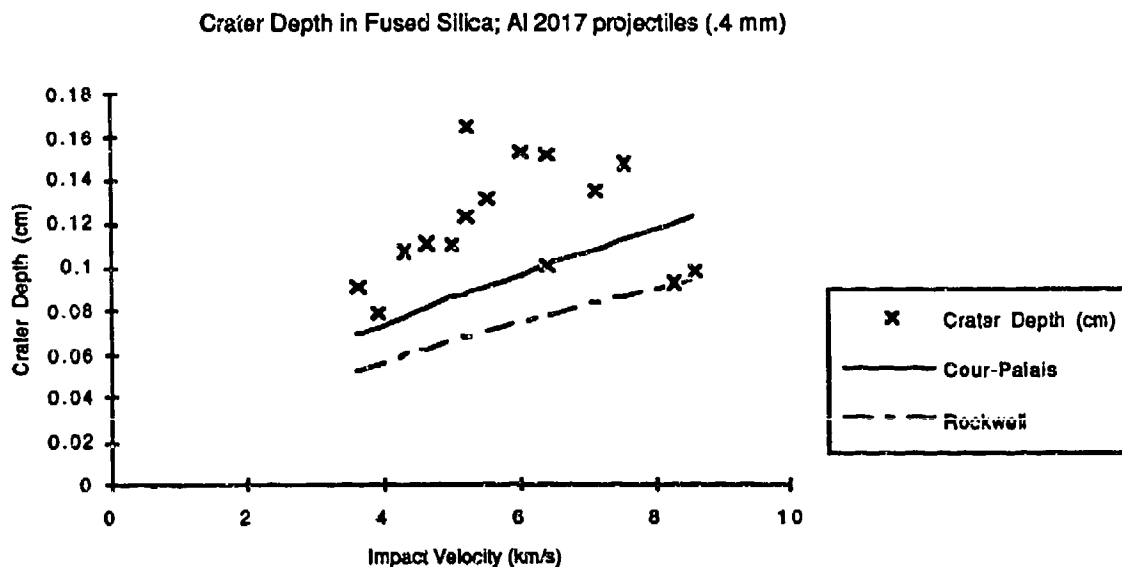


Figure 2

The two equations are limited in the velocity regimes they can be applied to; both were derived from data taken primarily between 6 and 7.5 km/s. Since the average velocity of orbital debris is 10 km/s, and the average velocity of micrometeoroids is 20 km/s, this data base is inadequate. Also, many, if not most, of the impacts experienced in low earth orbit are oblique. The normal velocities of these impacts could be well below the 6 km/s tested in previous years.

A word must be said about experimental error. The velocity, diameter and density measurements involved in this experiment, Rockwell's testing and Cour-Palais' work are all inaccurate to a certain degree. The measurement errors in the current work have been evaluated, and should yield a predicted crater depth value within 10% using equations (1) and (2). The plot in Figure 2 demonstrates that experimental error cannot account for the differences in test data versus predicted values.

### **Test Procedures**

The target disks were prepared at JSC using six fused silica panes scrapped from the Shuttle program (damaged thermal panes). One disk from each scrapped thermal pane was cut around the pre-existing damage which had caused the pane's removal. The flight-damaged disks were delivered to the SEM laboratory for analysis.

The remaining fused silica was cut into about twenty disks per window. These disks were used as targets in the light-gas guns at JSC's Hypervelocity Impact Test Facility (HIT-F).

The HIT-F supports three light-gas gun ranges, with 1.7 mm, 4.3 mm and 12.7 mm calibers. These guns can launch projectiles sized from 100 micron spheres to 12.7 mm cylinders, at velocities from 2 to 7 km/s; the smaller projectiles can be launched at even higher velocities.<sup>3</sup> The majority of the shots in this effort were done with the 1.7 mm gun; the remaining shots were on the 4.3 mm gun.

The velocity range used in this test was broad by design. Although many shots were done between 6 and 7 km/s, a good amount were also at normal velocities below 5 km/s. A few shots were done between 7 and 8 km/s, but high velocities are difficult to achieve and were often not possible due to the projectile size.

The projectiles were selected to vary material density and diameter. The sizes used ranged from 400 to 1000 microns, and the densities varied from 2.2 to 3.8 g/cm<sup>3</sup>. Since the crater depths from orbital impacts are of the order of .05 cm, the smaller projectiles were used more often than the large. Still, the crater depths produced in this experiment are at least an order of magnitude larger than those experienced in the Shuttle program. Only one Shuttle window has had a crater the size of those created in the laboratory.<sup>4</sup>

After the targets were shot at the HIT-F, the crater depth and diameters were measured using the same methods that technicians at KSC use following Shuttle flights. A mold impression of the crater is made, then the mold impressions are measured under an optical microscope. The front spall diameter was measured directly on the target disk using a digital micrometer and magnification.

A separate segment of the test was performed using a fractional factorial matrix design. This portion of the test was specially designed to determine which projectile parameter, velocity, diameter, or density, had the most effect on crater depth, crater shape factor and residual strength.

### **Data**

The experimental data can be found in Appendix A. Sixty-five targets were shot and fractured; data from fifty-eight of these were used in this analysis. Table 1 shows mean values of some of the test data.

Variable	projectile diameter (mm)	projectile mass (mg)	Velocity (km/s)	crater depth (cm)	front spall diameter (cm)
mean value	0.635	0.583	5.707	0.167	2.686

Table 1

## Penetration Equation

### Analysis of fractional factorial data

The "designed" segment of this experiment explored the qualitative effects of five variables on three results. The variables were projectile diameter, velocity, density and angle of incidence, and the target thickness. The results measured were crater depth, crater aspect ratio, and target residual strength. A binomial matrix was used with a half fraction design (16 runs). The variable settings are shown in Table 2:

Factor	proj. diameter mm	proj. velocity km/s	proj. density g/cm <sup>3</sup>	incidence angle degrees	target thickness in
low	0.395	4	2.8	normal	.56
high	1	7	3.9	45	.69

Table 2

Analysis of the crater depth measurements indicated that projectile diameter was the most influential variable in this result. Four other parameters were also significant: projectile velocity, density, momentum and mass. The mean crater depth in these 16 runs was .162 cm.

Although front spall diameter was not included in the results analyzed during this segment, the crater aspect ratio data can be examined for trends that would be true for spall diameter also (since aspect ratio is diameter divided by depth). The most influential variable for crater aspect ratio was projectile diameter, with impact momentum and normal velocity also significant. The mean aspect ratio in these 16 runs was 17.12.

### Dimensional analysis of all data

The penetration equations (1) and (2) are not dimensionally balanced. To correct this, and hopefully to find a better correlation to the test data, a dimensional analysis was attempted.

During a hypervelocity impact event, the kinetic energy and momentum of the projectile are transferred to the target material very rapidly through a longitudinal shock.<sup>5</sup> Extremely high pressures are generated in the shocked materials of both target and projectile. The projectile is either partially or fully shocked and may be entirely melted at the end of the event. The target craters as the shock front travels through the material, sending an overpressure wave towards the rear surface. The shock front attenuates as it propagates into the target and crater formation ends when compression no longer occurs. The longitudinal wave continues through the material without changing the phase of the material it passes through. At a certain level of impact velocity or momentum, a rear-surface spall is created by this longitudinal wave.

In considering what material properties might influence the cratering of glass during a hypervelocity impact event, the thermal effects appeared important. So in addition to the impact velocity, projectile and target densities, and the projectile diameter, the projectile and target specific heats were included. Also, the projectile and target bulk moduli were included, to provide some effect from the structural properties of the system. Equation (3) demonstrates the proposed function.

$$P = f(D_p, \rho_p, V_p, C_{vp}, K_p, \rho_t, C_{vt}, K_t) \quad (3)$$

Table 3 shows how each variable in the penetration equation is described in dimensional terms. A kg-m-s system is used in this analysis.

Physical Quantity	Symbol	Dimensional Formula			
Penetration Depth	P	L			
Projectile Diameter	D <sub>p</sub>	L			
Projectile Density	ρ <sub>p</sub>	L <sup>-3</sup>	M		
Projectile Velocity	V <sub>p</sub>	L		T <sup>-1</sup>	
Projectile Specific Heat	C <sub>vp</sub>	L <sup>2</sup>		T <sup>-2</sup>	θ <sup>-1</sup>
Projectile Bulk Modulus	K <sub>p</sub>	L <sup>-1</sup>	M	T <sup>-2</sup>	
Target Density	ρ <sub>t</sub>	L <sup>-3</sup>	M		
Target Specific Heat	C <sub>vt</sub>	L <sup>2</sup>		T <sup>-2</sup>	θ <sup>-1</sup>
Target Bulk Modulus	K <sub>t</sub>	L <sup>-1</sup>	M	T <sup>-2</sup>	

Table 3

$$P = D_p^a \rho_p^b V_p^c C_{vp}^d K_p^e \rho_t^f C_{vt}^g K_t^h \quad (4)$$

Using the dimensional formulas in the table above,

$$L = (L^a)(M^b L^{-3b})(L^c T^{-c})(L^{2d} T^{-2d} \theta^{-d})(M^e T^{-2e} L^{-e})(M^f L^{-3f})(L^{2g} T^{-2g} \theta^{-g})(M^h T^{-2h} L^{-h}) \quad (5)$$

Assuming  $c = 2/3$  and solving for the remaining variables:

$$\begin{aligned}
 a &= 1 \\
 b &= b \\
 c &= 2/3 \\
 d &= d \\
 e &= e \\
 f &= 1/3 - b \\
 g &= -d \\
 h &= -(1/3 + e)
 \end{aligned} \tag{6}$$

Starting with four independent equations and eight unknowns, after assuming a value for one of the unknown exponents, the dimensional analysis results in three remaining unknown exponents: b, d, and e.

The penetration equation can be simplified:

$$\begin{aligned}
 P &= D_p \rho_p^b V_p^{1/3} C_{vp}^d K_p^e \rho_t^{1-b} C_{vt}^{-d} K_t^{-(1+e)} \\
 P &= D_p V_p^{1/3} \left[ \left( \frac{\rho_p}{\rho_t} \right)^b \right] \left[ \left( \frac{C_{vp}}{C_{vt}} \right)^d \right] \left[ \left( \frac{K_p}{K_t} \right)^e \right]
 \end{aligned} \tag{7}$$

The final version used in the data analysis was:

$$P = D_p V_p^{1/3} \left( \frac{\rho_p}{K_t} \right)^{1/3} \left\{ \left( \frac{\rho_p}{\rho_t} \right)^b \left( \frac{C_{vp}}{C_{vt}} \right)^d \left( \frac{K_p}{K_t} \right)^e \right\} \tag{8}$$

Swift<sup>6</sup> derives the penetration equation by starting with the equivalence

$$V_c = k E_p \tag{9}$$

where  
 $V_c$  = crater volume  
 $E_p$  = energy of the projectile  
 $k$  = proportionality constant

Equation (9) is expanded by assuming that the crater has a hemispherical shape and its volume is proportional to the projectile's kinetic energy. Swift gives equation (10):

$$\frac{P}{D_p} = \left( \frac{\rho_p k}{4} \right)^{1/3} V_p^{1/3} \tag{10}$$

The energy relationship assumed here provides the rationale for assuming  $c = 2/3$  in equation (7) above. Equation (10) also shows that the linear relationship found between P and  $D_p$  is correct. (Swift notes that this linear relationship deviates slightly; careful investigation has determined that an

exponent of 1.06 on  $D_p$  is more accurate than 1.0. To maintain the dimensional balance, the linear relationship is retained.)

Swift also cites the Eichelberger equation, describing the crater depth produced by a long rod in a thick target:

$$\frac{P}{D_p} = \left( \frac{\rho_p}{\rho_t} \right)^{\frac{1}{2}} \quad (11)$$

This equation suggests assuming  $b = .5$  in equation (7).

The materials used in this experiment and their corresponding properties are given in Table 4.

Material ID	$C_v$ J/kg-C	E GPa	$\nu$	$\rho$ g/cc	K GPa
fused silica	740.6	73	0.17	2.202	36.87
Al 2017	962.2	71.7	0.33	2.796	70.29
pyrex	753.6	62.7	0.2	2.23	34.83
synthetic ruby	759	148.2		3.98	49.40

Table 4

Further reading in the literature of hypervelocity impact penetration<sup>7</sup> points out the importance of the shock during the impact. Changes in pressure, density and internal energy (heat) across a shock front are calculated using the shock velocity  $U_s$  and the particle velocity  $U_p$ . The Hugoniot curve for a material, sometimes referred to as the equation of state, is formed from a set of points that describe the pressure-density states attained by shock loading from a single initial state. This curve is regularly used in numerical modelling of impact events. The Hugoniot curve for a solid is often fit to experimental data with the form

$$U_s = a + bU_p \quad (12)$$

The constant  $a$  represents the wave velocity in an extended medium, and the constant  $b$  is related to the Gruneisen parameter  $\Gamma$ .

$$\Gamma = \frac{3\alpha K}{\rho C_v} \quad (13)$$

The appearance of the bulk modulus and specific heat in this relationship suggests that the exponents  $d$  and  $e$  in equation (8) could be equivalent and equal to 1. Equation (8) can then be written

$$P_c = D_F V_p^{\frac{1}{2}} \left( \frac{\rho_t}{K_t} \right)^{\frac{1}{2}} \left( \frac{\rho_p}{K_p} \right)^{\frac{1}{2}} \left( \frac{C_{v_p}}{C_{v_t}} \right) \left( \frac{K_p}{K_t} \right) \quad (14)$$

Using the properties from Table (4), an equation was written for each projectile type into the fused silica target. These equations were plotted vs. the test data. Figure (3) shows the same data as Figure (2), plotted against the new equation.

Crater Depth in Fused Silica; Al 2017 projectiles (.4 mm)

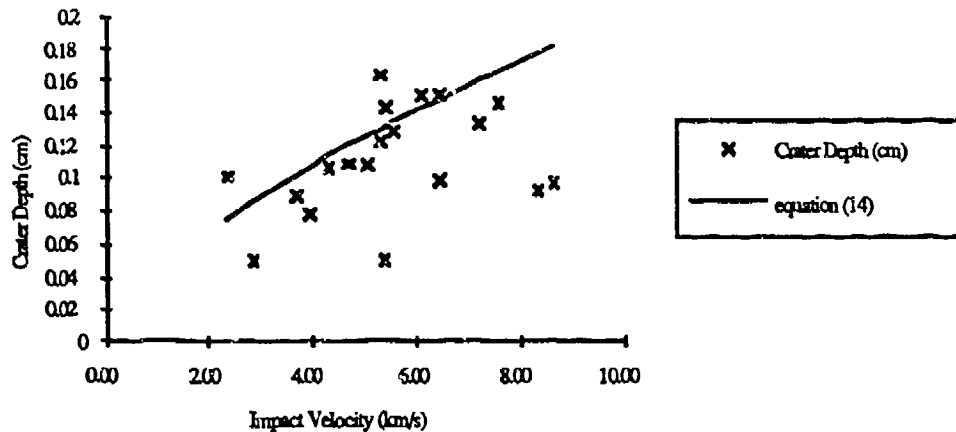


Figure 3

Similar results are found for the remaining projectile materials and sizes, except for the pyrex glass projectiles. The new equation underpredicted those four crater depths by about 50%. Further testing of this equation is planned with a different glass target material.

### Spall Diameter

After examination of both the data from shuttle window impacts and the data from the hypervelocity tests, two relationships have been proposed relating the frontal spall diameter of shuttle window impacts with the diameter of the impacting projectile. Both of these relationships relate the crater frontal spall diameter to an expression combining the mass and the velocity of the impactor (e.g., momentum and kinetic energy). The relationships were conjectured after relating the spall diameter to the impactor mass and the impactor velocity separately, and finding no sound correlation.

The first relationship relates the crater frontal spall diameter to the momentum of the impacting projectile, and is expressed by the equation:

$$D_{spall} = kP^{0.4445} \quad (15)$$

where  $D_{spall}$  = spall diameter (m)  
 $P$  = projectile momentum (kg-m/s)  
 $k = 0.41212$  (s/kg)

This expression was derived using a least squares linear regression of the natural logarithms of the spall diameters and the projectile momentums obtained from the hypervelocity tests. Momentum of the impacting projectile was found by assuming spherical projectiles for the given projectile diameters, computing projectile mass, and multiplying by the given velocity.



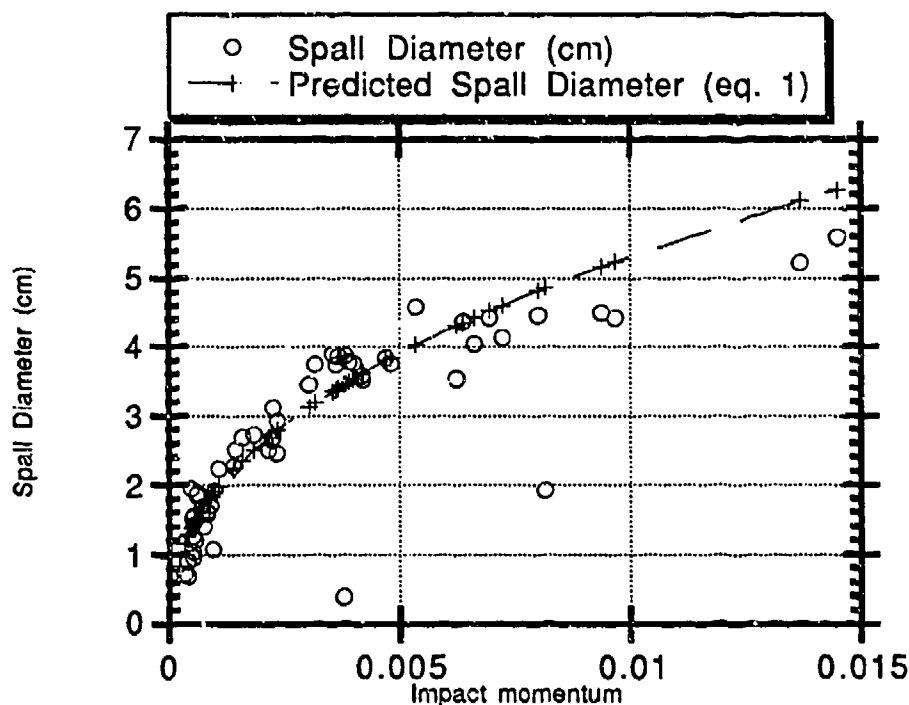


Figure 5

The second relationship relates the crater frontal spall diameter to the kinetic energy of the impacting projectile, and is expressed by the equation:

$$D_{spall} = kE^{0.4060} \quad (16)$$

where  $E$  = projectile kinetic energy ( $\text{kg}\cdot\text{m}^2/\text{s}^2$ )  
 $k = 0.01336$  ( $\text{s}^2/(\text{kg}\cdot\text{m})$ )

This expression was derived using a least squares linear regression of the natural logarithms of the spall diameters and the projectile kinetic energies obtained from the hypervelocity tests. Kinetic energy of the impacting projectile was found by assuming spherical projectiles for the given projectile diameters, computing projectile mass, and multiplying by one-half of the square of the given velocity.

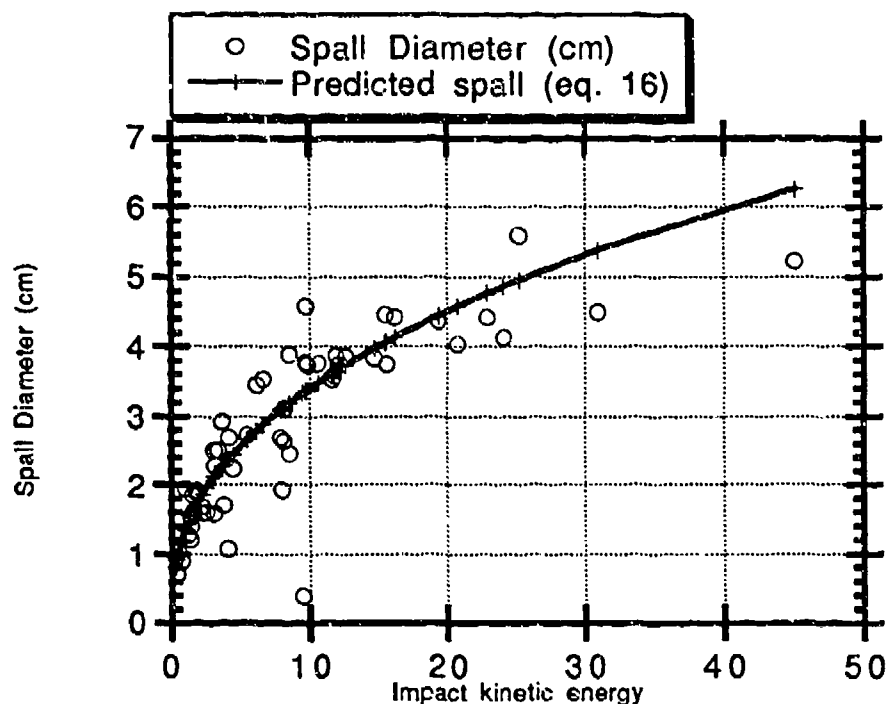


Figure 6

#### Comparison of the two equations

Table 5 summarizes the correlation coefficient R for each of the equations, and the mean deviation of each equation. The correlations were calculated in the logarithmic domain. The mean of the spall diameters from the hypervelocity tests is 0.028 meters (2.8 cm).

	correlation coefficient R	mean deviation
Equation (15)	0.937	0.00311 m
Equation (16)	0.936	0.00369 m

Table 5

Although these two equations give similar results when using the hypervelocity test data, the results given when using the spall diameter measurements from shuttle window impact craters are not identical. Table 6 shows four spall diameter measurements (in inches) taken from removed shuttle window thermal panes and the projectile diameters needed (in microns) as calculated by equations 1 and 2 to create that damage. The calculations assume spherical aluminum impactors.

	Disk #26-03-01 STS-31	Disk #26-23-01 STS-30	Disk #26-06-01 STS-41D	Disk #26-17-01 STS-41G
Spall Diameter (in)	.105	.118	.088	.074
Equation (15)	82-105	89-115	72-92	63-81
Equation (16)	55-73	63-77	47-63	41-55

Table 6

### Application to Shuttle Program

The Shuttle window damage is well described once it is discovered during vehicle inspections. However, the only information available from an inspection is a detailed description of the appearance of the crater, and a measurement of its size. Knowing the projectile material, velocity or incidence angle is not possible from a visual inspection. An SEM analysis can show what the projectile was and what range of velocity the event had, but more information can only be guessed at. The equations derived in this paper will help narrow the guesses and improve our understanding of the low-earth orbit environment. This knowledge will help us plan Shuttle missions more wisely, and not damage as many windows.

Figure 7 and table 7 show data from several flight windows. These windows have been examined with an SEM, and conclusive evidence has been found indicating debris damage. The spall diameter equation (15) and the new penetration equation (14) (for Aluminum projectiles in cases of debris) are used to predict the mass of the projectile that would have caused the respective damage. The two equations predict masses of the same order of magnitude, but the bar chart shows how much variation there is in the prediction. Part of the problem with the flight data is attributed to inconsistent measurement of the front spall diameter.

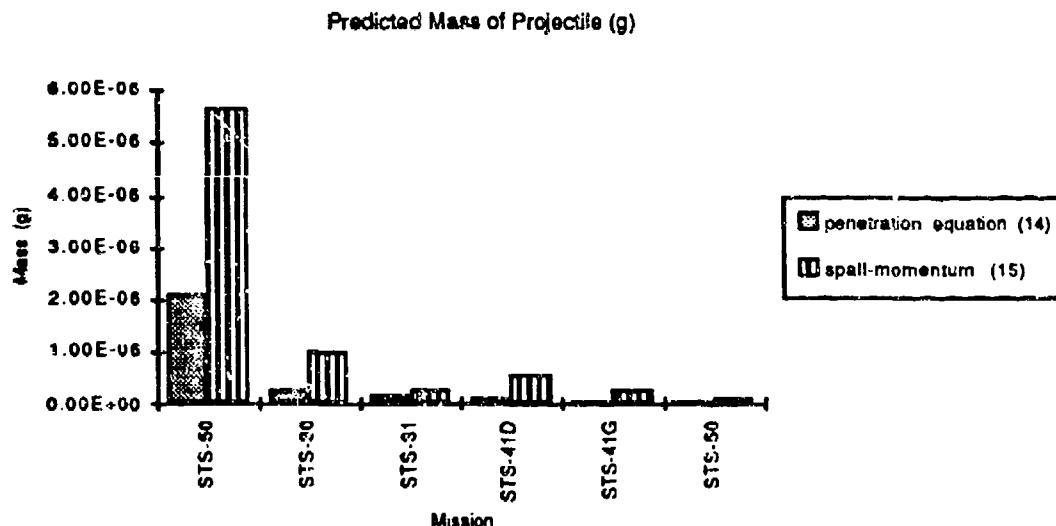


Figure 7

Mission	Disk	Spall Dia (cm)	Crater depth (cm)	Mass from (14) (g)	Mass from (15) (g)
STS-50	28-18-01	0.5334	0.0570	2.09E-06	5.66E-06
STS-30	26-13-01	0.2459	0.0292	2.81E-07	9.91E-07
STS-31	26-03-01	0.1410	0.0254	1.85E-07	2.83E-07
STS-41D	26-06-01	0.1905	0.0203	9.46E-08	5.58E-07
STS-41G	26-17-01	0.1334	0.0178	6.34E-08	2.50E-07
STS-50	26-31-01	0.0838	0.0080	5.77E-09	8.80E-08

Table 7

### **Conclusions**

A new penetration equation has been derived that includes both projectile and target parameters. This equation fits the data better than the previous equations found in the literature for fused silica.

A relationship for finding impact momentum from spall diameter has been demonstrated with great correlation.

These equations will be used in future analysis of Shuttle window impact damage. The information derived from these equations about the impact parameters in low-earth orbit will increase NASA's understanding of the low-earth orbit environment and will make space flight safer and window replacements fewer.

### **Acknowledgements**

The principal author wishes to acknowledge the employees of the NASA Hypervelocity Impact Test Facility and the Scanning Electron Microscopy Laboratory.

<sup>1</sup> Cour-Palais, Burton G., "Hypervelocity Impact in Metals, Glass, and Composites," *International Journal of Impact Engineering*, Vol. 5, 1987, pp. 221-237.

<sup>2</sup> McHugh, A.H., Richardson, A. J., "Hypervelocity Particle Impact Damage to Glass," North American Aviation report # STR 241, 1974.

<sup>3</sup> Crews, J.L. and Christiansen, E.L., "The NASA JSC Hypervelocity Impact Test Facility (HIT-F)," in *AIAA Space Programs and Technologies Conference*, March 1992, AIAA #92-1640.

<sup>4</sup> Christiansen, E.L., Bernhard, R.P., Hyde, J.L., Kerr, J.H., Edelstein, K.S., Ortega, J., and Crews, J.L., "Assessment of High Velocity Impacts on Exposed Space Shuttle Surfaces," in the proceeding of the *First European Conference on Space Debris*, April, 1993.

<sup>5</sup> Hill, D.C., Stevenson, T.C., Zarnecki, J.C., "Application of Laser Simulation of Hypervelocity Impacts to Space Particulate Damage to Metals and Optical Glasses," University of Kent at Canterbury, paper #A89-51121.

<sup>6</sup> Swift, H.F., "Hypervelocity Penetration Mechanics," in *Impact Dynamics*, Zukas, et. al., Krieger Publishing Company, Florida 1992.

<sup>7</sup> Zukas, J.A., "Stress Waves in Solids," in *Impact Dynamics* by Zukas, et. al., Krieger Publishing Company, Florida, 1992.

DEVELOPMENT OF A TRANSPARENCY DURABILITY TEST CRITERIA:  
COUPON SCALE TESTING, FIELD SERVICE DATA ANALYSIS, AND  
FULL SCALE TESTING

T. Whitney  
D. R. Bowman  
University of Dayton

R. A. Smith  
Flight Dynamics Directorate  
Wright Laboratory

# **DEVELOPMENT OF A TRANSPARENCY DURABILITY TEST CRITERIA: COUPON SCALE TESTING, FIELD SERVICE DATA ANALYSIS, AND FULL SCALE TESTING\***

*Thomas J. Whitney and Daniel R. Bowman  
University of Dayton Research Institute  
Dayton, Ohio 45469-0110  
(513) 229-3018*

*Richard A. Smith  
Flight Dynamics Directorate, Wright Laboratory  
Wright-Patterson Air Force Base, Ohio 45433  
(513) 255-4640*

**ABSTRACT:** The focus of the Transparency Durability Test Criteria Program is to develop a durability test methodology for aircraft transparency systems which will include laboratory coupon scale durability testing, full scale durability testing, and field service data acquisition. These three areas will be used to develop, measure, compare, and predict actual in service aircraft transparency durability, where durability is defined as the continued ability of the transparency to meet specified performance requirements. A goal of the Air Force is that future aircraft transparency systems have a four year service life (on the aircraft). This program is being conducted to provide better tools for the transparency community to understand, predict, and increase transparency durability.

## **INTRODUCTION**

The Transparency Durability Test Criteria Program is a three phase program. The first phase of the program included a literature review [1], a review of test programs, test data, and work relevant to transparency durability [2], coupon scale testing and field service data acquisition [3], field service and full scale data analysis and full scale testing critique [4], correlation of coupon and full scale data with field service data and methodology development and documentation [5]. Each of the successive phases is an iteration of the first phase, updating collected information, building on and improving the methodology. Currently the program is in the second phase. The purpose of the entire program is to develop the framework of a methodology which can be used for any type of transparency system.

This paper is a compilation of the information reported in [1-5], which are interim reports for the Transparency Durability Test Criteria Program. The overall methodology of predicting aircraft transparency durability is based on Figure 1. This methodology includes coupon scale testing, full-scale testing, and field service data acquisition and analysis.

The first step in assessing durability is coupon scale testing. Coupon scale testing can be conducted for one or many competing transparency cross-section designs. If coupon scale testing produces satisfactory results, then full scale durability testing is conducted. If full scale durability

---

\*Performed under Contract F33615-90-C-3410 for the Flight Dynamics Directorate, Wright Laboratory, Wright-Patterson AFB, Ohio.

testing produces satisfactory results, then the transparency design is ready for field service. If coupon scale or full scale testing reveal problems with a design, the design can be changed. If field service data reveals a problem, changes can be made not only to the transparency design, but the entire methodology, which includes choice of coupon scale tests and interpretation of the results of the coupon scale tests. Coupon scale and full scale durability testing are conducted with correlations made between both of these and field service data. The whole process is iterative and can change continuously as it is used to reflect lessons learned and improvements in testing and interpretation of test results. At this stage of the program, only the skeleton framework of the methodology is in place. Each of the components, coupon scale testing, full scale testing, and field service data collection and analysis are identified and recommendations are made for choosing test techniques and evaluating results; however, the parameters for and the interrelationships between the components are not well defined. The system must improve with implementation. The methodology is a general one which could be applied to any transparency system. The exact choice of tests and interpretation of results is system specific. The choice of tests and analysis of results for a new system must be based on experience with similar systems.

It should be noted that the current state of the art in aircraft transparency durability testing can be described as comparison testing, where a number of designs are subjected to the same tests and then ranked in terms of performance. Even though artificial weathering or laboratory conditioning is often conducted as part of the testing, no real attempt has been made to predict an actual service life based on that testing. This program will address the issue of actually predicting service life, realizing the extreme difficulties in doing so. Those include: development of a realistic artificial weathering, correlating coupon scale test results with field performance, and factors which affect durability that cannot be accounted for in coupon scale testing.

## **COUPON SCALE DURABILITY TESTING**

Coupon scale testing techniques have evolved and become more complex with the development and use of plastics and polymeric materials in all types of products. Reference [2] includes brief descriptions of many of the historical transparency coupon scale test programs. There are several ways to increase durability of a given part. The major ways are to choose the most durable material from a set of materials, to customize a material, or to coat the material to protect it from the environment. Plastics can be reformulated, or doped with additives to change specific characteristics. The most common examples are the use of (anti)plasticizers, UV stabilizers, and cross-linking agents. This type of work (formulation and additive packages) is usually conducted by the plastic suppliers or the transparency manufacturers.

The end user, in this case the government, rarely has any part in the material development, but is often involved in evaluating durability and also basic performance characteristics (such as Haze and Luminous Transmittance for transparent plastics), through different types of coupon testing. Coupon testing has long been recognized as an evaluation tool with reasonable cost; however, the choice of coupon tests and the interpretation of test data are not simple, are not refined to the point of being an exact science, and are not generally agreed upon by different groups within the transparency community.

The purpose of this section is to present coupon scale test methods which are available for transparencies; identify those which appear to be valuable for measuring durability; describe the proposed approach for evaluating durability with coupon tests; conduct proposed tests on a transparency system of interest (in this case the F-111 ADBIRT windshield system); present results of that testing; and finally, assess the effort to date and make recommendations for the future phases of this program.

## **Identification and Classification of Tests**

### **Material Property Testing**

There are a large number of test methods that deal with what are often thought of as basic material properties. These tests include mechanical tests such as tensile, compression, shear, flexure, Poisson's ratio, fatigue, fatigue crack growth, and fracture toughness, thermal tests such as coefficient of thermal expansion and thermal conductivity, optical tests such as index of refraction, and luminous transmittance and haze, and various electrical tests. For many common transparency materials such as glass, polycarbonate, and acrylic, most of these properties are well defined at room temperature and at static strain rates. For interlayers and new structural and surface ply materials, many of these properties have not been documented. The properties listed in this section do not by themselves indicate anything about durability. The exception may be high temperature tests of these properties which indicate that a material is not suitable for high temperature requirements. Rather, changes in these properties after natural or artificial aging, or simulated missions can be used to measure durability. The most useful of these tests for assessing durability may be tensile testing. Tensile tests of new and aged material can reveal many material changes and possible durability problems. For example, yield strength, initial modulus, and elongation are usually affected by aging of plastics. Luminous haze and transmittance are direct measures of transparency optical performance, and changes in these properties induced by aging can indicate significant durability problems.

### **Performance Testing**

The development of birdstrike resistant aircraft transparency systems produced a number of "performance" test methods. These methods were developed to evaluate impact strength and toughness, flexural stiffness and strength, interlayer strength, and edge attachment strength. These tests are related in a complex way to many of the basic material properties tests listed above. Specific tests included falling weight, three and four point loaded flexural beam, air cannon, torsional shear, flatwise tension, wedge peel, notched and unnotched Izod, edge attachment pull-out, and edge attachment flexure. These tests can also be used to evaluate durability by comparing the results of these types of tests before and after natural or artificial aging, or simulated missions.

### **Durability Testing**

A third class of test methods was developed or adopted that could be used to address service life, resistance to aging, and durability specifically. These methods often include the



measurement of certain material properties before and after natural and simulated weathering (or aging) or some type of simulated mission environment. Specific tests include rain erosion, dust erosion, hail impact, salt impingement, oscillating sand (Bayer) abrasion, Taber abrasion, tape peel, chemical stress craze, chemical attack (swelling), stress weathering, thermal shock, yellowness index, gel permeation chromatography (GPC), differential scanning calorimetry (DSC), thermal mechanical analysis (TMA), dynamic mechanical analysis (DMA), x-ray photoelectron spectroscopy (XPS), energy dispersive x-ray analysis (EDXA), Raman spectroscopy, gas chromatography mass spectroscopy, Fourier transform infrared (FTIR), and optical and scanning electron microscopy (SEM).

### Summary of General Test Methods

A list of test methods which have been used in the past for transparency testing is shown in Table 1. These test methods are used to characterize different properties of the transparency as a whole, or material by material. However, not all of these tests are necessarily applicable to durability testing or prediction. When choosing a test to evaluate durability, it is helpful to think in terms of what failure mode is being evaluated. A number of the tests listed in Table 1, although used often to characterize various properties of transparent materials, do not yield any particular information concerning transparency failure modes or durability. For instance, thermal conductivity, while perhaps important for calculating heat transfer through the transparency, does not significantly affect durability (although changes in thermal conductivity might be an indication of a durability problem such as polymer degradation), since transparencies are not removed due to changes in thermal conductivity.

Common failure modes as well as recommended tests to evaluate durability in terms of those failure modes are listed in Table 2 for the transparency types of interest. Tests shown in Table 2 are limited to those which have proven successful and are favored by many in the transparency industry, or which, although new and not entirely proven, appear to show promise for evaluating durability. An example is free volume. Free volume in a polymer is the empty space in the molecular structure. Thermal aging below the glass transition temperature for polycarbonate increases the order of the molecular structure, increasing the density of the material, while decreasing the free volume. Consequently, free volume can give an indication of thermal aging [6,7]. However, free volume testing and application are in their infancy and have not yet been applied to any great extent.

The tests listed in Table 2 for each failure mode are tests which can be used to address that mode. Where more than one test is listed per failure mode, the different tests may address that type of failure mode in subtle or grossly different ways. For example, air cannon, falling weight, flexure beam, and tensile testing are recommended to address structural degradation caused by aging. However, each of these tests has a different application, based on the strain rate of interest. As a second example, fatigue crack growth, fracture toughness, and tensile edge attachment tests are recommended to evaluate cracking as a failure mode. Where aging is affecting the *bulk* transparency acrylic face sheet or the polycarbonate, fatigue crack growth and fracture toughness tests are appropriate to determine if these properties are changing due to aging. However, where the bulk material is *not* degraded but the edge attachment is possibly

degraded, tensile edge attachment testing is recommended.

There are several failure modes which are not addressed in Tables 1 or 2. These include distortion and delamination caused by residual stress or wavy or out-of-contour plies; distortion, delamination, or surface degradation caused by in-flight and flight-line thermal effects; residual strength after fatigue, pressure, and flight load stresses; and multiple imaging. Distortion is caused by geometric anomalies such as waviness of the ply(s). Distortion can be present as manufactured, which is not a durability problem. Distortion can also be caused by in service temperature extremes for plastic or plastic faced transparencies, resulting in warping or contraction of the plastic. This failure mode as well as failure modes caused by pressure loads can generally only be addressed in full scale durability testing. Multiple imaging is a result of the different indices of refraction for the different plies in a laminate, occurring when light passes through the laminate at certain angles. Multiple imaging is not a durability problem, it is a design and manufacturing problem. Failure due to hail impact or fungus attack were not included in Table 2 as these are considered natural hazards and, while existent, are relatively rare. Fungus attack does not appear to be a problem for current USAF aircraft transparencies. The development of new face ply materials and coatings should include fungus testing for screening purposes.

Combat hazards are not addressed in this program. It should be noted that the ability of a transparency system to resist combat hazards may change as the transparency ages. If combat hazard protection is required for a transparency system, that system should be subjected to coupon scale artificial weathering and combat hazard testing, and then possibly full scale durability testing followed by combat hazard testing.

### Coupon Scale Methodology

The goal of the coupon scale testing is to conduct tests using coupon specimens from new and artificially weathered transparencies (from Table 2) which are related to the failure modes of interest for a type of transparency system. Changes in measured properties resulting from artificial weathering and conditioning are evaluated (conditioning may include parameters such as abrasion during weathering). Figure 2 is an example of how a given test property might degrade with time (under artificial weathering conditions). Note that for non-destructive tests such as haze and transmittance, data can be obtained at multiple intervals between zero and 4 years of aging, while destructive tests can only be conducted at one or two points for each specimen (to keep costs reasonable, only baseline, 2 year, and 4 year artificially aged specimens were destructively tested). Assuming that a transparency can be called "failed" when the property degrades to a specified value, and that the shape of the degradation curve remains constant independent of the baseline starting point, Figure 2 shows that any spread in the baseline data will result in spread in "time to fail". This "failure time" is simply the time required for the property to degrade to a specified minimum (or maximum, for tests such as haze).

Specification of a failure value for a given property will be determined from in service aged coupon tests. In Phase II of this program, for those tests where measured properties changed in Phase I artificially aged tests, similar tests will be conducted on a number of in service

aged transparencies. As shown in Figure 3, scatter will also be present in service aged data; there was significant scatter in coupon test results for coupons from in service aged F-111 windshields in the Reference [4] program. To characterize the scatter, a minimum of three windshields will be required for each in service age test data point. For instance, to characterize in service age test performance at one, two, three, and four years, three windshields would be tested with service lives of approximately one year, three would be tested with service lives of approximately two years, three would be tested with service lives of approximately three years, and three would be tested with service lives of approximately four years. Based on field service data, a failure time will be identified on the in service degradation curves and the measured value (or mean value with a confidence interval) of the property from coupon testing for that time will be identified. This value will be used as the failure value for artificially aged coupons, if a positive correlation exists between the property and the field service data. In this way the results of the testing of the in service aged transparencies will be correlated with the test results of the baseline and artificially aged specimens to provide a basis for predicting service life for a given test method and given failure mode.

The assumptions made and the discrepancies which will result from this approach are worth noting. The consistency of conditioning exposure will be better for the artificially aged specimens than for the in service aged specimens, since no two in service aged transparencies are exposed to exactly the same environment or conditioning. Until proposals for instrumenting transparencies with micro-sensors (to monitor actual exposure history) are implemented, the best measure of in service conditioning is time on the airplane, known as service life. It must be assumed that coupons from one or two transparencies with the same in service age will be representative of all transparencies with that same service age. This is obviously not true as one transparency might be from an airplane that was stationed in an arid environment and another might be from an airplane that was stationed in a sub-tropical environment. In addition, three years of service life on one airplane might be much more severe (in terms of flight line and in-flight thermal and pressure profiles) than five years of service life on another airplane, because of different climates and different missions that might be flown at different bases. In addition to scatter caused by in service aging, it is expected that there is scatter or variability among new (baseline) transparencies which could be caused by manufacturing process variables, lot to lot material variability, and other factors. While we can measure certain properties for baseline transparencies and for in service aged transparencies, we do not know what baseline values for these properties the service aged transparencies had when they were new. An average value and a confidence interval can be assumed based on testing of baseline transparencies now; however, the fact that scatter exists must be realized and interpretations based on test results of in service aged transparencies must be cautious. For example, a certain measured property for a failed transparency with one year of service life might be extremely low compared to average values for that property in baseline transparencies; however, that property might have initially been very low for that transparency (if it would have been measured when the transparency was new) possibly explaining the short service life; a second explanation for the low value after only a year of service life could be an exceptionally severe environment for that transparency. Scatter in the service aged degradation curves may make it difficult to establish a trend similar to that of artificially aged degradation curves. In a like manner, field data may also indicate that "failure times" or "service

lives" for a particular failure mode contain so much scatter that it may be difficult to find or establish a "failure value" for an identified property (or combination of properties).

### **Artificial Weathering Technique**

One of the most important parts of a coupon scale test program to evaluate durability is the choice of artificial weathering, or conditioning, techniques. Numerous past researchers have concluded that outdoor "life" (without respect to any particular failure mode) and "life" due to accelerated weathering do not directly correlate. The scatter in natural weathering data is too large, and the interacting factors too numerous, for calculations of universal "factors" which correlate natural and artificial "life" for all materials and environments. However, it is usually possible to correlate the ranking of material performance in artificial conditioning to that in natural conditioning as long as the artificial weathering adheres to critical factors found in the natural environment. In the long run, given sufficient statistical data on natural weathering and sufficiently large safety factors, it may be possible to develop conservative "life" values for natural exposure on the basis of artificial and accelerated exposure.

For transparency materials, the important factors include the spectral distribution of the sun's EM radiation, particularly in the UV region; temperature; and wet time (which includes dew condensation and is distinctly different from total precipitation or humidity of the air). Also important is the manner in which these factors vary on a daily basis over the course of a year. UDRI reevaluated artificial weathering techniques used in the past, in an effort to identify or develop a technique which has the following attributes: simple to operate, lab scale, commercially available, accelerated, reasonable cost, UV spectrum which is similar to the UV in the atmosphere, moisture included, and thermal environment of the transparency simulated as much as possible.

The evaluation showed the QUV [8,9] to have a number of advantages over other laboratory scale weathering systems. The QUV is readily available and is inexpensive to purchase and operate. Virtually all of the major transparency manufacturers have QUV machines at their facilities. The QUV can duplicate periods of high UV exposure and temperature and low moisture content, followed by periods of low UV exposure and temperature and high dew condensation. UV, temperature, and moisture (wet time) can be varied independently.

The artificial weathering profile for the QUV was developed by defining specific operating values for UV, temperature, and wet time, based on natural weathering data taken at two locations: New River, Arizona, and Miami, Florida. The former represents a location with high temperature and UV exposure. The latter experiences lower UV doses but significantly higher wet times. The basic approach, common to all three environmental parameters, was to examine data collected by DSET Laboratories at the above mentioned geographic sites, and reduce the daily data for each factor to a weighted average over a year's time. The weighting was dependent on the factor being considered and how it was perceived to affect polymer degradation. Specifically, monthly averages were calculated for 4 to 7 of the most recent years (depending on the environmental parameter) for which complete monthly data was available for at least 10 months. Using this monthly data, a weighted yearly average was calculated for each parameter.

These values were then correlated to QUV output measurements to calculate cycle times and temperatures which would produce an equivalent year of *wet time in Miami* and an equivalent year of *UV exposure and temperature induced degradation in New River*. QUV cycles could therefore be considered "worst case" by combining the most damaging environmental effects from each location.

Using simple degradation models [10,11] to perform the calculations, the QUV exposure cycle used in this program consists of alternating cycles of 8 hours of UV exposure at 70 degrees Celsius using UVA-340 bulbs, followed by 4 hours of dark/condensation at 50 degrees Celsius (this was the highest maintainable temperature in the UDRI QUV machines during the condensation cycle). Based on simple models, this cycle should roughly match the degradation due to average total UV radiation energy (300-380 nm) and temperature in New River, Arizona, and the average percentage wet time in Miami, Florida. Two weeks of exposure (336 hours) in the QUV is being used to represent one year of natural weathering. Routine cleaning was simulated by wiping the surface of the specimens 50 times with a 50/50 mixture of isopropyl alcohol every other day (after 48 hours of artificial weathering), using a Kimwipe paper towel.

The artificial conditioning scheme developed for this program is generic in the sense that it only includes weathering and could be applied to any transparency system. In the future, it is recommended that work be conducted to add transparency system-specific conditioning that includes equivalent thermal energy and other parameters which may be encountered during flight. For instance, if an aircraft mission profile produces transparency surface temperatures of, say, 300 °F, exposure of coupon test specimens to temperatures of 300°F (and possibly other simultaneous conditions) might reveal problems which would otherwise go undetected until full scale durability testing was conducted.

## PHASE I COUPON TESTING

### Failure Modes and Selected Tests

As an example of how test methods are chosen for a specific system, the tests which were chosen for evaluating the F-111 ADBIRT windshield are described below. The F-111 ADBIRT windshield is an acrylic faced laminate with two polycarbonate structural plies. While it would be desirable to conduct testing on all aircraft transparency types with many or all of the test methods discussed below, it was not economically feasible. The F-111 windshield was chosen to be used to develop and demonstrate a coupon scale test methodology as it represents a cross section design of interest, baseline (new) transparencies are available, this system has the most complete available field service data, and full scale durability testing has been conducted for the F-111. Test methods chosen for evaluating these transparencies were limited to those which were established or required minimal development and which addressed common failure modes for these (types of) transparencies.

Abrasion, aging, crazing, cracking, and delamination were chosen as the failure modes to be investigated for the F-111 transparencies. These failure modes are representative of failure

modes encountered in service; see Reference 4 for more complete analysis of F-111 failure modes. Abrasion failures due to dust and sand impingement were very common during Desert Storm. Cleaning abrasion scratches are often evident when transparencies are inspected on the aircraft during field service data acquisition trips. Cracking and delamination are the two most prevalent failure modes reported in the F-111 field service data. Cracking at the edge and in the vicinity of the bolt holes has become a reason for removal and is of special concern as cracks decrease birdstrike resistance (it is important to maintain birdstrike protection during the service life of a transparency).

Table 3 shows the Phase I coupon scale test matrix. Oscillating sand (Bayer) abrasion simulates rubbing or contact type of abrasion, such as might be caused by cleaning a dirty transparency or by a maintenance person rubbing up against the transparency during maintenance operations. Salt impingement simulates ice crystal, sand, or dust impact during flight or on the ground. These two types of abrasion tests are reasonable in cost and are used by many in the industry. Currently, both have several drawbacks. The standard sand used in the Bayer abrasion test and the standard salt used in the salt impingement test are no longer available. Consequently, replacements were chosen.

Haze and transmittance testing of new, laboratory aged, and in service aged coupons can be conducted as part of the salt impingement test, as these measurements are typically made at one corner of the specimen which is not abraded. This test alone was utilized to evaluate aging of the bulk laminate. Other tests have been used in the past and essentially no bulk polycarbonate degradation has been detected as noted below. Molecular weight of polycarbonate from F-111 in service aged windshields was evaluated in Reference [12], and molecular weight of polycarbonate from F-16 in service aged forward canopies was evaluated in References [13] and [14]. Molecular weight was not found to be significantly affected by in service aging in any of these programs. Reference [14] did report molecular weight degradation in one lot of canopies caused by an improper additive used by the sheet manufacturer. In that case, the material degraded significantly even when stored in the laboratory. Dynamic mechanical analysis (DMA) was also conducted in the Reference [12] program, and minimal thermal history effects were detected for the polycarbonate. Typically interlayers, coatings, and face plies screen out UV before it reaches the polycarbonate; however, it is possible that molecular weight could change for some types of transparencies such as glass faced polycarbonate or monolithic polycarbonate with a UV transparent coating.

Infrared (IR) and x-ray photoelectron (XPS) spectroscopy were identified as techniques to characterize the surface of the acrylic faced specimens before and after artificial weathering and after in service aging. These tests are surface sensitive techniques which can be used to identify changes in the polymer caused by weathering or chemical attack. Only XPS tests were conducted. After XPS testing was complete, another technique, gas chromatography mass spectroscopy, was chosen to evaluate acrylic aging. The most prevalent change in cast acrylic (PMMA, polymethyl methacrylate) with aging is reversion of the polymer to the monomer [15]. Initially PMMA would have a monomer concentration of approximately 0.7%, and with aging the concentration may increase as much as 2.5%. This increase in monomer decreases the craze resistance of the acrylic. Reversion to the monomer is reported to occur only at temperatures

near the glass transition temperature and is maintained only if the material is cooled rapidly. If the material is cooled slowly, the free monomer will recombine. Gas chromatography mass spectroscopy tests have been conducted on F-16 canopies with craze problems in the forward viewing area by Polycast. The crazed areas which were in the forward portion of the canopy had monomer concentrations of approximately 2.5% and the uncrazed areas had monomer concentrations of approximately 0.7%. Apparently the forward portion of the canopy is exposed to thermal conditions which result in reversion of some of the polymer to the monomer.

Chemical stress craze tests provide a straightforward evaluation of craze resistance for a given chemical; however, the tests have not been related to field service durability. A second technique to evaluate craze resistance is surface roughness. UDRI conducted a study of the effect of surface roughness on chemical stress crazing of cast acrylic [16]. As expected, craze resistance increased as surface roughness decreased; however, the technique used by UDRI to measure surface roughness was not sensitive enough to characterize surface roughness of extremely smooth optical surfaces. Other techniques exist such as the non-contacting laser profilometer [17]; however, these types of systems are expensive and have only been used for small coupon specimens to date. Other surface roughness measuring techniques were evaluated, including a  $\mu$  Scan scatterometer manufactured by TMA Technologies Inc. Craze resistance for acrylic is also dependent on the amount of monomer present. As acrylic ages, especially in the presence of elevated temperature, it reverts to the monomer, and the more monomer which is present, the lower the craze resistance of the acrylic. The amount of monomer can be evaluated using gas chromatography mass spectroscopy.

To evaluate the resistance of the edge attachment to degradation (cracking), coupon specimens were subjected to tensile edge attachment testing. As reported in Reference [12], fatigue crack growth and fracture toughness testing of the polycarbonate plies from baseline and in-service aged F-111 ADBIRT windshield transparencies indicated that there was no significant change in these properties in the bulk material with in service aging. These tests were not repeated in the current program.

Flatwise tension and differential scanning calorimetry (DSC) or dynamic mechanical analysis (DMA) were chosen to evaluate delamination. Flatwise tension measures mechanical strength and its changes with aging. This test was used in the Reference 4 program to evaluate changes caused by in service aging. DSC or DMA were identified as candidate techniques for this program to determine if aging changes the cross-link density of the interlayer. DMA is preferred as it gives more information about the polymer than DSC; however, it is very difficult to fabricate a DMA specimen from the interlayer. DSC was chosen as a backup technique to evaluate changes caused by aging, but was not used. Molecular weight is not a suitable test for silicone and urethane interlayers as they are probably not soluble and are highly cross-linked materials. It is possible that the changes which cause delamination are not in the bulk interlayer, but are at the interface between the interlayer and the substrate, and may involve primers. Changes at this location may be difficult to detect and may require surface analysis techniques such as IR spectroscopy and XPS.

## Results of Phase I Artificially Aged Coupon Testing

The goal of the coupon scale testing was to conduct tests of baseline and laboratory aged specimens, and identify trends in the measured test results that could be correlated with degradation and durability. The chosen coupon scale test methods and the chosen artificial weathering technique produced recognizable degradation trends in a number of the test methods. However, scatter existed in test values between different windshields with the same history, making measurement and identification of trends difficult. It appears that more specimens need to be tested for each condition to better quantify scatter, and that additional/different test methods must be identified to evaluate degradation and durability.

The oscillating sand and salt impingement tests were chosen to simulate abrasion. Results from these tests were consistent with the goal of the coupon testing. Artificial weathering combined with abrasion produced measurable decreases in optical properties, which followed easily recognizable trends (Figures 4 and 5). Haze values were higher and transmittance values were lower for baseline oscillating sand abrasion (no QUV exposure) than for oscillating sand abrasion combined with QUV exposure. Weathering and cleaning actually polish the transparency surface, resulting in better optics. Acrylic is very stable in UV light, and the moisture and temperature exposures do not seem to be affecting the acrylic. Field cleaning is important for maintaining transparency optical quality. This is evidenced by the drop in haze of the oscillating sand abrasion coupons each time they were subjected to weathering and cleaning after being subjected to oscillating sand abrasion.

The failure mode of crazing was evaluated utilizing chemical stress craze testing. As shown in Table 4, there is a definite trend of decreased craze resistance with increased artificial weathering. Two different types of crazing are reported in Table 4. The first has been referred to as transient crazing, and refers to crazing which was identified during the actual test. It is important to note that in some cases the transient crazing at high stresses was not detectable after removal of the chemical and completion of the test. The second type of crazing reported has been referred to as permanent crazing, and refers to crazing which was identified after testing was completed under very close examination with a flashlight as a light source. In many cases permanent crazing, though very faint, was detected at greater stresses than was detected during the test.

Flatwise tension and DMA were used to evaluate delamination as a failure mode. The effect of artificial weathering on flatwise tension strength varied from windshield to windshield. Minor changes in the interlayer between the acrylic surface ply and the outboard polycarbonate ply, as a result of artificial weathering, were detected using DMA. These changes in combination with the flatwise tension results indicate that properties of the interlayers are not changing enough to cause delamination concerns as a result of artificial weathering alone. Delamination problems as a whole are most prevalent along the edges of transparencies and may be caused by combination of moisture ingress, thermal effects (causing shrink-back, warping, etc.), and out-of-contour effects (especially for glass outer plies). These effects are not simulated in coupon scale tests.



To evaluate the resistance of the edge attachment to degradation (cracking), tensile edge attachment testing was conducted. The results of tensile edge attachment testing indicate that the edge attachment is not affected by artificial weathering. XPS and gas chromatography mass spectroscopy (GCMS) were used to evaluate aging of the acrylic surface ply. No significant changes in the acrylic surface ply were detected using XPS; this technique is not sensitive to subtle changes in acrylic. Gas chromatography mass spectroscopy analysis of the acrylic surface ply did not reveal any significant changes in the acrylic.

It should be emphasized that while some of the tests chosen did not provide definitive information about the specimens which were artificially aged in this effort, those tests still warrant consideration, as they may still be valid for analysis of other artificially aged specimens or specimens removed from service. For instance, thermal shock (rapid decrease in temperature from temperatures near  $T_g$ ) may occur often in service, increasing monomer reversion and decreasing durability. QUV artificial weathering does not include thermal shock capabilities. Phase II of this program will investigate the relationship of thermal shock to durability through the use of density, hardness, and GCMS testing.

### **FIELD SERVICE DATA ACQUISITION AND DATA ANALYSIS**

The collection and analysis of field service data is critical to the understanding of the actual performance of aircraft transparencies in the field. Accurate field service data is essential not only for understanding the durability problem, but is also essential to the development of coupon scale and full scale durability testing.

The foremost questions which field service data must answer are:

- (1) what is the overall average service life for a type of transparency,
- (2) what are the failure modes for that transparency, frequency of occurrence for each, and service lives associated with those failure modes,
- (3) what effect if any is there on service life, failure mode, and frequency of occurrence resulting from factors such as geographic location (home base), aircraft model, primary mission, transparency design, manufacturer, etc.

Answering these questions requires collection of specific data. An example of the data which has been collected in the past is shown in Table 5. Examples of the methods and recommended types of analysis which can be conducted using the data can be found in Reference [4], which included analysis of field service data for F-111, F-16, and B-1 transparencies.

## Data Acquisition

There are a number of traditional ways which field service data has been acquired. These include the Air Force Maintenance Data Collection System (MDCS), field trips to bases to examine transparencies and aircraft records, and field trips to warehouses where failed transparencies are stored. These techniques have a number of drawbacks. The MDCS has not proven to be useful in terms of accuracy or completeness of data [5]; field trips are expensive and time consuming; warehouse storage requires extensive space, shipping costs, and a concentrated effort by a significant number of persons at given time intervals to physically examine each failed part. At this point, field data collection trips give the most useful (although sometimes limited) data.

For the Durability Test Criteria Program, UDRI has accompanied WL/FIVR personnel on a limited number of data acquisition trips for F-111 and F-16 aircraft. However, even on-sight data collection requires piecing together information from a number of sources. For example, during each trip for F-111 data (Cannon AFB), the Weight and Balance (W&B) records, transparencies currently on aircraft on the flight-line, and the parts in the scrap yard must be examined to get service life and (some) failure mode data. These data, though, may be incomplete: serial numbers recorded in W&B records are often missing or incomplete; failure modes are rarely recorded in W&B records; the F-111 T.O. manual requires recording of the transparency changeout in W&B records only if the difference in weight between old and new transparencies is greater than 1/2 pound (so a data point may be completely missed); and the failure tags from parts in the scrap yard are often incomplete or missing. As a result, considerable effort is required to obtain complete field service data. However, data that is collected has proved valuable in selecting appropriate coupon scale tests.

The situation is less severe and is improving for F-16 canopies. Until recently, the F-16 canopies removed from service were shipped to Hill AFB, where every two years or so they were examined and the reparability/recoatability was assessed for each transparency. Field service data from such an assessment was acquired for approximately 1200 F-16 canopies removed in the two years prior to June 1992. Currently, removed canopies are shipped back to Texstar for evaluation.

The data acquired on these trips is being added to the database for these aircraft which was developed by WL/FIVR. This updated database will be analyzed during the next phase of the Durability program. Based on the experience gained from these trips and the analysis of the data obtained, field service data collection activities for the second and third phases of this program will be modified to improve field service data collection.

Also, UDRI is evaluating alternative data gathering techniques for the F-111, F-16, and B-1 aircraft transparency systems. A data card is being developed in-house at FIVR to provide a possible future data collection technique. UDRI is considering an interim data collection technique which would consist of transparency data cards that are filled out by maintenance personnel whenever a new transparency is installed in an aircraft. Example data cards for F-111, F-16, and B-1 aircraft transparency systems are shown in Figures 6, 7, and 8. These cards would

be pre addressed, stamped, and could be on hand for use at the base or depot. However, a better approach would probably be to include a data card with each new transparency that has all information about that transparency on the card (such as manufacturer, serial number, date of manufacture, weight, etc.). The maintenance personnel would complete the data cards, filling out all appropriate blanks which identify subject aircraft, transparency removed, reason for removal, etc., and return the card to the data collecting agency. To make it easier for field personnel to obtain the data from the transparency ID decal, a standardized decal which positively identifies each of the pertinent pieces of information could be incorporated. Currently, many of the decals are hard to read and interpret. In order for a system like this to work it is critical to obtain official Air Force approval, and that the people who actually are going to fill out these cards be made aware of the importance and reasons for collecting the data, and that they be motivated to collect the data consistently and accurately.

### Example F-111 Field Data

A portion of the F-111 field data analysis is discussed below. Figure 9 displays the average life, 95 percent confidence limits, and the number of cases for each specific failure mode. The horizontal line is the average life for the failure mode and the extent of the vertical line defines the 95 percent confidence limits on the average. The confidence limits are defined by the expression

$$\bar{T} = \frac{1.96s}{\sqrt{n_i}} \quad (1)$$

where  $\bar{T}$  is the average for mode  $i$ ,  $s$  is the standard error from the analysis of variance (i.e., the pooled estimate of the scatter of lives from all of the failure modes), and  $n_i$  is the number of cases for mode  $i$ . The factor of 1.96 is the Student's  $t$  value for the large sample size in the estimate of  $s$  of this analysis. Since the lengths of the confidence intervals are inversely proportional to the number of cases in the averages, the longer confidence intervals result from small sample sizes. Non-overlapping confidence limits are definite indicators that the averages lives are significantly different. This figure indicates that windshields removed for acrylic crazing (Mode 1) and delaminations (Mode 4) have longer lives on average than those removed for cracks (Modes 2 and 3).

Average lives with confidence bounds for the two windshield manufacturers with data are presented in Figure 10. The difference between these averages is not statistically significant for these relatively large sample sizes. To further investigate potential differences between the manufacturers, average lives for each manufacturer by failure mode combination were compared when data were available. None of the differences in average life for the specific modes were statistically significant and it can be concluded that there was no joint effect of manufacturer and failure mode on life.

To test whether last base of operation had a significant effect on windshield life, the average lives were compared for the five bases. The observed averages, confidence limits and sample sizes are shown in Figure 11. The differences between the averages are not significant.

The clear or metallic coating was specified in only 114 of the windshield records. Of these, 99 indicated a clear coating and 15 indicated a metallic coating. The analysis of variance indicated that the metallic coating average life of 36.4 months was significantly longer than the clear coat average life of 25.2 months. Due to the very small number of metallic coating records, comparisons of average life for failure modes was not generally possible. However, the average lives for the 9 clear coated windshields and seven metallic coated windshields with a delamination (Mode 4) failure mode were not significantly different.

In 224 of the records with a positive partlife, the time between windshield manufacture and installation was available. This wait or storage time was correlated with partlife. Figure 12 displays the correlation and indicates that storage time has a negative impact on the life (durability) of ADBIRT windshields. The correlation is significantly less than zero but, as can be seen in the figure, may well be a second order effect if the wait is less than 24 months. There are many other factors that affect service life.

### FULL SCALE DURABILITY TESTING

The Air Force utilizes a test facility to evaluate full scale durability of aircraft transparencies subjected to flight conditions. This test facility is known as the full scale durability test facility and is located at WPAFB, Area B, Building 68. This facility has been used to assess durability of F-111 ADBIRT transparencies, and B-1 windshield transparencies are currently being evaluated in the facility. A more complete discussion of full scale durability testing and the test facility, a critique of the facility, and correlations between full scale testing and in service aging are included in Reference 4.

The full scale durability facility simulates transparency flight temperatures and differential pressure on the transparencies during different types of standard missions. A mix of flight mission profiles are developed to simulate each year of typical aircraft usage. Schematics of the test system are shown in Figures 13 and 14. Temperature control is achieved by mixing air from a hot air loop and a cold air loop with the test loop which contains the test article. Each loop is controlled independently. Thermocouples on the transparency surface provide information to a control system which operates the hot and cold air loop valves to mix air so that the desired temperature profile can be obtained. The internal cockpit temperature is maintained at or near room temperature typically. Pressure loads on the cockpit are simulated by pressurizing or evacuating the cockpit to obtain the net pressure differential between internal cockpit pressure and external ambient plus aerodynamic pressure that would occur during flight. The transparency surfaces have typically been cleaned at the beginning of each eight hour shift utilizing authorized cleaning solutions. The surface area of the transparency is broken up into different regions, each of which is cleaned with a different solution. Periodically the transparencies are inspected, and damage is documented and photographed. In the past, durability testing has not included environmental effects such as flight line temperatures, UV exposure, rain, humidity, or dust impingement. Recommendations regarding these additional factors were made in Reference 4, and inclusion of some of these effects is being considered.

Full scale durability testing is the logical next step in the development of durable transparencies after coupon scale testing. Coupon testing cannot reveal every possible problem with a design, nor can the flight environment be simulated accurately. Often problems develop in full scale testing which are a direct result of the edge attachments, the size and geometry of the finished part, or the intense thermal profile associated with simulated flight. The three biggest drawbacks to full scale testing are the cost, the time required to test, and the limited number of designs and systems which can be tested due to schedule and time constraints. In the past little or no attempt has been made to document this type of testing, and there have been no correlations with field service data.

Full scale durability testing has evolved from simply putting the transparency on the airplane and flying it, to the development of a facility for conducting full scale durability testing on the ground. This facility has been criticized in terms of realism of testing, cost, time to test, and relatively small number of articles actually tested; however, improvements in most of these areas have taken place or are taking place. Full scale testing can reveal failure modes and system problems which cannot be detected with coupon scale tests.

One of the single most important areas which still needs to be addressed is that correlations need to be made between full scale durability testing and field service performance. This program, the Transparency Durability Test Criteria Program, will address this issue during the course of the contract. It is difficult to make suggestions to improve full scale durability testing when the relationships between simulated service and field service are unknown.

## CONCLUSIONS/RECOMMENDATIONS

Much of the work in this, Phase I, of the program was to develop the foundation of the overall Transparency Durability Test Criteria Program. The focus of Phase I has been the formulation of the methodology for assessing durability, and initiation of work in each of the component areas of that methodology. The component areas are coupon scale durability testing, field service data acquisition and analysis, and full scale durability testing. The major tasks are to identify how each of these component areas should be addressed. Common failure modes from field service data and coupon scale tests which address these failure modes have been identified. A laboratory scale artificial weathering technique utilizing the QUV machine has been developed for conditioning specimens. The formulation of and preliminary testing to validate a coupon scale test methodology has been completed. Field service data collection efforts have been initiated, along with conceptual development of an improved field service data collection technique. Extensive analysis of this field service data has been conducted, and full scale durability test practices and the facility have been reviewed and critiqued (Reference [4]). Integration of and correlation between each of these areas is critical to the completion of a methodology; however, integration and correlation are premature at this stage of the effort.

To reiterate, the methodology is a general one which could be applied to any transparency system and can be described as follows. The first step in assessing durability is coupon scale testing. Currently, coupon testing by itself cannot be used to predict durability in terms of time.

Coupon testing can and has been used to comparatively assess durability for competing materials or designs based on the premise that performance in a given test is a real measure of durability. The choice of coupon tests is based on the transparency system being evaluated and for a new system must be based on experience with similar systems. Coupon tests are chosen to address the failure modes which can occur with the transparency system. If coupon scale testing produces satisfactory results, then full scale durability testing can be conducted. If full scale durability testing produces satisfactory results, then the transparency design is ready for field service. If the coupon scale or full scale testing reveal problems with the design, the design can be changed. If field service data reveals a problem, changes can be made not only to the transparency design, but to the entire methodology, which includes choice of coupon scale tests and interpretation of the results of the coupon scale tests. The whole process is iterative and can change continuously as it is used to reflect lessons learned and improvements in testing and interpretation of test results.

Phases II and III of this program will continue to build on the foundation of this Phase I work to continue the development and validation of a complete aircraft transparency durability test methodology. Phase II test plans include testing of in-service aged F-111 windshields for identification and correlation trends similar to those found in the artificially aged coupon tests. Included in artificially aged coupon tests will be a series of Phase II tests investigating the role of thermal shock in transparency durability. In these tests, a statistical Design of Experiments approach will be taken to assess how thermal shock affects the results of various test methods.

## REFERENCES

1. Whitney, Thomas J. and Daniel R. Bowman, "Transparency Durability Test Criteria, Phase I: Literature Survey," UDR-TR-92-14, University of Dayton Research Institute, Dayton, Ohio, February 1992.
2. Bowman, Daniel R., "Transparency Durability Test Criteria, Interim Technical Operating Report (Data Review: Coupon Scale Data, Full Scale Durability Data, and Field Service Data)," UDR-TR-92-26, University of Dayton Research Institute, Dayton, Ohio, February 1992.
3. Bowman, Daniel R., "Transparency Durability Test Criteria, Interim Technical Operating Report (Phase I: Coupon Scale Test Plan and Field Service Data Acquisition Plan)," UDR-TR-92-26, University of Dayton Research Institute, Dayton, Ohio, February 1992.
4. Bowman, Daniel R. and Alan P. Berens, "Transparency Durability Test Criteria, Interim Technical Operating Report (Phase I: Field Service and Full Scale Durability Testing Data Analysis)," UDR-TR-92-97, University of Dayton Research Institute, Dayton, Ohio, August 1992.
5. Bowman, Daniel R. and Thomas J. Whitney, "Transparency Durability Test Criteria, Interim Technical Operating Report (Phase I Test Methodology)," UDR-TR-92-161, University of Dayton Research Institute, Dayton, Ohio, November, 1992
6. Heater, K. J. and P. L. Jones, "The Utility of Positron Annihilation Lifetime Spectroscopy in

Characterizing the Molecular Response of Glassy Polymers," Technical Seminar ASTM Sub-Committee F7.08, October 9-10, 1991, Arlington, Texas.

7. Hill, A. J., P. L. Jones, J. H. Lind, and G. W. Pearsall, "A Positron Annihilation Lifetime Study of Isothermal Structural Relaxation in Bisphenol-A Polycarbonate." **Journal of Polymer Science: Part A: Polymer Chemistry**, Vol. 26, 1541-1552, 1988.

8. "Standard Practice for Operating Light- and Water-Exposure Apparatus (Fluorescent UV-Condensation Type) for Exposure of Plastics," **ASTM D 4329-84**.

9. "Standard Practice for Operating Light- and Water-Exposure Apparatus (Fluorescent UV-Condensation Type) for Exposure of Nonmetallic Materials," **ASTM G 53-88**.

10. Whitney, Thomas J., "Definition of Accelerated Artificial Weathering Cycles for Durability Test Criteria Program," **UDR-TR-92-24**, University of Dayton Research Institute, Dayton, Ohio, September 1992.

11. Piekutowski, Andrew J., "Simulation of Exposure of Aircraft Transparencies to Flight Line Environment," Conference on Aerospace Transparent Materials and Enclosures, **AFWAL-TR-83-4154**, December 1983.

12. Bowman, Daniel R., "An Investigation Into the Structural Degradation of In-Service Aged F-111 ADBIRT Windshield Transparencies," **UDR-TR-90-34**, University of Dayton Research Institute, Dayton, Ohio, June 1990.

13. Bouchard, M. P., "Failure Analysis of Birdstrike-Tested Recoated Monolithic F-16A Forward Canopies," **AFWAL-TR-87-3050**, Air Force Wright Aeronautical Laboratories, Wright-Patterson Air Force Base, Ohio, August 1987.

14. Teten, Lance, "Methods for the Determination of the Degradation of Polycarbonate," Conference on Aerospace Transparent Materials and Enclosures, January 16-20, 1989, **WRDC-TR-89-4044**, Air Force Wright Aeronautical Laboratories, Wright-Patterson Air Force Base, Ohio, April 1989.

15. Private Communications with John Lee and Lance Teten, September 1992.

16. Poolmon, Kevin L. and Blaine S. West, "Crazing of Acrylic as a Function of Surface Smoothness," **UDR-TM-88-23**, University of Dayton Research Institute, Dayton, Ohio, July 1988.

17. Bristow, Thomas C., "Surface Roughness Measurements of Window Materials Using a Non-Contact Profiler," Technical Seminar ASTM Sub-Committee F7.08, September 12-14, 1989, Palm Springs, California.

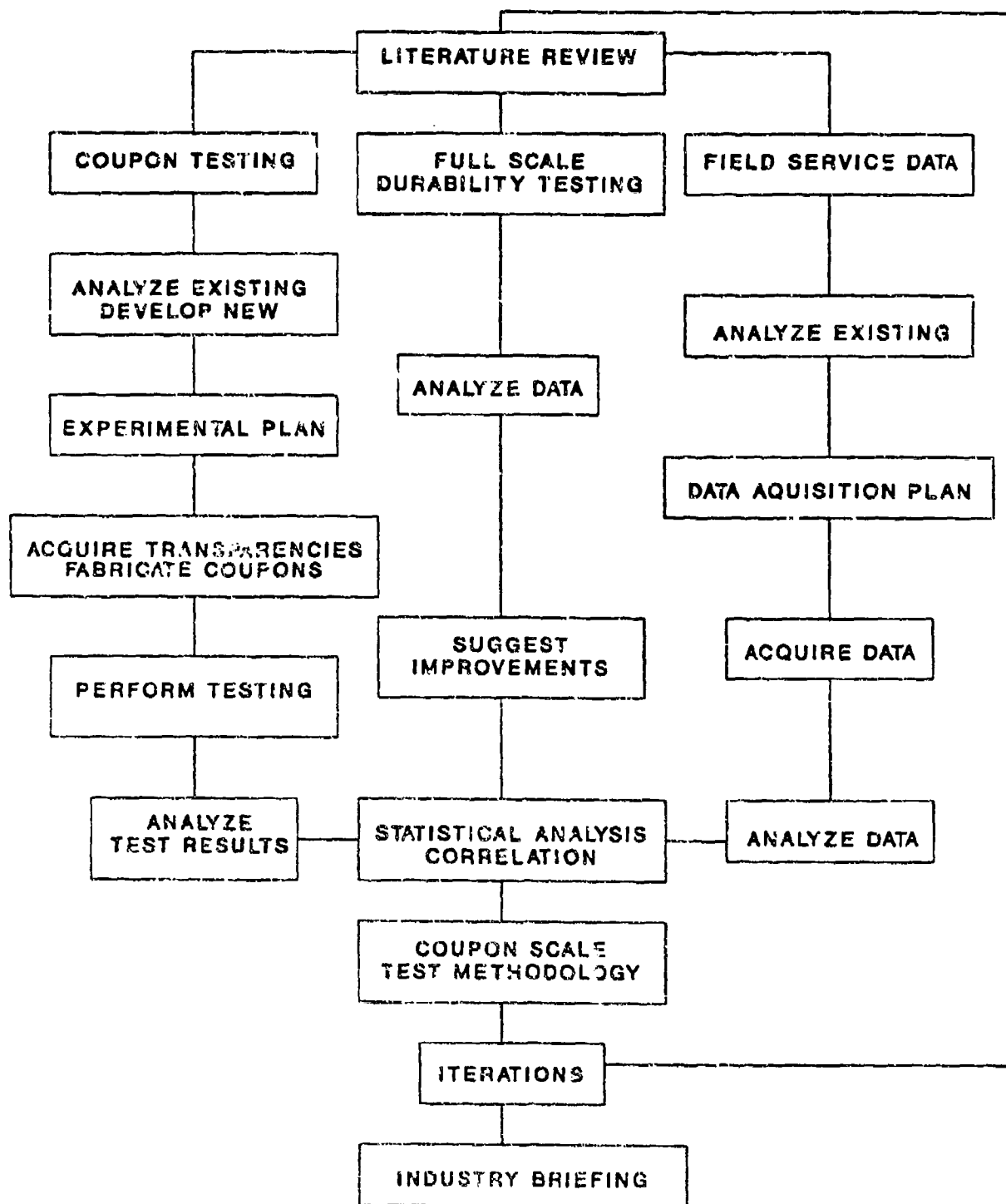


Figure 1. Transparency Durability Methodology.



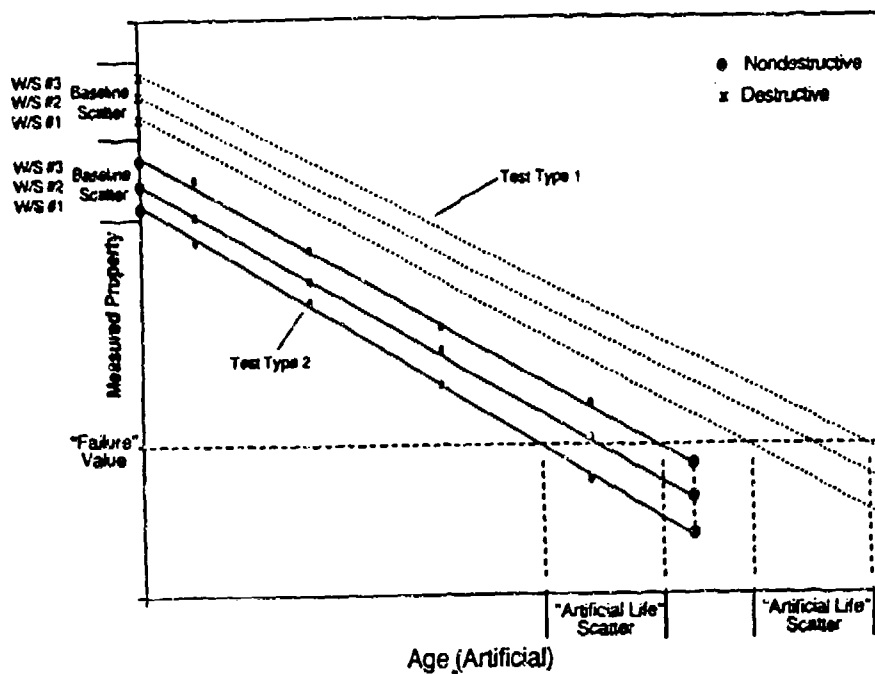


Figure 2. Hypothetical Degradation of Several Given Coupon Scale Test Properties with Artificial Aging.

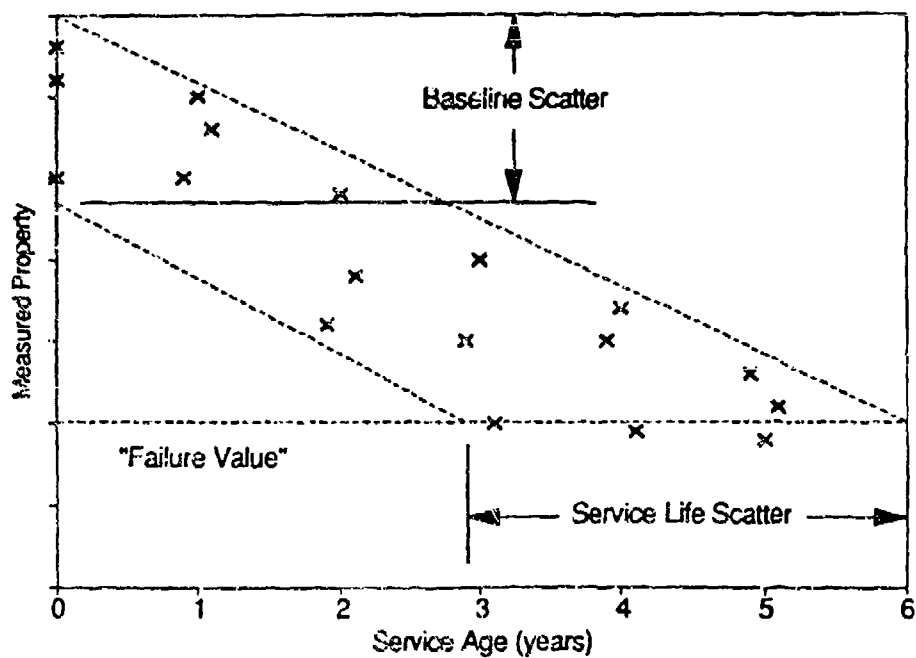


Figure 3. Hypothetical Degradation of Given Coupon Scale Test Property with In-Service Aging.

# PPG

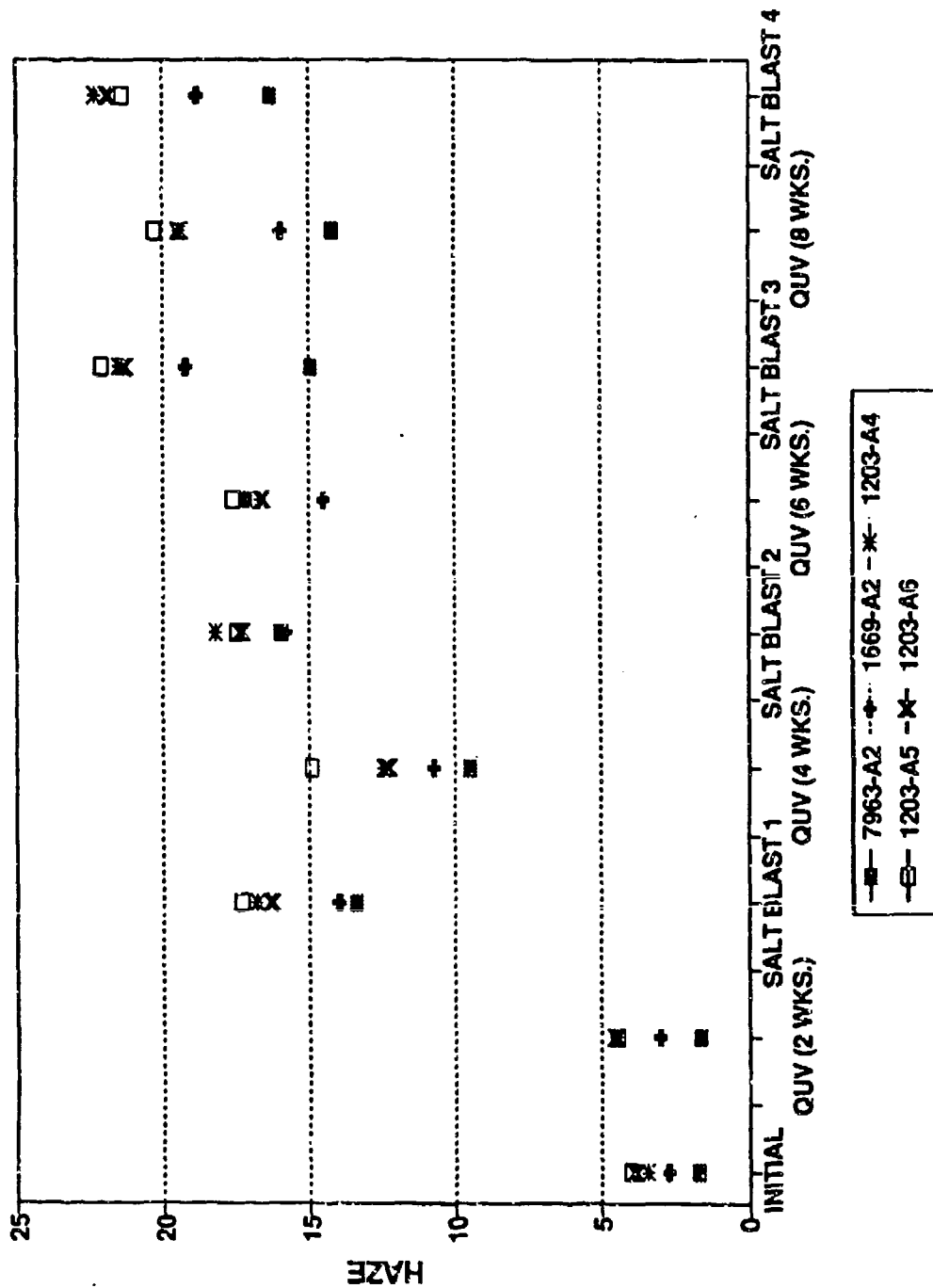


Figure 4. The Effect of Combined QUV Weathering and the Most Severe Salt Impingement (Location 4, 32 Blasts) for PPG Specimens.

# PPG

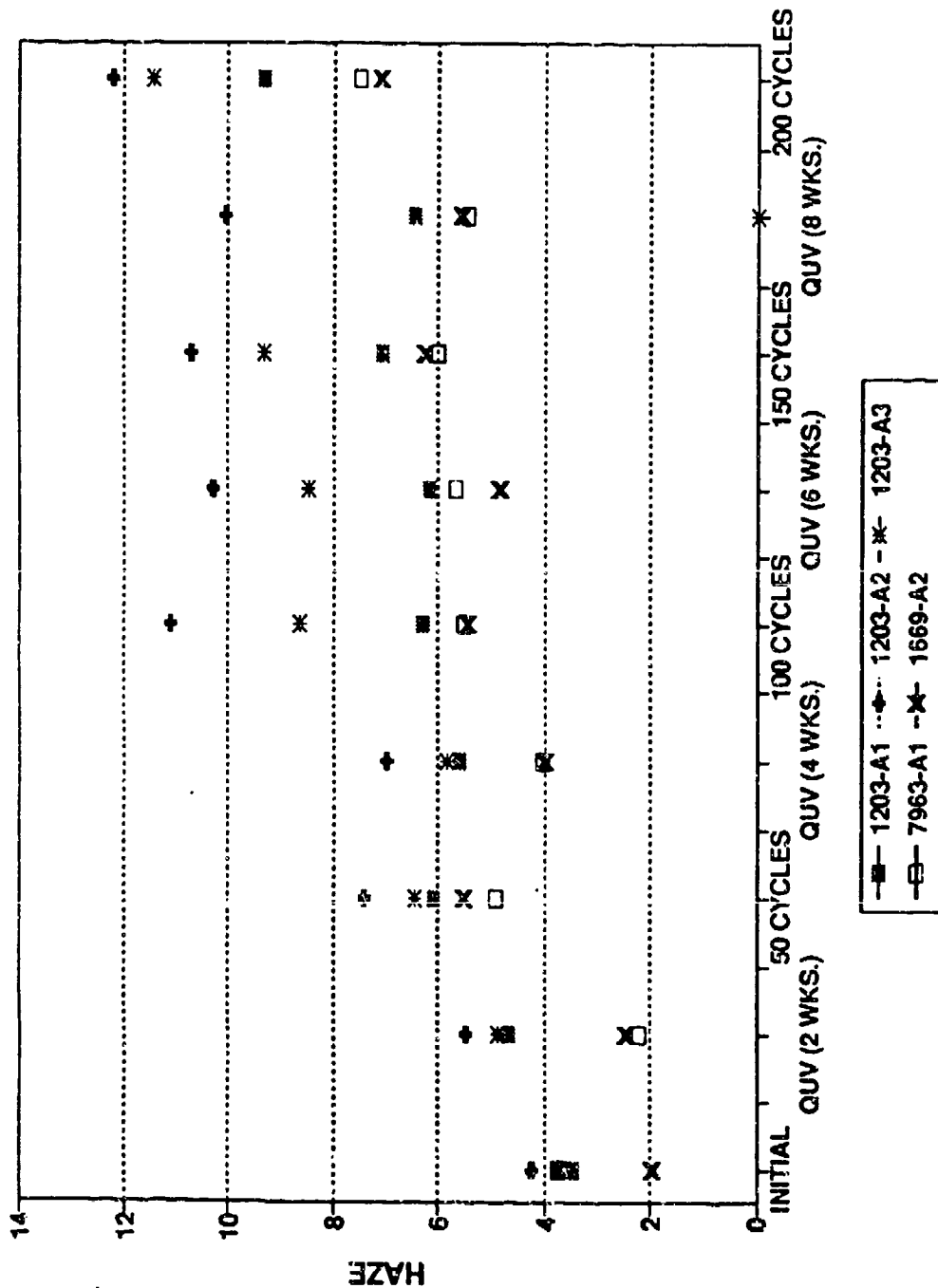
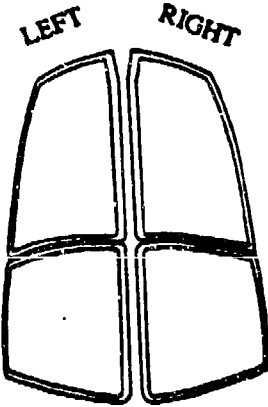


Figure 5. The Effect of Combined QUV Weathering and Oscillating Sand Abrasion for PPG Specimens.

# **IMPORTANT! MUST BE COMPLETED**

F-111 ADORIT TRANSPARENCY REMOVAL AND INSTALLATION DATA CARD

PLEASE COMPLETE ALL ENTRIES ON THIS CARD. YOUR INPUTS ARE NEEDED AND VALUABLE.

DATE:		TECHNICIAN NAME:		TRANSPARENCY REMOVED		TRANSPARENCY INSTALLED			
BASE:				MANUFACTURER:		MANUFACTURER			
AIRCRAFT TAIL NUMBER:				SERIAL NUMBER:		SERIAL NUMBER			
REASON FOR REMOVAL:				DATE OF MANUFACTURE:		DATE OF MANUFACTURE			
CHECK APPROPRIATE BOX(ES) BELOW:				WEIGHT:		WEIGHT			
<input type="checkbox"/> CRAZING		<p>INDICATE TRANSPARENCY REMOVED AND REPLACED AND INDICATE DAMAGED REGIONS</p> <div style="text-align: center;">  <p>LEFT      RIGHT</p> </div>							
<input type="checkbox"/> DELAMINATION OF EXTERIOR PLY									
<input type="checkbox"/> DELAMINATION BETWEEN INNER PLYS									
<input type="checkbox"/> ACRYLIC CRAZING (EXTERIOR PLY)									
<input type="checkbox"/> POLYCARBONATE CRAZING (INTERIOR PLYS)									
<input type="checkbox"/> HAZE									
<input type="checkbox"/> INNER PLY SCRATCHES									
<input type="checkbox"/> OUTER PLY SCRATCHES									
<input type="checkbox"/> BEND STRIKE									
<input type="checkbox"/> INNER COATING PEELING/DAMAGED									
<input type="checkbox"/> DAMAGED DURING REMOVAL									
<input type="checkbox"/> AGE/TIME CHANGE									
<input type="checkbox"/> OTHER									
NOTES:								TOP VIEW FORWARD ->	

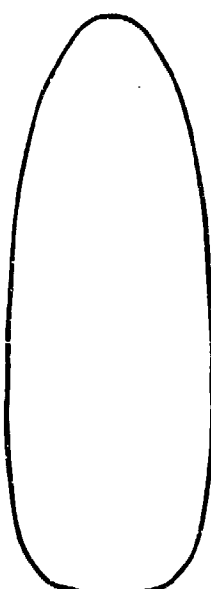
THIS DATA IS BEING COLLECTED SO THE AIR FORCE CAN IDENTIFY THE SERVICE LIFE AND CAUSE FOR REMOVAL FOR DIFFERENT TRANSPARENCY DESIGNS. EACH SUPPLIER CAN IMPROVE THEIR DESIGNS TO PREVENT PROBLEMS, AND THE AIR FORCE CAN BUY THE BEST DESIGNS. THIS WILL REDUCE COSTS AND MAINTENANCE MANHOURS. FILL THIS CARD OUT, TURN IT OVER FOLD IT UP SO THAT ADDRESS AND STAMP ARE VISIBLE, STAPLE ON TAPE CLOSED, AND MAIL THE CARD.

Figure 6. Field Service Data Acquisition Card, F-111.

# **IMPORTANT! MUST BE COMPLETED**

F-16 TRANSPARENCY REMOVAL AND INSTALLATION DATA CARD

PLEASE COMPLETE ALL ENTRIES. YOUR INPUTS ARE NEEDED AND VALUABLE.

DATE:		TECHNICIAN NAME:		TRANSPARENCY REMOVED		TRANSPARENCY INSTALLED	
AIRCRAFT TAIL NUMBER:		MANUFACTURER:		MANUFACTURER:		MANUFACTURER:	
REASON FOR REMOVAL:		MANUF PART NUMBER:		MANUF PART NUMBER:		MANUF PART NUMBER:	
CHECK APPROPRIATE BOX(ES) BELOW:		SERIAL NUMBER:		SERIAL NUMBER:		SERIAL NUMBER:	
<input type="checkbox"/> CRACKING		DATE OF MANUFACTURE:		DATE OF MANUFACTURE:		DATE OF MANUFACTURE:	
<input type="checkbox"/> DELAMINATION		NO. OF HOURS:		NO. OF HOURS:		NO. OF HOURS:	
<input type="checkbox"/> TACRYLIC CRACKING (EXTERIOR PLY)		LAMINATE:		LAMINATE:		LAMINATE:	
<input type="checkbox"/> POLYCARBONATE CRACKING (INTERIOR PLY)		<p>INDICATE TRANSPARENCY REMOVED AND REPLACED AND INDICATE DAMAGED REGIONS</p> 					
<input type="checkbox"/> HAZE							
<input type="checkbox"/> INTERIOR SCRATCHING							
<input type="checkbox"/> EXTERIOR SCRATCHING							
<input type="checkbox"/> COATING DAMAGE, INSIDE							
<input type="checkbox"/> COATING DAMAGE, OUTSIDE							
<input type="checkbox"/> STATIC DISCHARGE							
<input type="checkbox"/> HULL GOUGES							
<input type="checkbox"/> BIRDS/STRIKE							
<input type="checkbox"/> MAINTENANCE							
<input type="checkbox"/> FACE		NOTES:		TOP VIEW FORWARD ->			
<input type="checkbox"/> OTHER							

THIS DATA IS BEING COLLECTED SO THE AIR FORCE CAN IDENTIFY THE SERVICE LIFE AND CAUSE FOR REMOVAL FOR DIFFERENT TRANSPARENCY DESIGNS. EACH SUPPLIER CAN IMPROVE THEIR DESIGNS TO PREVENT PROBLEMS, AND THE AIR FORCE CAN BUY THE BEST DESIGN. THIS WILL REDUCE COSTS AND MAINTENANCE HOURS. FILL THIS CARD OUT, TURN IT OVER AND IT UP SO THAT ADDRESS AND STAMP ARE VISIBLE, STAPLE OR TAPE CLOSED, AND MAIL THE CARD.

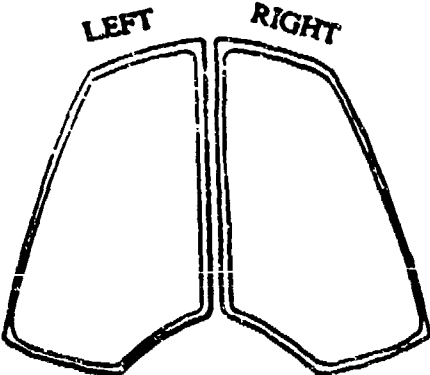
Figure 7. Field Service Data Acquisition Card, F-16.

# IMPORTANT! MUST BE COMPLETED

B-1 WINGFIELD REMOVAL AND INSTALLATION DATA CARD

PLEASE COMPLETE ALL ENTRIES ON THIS CARD. YOUR INPUTS ARE NECESSARY AND VALUABLE.

DATE:		TRANSPARENCY REMOVED		TRANSPARENCY INSTALLED	
BASE:		REMOVAL USER		MANUFACTURER	
REASON FOR REMOVAL		SERIAL NUMBER		SERIAL NUMBER	
CHECK APPROPRIATE BOXES IN BELOW		DATE OF MANUFACTURE		DATE OF MANUFACTURE	
<input type="checkbox"/> CRACKS					
<input type="checkbox"/> DECONTAMINATION CASE					
<input type="checkbox"/> DECONTAMINATION (RENTAL)					
<input type="checkbox"/> GLASS CRACKS (EXTERIOR FL)					
<input type="checkbox"/> POLYCARBONATE CRACKING (INTERIOR FL)					
<input type="checkbox"/> HAZE					
<input type="checkbox"/> INTERIOR SCORCHING					
<input type="checkbox"/> EXTERIOR SCORCHING					
<input type="checkbox"/> FOUL/DAMAGE					
<input type="checkbox"/> DISTORTION					
<input type="checkbox"/> FALLOUT OF ELECTRICAL HEATING					
<input type="checkbox"/> BRUISING					
<input type="checkbox"/> FOUL/DAMAGE					
<input type="checkbox"/> PUNCTURE/SCORCH					
<input type="checkbox"/> DAMAGED DURING FOAM REMOVAL					
<input type="checkbox"/> MAINTENANCE					
<input type="checkbox"/> PAGE					
<input type="checkbox"/> OTHER					



LEFT RIGHT

TOP VIEW FORWARD →

NOTES

THIS DATA IS BEING COLLECTED SO THE AIR FORCE CAN DETERMINE THE SERVICE LIFE AND CAUSE FOR REMOVAL FOR DIFFERENT TRANSPARENCY DESIGNS. EACH SUPPLIER CAN IMPROVE THEIR DESIGNS TO PREVENT PROBLEMS, AND THE AIR FORCE CAN BUY THE BEST DESIGN. THIS WILL REDUCE COSTS AND MAINTENANCE HOURS. FILL THIS CARD OUT, TURN IT OVERFOLD IT UP SO THAT ADDRESS AND STAMP ARE VISIBLE, STAPLE OR TAPE CLOSED, AND MAIL THE CARD.

Figure 8. Field Service Data Acquisition Card, B-1.

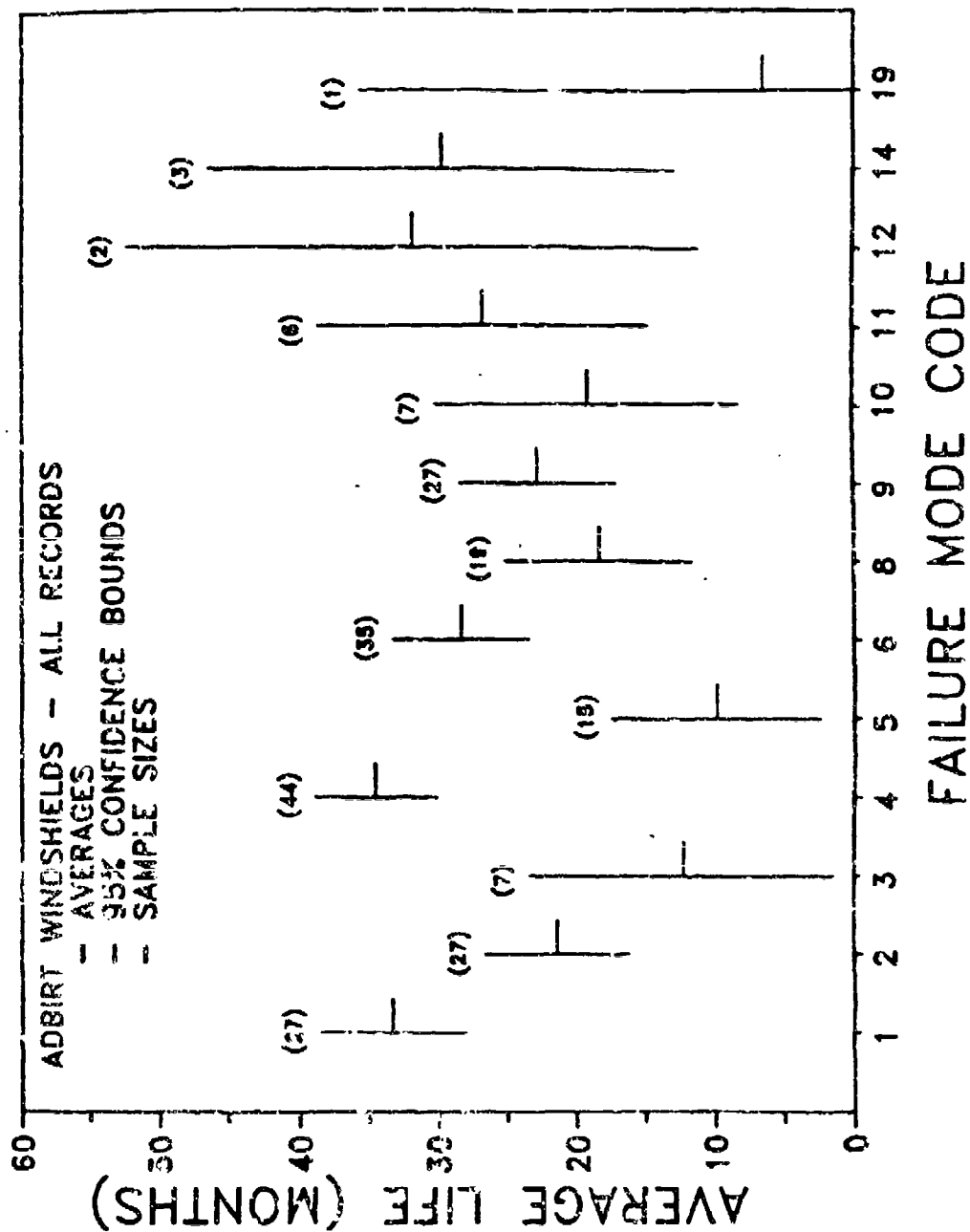


Figure 9. Service Life Statistics for Failure Modes - ADBIRT Windshields.

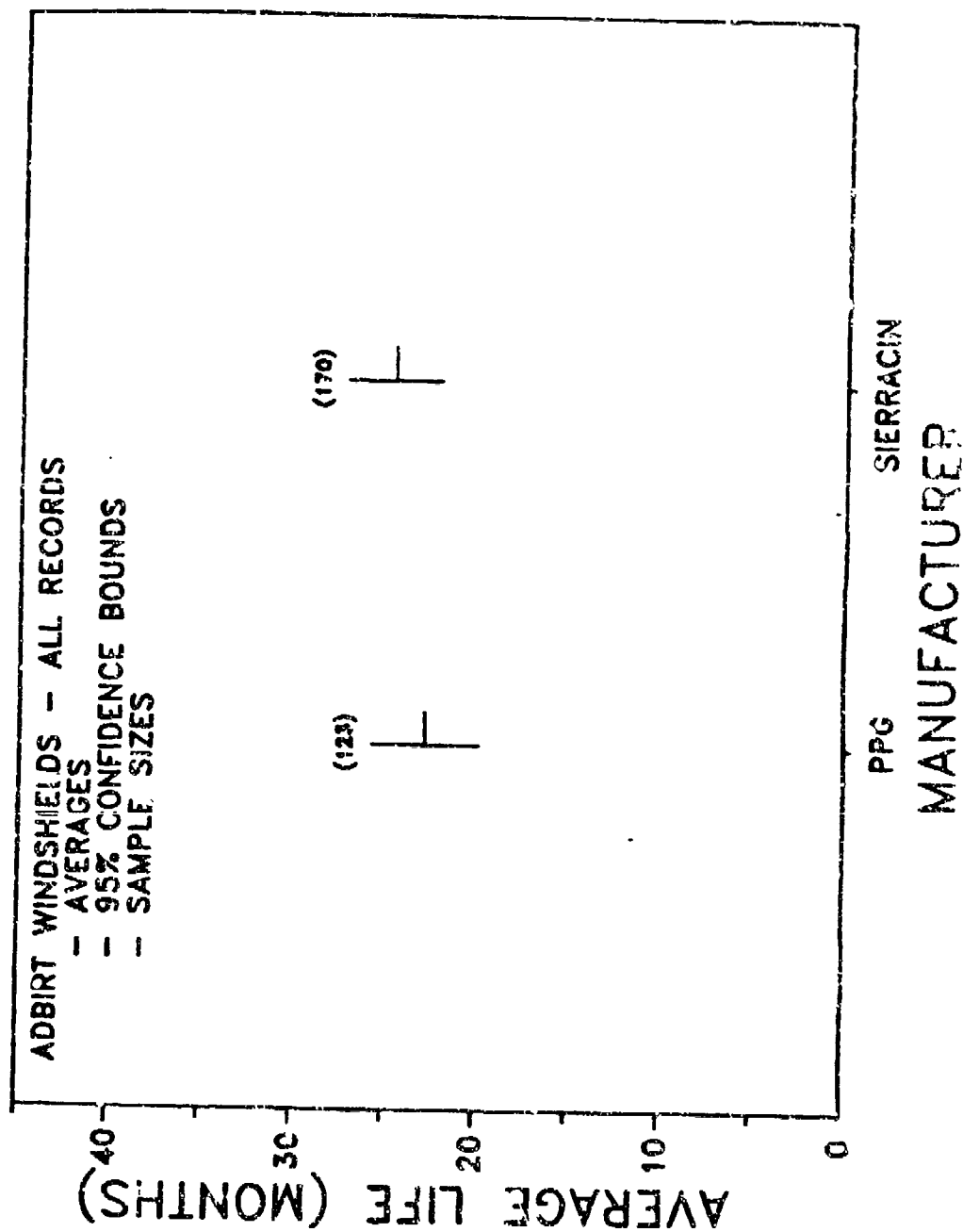


Figure 10. Service Life Statistics for Manufacturers - ADBI RT Windshields.



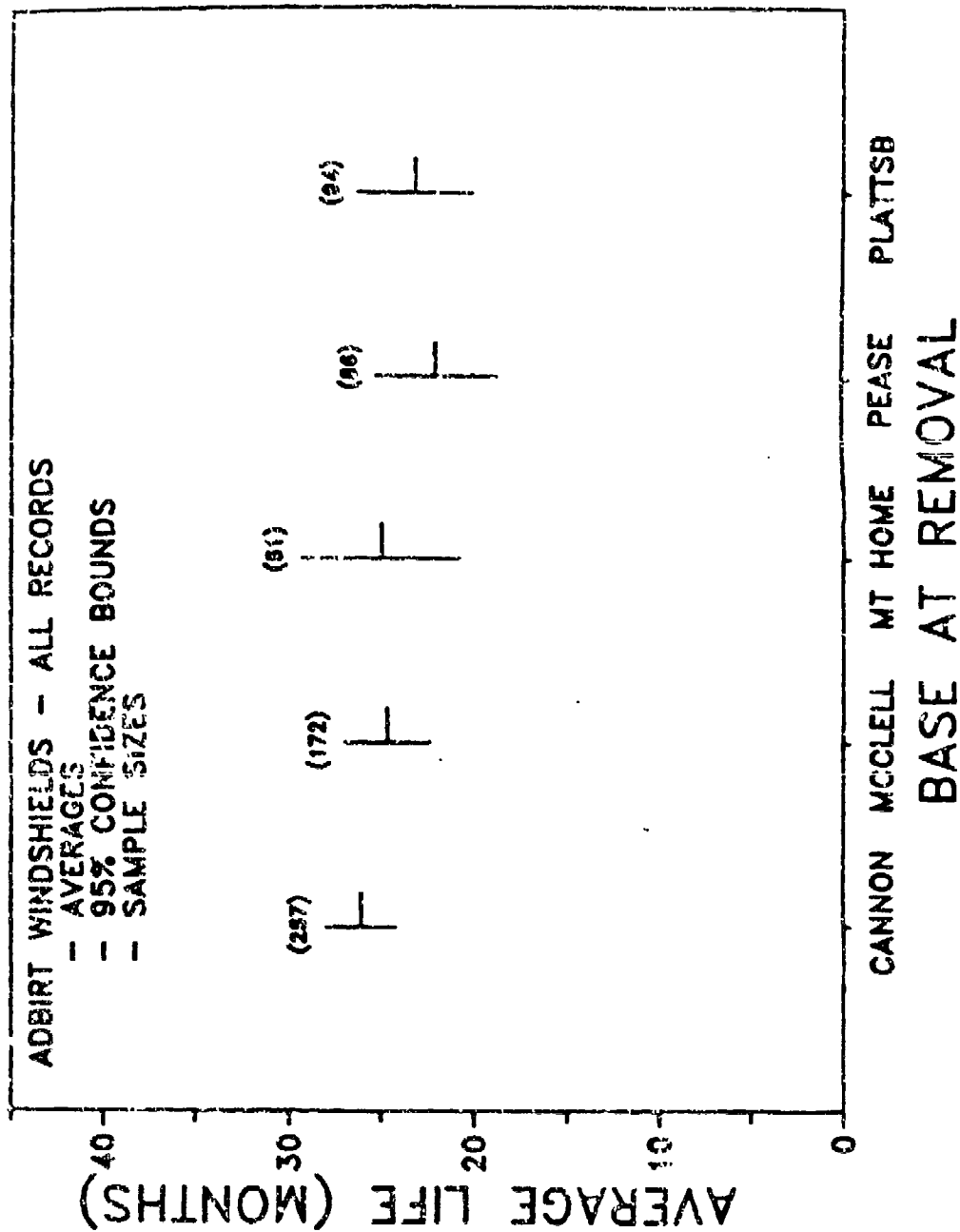


Figure 11. Service Life Statistics for Bases - ADBIRT Windshields.

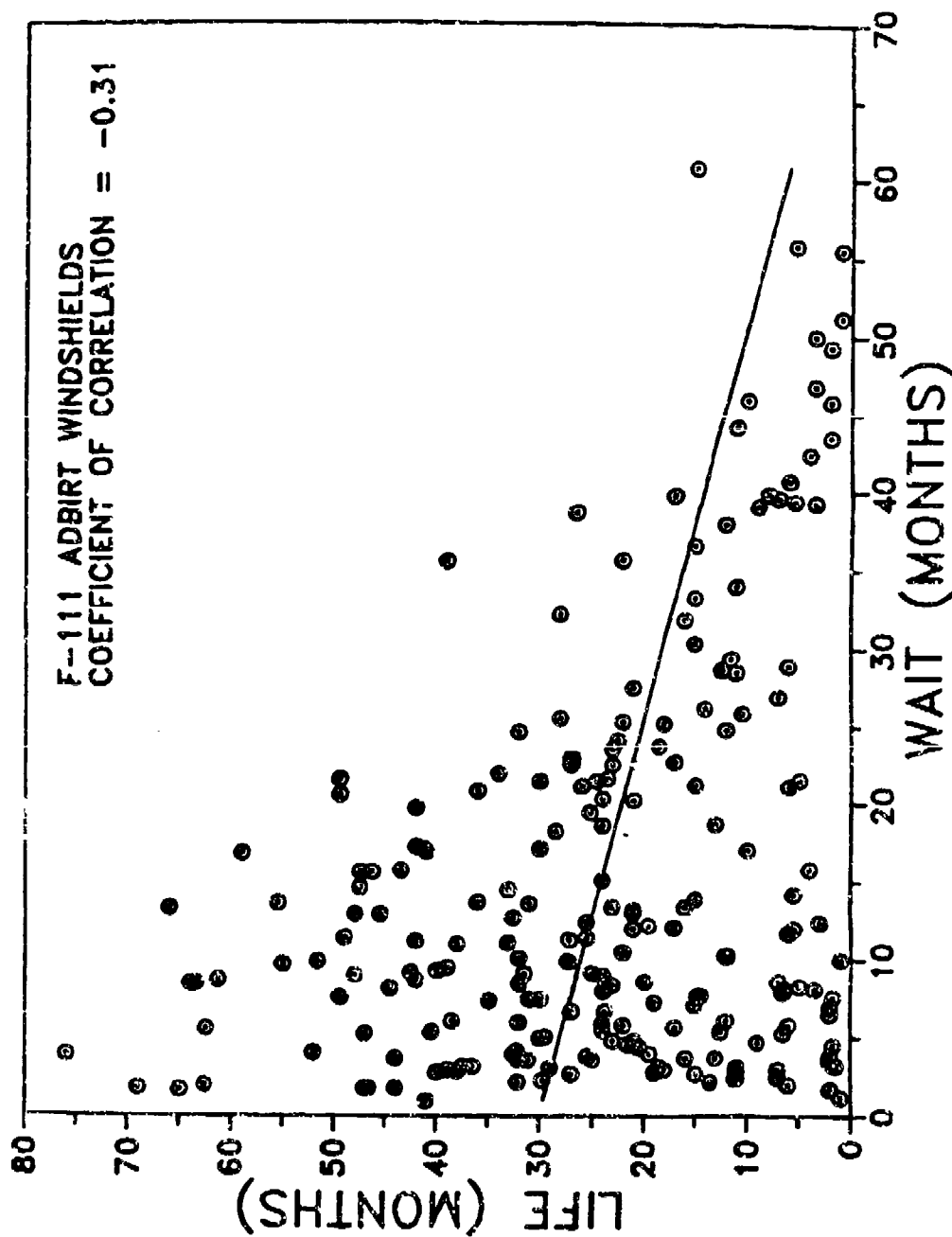
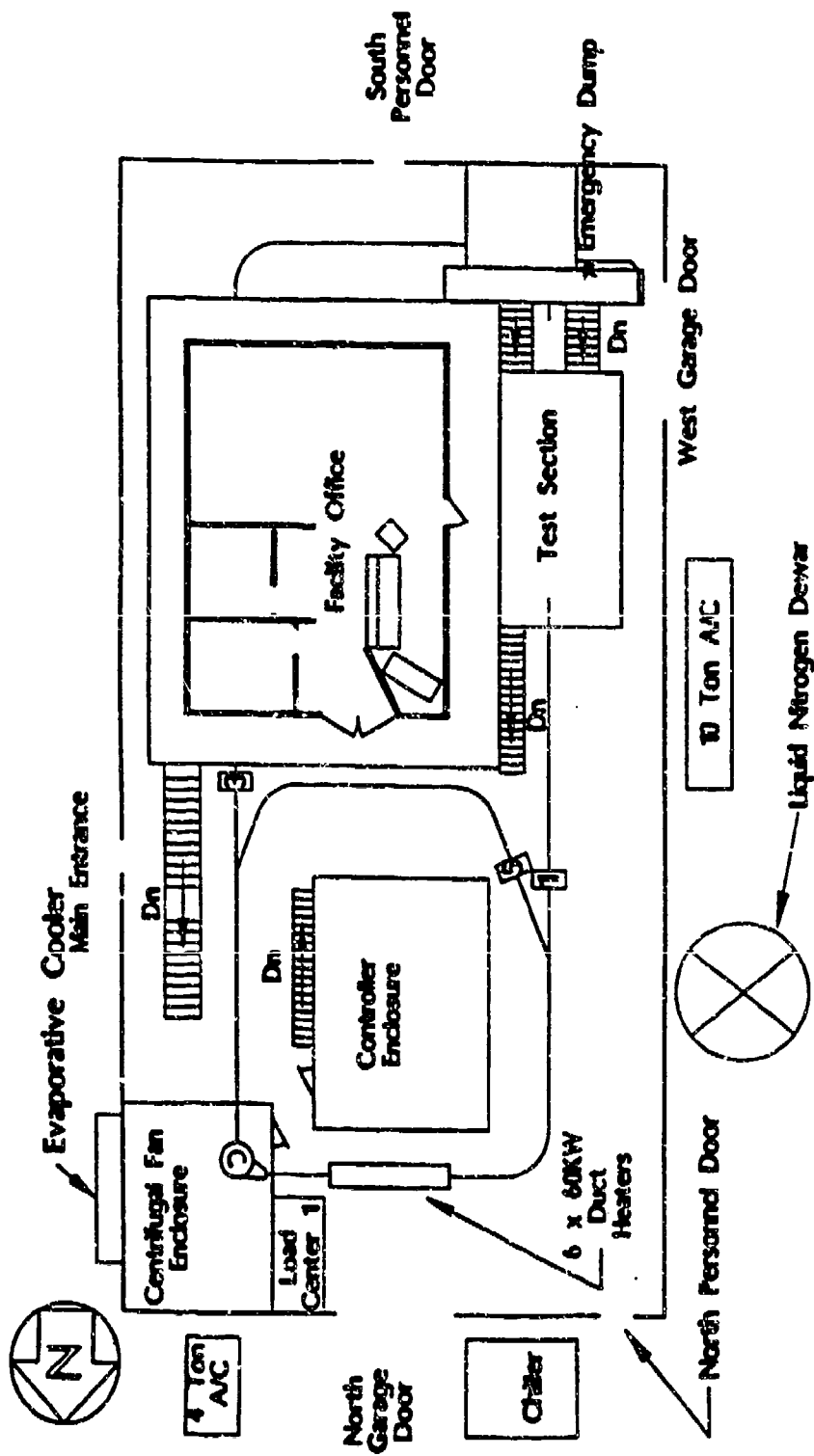


Figure 12. Correlation of Service Life with Installation Delay -  
ADBIRT Windshields.





20 Dec 89

Figure 14. Convection Heat Test Facility, WPAFB Area B, Bldg. 68  
System Layout - Mezzanine Level.

**TABLE 1**  
**COUPON SCALE TEST METHODS**

<b>GENERAL</b>	<b>CHEMICAL/SURFACE/RHEOLOGICAL</b>
DENSITY	DYNAMIC MECHANICAL ANALYSIS (DMA)
HARDNESS	DIFFERENTIAL SCANNING CALORIMETRY (DSC)
SURFACE ROUGHNESS (FINISH)	THERMAL MECHANICAL ANALYSIS (TMA)
	THERMAL GRAVIMETRIC ANALYSIS (TGA)
	GEL PERMEATION CHROMATOGRAPHY (GPC) - MOLECULAR WEIGHT
	INTRINSIC VISCOSITY
<b>OPTICAL</b>	FLOW INDEX
YELLOWNESS INDEX	INFRARED (IR) SPECTROSCOPY
LUMINOUS HAZE	X-RAY PHOTOELECTRON SPECTROSCOPY (XPS)
LUMINOUS TRANSMITTANCE	FREE VOLUME
INDEX OF REFRACTION	OPTICAL AND SCANNING ELECTRON MICROSCOPY (SEM)
<b>MECHANICAL</b>	<b>CHEMICAL ATTACK</b>
TENSILE (STANDARD AND FLATWISE TENSION)	CHEMICAL STRESS CRAZE
COMPRESSIVE	CHEMICAL EXPOSURE
BULK MODULUS	
SHEAR (STANDARD AND TORSIONAL SHEAR)	<b>THERMAL</b>
PLASTIC	GLASS TRANSITION TEMPERATURE
FATIGUE	HEAT DEFLECTION TEMPERATURE
FATIGUE CRACK GROWTH	COEFFICIENT OF THERMAL EXPANSION
FRACTURE TOUGHNESS	SPECIFIC HEAT
CREEP/STRESS RELAXATION	THERMAL SHOCK
<b>IMPACT</b>	<b>MISCELLANEOUS</b>
AIR CANNON	FUNGUS ATTACK
FALLING WEIGHT	TAPE PEEL
ROD	X-HATCH RAIN EROSION
CHIPPY	EDGE ATTACHMENT
BALLISTIC	MOISTURE ABSORPTION/DESORPTION
MAIL	ELECTRICAL AND LOW OBSERVABLE
<b>ABRASION/EROSION</b>	ELECTROSTATIC DISCHARGE
TAPER	DIELECTRIC STRENGTH/CONSTANT
COBALLASTING SAND (BAYER)	RESISTIVITY
SALT IMPINGEMENT	
DUST EROSION	<b>ENVIRONMENTAL</b>
RAIN EROSION	NATURAL WEATHERING
	ARTIFICIAL WEATHERING
	HEAT AGING
	HEAT/MOISTURE AGING
	SALT SPRAY
	STRESS WEATHERING

TABLE 2

## AIRCRAFT TRANSPARENCY FAILURE MODES AND APPLICABLE TEST METHODS

FAILURE MODE	AFFECTED TRANSPARENCY COMPONENT					TEST	APPLICABLE STANDARD
	COATING	FACE PLY	STRUCTURAL PLY	INTER LAYER	COMPLETE X-SEC.		
ABRASION ICE EROSION DUST EROSION RAIN EROSION	X	X				OSCILLATING SAND (BAYER) SALT IMPINGEMENT DUST EROSION RAIN EROSION	ASTM F 705 ASTM F 1120 ASTM G 73
AGING (PHYSICAL/WEATHERING)  OPTICAL YELLOWING HAZE INCREASE TRANSMITTANCE DECREASE  STRUCTURAL (TOUGHNESS DECREASE)					X	YELLOWNESS INDEX HAZE TRANSMITTANCE	ASTM D 1925 ASTM D 1003 ASTM D 1003
CHANGE IN POLYMER	X	X	X	X	X	AIR CANNON FALLING WEIGHT FLEXURE BEAM TENSILE  DENSITY (MICRO)HARDNESS DYNAMIC MECHANICAL ANALYSIS (DMA) FREE VOLUME MOLECULAR WEIGHT INTRINSIC VISCOSITY FLOW INDEX INFRARED (IR) SPECTROSCOPY X-RAY PHOTOELECTRON SPECTROSCOPY (XPS)	ASTM F 706 ASTM D 790 ASTM D 638 AND D 2783  ASTM D 3682 ASTM D 2867 ASTM D 1230
DECREASE IN ADHESION	X					TAPE PEEL PATCH RAIN EROSION	
EMBODIMENT OF STRUCTURAL PLY BY COATING					X	AIR CANNON FALLING WEIGHT FLEXURE BEAM	ASTM F 706 ASTM D 790
DECREASE IN COATING PERFORMANCE	X					ELECTRICAL AND LOW OBSERVABLE TESTS	
CRACKING		X				FATIGUE CRACK GROWTH FRACTURE TOUGHNESS TENSILE EDGE ATTACHMENT	ASTM E 647 ASTM E 399
CRACKING	X	X				CHEMICAL STRESS CRACK  SURFACE ROUGHNESS	ASTM F 46- AND F 180
CHEMICAL ATTACK	X	X				CHEMICAL EXPOSURE	ASTM D 543
DELAMINATION				X	X	MOLECULAR WEIGHT FLATWISE TENSION TORSIONAL SHEAR	ASTM D 388 ASTM F 87
MULTIPLE	X	X	X	X	X	STRESS WEATHERING COMBINED TESTS	

TABLE 3

## PROPOSED COUPON TEST PLAN

TRANSPARENCY MANUFACTURER	FAILURE MODES	TESTS	COMPONENT CONDITIONS	ENVIRONMENT BASELINE 2 EQ. YEARS ARTIFICIAL WEATHERING 4 EQ. YEARS	NUMBER OF HANDS HELD	REPLICATES	NUMBER OF COUPONS
F-111 PRO AND SEPPACON	ABRASION	OSCILLATING BAND (BAYER) SALT IMPINGEMENT	ACRYLIC ACRYLIC	X X	3 3	3 3	20 20
	AGING	HAZE AND TRANSMITTANCE IN SPECTROSCOPY OR X-RAY PHOTOELECTRON SPECTROSCOPY (XPS)	URANATE ACRYLIC	X X	3	1	18
	CRACKING	CHEMICAL STRESS CRACKS/ SURFACE ROUGHNESS	ACRYLIC	X	3	3	80
	CHIPPING	TENSILE EDGE ATTACHMENT	URANATE	X	3	5	42
	DELAMINATION	PLATINUM TENSION DIFFERENTIAL SCANNING CALORIMETRY (DSC) OF ULTRATHIN FILMS OF POLYMER (PMMA)	URANATE WHITE SLAYER	X X	3 3	5 1	42 18
						TOTAL	250

\* FROM FIRST HANDS HELD, ONLY 1 BROKEN TESTED FROM 2ND AND 3RD HANDS HELD  
 \*\* 1/2 OF 180 TRANSPARENT HAVE TESTING CONDUCTED AS PART OF SALT IMPINGEMENT

**TABLE 4  
CRAZE TEST RESULTS**

CHEMICAL APPLIED: TOLUENE								
VENDOR	BASELINE			4 WEEKS OF QUV			8 WEEKS OF QUV	
	SPECIMEN ID	RESULTS TRANSIENT (PSI)	PERMANENT (PSI)	SPECIMEN ID	RESULTS TRANSIENT (PSI)	PERMANENT (PSI)	SPECIMEN ID	RESULTS TRANSIENT (PSI) PERMANENT (PSI)
SIERRACIN	065-B-1	3500	2550	065-A/2-1	1700	180	065-A-1	2200 2100
	065-B-2	3350	3000	065-A/2-2	2800	2800	065-A-2	1900 1750
	065-B-3	3050	2850	065-A/2-3	2700	2000	065-A-3	1900 1750
	061-B-1	3200	3200	061-A/2-1	2400	2800	061-A-1	2500 2000
	065-B-1	3500	3400	065-A/2-1	2800	2550	065-A-1	2350 2000
	1203-B-1	2300	2250	1203-A/2-1	1350	1300	1203-A-1	1250 750
PPG	1203-B-2	2200	1800	1203-A/2-2	1800	1250	1203-A-2	1400 800
	1203-B-3	2250	2250	1203-A/2-3	450	450	1203-A-3	1200 900
	1869-B-1	2200	2400	1869-A/2-1	1450	1450	1869-A-1	1400 1250
	7963-B-1	2450	2050	7963-A/2-1	1400	1800	7963-A-1	1750 1750
CHEMICAL APPLIED: ETHYLENE GLYCOL								
VENDOR	BASELINE			4 WEEKS OF QUV			8 WEEKS OF QUV	
	SPECIMEN ID	RESULTS TRANSIENT (PSI)	PERMANENT (PSI)	SPECIMEN ID	RESULTS TRANSIENT (PSI)	PERMANENT (PSI)	SPECIMEN ID	RESULTS TRANSIENT (PSI) PERMANENT (PSI)
SIERRACIN	065-B-4	1500	1500	065-A/2-4	900	1050	065-A-4	2000 1400
	065-B-5	1500	1750	065-A/2-5	1000	950	065-A-5	1100 1300
	065-B-6	1100	1500	065-A/2-6	750	500	065-A-6	1200 1400
	061-B-2	1600	1850	061-A/2-2	400	2100	061-A-2	1500 1000
	065-B-2	1200	1400	065-A/2-2	1050	1450	065-A-2	1250 1400
	1203-B-4	500	1100	1203-A/2-4	300	400	1203-A-4	300 800
PPG	1203-B-5	550	1050	1203-A/2-5	850	800	1203-A-5	250 800
	1203-B-6	600	750	1203-A/2-6	250	750	1203-A-6	280 800
	1869-B-2	1250	1500	1869-A/2-2	1250	1150	1869-A-2	250 300
	7963-B-2	1300	2500	7963-A/2-2	250	500	7963-A-2	750 450
CHEMICAL APPLIED: ISOPROPYL ALCOHOL								
VENDOR	BASELINE			4 WEEKS OF QUV			8 WEEKS OF QUV	
	SPECIMEN ID	RESULTS TRANSIENT (PSI)	PERMANENT (PSI)	SPECIMEN ID	RESULTS TRANSIENT (PSI)	PERMANENT (PSI)	SPECIMEN ID	RESULTS TRANSIENT (PSI) PERMANENT (PSI)
SIERRACIN	065-B-7	2600	1950	065-A/2-7	1500	1000	065-A-7	1800 1800
	065-B-8	1800	1900	065-A/2-8	1800	1750	065-A-8	2000 1700
	065-B-9	1750	2000	065-A/2-9	1950	1800	065-A-9	1800 1500
	061-B-3	2350	2400	061-A/2-3	1250	1300	061-A-3	1750 1750
	065-B-3	2200	2400	065-A/2-3	1800	1550	065-A-3	1800 1750
	1203-B-7	1200	1100	1203-A/2-7	800	750	1203-A-7	850 800
PPG	1203-B-8	1300	1050	1203-A/2-8	850	1000	1203-A-8	850 800
	1203-B-9	1500	1400	1203-A/2-9	1400	1000	1203-A-9	850 300
	1869-B-3	1300	1250	1869-A/2-3	1400	1800	1869-A-3	1100 500
	7963-B-3	1500	1800	7963-A/2-3	750	1100	7963-A-3	1250 1250

\* 0.5X2.1 IN. SIZE AT FOLLOWS AFTER 10 MINUTES OF TESTING



TABLE 5  
EXAMPLE RAW FIELD SERVICE DATA FOR THE F-111

SEQ	MANUF	DOM	SN	WT	DATE REMOVED	ACFT & BASR	DATE INSTALLED FROM ACFT W48 RECORDS	SERVICE LIFE (YEARS)		COMMENTS
								DOM TO DATE REMOVED	DATE INST TO DATE REMOVED	
5	SIER	10/82	633	49.3	5.5/83	AC 161 380MPS F111 B/A (FB-111A)		2y 6m		
52	SIER	9/79	207	49.9	?	FB111 68-260 SM-ALC				
67	SIER	2/84	771	48.4	7.5/83	FB68-278 SM-ALC		1y 5m		
91	PPG	7.5/80	015-044	47.8	2/85	8066 F111B		4y 6.5m		
133	SIER	4/82	373	50.5	10.5/83	27EM5 F111D 68-162		1y 6.5m		
142	SIER	?	?	?	?	SM-ALC (NO OTHER INFO)				
152	PPG	7/81	015-374	2.8	12/84	27EM5 2A0102 F111D		3y 5m		
156	PPG	7/81	015-370	48.5	?	?				
158	PPG	8.5/81	015-423	47.9	5/83	(NO PAPERWORK) SM-ALC		1y 8.5m		

F-111 TRANSPARENCIES:  
FAILED PARTS AT SM-ALC WAREHOUSES 3 FEB 86 4 MAR 86

TRANSP: LHM3, SENT TO WPAFB

PAGE: 1

SESSION V

TESTING TECHNOLOGY - PART B

Chairman: S. Wortman  
McClellan Air Force Base

Co-Chairman: K. Clayton  
University of Dayton

Coordinator: G. Brockfeld  
Flight Dynamics Directorate  
Wright Laboratory

## ASSESSMENT OF DURABILITY OF FULL-SCALE TRANSPARENCY SYSTEMS

S. Hamilton  
G. Brockfeld  
Flight Dynamics Directorate  
Wright Laboratory

---

## **ASSESSMENT OF DURABILITY OF FULL SCALE TRANSPARENCY SYSTEMS**

LT SCOTT HAMILTON  
Durability Research Project Engineer  
WL/FIBT  
(513) 255-2318

LT GRETCHEN BROCKFELD  
Durability Research Project Manager  
WL/FIVR  
(513) 255-4926

Wright-Patterson Air Force Base, OH 45433

---

### **1. Introduction**

Today's high performance aircraft require increasingly complex transparency systems to meet changing mission requirements. At present, aircraft transparencies must meet a variety of specifications including birdstrike protection, optics, and weight. Many of these high performance, high cost transparency systems, however, are experiencing short service lives. A need exists for specifying the durability of a transparency system during the procurement process in order to reduce the overall life cycle costs of the system.

To meet this need, however, durability test methodologies and criteria must first be established. The Structures and Vehicle Subsystems Divisions of the Flight Dynamics Directorate, Wright Laboratory, have teamed up to develop and validate a full-scale transparency durability test methodology. Overall program management is provided by the Aircraft Windshield Systems Program Office (WL/FIVR), while testing technology is developed and applied by the Structures Test Branch (WL/FIBT).

The Aircraft Transparency Durability Research Facility (ATDRF) is an essential tool in the overall effort to develop durability test methodologies. In conjunction with several coupon-scale tests that are under development, it should provide a sound basis for assessing the durability of aircraft transparencies at the beginning of the procurement process. The main goal is to gain control of transparency durability at the point of acquisition rather than through belated correction of field problems. This can be accomplished by applying validated durability test methodology to enforce required product quality.

---

## **ASSESSMENT OF DURABILITY OF FULL SCALE TRANSPARENCY SYSTEMS**

---

### **2. Methodology/Purpose**

Wright Laboratory's Flight Dynamics Directorate began researching methods for evaluating the durability of aircraft transparencies in 1974. Initial testing methodology exposed the aircraft transparencies to typical flight pressures and temperatures by evacuating or pressurizing the cockpit module, and radiant heating with quartz lamps. The cockpit module consisted of an actual aircraft fuselage to insure that the transparencies were subjected to proper boundary conditions.

The structural use of composite and plastic materials in aircraft has increased over the years. These materials have a broad range of coefficients of absorption and reflectivity versus wavelength, which caused the results of tests using standard radiant heating techniques to be questioned. Radiant heating of laminated transparencies caused premature debonding at interlaminar boundaries, as each layer was affected differently by the radiant energy from the lamps. Under actual conditions, the heat transfer is mainly conducted from the outer surface through the transparency's thickness.

The need to develop a method of testing aircraft transparency lifetime durability with respect to thermal and pressure loads in a more realistic simulation of actual conditions led, in 1978, to the start of Work Unit No 24010508, Convection Heating Technology for Structural Testing. This development began with the concept of a one-loop system utilizing a single thermal conditioning unit upstream of the test section and eventually grew into a system utilizing two independent thermal conditioning loops and a dependent test loop. This system, called the Convection Heat Test Facility (CHTF), was developed to prove the concept of durability testing using convective heat transfer. Transparencies for the F-16 and F-111 were successfully tested in this system between 1980-1987.

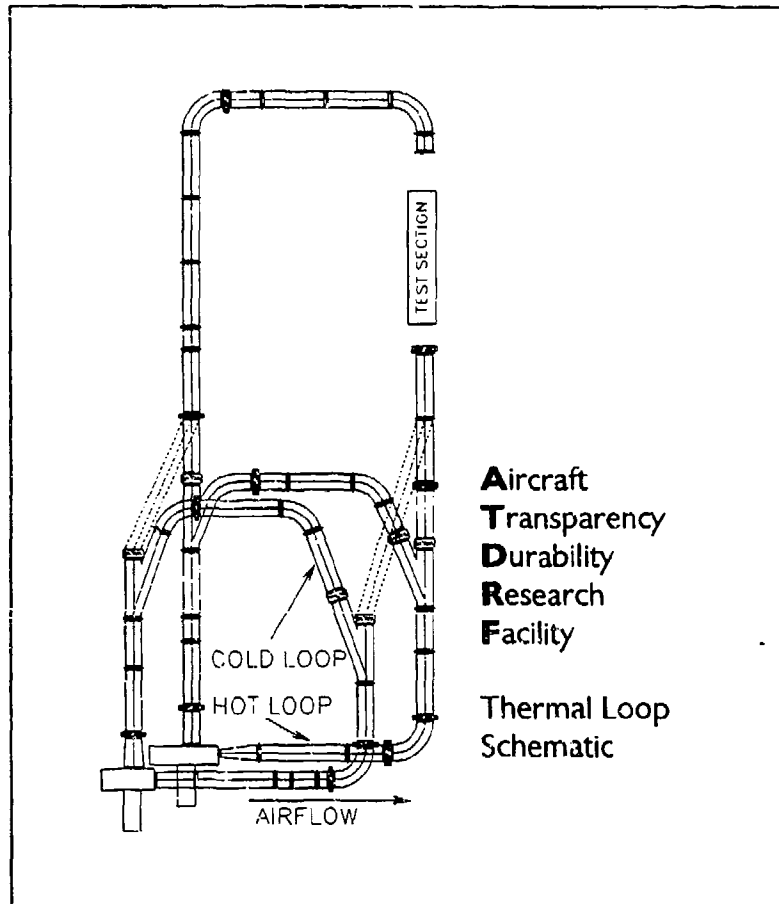
### **3. Facility Description**

This test facility was relocated to a separate building, mainly for space and noise considerations in 1987. The new facility was designed to overcome the limitations of original setup. The new design increased thermal efficiency, minimized pressure losses in the system and turbulence in the test section, and surpasses the performance and capabilities of the original system. The maximum temperature rating is 1000 °F, and minimum is -100 °F. The design maximum rate of change for the surface temperature of the glass is 5 °F/s.

The methodology used to guide the facility is based on attempting to recreate flight temperatures and loads experienced by the transparencies. To do this, the external transparency temperature is controlled, as well as the interior air temperature and interior air pressure (and vacuum). Each of these parameters has an associated set of centralized, computer-controlled hardware, and some independently controlled hardware. The external surface temperature control system has five subsystems dependent on the central

## ASSESSMENT OF DURABILITY OF FULL SCALE TRANSPARENCY SYSTEMS

Vax and no independent hardware. The internal air temperature control system has two dependent subsystems and one associated set of independent hardware. The internal pressure control system has three dependent subsystems and two associated sets of independent hardware.



The centralized computer resource is a Vax 4200 with 32 megabytes of RAM and 700 megabytes of hard disk storage. An ADAC expansion bus controls all output signals, and all input signals are through a NEFF 470 signal conditioning unit.

The external surface temperature is controlled by passing hot or cold air through the test section. Air flow in the facility is through two independent loops (hot and cold thermal conditioning loops) and one dependent loop (test section). The test section contains the transparencies, mounted in a sealed cockpit fuselage, and a shroud that covers the cockpit and forms a closed loop system. The shroud is unique for each aircraft tested and is designed to provide for a 10% per linear foot decrease in the cross-sectional area of the airstream, providing for a more realistic front-to-rear temperature distribution over the surface of the transparencies. The ductwork is made of 10 gage 24" diameter stainless steel. Air flow is provided by two variable speed, low pressure centrifugal fans which comprise the first two dependent subsystems of the external temperature control loop.

## **ASSESSMENT OF DURABILITY OF FULL SCALE TRANSPARENCY SYSTEMS**

---

Each fan provides continuously variable airflow from 12,000 to 24,000 CFM at the extreme service temperature for each loop. The fans use variable speed (frequency control) motors. The Vax outputs 1-10 volts through an ADAC card to adjust the speed. A proximity switch on each fan measures the speed, and feeds back a 1-10 volt signal into the Vax through the NEFF 470.

The third dependent subsystem of the external temperature control loop is the Hot Loop SCRs. The Hot Loop continuously circulates air at temperatures up to 1000 °F. The air is heated by six 60 kW resistance type duct heaters. The heaters are controlled by two 300 amp, 480 v SCR controllers. The 0-5 volt drive for the SCRs is generated by the Vax microcomputer through an ADAC card. Feedback to the Vax is provided by averaging three J-type thermocouples probes inserted into the ducting. The setpoint for the Hot Loop is approximately 20% to 40% higher than the maximum surface temperature required, dependent upon the maximum temperature rise rate required. The Hot Loop will follow a profile loaded into the Vax so that more (or less) heat is available as required by the mission profile.

The Cold Loop, the fourth dependent subsystem of the external temperature control loop, continuously circulates air at temperatures as low as -100 °F. Liquid nitrogen, supplied by a local 11,000 gallon dewar, is injected into the airflow immediately downstream of the Cold Loop fan to cool the loop. A two inch cryogenic globe valve is operated by a 0-5 volt control signal generated by the Vax microcomputer through an ADAC card to maintain the loop temperature. Three T-type thermocouple probes inserted into the airstream are averaged for control feedback. The setpoint for the Cold Loop is approximately 20 °F to 50 °F lower than the minimum surface temperature required, dependent upon the maximum temperature fall rate required. The Cold Loop follows a profile loaded into the Vax so that more (or less) cooling capability is available as required by the mission profile.

Six sets of 24-inch opposed louver valves control the airflow, three on each thermal conditioning loop. The first allows for airflow into the test section, the second controls the bypass section, and the third allows returning airflow to enter the thermal conditioning loop. These valves are the fifth and final dependent subsystem of the external temperature control loop which consists of two parts: controlling valve movement and determining valve position. In order to control valve movement, each valve has a resolver that reads valve position and outputs a corresponding 0-1000 hertz analog signal on a 10 volt carrier wave to an Autotech valve position unit, which outputs 0-900 millivolts to the Vax. The Vax sends out  $\pm 10$  volts from an ADAC card to an AC/DC servo amp which drives a 5 horsepower DC motor to move the valve. Valve position is calculated by the Vax based on feedback from T-type ribbon thermocouples on the surface of the canopy.

The cockpit interior temperature is controlled so that the transparencies experience the correct through-the-thickness thermal gradient. The interior temperature control loop has two dependent subsystems and one independent associated set of hardware. The

---

## **ASSESSMENT OF DURABILITY OF FULL SCALE TRANSPARENCY SYSTEMS**

---

temperature extremes required to simulate extended exposure to both hot and cold runway cockpit temperatures necessitated using 5 kW duct heaters and gaseous nitrogen instead of the prior unit, a conventional air conditioning coil, to cool the cockpit. Four, 10 inch DC fans provide for 3800 cfm of air circulation.

The heaters are controlled by one 100 amp, 480 volt SCR controller which the Vax drives with a 0-5 volt signal from an ADAC card. The gaseous nitrogen is controlled by a 1 inch cryogenic ball valve, operated by a 0-5 volt control signal generated by the Vax. These two dependent subsystems use three T-type thermocouples suspended in the cockpit to provide feedback to the Vax.

The nitrogen is fed from a one inch line from a local 11,000 gallon dewar, and goes through an independent heating manifold prior to entering the cockpit to insure that the nitrogen is gaseous. A thermocouple reads the temperature in the manifold, and trips a relay to activate a bank of 10, 1500 watt nichrome heater lamps as long as the gas temperature remains below -280 °F.

The transparencies are subjected to a net pressure loading based on the calculated net dynamic pressure loading from cockpit pressurization, altitude, and aircraft velocity at that point in the profile. The pressure load is applied by evacuating or pressurizing the cockpit as necessary. The cockpit pressure control loop consists of three dependent subsystems and two associated set of independent hardware.

The air compressor, rated for a continuous duty cycle at 125 cfm at 120 psig, maintains a 640 gallon air reserve at 105 psig. The vacuum pump, rated at 475 cfm at 24 inHg, maintains a 200 gallon vacuum reserve at -14.7 psig. These two independent subsystems are both connected to the cockpit fuselage section by a single two inch pipe, the pressure feed line.

The pressure and the vacuum lines each have individual two-inch, normally closed globe valves, driven by a 4-20 milliAmp signal generated by an ADAC card in the Vax. Two LVDT transducers, reading -2 to +15 psig, output 0-30 millivolts to provide feedback to the Vax. The pressure and vacuum line valves are positioned prior to the junction where the individual pressure and vacuum lines tee into the pressure feed line. These two dependent subsystems are controlled to follow the pressure profile appropriate to the mission loaded into the Vax.

The cockpit also has two two-inch vent lines that are open to the atmosphere. The vent lines are controlled by two-inch normally open globe valves driven by 4-20 milliAmp signals generated by an ADAC card in the Vax. The vent lines allow the control system to compensate for the pressure fluctuations caused by the use of gaseous nitrogen to cool the cockpit, and to provide for emergency dump capability for pressure in the cockpit. Also, the pressure feed line has a two-inch, normally closed ball valve to allow for additional emergency venting. It is controlled by the abort circuitry (discussed below) and opens immediately whenever an abort relay is tripped.

---



## **ASSESSMENT OF DURABILITY OF FULL SCALE TRANSPARENCY SYSTEMS**

The Vax monitors all data channels ten times each second, and alerts the Test Operators if any critical test parameters are deviating from normal conditions. Critical test parameters are defined as those measured conditions directly affecting the test article, namely the external surface temperature, the cockpit air temperature, and the cockpit pressure. The Vax will show three levels of error: follow, warning, and abort. Following errors indicate that the control channel is experiencing small, acceptable variations. Warning errors indicate that the control channel is experiencing conditions that, if sustained, may jeopardize the validity of the test. Abort level error is triggered to prevent damage to the test articles.

When a critical test parameter reaches abort level, the control system engages a digital dump which trips a relay, engaging the abort circuitry. The abort circuitry sends a five volt signal to open the dump valve on the pressure feed line and cuts all drive signals to the pressure control subsystems, closing the pressure feed valves and opening the vent valves. The control system automatically begins to ramp the internal/external temperatures to a safe level (70 °F). If the control system cannot do this automatically, the Test Operators can engage Manual Control Circuitry, which immediately disconnects all computer drive signals, and manually adjust the drive signals. Once the test articles are secured, all subsystems are set to a dump condition; that is, they are disconnected from all drive signals, computer and manual.

Two thirty-two channel data loggers act as a redundant data system. The data loggers have relays which can activate the Facility Control Console safety circuitry. The pressure system has a mechanical Dwyer set to -1/-7 psig to act as an independent redundant dump system.

Due to the amount of data being monitored, it is only recorded every ten seconds. However, the last 100 data points for 28 critical data channels, representing the last ten seconds of testing, are saved separately in case of an abort. This allows for detailed examination of the final conditions that led to the abort.

### **4. Summary of Past Test Results**

The F-16A began pressure fatigue cycle testing in February 1980 and continued until August 1980, when preparations were made to begin full scale flight test simulation. Full scale testing began in conjunction with runway soak and ultraviolet conditions in April 1982 and ended in August 1983. The previously unreported failure mechanisms that occurred in this test, cracking of the acrylic ply, began to show up in the field within one year, showing the applicability of the convective heat test method.

The F-111 transparency began full scale flight test simulation in August 1985 and ran through September 1987. At this time, due to space constraints and growing requirements for other test programs, the facility was moved from inside Building 65 to Building 68.

After the new facility became fully operational in May 1990, the final set of F-111

## **ASSESSMENT OF DURABILITY OF FULL SCALE TRANSPARENCY SYSTEMS**

---

transparencies was tested. These tests continued through September 1990. All F-111 tests showed a good correlation to field service failures. One particular test article experienced a large growth in delaminations, especially after high-speed missions. A limited number of similar transparencies test were flown in Upper Heyford and Lakenheath, England, and were removed after as few as 100 hours for delaminations. The crew chief confirmed that he first noticed the delamination upon the aircraft's return from a high-speed mission.

The B-1B transparency underwent full-scale flight test simulation from June 1992 through January 1993. Both pilot and copilot production and prototype transparencies were tested. None of these transparencies experienced the delamination problem to the extent as reported on aircraft in the field. This test and its ramifications will be more fully discussed in the next section.

Currently, the F-16 transparencies are undergoing durability testing. Testing of the F-16 began in August 1993 and is scheduled to go through November 1994.

### **5. B-1B Test Results**

B-1B full-scale durability testing was conducted at Wright-Patterson AFB from 16 Jun 1992 to 29 Jan 1993. The results of the full-scale testing are inconclusive, since the failure mechanism most common in the field (delamination between the polycarbonate structural layer and the exterior glass ply) was not the cause for removal for either of the production windshields or either prototypes.

After the conclusion of the full-scale testing, representatives from WL/FIBT and WL/FIVR met to account for the discrepancy between the test results and the field data. According to B-1B IMPROVED WINDSHIELD DEVELOPMENT: VOLUME I, REQUIREMENTS AND ALTERNATE SYSTEM DEFINITION (CLAYTON AND BOUCHARD, WL-TTR-91-3087), the thermally tempered outer glass ply is responsible for the delaminations in the field, since the thermally tempered glass does not conform exactly to the compound curvature of the B-1B windshield. The interior stresses caused by this enforced displacement from the natural position of the glass ply were found, using finite element analysis, to be greater than the ultimate strength of the silicone interlayer. Changing the outer ply to chemically tempered glass, which can be more easily formed to match the compound curvature of the polycarbonate structural ply, was the recommended solution and was implemented on all prototypes. This theory would indicate that delamination was mainly a function of time, which could very possibly be accelerated by the induced thermal and mechanical stresses inherent to the full-scale testing environment. The results of the full-scale testing, however, do not reinforce this assertion.

The production B-1B windshields in the field exhibited lifetime of six to eighteen months, where one year is equivalent to 350 flight hours. However, the production windshields tested in the full-scale facility did not experience any delamination greater than 1/4" deep and 3/4" wide until well into the third simulated year of testing (917 hrs total simulated flight time). The delaminations occurred only after the decision was made to attempt to

---

## **ASSESSMENT OF DURABILITY OF FULL SCALE TRANSPARENCY SYSTEMS**

---

increase the presence of humidity on the test articles. This was accomplished by cutting the edge sealant back to expose the edge of the copilot transparency and spraying water directly on the exposed surface at each inspection (roughly six to eight hour intervals). After 963 hours of simulated flight, the copilot windshield experienced a delamination approximately 1/4" deep that ran along most of the lower, outer edge. This delamination showed no further signs of growth.

Neither prototype windshield experienced any delamination and both were removed after 607 hours of simulated flight. The prototypes were not expected to sustain any significant damage at this point, based on the results of the baseline testing.

### **6. Lessons Learned from B-1B Full-Scale Testing**

The lack of correlation between damage sustained by the test articles and the damage experienced by windshields in actual field service indicated that either the facility was not exposing the test articles to a condition (or conditions) critical to failure, or that the facility's conditions were not severe enough to promote gross delamination. The latter condition was dismissed by WL/FIVR personnel, who expressed a high degree of confidence in the temperature range of the flight profiles.

The decision to go ahead with full-scale testing was not preceded by much analysis or any testing. Ideally, the expected failure modes should be listed, and the expected conditions that cause such failures. Then, realizing that both methods have inherent strengths and limitations, coupon or full-scale testing should be identified as the most advantageous method with which to continue. Neither this, nor any similar procedure, was done prior to the B-1B testing. The lack of communication and shared knowledge between the coupon and full-scale personnel contributed greatly to the lack of an orderly approach.

### **7. Follow-on B-1B Testing**

Since the conditions in the facility did not cause the transparencies to delaminate, various possible synergistic conditions were investigated through system analysis, literature surveys and contact with the vendors for the B-1B windshields. The following specific factors were investigated:

#### **Factor: UV**

- ♦ Theory: Exposure to UV degrades silicone/glass adhesion.
  - One vendor reported testing the silicone layer after combined UV/humidity exposure, and reported that it did decrease the effective strength of the interlayer in peel tests.

#### **Factor: A/C structural loads carried by transparencies**

- ♦ Theory: Torsion/bending loads in A/C add shear/tension forces to interlayer.
  - The B-1 windshield was originally designed to be a load-carrying member. This requirement was later removed, but the windshield design was not changed. However, vendors report that the actual loads carried by the transparencies are minimal.

## ASSESSMENT OF DURABILITY OF FULL SCALE TRANSPARENCY SYSTEMS

---

### Factor: A/C vibrations

- ♦ Theory: Harmonics affect normal stresses present in transparency interlayers.
  - No support for this theory could be found.

### Factor: Structural changes to B-1B test module

- ♦ Theory: The test module was modified from a B-1A ejection seat module test fixture, and was refitted to conform to B-1B structural specifications around the transparencies. However, the entire underside of the module was rebuilt with 3/8" stainless steel to hold test equipment and a 6 psi positive pressure load condition. This considerable mass of metal did act as a large heat sink, which resulted in some unusual temperature gradients across the transparency during hot missions.
  - All the non-standard modifications were structurally removed from the edges of the frames, so the pressure load distribution applied to the transparencies should not differ from that in an actual aircraft.
  - The temperature gradients caused by the heat sink, while not representative of conditions experienced in flight, were not significant enough to affect the interlayer directly.

### Factor: Humidity

- ♦ Theory: Exposure to humidity degrades silicone/glass adhesion.
  - Silicone adhesion is due to weak molecular forces and therefore resists absorption of liquid water due to low surface energy, but water vapor readily migrates into silicone elastomers. Degradation of bonds may occur by hydrolysis of silicon/oxygen bonds or disruption of electrostatic bonding sites. Additionally, testing has shown that water exposure caused a rapid reduction in peel strength with SS 6569, a conventional glass primer used by one of the vendors initially. "SILICONE INTERLAYER ADHESION CHARACTERISTICS," JUENGST, LEMASTERS, AND WANG; WRDC TR-89-4044
  - "... humidity exposure. . . is considered the most adverse environment for interlayer adhesion." "HEAT RESISTANT SHEET INTERLAYER," JE MAHAFFEY; AFML TR-76-54
  - Failure mode in field experience is adhesive (between silicone and glass), not cohesive, indicating a degradation of the silicone-primer bond or the primer-glass bond, or both.

All investigations showed that humidity is a major factor (if not the main factor) in silicone interlayer degradation. If the B-1B delaminations were solely a function of humidity, this would explain the full-scale testing results, but not the depth of the problem as reported in the field. Cases were reported to WL/FIVR where a transparency had delaminated in the crate, awaiting installation. These cases occurred early in the cycle, and were never wide-spread. Possible explanations for this are:

Different primers/adhesives used by manufacturers during production run:

- ♦ Increased capabilities of newer materials provided increased performance.
- ♦ All primers/adhesives are proprietary, and information about changes is not readily available.

Thermally tempered glass contours of test articles more closely match polycarbonate structural ply contours of test articles:

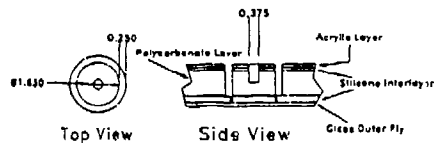
---

## ASSESSMENT OF DURABILITY OF FULL SCALE TRANSPARENCY SYSTEMS

- ♦ Since the test articles were from the end of the production run, constantly improving techniques throughout production run decreased amount of deviation of glass contour from polycarbonate structural ply contour.

Since no published data exists in the public domain on the effects of humidity on the interlayer of the B-1B transparencies, WL/FIBT, WL/FIVR, and UDRI decided to perform a joint investigation using actual B-1B transparencies as test articles. The test will involve pulling plugs from actual B-1B windshields so as to test the strength of the silicone interlayer/primer/glass system. Multiple tests will be performed on each windshield, allowing the windshield to be exposed to a progressive controlled

heat/humidity environment. A series of tests will then show the effect of humidity exposure over time on the strength of the silicone interlayer/primer/glass system over time.



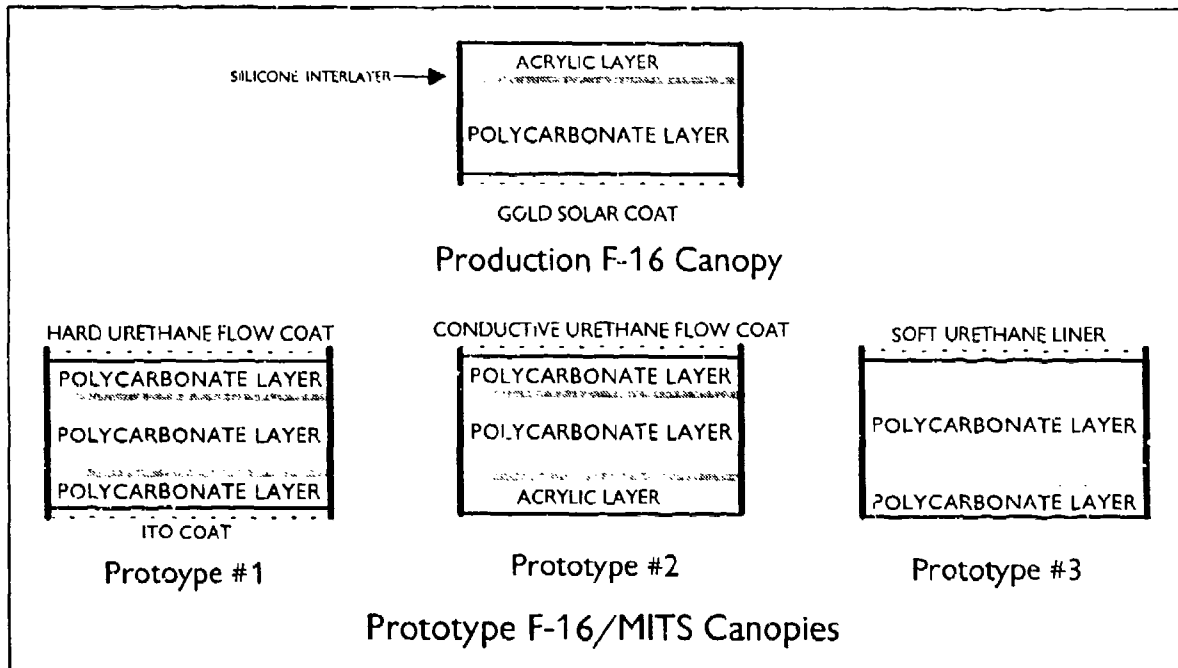
B-1B Follow-on Test Article Diagram

### 8. F-16 Advanced Canopy Coatings Project

The current full-scale durability testing is being conducted on the F-16 advanced canopy coatings project (in conjunction with the Mission Integrated Transparency System - MITS - project). The objective of this test is to evaluate the capability of three separate multi-functional durable coatings systems to withstand pressure and thermal load cycling of simulated F-16 a/c mission environments. The coatings are intended to protect the polycarbonate canopy structure against abrasion, crazing, and electrostatic discharge (ESD).

A total of four F-16 canopies will be tested in the facility. The test articles include one current production F-16 canopy and three canopies with prototype durable coatings. The current production canopy structure consists of a bare acrylic face ply with a polycarbonate structural ply and a gold solar coating on the inside (see figure below). The first prototype canopy design consists of a hard urethane flow coat on polycarbonate with an indium tin oxide (ITO) coating on the inner ply. The second is a conductive urethane flow coat applied to polycarbonate with a bare acrylic inner ply. The third is a soft urethane liner on polycarbonate. These prototype designs were selected because of their superior performance in coupon scale testing (rain erosion, abrasion, craze, hail impact, flex beam).

## ASSESSMENT OF DURABILITY OF FULL SCALE TRANSPARENCY SYSTEMS



The durability testing will subject the full-scale canopies to the pressure and thermal load cycling representative of the F-16 a/c mission environment. By using a full-scale test article, the effects of the canopy geometry and edge effects of the frame are accounted for, which is not possible in coupon-scale testing. Previous F-16 full-scale durability testing (in 1980) indicated that pressure and thermal cycling was a significant contributor to the failure of the older F-16 canopy designs.

For the first time, coupon-scale durability testing will be performed in parallel with the full-scale testing in an attempt to further understand mechanics involved in the failure of transparencies in the field. The thermal and pressure mission profiles will be applied to coupon samples of the prototype canopies in order to establish a correlation between coupon- and full-scale testing. In addition, half of the coupon samples will be exposed to ultraviolet weathering prior to durability testing. Coupon-scale testing of the prototype designs indicated that artificial weathering (QUV) was an important factor in the degradation of coating performance in most the tests (rain erosion, abrasion, flex beam).

Full-scale testing is scheduled to begin in early Aug 1993. Each canopy will be subjected to the equivalent of four year's worth of flight time (approximately three months of facility time). Testing should be completed by Nov 1994. The test methodology for the coupon-scale durability testing is still under development, but actual testing should take approximately three months total.

### 9. Facility Outlook - the Future

The mission of the ATDRF is to develop and validate test methodology and criteria to assess the service life of a transparency system. To successfully carry out this mission, several goals must be met.

## **ASSESSMENT OF DURABILITY OF FULL SCALE TRANSPARENCY SYSTEMS**

---

### **Short-term goals:**

- ♦ Establish a standardized method for gathering field data to verify mission profile calculations (temperature and pressure). This eliminates the last-minute scramble for information that can verify/disprove any questionable calculations.
- ♦ Establish a standardized procedure for calculating the mission profiles. Each test series, thus far, has used a different method for calculating the temperature and pressure profiles. It is important to first obtain valid aircraft mission profiles and then use the proper analytical methods to obtain the test profiles. STAPAT II, a transient, three-dimensional aero-thermal analysis code, was used to obtain the test profiles for both the B-1B and F-16 transparency tests.
- ♦ Establish a standardized procedure for determining the potential value of testing a transparency system in the ATDRF. Full-scale durability testing is too costly and time-consuming to test every new transparency system. There needs to be an established set of criteria for determining if the temperature and pressure cycling could potentially be a significant driver of the failure of the particular transparency design. This will be based on past experience of results from similar designs. Coupon-scale test methods are being looked at to assist in this determination.

### **Long-term goals:**

- ♦ Develop a coupon-scale durability test method that correlates to the full-scale method as well as the field service life data, potentially eliminating the need for full-scale testing. Full-scale testing is very expensive and, currently, transparencies can be tested only one at a time. A validated coupon-scale durability test method would save time and money.
- ♦ Increase efficiency of test preparations to minimize changeover time between tests. Currently, changeover time is about six months between different aircraft windshield tests. The time is used to install the new test stand, rewrite control system codes, and check out system functions. To reduce the backlog of upcoming tests, changeover time can be minimized by advance planning and preparations.
- ♦ Develop quantitative evaluation measures that can be used to evaluate new transparency designs independently, eliminating the need for a current production baseline test. The F-16 canopy test will be the first to utilize quantitative techniques (haze index, optical distortion, and birdstrike) to evaluate and monitor transparency degradation in the facility.
- ♦ Develop standardized durability test criteria that can be used in the procurement of transparency systems. The culmination of all durability efforts will be the establishment of durability requirements to be used in the procurement process of aircraft transparency systems.

## **10. Conclusion**

The Aircraft Transparency Durability Research Facility is a one-of-a-kind, state-of-the-art R&D test facility. Full-scale testing is less expensive than test-flying aircraft, but it is not suited to the variety of conditions applied to coupon testing (abrasion, rain-erosion, etc.).

---

## **ASSESSMENT OF DURABILITY OF FULL SCALE TRANSPARENCY SYSTEMS**

---

The development and validation of durability test methodologies and criteria will lead to the establishment of durability requirements for future transparency systems, but this will only happen with an integrated testing methodology. The various aspects of full-scale testing need to be fully investigated so that future transparency research can easily choose the proper technique for the most accurate and efficient results.

---

### **REFERENCES:**

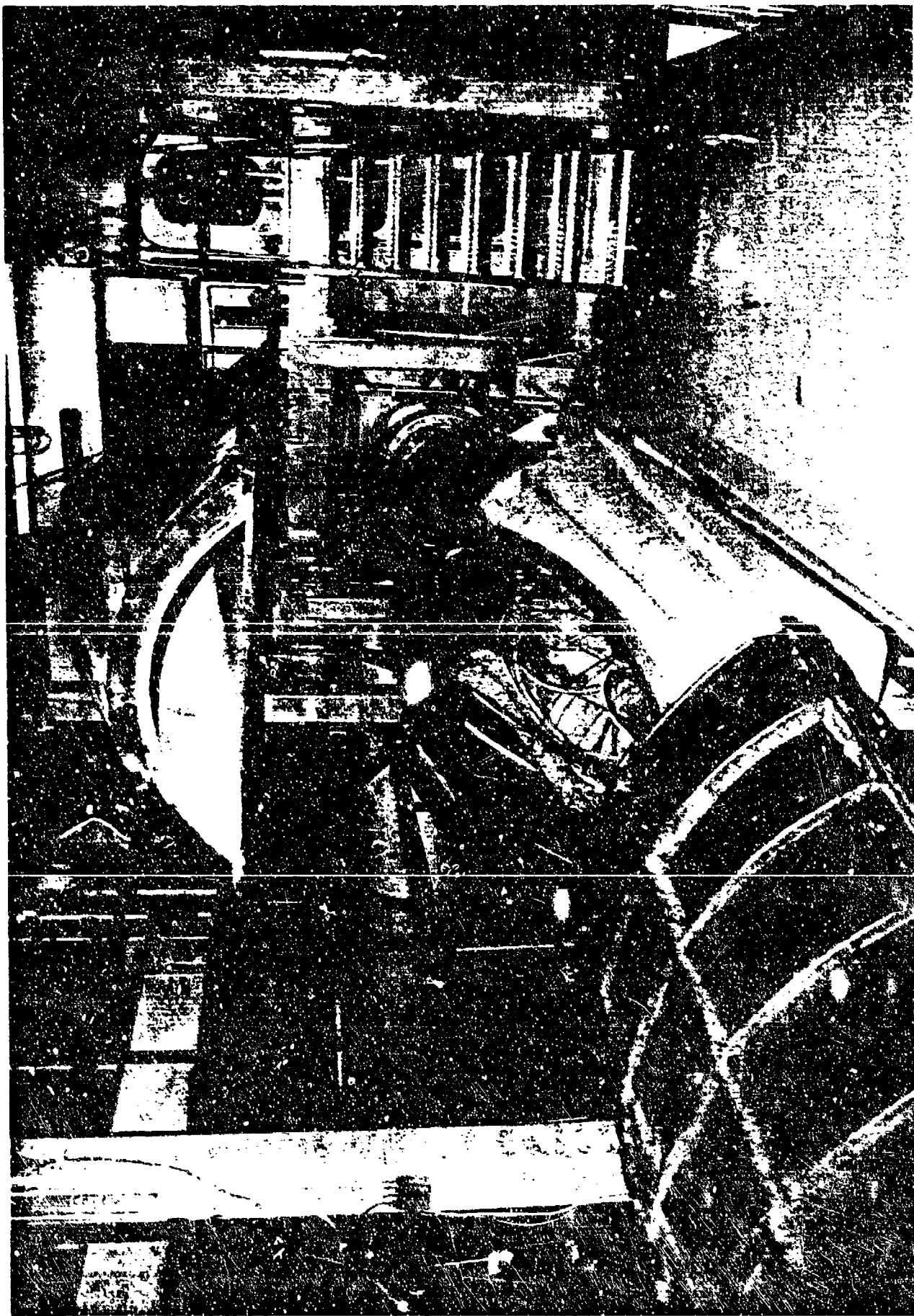
Clayton, K. I. and M. P. Bouchard: "B-1B Improved Windshield Development: Volume I, Requirements and Alternate System Definition," WL-TR-91-3087.

Juengst, C., D. LeMasters and H. T. Wang: "Silicone Interlayer Adhesion Characteristics," WRDC TR-89-4044.

Mahaffey, J. E.; "Heat Resistant Sheet Interlayer," AFML TR-76-54.

---

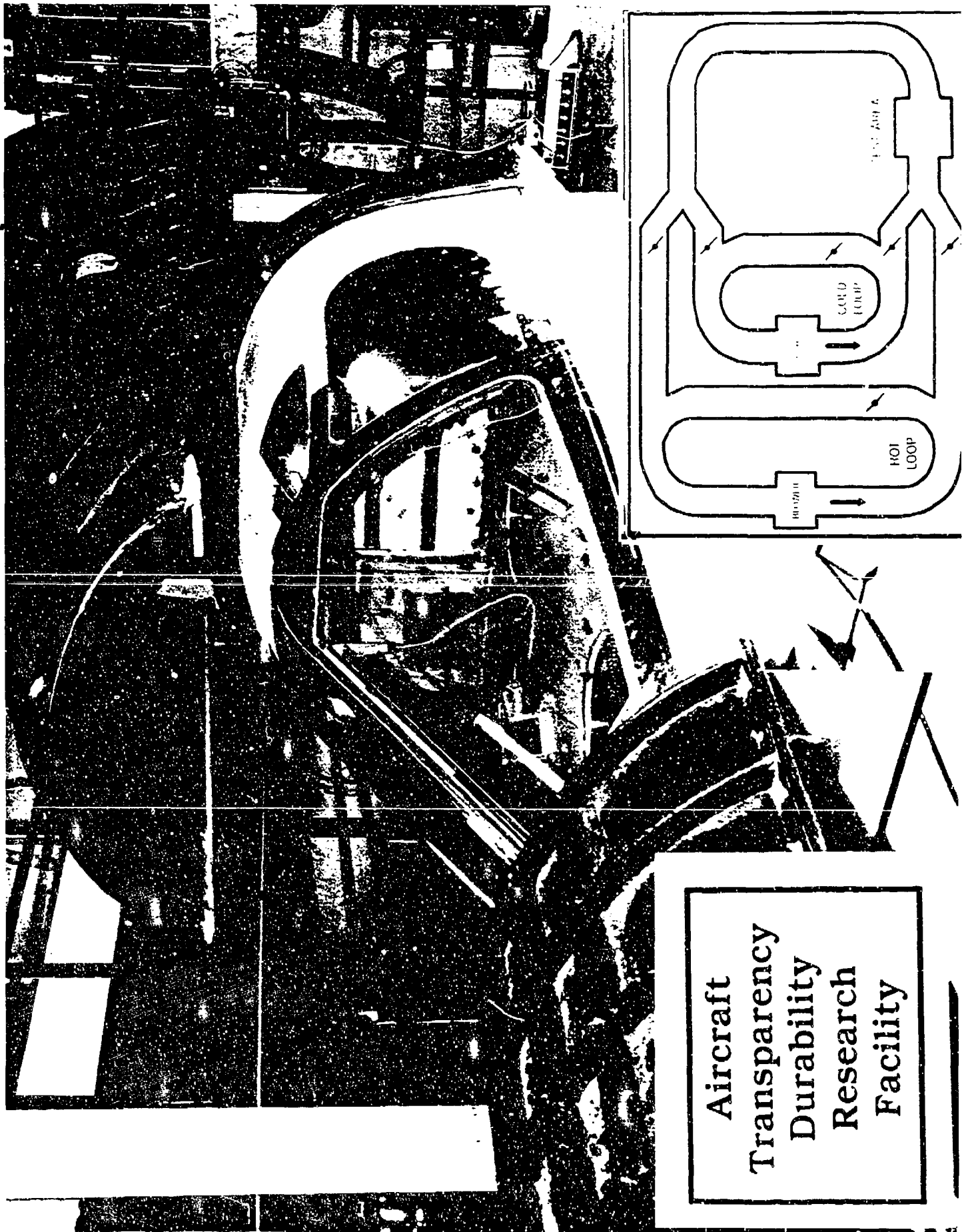




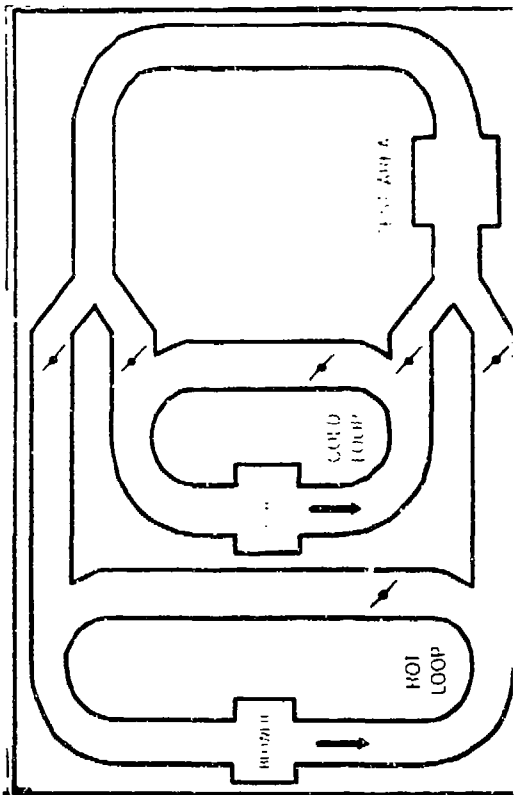
1. Full-scale Test Section - F-16 module



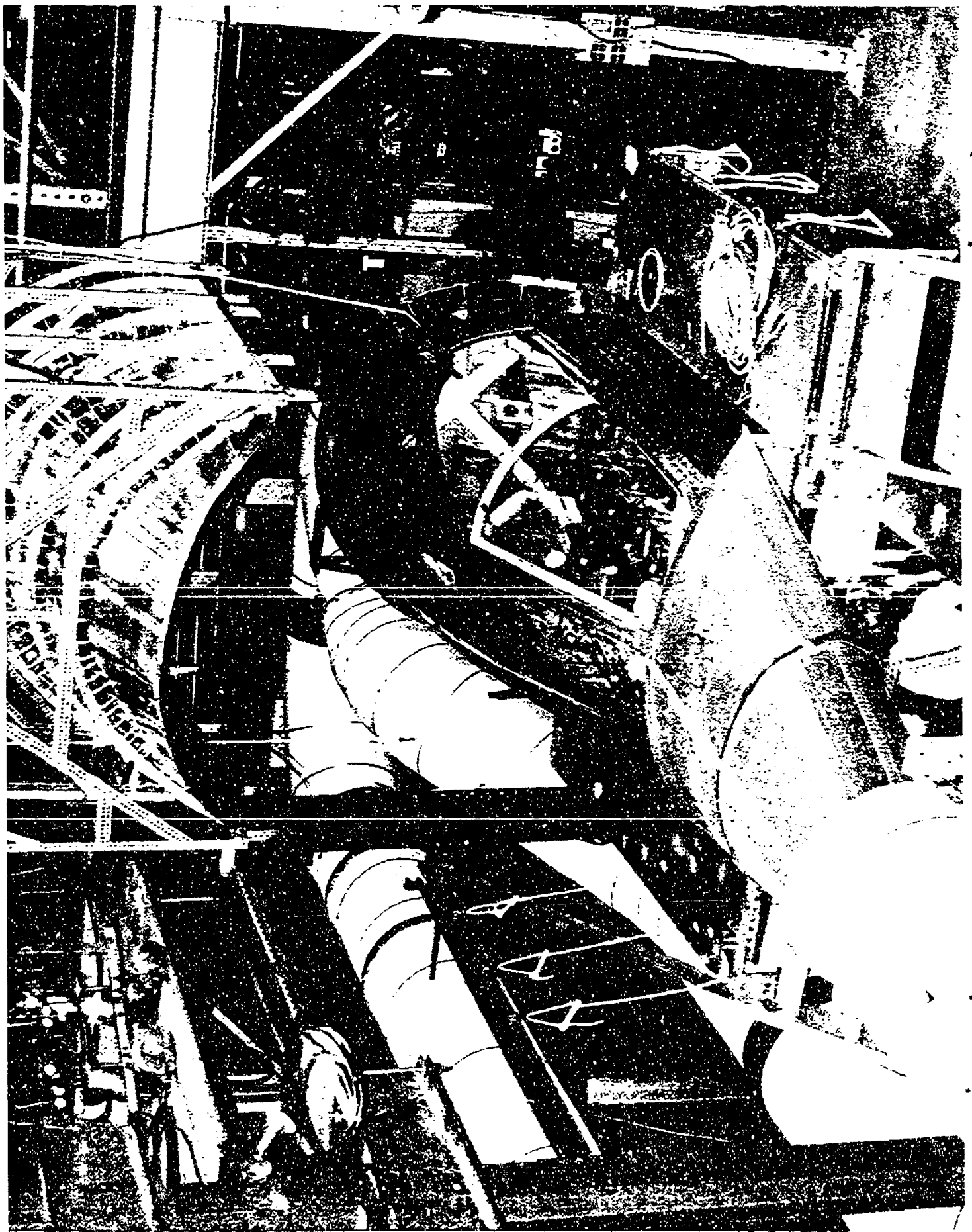
2. Control Room



**Aircraft  
Transparency  
Durability  
Research  
Facility**



3. Test Section - B-1B Module



4. Test Section -- Old Facility. F-111 Module

PRESSURE BURST TESTING OF KC-135 CELESTIAL NAVIGATION WINDOWS

T. J. Whitney  
D. R. Bowman  
University of Dayton

R. Urzi  
Flight Dynamics Directorate  
Wright Laboratory

# PRESSURE BURST TESTING OF KC-135 CELESTIAL NAVIGATION WINDOWS\*

*Thomas J. Whitney  
Daniel R. Bowman  
University of Dayton Research Institute  
300 College Park Ave.  
Dayton, Ohio 45469-0110*

*Russell Urzi  
WL/FIVR  
Wright-Patterson AFB, Ohio 45433*

**ABSTRACT:** The objective of this work was to contribute to the development of a removal for cause criteria for the KC-135 celestial navigation window by investigating the relationship between service-age and interlayer burst strength. The testing conducted in this program included pressure proof testing of the celestial window, and burst testing of the PVB interlayer. A suitable test system was developed which could be modified to test other transparency systems. Statistical analysis of the data was performed to estimate confidence intervals and extrapolate a lower age limit below which burst failure would not occur. A risk analysis based on the test data was also conducted.

## INTRODUCTION

There have been two catastrophic in-flight failures of KC-135 celestial windows, one in 1974 and one in 1988. Each of these failures has resulted in rapid decompression of the aircraft and a fatality. The location of the KC-135 celestial window on the aircraft is shown in Figure 1. The window is a 13"x15" glass/PVB/glass laminate, see Figure 2. No information was obtained regarding the failure of the first window in 1974. The cause of the glass ply failure was unknown for the 1988 failure; however, the cause of the failure of the fail/safe PVB ply was determined to be PVB degradation and subsequent fatigue cracking of the PVB at the periphery of the window [1]. In 1974 an engineering change was made to the window, which consisted of changing the bumper from PVB to a sealant and covering the PVB at the edge attachment with a sealant. Both transparency failures were the pre-1974 design.

During the life of the KC-135, celestial windows have been removed and replaced only if they no longer met the optical requirements. There is no requirement for removal and replacement after a given structural service life. In December 1988, for flight safety reasons, the interior surfaces of the celestial windows were covered with an aluminum skin to prevent additional failures. Also, a directive was issued to remove the celestial windows and replace them with an aluminum plate as plates became available. The celestial window failures coupled with the high average age of the fleet have led to general concerns over the effects of aging on interlayer materials' resistance to degradation, since there are a number of Air Force aircraft with windows of similar design which may be subject to similar degradation problems.

---

\*Performed under Contract F33615-90-C-3410 for the Flight Dynamics Directorate, Wright Laboratory, Wright Patterson AFB, Ohio.

While the use of aluminum skins provided a short term resolution to flight safety concerns, understanding the long-term degradation of fail-safe interlayers would allow use of these (and other similar) windows by specifying limits for their useful structural life. The objective of this work was to contribute to the development of a removal for cause criteria for the KC-135 celestial navigation window by investigating the relationship between service-age and interlayer burst strength. With this strength vs. age data and appropriate limits for acceptable risk, a removal for cause criteria based on structural durability can be developed.

## TEST ARTICLES

Table 1 lists the KC-135 celestial navigation windows obtained for testing, and includes manufacturing dates, approximate dates-of-removal, and approximate service age. Service age is defined as the difference between date-of-removal and date-of-installation, minus a value representative of the uncertainty in removal and installation dates. Uncertainty ranged from  $\pm 4.5$  months to  $\pm 6$  months depending on the manufacturing, installation, removal, and shipping data available for each window. Most specimens were received with the aluminum plate still attached. The amounts of adhesive remaining on the inner structural glass plies after plate removal were considered small and were thought not to affect PVB burst pressure results. Visual observations of the pre-test conditions of the windows showed a number of apparent delaminations between the PVB and the aluminum frame piece near the window edges (see Figure 2). Large voids (bubbles) were also present in the center portion of some windows, apparently between the glass and PVB plies. Rubber sealing compound on the edge mounting surfaces was often peeled away. When required, butyl rubber strips were placed in these locations to aid in sealing during the pressure tests. With the exception of the use of butyl rubber, no other specimen preparation was performed.

The majority of specimens were manufactured in the mid 1970's, and represented service ages of roughly 15 years. Figure 3 shows the distribution of estimated service ages of specimens used in this study. Note that the histogram is shifted toward the high service age end. This shift is a result of the availability of windows for testing: a far greater number of "older" windows have been removed since criteria for removal are based on the optical condition of the window.

## PRESSURE BURST TEST SYSTEM

The Pressure Burst Test System, Figure 4, was designed and fabricated specifically for this test program. The system consists of a two test cells fabricated to match the curvature of the left and right side KC-135 windows; a holding tank with an impact resistant polycarbonate lid in case of catastrophic failure; a portable air pressure source; pressure control hardware with computer controlled pressurizing of the test cell; and digital recording of pressure data. A video camera was used to record the test.

The test article (celestial window) was mounted inside the two-part test cell against flanges that matched the geometry of the transparency edges. The sealed test cell was placed

inside the 4'x4' steel containment box for testing. The box included a transparent, impact resistant polycarbonate lid through which the test was recorded on videotape. The system was designed to allow future expansion of capabilities. The containment box size can accommodate larger aircraft windows as well as other test hardware such as environmental controls. Computer system hardware and software can be used to acquire any analog signal, such as strain gages and thermocouples, and control numerous analog devices.

## TEST PROCEDURE

Proof tests of the windows in as-received condition and burst tests of the PVB interlayer were conducted on each window received. Proof tests were conducted first to assess the ability of the window as a unit to withstand high pressure. Pre-test calculations indicated that the inner structural glass ply should be capable of withstanding 60 psi. The proof test cycle consisted of a pressure ramp to 50 psi over 5 minutes (0.167 psi/sec), a 1 minute dwell time, and a depressurizing ramp back to 0 psi over 5 minutes. Ramp times were chosen to assure quasi-static loading. Visual inspections were made before and after each test.

If the window passed the proof test (completed the cycle with no pressure losses), a PVB interlayer burst test was conducted. Loading of the interlayer was assured by fracturing the inner glass structural ply prior to the burst test. A simple hammer blow on the inside surface at a corner, where the glass meets the phenolic edge material, resulted in a networks of cracks and minimal local chipping (Figure 5). The burst test cycle consisted of a ramp of 0.333 psi/sec until the interlayer could no longer hold pressure, at which point the test was terminated. Pre- and post- test visual assessments of the windows were made, including failure descriptions and locations.

Reference [2] provides further details on the Pressure Burst Test System and procedures used in conducting the tests.

## TEST RESULTS AND ANALYSIS

Table 2 lists the results of Proof Tests, PVB burst pressure for the Fail/Safe Tests, and descriptions of the PVB failure modes. The failure modes ranged from small PVB tears near the phenolic edge to "blowout" of the window, characterized by complete tearing of the PVB interlayer and large window pieces completely separated from the frame. Figures 5 and 6 show typical specimens after PVB failure.

Figure 7 shows the PVB burst pressures as a function of approximate service life. The data have been fitted with a least squares linear regression. The 99% and 99.9% confidence intervals on the burst pressures are also shown. The data indicate a gradual reduction of burst strength over long periods of time. In using linear regression to characterize the data the assumptions were made that the trend in strength with service age can be accurately represented linearly, and that the burst strength for a given age can be represented by a Normal distribution. The 99% confidence interval lower bound indicates the pressure below which, on average, 1% of



the windows in a random sampling of a specific service-age will likely burst. In other words, based on the observed variance of burst pressures, it is reasonable to expect that (on the order of) 1 window out of 100 randomly selected windows will have developed burst pressures below the 99% lower bound.

For a minimum burst pressure of 10 psi, the 99% confidence interval lower bound extrapolates to a service-age of 313 months. Equivalently, a 313 month-old window has a "Failure Risk" of 1 in 100 at 10 psi. For any service-age, a "Failure Risk" at 10 psi can be calculated by finding the confidence interval which passes through 10 psi at that service-age. Figure 8 shows the results of these calculations for service-ages from 0 to 500 months.

"Failure Risk" can also be established on a flight hour basis by simply dividing the number of flight hours at any particular service-age ( $A$ ) into the Failure Risk ( $R$ ). Assuming an average of 22.92 flight hours per month (275 per year), Flight Hour Failure Risk ( $R_{FH}$ ) is given by

$$R_{FH} = \frac{R}{(22.92)(A)} \quad (1)$$

The results of this calculation are given in Figure 9. Note that the graph does not include risk for service lives less than 100 months. Equation (1) results in artificially high risk for short service lives, since the graph of Failure Risk ( $R$ ) vs. Service Life ( $A$ ) is relatively flat for low service lives (Figure 8). From (1), no change in  $R$  results in increasing  $R_{FH}$  as  $A$  gets very small.

## RISK ANALYSIS

Testing of KC-135 celestial navigation window fail-safe interlayers demonstrated a gradual reduction in pressure retaining capabilities with increasing service life of the window. The following risk assessment was performed to assist in the definition of a removal-for-cause criteria, based on service life, for these windows. The risk assessment procedure follows MIL-STD-882C, Military Standard for System Safety Program Requirements.

### Hazard Severity

Hazard severity categories are defined to provide a qualitative measure of the worst credible mishap resulting from component failure. The severity categories defined in MIL-STD-882C are given in Table 3. Two previous in-flight failures have resulted in rapid cabin decompression and death of a crew member. Given this history, pressure bursting of the PVB interlayer is considered Category I, Catastrophic.

### Hazard Probability

The probability that a hazard will be created during the life of a transparency system can be described in terms of potential occurrences per unit of the population of windows in the field. It can also be described in terms of occurrences per flight hour of the fleet. In the pressure burst testing, linear regression analysis was used to identify confidence intervals for the reduction in

burst strength with service age. Using hazard probability definitions suggested by MIL-STD-882C [2], Hazard Probability Levels were defined and are shown in Table 4. Probability levels were assigned based on the proposition that more than 2 failures per year fleet-wide is considered "Frequent." The Failure Risk associated with 2 failures per year is approximately 5/100 (95% confidence bound). The remaining Hazard Probability Levels were based on decade or half-decade increments of Failure Risk. Number of Fleet occurrences and Service Ages were obtained from Figures 8 and 9. It must be emphasized that the actual distribution of service-ages in the fleet is not accounted for in this analysis. That is, Number of Flight-Hour Occurrences assumes that all windows have service-ages equal to that given in the Service Age column. For removal-for-cause criteria purposes, this represents a conservative approach, since at any given time, some windows will have service lives less than the recommended removal age. It must also be emphasized that the confidence bounds, and therefore the Failure Risk and Service Age estimates, are based on the variance in burst pressure demonstrated in actual pressure burst testing.

### **Hazard Risk Index**

The Hazard Risk Assessment Matrix from MIL-STD-882C is shown in Table 5. For the Catastrophic category, of which interlayer burst is a part, probability levels down through Level C (0.1 to 0.5 failures for every 1000 windows) must be prevented. Risk associated with Level D (0.05 to 0.1 failures for every 1000 windows) is undesirable, while risk associated with Level E is acceptable.

### **Removal-for-Cause Criteria**

Based on Tables 3, 4, and 5, risk analysis indicates that requirements to prevent failures numbering 0.5 per 1000 service aged windows (0.017 per 100,000 flight hours) would be satisfied by replacing the window when service life reached 126 months, or 10.5 years. A ten-year change-out cycle would eliminate Unacceptable and Undesireable risk, as estimated by the pressure burst test results. However, risk defined as Acceptable with Review would still remain.

## **CONCLUSIONS AND RECOMMENDATIONS**

Currently, KC-135 celestial navigation windows are replaced only if the window fails to meet optical requirements. Like many other windows of this design, no criteria exist which specify removal based on likelihood of structural failure due to material degradation. This work is a first step in establishing such criteria. A removal for cause criteria based on a 10 psi minimum for the 0.05% Failure Risk level would require replacement of the window after 10.5 years of service-age had elapsed. However, it must also be recognized that this program addresses only the PVB fail-safe layer of the window. For a window blow-out to occur, both the inner and outer glass plies must also fail. No effort has been made to assess the risk associated with glass ply failure.

A planned changeout of 10.5 years represents a considerable reduction in risk compared to current optical criteria, which may have windows in service for 25 years or more. Two points

help to underscore this reduction. First, two catastrophic failures have occurred in the estimated 13.5 million flight-hour life of the fleet (through 1990). Therefore, the historical *combined* risk of having a glass ply failure and a PVB interlayer failure occur simultaneously is approximately 0.015/100,000 flight hours. The 10.5 year changeout has an associated risk alone of 0.017/100,000 flight-hours, which is nearly the same as the historical *combined* risk. The risk associated with 10.5 year changeout is therefore conservative. Second, as of 1990, as many as 110 windows still in the fleet had service ages over 22 years (264 months). These parts were at a high risk for PVB failure. According to Table 4, the Flight-Hour Failure Risk can be reduced by a factor of almost 5 (compared to 264 month-old parts) by removing parts at 10.5 years (126 months). This represents a substantial reduction in risk while maintaining reasonable service-life over which to spread replacement costs.

In establishing a more reliable removal for cause criteria, other factors would ideally be accounted for. While difficult to track, actual flight hours (rather than estimated or averaged) may be a more appropriate parameter on which to base a criteria. Exposure to thermal, moisture, and chemical environments would be important and should ideally be considered for a true understanding of degradation phenomenon. However, it must be kept in mind that the goal of a criteria is not to improve the performance of a part, but merely to indicate when the chances of performance degradation increase. The degradation of the PVB burst strength appears to be long-term phenomenon, not a sudden decrease in performance which can be traced to specific causes. Therefore, understanding specific causes of degradation may not be as important as knowing when the degradation will occur. In this light, any further work should be directed toward additional support for the observed trend. Most notably, burst data covering a wider and more complete range of service lives should be obtained in order to verify the trends and confirm the extrapolations.

It should be emphasized that the PVB in the KC-135 windows provides a fail safe component for the windows. If the glass fails, the PVB is supposed to maintain structural integrity and hold cabin pressure. The testing reported in this effort provides evidence that there is a limited lifetime to this fail-safe protection. It is recommended that service life be limited for this type of window. Other similar windows should also be investigated.

## REFERENCES

1. Griffen, Sandra J., Analysis of KC-135 Navigator's Window In-Flight Mishap, Materials Engineering Report 88-417, December 5, 1988.
2. Whitney, Thomas J. and Daniel R. Bowman, "Pressure Burst Testing of KC-135 Celestial Navigation Windows," UDR-TR-93-27, University of Dayton Research Institute, Dayton, Ohio, March 1993.
3. Military Standard for System Safety Program Requirements, MIL-STD-882C, October 1991.

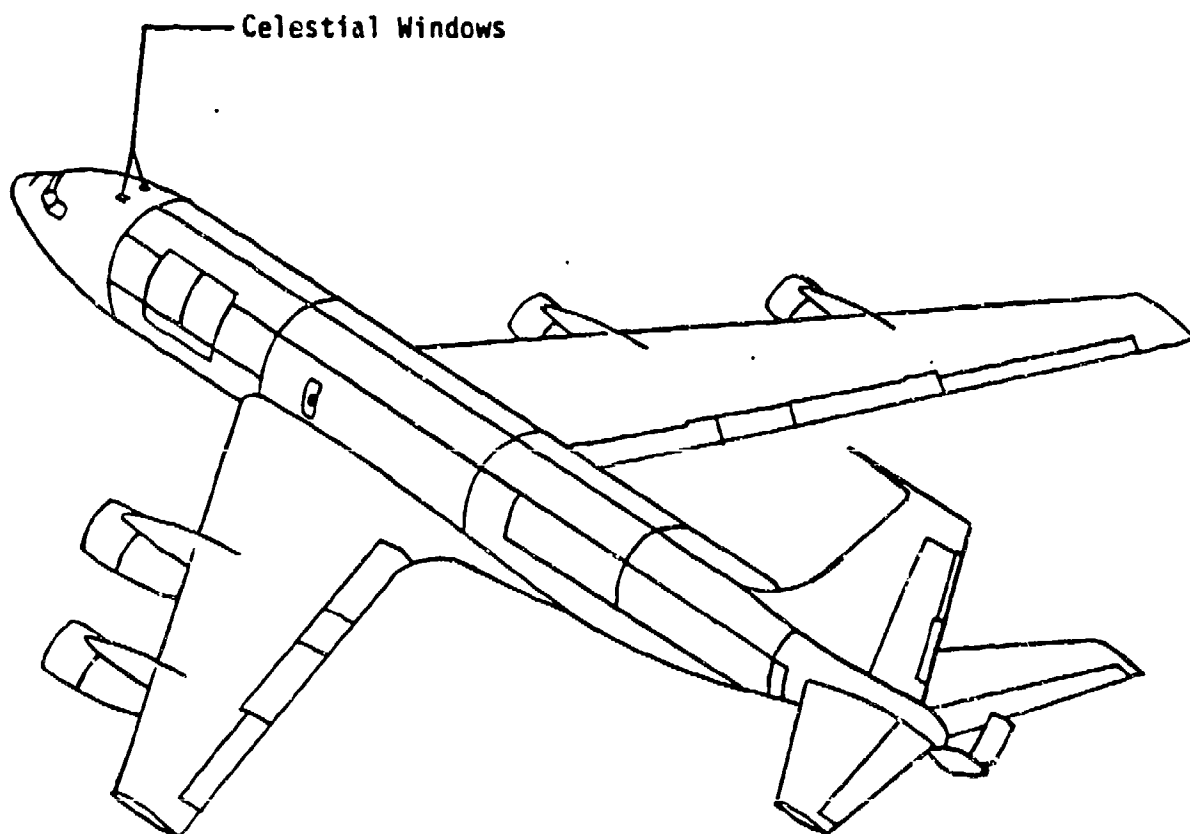
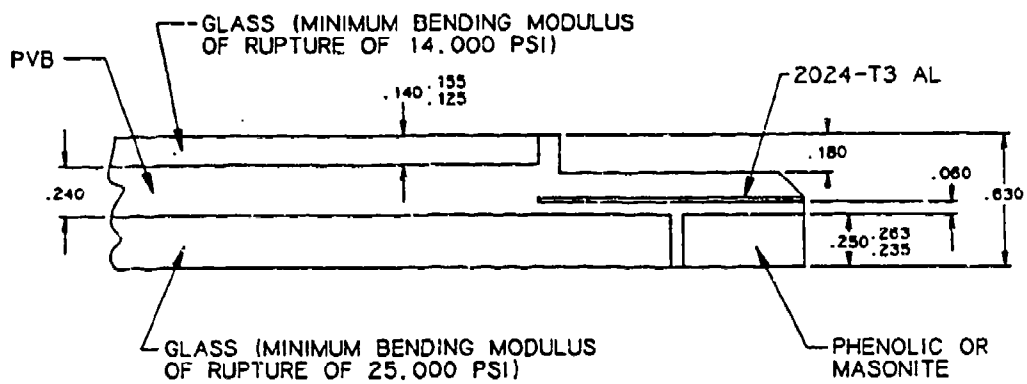
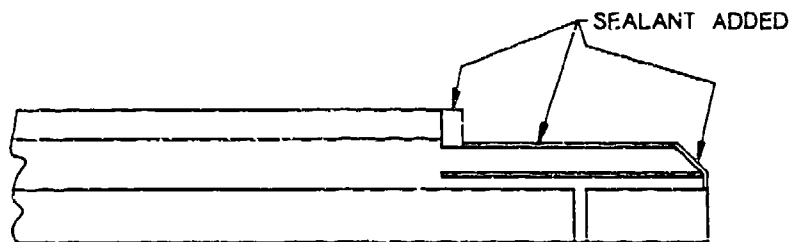


Figure 1. KC-135 Celestial Navigation Window Location



PRE - 1974 DESIGN



POST - 1974 DESIGN

Figure 2. KC-135 Celestial Navigation Window Cross-Section

### KC-135 Celestial Navigation Window Specimen Age Profile

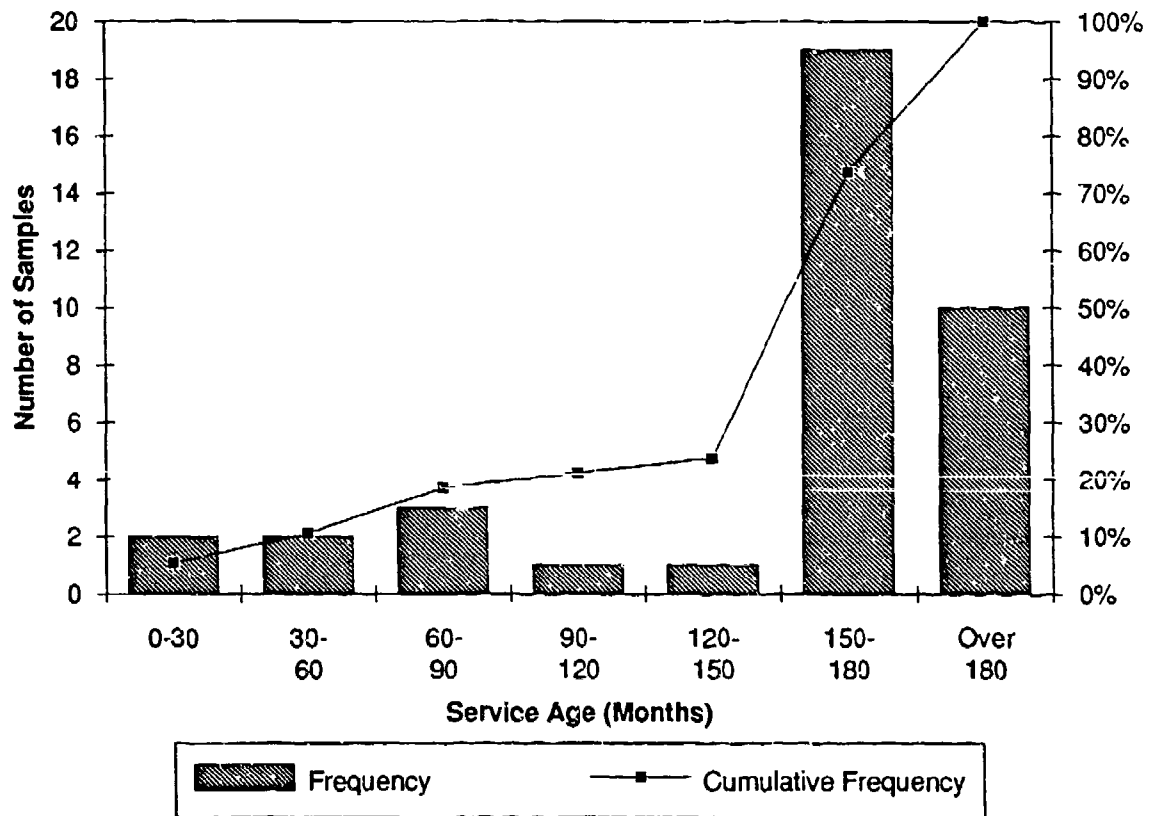


Figure 3. Distribution of Service Ages

# KC-135 Pressure Burst Test System

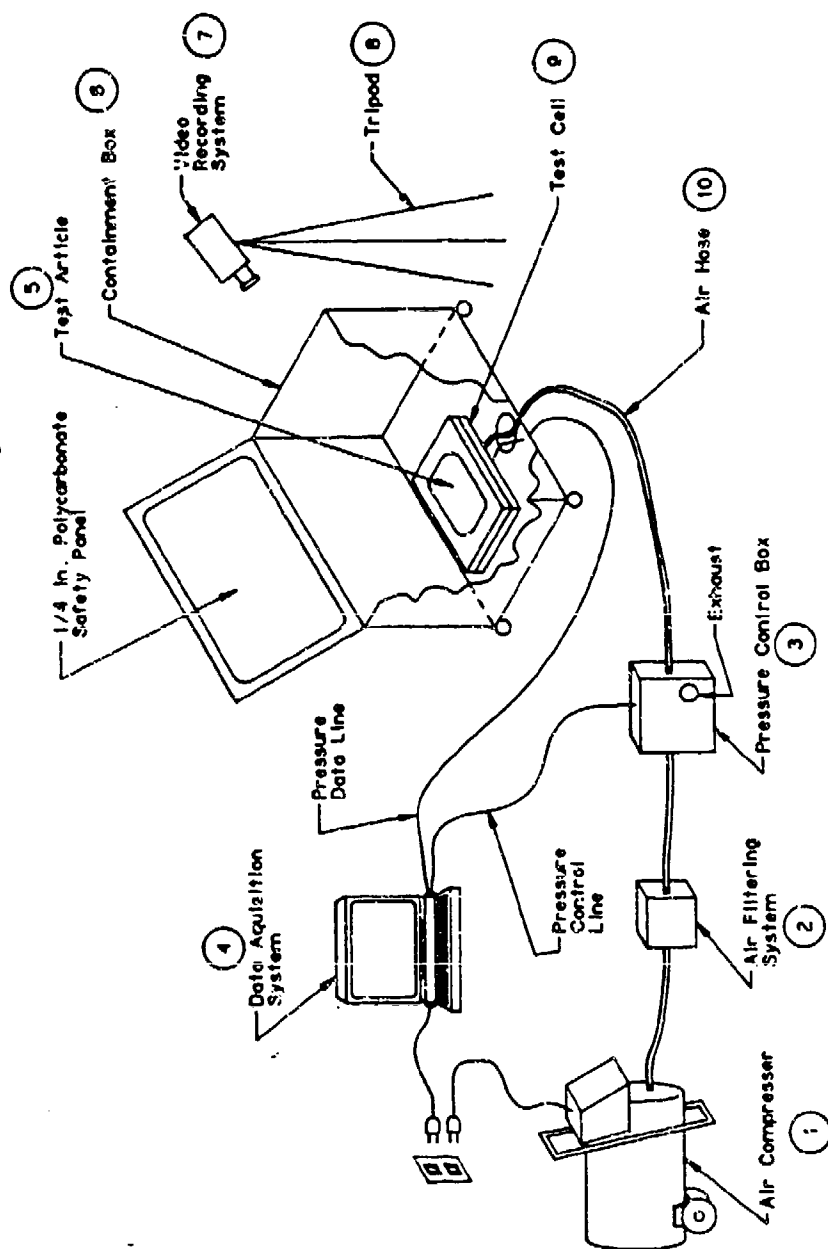
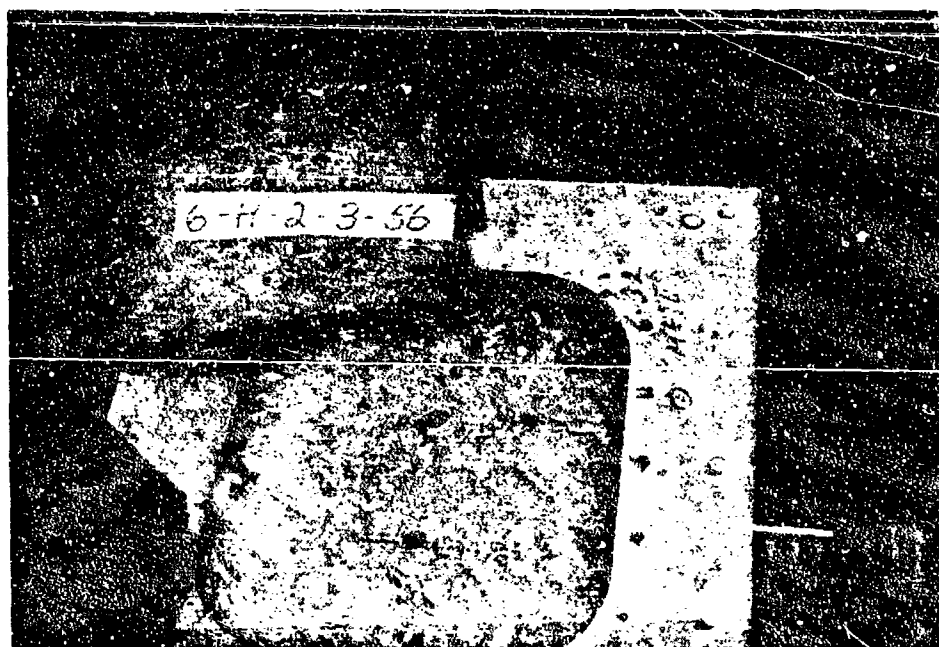


Figure 4. Pressure Burst Test System



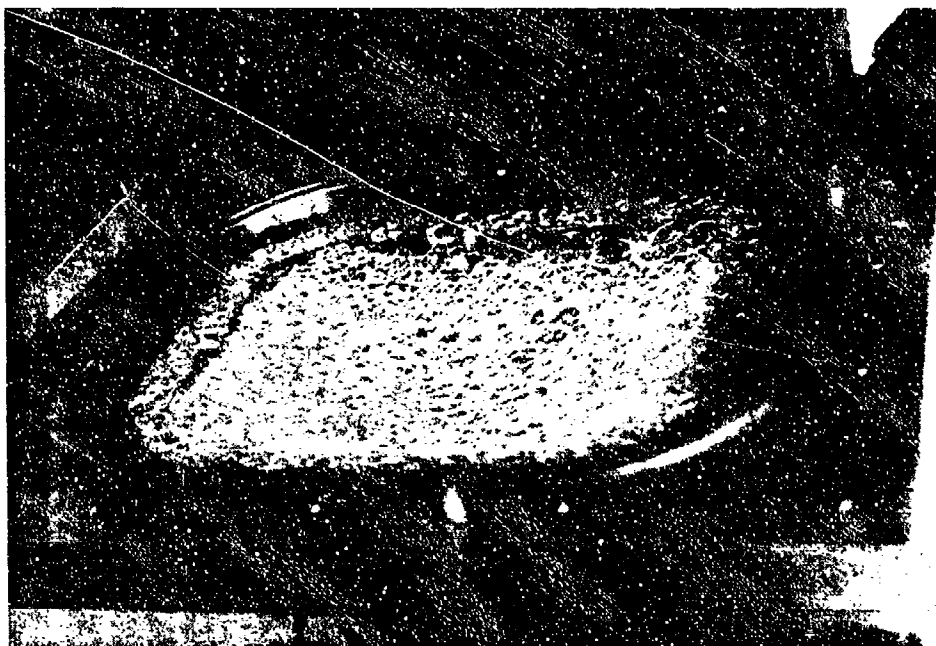
Specimen 6-H-2-3-56 Showing Typical Fracture of Inner Glass Ply Prior to Burst Testing



Specimen 6-H-2-3-56 Showing Complete Separation of Window from Frame During Burst Testing

Figure 5. Pre- and Post- Burst Test Appearance of KC-135 Window





Specimen 6-H-11-9-12. Typical Edge Tear During Fail-Safe Test



Specimen 83-H-6-20-210. Typical Complete PVB Tear During Fail Safe Tests.

Figure 6. Typical PVB Interlayer Failures

### KC-135 PVB Burst Strength Results

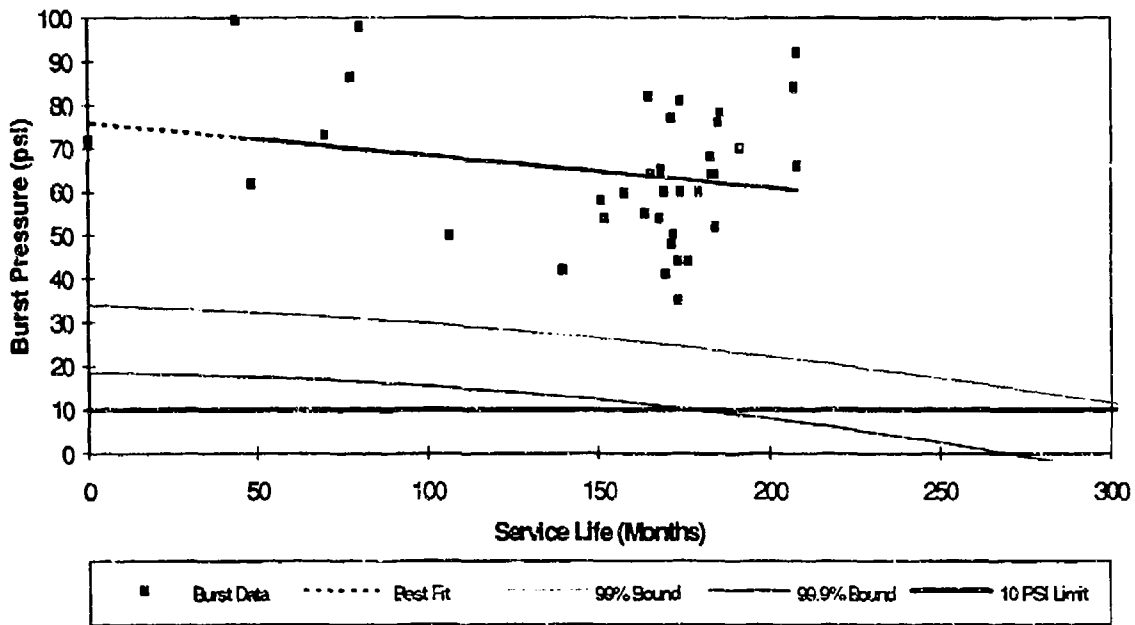


Figure 7. Reduction in PVB Burst Strength

### Effect of Service Age on PVB Failure Risk (for failure at 10 psi)

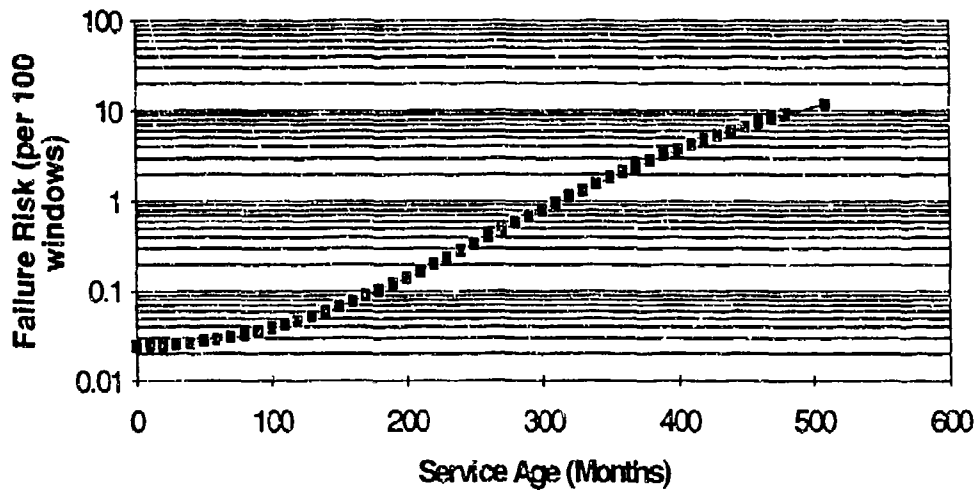


Figure 8. PVB Failure Risk

### Effect of Service Life on PVB Flight-Hour Failure Risk

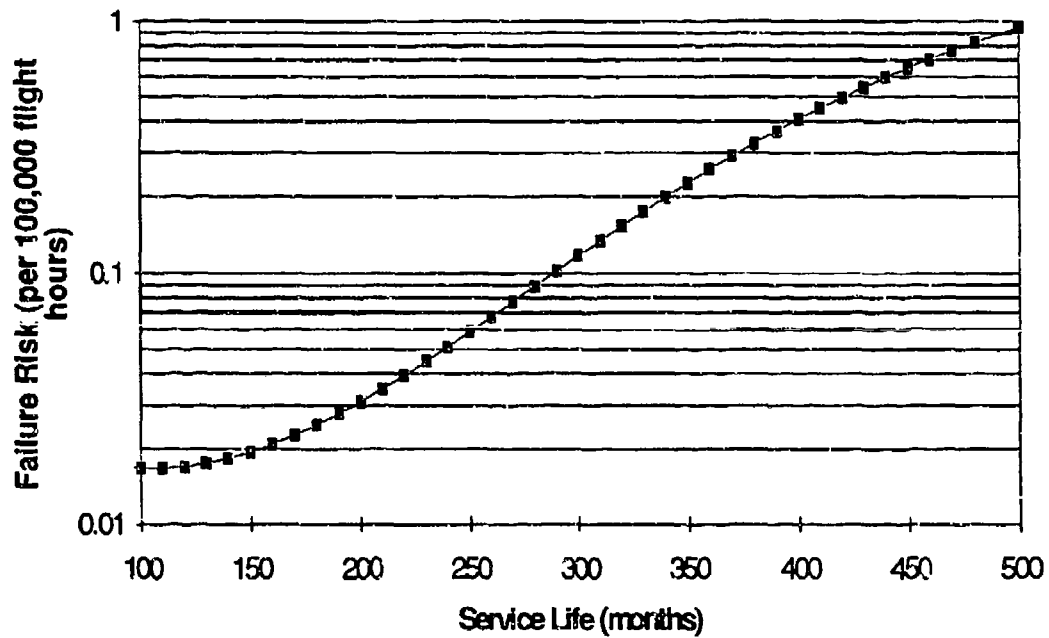


Figure 9. PVB Flight Hour Failure Risk

Table 1. KC-135 Celestial Window Inventory

UD#	USAF#	L/R	DATE of MANUFACTURE	DATE of REMOVAL	DATE of SHIPMENT	LIFESPAN (Months)	PVB Burst (psi)
1	6-H-8-21-30	R	Aug-76		May-91	168	54
2	6-H-11-9-12	R	Nov-76		May-91	165	82
3	6-H-2-11-31	R	Feb-76		May-91	174	81
4	88-H-12-12-027	R	Dec-86		May-91	44	99.6
5	6-H-6-14-13	R	Jun-76		May-91	170	41
6	83-H-6-20-335	R	Jun-83	Jul-90		77.5	86.4
7	87-H-03-09-169*	Burst Tested as Window #43 Below					71
8	6-H-12-11-17	R	Dec-76		May-91	164	55
9	6-H-5-13-52	R	May-76		Jun-91	172	50
10	6-H-12-11-11	Burst Tested as Window #44 Below					72
11	6-H-2-12-132	L	Feb-76	Jul-90		165.5	64
12	6-H-2-3-56	L	Feb-76	Jun-91		176.5	44
13	6-H-8-2-12	L	Aug-76	May-91		169.5	60.1
14	86-H-09-22-583	L	Sep-86	May-91		48.5	61.8
15	6-H-12-17-93	L	Dec-76		Nov-90	158	59.6
16	8-H-1-06-88	L	Jan-78		May-91	151	58
17	6-H-12-6-101	L	Dec-78		May-91	140	42
18	83-H-6-20-204	L	Jun-83	Oct-90		80.5	98
19	6-H-2-3-58	L	Feb-76		May-91	174	60
20	6-H-4-1-56	L	Apr-76	May-91		173.5	35
21	84-H-8-20-469	L	Aug-84		Mar-91	70	73
22	#2 (NO SN)				May-91	-	67
23	7-H-12-07-91	L	Dec-77		May-91	152	54
24	#1 (NO SN)	L	Jan-00	Nov-90		-	72
25	5-H-2-20-11	L	Mar-75		May-91	186	78
26	#3 (NO SN)				May-91	-	66
27	6-H-6-18-51	L	Jun-76	Jan-92		179.5	60
28	8-H-1-06-85	L	Jan-78	Dec-92		171.5	48
29	7-H-11-02-10	L	Nov-77	Dec-92		173.5	44
30	83-H-6-20-210	L	Jun-83	Dec-92		106.5	50
31	6-H-12-6-98	L	Dec-76		Dec-92	183	68
32	8-H-1-06-71	L	Jan-78	Dec-92		171.5	77
33	6-H-12-11-08	R	Dec-76	Dec-92		184.5	52
34	6-H-11-9-41	R	Nov-76	Oct-92		183.5	64
35	6-H-11-9-37	R	Nov-76	Dec-92		185.5	76
36	6-H-5-14-38	R	May-76	Dec-92		191.5	70
37	4-H-12-19-104	L	Dec-74	Dec-92		208.5	92
38	6-H-12-11-15	R	Dec-76	Dec-92		184.5	64
39	4-H-12-19-90	R	Dec-74	Dec-92		208.5	66
40	5-H-1-29-40	R	Jan-75	Dec-92		207.5	84
41	8-H-1-11-120	R	Jan-76	Sep-92		168.5	65
42	#4 (NO SN)					-	73
43	87-H-03-09-169	R	Mar-87	Never Installed		0	
44	6-H-12-11-11	R	Dec-76	Never Installed		0	
45	#5 (NO SN)						
46	#6 (NO SN)						
47	#7 (NO SN)						
48	#8 (NO SN)						

\*Also labeled 90-092H0 965

Table 2. KC-135 Celestial Window Test Summary

UDs	USAFs	LIFESPAN (Months)	PROOF TEST RESULT (P/F)	PVB Burst (psi)	OUTER PLY BURST (psi)	PROOF and BURST TEST COMMENTS	DATE of REMOVAL	DATE of SHIPMENT
1	6-H-8-21-30	186	P	54	41	PVB leak around edge at 54 psi.		May-91
2	6-H-11-9-12	165	P	82	46	PVB pulled away from edge.		May-91
3	6-H-2-11-31	174	P	81	-	Inner ply NOT broken prior to burst test. Catastrophic (blowout) failure. Video failure immediately after test.		May-91
4	86-H-12-12-027	44	P	99.6	-	Compressor delay near 80 psi. PVB leak near edge at 99.6 psi.		May-91
5	6-H-6-14-13	170	P	41	41	Outer ply and PVB pulled away from edge.		May-91
6	83-H-6-20-335	77.5	P	86.4	-	Seal failure on first Proof Test. Passed a second proof test. PVB pulled away from edge at 86.4 psi during burst test.	Jul-90	May-91
7	37-H-03-08-169*	0	P	-	-	Burst Tested as UD #43.	Never Installed	May-91
8	6-H-12-11-17	164	P	55	-	PVB edge leak.		May-91
9	6-H-5-13-52	172	F	48	-	Failed Proof test at 48 psi. Catastrophic. Large tear of PVB layer through window center.		Jun-91
10	6-H-12-11-11	0	P	-	-	Burst Tested as UD #44.	Never Installed	Jun-91
11	6-H-2-12-132	165.5	P	64	-	Catastrophic failure at 64 psi.	Jul-90	
12	6-H-2-3-56	176.5	P	44	-	Initial loss of seal at 42 psi. Appeared to re-seal and failed at 55 psi. Catastrophic: complete separation of glass plate from frame.	Jun-91	
13	6-H-2-2-12	169.5	P	60.1	-	PVB edge leak at 60 psi.	May-91	
14	86-H-02-22-583	48.5	P	61.8	-	Catastrophic failure at 61 psi.	May-91	
15	6-H-12-17-93	158	P	59.6	-	Catastrophic failure at 60 psi.		Nov-90
16	6-H-1-06-88	151	P	58	-	PVP edge leak.		May-91
17	6-H-12-6-101	140	P	42	50	Outer ply fracture during Proof. PVB edge rupture at 43 psi.		May-91
18	83-H-6-20-204	80.5	P	98	-	PVB edge rupture at 95 psi.	Oct-90	
19	6-H-2-3-58	174	P	60	-	PVB edge rupture at 60 psi.		May-91
20	6-H-4-1-56	173.5	P	35	40	Outer ply fracture during Proof. PVB edge rupture at 35 psi.	May-91	
21	84-H-6-20-489	70	P	73	-	Catastrophic failure at 73 psi.		Mar-91
22	#2 (NO SN)	-	P	67	-	PVB edge rupture at 67 psi.		May-91
23	7-H-12-07-91	152	P	54	-	Catastrophic failure at 55 psi.		May-91
24	#1 (NO SN)	-	P	72	-	PVB edge rupture at 72 psi.	Nov-90	
25	5-H-2-20-11	186	P	78	-	PVB edge rupture at 82 psi.		May-91
26	#3 (NO SN)	-	P	55	-	Inner and Outer glass ply fractured prior to burst test. PVB edge leak at 66 psi.		May-91
27	6-H-6-18-51	179.5	P	60	-	PVB edge rupture at 60 psi.	Jan-92	
28	6-H-1-06-85	171.5	P	48	-	PVB edge rupture at 50 psi.	Dec-92	
29	7-H-11-02-10	173.5	P	44	-	PVB edge rupture at 42 psi.	Dec-92	
30	83-H-6-20-210	106.5	P	50	-	Catastrophic failure at 50 psi.	Dec-92	
31	6-H-12-6-98	183	P	68	-	Slight seal loss at 45 psi. PVB edge rupture at 65 psi.		Dec-92
32	6-H-1-06-71	171.5	P	77	-	PVB edge rupture at 77 psi.	Dec-92	
33	6-H-12-11-08	184.5	P	52	-	PVB edge rupture at 52 psi.	Dec-92	
34	6-H-11-9-41	183.5	P	64	-	PVB edge rupture at 64 psi.	Oct-92	
35	6-H-11-9-37	185.5	P	76	-	PVB edge rupture at 76 psi.	Dec-92	
36	2-H-5-14-38	191.5	P	70	-	PVB edge rupture at 70 psi.	Dec-92	
37	4-H-12-19-104	208.5	P	92	-	Pressure loss at 90 psi. Re-sealed at 75 psi and climbed to 85 psi before catastrophic failure.	Dec-92	
38	6-H-12-11-15	184.5	P	64	-	Catastrophic failure at 64 psi.	Dec-92	
39	4-H-12-19-90	208.5	P	86	-	PVB edge rupture at 86 psi.	Dec-92	
40	5-H-1-29-40	207.5	P	84	50	Inner ply broken during proof test. Window lost pressure during proof test but re-sealed and completed proof test. PVB edge rupture at 84 psi during burst test.	Dec-92	
41	6-H-1-11-120	168.5	P	65	-	Catastrophic failure at 60 psi.	Sep-92	
42	#4 (NO SN)	-	P	73	-	PVB edge rupture at 73 psi.		
43	87-H-03-08-169	0	-	71	-	Proof Tested as UD #7. Catastrophic failure at 71 psi.		
44	6-H-12-11-11	0	-	72	-	Proof Tested as UD #10. Initial seal loss at 50 psi. Re-sealed itself, followed by PVB edge leak at 70 psi.		
45	#5 (NO SN)		F			Inner and outer glass badly damaged prior to test. Failed to seal even with additional sealing (butyl rubber) compound.		
46	#6 (NO SN)		F			Inner and outer glass badly damaged prior to test. Failed to seal even with additional sealing (butyl rubber) compound.		
47	#7 (NO SN)		F			Failed proof test at 50 psi.		
48	#8 (NO SN)		F			Inner and outer glass badly damaged. Failed proof test at 50 psi.		

\*Also labeled 90-092H0 965

Table 3. Hazard Severity Categories

Description	Category	Definition
Catastrophic	I	Death, system loss, or severe environmental damage
Critical	II	Severe injury, severe occupational illness, major system or environmental damage
Marginal	III	Minor injury, minor occupational illness, or minor system or environmental damage
Negligible	IV	Less than minor injury, occupational illness, or system or environmental damage

Table 4 Hazard Probability Levels and Corresponding Service Lives

Probability	Level	Fleet Description	Number of Occurrences*	Number of Fleet Occurrences**	Service Age***
Frequent	A	Continuously experienced	> 5	More than 0.5 (>2 per year)	>424
Probable	B	Will occur frequently	0.5-5	0.08-0.5 (0.32-2 per year)	273-424
Occasional	C	Will occur several times	0.1-0.5	0.025-0.08 (0.1-0.32 per year)	178-273
Remote	D	Unlikely, but can reasonably be expected to occur	0.05-0.1	0.017-0.025 (0.068-0.1 per year)	126-178
Improbable	E	Unlikely to occur, but possible	< 0.005	Less than 0.017 (<0.068 per year)	<126

\* Per 100 windows in service.

\*\* First Row: Per 100,000 flight hours.

Second Row: Assuming 275 Flight Hours/Year, 1460 windows in service

\*\*\* Based on Figure 8. Service Age in Months.

Table 5. Hazard Risk Assessment Index

Probability		Category			
		Catastrophic 1	Critical 2	Marginal 3	Negligible 4
Frequent	A	1A	2A	3A	4A
Probable	B	1B	2B	3B	4B
Occasional	C	1C	2C	3C	4C
Remote	D	1D	2D	3D	4D
Improbable	E	1E	2E	3E	4E

Hazard Risk Index	Criteria
1A 1B 1C 2A 2B 3A	Unacceptable risk
1D 2C 2D 3B 3C	Undesirable risk
1E 2E 3D 3E 4A 4B	Acceptable with review
4C 4D 4E	Acceptable

SESSION VI

BIRDSTRIKE HAZARDS AND OPTICS - PART A

Chairman: D. J. Rubin  
Spectrum Sciences & Software

Co-Chairman: L. Task  
Armstrong Labs

Coordinator: D. Hamershock  
Flight Dynamics Directorate  
Wright Laboratory



**BIOLOGICAL VALIDATION AND STANDARDISATION OF  
INTERNATIONAL BIRDSTRIKE TESTING TECHNIQUES**

J. Allan  
Central Science Laboratory (MAFF)

D. M. Hamershock  
Flight Dynamics Directorate  
Wright Laboratory

## 1. Introduction

Collisions between aircraft and birds are costly and potentially dangerous events. The US Air Force alone suffers some 3,500 birdstrikes per year at an estimated cost of 65 million dollars. More seriously, the USAF has lost seven lives to birdstrikes since 1987 (Merritt & Dogan 1992). Thorpe (1990a, 1992) summarises recent serious birdstrike incidents involving civil airliners. These include the total loss of a Boeing 737 at Bahar Dar, Ethiopia, in 1988 which left 35 passengers dead and 27 seriously injured. A total of 96 passenger lives have been lost in birdstrike related incidents since 1960 (Thorpe 1990b).

A great deal of research effort is put into improving the performance of aircraft components either by developing new designs or incorporating new materials into existing assemblies. For reasons of safety, the performance of such new designs and materials in withstanding birdstrike damage needs to be evaluated. Many aircraft components are therefore required to pass certification tests before being allowed into service. Such tests involve maintaining a certain level of performance following impact with a specified number of birds of a given weight. Most manufacturers undertake preliminary tests using dummy birds: cylinders or spheroids made of gelatin. Dummy birds have a number of advantages for the testing process. They are continuously available, of identical mass shape and density, are clean in use and do not involve killing of birds for testing (Deveaux 1992).

The number, mass and density of the real and dummy birds used in certification testing is the subject of continued debate (Deveaux 1992). There are no regulations on the species of birds that are used in testing; nor on the size, shape or density of dummy birds. This has resulted in different companies employing a wide variety of bird species for their tests. Birds as diverse as Herring Gulls (*Larus argentatus*), Mallard Ducks (*Anas platyrhynchos*), Canada Geese (*Branta canadensis*), Quails (*Colinus sp.*), Pheasants (*Phasianinae*), Plover species (*Charadriidae*), and domestic ducks and chickens have all been employed. Similarly, the size and shape of dummy birds vary from cylindrical to spheroid and differing densities of gelatin are used. It is unclear whether the bird species used in birdstrike tests are representative of those struck in operation in terms of their size, shape and density or, indeed, whether the different bird species and dummy birds used by various companies are comparable with each other.

In the aeroengine field, the advent of the large high bypass ratio (HBPR) engine and the increasing use of 'big twin' airliners for transatlantic travel have resulted in proposals to increase the weights of the medium and large sized birds used in tests from 1.5 and 4lbs to 2 and 8lbs respectively. These proposals prompted Rolls Royce Aeroengines plc. and the U.K. Civil Aviation Authority to commission research from the Central Science Laboratory, Ministry of Agriculture Fisheries and Food (CSL) into the flocking habits and flock structures of different bird species. The work was designed to determine the true probability of encountering a given number of birds during a strike with a particular species. These data are independent of reporting biases present in birdstrike databases, and can be used to help determine the numbers and weights of birds used in certification tests.

At the same time, research was being conducted in the USA by the USAF Wright Laboratory and the US Department of Agriculture into the mass, shape and density of wild birds. The work was designed to determine whether domestic chickens used in windshield testing were representative of the bird species being struck in operation by the USAF. The data were also to be used to determine whether dummy birds used in preliminary tests were of a comparable shape and density to wild birds.

Rolls Royce also have an interest in the development of dummy birds for use in engine testing. They have found that the results obtained from tests with real birds are more variable than those from preliminary tests with dummies. CSL was commissioned to study the structure and tissue density within bird bodies in order to investigate this phenomenon. Three-dimensional computer reconstructions of bird bodies were developed to determine the mass, shape and density of the slices cut through a bird's body by turbine blades during a birdstrike. These data can be used to compare slice densities from wild birds with those from domesticated species used for engine testing. They also allow density of dummy birds used for preliminary tests to be related directly to slice densities likely to be encountered in operation.

Preliminary findings from the three studies described above have generated considerable interest from both manufacturers and the regulatory authorities. It was therefore decided to develop a research program that would combine the three projects in order to provide the data needed to validate biologically the test procedures currently used, and on which future test criteria could be set. The research has the following objectives:

- 1) To identify the bird species which pose the most problems to the aviation industry world-wide.
- 2) To measure the shape, mass, volume and hence density of these species and to compare these with the bird species and dummy birds currently used in birdstrike testing.
- 3) To determine how internal density is distributed for each species and calculate the size, mass and density of slices cut by turbine blades passing through the body at different angles.
- 4) To measure the three-dimensional structure of flocks of these species so that the probability of striking a given number of birds can be estimated.

## **2. Methods and preliminary results**

The development of the techniques to be used in this project has been carried out by CSL, USAF and USDA under a variety of research contracts. The methods to be used to achieve objectives 1 to 4 are outlined below and, where commercial considerations permit, examples of the preliminary data obtained are given.

### **2.1 Identification of the bird species causing the greatest problems to aviation world-wide.**

In order to evaluate which species merited further study, it was necessary to identify the species most frequently involved in birdstrikes, those of relatively high weight, and those most often involved in multiple impacts. It was important to ensure that the datasets used were as representative of the true world situation as possible. For this reason, a total of twelve birdstrike databases were employed. These included US and UK military databases, the UK civil database and the ICAO international civil database split by region. These were supplemented by reference to databases kept by manufacturers, such as Rolls Royce and to other sources of published information where reporting standards were known to be reasonably high.

Table 1. The 40 bird species ranked as most hazardous to aircraft world-wide. See section 2.1 for an explanation of the ranking method used and sources of data.

SPECIES	MEAN RANK	No. OF DATASETS WHERE PRESENT	FINAL RANK
Larus argentatus (Herring Gull)	2.75	8	1
Larus ridibundus (Black-headed Gull)	2.71	7	2
Milvus migrans (Black Kite)	4.00	7	3
Anas platyrhynchos (Mallard)	2.33	3	4
Columba palumbus (Woodpigeon)	4.67	6	5
Vanellus vanellus (Lapwing)	6.71	7	6
Columba livia (Rock Dove)	6.33	6	7
Larus canus (Common Gull)	7.50	8	8
Buteo buteo (Buzzard)	6.00	3	9
Gyps bengalensis (White-backed Vulture)	1.00	1	10
Cacatua roseicapilla (Galah)	1.00	1	11
Buteo jamaicensis (Red-tailed Hawk)	2.00	1	12
Larus marinus (Great Black-backed Gull)	6.33	3	13
Hagedashia hagedashia (Hadada Ibis)	2.00	1	14
Asio otus (Long-eared Owl)	3.00	1	15
Corvus frugilegus (Rook)	8.80	5	16
Bubulcus ibis (Cattle Egret)	6.50	2	17
Coragyps atratus (Black Vulture)	3.00	1	18
Haematopus ostralegus (Oystercatcher)	4.00	1	19
Corvus cornix (Hooded Crow)	8.67	3	20
Haliastur indus (Brahmany Kite)	4.00	1	21
Eupodotis australis (Australian Bustard)	4.00	1	22
Apus apus (Swift)	9.75	4	23
Sturnus vulgaris (European Starling)	11.71	7	24
Burhinus oedecnis (Stone Curlew)	5.00	1	25
Branta canadensis (Canada Goose)	9.33	3	26
Falco cenchroides (Australian Kestrel)	5.00	1	27
Asio flammeus (Short-eared Owl)	6.00	1	28
Turdus merula (Blackbird)	9.00	2	29
Phasianus colchicus (Pheasant)	6.00	1	30
Falco tinnunculus (Kestrel)	12.00	5	31
Alauda arvensis (Skylark)	12.50	6	32
Larus fuscus (Lesser Black-backed Gull)	10.67	3	33
Cathartes aura (Turkey Vulture)	9.50	2	34
Vanellus indicus (Red-wattled Lapwing)	6.00	1	35
Larus delawarensis (Ring-billed Gull)	10.67	3	36
Larus dominicanus (Kelp Gull)	6.00	1	37
Apus affinis (House Swift)	7.00	1	38
Larus novaehollandiae (Silver Gull)	11.50	2	39
Gyanorhina tibicen (Australian Bell Magpie)	7.00	1	40

A ranking system was developed in which each species which constituted more than 1% of recorded strikes in a dataset was ranked by strike frequency, mass and the proportion of the strikes involving multiple impacts. The mean of these three ranks was calculated to produce a final rank score for each species. An overall rank score was computed by taking the average final rank for each species across the twelve datasets and combining this with a ranking based on the number of datasets in which the species occurred, the latter score reflecting how widespread the problem posed by a particular species is. The final table includes some 86 species. The top 40 species are shown in table 1.

This ranking system gives equal weight to frequency, mass and proportion of multiple impacts in calculating the final listing. The system can be adjusted to give a greater weighting to one or more of these variables if required. For example, those interested in impacts with windshields may be more concerned with birds of high body mass, whilst those involved in engine manufacture may give more weight to species frequently involved in multiple impacts.

Table 1 shows that the ranking technique employed here produces a species list broadly in line with current thinking concerning which species constitute the greatest hazard to aircraft. Large, flocking species, e.g. gulls (*Larus* sp.), identified by Milsom (1990) as the 'priority group' for bird controllers feature prominently in the list as do larger raptors, e.g. kites (*Milvus* sp.). The presence of some species (e.g. the Galah) reflects the reporting biases inherent in datasets of this type (Thorpe 1990b). The Galah features only in the ICAO Asian/Australasian database but, because of more rigorous reporting standards in Australia compared to the rest of Asia, strikes with this species are more often reported to ICAO. This gives the impression that the Galah is an important species throughout Asia which is not in fact the case as it occurs only in Australia. It is also likely that similar reporting inconsistencies will result in species which form a significant hazard in parts of the world where reporting standards are poor being omitted from the list. Despite the acknowledged shortcomings of such a method, there are no alternative means of establishing which bird species are struck world-wide.

## **2.2 Measurement of whole body mass, volume and density**

This work has already been accomplished by USAF and USDA staff on twelve North American species (Hamerschock et al. 1993). Ten individuals of each species were obtained and the total length, wingspan and body circumference at the widest point measured. Birds were then weighed with feathers in place and the volume of each bird determined by displacement in water. This measurement was then repeated with the feathers fully wetted to remove as much trapped air as possible. Finally, the bird was plucked and both mass and volume re-measured. Three density measurements; dry, wetted and plucked could thus be calculated. Table 2 shows the data obtained for the species examined so far.

Table 2 Dry, wetted and plucked densities (g/cc) of twelve North American bird species. Data are means for ten birds. Figures in brackets are standard deviations (From Hamershoek et al. 1993).

SPECIES	DRY BIRD DENSITY	WET BIRD DENSITY	PLUCKED BIRD DENSITY
Herring Gull	0.602 (0.053)	0.743 (0.046)	0.879 (0.054)
Ring-billed Gull	0.644 (0.031)	0.786 (0.028)	0.928 (0.034)
Rock Dove	0.648 (0.032)	0.802 (0.026)	0.987 (0.022)
Canada Goose	0.669 (0.041)	0.807 (0.023)	0.917 (0.023)
Laughing Gull	0.700 (0.043)	0.831 (0.027)	0.935 (0.038)
Turkey Vulture	0.700 (0.018)	0.803 (0.024)	0.916 (0.025)
Mallard	0.739 (0.040)	0.877 (0.026)	0.959 (0.016)
Brown-headed Cowbird	0.750 (0.029)	0.915 (0.024)	1.042 (0.028)
House Sparrow	0.751 (0.042)	0.913 (0.035)	1.058 (0.032)
European Starling	0.776 (0.035)	0.947 (0.024)	1.027 (0.020)
Common Grackle	0.809 (0.030)	0.924 (0.023)	1.005 (0.024)
Domestic Chicken	0.918 (0.041)	no data	1.044 (0.011)
Analysis Of Variance Between Species	F = 64.14 P < 0.0001	F = 66.54 P < 0.0001	F = 46.83 P < 0.0001

The data show significant differences between the densities of the twelve species studied. The Herring Gull, used by some organisations as a test species, is 34% less dense than the domestic chicken which is used by other companies. The average dry density for wild birds is 0.708 g/cc compared to 0.918 g/cc for the domestic chicken. There is clearly a need to consider whether the test species used by different companies are comparable both with each other and with the wild species most frequently struck. The gathering of more data on a wider range of species would allow the standardisation of size and density as well as mass for certification testing, and a representative bird species could then be chosen. Similarly, these data could be used to produce dummy birds of a size, mass and density more typical of those species likely to be struck in operation.

### 2.3 Determination of internal density distribution within bird bodies

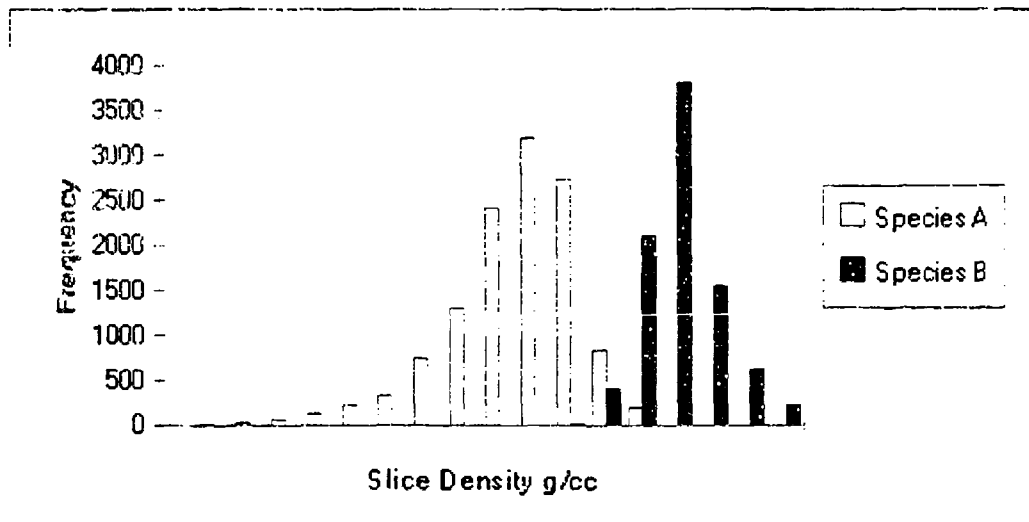
In order to determine how the internal distribution of tissue density varies between bird species, and to model the passage of engine fan blades through their bodies, it was first necessary to develop a three-dimensional computer reconstruction of the internal structure of each bird. This was achieved by first freezing the bird, removing the neck, wings and legs, and then slicing the torso at 0.5cm intervals perpendicular to the longitudinal axis. After each slice was removed, the exposed surface was photographed. Each photograph was digitised on a computer and the resulting tissue map fed into a specially modified 3-D reconstruction program. A second bird was dissected and samples of the different tissues removed. Each tissue sample was weighed, its volume measured by displacement in water and its density determined. The density

of each tissue type was then fed into the computer reconstruction to produce a three-dimensional density map of the bird body.

The 3-D density map can then be used to model the passage of turbine blades at any angle through the bird's body. A total of over 8,000 slices were modelled for each species tested (the precise number of slices depending upon the size of the bird involved). Figure 1 shows the distribution of mean slice density for two of the bird species tested. Commercial confidentiality prevents the disclosure of the exact values obtained, but statistically significant differences exist between the two species shown.

The process of slicing, photographing and digitising each individual bird is extremely time consuming and expensive. It is hoped that the software can be adapted to take data from a Magnetic Resonance Imager (MRI) so that a simple scanning procedure can be used to generate the initial three-dimensional model. Work on the adaptation of MRI data for use in the modelling process is continuing.

Figure 1. Graph showing the distribution of slice densities obtained from modelling the passage of a turbine blade through the bodies of two frequently struck European bird species.



#### 2.4 Measurement of the three-dimensional structure of bird flocks and calculation of the probability of multiple impacts.

Banilower and Goodall (1992) reviewed recent birdstrikes to a variety of HBPR engines and compared data from 1981-83 with that from 1989-90. They concluded that the species and thus mass of birds involved in strikes had not changed significantly over the period. The poor reporting levels of birdstrike incidents from some countries, and the lack of specific identification of the birds involved, raises questions concerning the reliability of such data, however (Thorpe 1990b). For example, the information used to calculate the masses of birds ingested by aircraft in the USA during the study is based on only 16 reported incidents where the birds involved were identified to species. Even in countries where the reporting of all birdstrikes is mandatory, relying on existing datasets where accuracy levels vary by factors of ten (the UK birdstrike reporting form has categories of 1, 2-10 and 10-100 birds hit) to determine how many birds should be used in certification tests is itself questionable. To use data gathered on aircraft of an existing design and flying existing routes to establish standards for new designs or new routes is clearly undesirable. If we are to accurately predict the probability of striking a given number of birds of a particular species in the future, independent data without the biases imposed by the current reporting system are required. Detailed measurements of the flock sizes and structures adopted by bird species allow such predictions to be made.

Extremely limited data exist on the flock structure of birds. Van Tets (1966) used single still photographs to estimate the flock sizes of a wide range of species but with limited accuracy, whilst Dill & Major (1977) used stereo still photography with high speed cameras to obtain accurate data on a very limited range of species in level flight. The species range studied was limited by difficulties with gathering photographic information in the field and with processing the large amounts of information needed to follow the movements of a flock in three dimensions.

Advances in video recording techniques, and the advent of powerful computers capable of running image analysis software mean that these problems can now be overcome. CSL, under contract to Rolls Royce and the Civil Aviation Authority, has developed a portable video system that can record stereo images of bird flocks as they move in response to aircraft or other stimuli. An automated image analysis system allows the three dimensional position of each bird in a flock to be calculated automatically and statistics such as flock size, flock density and inter-bird distances calculated. The system can also be used to model the passage of an aircraft or engine through a flock at any desired angle or speed. The number and location of any resulting strikes can thus be determined.

Data need to be gathered on the flock structures of the widest possible range of species. The changes in flock structure that occur whilst birds perform their various daily behaviours also need to be monitored. These data will allow an independent estimate of the probability of striking a particular number of birds of a given species to be made. The most hazardous species will thus be able to be identified and the data used to help set certification standards. The ability to model different aircraft configurations may also shed light on why some suffer more birdstrikes than others.



### **3. Organisation and timescale of future research**

The proposed research involves capturing a number of birds of each species at the top of the priority listing (subject to obtaining the necessary licenses, etc.). Whole body density will be measured and physical dimensions such as wingspan and cross-sectional area recorded. Internal density distribution will be modelled for each species and the density of the slices cut through the body by turbine blades determined. For flocking species, stereo video recordings will be made of as wide a range of behaviours as possible, with particular reference to behaviour on or near airports. Flock sizes and densities will be calculated and the passage of a variety of aircraft, engines, etc. through the flocks will be modelled to determine the numbers of birds likely to be hit.

#### **3.1 Funding**

Since the research is of general interest to the whole industry, we propose that the project should be funded by an 'industry club' consisting of manufacturers, airlines, regulatory authorities and other interested organisations each contributing annually a modest sum of money. Subscription to the club would buy full access to all data gathered, and the right to suggest changes to research priorities (e.g. to alter the list of species to be studied or to have a particular aircraft or engine type modelled for passage through flocks of a particular species). The project is scheduled to last for three years, with the possibility of extension if a greater range of species needs to be studied. It is hoped that the project will commence in 1993-4, with North American and European birds from the top of the priority listing being selected as the first targets for study. This is because USAF Wright Laboratory, UK Civil Aviation Authority and Rolls Royce Aeroengines have already invested in the project. The cost to individual subscribing organisations would obviously depend on the number of members of the industry club and the number and location of the bird species finally chosen for study.

### **4. Conclusion**

This proposal constitutes the first comprehensive study of those species which cause the greatest problems to the aviation industry world-wide. It is designed to gather the biological information needed by manufacturers, and regulatory authorities to help them make decisions about design, testing and certification against birdstrikes. It will also assist airlines, who must meet the cost of birdstrike damage, to minimise the impact of birdstrikes on their operation.

### **5. References**

Banilower H. & Goodall C. (1992) Bird Ingestion Into Large Turbofan Engines. DOT/FAA/CT-91-17. FAA Technical Centre, Atlantic City, New Jersey.

Deveaux J-P (1992) Substitute Bird Objectives And Constraints. Proc. 21st. Bird Strike Committee Europe. Jerusalem 413-424.

Dill & Major (1977) Spatial Structure Of Bird Flocks. Report to NRC Committee on Bird Hazards To Aircraft. Canada.

Hamershock D.M. Seamans T.W. & Bernhardt G.E. (1993) Determination of body density for twelve bird species. WL-TR-93-3049. Wright-Patterson A.F.B. Dayton Ohio.

**Merritt R.L. & Dogan R.L. (1992)** Bird Strikes to US Air Force Aircraft 1987-1991. Proc. 21st. Bird Strike Committee Europe. Jerusalem. 393-401.

**Milsom T.P. (1990)** The Use Of Birdstrike Statistics To Monitor The Hazard And Evaluate Risk On UK Civil Aerodromes. Proc. 20th. Bird Strike Committee Europe. Helsinki 303-320.

**Thorpe J. (1990a)** Serious Birdstrikes To Civil Aircraft 1987-1989. Proc. 20th. Bird Strike Committee Europe. Helsinki 295-301.

**Thorpe J. (1990b)** Analysis of Birdstrikes Reported By European Airlines 1981-1985. Proc. 20th. Bird Strike Committee Europe. Helsinki. 263-294.

**Thorpe J. (1992)** Serious Bird Strikes To Civil Aircraft 1989-1991. Proc. 21st. Bird Strike Committee Europe. Jerusalem. 291-302.

**Van Tets (1966)** A Photographic Method Of Estimating The Densities Of Bird Flocks In Flight. CSIRO Wildl. Res. 11: 103-110.

**INTEGRATION OF BIOLOGICAL AND ENGINEERING TECHNOLOGIES:  
X3D ANALYSIS OF SIX BIRD SPECIES IMPACTING AIRCRAFT TRANSPARENCIES**

**D. M. Hamershock  
Flight Dynamics Directorate  
Wright Laboratory**

**Steven E. Olson  
Michael P. Bouchard  
University of Dayton**

**INTEGRATION OF BIOLOGICAL AND ENGINEERING TECHNOLOGIES: X3D  
ANALYSIS OF SIX BIRD SPECIES IMPACTING AIRCRAFT TRANSPARENCIES**

**David M. Hamershock<sup>1</sup>  
Steven E. Olson<sup>2</sup>  
Michael P. Bouchard<sup>2</sup>**

<sup>1</sup>USAF Windshield Systems Program Office  
WL/FIVR Bldg 255, 2079 Tenth St  
Wright-Patterson AFB OH 45433-6553 USA

<sup>2</sup>Structures Group, Aerospace Mechanics Division  
University of Dayton Research Institute  
Dayton OH 45469-0110

**Abstract**

Recently determined bird density, mass, length, and diameter data were utilized to create cylinder models of six bird species often struck by aircraft. These models were used to conduct X3D finite element analysis on computer models of the 350-knot capability current production model F-16 canopy. The results, conclusions, and recommendations from these analyses are presented. This report is useful to advance aircraft birdstrike testing techniques, regulation, and threat characterization.

## INTRODUCTION

Each year collisions between aircraft and birds cause millions of dollars of damage and, occasionally, loss of human life. In the USAF, since 1987, seven deaths have occurred due to birdstrikes. Losses have increased from use of jet propelled aircraft at high speeds and low levels. This has resulted in engineers and biologists seeking solutions to prevent future losses. One engineering solution has been to develop birdstrike resistant aircraft components, including transparencies. Numerous computer codes have been written as a method to accomplish resistance testing of these components. One of these codes is X3D.

The X3D finite element analysis computer code, developed by the University of Dayton Research Institute, Dayton, Ohio, is "an explicit finite element program suitable for analyzing transient dynamic and impact problems in solids" (Reference 1). X3D has been demonstrated to be useful as a modeling tool to augment and possibly reduce the amount of costly and time consuming full-scale transparency testing (Reference 2). X3D permits models of both the canopy and the bird (typically as a cylinder). It propels the bird at the canopy at a precise user-defined velocity and impact point. The bird is modeled using a number of values, including: mass, density, length, diameter, shear strength, and elasticity (Reference 3).

Until the last year, values for bird properties have been determined using mostly unreferenced sources and drawing from a largely incomplete resource of biological data. A recent study was conducted to begin to validate and standardize some of the biological unknowns (Reference 4). The objective of this study was to incorporate the new biological data into the X3D program to discover limitations, assess results, and to determine if improvements in biological and engineering technologies will allow significant advancements to aircraft birdstrike modeling techniques.

## MATERIALS AND METHODS

Bird mass, density, length, and diameter values were used from six bird species, including: Canada Goose (*Branta canadensis*), Domestic Chicken (*Gallus gallus*), Herring Gull (*Larus argentatus*), House Sparrow (*Passer domesticus*), Ring-billed Gull (*L. delawarensis*), and Turkey Vulture (*Cathartes aura*). The length was measured from the tip of the bill to the tip of the tail (plucked). The diameter was of plucked birds at its location of greatest magnitude. To compare the Domestic Chicken to previous model applications, a mass of exactly 4-lbs was used.

The typical bird modeling assumption of right circular cylindrical geometry constrains the bird mass, density, and volume inputs to be dependent upon each other. Therefore, to

work with the available biological data, one of the bird geometry inputs had to be altered to fit the cylindrical assumption. Diameter was slightly altered for each species to fit this dependence (Table 1). Each bird model was impacted, at a simulated 350-knots, against the 350-knot capability current production F-16 aircraft canopy computer model.

Historically the assumed cylindrical bird length-to-diameter ratio has been 2:1; therefore, a second set of bird models was developed to accept mass, density, and volume values conforming to this ratio. Using measured mass and density values from the same six species, volume values were calculated to correspond with a 2:1 ratio (Table 2). Each bird model was impacted, at a simulated 350-knots, against current production F-16 aircraft canopy computer model (without head-up-display).

For all 12 simulations a "weak" bird model with a  $\sigma_{ult} = 3,000$  psi was used. All other values and procedures were accomplished consistent with X3D analysis of the F-16 current production canopy accomplished by References 1 and 2. Cylinders were directed to impact the canopy head-on, at Fuselage Station (FS) 113.5. The canopy cross-section used was 0.530" polycarbonate (inner layer), 0.055" polyurethane, 0.125" acrylic (outer layer).

Table 1. Bird geometry based on measured mass, density, and length (Reference 4). Diameter adjusted to fit cylinder model.

Species	Mass (lb)	Density (g/cm <sup>3</sup> )	Length (in)	Diameter (in)
House Sparrow	0.0496	9.827E-05	4.0866	0.6383
Ring-billed Gull	0.8807	8.685E-05	12.6772	1.6243
Herring Gull	2.0767	8.236E-05	16.9409	2.2158
Turkey Vulture	3.7337	8.573E-05	16.1772	2.9800
Domestic Chicken	4.0000	9.771E-05	14.6969	3.0312
Canada Goose	8.4471	8.582E-05	30.1299	3.2826

Table 2. Bird length and diameter geometry adjusted to fit 2:1 ratio model.

Species	Length (in)	Diameter (in)
House Sparrow	1.8814	0.9407
Ring-billed Gull	5.1146	2.5573
Herring Gull	6.9292	3.4646
Turkey Vulture	8.3137	4.1569
Domestic Chicken	8.1439	4.0720
Canada Goose	10.9102	5.4551

Canopy deflection was assessed at FS 113.5 (Node 273) and FS 140.5 (Node 579) due to requirements established by Reference 5. FS 113.5 is the straight-on, center point of contact with the canopy, in-line with the pilot design eye location and FS 140.0 is directly above the pilots head.

## RESULTS

Tables 3-4 list maximum deflections for all 12 impacts. Figures 1-6 graphically display deflection results. In Figures 1-6 substitute "Canada Goose" for "Canadian Goose." Figures 7-8 display size relationships between bird models.

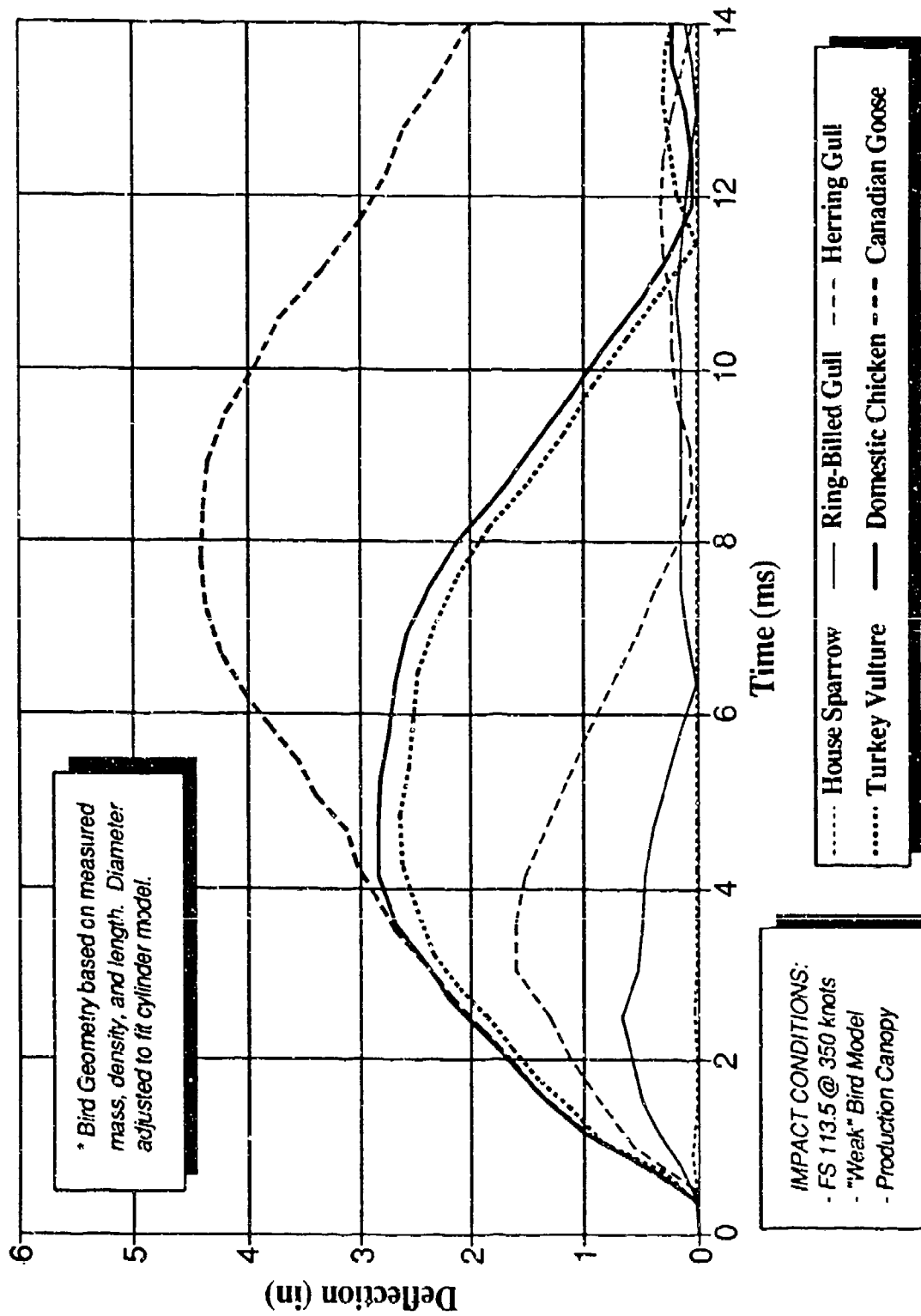
Table 3. Maximum deflections (in inches) of bird models impacting model current production F-16 canopies. Models have diameter adjusted.

<u>Species</u>	<u>Node 273 FS 113.5</u>	<u>Node 579 FS 140.5</u>
House Sparrow	0.05	0.01
Ring-billed Gull	0.67	0.08
Herring Gull	1.61	0.23
Turkey Vulture	2.63	0.67
Domestic Chicken	2.84	0.76
Canada Goose	4.40	2.94

Table 4. Maximum deflections (in inches) of bird models impacting model current production F-16 canopies. Models adjusted to 2:1 length-to-diameter ratio.

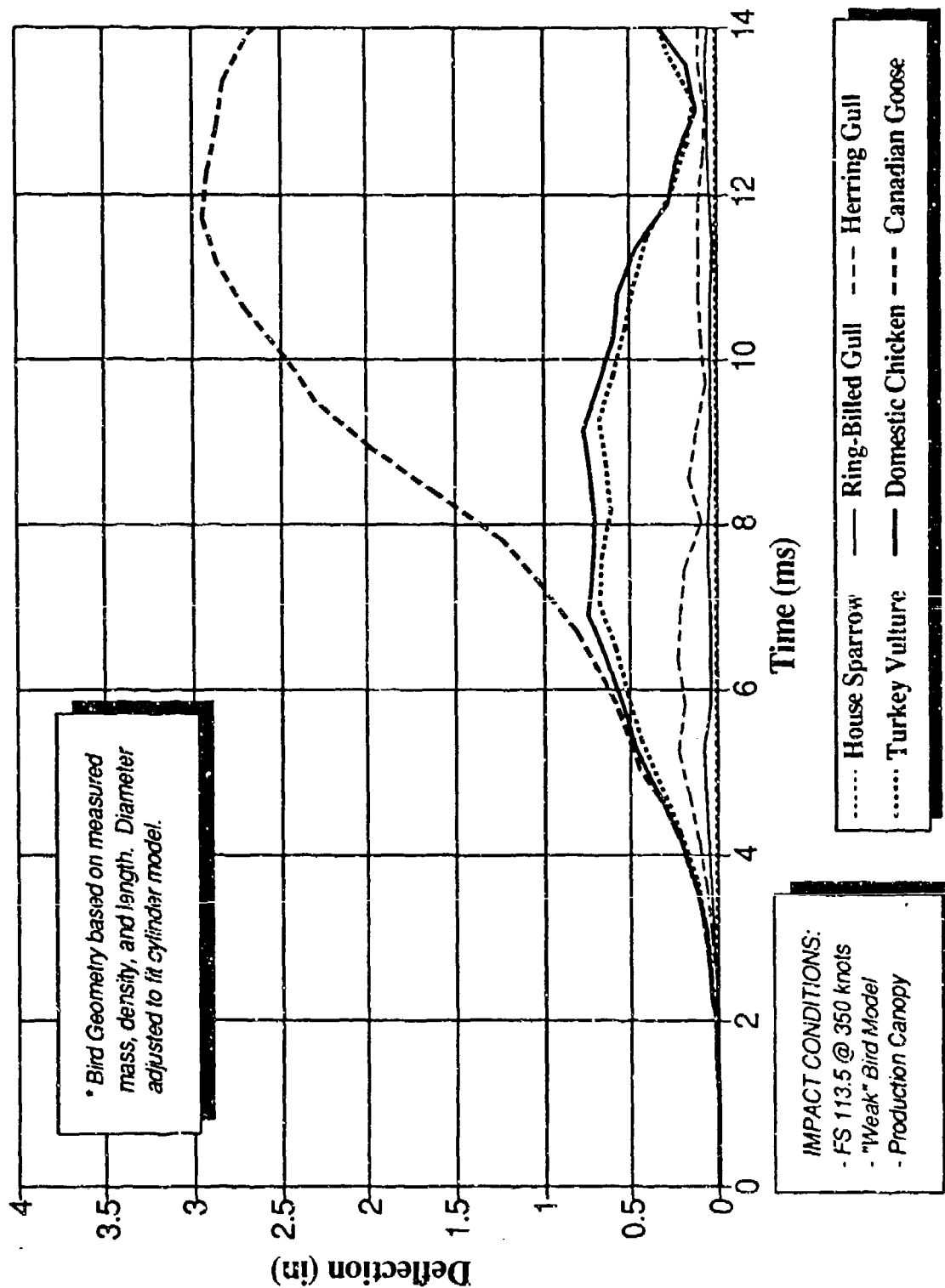
<u>Species</u>	<u>Node 273 FS 113.5</u>	<u>Node 579 FS 140.5</u>
House Sparrow	0.06	0.01
Ring-billed Gull	0.85	0.22
Herring Gull	1.98	0.48
Turkey Vulture	2.62	0.80
Domestic Chicken	2.90	0.89
Canada Goose	5.23	3.57

**Figure 1.**  
**Comparison of Various Bird Species**  
**Deflection Time Histories at FS 113.5**

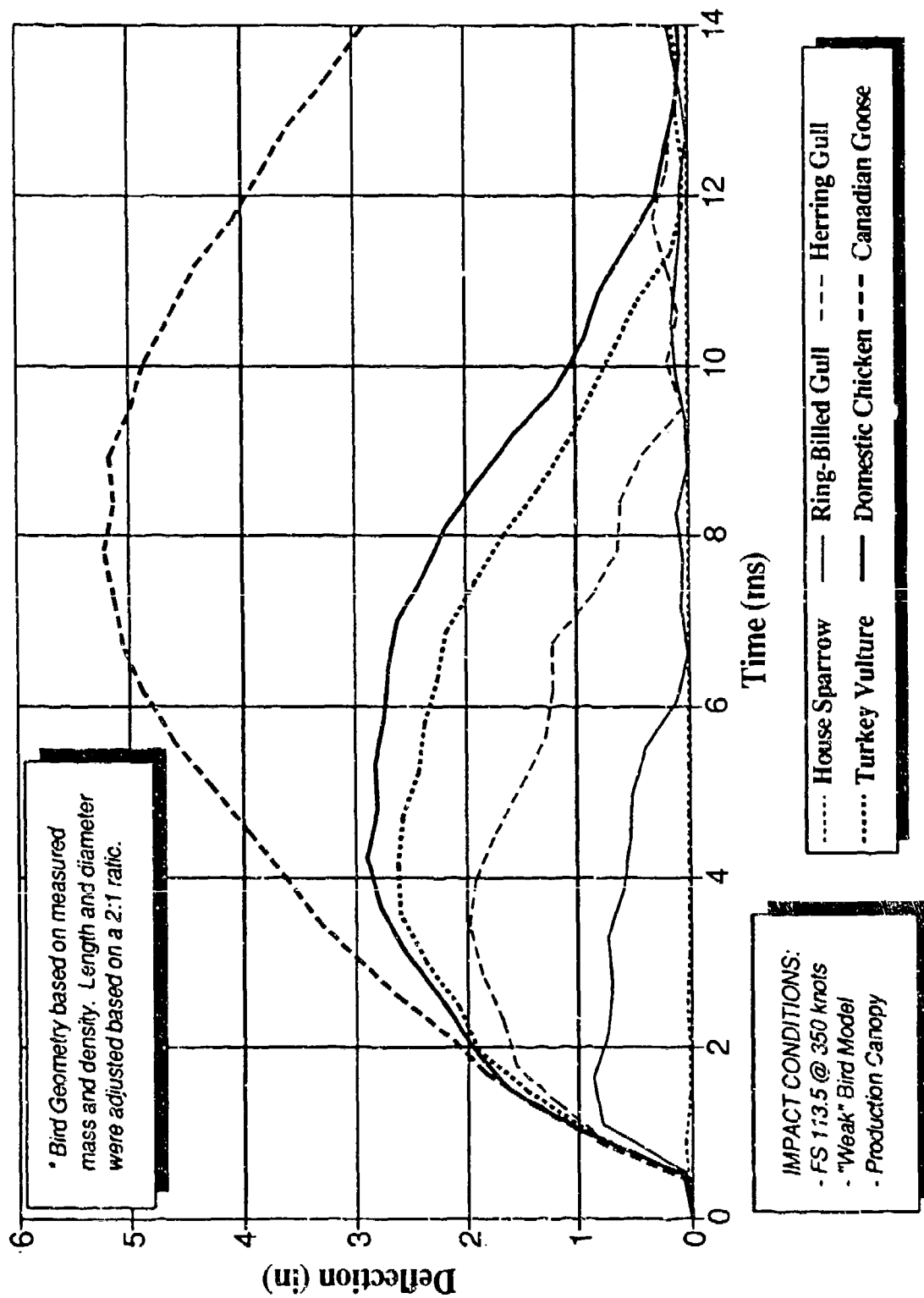




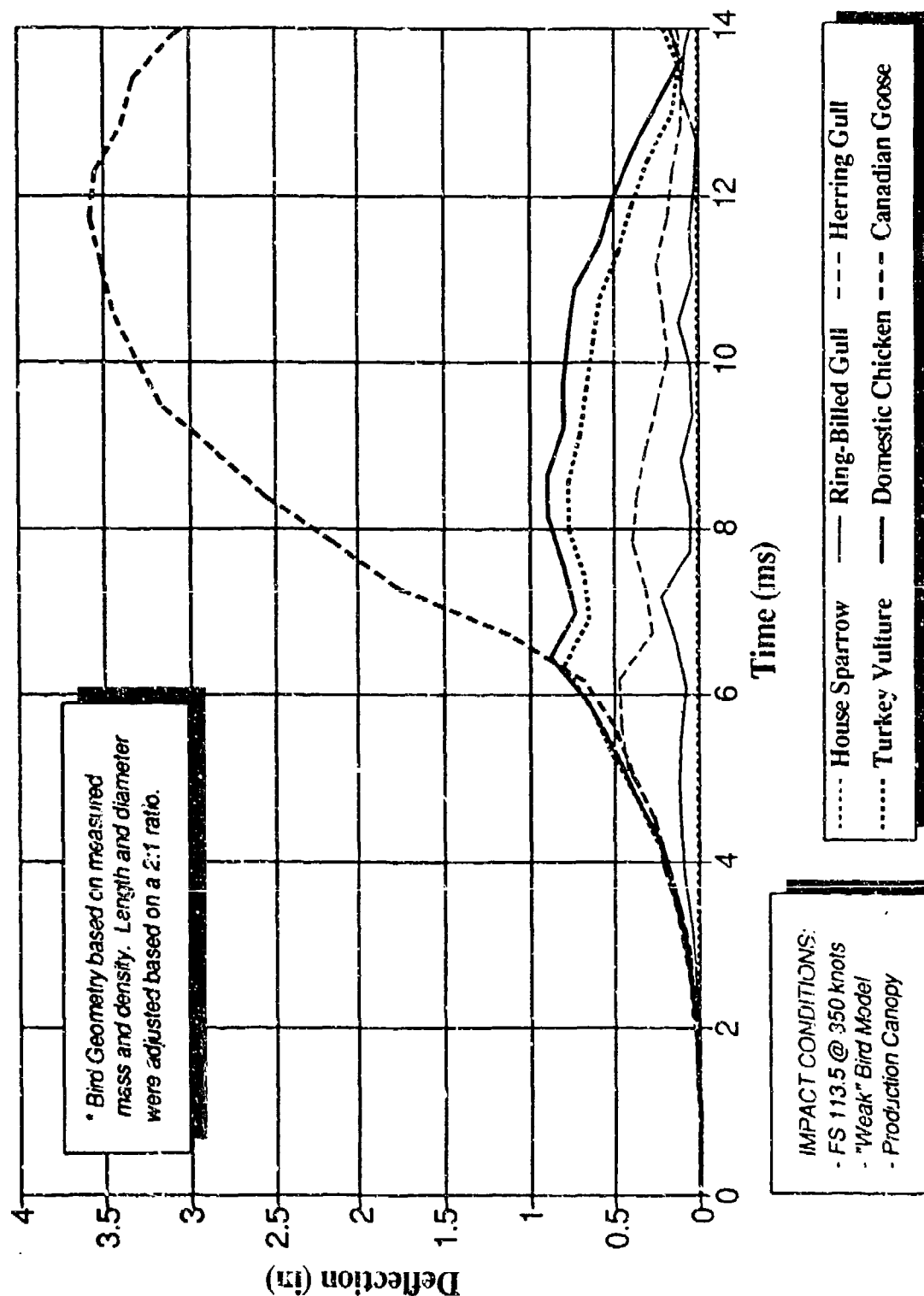
**Figure 2.**  
**Comparison of Various Bird Species**  
**Deflection Time Histories at FS 140.5**



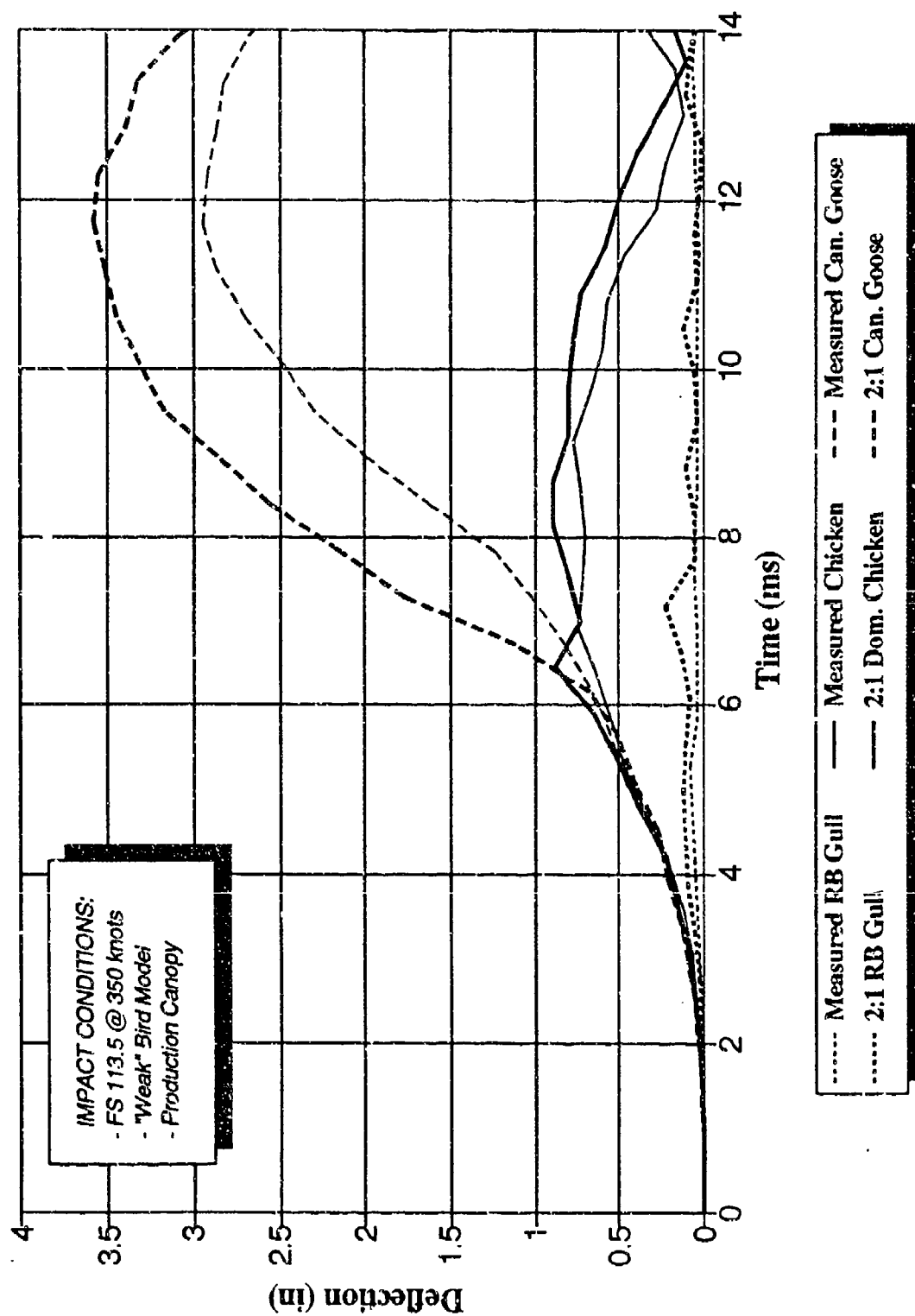
**Figure 3.**  
**Comparison of Various Bird Species**  
**Deflection Time Histories at FS 113.5**



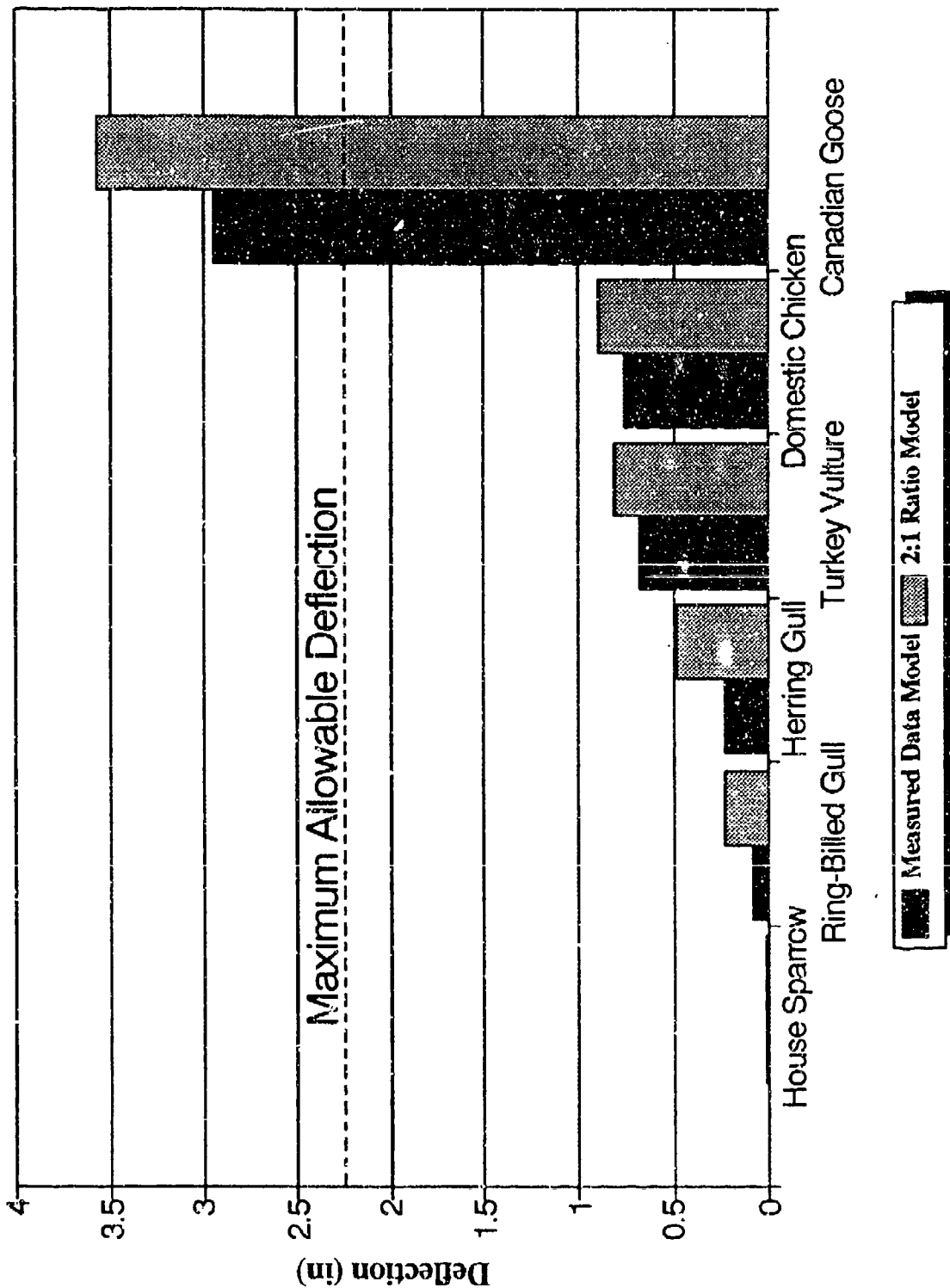
**Figure 4.**  
**Comparison of Various Bird Species**  
**Deflection Time Histories at FS 140.5**

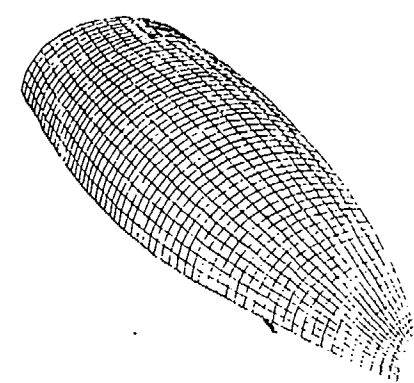


**Figure 5.**  
**Comparison of Various Bird Models**  
 Deflection Time Histories at FS 140.5

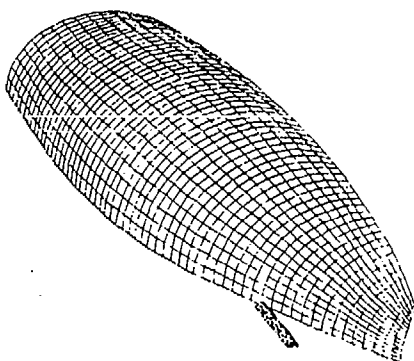


**Figure 6.**  
**Maximum Deflections at FS 140.5**  
**for Various Bird Species and Models**

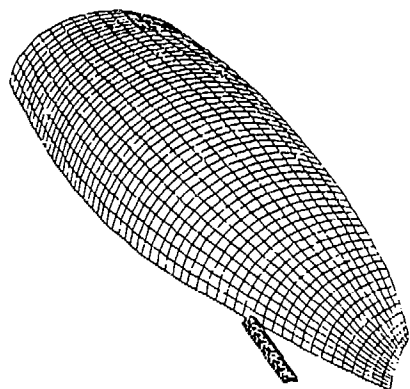




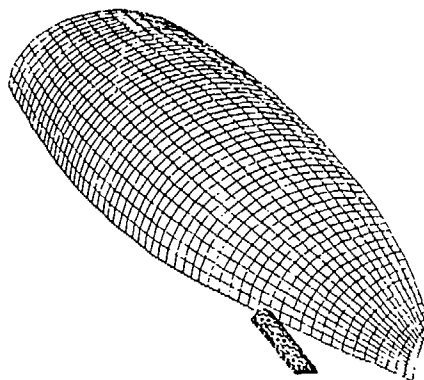
**House Sparrow**



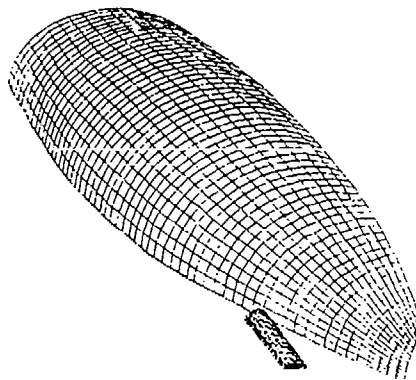
**Ring-billed Gull**



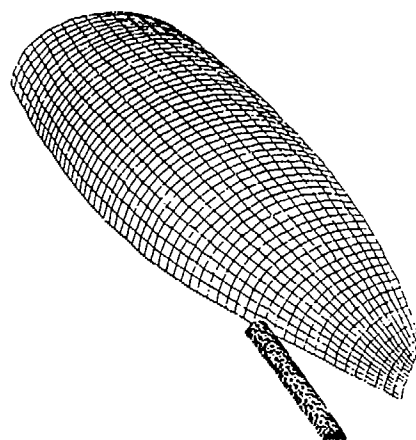
**Herring Gull**



**Turkey Vulture**

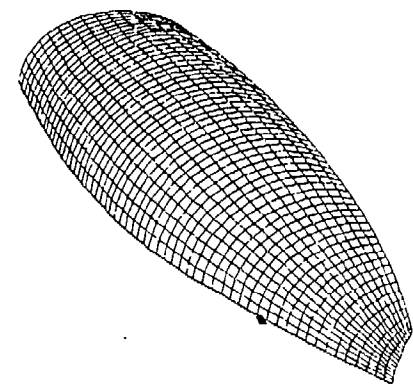


**Domestic Chicken**

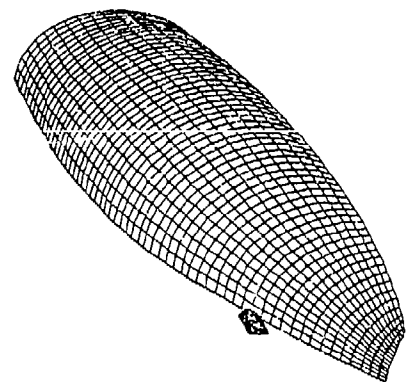


**Canada Goose**

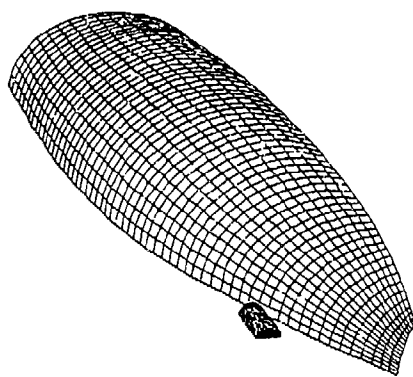
**Figure 7. Size relationship of six diameter adjusted bird models to F-16 canopy before impact.**



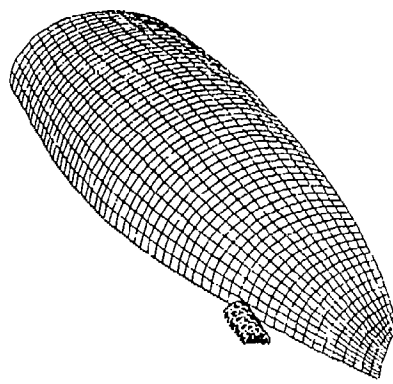
**House Sparrow**



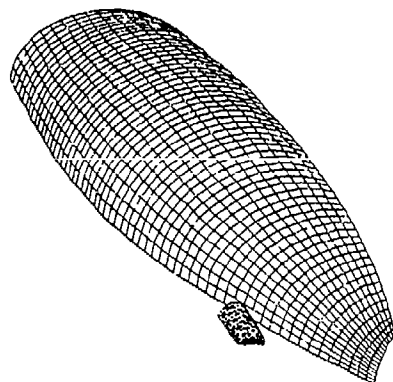
**Ring-billed Gull**



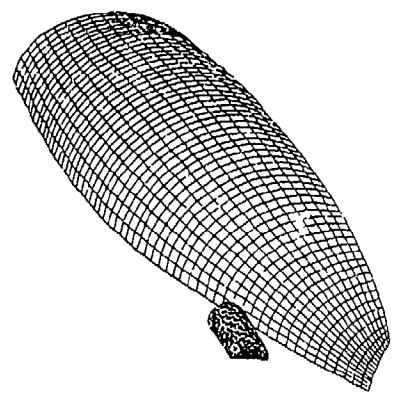
**Herring Gull**



**Turkey Vulture**



**Domestic Chicken**



**Canada Goose**

**Figure 8. Size relationship of six 2:1 length-to-diameter ratio adjusted bird models to F-16 canopy before impact.**

## DISCUSSION

At FS 140.5 the "diameter adjusted" and "2:1 ratio" Canada Goose exceeded the 2.25" maximum deflection requirement established for safe operation of the F-16 canopy by Reference 5. All other species passed the requirement. None of the 12 tests resulted in bird penetration.

Deflections for the Domestic Chicken at FS 140.5 were 0.76" "measured" and 0.89" for the "2:1 ratio." Reference 2 shows a deflection of approximately 1.1" for a similar simulation using a 3100 psi "2:1 ratio" bird and slightly different canopy properties. Deflection data from full-scale testing of F-16 canopies of 0.125" acrylic, 0.060-0.080" interlayer, and 0.500" polycarbonate composition show results of  $\geq 0.63$ " for a 352-knot test and  $\geq 0.94$ " for a 356-knot test (Reference 6). Data "dropout" did not permit peak deflection to be ascertained; therefore, actual deflection may have surpassed these test values.

At FS 113.5, all 12 tests resulted in a pass (no penetration). We expected the Canada Goose to penetrate. Why it did not is not understood; however, the low density, use of "weak" bird model, and uncertainty associated with the polycarbonate failure criterion may be major factors. To model birds,  $\sigma_{ult}$  values of 3,000-4,500 psi have been tried. Reference 7 found the "weak" model to be favorable in analysis of bird impacts on flat plate injection molded panels. More analysis of bird ultimate strength and polycarbonate failure criteria are needed to understand the non-penetration of an 8.5-lb bird.

The deflection time histories appear to be only slightly sensitive to whether the bird model is based on as-measured or 2:1 length-to-diameter ratio data. Modeling with a 2:1 ratio produced more conservative results than modeling based entirely on the as-measured data. Until these simulations are compared to data from equivalent full-scale tests statements concerning accuracy are difficult to make.

The Domestic Chicken had slightly higher deflection results than the Turkey Vulture. The Turkey Vulture is the most important species for the USAF to protect against. Turkey Vultures cause 20% of damaging USAF birdstrikes and have caused at least of \$21M of damage since 1985. Since 1989, collisions with Turkey Vultures have resulted in one pilot fatality and the loss of two F-16's (USAF Bird/Aircraft Strike Hazard Team Data, Tyndall AFB FL). Reference 4 recorded the average mass of 12 Sandusky, Ohio, Turkey Vultures to be 3.7 lbs (plucked mass used). However, the USAF Bird/Aircraft Strike Hazard Team, Tyndall Air Force Base, Florida, considers the US average to be 4.5-lbs. A 4.5-lb Turkey Vulture may cause more damage than the 4-lb Domestic Chicken. This should be a concern of future analysis and decision-making.

Choosing a cylinder to model the bird has limited researchers to adhering to mathematical relationships governing



it. The result of this is not allowing for input of independent biological variables. However, our preliminary results do not show too much sensitivity to model geometry.

The biological data currently available for use during modeling is relatively scarce. During model development, biological data was generally unavailable; therefore, model design did not have to incorporate the ability to input specific values such as "length" and "diameter." Scientists should aim to make the model fit the bird, not make the bird fit the model.

It is important for engineers to make their needs known to the biological field. Density, ultimate strength, shear strength, compressibility, body dimensions, and elasticity are all areas that need to be better defined to advance bird modeling. It is important for the biologists to understand the limitations engineers work under and the high quality of data needed. These investments will eventually save user time and money during development of transparency systems.

The potential rewards for effective integration of biological and engineering technologies are numerous and include: improved accuracy of advanced computer modeling of birdstrikes, aiding international standardization of full-scale testing techniques, increased acceptability and validity to the use of "artificial" birds for full-scale birdstrike testing, and improving standards of birdstrike resistance. This paper is just the beginning of showing how integration of current biological and engineering technologies can benefit flight safety research.

## REFERENCES

1. Brockman, R. A. and T. W. Held. 1992. X3D user's manual. UDR-TR-92-59, University of Dayton Research Institute, Dayton, Ohio.
2. Bouchard, M. P. and J. C. Davisson. 1993. Advanced transparency development for USAF aircraft. Presented at the 34th Structures, Structural Dynamics, and Materials Conference, La Jolla, California, April 19-22.
3. Brockman, R. A. and T. W. Held. 1991. Explicit finite element method for transparency impact analysis. WL-TR-91-3006, Wright-Patterson Air Force Base, Dayton, Ohio.
4. Hamershock, D. M., Seamans, T. W., and G. E. Bernhardt. 1993. Determination of body density for twelve bird species. WL-TR-93-3049, Wright-Patterson Air Force Base, Dayton, Ohio.
5. Lockheed Fort Worth Specification No. 16ZK002F. 1992. Critical Item Development Specification for F-16 A/B/C/D Transparencies. Fort Worth, Texas.
6. Bouchard, M. P. 1989. F-16 500 knot canopy development design recommendations. UDR-TM-89-16, University of Dayton Research Institute, Dayton, Ohio.
7. Braisted, W. R., Stenger, G. J., and P. G. Szalek. 1992. Birdstrike resistance evaluation of flawed injection molded transparent panels. UDR-TR-92-44, University of Dayton Research Institute, Dayton, Ohio.

**ASSESSMENT OF MATHEMATICAL BIRD MODELS FOR BIRD IMPACT  
ANALYSIS WITH AN EXPLICIT FINITE ELEMENT CODE**

F. Stoll  
R. A. Brockman  
University of Dayton

# **Assessment of Mathematical Bird Models for Bird Impact Analysis with an Explicit Finite Element Code**

**Frederick Stoll and Robert A. Brockman  
University of Dayton Research Institute**

## **ABSTRACT**

Military fighter aircraft occasionally suffer collisions with birds, sometimes at near-sonic relative velocities. These collisions pose a threat to the structural integrity of the aircraft, and thus are of concern to designers. An explicit three-dimensional finite element code for dynamic impact analysis, named X3D, has been under continuous development for several years at the University of Dayton Research Institute, with a major area of emphasis being the ability to analyze birdstrikes of crew enclosure transparencies of fighter aircraft. The bird model used in these analyses is critical only to the extent that appropriate loads are applied to the impacted surface, but even with this limited requirement for modelling accuracy, the bird poses modelling difficulties because of the tendency of bird bodies to behave as liquids during high speed impacts. This paper presents the results of a study of two different bird models available within X3D, one of which uses a conventional solid finite element representation, and the other which models the bird as a closest-packed assemblage of spherical elements. Various modelling parameters are studied, including element size and material constitutive properties. Contact forces computed analytically are compared with experimental data to assess the two different bird models, and to establish improved guidelines for the specification of the various modelling parameters.

## **INTRODUCTION**

Military fighter aircraft occasionally suffer mid-air collisions with birds, sometimes at near-sonic relative velocities. These collisions pose a threat to the structural integrity of the aircraft, and thus are of concern to designers. As part of a long-term effort to improve the resistance of fighter aircraft crew enclosure transparencies to birdstrikes, a finite element code for the analysis of high-speed impacts has been under continuous development for several years at the University of Dayton [1]. The finite element code, named X3D, is capable of performing three-dimensional nonlinear transient analysis of dynamic events including impact, using an explicit time integration scheme. Finite element bird models have been used in X3D in the simulation of birdstrike events [1]. However, from the standpoint of engineering materials and finite element modelling practices, the response of a bird body during a high-speed impact event is quite unusual. Thus, there remain questions as to the best method for modelling the bird body, and what material properties to assign to it. This paper presents the results of an analytical study intended to help answer these questions, and to provide the basis for developing and implementing improved bird models for use in impact simulations with X3D.

The scope of concern here is limited to the structural loads experienced by an aircraft component during high-speed birdstrikes. Thus, the bird's physical characteristics and behavior during impact are important only to the extent that they influence aircraft structural loads. High-speed here refers to velocities equal to and greater than the low-altitude cruise velocity of typical

fighter aircraft. The basic work on high-speed bird impact loads was done during the mid-to-late 1970's using rigid-wall impact experiments [2-6]. Important conclusions of this work are noted here. The stresses generated during an impact event so greatly exceed the tissue strength of the bird that the bird behaves as a fluid with negligible viscosity [2,4,5,6]. The loads produced by the bird are adequately duplicated by representing the bird as a right circular cylinder with the same mass, density, and compressibility as the bird [4]. The bird may be modelled as a material with 10% porosity (containing air) having an average specific density of 0.95 [2,4,6]. In rigid-wall impacts, the impact event is characterized by an initial shock load, followed by a steady-flow load, with the impact duration approximately equal to the length of the bird divided by the initial velocity (assuming end-on impact) [5,6].

In the current investigation, two general mathematical soft-body bird models available within the X3D code are studied through rigid-wall impact simulations. The bird models are assessed by comparing their impact response with the behavior expected based on the conclusions noted in the previous paragraph. Computed values for contact forces and pressures are used to quantify various aspects of the impact event, and visualization of the impact is used to establish qualitative aspects of the bird-model behavior. For each of the two general bird models considered, the parameters which characterize the material behavior are varied in order to create a variety of specific bird models. Section 2 provides a brief description of key characteristics of the X3D finite element analysis code, the bird models available, and post-processing parameters used in the current investigation. Section 3 includes a presentation and discussion of impact-simulation results for a variety of bird-model configurations. Conclusions from the current study and recommendations for future work are summarized in Section 4.

## FINITE ELEMENT ANALYSIS

### Overview of the X3D Finite Element Code

The finite element code X3D [1] is capable of performing three-dimensional dynamic analysis of materially and geometrically nonlinear systems. The code uses an explicit time-integration scheme which avoids the need to form large systems of equations for expressing the equations of motion of the discretized system. This formulation is well suited to short-duration dynamic events such as wave propagation and impact simulation but requires the use of very small time increments, making the method unattractive for long-duration events. X3D incorporates both solid and shell finite elements, and can simulate a variety of material models. Advanced pre-processing and post-processing features are available for finite-element model development and output review. A full discussion of the basis and capabilities of X3D is included in [1].

The explicit time-integration scheme is carried out in a three-step procedure for each time increment, as summarized in the following equations for a single degree of freedom:

$$a(t) = (f_{ext}(t) - f_{int}(t)) / m \quad (1)$$

$$v(t + \Delta t/2) = v(t - \Delta t/2) + \Delta t a(t) \quad (2)$$

$$u(t+\Delta t) = u(t) + \Delta t v(t+\Delta t/2) \quad (3)$$

where  $u$ ,  $v$ , and  $a$  are the generalized displacement, velocity, and acceleration, respectively,  $m$  is the generalized mass,  $t$  is the time at which the solution  $u$  is initially known, and  $\Delta t$  is the nominal time increment between successive solutions. Quantity  $f_{ext}$  is the externally applied generalized force, and  $f_{int}$  is the internal generalized force which would arise, for example, due to non-zero stresses in an elastic body.

In the actual implementation of the time-integration scheme, the time increments need not be uniform from one step to the next. In order to maintain stability of the time-integration scheme, the time increment is kept less than or equal to the value

$$\Delta t = \frac{2}{\omega_c} \quad (4)$$

where  $\omega_c$  is the largest element natural frequency among all finite elements in the model. The natural frequencies of each element are affected by the deformation history of the element, and so the frequencies must be computed at each time step. The constraint on the time increment is an issue in assessing the different bird models, as will be shown later.

A contact algorithm is incorporated in X3D to facilitate impact simulation. A control surface through which no penetration may occur is defined in terms of "master elements." For solid master elements, one surface is designated as the contact surface; for shell master elements, the element reference surface is the contact surface. The opposing body in an impact is designated in terms of "slave nodes;" these nodes are generally the nodes of some finite element body, such as one of the finite-element bird models discussed later in this paper. The contact constraint is that no slave node may lie in a specified region "behind" any master-element surface. After the computation of the displacement solution at each time step, the contact constraints are evaluated. Where the constraint is violated, the translational velocities of the slave node and the nodes connected to the contact surface of the master element are adjusted so that the following conditions are met: i) the relative velocity of the slave node normal to the contact surface is zero, and ii) the linear and angular momenta of the system are preserved. (All mass in the system is lumped at the finite element nodes.) Contact forces at a node are computed as the sum of the internal forces and the forces required to accelerate the node to its corrected velocity over the time increment just completed. From these contact forces, contact pressures are computed.

X3D has a variety of ways to handle predicted material failure, and these are described in [1]. Of interest in assessing mathematical bird models is the treatment of material failure in the solid elements typically used to model birds in impact simulations. When the effective stress in an element surpasses the specified ultimate stress (see [1] for a complete discussion), the element is deleted from the finite element model. However, any slave nodes which are freed by the deletion of an element remain in the model as point masses, and thus are able to further interact with the master elements through the contact algorithm described above.

## Description of Mathematical Bird Models

*Tetrahedral-element bird models:* It has been a common practice among X3D users to model birds and other impacting bodies using solid tetrahedral elements. Most commonly, a circular cylindrical shape is used for bird models, though this is not a limitation of the method. A quarter-cylinder model which is used with two symmetry planes in the current study is depicted in Figure 1. This model has 480 elements and 171 nodes. (Simulations of windshield birdstrikes are usually performed with one symmetry plane using a half-cylinder bird model.)

Tetrahedral elements have four corner nodes and use linear interpolation functions for displacements, so strain and stress measures are constant within an element. Common to all material models for the element is the use of an elastic pressure-volume relation. Define a compressions ratio  $\eta$  as

$$\eta = \rho/\rho_0 - 1 \quad (5)$$

where  $\rho$  is the material density,  $\rho_0$  is the initial density, and positive and negative values of  $\eta$  correspond to compression and tension, respectively. The elastic pressure-volume relation is given by

$$p = K_1 \eta + K_2 \eta^2 + K_3 \eta^3 \quad \eta > 0 \quad (6)$$

$$p = K_t \eta \quad \eta < 0 \quad (7)$$

It can be seen that a cubic relation is accommodated for compression, whereas a linear relation is used for tension. For all results presented in this paper, the following coefficient values were used:

$$K_1 = 337,000; \quad K_2 = 729,000; \quad K_3 = 2,202,000; \quad K_t = 1000 \quad (8)$$

where  $p$  is given in lbs./in.<sup>2</sup>. The compressive behavior defined by these coefficients is that of water. The coefficient  $K_t$  was selected without any particular quantitative basis; however the impact simulations performed in this study have shown little sensitivity to the selection of this parameter.

It remains to relate the deviatoric stresses  $\sigma'_{ij}$  to the deformation of the material. The deviatoric stresses are defined by

$$\sigma'_{ij} = \sigma_{ij} - p \delta_{ij} \quad i, j = 1, 2, 3 \quad (9)$$

where  $p$  is the hydrostatic pressure of equation (6) or (7) and  $\delta_{ij}$  is the Kroniker delta function. Two different general models for this aspect of material behavior were used in the simulations reported here. The first is an elastic-plastic deviatoric stress model. Four key parameters are used to specify the material properties: 1) elastic shear modulus  $G$ , ii) yield stress  $\sigma_y$ , iii) ultimate stress  $\sigma_u$ , and iv) hardening modulus  $H$ , defined by

$$H = \frac{EE'}{E - E'} \quad (10)$$

where  $E'$  is the slope of the stress-strain curve past the point of yielding. The details of this stress model, described in [1], are relatively complex, and thus are not repeated here. Instead, a degenerate case is used to illustrate some key aspects of the material model. Consider the case of uniaxial tension with axial stress  $\sigma$  and axial strain  $\epsilon$ , with a linear pressure volume relation defined by the coefficients  $K_1=K_2=K$ ,  $K_3=0$ . For this case,  $K$ ,  $E$ ,  $G$ , and Poisson's ratio  $\nu$  are related by the equations

$$K = \frac{E}{3(1-2\nu)} ; \quad G = \frac{E}{2(1+\nu)} \quad (11)$$

For this degenerate case, a schematic stress-strain diagram is shown in Figure 2. If the axial stress reaches  $\sigma_u$ , the material is assumed to have failed. The plastic strain  $\epsilon_p$  defined in Figure 2 (ultimate strain minus yield strain) is a measure of the plasticity of the material. As can be seen in the figure, small differences between  $\sigma_y$  and  $\sigma_u$  can result in relatively large values of  $\epsilon_p$  if  $E'$  is small compared to  $E$ .

The second general material model used here is a viscous liquid model. For this model, the stress components are given by

$$\sigma_{ij} = -p\delta_{ij} + 2\mu d'_{ij} \quad (12)$$

where  $\mu$  is the dynamic viscosity of the fluid and  $d'_{ij}$  are components of the deviatoric portion of the rate of deformation tensor. These are defined by

$$d'_{ij} = d_{ij} - \frac{1}{3}\delta_{ij}d_{kk} ; \quad d_{ij} = \frac{1}{2}\left(\frac{\partial v_i}{\partial x_j} + \frac{\partial v_j}{\partial x_i}\right) ; \quad i, j = 1, 2, 3 \quad (13)$$

where  $v_i$  are the velocity components,  $x_i$  are the spatial coordinates of a material point, and summation over repeated index  $k$  is implied.

*Martin's spherical-element soft-body model:* In [7], Martin presents a soft-body model which is fundamentally different from a traditional finite element model, but which can be used in conjunction with finite elements. The model has been implemented, with some alterations, in the X3D analysis code. The model uses spherical elements, each one of which is centered around a node used to track the element motion. Initially, the spherical elements are in a closest-packed configuration, so that each internal element (not on a surface) is just touching 12 adjacent elements. Denoting the initial radius of each element as  $R_0$ , the initial node-to-node spacing of adjacent elements is  $2R_0$ . The mass of the body is assumed to be distributed evenly among all elements. The density of each spherical element is greater than the average density of the body in order to compensate for the unfilled space which remains in the closest-packed model. A visualization of a half-cylinder model is shown in Figure 3. The nodes at the center of each element are shown as small circles; the elements themselves are not shown.

A search distance  $D_s$  is specified; after deformation has begun, only element pairs with a node spacing of less than  $D_s$  will interact directly. For all results discussed here,  $D_s = 2R_0$ . Assuming that an element has  $n$  neighboring elements which fall within the check distance, the



radius  $R_i$  assigned to that element for purposes of determining volume, density, etc. is given by

$$R_i = \frac{1}{n} \left( \frac{D_1}{2} + \frac{D_2}{2} + \dots + \frac{D_n}{2} \right) \quad (14)$$

where  $D_j$  is the node-to-node distance to the  $j^{\text{th}}$  neighbor. The pressure for the element is then given by

$$p = K_1 \eta + K_2 \eta^2 + K_3 \eta^3 \quad \frac{d\eta}{dt} > 0 \quad (15)$$

$$p = K_1 \eta \quad \frac{d\eta}{dt} < 0 \quad (16)$$

where  $\eta$  is given in equation (8). Equations (15) and (16) are identical to equations (6) and (7), respectively, except that the decision of which equation to use is based on the sign of the rate  $d\eta/dt$  rather than on the sign of  $\eta$ . For each pair of interacting elements, a contact area  $A$  is defined, given by

$$A = \pi \left[ R_o^2 - \left( \frac{D_j}{2} \right)^2 \right] \quad , \quad \frac{D_j}{2} \leq R_o \quad (17)$$

where  $D_j$  is the node-to-node spacing. The force acting on an element due to the interaction is the internal pressure of the neighboring element multiplied by the contact area, directed toward the first element along a line between the two nodes.

There is a significance to the use of the rate  $d\eta/dt$  in deciding whether to use equation (15) or equation (16). Martin [7] found it necessary to use reduce the pressure in expanding elements relative to the pressure in contracting elements in order to stabilize the response of the soft body (to keep it from flying apart). Martin's pressure-volume relationship [7] is somewhat different from that of equations (15) and (16), but his basic approach is to reduce the compression-induced pressure of an element which is expanding to 1/3 the value of an element which is contracting. For that reason, two different bird models are investigated here: i) an "Undamped model" for which  $K_1 = K_1$ , and ii) a "Damped model" for which  $K_1 = K_1/3$ .

### Results Presentation Parameters

A few parameters are described here which are used in assessing the performance of the various bird models. These parameters are geared toward the nominally axisymmetric impact event modelled here, namely a circular cylinder impacting a rigid wall end-on. It is assumed that the rigid wall target lies in the  $z=0$  plane, and that coordinates  $(x,y)$  or  $(r,\theta)$  are measured with respect to the impact center. The cumulative impulse  $I(t)$  is given by

$$I(t) = \int_0^t \int_A p(x,y,t) \, dA \, dt \quad (18)$$

where  $p(x,y,t)$  is the contact pressure. (The contact forces/pressures computed in an analysis are extremely spiky with respect to time; the integration used in equation (18) provides a variable which is much easier to interpret.) In the results presented,  $t=0$  corresponds to the initial impact.

Two additional parameters are used in order to quantify the "spreading" of the bird during impact. These are called "radial moments of impulse"  $H1$  and  $H2$ , and are defined by

$$[H1, H2] = \int_0^{t_f} \int_A p(x,y,t) [r, r^2] dA dt \quad (19)$$

where  $t_f$  is the time at the end of impact. Because of the weighting of the pressure by  $r$  or  $r^2$ , the more the bird has spread, the larger the measures  $H1$  and  $H2$  become. Normalized values for the radial moments of impulse are used for actual presentation of results:

$$\overline{H1} = \frac{H1}{I(t_f) R} ; \quad \overline{H2} = \frac{H2}{I(t_f) R^2} \quad (20)$$

## RESULTS AND DISCUSSION

### Description of Test Case

A standard test case was used for all results presented here. The bird model is a right circular cylinder with a length  $L=6$  in., diameter  $D=3.5$  in., and mass  $m=.005126$  lbs.-sec.<sup>2</sup>/in.= 2 lbm.. The initial velocity is  $V=300$  kts. (6076 in./sec.), and the cylinder impacts a rigid wall end-on. The resulting impact event is nominally axisymmetric, although the finite element models are three-dimensional. For the tetrahedral-element models, the quarter-cylinder model of Figure 1 is used (except where otherwise noted). For Martin models, the half-cylinder model of Figure 3 is used (except where other wise noted).

All analytical results are referred to full-cylinder values. The reference impulse value is the initial momentum of the model,  $M_{ref}=mV=31.1$  lb.-sec.. The reference time is the nominal "squash-up" time,  $t_{ref}=L/V=0.00099$  sec..

### Standard In-House Bird Models

The first models investigated are three tetrahedral-element models representative of bird models which have been used at the University of Dayton Research Institute (UDRI) in birdstrike investigations. These all use the elastic-plastic material model. As mentioned previously, these models use the pressure-volume relationship of water for compressed elements (see equations (6-8) and the accompanying discussion). Other material parameter values include  $G=3000$  psi.,  $\sigma_y=3000$  psi., and  $H=300$  psi., and three different values for  $\sigma_u$  corresponding to three named bird models. The values for  $\sigma_u$  and the corresponding values of plastic strain  $\epsilon_p$  (defined in Figure 2) are indicated in Table 1 for the three bird models. The parameter values noted here were selected without any particular quantitative basis, except that they provide impact simulation results which appear to be reasonable, and the relative values of the parameters give the ability to adjust the plastic strain at failure in the manner indicated. The lack of a better quantitative bases for the parameter values was part of the motivation for the current study.

Name	$\sigma_u$	$\epsilon_p$
"Weak Bird"	3000	0
"Semi-Strong Bird"	3100	33 %
"Strong Bird"	4500	500 %

Table 1. Ultimate stress and plastic strain levels for three standard in-house bird models.

Visualizations of impact simulations at five time steps are shown in Figure 4 for each of the standard in-house bird models. Nodes which have been freed by element failures are depicted as small isolated circles. A remarkable variety in the responses of the three models is apparent. As each element layer of the Weak bird impacts the wall, the element layer is quickly deleted due to predicted material failure. As a result of the loss of effective material volume which accompanies element deletion, there is very little spreading induced, and the entire bird collapses against the wall with little outward momentum. With the Semi-Strong bird, there is some degree of outward momentum (spreading) induced as elements contact the wall, but the elements are deleted before the spreading is significant. The energy absorbed during material deformation is significant, because at the end of the impact event, a large chunk of the cylinder remains against the wall with zero velocity. With the Strong bird, there is significant spreading, and indeed the plastic strain to failure is so large that the momentum is absorbed with the failure of a single element. The deformed bird actually bounces off the wall with a small amount of reverse velocity. None of the three standard bird models exhibits the fluid-like behavior expected based on the conclusions of [2-6] noted in the introduction.

Plots of normalized cumulative impulse versus normalized time for the three standard bird models are included at the bottom of Figure 4. Both the Weak and Semi-strong model are successful in recapturing the initial momentum in terms of total impulse, and both models complete the impact event at the approximate time  $t=t_{ref}$ . In contrast, the Strong model accumulates a total impulse in excess of the initial momentum, because of the "bounce" which it exhibits, and the impact duration is only about 60% of the expected value. The stairway profile for the Weak bird clearly reflects the sharp contact-load spike associated with the impact of an element layer and subsequent failure of all elements in the layer. The Semi-Strong model also reflects an extremely spiky contact force history, though it is irregular compared to the Weak model behavior. The spiky contact forces for the Weak and Semi-Strong models are not consistent with fluid-like bird-model response which is sought.

### Flattening-Limited Element Models

As discussed earlier, a viscous-fluid material model is available within X3D, and this model should, ostensibly, provide the fluid-like bird-model behavior which is sought. However, the finite elements use a Lagrangian reference frame; this means that the elements move with the fluid material and are thus subjected to extreme element distortion which ultimately causes numerical failure. Because of this fact, an effort was made to establish a set of parameter values which could be used with one of the existing material models (thus allowing a quick proof-of-

concept) to create tetrahedral elements with the following two characteristics: i) the elements should simulate low-viscosity fluid behavior, and ii) the element material should "fail" (and the element deleted from the finite-element model) before the element distortion becomes so large as to cause numerical failure.

The elastic-plastic solid material model discussed previously has a stress-based material failure criterion available, so this feature is exploited in order to effect the element deletion which is sought. Limited fluid-like behavior can be simulated with this material model by setting the shear modulus  $G$  to a sufficiently low number. In order to specify a measure of element distortion at which an element is deleted, the following procedure is used. The yield stress  $\sigma_y$  is set equal to the ultimate stress  $\sigma_u$  in all cases, so that the plastic hardening does not come into play. The value of  $\sigma_u$  is set so that in an incompressible squashing of the material in one direction (with expansion of the material in the remaining two directions) the material fails at a pre-specified value of flattening  $f$ , defined by

$$f = \frac{h_{fail}}{h_{initial}} \quad (21)$$

where  $h$  is the dimension of a material element in the direction of the squashing. The corresponding value of ultimate stress, derived in the Appendix, is given by

$$\sigma_u = 3G \ln(1/f) \quad (22)$$

Impact simulations were performed with the flattening-limited tetrahedral element bird models for a range of values of  $f$ . For comparison purposes, an impact simulation was performed with a viscous-liquid bird model, using a dynamic viscosity value ten times that of water. Visualizations of impact simulations with the liquid bird model and with flattening-limited element models for  $f=1/10$  and  $f=1/3$  are shown in Figure 5. The liquid model experiences numerical failure at a normalized time of 0.8, due to the extreme element distortion which develops. For the  $f=1/10$  flattening-limited elements, the response looks similar to that of the liquid bird, but the deletion of the elements associated with material "failure" prevents numerical problems. The  $f=1/3$  flattening limited element model behaves similarly to the  $f=1/10$  model, except that the earlier element failures appear to reduce the spreading somewhat. A plot of normalized cumulative impulse versus normalized time for the three models is shown in Figure 6. The curves for the liquid model and the  $f=1/10$  model are very similar up to the point of numerical failure of the liquid model, and these curves are much smoother than the curves for the Weak and Semi-Strong standard models, indicating a smoother contact-force history. The curve for  $f=1/3$  is less smooth than the curve for  $f=1/10$ , but is still smoother than the curves for the Weak and Semi-Strong standard models.

The normalized radial moments of impulse for several flattening-limited element models are plotted versus  $f$  in Figure 7. It was expected that the normalized moments would vary monotonically with  $f$ , but they actually oscillate somewhat; nonetheless, the normalized moments generally increase with decreasing  $f$  indicating, as expected, increased "spreading" as greater element flattening is allowed. Assuming that, for small values of  $f$ , the radial moments of impulse are close to physically realistic values, the results shown in Figure 7 are used to establish

reference values  $\overline{H1}_{ref}=0.98$  and  $\overline{H2}_{ref}=1.33$  for comparison with other results.

The regimes of initial shock loading and the steady-flow loading are generally treated independently in the basic literature [2-6], so experimental data have not been located which are directly suitable for computing  $H1$  and  $H2$ . However to provide some measurement-based values for comparison, nondimensionalized steady-flow radial pressure distributions from gelatin-bird impact tests from Figure 3.11 of [3] were used to compute the radial moments of impulse, and these values are indicated in Figure 7. These radial moments are shown as ranges, reflecting the uncertainty in the pressure distribution at large radius values. The selected reference values of the radial moments are somewhat lower than the steady-flow-based values; however this is appropriate because the reference values include the contribution of the initial shock loading which occurs before significant spreading takes place.

A comparison of the normalized radial moments of impulse of the Weak and Semi-Strong standard models with the reference values from Figure 7 is presented in Figure 8. The radial moments of impulse of the standard models fall significantly below the reference values. This gives quantitative evidence that the two standard models exhibit inadequate spreading on impact, and these models can be expected to produce a load footprint on a target structure which is somewhat smaller and more concentrated than would occur in reality. Results from a refined-grid Semi-Strong bird model, for which the nominal element dimensions were reduced by 1/3, are included in Figure 8. These results agree closely with the results for the baseline Semi-Strong model.

The results presented here support the use of flattening-limited elements in preference to the standard in-house bird models. However, in some cases there is a penalty for using the flattening-limited elements. As a tetrahedral element is flattened or distorted, the element's natural frequency  $\omega_e$  is generally increased. Because the highest natural frequency of all elements in the model is used to set the time increment per equation (4), the flatter an element is allowed to become the smaller the time increment may become. This directly affects the computational expense of an analysis which spans a particular time interval. (Whether or not the bird elements actually determine the allowable time increment depends on the rest of the finite element model.) It would thus be advisable to use the largest value of  $f$  (the least flattening) judged to be accurate based on Figure 7, perhaps a value of 0.2 or 0.25. An alternate approach to flattening-limited elements would be to delete bird-model elements whose natural frequency exceeded a specified value. This method has the advantage that it weeds out the occasional element which is much higher in natural frequency than all others.

### Martin Soft-Body Model

Visualizations of impact simulations using the Undamped and Damped Martin bird models are presented in Figure 9. As expected, the Undamped model exhibits inappropriate behavior; the outer layer of elements is expelled upon impact, and the model in general seems to expand too much. The Damped model appears to have qualitatively correct behavior. However, whereas the initial outward expansion of the liquid element bird model is concentrated near the wall (see Figure 5), the Martin model seems to expand outward along much of its length.

The cumulative impulse histories of the two Martin bird models and two flattening-limited element models are plotted in Figure 10. The Undamped Martin model has not recaptured its initial momentum (in terms of impulse) in the plotted time range, and appears unlikely to do so. The Damped Martin model recaptures most of its initial momentum, although the impact duration somewhat exceeds the nominal value of  $t_{ref}$ . There is a large initial build-up of impulse for the Martin models as compared to the tetrahedral-element models; the Damped Martin model accumulates 37% normalized impulse in the first tenth of the nominal impact duration, compared with 18% for the flattening-limited element models. The following explanation is offered for this behavior: because of the initial closest-packing of the spherical elements, the inclination of the forward elements to splay outward upon impact is suppressed by a resistance to material shearing caused by mechanical interference associated with the closest-packed configuration. In order for the forward elements to expand outward, there must be a general expansion of the body along the length. This is exactly the behavior noted in the previous paragraph based on impact visualizations.

The normalized radial moments of impulse for the Martin bird models are compared with the reference values in Figure 11. The values for the Damped model match very closely the reference values, indicating that, in a time-averaged sense, the Damped Martin model spreads in the desired manner. Results are also presented in Figure 11 for a refined Damped model which used 840 elements/nodes as opposed to 344 for the baseline model. The radial moments of impulse for the two models agree closely.

An attraction of the Martin bird model compared with the conventional tetrahedral element models is that the volume loss associated with deletion of tetrahedral elements is avoided. The model is difficult to assess in theoretical terms, because it does not have quantified continuum properties outside of the pressure-volume relationship, and because it requires input parameters, such as the damping ratio and the search radius, which have no direct physical meaning. The Damped Martin model seems to spread in the desired manner, but there is other evidence that the expected fluid-like behavior is not closely represented. It may be possible through experimentation to determine input parameter values which improve the response of the model.

## CONCLUDING REMARKS

### Summary

An analytical assessment of bird models used in finite-element impact simulations was conducted by performing high-speed rigid-wall impact simulations and inspecting the qualitative bird-model behavior and the contact pressure results. Bird models considered included solid tetrahedral-element models with a variety of material properties, and the Martin spherical-element model. Based on this study, several observations are made.

1. The standard in-house bird models used at UDRI incorporate a shear modulus value which is too large, thus precluding the liquid-like behavior expected in a high-speed impact. The weaker two models of the three considered experience early element deletion (associated with

predicted material failure) which prevents the expected spreading of the bird model as it squashes against the impact surface. The strong bird model suffers no material failure, and actually bounces off the impact surface, which is not consistent with experimental observations.

2. Material property values were established for a flattening-limited tetrahedral element model which behaves similar to a liquid, except that material "failure" occurs for highly flattened or distorted elements, leading to their deletion from the model before numerical problems occur. This model appears to exhibit more realistic behavior than the standard in-house models, and is recommended for use in conjunction with a flattening limit of 0.2 to 0.25. The drawback of this model is a possible decrease in the mean time increment used between time steps in the dynamic analysis.
3. The damped Martin spherical-element model exhibits some aspects of the qualitative behavior which is sought, but some quantitative results for the model are at odds with results obtained using continuum-based finite-element representations.

#### **Future Work**

Future work on this topic is planned at UDRI in the following areas:

1. Reduce the contact-force spikes caused by the sudden velocity correction when a node (with finite mass) penetrates a contact surface. Do this by imposing the contact constraint gradually in a buffer zone above the contact surface, i.e., by regularizing the constraints.
2. Investigate the influence of air compressibility in a 10% porous bird material.
3. Establish realistic strength properties for various soft-body materials (bird tissue, gelatin, etc.)
4. Explore the performance of the Martin model with different parameter values, different initial packing, etc.
5. Further assess bird models through simulations of oblique impacts, and using deformable targets.

#### **ACKNOWLEDGEMENTS**

The support of WL/FIVR Contract No. F33615-92-C-3400 is gratefully acknowledged. The first author wishes to thank William Braisted and Marc Huelsman of UDRI for their help in understanding the bird models, and their instruction in using the X3D procedures.

## APPENDIX - Ultimate Stress for Flattening-Limited Elements

Consider an element of material which is initially undeformed with uniform dimensions  $a \times a \times a$ . The element undergoes an incompressible flattening in the  $z$ -direction and uniform expansion in the  $x$ - and  $y$ -directions, so that the deformed dimensions are given by

$$a\left(\frac{1}{\sqrt{f}} \times \frac{1}{\sqrt{f}} \times f\right) \quad (A1)$$

where  $f=f(t)$  is now a variable flattening measure which is initially unity. The von Mises effective stress  $\sigma_e$  corresponding to this flattening is now computed, because this value is compared against the material ultimate stress in order to predict failure in the X3D code.

Define  $\bar{x}$ ,  $\bar{X}$ , and  $\bar{u}$  to indicate the vectors of spatial coordinates, material coordinates, and displacements, respectively, in a Lagrangian reference frame, so that

$$\bar{x} = \bar{X} + \bar{u} \quad (A2)$$

The displacement field for the problem defined is given by

$$\bar{u} = \begin{bmatrix} (1/\sqrt{f} - 1)X_1 \\ (1/\sqrt{f} - 1)X_2 \\ -(1-f)X_3 \end{bmatrix} = \begin{bmatrix} (1-\sqrt{f})x_1 \\ (1-\sqrt{f})x_2 \\ -(1/f-1)x_3 \end{bmatrix} \quad (A3)$$

Velocities are defined by

$$\bar{v} = \frac{\partial \bar{u}}{\partial t} \bigg|_{\bar{X}} \quad (A4)$$

For the incompressible case here, the rate-of-deformation tensor components  $d_{ij}$  and their deviatoric contributions  $d'_{ij}$  are identical, and are given by [1]

$$d_{ij} = d'_{ij} = \frac{1}{2} \left( \frac{\partial v_i}{\partial x_j} + \frac{\partial v_j}{\partial x_i} \right) \quad (A5)$$

For the rotation-free case under consideration, the deviatoric stresses are governed by [1]

$$\frac{d\sigma'_{ij}}{dt} = 2Gd'_{ij} \quad (A6)$$

and the deviatoric stresses can be evaluated in terms of the flattening  $f$  using the equation

$$\sigma'_{ij} = \int_0^t \frac{d\sigma'_{ij}}{dt} dt \quad (A7)$$



subject to  $f=1$  at  $t=0$ . The von Mises effective stress  $\sigma_e$  is defined as [1]

$$\sigma_e = \sqrt{3/2 \sigma'_{ij} \sigma'_{ij}} \quad (A8)$$

where summation over the repeated indices is implied.

When the equations given above are used to evaluate  $\sigma_e$  for the displacement field initially described, it is found that

$$\sigma_e = 3G \ln(1/f) \quad (A9)$$

Based on this result, the ultimate stress is specified according to the desired flattening limit  $f$  and the specified shear modulus  $G$  using the following equation:

$$\sigma_u = 3G \ln(1/f) \quad (A10)$$

## REFERENCES

1. Brockman, R.A., and Held, T.W., "X3D User's Manual," Report no. UDR-TR-92-59, University of Dayton Research Institute, Dayton, OH (1992).
2. Wilbeck, J.S., "Impact Behavior of Low Strength Projectiles," Report no. AFML-TR-77-134, Air Force Materials Lab., Air Force Wright Aeronautical Lab's, Wright-Patterson Air Force Base, OH (1977).
3. Bauer, D.P., and Barber, J.P., "Experimental Investigation of Impact Pressures Caused by Gelatin Simulated Birds and Ice," Report no. UDR-TR-78-114, University of Dayton, final technical report for Contract 200-FBA-14K-47884 for General Electric Aircraft Engine Group, March, 1979.
4. Barber, J.P., Taylor, H.R., and Wilbeck, J.S., "Bird Impact Forces and Pressures on Rigid and Compliant Targets," AFFDL-TR-77-60, May, 1978.
5. Challita, A., and Barber, J.P., "The Scaling of Bird Impact Loads," Report no. AFFDL-TR-79-3042, June 1979.
6. Wilbeck, J.S., and Barber, J.P., "Bird Impact Loading," The Shock and Vibration Bulletin, Vol. 48, Part 2, Sept. 1978, pp. 115-122.
7. Martin, N.F. Jr., "Nonlinear Finite-Element Analysis to Predict Fan-Blade Damage Due to Soft-Body Impact," J. Propulsion, Vol. 6, No. 4, July-Aug. 1990, pp. 445-450.

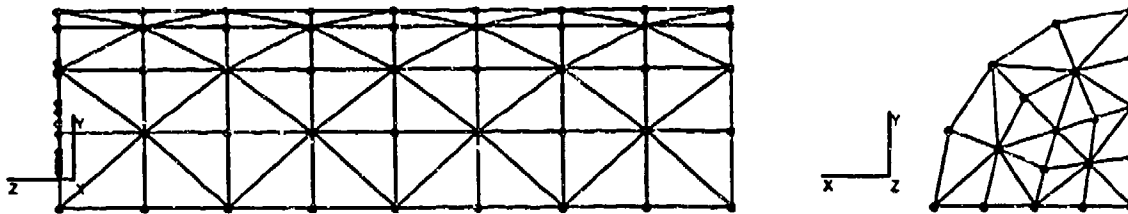


Figure 1. Quarter-cylinder tetrahedral-element bird model, 480 elements, 171 nodes (used with two symmetry planes).

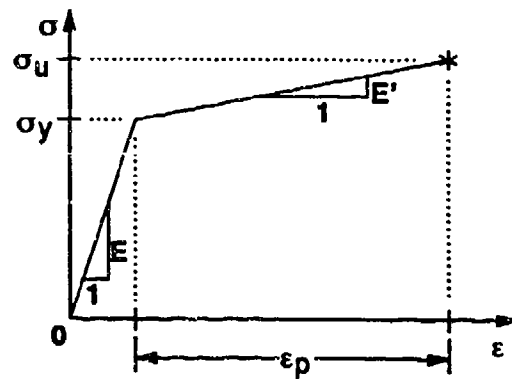


Figure 2. Schematic stress-strain curve for the elastic-plastic material model.

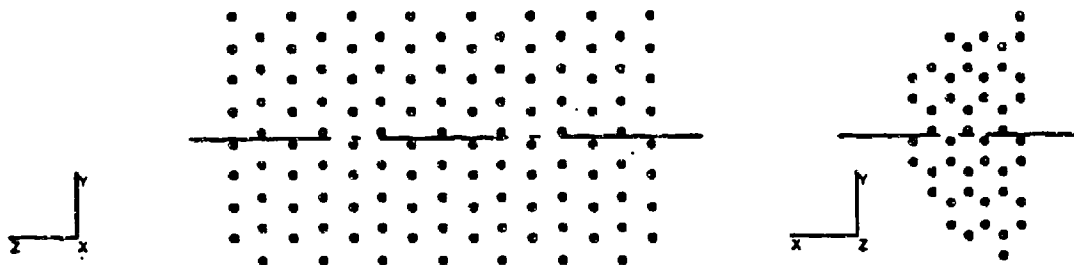


Figure 3. Half-cylinder spherical-element bird model, 344 elements/nodes (used with one symmetry plane).

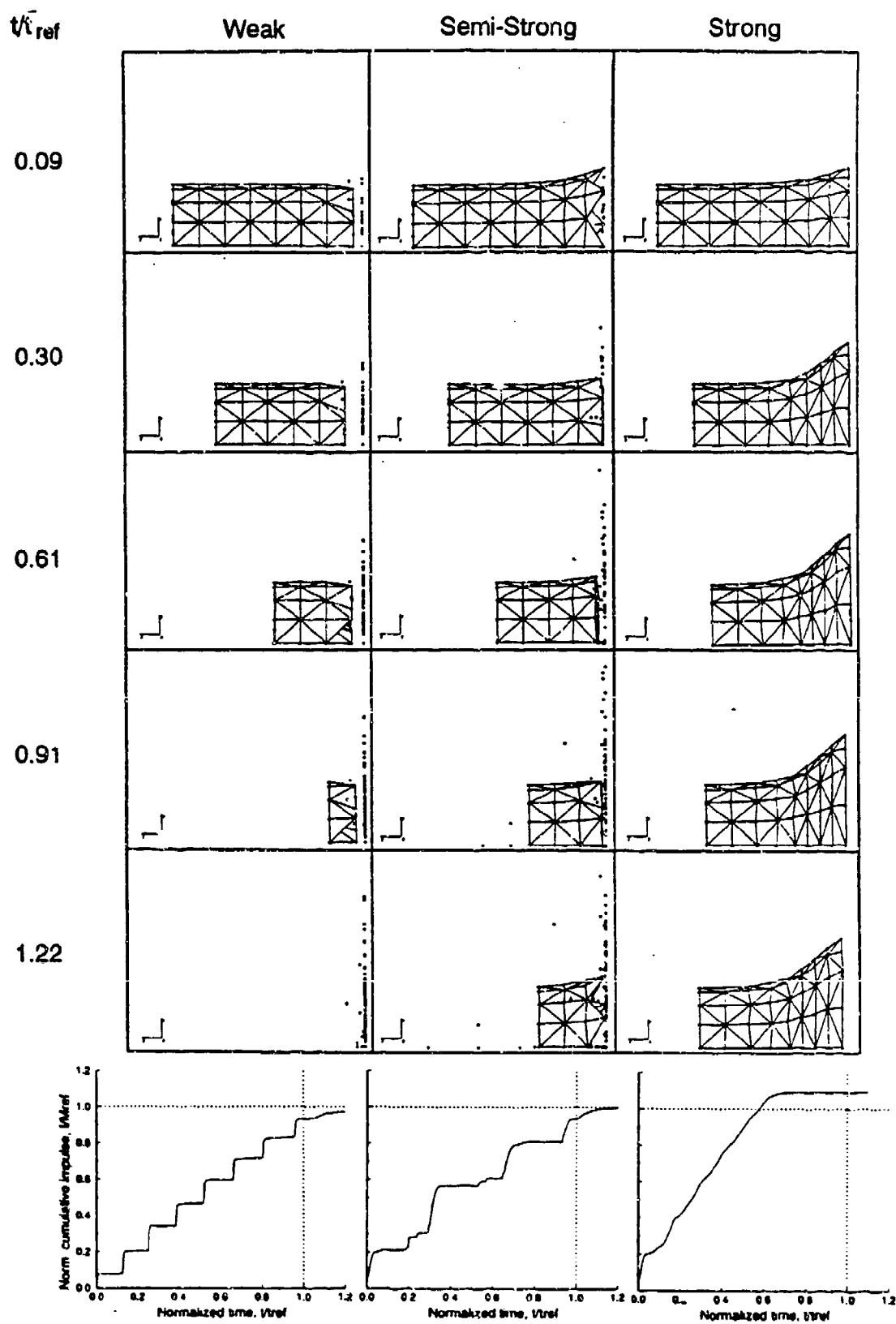


Figure 4. Visualizations of impact simulations and normalized cumulative impulse vs. time for UDRI standard in-house bird models.

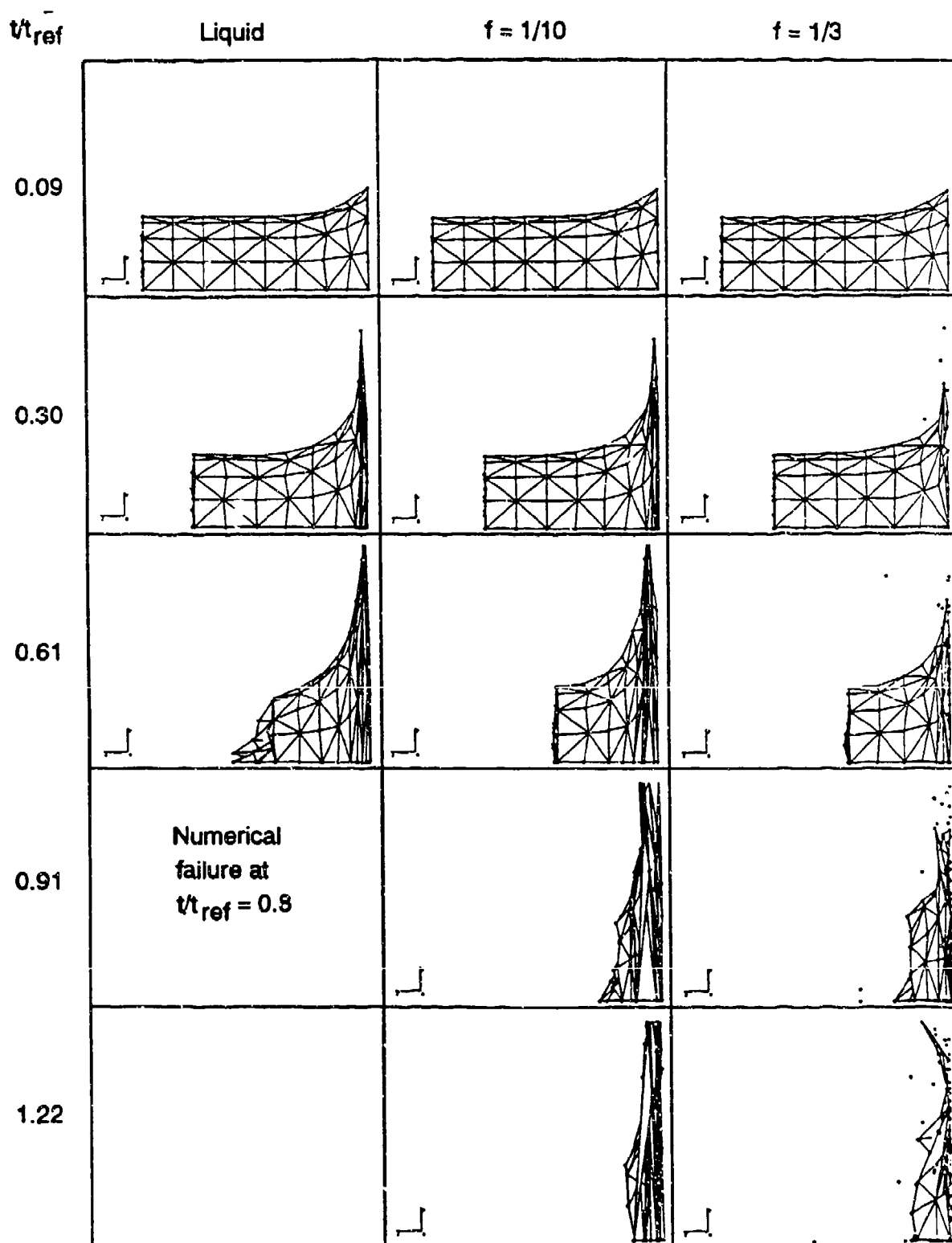


Figure 5. Visualizations of impact simulations for liquid and flattening-limited element models.

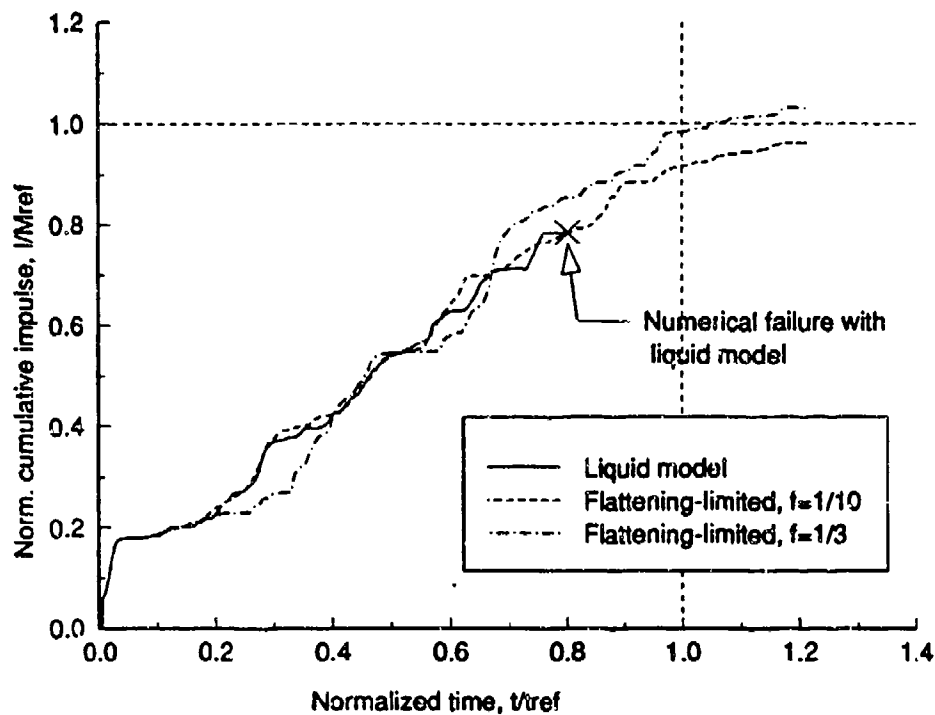


Figure 6. Normalized cumulative impulse versus normalized time for liquid and flattening-limited element models.

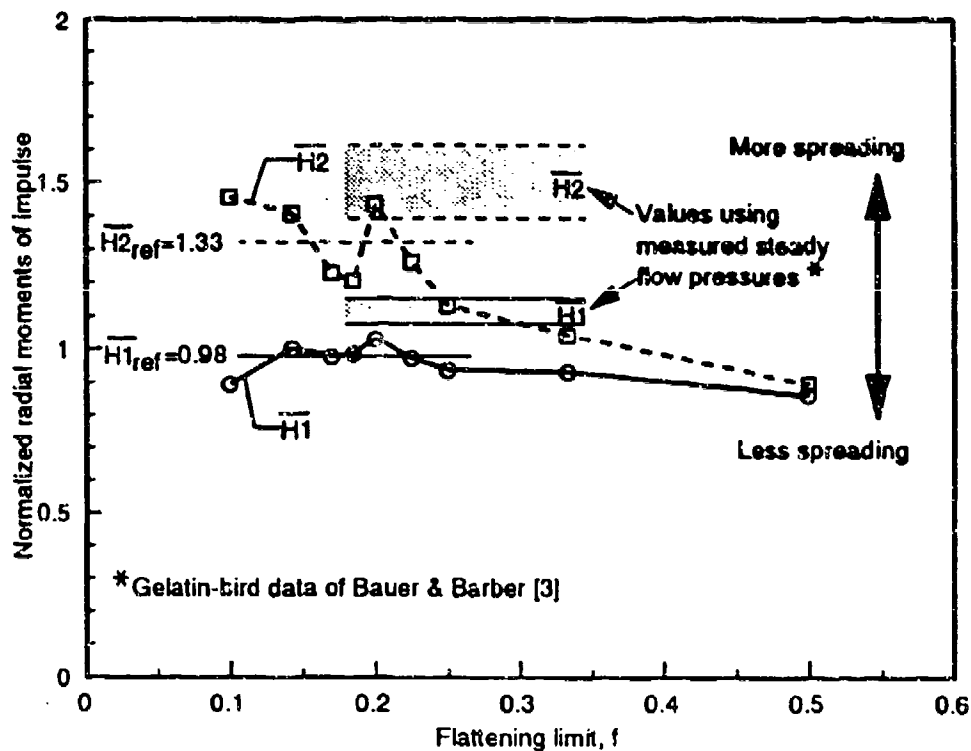


Figure 7. Normalized radial moments of impulse versus flattening limit for flattening-limited element models.

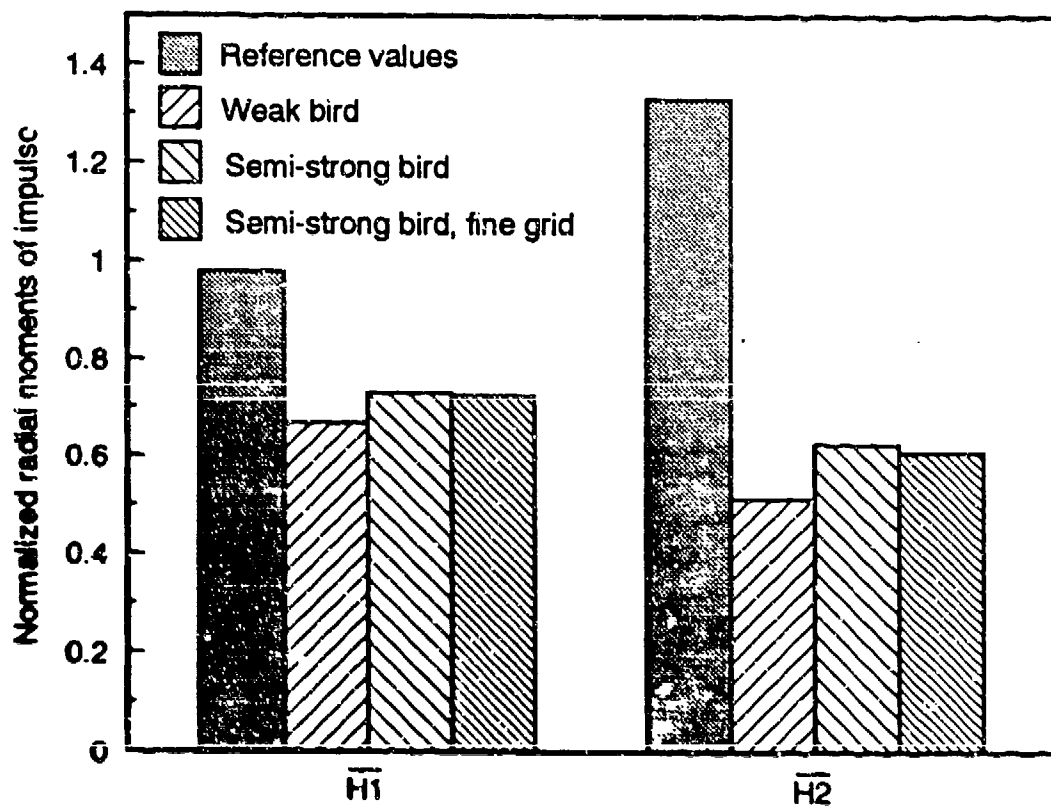


Figure 8. Comparison of normalized radial moments of impulse of UDRI standard in-house bird models with reference values.

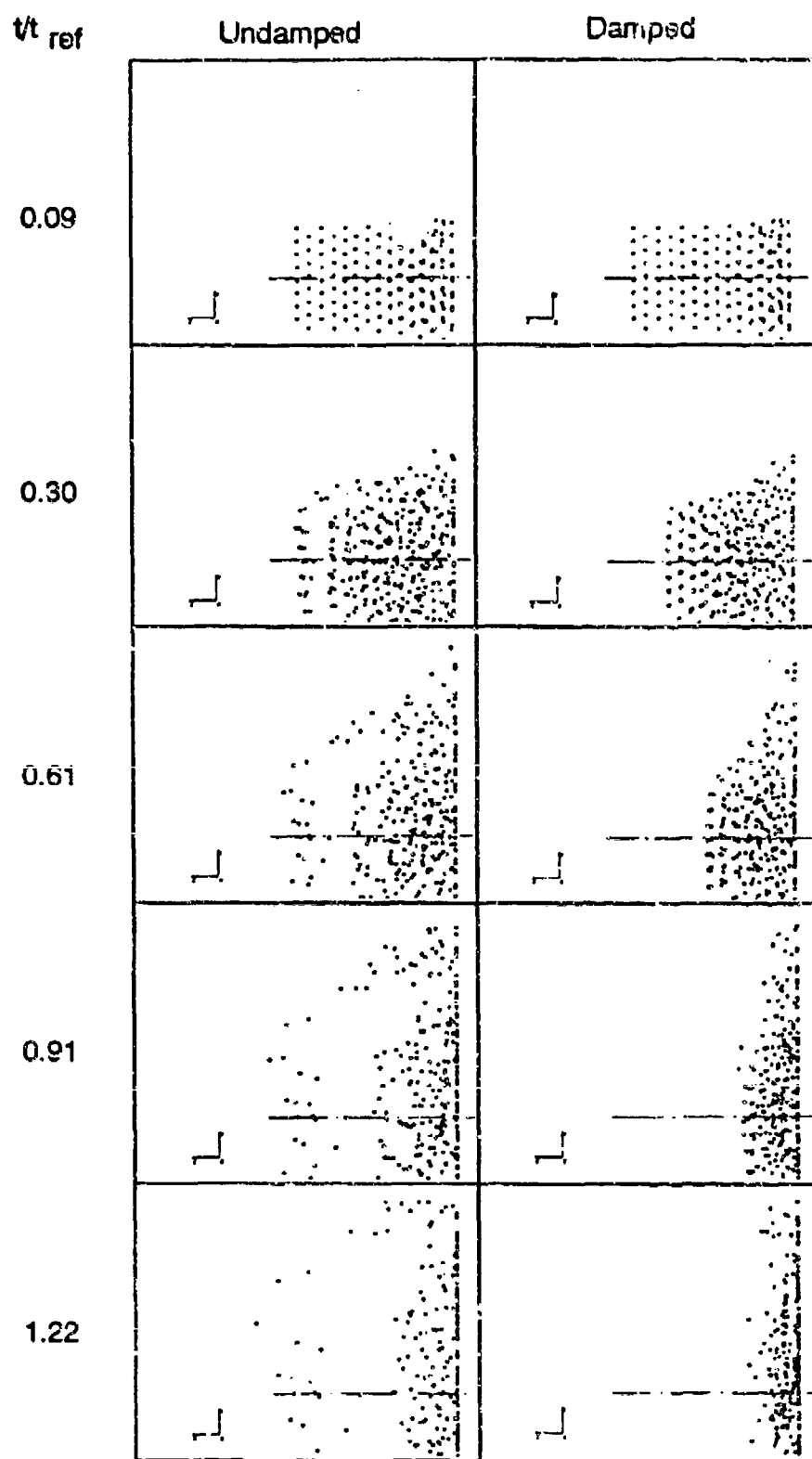


Figure 9. Visualizations of impact simulations for Martin bird models.

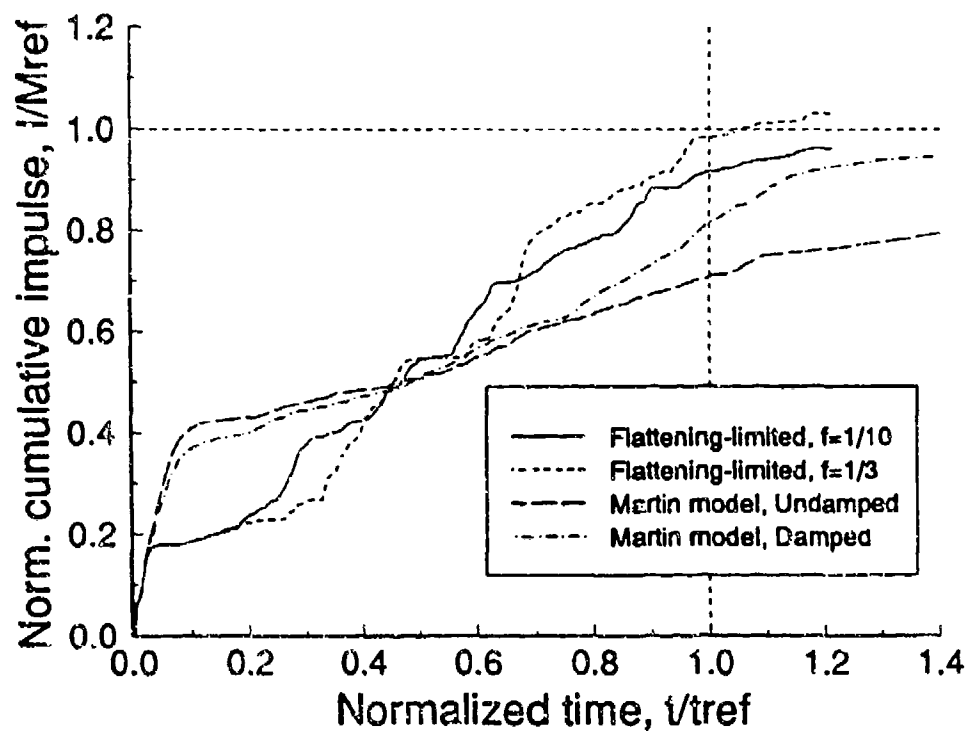


Figure 10. Normalized cumulative impulse versus normalized time - Martin model versus flattening-limited element model.

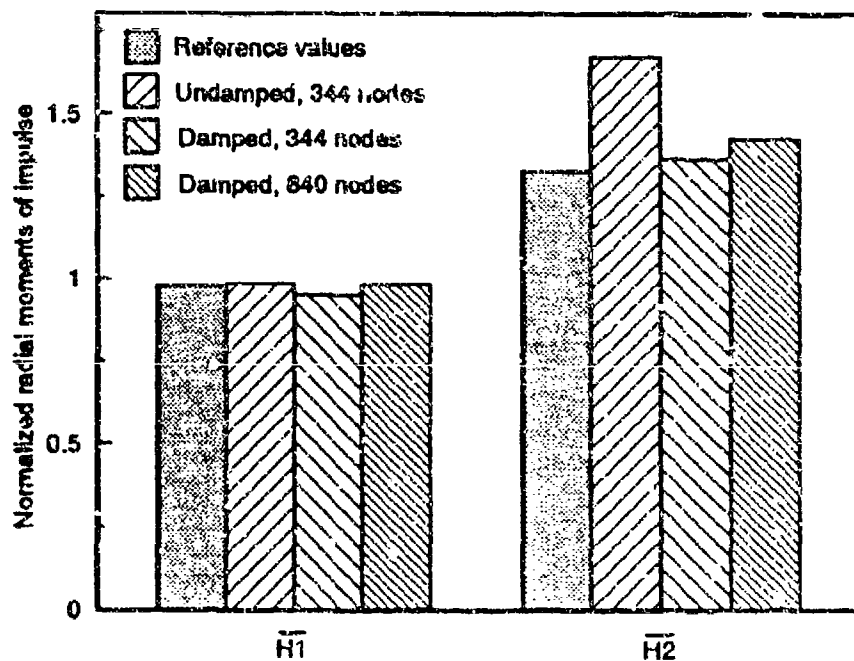


Figure 11. Comparison of normalized radial moments of impulse of Martin bird models with reference values.



SESSION VI

BIRDSTRIKE HAZARDS AND OPTICS - PART B

Chairman: L. Task  
Armstrong Labs

Co-Chairman: D. J. Rubin  
Spectrum Sciences & Software

Coordinator: D. Hamershock  
Flight Dynamics Directorate  
Wright Laboratory

**BIRD STRIKE HAZARDS:  
SUPPORT FOR A 4.5 POUND BIRD TEST CRITERIA**

R. L. Merritt  
Bird Aircraft Strike Hazard  
Tyndall Air Force Base

J. J. Short  
Flight Dynamics Directorate  
Wright Laboratory

BIRD STRIKE HAZARDS: SUPPORT FOR A 4.5 POUND BIRD TEST CRITERIA

Ronald L. Merritt, Maj, USAF  
HQ AFCESA/DMPS  
Tyndall AFB, FL 32403

and

Jeffrey J. Short, LtCol, USAFR  
WL/FIVR  
Wright-Patterson AFB, OH 45433

ABSTRACT

Over 20 percent of all U.S. Air Force (USAF) birdstrikes occur during low-altitude, high speed training flights. These low-level birdstrikes are usually the most damaging in terms of aircraft damage and loss of aircrews. Since 1987, these birdstrikes have resulted in the loss of nine aircraft and six aircrew fatalities and an average annual cost of over \$45 million during low-level and range training flights.

The 4-pound (1.8 kg) bird is usually considered the design standard for the aircraft structures and transparency systems. The 4-pound birdweight distribution represents approximately 95 percent of all recorded birdstrikes (pre-1970) which were collected during a joint study by the USAF and the Federal Aviation Administration. The Bird Aircraft Strike Hazard (BASH) Team collects data from both damaging and non-damaging bird strikes. These data are used to identify installations with hazardous wildlife hazard trends, develop local control procedures, and as a baseline for bird avoidance modelling.

The objective of this study is to reassess the birdweight distribution for low-level birdstrikes. Analysis of the data extracted from the database from 1985-1992 for strikes occurring during high speed, low-level flight and with identified bird species and weights produces a cumulative distribution frequency curve that strongly supports using a 4.5 pound test standard.

## BACKGROUND

Each year the Air Force reports approximately 3,000 bird strikes to aircraft worldwide. Since 1987 these strikes have resulted in the loss of nine aircraft, six aircrew fatalities, and an average annual cost of over \$45 million. The Bird Aircraft Strike Hazard (BASH) Team collects data from both damaging and non-damaging bird strikes. These data are used to identify installations with hazardous wildlife hazard trends, develop local control procedures, and as a baseline for bird avoidance modelling. The data are also helpful in assessing damage to various aircraft components such as engines and windshield/canopy systems.

A four pound bird strike capability has long been the standard maximum bird weight for testing aircraft components. The four pound weight distribution represents approximately 95 percent of all recorded bird strikes (pre-1970) collected during a joint study by the U.S. Air Force and the Federal Aviation Administration. Also, about 95 percent of bird species in North America weigh less than 4 pounds.

The bird strike records supporting the four pound criteria were scanty with regards to species struck as well other aspects of the incident. The pre-1970 bird strike sample included mishaps near airfields where aircraft operations and (in general) bird habits are different than at low-level flight altitudes. Different bird behaviors or population distribution dynamics could affect the type and weights of birds struck.

A study conducted in 1990 by the second author (and reported at the 20th Bird Strike Committee Europe, Helsinki, Finland) of over 700 low-level bird strikes found a significant difference in the bird weight frequency distribution when comparing all phases of military aircraft operation and low-level only (Figure 1). The bird weight frequency distribution showed a much flatter curve indicating that heavier birds are hit more often during low-level operations. Also, there was a significant difference between the F-4 and B-52 bird weight distributions that could be attributed to mission differences. Bomber aircraft, such as the B-52, fly longer, further, and more night missions than fighter aircraft (e.g.; F-4) which exposes them to heavier birds.

An analysis of data extracted from the USAF bird strike database for 1985-1992 was conducted to examine bird strikes that occur during low-level flight operations. The low-level flight phase was chosen because it represents the worst case scenario for energy impacts due to the high speed of the aircraft. Only bird strikes with identified species (and thus weights) were included in the analysis. A sample for 402 bird strikes were analyzed using Statistical Analysis System software. The mean weight of birds struck was 46.3 ounces (std dev = 38.58 oz.), the median weight was 40 ounces and the mode was 72 ounces (Table 1). A cumulative frequency plot (Figure 2) shows a sharp break at 64 ounces (a weight represented by the Double-Crested Cormorant) and at 72 ounces (representing Black Vultures and Turkey Vultures).

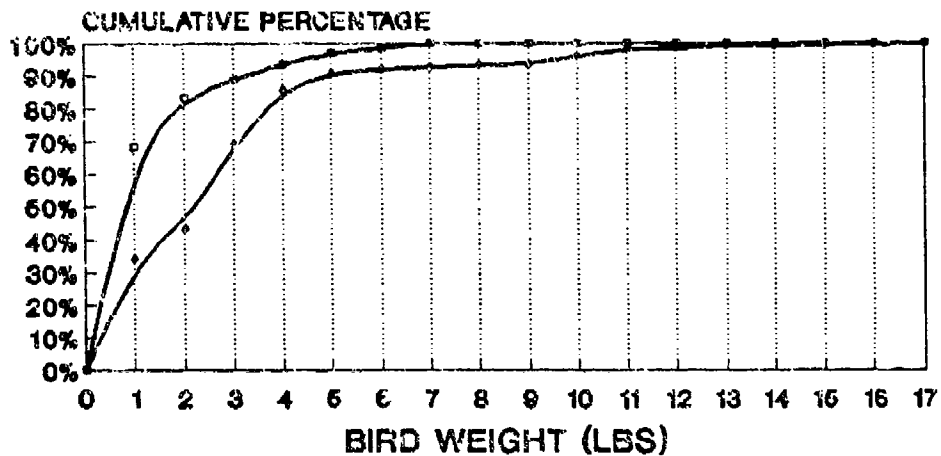
A significant shift in frequency occurs between the weight range of 64 ounces or less (54.5%) and 72 ounces or less (94.3%).

#### CONCLUSIONS

These data clearly reflect the importance of the 72 ounce bird as a basis for aircraft component testing. Birds in the 72 ounce weight class (n=160) accounted for 39.8 percent of all birds struck during low-level flight. These data also reflect the altitudinal distribution by weight class: large birds such as vultures use thermal lift for soaring and subsequently have greater exposure to aircraft flying low-level missions. Analysis of data collected from the most current bird strike database clearly support the use of a 4.5 pound standard as a minimum for aircraft that fly low-level missions.

FIGURE 1

# FREQUENCY DISTRIBUTION OF LOW-LEVEL BIRDSTRIKES



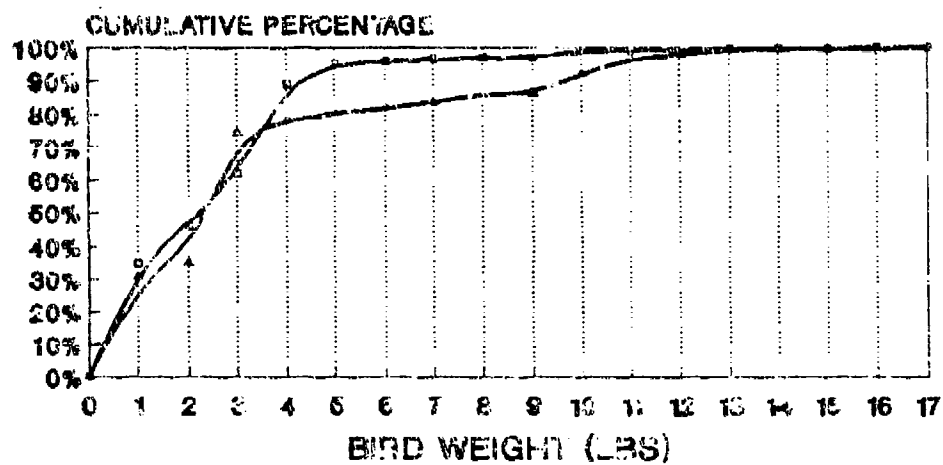
--- MISSION • --- MERGED ••

KOLMOGOROV-SMIRNOV TEST ( $P < 0.001$ )

• LOW-LEVEL ONLY (1976-89)

•• ALL PHASES (1970-81)

# FREQUENCY DISTRIBUTION OF LOW-LEVEL BIRDSTRIKES



--- F-4 •--- E-62

KOLMOGOROV-SMIRNOV TEST ( $P < 0.005$ )

F-4 - 186 IDENTIFIED

E-62 - 160 IDENTIFIED

## SAS

## UNIVARIATE PROCEDURE

Variable=WEIGHT

## Moments

N	402	Sum Wgts	402
Mean	46.38109	Sum	18645.2
Std Dev	38.58842	Variance	1489.066
Skewness	1.522114	Kurtosis	7.124787
USS	1461900	CSS	597115.4
CV	83.19859	Std Mean	1.924615
T:Mean=0	24.09889	Prob> T	0.0001
Sgn Rank	40501.5	Prob> S	0.0001
Num ^= 0	402		

## Quantiles(Def=5)

100% Max	288	99%	153
75% Q3	72	95%	80
50% Med	40	90%	72
25% Q1	7.7	10%	1.5
0% Min	0.3	5%	1
		1%	0.5
Range	287.7		
Q3-Q1	64.3		
Mode	72		

## Extremes

Lowest	Obs	Highest	Obs
0.3 (	259)	153 (	247)
0.5 (	388)	160 (	236)
0.5 (	375)	210 (	59)
0.5 (	324)	288 (	109)
0.5 (	287)	288 (	308)

## SAS

## UNIVARIATE PROCEDURE

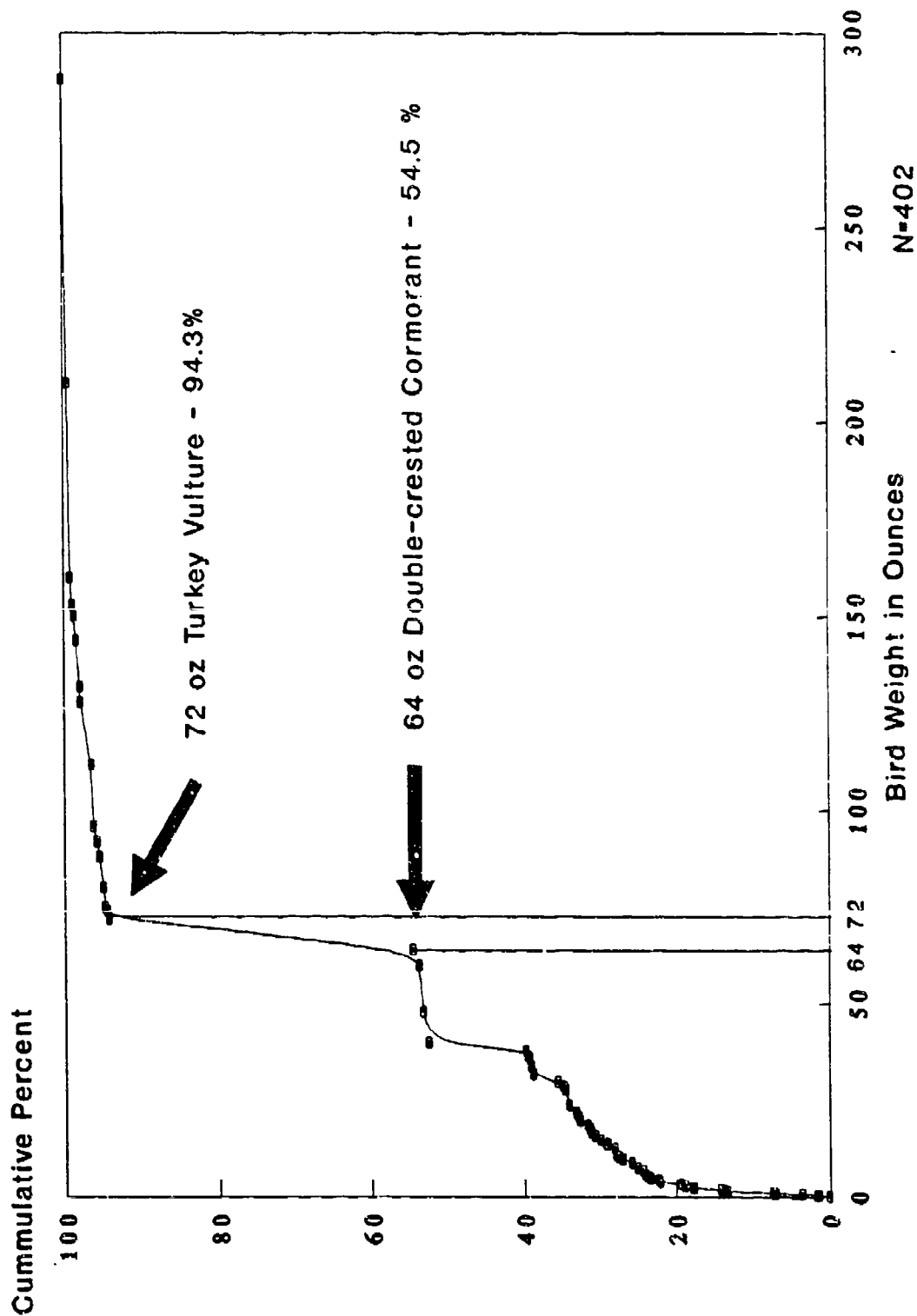
Variable=WEIGHT

## Frequency Table

Percents				Percents			
Value	Count	Cell	Cum	Value	Count	Cell	Cum
0.3	1	0.2	0.2	20	4	1.0	32.6
0.5	5	1.2	1.5	21	1	0.2	32.8
0.7	1	0.2	1.7	22	1	0.2	33.1
0.8	8	2.0	3.7	24	4	1.0	34.1
1	14	3.5	7.2	28	2	0.5	34.6
1.4	1	0.2	7.5	28.8	1	0.2	34.8
1.5	24	6.0	13.4	30	3	0.7	35.6
1.8	1	0.2	13.7	32	13	3.2	38.8
2	2	0.5	14.2	34	1	0.2	39.1
2.5	14	3.5	17.7	36	1	0.2	39.3
2.6	1	0.2	17.9	36.6	1	0.2	39.6
3	4	1.0	18.9	38	1	0.2	39.8
3.5	2	0.5	19.4	40	51	12.7	52.5
4	11	2.7	22.1	48	2	0.7	53.2
4.5	1	0.2	22.4	60	2	0.5	53.7
5	4	1.0	23.4	64	3	0.7	54.5
5.3	1	0.2	23.6	72	160	39.8	94.3
5.5	1	0.2	23.9	74	1	0.2	94.5
6	1	0.2	24.1	75	1	0.2	94.8
7	1	0.2	24.4	80	1	0.2	95.0
7.7	3	0.7	25.1	88	2	0.5	95.5
9	3	0.7	25.9	92	2	0.2	95.8
10	5	1.2	27.1	96	2	0.5	96.3
10.5	2	0.5	27.6	112	1	0.2	96.5
11	1	0.2	27.9	128	6	1.5	98.0
12.7	1	0.2	28.1	132	1	0.2	98.3
14	4	1.0	29.1	144	1	0.2	98.5
15	3	0.7	29.9	150	1	0.2	98.8
16	3	0.7	30.6	153	1	0.2	99.0
17	2	0.5	31.1	160	1	0.2	99.3
18	1	0.2	31.3	210	1	0.2	99.5
19	1	0.2	31.6	288	2	0.5	100.0



**FIGURE 2.** Frequency Distribution of Bird Weights  
Low-level Phase of Flight



TURKEY VULTURE BIRD STRIKE HAZARD AND  
USING SATELLITE TELEMETRY FOR BIRD AVOIDANCE

D. J. Rubin  
Spectrum Sciences and Software

Turkey Vulture (*Cathartes aura*) Bird Strike Hazard and Using Satellite  
Telemetry for Bird Avoidance

David J. Rubin  
USAF Bird Aircraft Strike Hazard (BASH) Team  
Spectrum Sciences and Software Inc.  
HQ AFCEA/DMPS, Tyndall AFB, Florida

ABSTRACT:

Turkey Vultures (TV) (*Cathartes aura*) have accounted for approximately twenty percent of all USAF damaging bird strikes from 1985-1992 resulting in the loss of two aircraft, one pilot fatality, and more than 21 million dollars in damage. The majority of these strikes (72.5%) have occurred during the low-level phase of flight. The pilot fatality and the loss of an F-16 aircraft resulted from windscreen penetrations (1.2% of total TV strikes). Bird avoidance during low-level training can reduce the exposure of aircraft components to bird species such as the Turkey Vulture (4.5 lbs.), which surpass the standard bird weight used for windshield development. Bird avoidance is based on an understanding of the behavior patterns of hazardous bird species. These patterns have not been adequately studied for Turkey Vultures. The USAF BASH Team has proposed research to study the long-distance seasonal movement patterns and altitude distribution of Turkey Vultures using satellite telemetry. The ARGOS Data Collection and Location System will be used to gather remote data. Meteorological data will be collected to evaluate the impacts of weather on TV movements and altitudes of flight. Additionally, correlation between TV movements and habitat and topographic variables will be examined. These data will be integrated with additional geophysical and biological data on a Geographic Information System (GIS) to improve the USAF BASH Team's Bird Avoidance Model (BAM). Component design and bird avoidance are integral in protecting mission resources during low-level operations.

## TURKEY VULTURE (*Cathartes aura*) BIRD STRIKE HAZARD AND USING SATELLITE TELEMETRY FOR BIRD AVOIDANCE

### INTRODUCTION:

Each year the U.S. Air Force reports more than three thousand bird strikes resulting in approximately sixty-five million dollars a year in damage. Based on microscopic identification of bird strike remains from 1985-1992, twenty percent of all damaging bird strikes (>\$10,000) have been found to involve Turkey Vultures. Most of these damaging strikes (72.5 %) occurred during the low-level phase of flight. Current mission emphasis on low-altitude, high speed training flights has significantly increased aircrew vulnerability to serious bird strike mishaps. Aircraft collisions with Turkey Vultures have resulted in the loss of two aircraft and one pilot fatality since 1989. One of these aircraft losses and the pilot fatality were due to windscreen penetrations during low-level operations. Bird avoidance during low-level flights can reduce the exposure of aircraft components to bird species such as the Turkey Vulture, which exceed the standard bird weight used for windshield development.

The Bird Avoidance concept is based upon an understanding of the behavior patterns of hazardous bird species. The reproductive biology, foraging behavior and flight strategies of both migratory and resident birds must be examined in great detail for each species. Bird behavior is often predictable and once the factors influencing that behavior are identified, bird avoidance measures can be implemented to reduce the bird strike hazard potential. These influences have not been adequately studied for Turkey Vultures.

### DISCUSSION:

The USAF BASH Team has proposed research to study the long distance seasonal movement patterns and altitude distribution of Turkey Vultures using satellite telemetry. The ARGOS Data Collection and Location System will be used to monitor up to ten birds for up to one year. Bird locations will be determined from calculations of the doppler shift associated with the satellite's movement past the transmitter. Transmitters will be modified to incorporate altimeters that will be used to determine the bird's altitude above ground level (AGL) at each location. Meteorological data will be collected to evaluate the impacts of weather phenomena on vulture movements and altitudes of flight. Additionally, relationships between vulture movements and habitat and topographic variables will be examined. Significant data will be integrated with existing geophysical and biological data in the USAF BASH Team's Bird Avoidance Model (BAM) on a Geographic Information System (GIS). The BAM is designed to calculate the relative risk for an aircraft collision with a bird. Risk is calculated based on population density, bird weight, and specific flight behaviors. The temporal aspects of hazard, including time of year (seasonal variation) and time of day (diurnal variation) with altitude distribution for each temporal component, is incorporated into the risk assessment. These Turkey Vulture behavioral data will fill the largest data gap that has been identified (USAF BASH Team) in the new Bird Avoidance Model.

ROUND ROBIN TESTING TO DETERMINE THE PRECISION AND ACCURACY  
IN MEASURING MULTIPLE IMAGES IN AIRCRAFT TRANSPARENCIES

W. N. Kama  
Armstrong Laboratory

ROUND ROBIN TESTING TO DETERMINE THE PRECISION  
AND ACCURACY IN MEASURING MULTIPLE IMAGES IN  
AIRCRAFT TRANSPARENCIES

William N. Kama  
Visual Display Systems Branch  
Human Engineering Division  
Armstrong Laboratory  
Wright-Patterson Air Force Base, Ohio 45433-7022

ABSTRACT

A round robin testing study was conducted to determine the precision and accuracy of a test method used to measure multiple images in aircraft transparencies. A total of 12 measurement technicians from 6 laboratory facilities served as subjects. Stimulus materials for this study were four 8 x 10, black and white, multiple imaging photographs which represented 4 different camera-to-array distances - 15, 23, 23.5 and 25 feet. Each photo was created by photographing a light array of known size at a specified distance from the design eye position of the windshield. The subject's task included (1) determining a scale factor (used to relate linear distances on the photograph to actual angular distances as seen from the design eye position) for each of the 4 photos to be measured and (2) making linear measurements in millimeters (mm) for each light on the photograph to determine the separation between the secondary and primary images. The linear measurements were made using a pair of digital calipers. All subjects were carefully instructed on how to calculate the scale factor, how to use the digital calipers, and the manner in which they were to make the linear measurements, from the "center" of the secondary image to the "center" of the primary image. Subjects measured each photo twice so that a determination of the repeatability of their measurements could be made. Subject performance was evaluated with respect to the performance of two measurement technicians who were highly skilled and proficient in using this measurement technique. Their scores were used as the baseline for this study. Findings from this study indicated that (1) measurements were highly accurate, differing on average from the baseline score by 0.37 mm, (2) repeatability (precision) was also high, scores differing, on average, between trials 1 and 2 by 0.08 mm, and (3) the calculated scale factors were larger, on average, by 0.24 mrad/mm, than the baseline scores.

## INTRODUCTION

Multiple imaging is caused by multiple reflections of light from external sources (e.g., runway marker lights and VASI lights). As shown in Figure 1, the light travels through the outer surface of the windshield to the inner surface where part of it is reflected back towards the outer surface where it is partially reflected back towards the pilot's eyes. This process may occur several times so that a third or fourth image may be visible under the right conditions. A pilot looking through a windshield under these conditions will see two or three images of each external light source.

Although multiple imaging occurs both in the daytime as well as at night, it is typically visible only at night because the secondary and/or higher images are masked by the brightly lit daytime scene. Indeed, this effect might not be seen, even at night, if the secondary or higher images happen to fall directly on top of the primary image. In this situation, there is no angular separation so that the secondary (and higher) images cannot be distinguished from the primary image and only one image is perceived.

The severity of the multiple imaging occurring in a windshield is dependent on (1) the materials involved, (2) the curvature and thickness of the windshield, (3) the intensity of the light source, and (4) the darkness of the surroundings around the light source.

During late 1985 and early 1986, the Armstrong Laboratory developed a technique for measuring and determining the severity of multiple images noted in aircraft windshields, specifically the B-1B windshield. Development of this technique was based on the two characteristics that are most noticeable in multiple images - the ratio of intensity of the secondary image to the primary image and the magnitude of separation between the secondary and primary images. Based on laboratory data gathered on 3 windshields that had been removed from service because of multiple imaging, the angular displacement between the secondary and primary images was selected as the basis for this measurement technique (Ref. 1).

The measurement technique developed consisted of the following steps: First, a photograph is taken of a light array (Figure 2) of known size that is located at some specified distance from the design eye position of the windshield being evaluated. Second, an 8 x 10, black and white, matte-finished photograph of the light array is used to obtain linear measurements of the image separations as well as for determining a scale factor. Finally, the linear

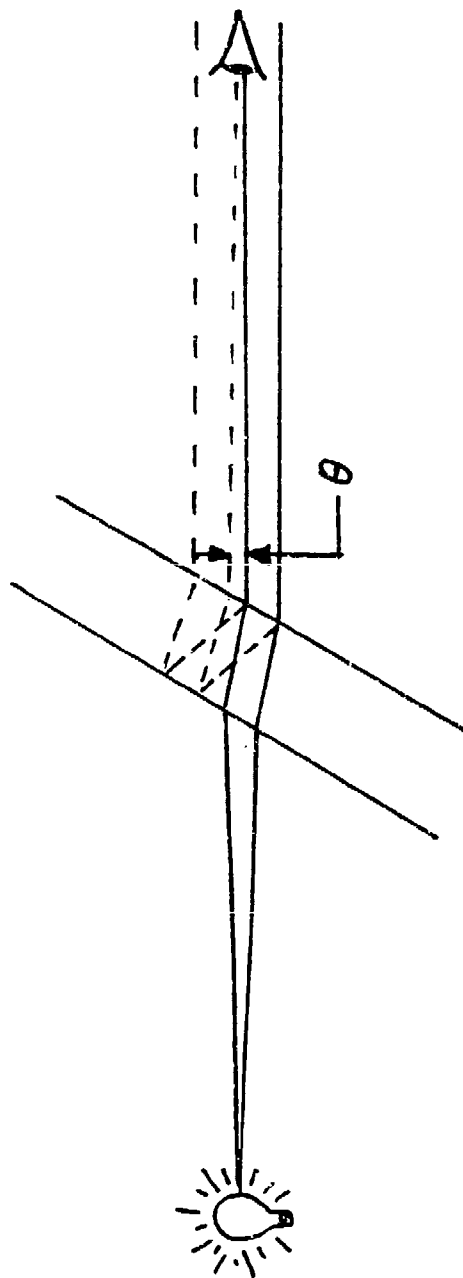


FIGURE 1. HOW MULTIPLE IMAGING OCCURS



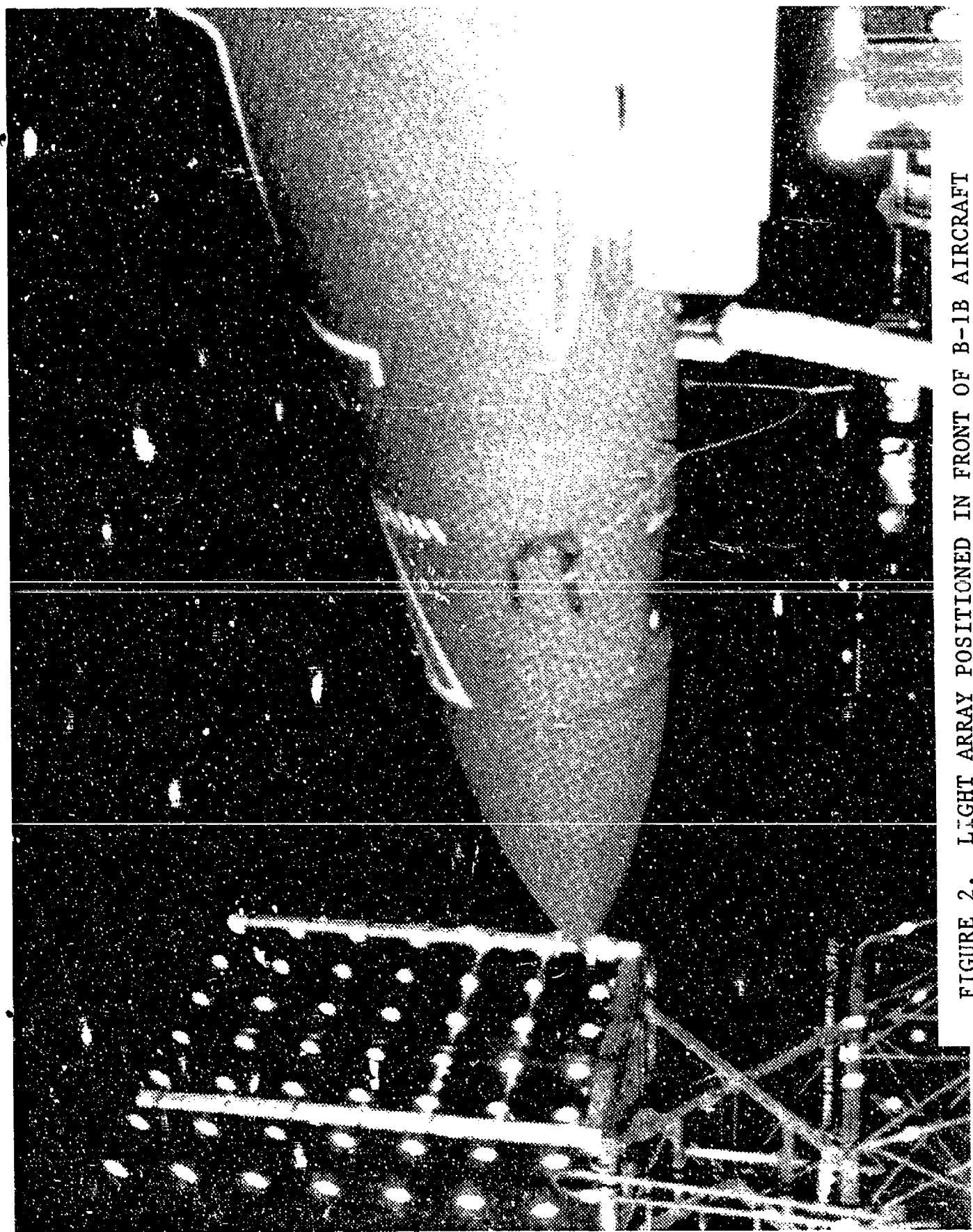


FIGURE 2. LIGHT ARRAY POSITIONED IN FRONT OF B-1B AIRCRAFT

measurements are converted to angular units using the scale factor obtained in step 2. In 1988, this technique was accepted as a Standard Test Method by the American Society for Testing and Materials (ASTM) and is identified as ASTM F 1165-88, "Standard Test Method for Measuring Angular Displacement of Multiple Images in Transparent Parts" (Ref. 2).

As an accepted test method, this technique had to meet an ASTM requirement that all test methods contain a precision and bias statement. To meet this requirement, this round robin testing was conducted. Its purpose was to determine the precision and accuracy of measurements made of multiple images from multiple imaging photographs.

## METHODOLOGY

### Subjects

A total of 12 subjects were used in this study. All were measurement technicians from 6 laboratory facilities: Armstrong Laboratory at Wright-Patterson AFB, OH; PPG, Inc. at Huntsville, AL; NORDAM, Inc. at Tulsa, OK; Texstar, Inc. at Grand Prairie, TX; Sierracin Corp. at Sylmar, CA; and Pilkington Aerospace at Garden Grove, CA. Each of the facilities provided 2 technicians. No attempt was made to assess the experience level of each of these technicians regarding the measurement of multiple images.

Two technicians from the Armstrong Laboratory who were highly skilled and proficient in the use of this measurement technique performed the same task as our 12 subjects. Their scores served as the baseline performance against which subjects were evaluated.

### Stimulus Photos and Equipment

The stimulus material used consisted of 4 multiple imaging photographs. These were 8 x 10, black and white, matte-finished photos that were created by photographing a 7 x 7 light array grid board (see Figure 2) through 3 different B-1B windshields from the design eye position. Three of the photos were taken in the windscreen facility at the Armstrong Laboratory and one was taken in the field at Dyess AFB, TX. Each photo represented a different camera-to-array distance. The distances depicted were 15 feet (photo 4), 23 feet (photo 3), 23.5 feet (photo 1), and 25 feet (photo 7). Figure 3 shows all four of these photos.

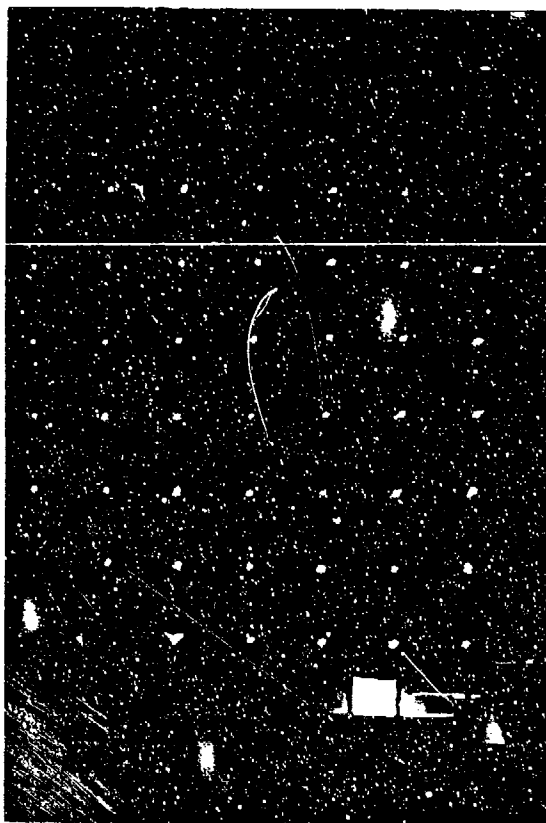


PHOTO 1

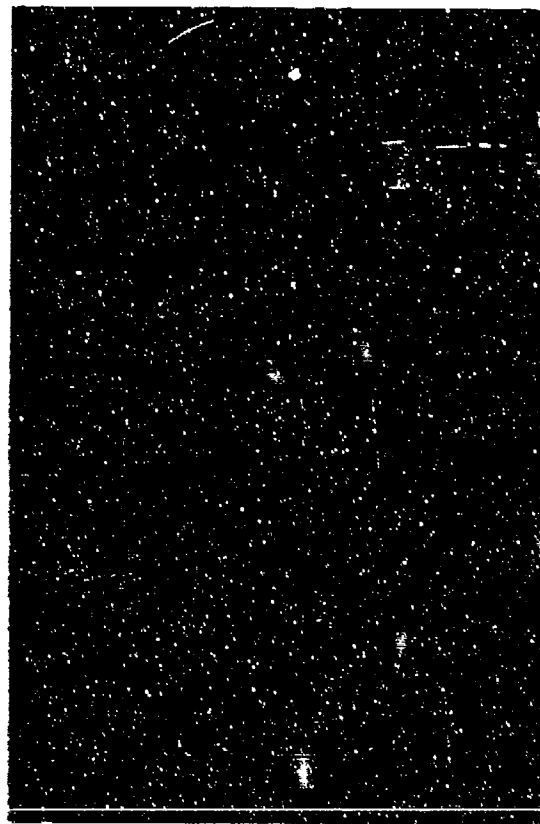


PHOTO 3

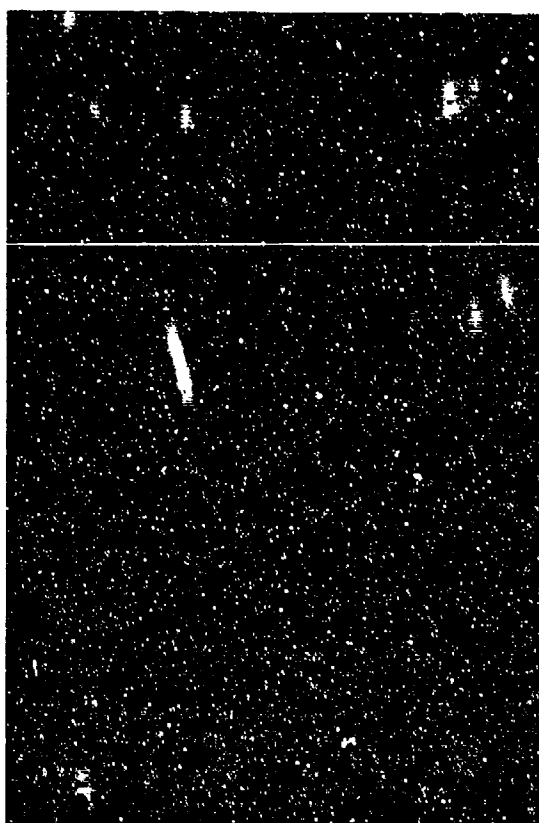


PHOTO 4

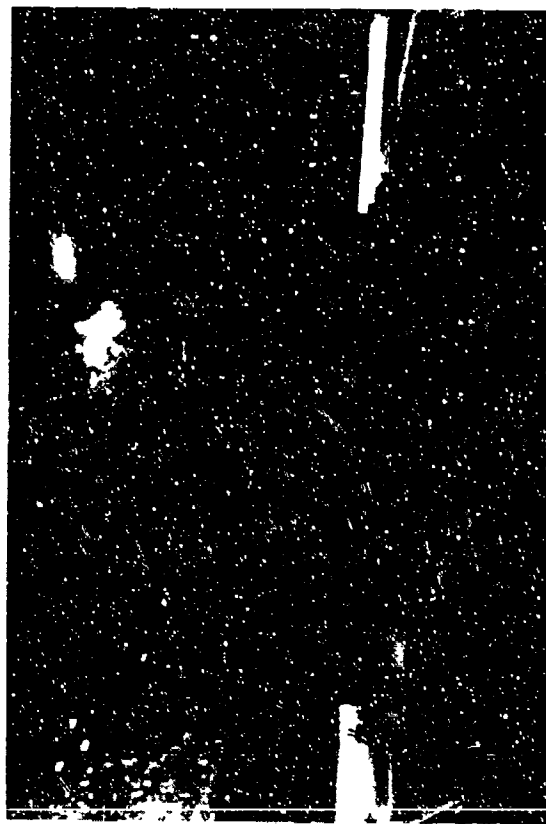


PHOTO 7

FIGURE 3. STIMULUS PHOTOS USED IN STUDY

Two pieces of equipment that made using this technique simpler and easier were a scientific hand held calculator and a pair of digital calipers (Figure 4). The calculator was used to facilitate the calculation of the scale factor that is used to convert the linear measurements made from each photo to angular separations that are seen from the pilot's eye position. The digital calipers made the measurement of the linear separations much more precise and faster.

## Procedure

The procedure employed during the conduct of this study was as follows: The experimenter traveled to each of the facilities that were participating in this study and spent approximately 3 to 4 hours there. He brought with him a hand held scientific calculator, two pairs of digital calipers, clear document protectors, several sets of the stimulus photos, and other necessary items. The experimenter apprised each subject of the purpose of the study, the task that they were to perform, how to use the digital calipers, how each measurement was to be done, and most importantly, how to calculate the scale factor. If the subjects had any questions, they were answered at this time. Both technicians at each facility were tested at the same time in the same room. To combat order, practice or fatigue effects, the order in which subjects measured each of the 4 photos was counterbalanced. Each subject measured each photo twice in order that we might be able to determine the repeatability of their measurements. The following task was performed by each subject:

First, they were required to calculate the scale factor for each of the four photos in units of milliradians (mrad) per mm that is based on the photographic geometry conditions and the enlargement process. Calculation of this scale factor required the completion of the following two steps:

Step 1 involved determining the angular subtense, in mrad, of the separation between 5 lights on the light array grid board for a specified camera-to-array distance, i.e., 15, 23, 23.5 or 25 feet.

Step 2 involved measuring the distance between 5 lights on the photo being measured in mm. For purposes of uniformity, the fourth row of the array was selected for this measurement. The distance between the lights in column 2 and 6 (4 segments between lights) for this row was then measured. The measurement was made from the "center" of the primary image of light 2 to the "center" of the primary image of light 6. The distance measured was then divided into the angular subtense value obtained in step 1 to determine the scale factor.



FIGURE 4. PHOTO OF HANDHELD CALCULATOR AND DIGITAL CALIPERS

Appendix 1 presents a detailed, yet simple, explanation on how to calculate the scale factor.

After calculating the scale factor for the photo being measured, the subject then measured the linear separations between the secondary and primary images for each light on the photo. The photo was placed in a clear document protector before these measurements were made to prevent them from being scratched or marred by the calipers. Excluding the two topmost rows (rows 1 and 2), they were instructed to measure all lights on the photo which exhibited multiple imaging. They were to make these measurements from the "center" of the secondary image to the "center" of the primary image. If no secondary images were visible or a light was occluded, its position on the data matrix sheet was left blank or a line was drawn through that location.

## RESULTS

As stated earlier, the accuracy of the measurements made by subjects was determined by comparing their performance to that of two highly skilled measurement technicians. Both of these technicians were proficient and experienced in the use of this measurement technique and had been making multiple imaging measurements since this technique was first developed, a period of approximately 7 years. Both of these technicians calculated the scale factor and made linear measurements on each of the photos that were used. Their obtained scores were used as the baseline scores for each photo and the standard against which subject performance was judged. The scale factors and the overall mean for the linear measurements obtained on each photo by these two technicians are shown in the Table below.

Table 1

Baseline Scores for Two Highly Skilled  
Measurement Technician

	Photo 1	Photo 3	Photo 4	Photo 7
Scale Factor (mrad/mm)	2.33	2.34	2.32	1.85
Overall Mean (mm)	4.12	3.66	3.83	3.04

Subject performance was evaluated using two performance measures - (1) the magnitude of the difference between the calculated scale factors and the baseline scale factor and (2) the difference between the overall mean value (for all the linear measurements made on each photo) and the baseline mean value. Repeatability of the measurements was determined by comparing the overall mean for the first trial to that of the second trial for each photo. Since we were concerned primarily with the accuracy of the measurements made, only the linear measurements are used to evaluate performance. The conversion to angular separations involved performing the mathematical process of multiplying the linear measurements by the scale factor (e.g, multiplying 4.12 by 2.33 yields an angular separation value of 9.60 mrad). This step was not included in this study.

The scale factors obtained by each subject for each photo are shown in Table 2 along with the baseline values. Inspection

Table 2  
Scale Factors (MRAD/MM) Calculated By  
Each Subject for Each Photo

Subject	Photo 1	Photo 3	Photo 4	Photo 7
1	2.33	2.34	2.32	1.84
2	2.33	2.34	2.32	1.84
3	2.54	2.56	2.53	2.50
4	2.53	2.54	2.53	2.49
5	2.03	2.05	2.53	1.99
6	2.53	2.05	2.03	2.00
7	2.55	2.55	2.52	2.48
8	2.53	2.55	2.53	2.50
9	2.53	2.56	2.53	2.50
10	2.53	2.55	2.53	2.48
11	2.55	2.50	2.54	2.50
12	3.34	2.55	3.35	2.50
Mean	2.53	2.43	2.52	2.30
Variance	0.09	0.04	0.09	0.08
Baseline	2.33	2.34	2.32	1.85

of the data in this table indicates that 75% (36 of 48) of the calculated scale factors were larger than the baseline

scale factor for each photo, averaging 0.26 mmrad/mm more. The data also indicates that the variability of the calculated scale factors were quite small, averaging 0.08. For photo 1, the scale factors ranged from 2.03 to 3.34 with a mean value of 2.53 and a variance of 0.09. For photo 3, the factors ranged from 2.05 to 2.56 with a mean value of 2.43 and a variance of 0.04. Photo 4 ranged from 2.03 to 3.35 with a mean value of 2.52 and a variance of 0.09 while photo 7 had a range of 1.84 to 2.50 with a mean of 2.30 and a variance of 0.08.

To determine the repeatability of subjects' measurements, the difference in linear measurements made in trial 1 versus trial 2 was determined. These differences are shown in Table

Table 3  
Difference Scores Between Trials 1 and 2 for Each  
Photo (mm)

Subjects	Photo 1	Photo 3	Photo 4	Photo 7
1	0.09	0.11	0.09	0.09
2	0.20	0.02	0.05	0.01
3	0.10	0.10	0.01	0.00
4	0.12	0.00	0.04	0.14
5	0.04	0.07	0.14	0.19
6	0.16	0.07	0.16	0.15
7	0.02	0.04	0.13	0.03
8	0.10	0.01	0.09	0.11
9	0.16	0.07	0.13	0.01
10	0.00	0.08	0.07	0.02
11	0.00	0.06	0.21	0.00
12	0.17	0.03	0.04	0.10
Mean	0.10	0.06	0.10	0.07

3. Inspection of the data in Table 3 indicates that the repeatability of the measurements were very high, averaging 0.08 mm. For photo 1, the average difference was 0.10 mm; for photo 3, it was 0.06; for photo 4, it was 0.10 and for photo 7, it was 0.07 mm.

Table 4 shows the data for the linear measurements made on each photo. The score shown is the mean of subjects' measurements for both trials. This mean score is compared with our baseline score to determine how accurate each subjects' measurements were.



Inspection of the data in Table 4 indicates that subjects, on average, tended to make larger measurements (than the baseline) on photo 1; smaller measurements for photos 4 and 7; and had the same average measurements on photo 3. For photo 1, the measures ranged from 4.13 to 4.79 with a mean of 4.46 and a variance of 0.04. For photo 3, they ranged from 3.44 to 3.87 with a mean of 3.66 and a variance of 0.02. For photo 4, they ranged from 2.84 to 4.13 with a mean of 3.32 and a variance of 0.12 while for photo 7 they ranged from 2.13 to 3.01 with a mean of 2.42 and a variance of 0.09.

Table 4

Mean Linear Measurements for Two Trials  
for Each Photo (mm)

Subjects	Photo 1	Photo 3	Photo 4	Photo 7
1	4.25	3.87	3.11	3.01
2	4.58	3.80	2.88	2.95
3	4.56	3.51	2.84	2.30
4	4.45	3.79	4.13	2.55
5	4.70	3.71	2.98	2.55
6	4.39	3.57	3.45	2.25
7	4.79	3.79	3.51	2.32
8	4.50	3.64	3.46	2.23
9	4.34	3.63	3.41	2.24
10	4.53	3.72	3.52	2.39
11	4.13	3.49	3.29	2.13
12	4.24	3.44	3.21	2.15
Mean	4.46	3.66	3.32	2.42
Variance	0.04	0.02	0.12	0.09
Baseline	4.12	3.66	3.83	3.04

## DISCUSSION

As stated earlier, the purpose of this study was to determine the precision and accuracy with which multiple imaging measurements could be made using the only available measurement technique. To determine the accuracy of the measurements made, subjects' scores were compared to those of two highly skilled and proficient multiple imaging measurement technicians. Table 4 presents the measurements made by each subject on each photo (over two trials) and the

baseline scores of our two experienced technicians. Taken by photos, the data shows that the largest difference was for photo 7, where subjects showed a reading that averaged less than 0.62 mm than the baseline score. Photo 4, showed readings that were less than the baseline an average of 0.51 mm. Photo 3 showed the same average reading as the baseline while the readings on photo 1 averaged 0.34 mm more. Since we are dealing with mm, the difference observed does not seem unreasonable and indicates that subjects were fairly accurate in their measurements. Taking the difference between the overall mean and the baseline and dividing the result by the baseline value yields an average error of approximately 10% between the observed scores and the baseline values.

To determine the precision with which the measurements were made, the repeatability of subjects' measurements were determined. This data is presented in Table 3, where the difference in scores made on trial 1 and trial 2 is presented. Examination of the data in this Table indicate that the average difference for the first and second trial for photo 1 was 0.10 mm. For photo 3, the average difference was 0.06 mm; for photo 4, it was 0.10 mm; and for photo 7, it was 0.07 mm. With the average difference for all measurements made on all photos being equal to 0.08 mm, it is not unreasonable to assume that the measurements were highly repeatable and hence indicates some precision in the measurement process.

In using this measurement technique, calculating the scale factor as accurately as possible is of great importance. This is because the scale factor is used to convert our linear measures to angular units, which in turn are used to meet the optical specifications for multiple imaging. An incorrect scale factor can bias the angular separation scores in one direction or the other if not detected. For example using the two scale factors calculated by subjects 1 and 12 for photo 1 (Table 2) and multiplying a linear measurement of 4.12 mm by these scale factors yields an angular separation value of 9.60 for subject 1 and a value of 13.76 for subject 12. Clearly the larger the scale factor the larger the angular separation value becomes. This could lead to the rejection of a windscreen that may be optically acceptable. Conversely, a scale factor that is too small can lead to the acceptance of a windshield that should be rejected.

Examination of the data in Table 2 indicates that the calculated scale factors were larger than the baseline scale factors. For photo 1, the scale factor was 0.20 mrad/mm larger than the baseline; for photo 3, 0.09 larger; for photo 4 it was 0.20 while for photo 7, it was 0.45 mrad/mm.

## CONCLUSIONS

Based on the results from this study, the following conclusions may be drawn:

1. Accuracy of the measurements was determined to be fairly high, the average difference between the measured values and the baseline value being 0.37 mm. Additionally the average error of all the measurements made was only 10%.

2. The precision of the measurements, as determined by the repeatability of the measurements, is also high. The average difference for all measurements was equal to 0.08 mm.

3. The calculated scale factors averaged 0.24 mrad/mm more than our baseline scale factor. This can lead to larger angular separation scores which, in turn, can lead to the rejection of an optically acceptable windscreen.

## REFERENCES

1. Kama, W.N., Task, H.L. & Merkel, H. *Field and Laboratory Evaluation of the Optical Qualities of the B-1B Winshield (U)*, AAMRL Technical Report 88-050, Armstrong Aerospace Medical Research Laboratory, Wright-Patterson AFB, OH, Jan 1988. (DTIC No. B147487)
2. ASTM F 1165-88, *Standard Test Method for Measuring Angular Displacement of Multiple Images in Transparent Parts*, American Society for Testing and Materials, 1916 Race St., Philadelphia, PA, Dec 1988.

## APPENDIX 1

This appendix documents the steps used to calculate the scale factor.

The first step is to find the angular subtense of the distance between 5 lights on the light array. For the Armstrong Laboratory Light array, the distance between each light is 16 inches or 1.33 feet measured on-center to on-center. Therefore the distance between 5 lights is 64 inches or 5.33 feet. The angular subtense, in degrees, for the distance between these 5 lights (at a specified distance) is determined using the following formula:

$$A = 2 \arctan (x/2y) \quad \text{where} \quad \begin{array}{l} A = \text{angular subtense in} \\ \text{degrees} \\ x = \text{distance between 5} \\ \text{lights (5.33 ft in this} \\ \text{case)} \\ \text{and } y = \text{camera-to-array} \\ \text{distance (15, 23, 23.5} \\ \text{or 25 ft)} \end{array}$$

The second step is to convert the degrees to milliradians by multiplying the angular subtense obtained in step 1 by 17.45 mrad/degree. Hence,

$$A' = A \times 17.45 \text{ mrad/degree} \quad \text{where} \quad \begin{array}{l} A' = \text{angular subtense} \\ \text{in mrad} \\ \text{and } A = \text{angular subtense} \\ \text{in degrees} \end{array}$$

The third step involves measuring the distance between 5 lights on the photo being evaluated. For purposes of uniformity, the distance between the 2nd and 6th lights of the middle or fourth row of the array is selected for this purpose.

The last step involves dividing the angular subtense in mrad ( $A'$ ) by the distance found between 5 lights on the photo. Hence,

$$S = A'/d \quad \text{where} \quad \begin{array}{l} S = \text{scale factor in mrad/mm} \\ A' = \text{angular subtense in} \\ \text{mrad} \\ \text{and } d = \text{distance between 5 lights} \\ \text{measured on photo} \end{array}$$

Using a scientific calculator, this process becomes rather simple. Using photo 1 as an example, the following steps are inputted to the calculator:

- Step 1 - ensure that calculator is in degrees mode
- Step 2 - enter 5.33 (distance between 5 lights on array)
- Step 3 - divide 5.33 by 47 (the camera-to-array distance for photo 1 [23.5 ft] which has been doubled)  
This yields the tangent value of 0.1134.
- Step 4 - using the 2nd function, find the arctan value by initiating the tangent button. This gives us a value of 6.4699.
- Step 5 - multiply the obtained value by 2 to get the angular subtense in degrees or 12.9399
- Step 6 - multiply this result by 17.45 mrad/degree to get the angular subtense in mrad, 225.80 mrad
- Step 7 - measure the distance between 5 lights on the photo (for photo 1 it was 96.93 mm)
- Step 8 - divide this distance 96.93 into the angular subtense 225.80 to get the scale factor. In this case 2.33 mrad/mm

SESSION VII

NEW MATERIALS AND PROCESSES - PART A

Chairman: T. Reinhart  
Materials Directorate  
Wright Laboratory

Co-Chairman: R. Nelson  
Air Logistics Command  
Hill Air Force Base, UT

Coordinator: E. Joy  
Flight Dynamics Directorate  
Wright Laboratory

A SURVEY OF NEW HIGH USE TEMPERATURE THERMOPLASTICS  
FOR STRUCTURAL TRANSPARENCY APPLICATIONS

M. R. Unroe  
Materials Directorate  
Wright Laboratory



# A SURVEY OF NEW HIGH USE TEMPERATURE THERMOPLASTICS FOR STRUCTURAL TRANSPARENCY APPLICATIONS

Marilyn R. Unroe

Polymer Branch, Materials Directorate, Wright Laboratory  
WL/MLBP, 2941 P Street Ste 1, Wright-Patterson AFB, OH 45433-7750

## ABSTRACT

Current and future performance and maintenance requirements for transparent thermoplastics to use as novel canopy designs and retrofits has pushed the limit of the current state-of-the-art polymeric transparency materials beyond their physical capabilities. A new genre of high use temperature materials will be required to face the design parameters such as light weight, structural integrity beyond speeds of Mach 2, compatibility with other structural and nonstructural plies in a laminated canopy, particle crazing, and logistics needs such as resistance to flight line cleaning solvents and aircraft maintenance fluids, and longer life cycles to cost. Most new transparent engineering thermoplastics are currently limited by their commercial availability in bulk quantities, high cost, or by significant data gaps concerning transparency performance parameters.

The purpose of this report is to summarize data on some of the transparent materials currently advocated for high use temperature (i.e., 450°F (232°C)) applications. Emphasis shall be given to novel aromatic heterocyclic polymers with glass transition temperatures in the region of 572°F (300°C) or greater. One particular set of heterocyclic polymers discussed is the polybenzazoles with hexafluoroisopropylidene groups, also known as the 6F-PBO's. The Materials Directorate of Wright Laboratory is currently sponsoring an R and D effort to exploit the useful technologies of 6F-PBO's at use temperatures in the realm of 450°F and a summary of the historical work in the Directorate on 6F-PBO's is discussed.

## INTRODUCTION AND BACKGROUND

Current state-of-the-art thermoplastic polymers used in structural transparency applications have been pushed to the limits of their respective performance characteristics by the demands for speeds at or beyond Mach 2 and by demands for tighter maneuvers in the existing fighter aircraft. Typically the thermal limitations of the laminated canopy are dictated by the service ceiling of the lowest use temperature structural ply. For high performance aircraft such as the F-16 fighter, the service ceiling of the canopy is established by the outer acrylic ply with a very short term use temperature of 200°F (93°C).

The interests of the Polymer Branch were historically concentrated upon high use temperature polymeric reinforcements and matrices for structural composite applications. Usual estimations of the maximum use temperatures of structural composite materials are set at 50°C below the glass transition temperature ( $T_g$ ) of the polymers and/or the loss of 50-60% of the room temperature mechanical properties. While the application of the latter estimation is not necessarily the best approach for determination of the service ceiling of a canopy ply, the former estimate is a good point of departure for focus of any initial physical property determinations in novel materials. At the Polymer Branch, we have taken an even more conservative estimate for service ceiling of transparency materials at 75-100°C below the  $T_g$ . The goal of our research is to examine any materials with  $T_g$ 's near 300°C (572°F) which translates to use temperatures in the realm of 400-450°F (204-232°C), an increase of at least 200°F for the service ceiling of the canopy when the acrylic ply is replaced. The

research also targets to substitute the acrylic ply with a material which either meets or exceeds the current mechanical and inherent optical properties of the polyacrylates.

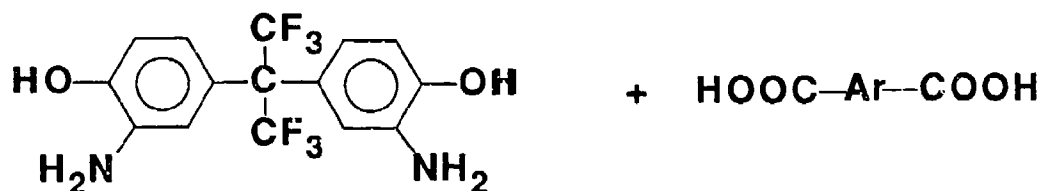
The Polymer Branch's entry into basic research and development with the ultimate goals of improved transparency materials was coincidental with a mission needs statement from Aeronautical Systems Division (now Aeronautical Systems Center) to the Materials Directorate in 1990 for internal support to explore future canopy materials. There are many problems associated with canopy materials; the work at first blush is very basic with much effort required in the future to improve the current data base on chemical structure-property correlations and how chemical structure affects intrinsic optical properties of new polymer compositions. Other constraints such as purification processes and fabrication processes which affect optical quality of the final polymers are also under consideration.

This report not only incorporates work performed at the Materials Directorate, but also includes the current work reported in the open literature on new high temperature thermoplastic materials which, as a family of polymers, may be under consideration for canopy structural plies. What is not addressed in this report are any proprietary materials which are known but are not protected by patent law and therefore not publicly releaseable.

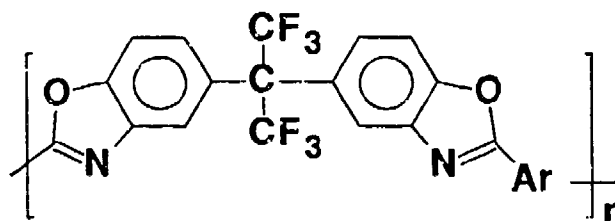
## DISCUSSION

### A. 6F-PBO's

Since the mid-1980's the Polymer Branch of the Materials Directorate has been interested in examining polymeric materials with  $T_g$ 's in the range of 300°C (572°F) for use as guest host matrices in nonlinear optical (NLO) applications. From a chemical structure-property correlation perspective, this temperature requirement would limit chemical structures to those polymers with aromatic character in the polymer backbone. In addition, one of the goals of the in-house efforts in the NLO area was to prepare polymers with aromatic fused ring heterocycles in the backbone of the polymer. While high use temperature is realized, the presence of fused ring heterocycles may impart high degrees of electronic conjugation in the polymer backbone and may result in highly colored materials. About a decade ago it was reported that the incorporation of hexafluoroisopropylidene (6F) groups in the polymer backbone could render the resulting polymers less colored by disturbing the electronic environment of the  $\pi$ -electrons of the backbone and improving solubility in common organic solvents without sacrificing thermal stability.<sup>1</sup> During some in-house work into the preparation of the fused ring polybenzazoles in nonacidic media, a literature reference for the preparation of simple benzoxazoles using trimethylsilyl-polyphosphate (PPSE) in 1,2-dichlorobenzene was utilized.<sup>2</sup> This preparative procedure was not proven for the preparation of polybenzoxazoles with 6F groups (6F-PBO's) until personnel at the Polymer Branch synthesized such polymers.<sup>3,4</sup> A family of 6F-PBO homopolymers with various aromatic spacers was prepared by this method.



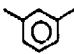
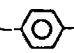

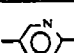
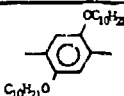
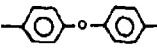
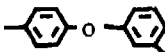
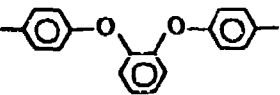
o-dichlorobenzene,  
 trimethylsilyl-  
 polyphosphate  
 RT → 135°C, 24 h  
 135° → 165°C, 24 h



The beauty of the preparative procedure is that one is limited in the chemical composition of the 6F-PBO polymer only by the availability of the diacid monomers. Many such monomers are commercially available through commodity or specialty chemical vendors in a purity grade such that the monomers can be used as received or purified by multiple recrystallizations to obtain monomer grade material. The procedure also allows for the use of dicarboxylic acid monomers that degrade in strong acid media such as polyphosphoric acid. Other cost advantages of the one-pot PPSE procedure are the commercial availability of the 6F monomer (6FAP), PPSE, and 1,2-dichlorobenzene. Since the materials are prepared in an organic solvent rather than a strong acid medium, waste volume is minimized and neutralization of acid before disposal is avoided. Despite the advantage of the synthetic procedure using nonacidic media, several 6F-PBO homopolymers have been prepared using highly polar, strong acidic media<sup>5,6</sup> with the final result of obtaining higher molecular weight material. Because the mechanical properties were not determined for these polymers, a reasonable conclusion about the superiority of one procedure over the other cannot be drawn.

The homopolymers exhibited a range of thermal properties such as  $T_g$  from 93-382°C (199-720°F), a range of long term (i.e., 200 h) thermooxidative stabilities at 346°C (655°F), and variations in solubility in acidic and nonacidic media (Tables 1 and 2).<sup>4,5,7</sup>

TABLE 1. SUMMARY OF 6F-PBO'S PREPARED.<sup>7</sup>

Polymer	Ar Spacer	Analysis Calc. (Found)	$\eta_{inh}^{a,d,f}$ or $[\eta]$ (dl/g) <sup>b</sup>	Solubility
1 <sup>c</sup>		C, 60.01 (59.68) H, 2.19 ( 2.38) N, 6.09 ( 5.79) F, 24.77 (23.60)	2.82 <sup>a</sup>	MSA TCE-phenol H <sub>2</sub> SO <sub>4</sub>
2 <sup>c</sup>		C, 60.01 (59.55) H, 2.19 ( 2.53) N, 6.09 ( 5.80) F, 24.77 (23.60)	2.23 <sup>a</sup>	MSA
3 <sup>c</sup>		C, 57.28 (56.75) H, 1.97 ( 2.13) N, 9.11 ( 8.93) F, 24.71 (23.59)	1.82 <sup>a</sup>	MSA H <sub>2</sub> SO <sub>4</sub>
4 <sup>c</sup>		C, 57.28 (56.00) H, 1.97 ( 2.29) N, 9.11 ( 8.54) F, 24.71 (23.40)	2.18 <sup>a</sup>	MSA H <sub>2</sub> SO <sub>4</sub>
5 <sup>c</sup>		C, 65.82 (66.14) H, 6.52 ( 6.56) N, 3.63 ( 3.37) F, 14.75 (14.27)	0.92 <sup>a</sup> 0.52 <sup>d</sup>	MSA CHCl <sub>3</sub> THF
6 <sup>c,e</sup>		C, 63.05 (62.82) H, 2.55 (2.68) N, 5.07 (5.20) F, 20.64 (20.72)	1.43 <sup>a,c</sup> 0.75 <sup>c,f</sup> 7.9 <sup>b,e</sup>	MSA H <sub>2</sub> SO <sub>4</sub> CHCl <sub>3</sub> , THF
7 <sup>e</sup>		C, 63.05 (62.83) H, 2.55 (2.53) N, 5.07 (4.35) F, 20.64 (20.70)	4.1 <sup>b</sup>	MSA H <sub>2</sub> SO <sub>4</sub> CHCl <sub>3</sub> , THF
8 <sup>g</sup>		C, 65.22(63.15) H, 2.81(2.83) N, 4.34(4.14)	6.0 <sup>b</sup>	MSA H <sub>2</sub> SO <sub>4</sub> CHCl <sub>3</sub> , THF

(a) Inherent viscosity in methanesulfonic acid (0.15 g/dL) at 30°C.

(b) Intrinsic viscosity in methanesulfonic acid at 30°C.

(c) Prepared in PPSE/*o*-dichlorobenzene.(d) Inherent viscosity in *o*-dichlorobenzene (0.15 g/dL) at 30°C.

(e) Prepared in phosphorus pentoxide/methanesulfonic acid.

(f) Inherent viscosity in 1,1,2,2-tetrachloroethane (0.15 g/dL) at 30°C.

(g) Prepared in 83% polyphosphoric acid.

TABLE 2. THERMAL CHARACTERISTICS OF 6F-PBO THERMOPLASTICS.<sup>7</sup>

Polymer	T <sub>g</sub> <sup>a</sup> (°C)	TGA <sup>b</sup> (°C)	ITAC <sup>c</sup> (%)
<u>1</u>	300	532 air 524 He	95
<u>2</u>	382	533 air 525 He	94
<u>3</u>	329	539 air 528 He	92
<u>4</u>	352	530 air 547 He	59
<u>5</u>	94	414 air 426 He	50 <sup>d</sup>
<u>6</u>	301	564 air	---
<u>7</u>	266	535 air	---
<u>8</u>	245	545 air	---

(a) Glass transition temperature determined by DSC ( $\Delta T = 10^\circ\text{C}/\text{min}$ ).

(b) Extrapolated onset of major decomposition determined in air and/or helium.

(c) Isothermal aging, weight retention after 200 h at  $346^\circ\text{C}$  ( $655^\circ\text{F}$ ) in circulating air.

(d) Weight retention after 50 h at  $346^\circ\text{C}$  ( $655^\circ\text{F}$ ) in circulating air.

The neat resin mechanical properties of some of the 6F-PBO's were evaluated under the rigorous conditions applied to composite matrices (Table 3)<sup>8</sup> and the values obtained were

TABLE 3. NEAT RESIN TENSILE PROPERTIES<sup>a</sup> OF 6F-PBO<sup>b</sup> AT VARIOUS TEMPERATURES AND CONDITIONS.<sup>8</sup>

Test Temperature, °C (°F)	Condition (Dry/Wet) <sup>c</sup> <sup>d</sup>	Tensile Strength, MPa (Ksi)	Tensile Modulus, GPa (10 <sup>3</sup> Ksi)	Strain-To-Failure (%)
24 (75)	Dry	103 (14.9)	2.63 (0.38)	5.93
	Wet	103 (14.9)	3.14 (0.46)	4.56
	<b>Dry</b>	<b>108 (15.6)</b>	<b>2.90 (0.42)</b>	<b>11.6</b>
	<b>Wet</b>	<b>106 (15.4)</b>	<b>3.03 (0.44)</b>	<b>11.6</b>
177 (351)	Dry	60.6 (8.8)	2.13 (0.31)	5.06
	Wet	65.5 (9.5)	2.43 (0.35)	4.75
	<b>Dry</b>	<b>51.2 (7.4)</b>	<b>1.88 (0.27)</b>	<b>5.14</b>
	<b>Wet</b>	<b>50.3 (7.3)</b>	<b>1.91 (0.28)</b>	<b>4.95</b>
260 (500)	Dry	29 (4.2)	1.96 (0.28)	2.62 <sup>e</sup>
	Wet	29 (4.2)	1.67 (0.24)	3.07 <sup>e</sup>
	<b>Dry</b>	<b>21 (3.0)</b>	<b>1.58 (0.22)</b>	<b>2.41<sup>e</sup></b>
	<b>Wet</b>	<b>22 (3.2)</b>	<b>1.51 (0.23)</b>	<b>2.50<sup>e</sup></b>
288 (550)	Dry	16 (2.3)	1.01 (0.15)	2.00 <sup>e</sup>

(a) Standard deviations omitted for brevity. For details see Reference 8.

(b) Both Polymers 1 and 6, Table 1.

(c) Specimens saturated 14 days in water at 71°C (160°F).

(d) 6F-PEO-1 (Reference 9) (Polymer 6, Table 1) in bold values.

(e) Strain-to-yield values. Polymers have entered onset of respective T<sub>g</sub>'s at test temperatures.

found to approximate the reported room temperature values for the polyacrylates. When all the data is compiled, the 6F-PBO's meet or exceed the neat resin mechanical properties of the polyacrylates and some of the properties of polycarbonates<sup>10</sup> (Figure 1 and Table 4). In addition, the polymer's equilibrium moisture uptake at temperatures up to 71°C (160°F) was in the range of 0.8 wt percent maximum. Resistance to aliphatic and aromatic hydrocarbons as well as ketones was limited to a maximum of 6.5 wt percent uptake over two weeks of immersion.<sup>7</sup>

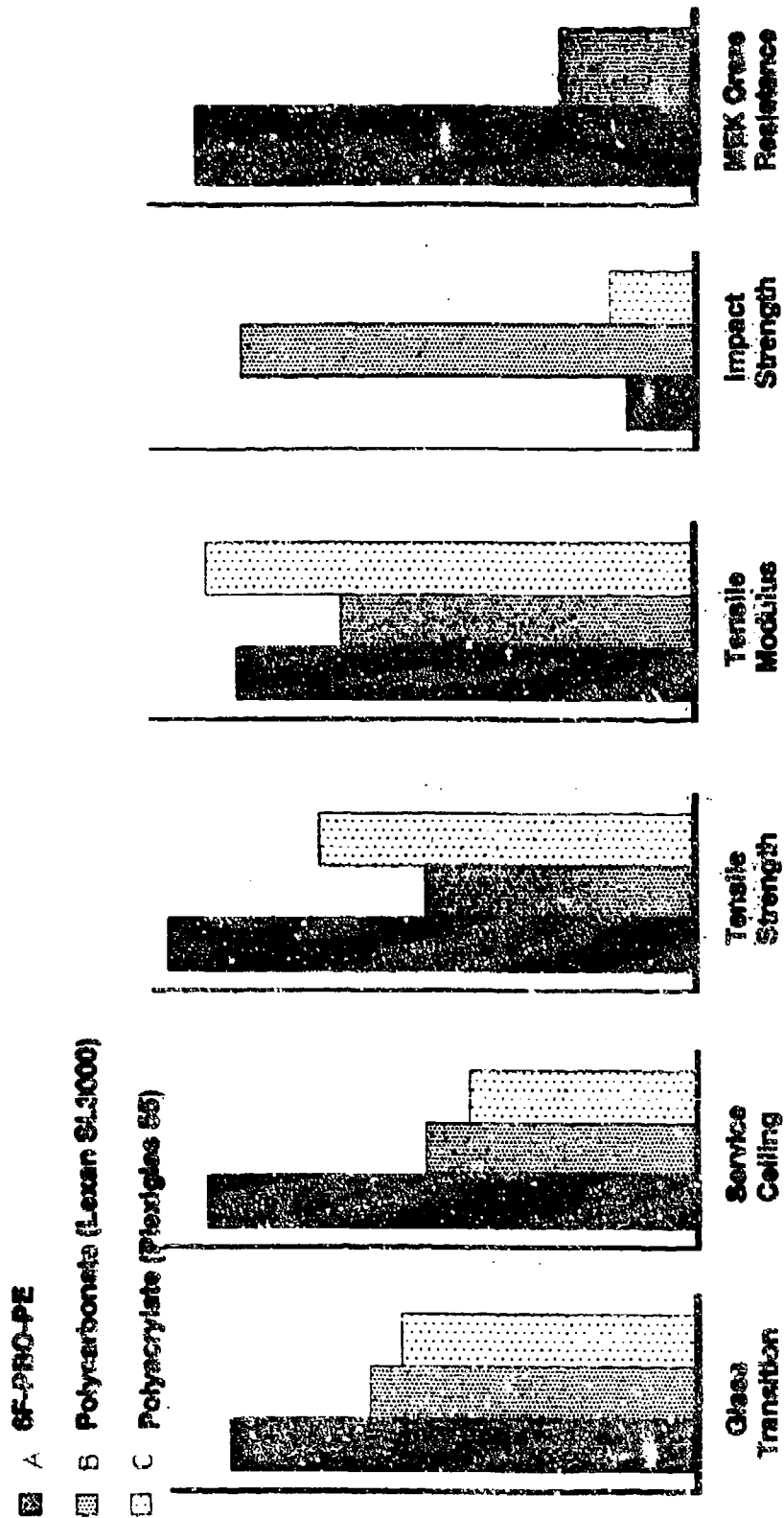


FIGURE 1. Comparison of 6F-PBO (Polymer 6, Table 1) With Other State-of-the-Art Transparency Materials.

TABLE 4. IMPACT TESTING<sup>10</sup> OF 6F-PBO-1.

PROPERTY	6F-PBO-1	LEXAN SL 3000	PLEXIGLAS 55
T <sub>g</sub> (°C)	293		
Continuous Service Temperature (°F)	450-500	250	
Tensile Strength (Ksi), RT, dry	15.6 ± 0.6	8.00 (min)	11.1
Tensile Modulus (Ksi), RT, dry	421 ± 46	325	450
Strain-to Failure (%), RT, dry	11.6 ± 0.8	90	4.7
Notched Izod (ft-lb/in), ASTM D256-88	0.32 ± 0.03	2.09 ± 0.4	0.40
Falling Dart Impact ASTM F736-81	Impact site broken out at 6.22' with min. 20'/s vel and 25 ft-lb impact E	No cracks observed at similar or greater impact E's and heights	
Solvent Crazeing (50% aq. MEK), ASTM 791-82	Crazing at 5500 psi stress, 25 min under stress	Fully crazed at 1500 psi under similar stress and < 25 min	
Solvent Crazeing (50% aq. IPA), ASTM 791-82	none at 3750 psi stress max, 25 min under stress	Fully crazed at 1500 psi under similar stress and < 25 min	
Salt Abrasion, ASTM 1128	Inconclusive	83% T (81% haze) after 100 cycles of blast	

What was not known at the time this effort was performed was the origin of the coloration of the 6F-PBO's in the composite matrix. When high T<sub>g</sub> thermoplastic 6F-PBO's are processed via standard compression molding techniques, they require at least 2500 psi pressures to produce consolidated resin and the temperature at which they are processed must be near or above the T<sub>g</sub> for complete consolidation. These high pressures are expected for the processing of high T<sub>g</sub> thermoplastic materials with stiff heterocyclic units in the backbone. However, the 6F-PBO's homopolymers that have been currently processed as consolidated neat resin tensile specimens exhibit a drastic color change about 50°C below the respective T<sub>g</sub>'s of the polymers.<sup>9</sup> Free standing, solution cast films of 6F-PBO's do exhibit coloration at room temperature as evidenced by the transmission data of ASTM D1925<sup>9</sup>, but the film must be of sufficient thickness (≥ 10 mil) to discern coloration with the naked eye.

The origin of the color in the neat resin 6F-PBO's is a source of much speculation at this time. From the data presented in a subsequent paper in this symposium<sup>9</sup> and in some unpublished data internal to the Polymer Branch, the source of coloration may originate from several possibilities. Those possibilities are intrinsic coloration in the



structure of the polymer backbone, chromophoric impurities in the monomers or polymerization media, simultaneous oxidative-degradation mechanisms, density and packing behavior of the polymer chains, or charge transfer effects between chains.

## B. Other Fluorinated and Nonfluorinated Polymers

There are other polymer compositions which employ the use of 6F groups in the backbones or 3F groups as pendants of aromatic groups in the backbones of polymers. Some of these materials are known to possess  $T_g$ 's in the range of 200°-250°C (392-482°F) and good thermal stabilities based upon their chemical architecture. Some of these polymers include 6F-polyarylene sulfones,<sup>9</sup> 6F-polyesters,<sup>9</sup> and 3F-pendant polyamides.<sup>11</sup> 6F-44 Polyimide,<sup>12</sup> with a  $T_g$  above 300°C (572), may be another candidate material, but it is known that the elongation-to-break of this polymer is low. Low break values empirically translate into reduced toughness and low impact strength. In addition, the cost of fully fluorinated polymers is very high in comparison to hydrocarbon analogs.

There are some nonfluorinated polymers recent to the literature. These include the polyarylene ether ketone homopolymers and copolymers,<sup>13</sup> and the polyarylene carbonates.<sup>14</sup> Again thermal stability and thus use temperature may be compromised, but the advantage to these materials choices may lie in the wealth of literature available on the structure-property characterizations of such materials. One promising new criterion for predicting impact toughness has developed from some recent research on the polyarylene carbonates which relates a  $T_g/T_f$  ratio for polymers to the impact strength.<sup>14</sup>

## CONCLUSIONS

### A. 6F-PBO's

If intrinsic coloration of the heterocyclic portion of the backbone is at fault, then benzoxazoles, even with 6F moieties in the backbone, will not be candidate materials for transparent canopies. There is some empirical evidence to support intrinsic coloration due to the very pale yellow color of solutions of benzoxazole ([273-53-0], mp 27-30°C). What this evidence implies is that the incorporation of 6F groups into the backbone of aromatic-heterocyclic polymers may not always impart colorlessness through the disturbance of the  $\pi$ -electrons. The absence of color is also determined by the choice of spacer. Classic examples from the previous synthetic efforts are the structures of the very yellow powder of Polymer 5 and the green-white powder of Polymer 3 (Table 1). Each 6F-PBO polymer, therefore, must be carefully examined as a significantly thick film or consolidated specimen and not taken at face value because the solid phase of the polymer is white. Despite the intrinsic color, there may be structural alterations which allow the disturbance of the electronic environment in the polymer chain. Incorporation of highly electron-withdrawing groups into the aromatic spacers of the 6F-PBO's is one possible route to investigate by synthetic methods.

Many of the other possibilities listed above for color contribution to 6F-PBO are currently being examined in-house. The status of this effort will be published at a later

date. There are analytical means by which the contributions of any impurities may be examined; however, there are limitations on the detection limits of certain analytical instruments. Since charge transfer effects have been examined by electron spin resonance (ESR) studies in polyimides,<sup>15</sup> a method exists by which to study charge transfer in 6F-PBO. Packing behavior of consolidated specimens may be explored by x-ray diffraction techniques. Some solutions to dense packing in consolidated samples may lie in the preparation of 6F-PBO's with very bulky but thermally stable spacers; work is currently proceeding on such novel spacers.

If the coloration problem is solved, choices will also have to be made between the desire for ultimate optical, physical and mechanical properties. After all the canopy issues are resolved, the presence of fluorine in the outgases of a catastrophic failure of the canopy by thermal degradative means must be weighed against the use of such a canopy material. During normal use temperatures, there would be no problems with 6F-PBO in a canopy ply since a low oxygen index and flame resistance are dictated by the inherent chemical structure. However, if temperatures exceeded 500°C, there would be generation of HF radicals during the combustion process and subsequent unhealthy personnel exposure to such gases.

#### B. Other Fluorinated and Nonfluorinated Polymers

There is some promising data for the incorporation of 6F and other fluorinated polymers into consideration for canopy materials. However, some thermal stability and thus use temperature may be sacrificed if lower  $T_g$  materials are chosen. At this time most mechanical properties as well as any optical properties are unknown for these materials. Toxicity problems upon catastrophic degradation of the fluorinated material will still come into effect.

For the consideration of nonfluorinated materials, stringent structure choices will be needed to be made to balance processability with high use temperature and cost. Again some compromises may have to be made in use temperature to get the desired optical properties.

## REFERENCES

1. P. E. Cassidy, T. M. Aminabhavi, and J. M. Farley, *Rev. Macromol. Chem. Phys.*, **C29** (2,3) **1989** 365.
2. J. M. Aizpura and C. Palomo, *Bull. Soc. Chim. Fr.* 3-4 pt 2 **1984** 142.
3. B. A. Reinhardt, *Polym. Commun.* **31** (12) **1990** 453.
4. U.S. Patent 4,931,532, "Method of Synthesis of Thermoplastic Aromatic Benzoxazole Polymers," B. A. Reinhardt (to U. S. Air Force), **1990**.
5. M. Dotrong, M. H. Dotrong, R. C. Evers, and G. J. Moore, *Polym. Prepr.* **31** (2) **1990** 675.
6. M. Ueda, H. Sugita, and M. Sato, *J. Polym. Sci., Part B: Polym. Chem. Ed.* **24** (5) **1986** 1019.
7. L.R. Denny, R. C. Evers, B. A. Reinhardt, M. R. Unroe, M. Dotrong, and M. D. Houtz, *22nd Int. SAMPE Tech. Conf.* **22** **1990** 186.
8. L.A. Hunter, P. J. Dynes, and M. R. Unroe, *23rd Int. SAMPE Tech. Conf.* **243** **1991** 104.
9. R. Gupta *et al.*, this symposium.
10. Internal report to WL/MLSE from the University of Dayton Research Institute, UDR-TM-91-07, 21 February 1991.
11. H. G. Rogers, R. A. Gaudiana, W. C. Hollinsed, P. S. Kalyanaraman, J. S. Manello, C. McGowan, R. A. Minns, and R. Sahatjian, *Macromolecules* **18** **1985** 1058.
12. Trademark name of Hoechst-Celanese.
13. P. Hergenrother, B. J. Jensen, and S. J. Havens, *Polymer* **29** (2) **1988** 358.
14. D. Freitag, G. Fengler, and L. Morbitzer, *Angew. Chem. Int. Ed. Engl.* **30** **1991** 1598.
15. D. Erskine, P. Yu, and S. C. Freilich, *J. Polym. Sci., Part C: Polym. Lett.* **26** **1988** 465.

LASER-PROTECTIVE AIRCRAFT TRANSPARENCIES

J. A. Brown  
John Brown Associates, Inc.

## LASER-PROTECTIVE AIRCRAFT TRANSPARENCIES

John A. Brown  
JOHN BROWN ASSOCIATES INC.

### ABSTRACT

A new class of laser-protective optical filters consists of thin-film stacks of organic polymers of alternating high and low refractive indices applied in open-to-the-air chemical process equipment. The process is amenable to the fabrication of sheets large enough to be laminated into aircraft transparencies.

\*\*\*\*\*

With the emergence of Limited Warfare and Special Operations type conflicts as major challenges, there is a growing need to provide airmen with laser eye protection; because lasers are cheap weapons. Figure 1 shows the beam wavelengths of several commercial lasers that someone might use as battlefield weapons.

Many approaches to laser protective filters have been explored, including holographic interference filters, absorptive dye filters, conventional dielectric stack interference filters that reject specific threat wavelengths, and the "Tristimulus" interference filter that blocks all popular laser wavelengths yet permits full natural color vision. Figure 2 shows the transmission spectrum of the Army's Sun-Wind-and-Dust (SWD) goggle which incorporates some laser protection, and Figure 3 shows the transmission spectrum of the JBA Tristimulus filter.

Most of the current laser-protection R&D is going into protective goggles and visors, but an attractive alternate approach would be to build the protection into the aircraft windows and canopies. The problem is how to do that. The darkness of the SWD goggle cannot be tolerated, and conventional interference filters would be prohibitively expensive in such large sizes.

Conventional interference filters are made by evaporative deposition of dielectric pairs such as zinc sulfide-and-cryolite or silica-and-titania in high-vacuum equipment, are limited to small sizes, and are very expensive. But this laboratory has recently demonstrated the fabrication of interference filters from thin films of organic polymers (nitrocellulose and polystyrene) in the open air - literally in Mason jars!

Two different proof-of-principle interference filters were made, one reflective in the green and one reflective in the red. Their transmission spectra are shown in Figure 4. They were abbreviated stacks of only 13 layers and were not intended to be protective filters, but they proved the feasibility of making interference filters in open-to-the-air chemical process equipment rather than in the usual high-vacuum equipment.

The proof-of-principle filters were small - one inch by two inches - and were made on glass microscope slides by dip-coating. Very large filters could be made on thin sheets of Mylar or polyurethane on conventional gravure machines, and then laminated between sheets of polycarbonate or acrylic to make all-plastic, laser-protective, aircraft transparencies.

Nitrocellulose and polystyrene were used for the proof-of-principle work, but better polymers are needed for practical filters. We are currently working on two UV-cure polymers, one with a refractive index of 1.4 and one with a refractive index of 1.6. One film is laid down and cross-linked with UV, and the other film is then laid down on top of the first and cross-linked. And so on in alternation until the complete stack is assembled.

Filters can be designed to block virtually any desired wavelengths by suitable choices of layer sequences. Figure 5 shows a design to block a narrow band around 532nm, and Figure 6 shows a design to block a wider band. Figure 7 shows a design to block solar infrared without attenuating visible light. The possible combinations of passbands and stopbands are virtually unlimited.

The filters are not in production; current work is focussed on optimizing the two UV-cure polymers and the deposition technique. We would welcome comments and suggestions as well as specific requirements and applications.

# SELECTED INDUSTRIAL LASERS

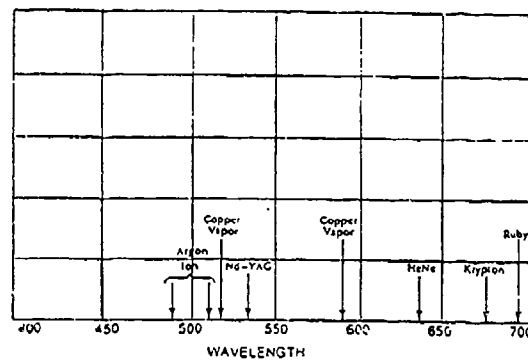


FIGURE 1

JOHN BROWN ASSOCIATES

# ARMY SUG-VID-DUST LASER GOGGLE

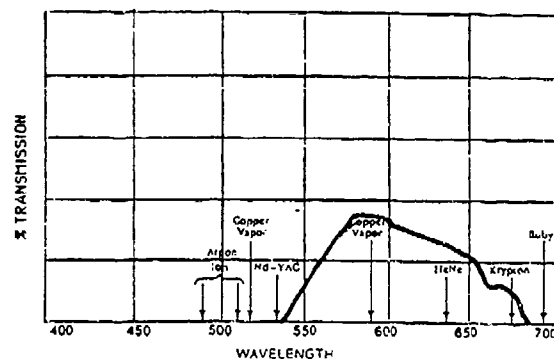


FIGURE 2

JOHN BROWN ASSOCIATES

# BROADBAND LASER EYE PROTECTION

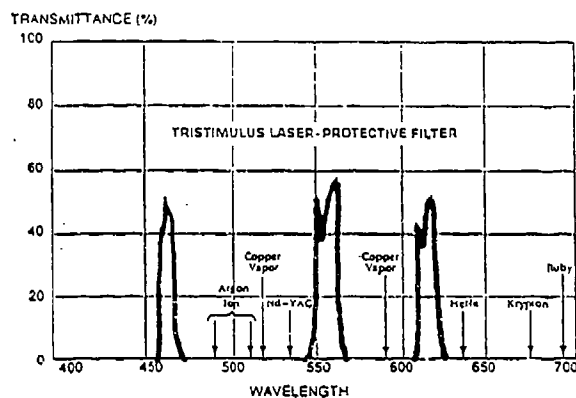


FIGURE 3

JOHN BROWN ASSOCIATES

# INTERFERENCE FILTERS MADE IN MASON JARS

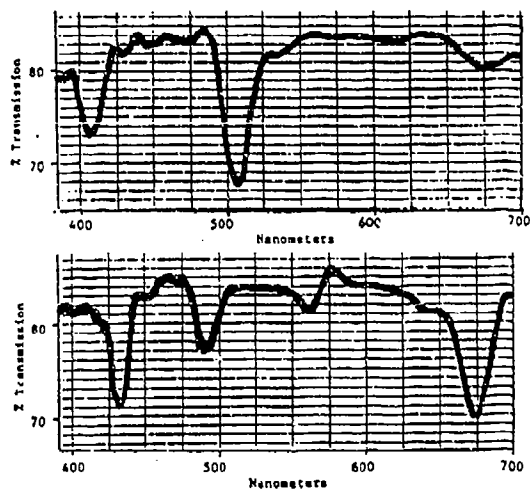
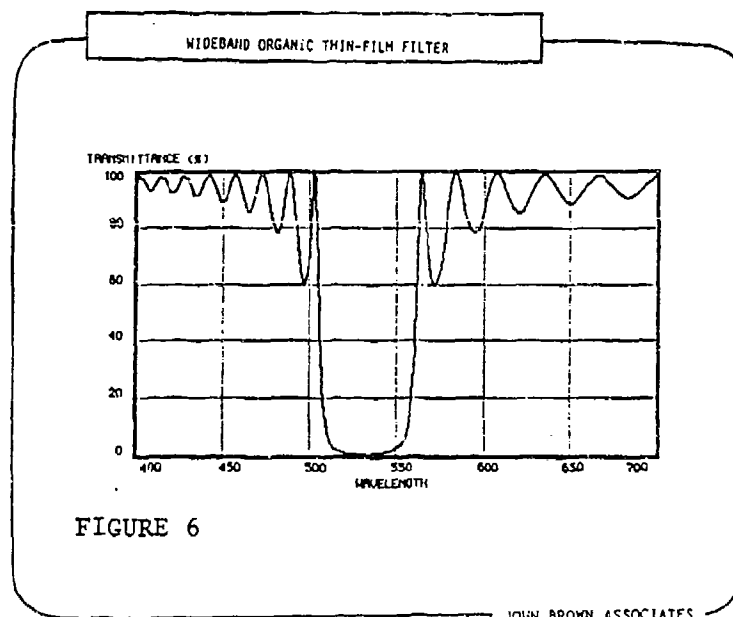
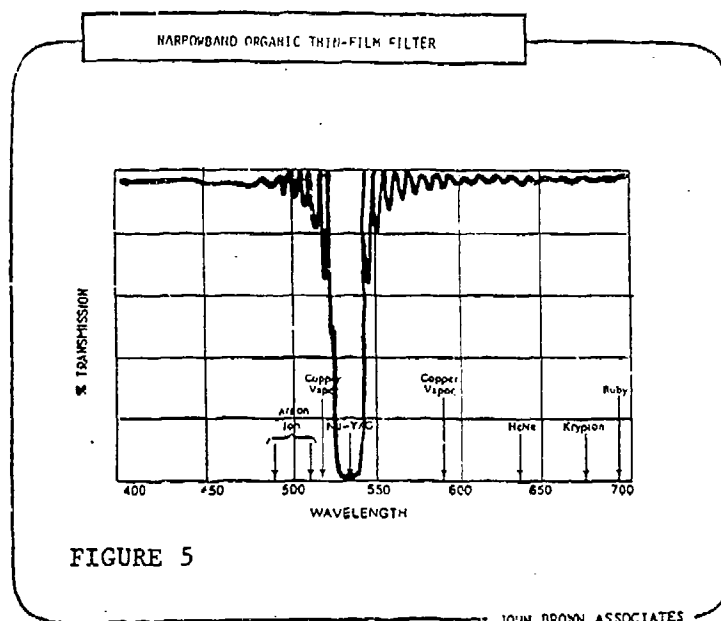


FIGURE 4

JOHN BROWN ASSOCIATES





ORGANIC THIN-FILM SOLAR HEAT REFLECTOR

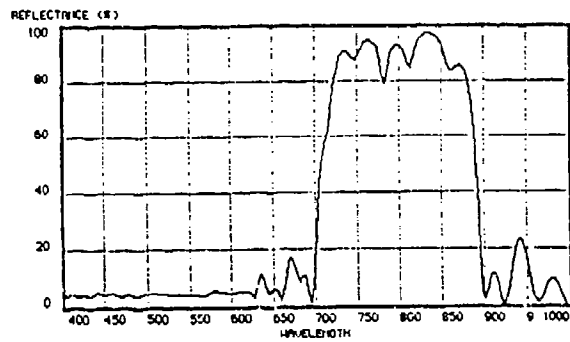


FIGURE 7

JOHN BROWN ASSOCIATES

**FAILURE ANALYSIS OF DIAMOND-LIKE CARBON (DLC)  
COATED POLYCARBONATES: MECHANICAL CHARACTERIZATION**

**Note: Manuscript of this paper was not submitted.**

**A. J. Hsieh  
Army Research Laboratory**

NEW HIGH TEMPERATURE HEXAFLUORINATED POLYBENZOXAZOLES  
FOR CANOPY APPLICATIONS

R. K. Gupta  
P. J. King  
Daychem Laboratories

M. R. Unroe  
Materials Directorate

**New High Temperature  
Hexafluorinated polybenzoxazoles  
for Canopy Applications**

**Rakesh K. Gupta**

**Pamela J. King**

**Daychem Laboratories, Inc.**

# NEW HIGH TEMPERATURE 6F-PBO MATERIALS FOR CANOPY APPLICATIONS

Rakesh K. Gupta, Ram B. Sharma, and Pamela J. King

Daychem Laboratories, Inc., 143 Westpark Road, Dayton, Ohio 45459-4814

and

Marilyn R. Unroe

Polymer Branch, Materials Directorate, Wright Laboratory,

WL/MLBP, 2941 P Street Ste 1, Wright-Patterson AFB, Ohio 45433-7750

New Transparent thermoplastic materials suitable for higher use temperature (350-500°F) are required in airframe applications to replace the existing state-of-the-art canopy materials. These materials must retain or surpass the physical properties of polycarbonates and acrylics at higher use temperature. Several candidates from the families of thermally stable aromatic/heterocyclic polymers without extended conjugation are being evaluated for this application.

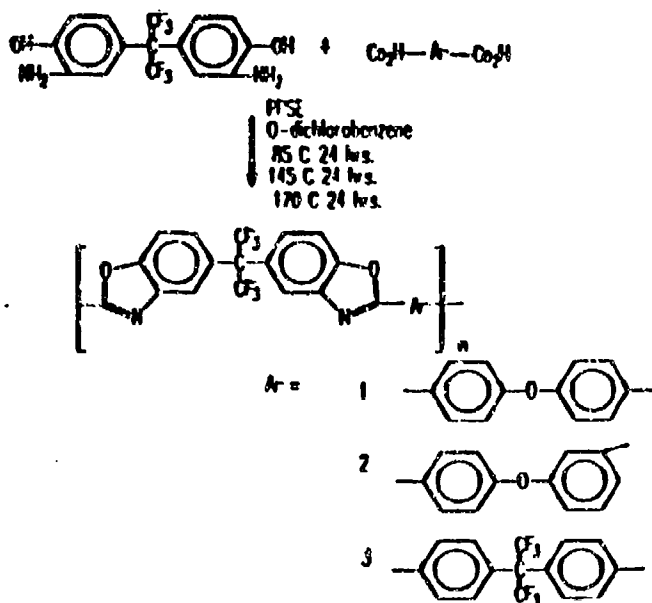
In this report a family of polybenzoxazoles with hexafluoromoieties (6F-PBO) has been synthesized and evaluated as transparency materials for canopy applications. Several candidate 6F-PBO systems are synthesized with different spacers, as homopolymers, copolymers and terpolymers with other thermally stable polymer systems. The processing parameters, thermal data, mechanical and optical properties of these systems are presented in this report. This is an ongoing effort, the data established to date is presented.

## Introduction

Future aircraft will require strict demands on composite materials such as strength, service temperature capability, and durability. The materials that are being developed are meeting these demands and are far superior to the currently available materials. The new thermoplastics are being developed in such a way so as to minimize the cost in manufacturing and processing. The polymer systems most emphasized are hexafluorinated polybenzoxazoles (6F-PBO's). A group of 6F-PBO's have been analyzed for mechanical strength, thermal stability, and optical quality. All data obtained was evaluated and summarized in this paper.

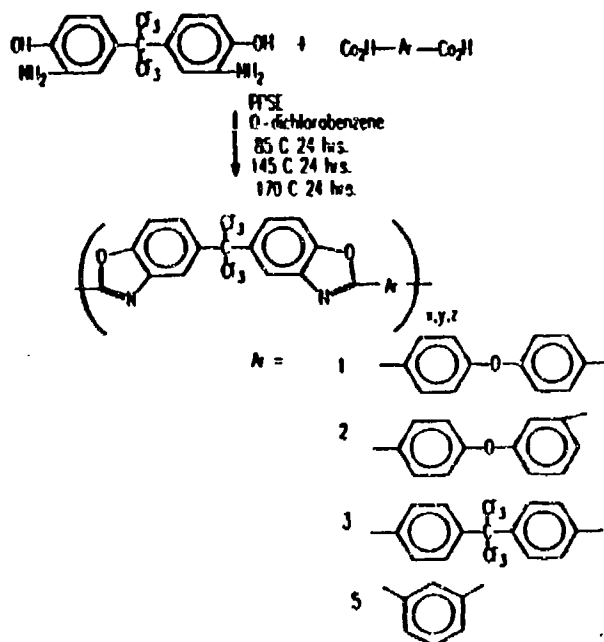
## Discussion

Research is currently being done at Daychem Laboratories, Inc. in scale-up synthesis, processing, and characterization of 6F-PBO systems as well as other candidate polymers. 6F-PBO systems synthesized (Reference 1) are shown below:



Polymers synthesized that have had desirable physical appearance were further analyzed (Table 1). Elemental analysis for 6F-PBO-1, 6F-PBO-2, and 6F-PBO-3 showed that the materials have high purity. Semi-quantitative analysis also confirmed this data. Solution viscosity data for the materials was obtained. The inherent viscosity measurements fall within the range for this type of polymer system.

Other polymer systems that were synthesized would include terpolymer 6F-PBO's, hexafluoro polyesters (Reference 2), and hexafluoro polysulfones (Reference 3) as shown below.

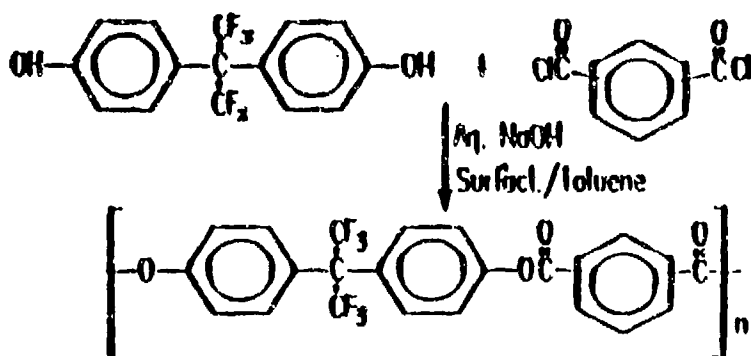


	<u>Monomers</u>			
	<u>1</u>	<u>2</u>	<u>3</u>	<u>4</u>
6F-PBO-X1	40%	40%	0%	20%
6F-PBO-X2	0%	0%	20%	80%
6F-PBO-X3	30%	0%	20%	50%



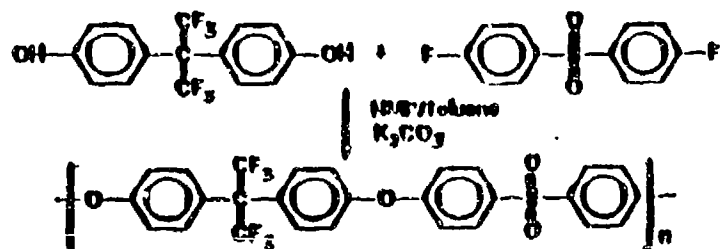
Table 1. Physical Characterization of Selected  
6F-PBO's

POLYMER	ELEMENTAL ANALYSIS		$\eta_{inh}$ (.180 g/dl) in MSA (30°C±1°C)	APPEARANCE	SOLUBILITY in THF
	CALC'D	(FOUND)			
6F-PBO-1	C 63.05	(62.91)	1.27 dl/g	white beaded powder	total (light yellow solution)
	N 5.07	( 5.19)			
	H 2.55	( 2.45)			
	Si 0.00	( 0.007)			
	P 0.00	( 0.19)			
	Cl 0.00	( 0.021)			
6F-PBO-2	C 63.05	(62.45)	0.51 dl/g	off- white beaded powder	total (medium yellow solution)
	N 5.07	( 5.08)			
	H 2.55	( 2.43)			
	Si 0.00	( 0.008)			
	P 0.00	( 0.10)			
	Cl 0.00	( 0.35)			
6F-PBO-3	C 55.99	(56.13)	0.91 dl/g	white beaded powder	total (light yellow solution)
	N 4.08	( 4.21)			
	H 2.06	( 1.92)			
	Si 0.00	( 0.005)			
	P 0.00	( 0.11)			
	Cl 0.00	( 0.17)			
6F-PBO-X1			1.20 dl/g	off-white beaded powder	partial (medium yellow)
6F-PG-1			0.706 dl/g	stark white beaded powder	total (color- less)



1,3-diacid chloride 6F-PE-1

1,4-diacid chloride 6F-PE-2



6F-PBO-X1, 6F-PE-1, and the 6F-Polysulfone all had desirable physical appearance and were further analyzed.

The thermal characteristics of 6F-PBO-1, 6F-PBO-3, and 6F-PBO-1E (6F-PBO-1E homopolymers endcapped with aromatic moieties) show high use temperatures for these materials. The glass transition temperature as shown by thermomechanical analysis (TMA) ranged from 309°C for 6F-PBO-3 to 295°C for 6F-PBO-1. Both 6F-PE-1 and 6F-Polysulfone have a glass transition temperature slightly above 200°C. Thermogravimetric analysis (TGA) was performed on 6F-PBO-1 and 6F-PBO-3 to 850°C maximum in air and both materials retained 95% of their weight up to 550°C. Decomposition onset was above 500°C (Table 2) by TGA.

Table 2. Thermal Data

	Glass Trans. Temp. $\Delta T = 10^\circ\text{C/min.}$		TGA (air) $850^\circ\text{C}$	Decomposition
	DSC	TMA (air)	95% wt. retention	Onset TGA (air)
6F-PBO-1	293°C	295°C	550°C	564°C
6F-PBO-1E	-----	278°C	525°C	572°C
6F-PBO-3	-----	309°C	575°C	518°C

Oxidative isothermal aging was performed on 6F-PBO-1, 6F-PBO-2, and 6F-PBO-1E. All of the polymer samples showed signs of discoloration starting at  $600^\circ\text{F}$ . Weight loss was not apparent until  $650^\circ\text{F}$ . At this temperature, 6F-PBO-3 was the only sample that retained 95% of its initial weight. Unconsolidated powders of 6F-PBO-1 and 6F-PBO-3 remained colorless for 200 hours at  $500^\circ\text{F}$  (Table 3).

Table 3. Isothermal Aging Properties of 6F-PBO Materials (200 Hours, Total Weight Loss).

	$500^\circ\text{F}$	$600^\circ\text{F}$	$650^\circ\text{F}$	$700^\circ\text{F}$
6F-PBO-1	white	pale yellow <2%	red brown 5%	black 86%
6F-PBO-2	light tan	red brown 1%	black 7%	black 76%
6F-PBO-3	white	off white <1%	yellow <2%	yellow gold 10%
6F-PBO-1E	white	yellow brown <1%	black 6%	black 70%

Mass spectroscopy/TGA was also performed for the same group of polymers. Major degradation at  $512^\circ\text{C}$  for all of the samples followed the same pattern. Degradation of the benzoxazole

ring was apparent at a temperature of 650°C. This data is summarized in Table 4.

Table 4. Occurrence and Relative Abundance of Major Products for 6F-PBO's

	<u>6F-PBO-1</u>		<u>6F-PBO-2</u>		<u>6F-PBO-3</u>		<u>6F-PBO-1E</u>	
TLC max (°C)	550	660	550	660	550	760	560	650
Sample Weight Loss (~ %)	19	15	21	14	50	<2	20	15
HF	100		100		100		100	
CO	60	60	50	50	50	33	50	50
H <sub>2</sub> O	14	14	23	23	10		15	15
CO <sub>2</sub>	16		18		8		15	13
HCN		18		15		7		8
NH <sub>3</sub>		6		8	3			10
CF <sub>3</sub> H	4		5		5		3	

6F-PBO-1 was processed by thermal compression molding. It was apparent from the thermal data that temperatures close to the glass transition temperatures would cause discoloration during processing. For this reason processing was difficult. To obtain complete consolidation without discoloration required pressures of 75,000 psi at a temperature of 575°F. These processing parameters gave a molded specimen with the least amount of discoloration; however, the molded specimen still possessed medium yellow color and was translucent. Processing of these materials is being investigated further at

this time. Transmission data shows that there is a decrease in transmission as film thickness is increased. The yellowness index of 6F-PBO's was compared to polycarbonates (Table 5). It is desired to replace the polyacrylate outer ply of the aircraft canopy with 6F-PBO materials. The polyacrylates have a yellow index of one; as can be seen by the data, 6F-PBO's have higher index values.

Table 5. Yellowness Index for 6F-PBO's Vs.  
Polycarbonate (ASTM D1925)

	<u>Thickness</u>	<u>Yellowness Index</u>
Polycarbonate "Blue"	0.25"	0.821
Polycarbonate "Yellow"	0.25"	9.424
F-16 Laminate with Solar Coating		39.031
6F-PBO-1	0.005"	16.450
6F-PBO-3	0.003"	7.940
6F-PBO-X1	0.005"	20.620
6F-PE-1	0.012"	3.520
6F-PBO-1E	0.005"	10.870

Processing was also done on 6F-PE-1 as well as 6F-Polysulfone. Both polymer materials were processed at temperatures approximate to their glass transition temperatures. The processed specimens were both colorless and transparent.

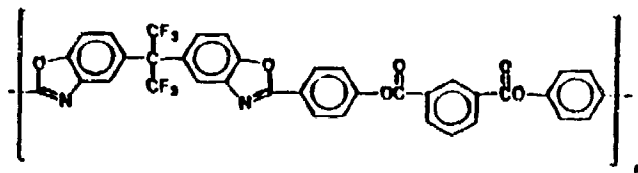
## Conclusions and Recommendations

The discoloration of 6F-PBO-1 during thermal processing is a problem that needs to be further investigated. The source of this color can possibly be attributed to several factors. One possibility is that impurities may have remained from the synthesizing process. The likelihood of this explanation; however, is diminished due to undetectable signs of impurity from the physical data. Another possibility is that the polymer itself may inherently be colored. There are two reasons for this. Initially, conjugation between the nitrogen in the benzoxazole ring and the aromatic ring of the diacid may cause a certain amount of discoloration. Secondly, color may also be attributed to the thickness of the molded specimens. Transmission data shows that thicker films have less transmission than a thin film. If inherent color is determined definitely one possible solution may be the addition of additives to counteract the color. This process is considered commonplace in the processing of many polymers. One final explanation for discoloration could be in the existence of trace amounts of oligomers or lower molecular weight polymer chains. These oligomers may have a tendency to break down at the processing temperatures that are needed to get complete consolidation of materials.

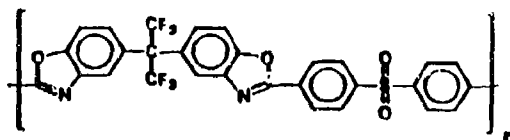
In conclusion, the 6F-PBO system needs to be investigated further to determine its likelihood as an aircraft canopy transparency. Other likely polymer systems with similar properties also need to be studied. Copolymer systems that

have potential for mechanical strength as well as transparency qualities are being investigated at this time. A few examples are shown below:

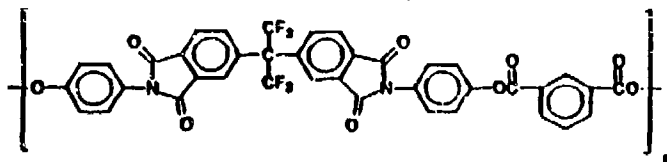
**Polybenzoxazole-ester copolymer**



**Polybenzoxazole-sulfone copolymer**



**Polyimide ester copolymer**



Finally, other commercially available candidates also require analysis to determine their feasibility in regards to desired applications.

#### Acknowledgement

This work was performed for contract F33615-92-C-5907 sponsored by the Materials Directorate, Wright Laboratory, Air Force Material Command, Wright-Patterson Air Force Base, Ohio 45433-6533 with Marilyn Unroe as the Project Engineer. The work described here was performed at Daychem Laboratories,

Inc. Transparency characterization and mechanical property determinations were performed at the site of the subcontractor, Texstar, Inc., Dallas, Texas, under the supervision of Mr. Lance Teten. Thermal data was provided by Marlene Houtz from Wright Laboratory.



## References

1. M. Zhao, M. Samoc, P. Prasad, B. Reinhardt, M. Unroe, M. Prazak, R. Evers, J. Kane, C. Jariwala and M. Sinsky, *Chem Mater.*, Vol. 2, 670 (1990).
2. W. M. Eareckson, III, *J. Polym. Sci.*, Vol. 40, 399 (1959).
3. S. Maiti and B. K. Mandal, *Prog. Polym. Sci.*, Vol. 12, 111-153 (1986).

SESSION VII

NEW MATERIALS AND PROCESSES - PART B

Chairman: R. Nelson  
Air Logistics Command  
Hill Air Force Base, UT

Co-Chairman: T. Reinhart  
Materials Directorate  
Wright Laboratory

Coordinator: E. Joy  
Flight Dynamics Directorate  
Wright Laboratory

## ADVANCED CANOPY COATINGS

K. Alexander  
Flight Dynamics Directorate  
Wright Laboratory

G. C. Stone  
Lockheed Fort Worth Company

## ADVANCED CANOPY COATINGS

Kristen K. Alexander  
Flight Dynamics Directorate  
Wright Laboratory, WPAFB OH, 45433

Dr. Gordon C. Stone  
Lockheed Fort Worth Company  
Fort Worth, Texas 76101, U.S.A.

### Abstract

Advanced Canopy Coatings will reduce the vulnerability of flight vehicles in the natural and combat environments which cause abrasion and cracking of transparency systems. The advanced coatings will be one of the main contributors to doubling the current nominal two year service life of transparency systems to meet the four year service life goal. The Air Force's Windshield Program Office, Flight Dynamics Directorate/ Wright Laboratory, WPAFB, Ohio started the MITS Advanced Canopy Coatings Program to design a transparency system using these coatings and to develop a test methodology for accepting them. This paper will discuss the various coatings tested and detail the test methodology developed. The payoffs include reduced replacement time, increased mission ready status, and considerable cost savings. This paper covers the sub scale screening and larger coupon tests, full scale test results will be presented in a separate report.

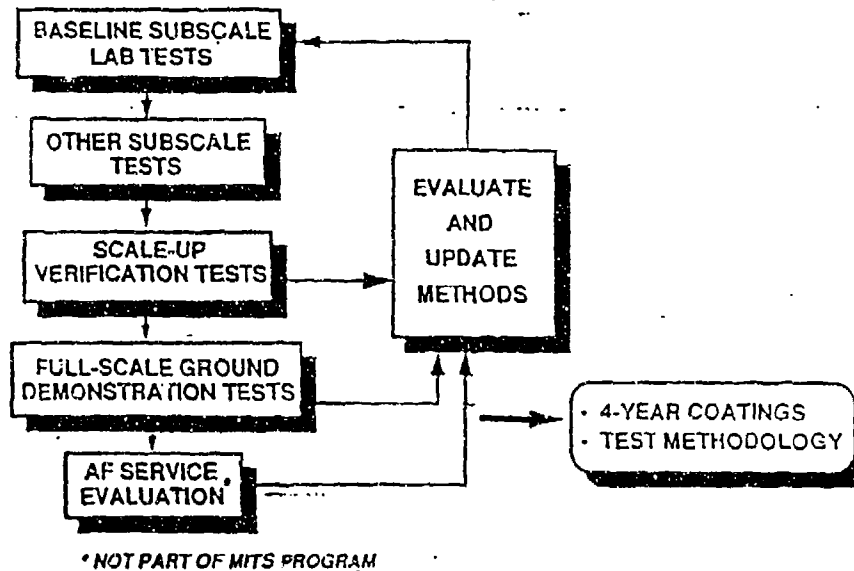
## INTRODUCTION

Advance Canopy Coatings reduce the vulnerability of flight vehicles in the natural and combat environments which cause abrasion and cracking in transparency systems. These coatings are one of the main contributors to doubling the current nominal two year service life of transparency systems to meet the four year service life goal. The coatings will protect the transparency from external environmental and chemical damage. The Mission Integrated Transparency System (MITS) Advanced Canopy Coating Program was focused on increasing the service life of transparency systems. The first of two objectives for this program was to demonstrate a coating with a four year service life. The second was to develop a test methodology to validate the service life.

There were some general principals followed in the development and completion of this program. First materials were off-the-shelf, no new materials were to be developed. Multiple sources were used for manufacturing and testing the coatings. Service life was the single most important goal. The MITS Program requirements were used as pass/fail criteria. Finally near term demonstration on the F-16 transparency was planned. A bare (non medalist) polycarbonate substrate was used as the baseline, but medalist versions were also included in the testing effort for future (and in reality selected) implementation.

The overall technical approach is summarized in Figure 1 and the participants in the program are shown in Table 1. First Baseline Subscale tests were conducted, followed by additional subscale tests and scaled up verification tests. Full-scale ground tests and flight test evaluation are on going currently. All of these test lead to an evaluation and updating of test methods and ultimately a four year coating test methodology. The Program was managed be the Flight Dynamics Directorate with the prime contractor being General Dynamics (now Lockheed). Most testing materials were provided by PPG, Sierracin/Sylmar, Swedlow (now Pilkington), and Texstar. Testing was conducted by the University of Dayton Research Institute, General Dynamics, PPG, Sierracin/Sylmar, Swedlow, and Texstar. Evaluation was conducted by everyone involved.

Eighteen candidate coating/substrate combinations were evaluated. Both polycarbonate and acrylic substrates were employed in bare and metalized (enhanced gold and indium tin oxide ITO) conditions. The type coatings tested included hard coats, liners, and thin films. The application/processing requirements for the candidates included casting, lamination, and flow coat. Tables 2 and 3 show the general characteristics of the tested candidates. The samples were coded by manufacturer and type, specific details must be obtained directly from the manufacturing company.



Overall Technical Approach for Advanced Coatings Investigations

FIGURE 1

Advanced Coatings Project Team

PARTICIPANT	T A S K		
	MATERIALS	TEST	EVALUATE
UNIVERSITY OF DAYTON		✓	✓
PPG	✓	✓	✓
SIERRACIN / SYLMAR	✓	✓	✓
SWEDLOW	✓	✓	✓
TEXSTAR	✓	✓	✓
GENERAL DYNAMICS	-	✓	✓

- GD & UDRI Conducted "Baseline" Tests
- Others Conducted "Preferred" Tests

TABLE 1

DESCRIPTION OF CANDIDATE COATINGS DESIGNS ON BARE  
POLYCARBONATE

MANUFACTURER	CODE	TYPE	PROCESSING
PPG	A1	POLYURETHANE LINER	CELL CAST FLAT
SWEDLOW	D1 D2 D3	POLYURETHANE " "	APPLIED TO FINISHED-CONTOUR PARTS
SIERRACIN	E3	POLYURETHANE SOFT COAT	FLOW COAT
TEXSTAR	F1 F2 F3 F4	COMPLEX ACRYLIC THIN FILM SAME AS F4 THIN-FILM POLYURETHANE POLYURETHANE LINER	FLOW COAT — FLOW COAT LAMINATED

TABLE 2

DESCRIPTION OF COATINGS DESIGNS ON ACRYLIC AND/OR  
METALLIZED SUBSTRATES

MANUFACTURER	CODE	TYPE	SUBSTRATE	PROCESSING
SWEDLOW	D4 D5 D6 D7 D8 D9 D10	POLYURETHANE (D1) ↓ (D2) (D3) (D1) (D2) (D1) ↓ (D1)	EG / POLYCARBONATE EG / POLYCARBONATE EG / POLYCARBONATE ITO / POLYCARBONATE ITO / POLYCARBONATE ACRYLIC EG / ACRYLIC	APPLIED TO FINISHED-CONTOUR PARTS ↓
SIERRACIN	E1 E2 E4	POLYSILICATE HARD COAT POLYSILICATE METAL SYSTEM (ITO) POLYSILICATE METAL SYSTEM (ITO)	ACRYLIC ACRYLIC POLYCARBONATE	FLOW COAT FLOW COAT / VACUUM SPUTTER FLOW COAT / VACUUM SPUTTER

Table 3

Although each of the participating suppliers conducted their own tests on their candidate materials, only those tests that were conducted by the University of Dayton (UDRI) and General Dynamics (GDFW) on all candidates will be summarized.

### DISCUSSION

The testing conducted on the MITS Advanced Canopy Coating Program was based on a methodology developed for this program, but with a more general goal of defining a comprehensible testing methodology for estimating the potential service life of transparency materials. In order to define this methodology we solicited inputs from both the MITS subcontractors and the transparency community in general through ASTM Subcommittee F7.08. After a survey of these participants regarding the most important natural hazards that limit service life and the most effective way of testing resistance to these hazards, we selected the baseline laboratory tests listed in Table 4 as the initial "combined-environment" tests. These tests may be updated and revised in the future as results and feedback from full-scale testing becomes available.

Although baseline tests on unweathered samples were conducted, all the testing included simulated weathering plus testing in another environment. A QUV, Q-Panel Co., machine that combines the effects of UV wavelengths of sunlight with heat and condensation was used to simulate accelerated weathering. The test operates in alternating cycles of 7 hours UV followed by 5 hours condensation, with 168 hours run time equal to one year. We used four years, 672 hours, accelerated weathering time. It is interesting to note that artificial weathering by itself has very little effect on the haze characteristics of all the coatings tested. All coatings, as shown in figures 2 and 3, passed the MITS requirement of less than 6 % haze after 4 years of QUV. Artificial weathering by itself then is not a good discriminator to aid in service life estimation.

Rain erosion tests were conducted at the University of Dayton Research Facility located at Wright Patterson AFB. This facility uses a 1 inch/hour rainfall rate. Samples were tested at a 30 degree installation angle at 350 knots (400 mph), 500 mph, and 500 knots (576 mph). The test was conducted at 1, 5, 10, 30, and 60 minute intervals, with a 20% coating removal, pitting or delamination criteria used for failure. The minimum screening criteria was no damage after 5 minute exposure at 350 knots. Cast acrylic samples were used for comparison and appear in the following tables with the designation G1. Figures 4 and 5 summarize the rain erosion results for the coatings at the 576 mph (500 knots).

The stress-craze tests were conducted using ASTM F-484 and F-791 as guidelines. A maximum fiber stress (cantilever-beam loading) of 4000 psi was used to accelerate failure. Our goal was to cause failures and provide a severe screening environment for the coating



# SUMMARY OF BASELINE SCREENING TESTS

- QUV\* + RAIN EROSION
  - ✓ 350-500 knots, 1-inch/hour Rain
- QUV\* + SALT BLAST
- QUV\* + STRESS CRAZE
  - ✓ 4000 psi Maximum (Accelerate Failure)
  - ✓ Five Fluids
    - Ethylene Glycol, Isopropyl Alcohol, Toluene, JP-4, 20% MEK in water
- QUV\* + OSCILLATING SAND

\* Daily Cleaning of Samples During QUV (4-Year Equivalent)

TABLE 4

# HAZE AND TRANSMITTANCE OF WEATHERED COATED POLYCARBONATE ARE ACCEPTABLE

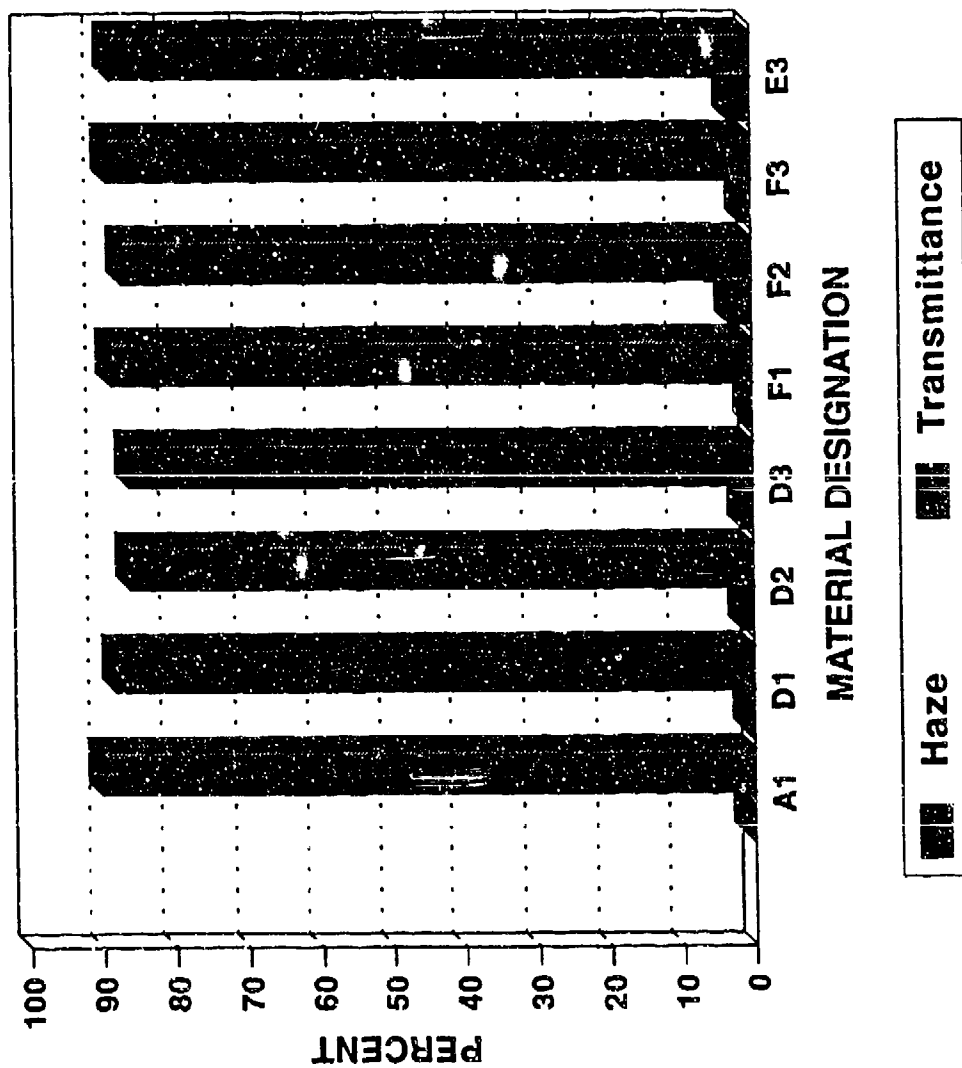


FIGURE 2

# HAZE & TRANSMITTANCE OF WEATHERED MET. COATED PC & AC ARE ACCEPTABLE

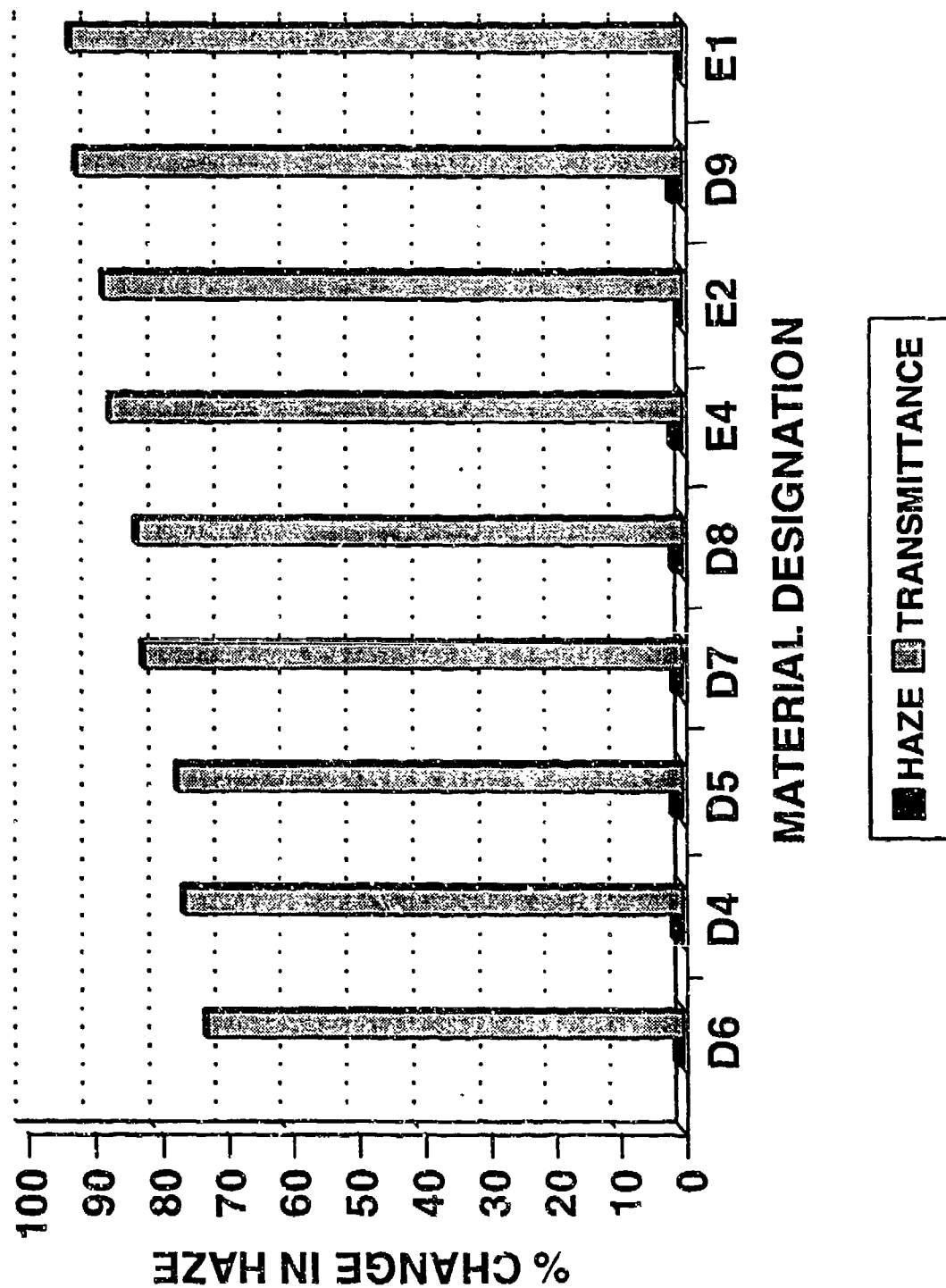
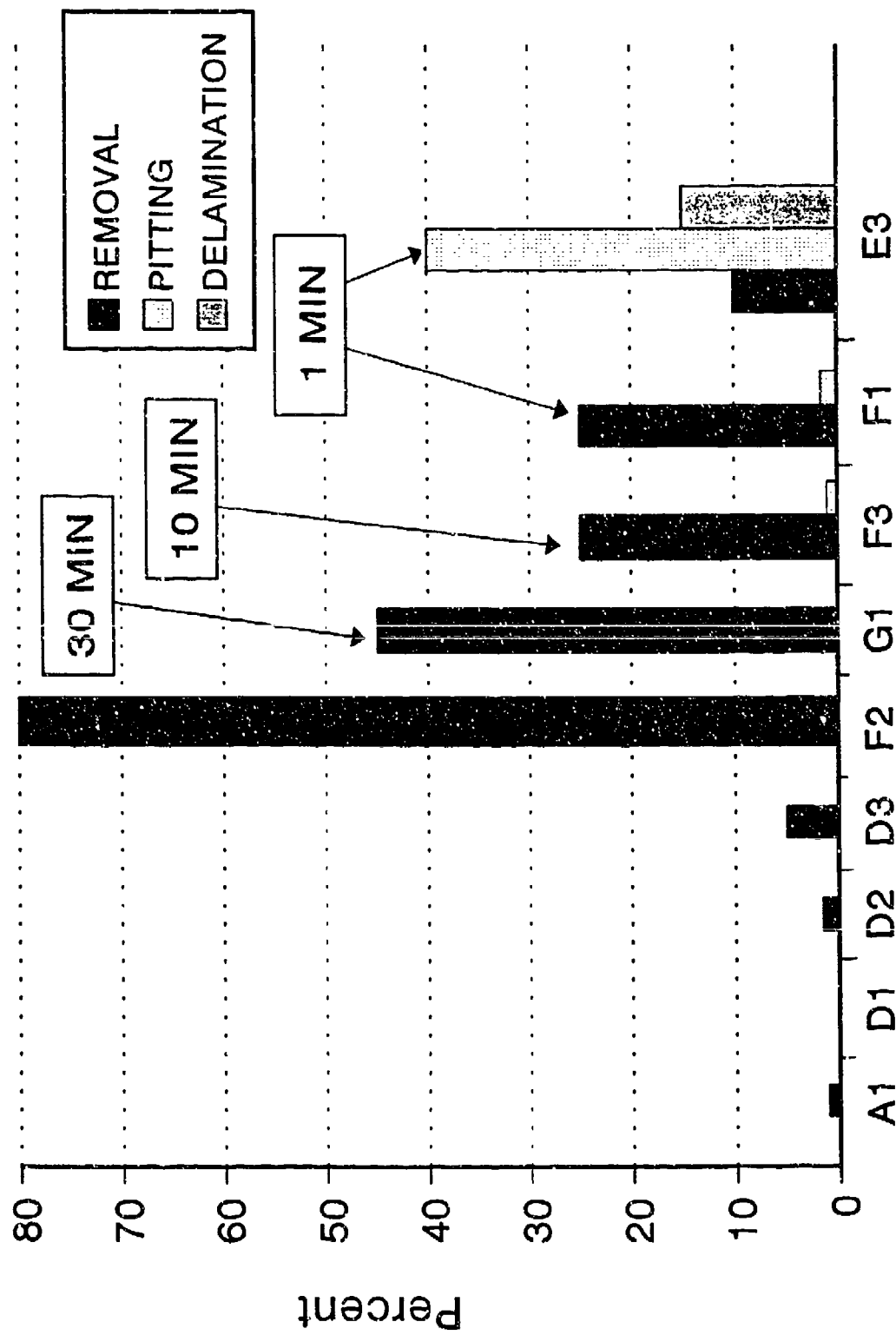


FIGURE 3

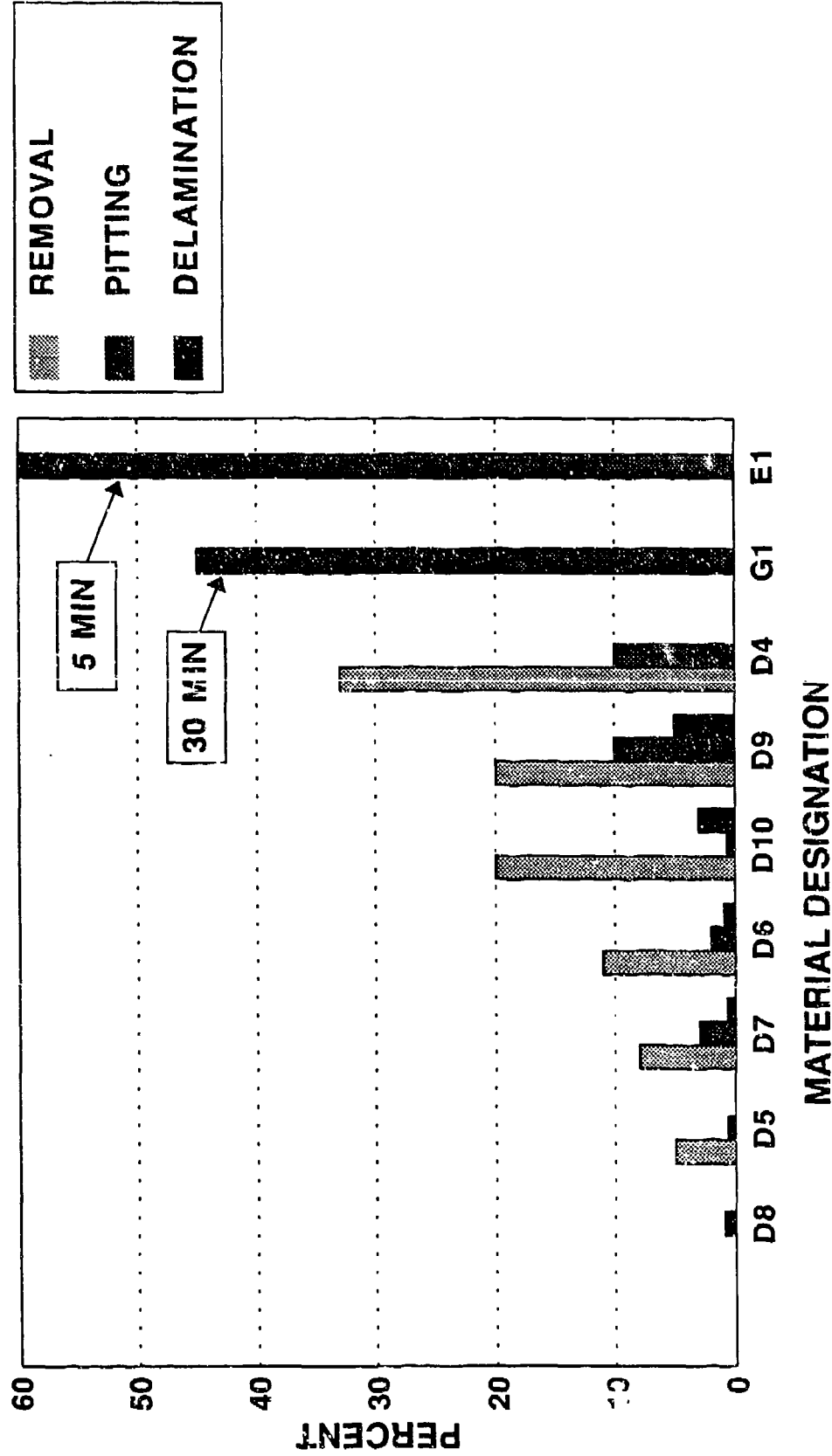
# RAIN EROSION TEST RESULTS, 576 MPH 1"/HR RAIN, 30 DEGREE IMPACT, 60 MINUTE



Material Designation

FIGURE 4

# **RAIN EROSION TEST RESULTS, 576 MPH 1"/HR RAIN, 30 DEGREE IMPACT, 60 MINUTE**



**FIGURE 5**

candidates. The chemicals tested (ethylene glycol, isopropyl alcohol, toluene, JP-4 jet fuel, and an MEK/Water mix) were selected as representative hazards on the flight line environment. Testing was done at room temperature, and the coating surface was kept continually covered with fluid for 30 minutes, and the lowest stress level to which crazing occurred was noted. Tables 5 and 6 summarize results of the stress craze tests after 4 equivalent years of QUV weathering.

The salt impingement (salt blast) tests were conducted with a grit blast gun operating with controlled pressure, duration, interval, and number of blasts. ASTM F-1128 was used as a guideline. Figure 6 summarizes the most severe salt blast testing used. The 4-inch X 4-inch sample is subjected to a different number of salt blasts on each four locations. Referring to the figure, location 3 on the sample received 8 blasts after each "year" (week in real time) of QUV weathering for a total of 32 blasts after 4 equivalent years. Figures 7 and 8 summarize the worst case results for the coating candidates. Figure 9 shows, for reference, baseline (unweathered) results for bare (uncrated) polycarbonate, stretched acrylic, and two types of cast acrylic (Poly-76 and Poly-84).

Figures 10 and 11 show the results for haze after 4 equivalent years of accelerated weathering and 600 cycles oscillating sand abrasion. The Bayer Abrasion criteria used was ASTM F735-81, this test is essentially a shaking table test, not a rolling sand test as in Taber abrasion. Changes in luminance transmission for these samples were insignificant and one notes that only 2 of the candidate coatings on bare substrate has changes in haze greater than 4 %.

Ultra violet, visual, and infrared (UV/VIS/IR) spectrum transmission measurements were taken on all coatings before and after accelerated weathering. These measurements (300-900 nanometer wavelengths) showed that all the coatings on polycarbonate and acrylic had good transmission, greater than 85% on the average. Figures 12 and 13 illustrate the difference in UV/VIS/IR transmissions for weathered and baseline samples for bare polycarbonate and metalized polycarbonate respectively. Negligible differences were noticed between the baseline and weathered samples. There was a slight difference in the transmission levels on samples with metallic services, this was expected, and the transmission measurements were acceptable.

Thermal cycling tests were conducted in which the candidate coatings designs on polycarbonate were cycled between room temperature and an elevated temperature that ranged from 250 to 350 degrees F, with a level time of 10 minutes at the elevated temperature. Visual inspection revealed no significant delamination or optical deterioration in the coatings after this cycling, although most coatings became soft near the 350 degree level. Some self healing was noted on samples that had surface blemishes prior to the elevated-temperature exposures.

# CHEMICAL STRESS CRAZE TEST RESULTS FOR QUV WEATHERED, COATED POLYCARBONATE

Specimen Design	Ethylene Glycol	Isopropyl Alcohol	Toluene	JP-4 Jet Fuel	20% MEK/ 80% Water
F3	X	•	•	X	X
D2	•	X	•	X	X
A1	•	•	•	X	X
D3	•	•	3700 Psi	X	X
F4	•	•	3600 Psi	X	X
D1	2910 Psi	•	2510 Psi	X	X
F1	3440 Psi	X	2490 Psi	3500 Psi	X
E3	2260 Psi	1300 Psi	750 Psi	1800 Psi	2000 Psi

X - Denotes no crazing

• - Denotes no crazing with coating softening

Values in table are minimum stress to craze in 30 minute test

TABLE 5

# CHEMICAL STRESS CRAZE TEST RESULTS FOR QUV WEATHERED METALLIC COATED POLYCARBONATE AND ACRYLIC

Specimen Design	Ethylene Glycol	Isopropyl Alcohol	Toluene	JP-4 Jet Fuel	20% MEK/ 80% Water
D10	3700 Psi	•	•	X	X
D9	2300 Psi	•	•	X	X
D5	•	3720 Psi	3700 Psi	X	X
D8	•	1510 Psi	2730 Psi	X	X
D6	3720 Psi	3700 Psi	3720 Psi	X	X
D4	2410 Psi	3610 Psi	3200 Psi	3600 Psi	X
D7	2500 Psi	2290 Psi	2240 Psi	2100 Psi	X
E2	2200 Psi	2900 Psi	2760 Psi	3260 Psi	2900 Psi
E1	2100 Psi	1800 Psi	2300 Psi	3720 Psi	3680 Psi
E4	1790 Psi	2300 Psi	1610 Psi	2500 Psi	2620 Psi

X • Denotes no crazing

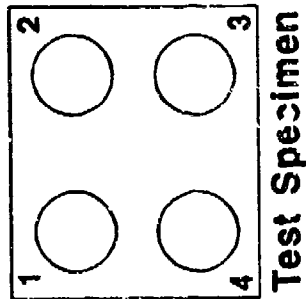
• • Denotes no crazing with coating softening

Values in table are minimum stress to craze in 30 minute test

TABLE 6



# SALT IMPINGEMENT



Measure of Abrasion  
Resistance

ASTM F-1128 used as  
Guideline

Number of Salt Blasts Per Cycle

Location				
1	2	3	4	
0	4	8	16	

Salt Blasting with  
Controlled Pressure  
Duration, Interval  
and Number of Blasts

Cumulative Number of Salt Blasts

QUV Weeks	1	2	3	4
1	0	4	8	16
2	0	8	16	32
3	0	12	24	48
4	0	16	32	64

FIGURE 6

# SALT IMPINGEMENT RESULTS QUV WEATHERED, COATED POLYCARBONATE

At location four (64 total salt blasts and 4 weeks of QUV)

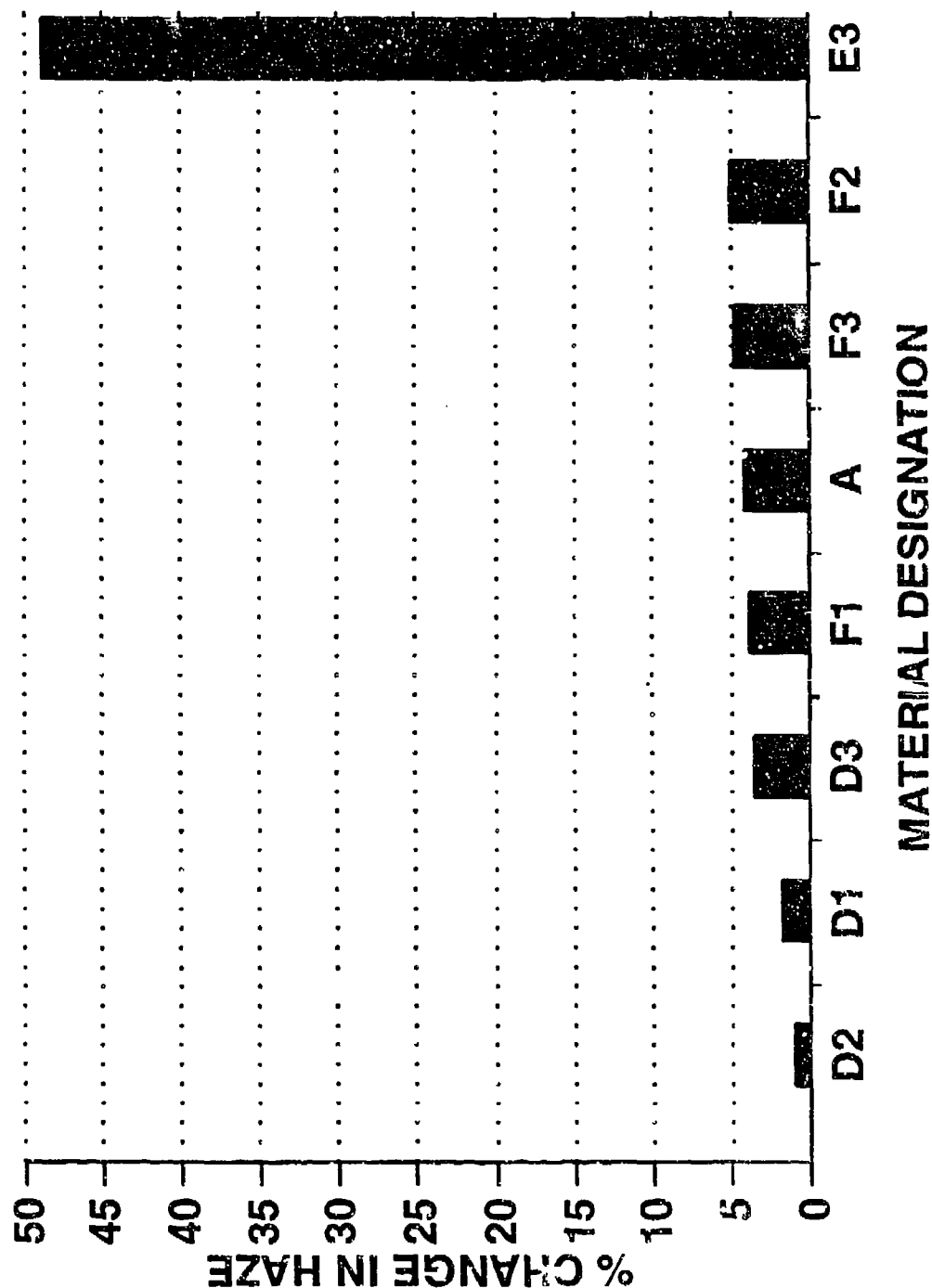


FIGURE 7

# SALT IMPINGEMENT RESULTS

## QUV WEATHERED, MET. COATED PC AND AC

At location four (64 total salt blasts and 4 weeks of QUV)

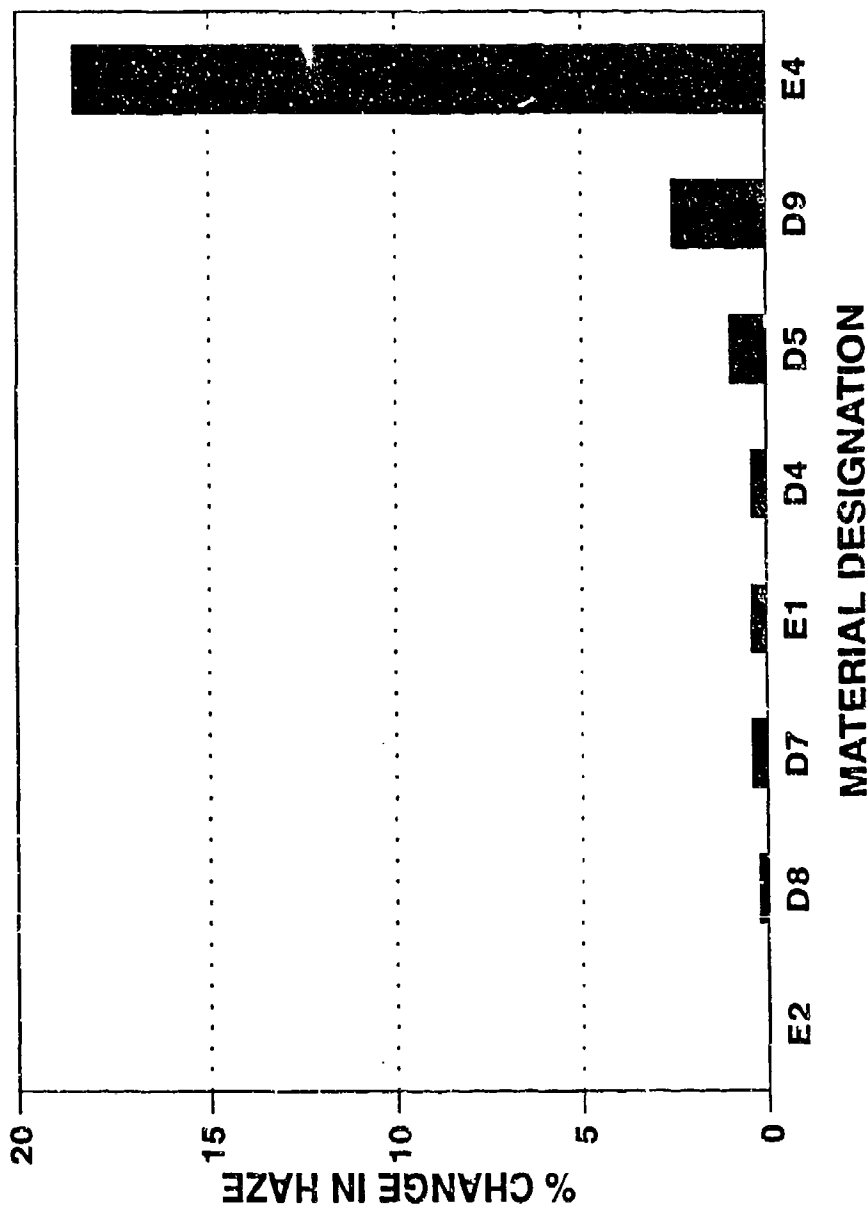


FIGURE 8

# TYPE II SALT IMPINGEMENT OF COMMON BASELINE AIRCRAFT WINDSHIELD MATERIALS

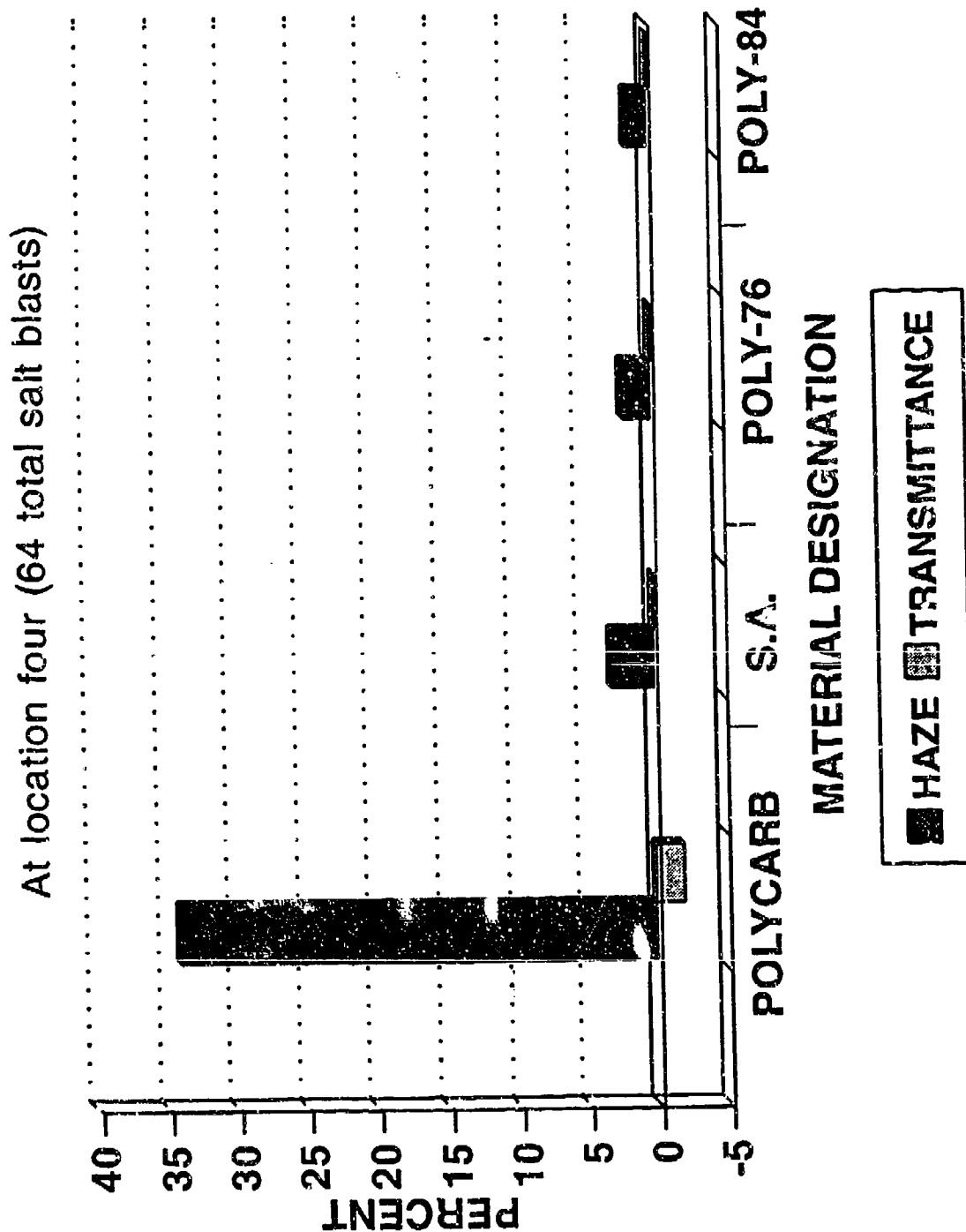


FIGURE 9

**METAL-COATED PC AND AC  
SHOW GOOD RESISTANCE TO  
OSCILLATING SAND ABRASION**

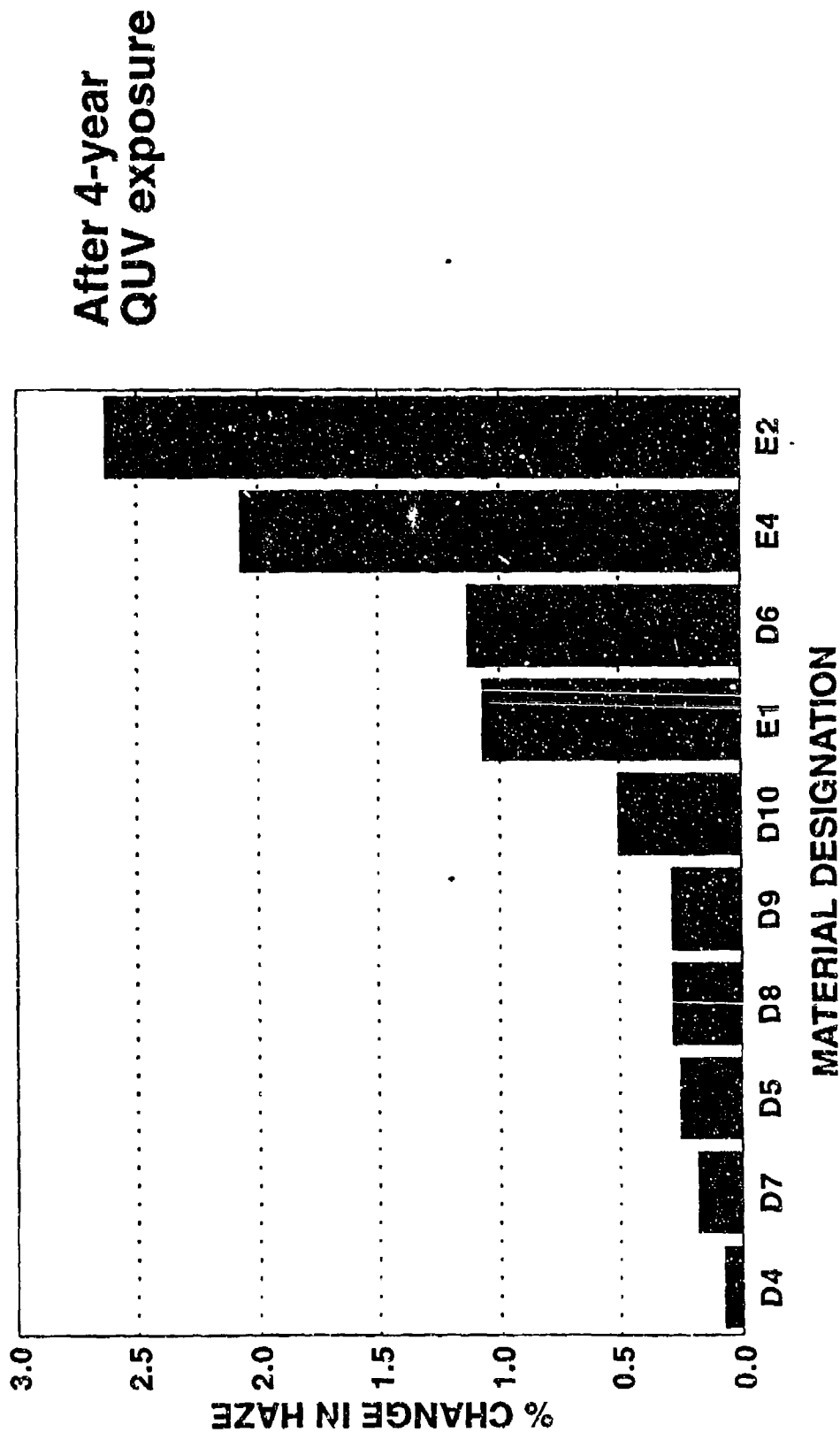


FIGURE 10

# **ANY COATINGS ON POLYCARBONATE SHOW GOOD RESISTANCE TO OSCILLATING SAND ABRASION**

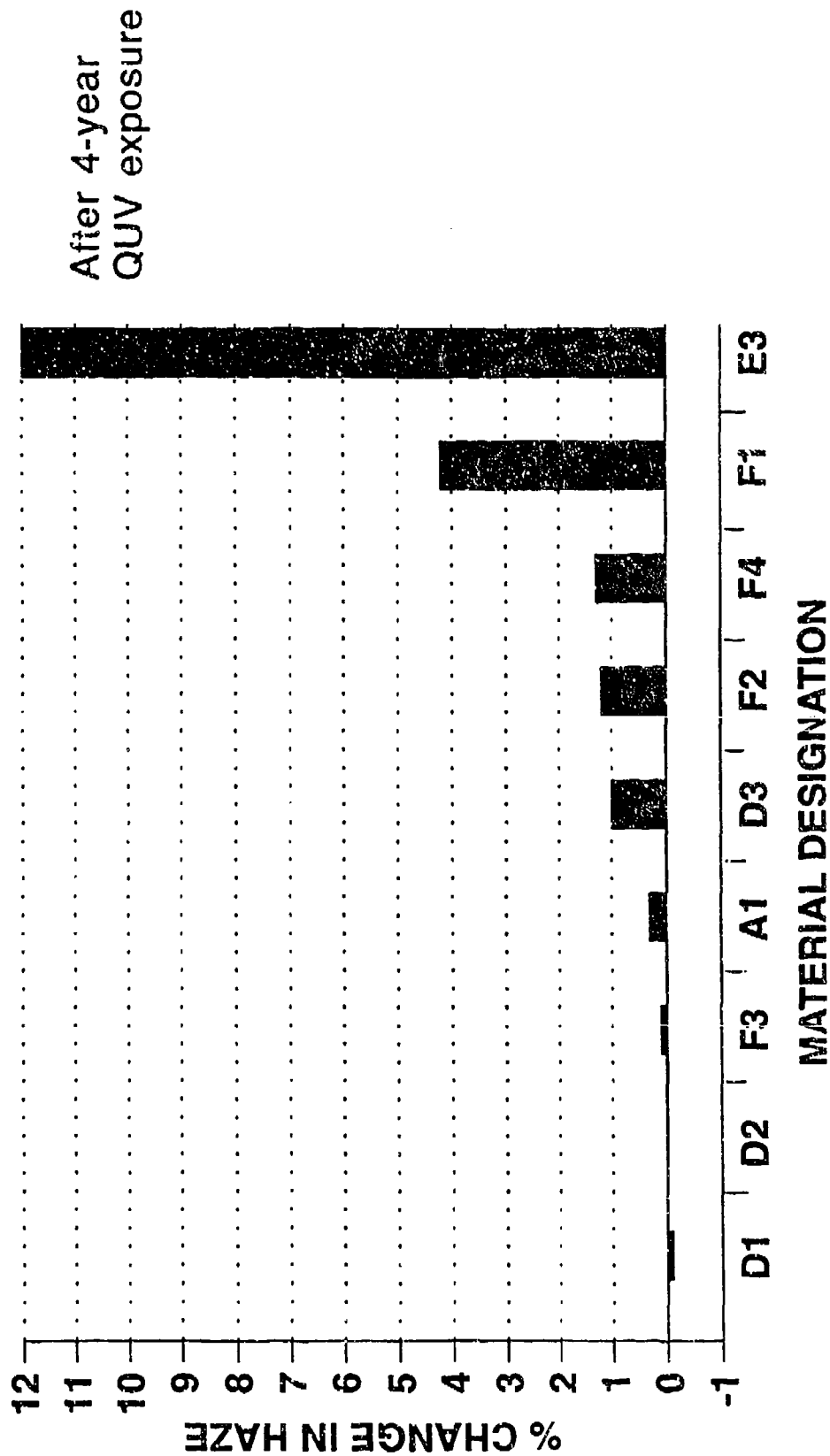


FIGURE 11

# EXAMPLE OF GREATEST DIFFERENCE BETWEEN QUV AND BASELINE UV/VIS/NIR TRANSMISSION FOR COATED PC

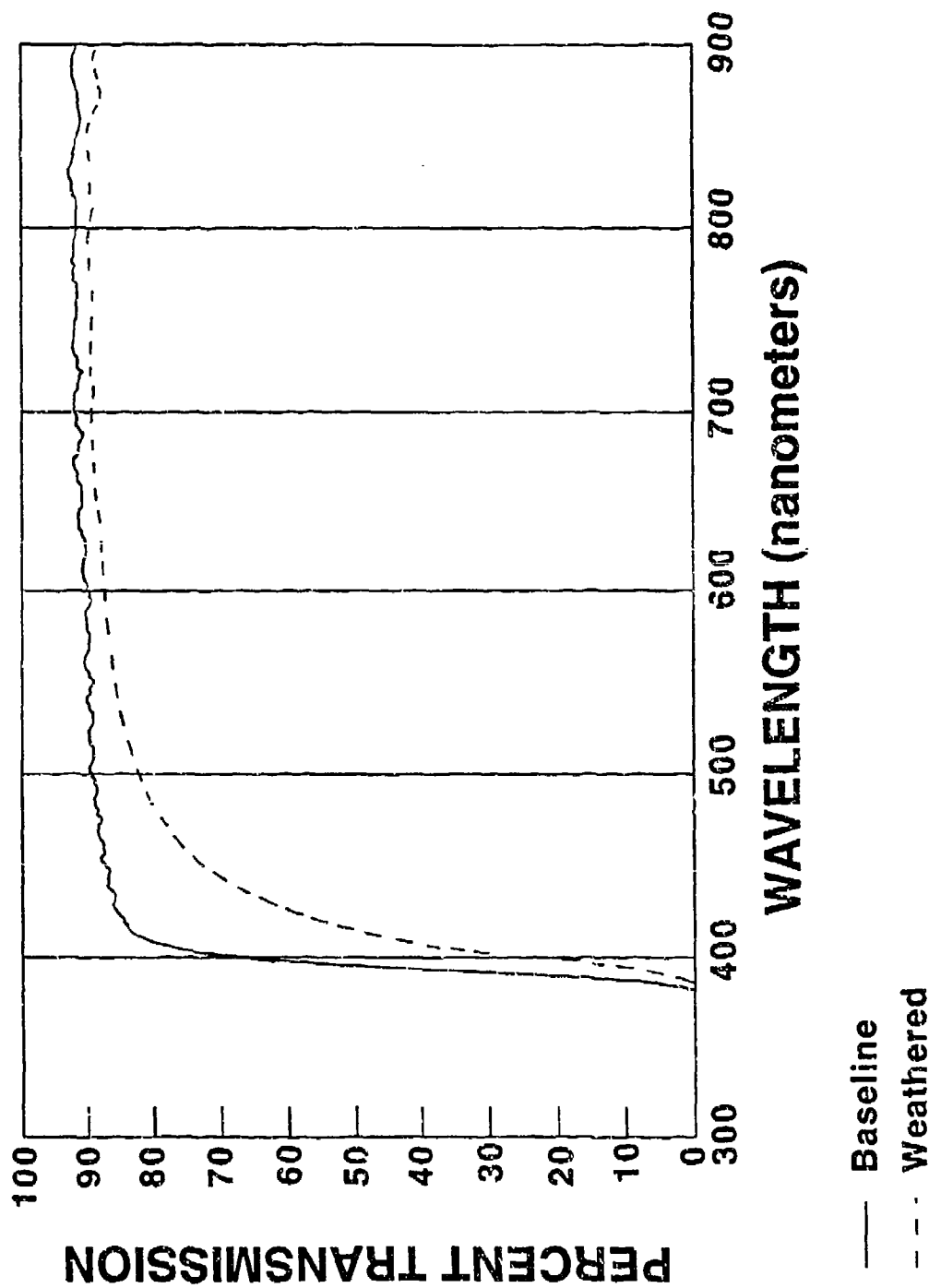
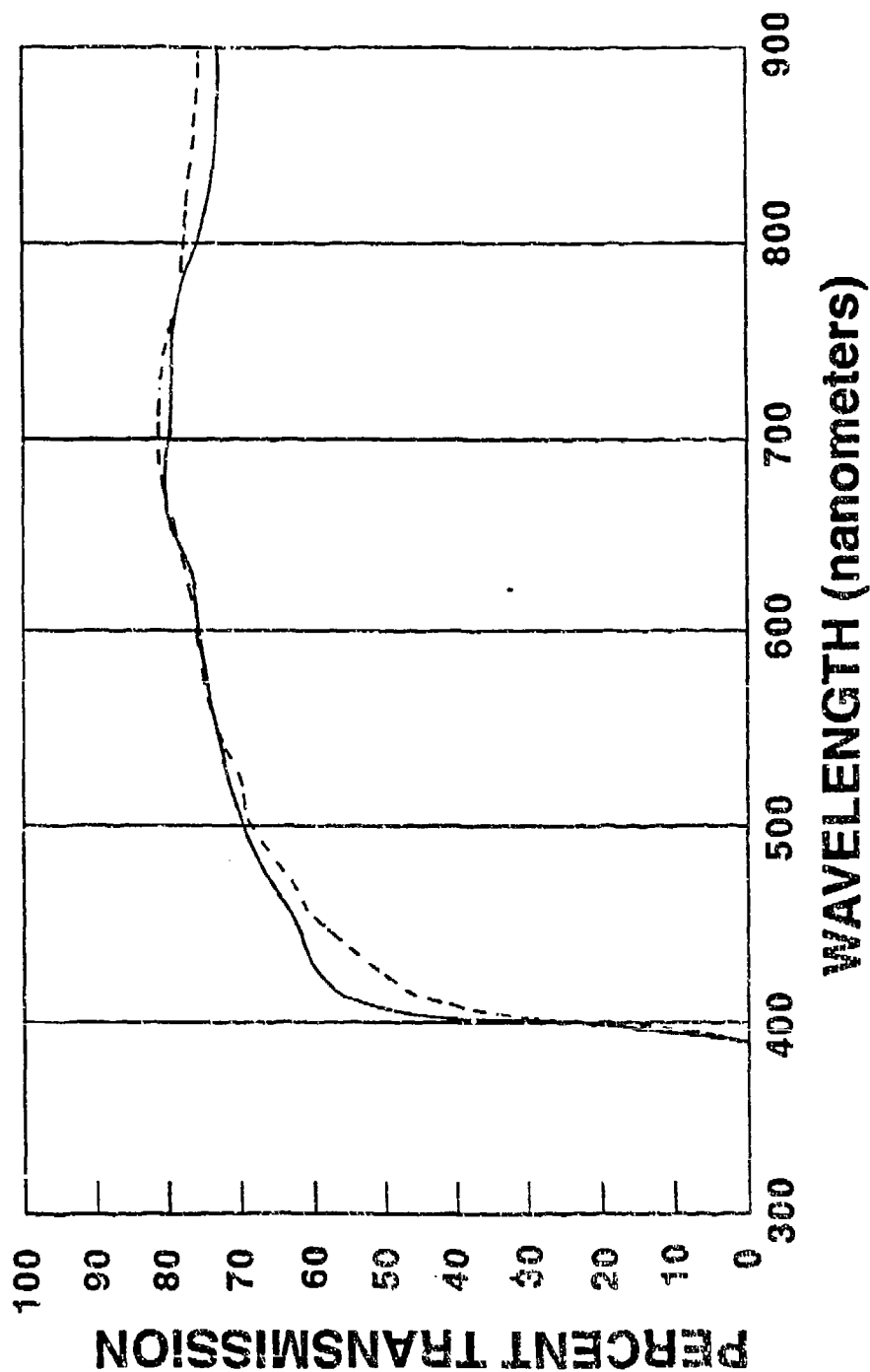


FIGURE 12

# TYPICAL DIFFERENCE BETWEEN QUV & BASELINE UV/VIS/NIR TRANSMISSION FOR METAL-COATED SAMPLES



— Baseline  
--- Weathered

FIGURE 13



The MITS team selected five coating designs on bare polycarbonate were D2, D3, A1, D1, and F3 as the top candidates based on a summary of all these tests. These candidates represent three manufactures and coating types, slight differences in thickness are the differences between D1, D2, and D3. On a metalized polycarbonate top two designs were D5 and D8. It should be noted that D2, D1, D5, and D8 are all variations (thicknesses) of the same material. These coatings not only passed each criteria, they all demonstrated outstanding performance under quite severe test conditions.

Following these coupon level results, scaled up testing was conducted on types A1, D2, and F3. The coatings were applied to a complex curvature (dome shaped) samples approximately 24 inches square. After accelerated weathering, rain erosion samples were prepared and tested under the same conditions described earlier. All of these coatings again achieved better performance than the MITS minimum requirements.

In MITS Phase III the two remaining best coatings candidates are being applied to F-16 canopies for full scale evaluation. The MITS Program has combined with the F-16 540 knot canopy program to evaluate a third coating full scale. Two coatings will be on bare polycarbonate, while one selected will be over a metalized polycarbonate. Three full-scale ground test are planned: Optical evaluation by Armstrong Laboratory personnel (AL/CFHO); Structural integrity/durability testing by Wright Laboratory personnel (WL/FIVR); and Birdstrike testing at AEDC in Tullahoma, Tennessee. The Air Force intends to conduct flight evaluations of these coatings, once they have passed full scale evaluation, at two different bases.

Throughout these scale-up and full scale evaluations we will revisit our initial laboratory testing baseline and correlate the results to update the lab test methodology as appropriate.

In addition, the Air Force is evaluating additional coatings at the time of this papers writing. The results of the full scale testing and the additional testing will be presented in a separate report at a later date.

CAUTION: An assumption that a coating will provide comparable performance on another substrate -or even the same substrate- is risky in this rapidly changing technology area. It is strongly suggested that a coating being considered for a specific point design be screened using this MITS criteria.

**SULLINER (UE-100) ANTI-CRAZING COATING FOR ACRYLICS**

**J. J. Demeester  
Sully Produits Speciaux**

## **SULLINER (UE-100) ANTI-CRAZING COATING FOR ACRYLICS**

Jean J. Deneester  
Engineering Manager  
SULLY Produits Spéciaux

Acrylic transparencies are currently affected by crises of premature crazing, a phenomenon commonly ascribed to the flight environment becoming temporarily more aggressive.

A durable protection of acrylics against crazing is provided by SULLINER (UE-100), a chemically resistant, "self-healing", soft coating. Gone into service in March 1987, coated cabin windows still do not show any trace of crazing in spite of the considerable number of flight hours they have logged. A service life several times that of similar uncoated parts is already proven.

## 1. SCOPE

Acrylic materials are largely employed to produce aircraft transparencies as they show good mechanical and thermal properties, can be easily formed and machined and have a low density. Unfortunately, like many other plastic materials, acrylics may be affected by crazing, a pattern of tiny superficial fissures caused by the combined effects of tensile stresses and chemical attacks. The moderate resistance of acrylics to abrasion contributes also to initiate crazing, as surface flaws are produced that open the way for water and chemicals to penetrate the material. Fissures tend then to grow from the flaws and connect to each others to form a craze pattern. This awkward phenomenon grows with service life (flight hours and cycles) and progressively impairs visibility. Eventually, operators are forced to remove the windows for periodical refurbishing or replacement. Whenever volcanic emissions and/or other atmospheric phenomena make the flight environment temporarily more aggressive, crises of premature crazing may occur that tremendously increase the maintenance costs of acrylic transparencies.

Coating acrylics with another material, more resistant to chemicals and abrasion, is undoubtedly the best method to avoid crazing. This is why Sully/Saint-Gobain have developed SULLINER. Formerly referenced UE-100, SULLINER is a soft coating of low cross-linked urethane that is featured by astonishing "self-healing" properties and appears remarkably resistant to abrasion, chemicals and weathering. Extensive laboratory testing and flight evaluations have shown that SULLINER fully protects acrylics from crazing with no degradation of the basic material properties. The latter feature allows any existing parts to be coated with no requalification.

The SULLINER coating process permits "pre-coated" or "post-coated" transparencies. This provides an appreciable flexibility in SULLINER applications and all cockpit and passenger windows, either new or properly repaired, can be coated.

## 2. PROPERTIES OF COATED ACRYLIC

Hard coatings for acrylics intrinsically have limited capabilities of elongation and may develop tensile cracks. Even, in some cases, catastrophic failures have been observed, due to crack propagations from the coating to the acrylic. It is therefore essential to make sure that the original properties of the coated material are preserved.

Although no deterioration of acrylic was feared from SULLINER, due to its favourable softness and chemical composition, tests have been conducted to validate this assumption. From the results in table 1, it appears that applying SULLINER on stretched acrylic does not modify significantly the material properties and all MIL-P-25690 requirements are met or exceeded by the coated material.

	MIL-P-25690 requirement	ACRYLEX *	
		BARE	COATED
Thermal relaxation 24 hours - 200°F (93°C)	< 0.5%	0.18%	0.1%
Craze resistance / 3000 psi			
30 min isopropyl alcohol	no crazing	no crazing	no crazing
30 min toluene/isobutyl acetate	no crazing	no crazing	no crazing
20 min sulfuric acid (75%)	no crazing	no crazing	no crazing
Crack propagation resistance			
average (lb/in <sup>3/2</sup> )	>2550	2748	2550
minimum -	>2400	2420	2400
Tensile strength - 70°F(21°C)	>9000 psi	12730 psi	12500 psi
In-plane shear strength - 70°F	>3000 psi	3625 psi	3625 psi

TABLE 1

\* ACRYLEX is the stretched acrylic material produced by Sully. ACRYLEX has been approved to the MIL-P-25690 specification by the US Naval Research Laboratory in 1988.

### 3. ADHESION

SULLINER shows an excellent adhesion on stretched acrylic as 100% adhesion at crosshatch test has been found.

### 4. ABRASION RESISTANCE

Because of its low cross-linked molecular structure, SULLINER shows an uncommon ability to spontaneously recover from scratches after a short period of time. This "self-healing" capability provides SULLINER with an excellent abrasion resistance: abraded according to ASTM D 1044, Taber test method, using a C3 10F wheel loaded at 500 g (1.1 lb) for 100 cycles, the coated samples feature 12 times less haze than the uncoated samples.

	unabraded	abraded	delta
uncoated ACRYLEX *			
light transmission	93.2%	89.2%	-4.0%
haze	0.5%	29.1%	+28.6%
SULLINER coated ACRYLEX *			
light transmission	92.7%	92.0%	-0.7%
haze	0.7%	2.3%	+1.6%

\* Stretched from Röhm 249 cast acrylic

TABLE 2

### 5. ENVIRONMENT EFFECTS

The possible effects on SULLINER of humidity, UV radiations, temperature changes, salt spray, fungi and usual contaminants have been carefully investigated.

#### 5.1 Humidity

SULLINER coated samples have been maintained for two weeks at 54°C (130°F) and 100% relative humidity.

No deterioration, no loss of adhesion, no reduction of abrasion or craze resistance have resulted from this exposure.

## 5.2 UV radiations

SULLINER coated samples have been exposed for 1000 hours at 40°C (104°F) and 100% relative humidity with UV radiations 50% of the time. No deterioration, no loss of adhesion, no reduction of abrasion or craze resistance have resulted from this exposure.

## 5.3 Temperature cycles

SULLINER coated samples have been submitted to temperature cycles. Each cycle consisted of 4 hours at 80°C (176°F), followed by 4 hours at -50°C (-58°F).

No deterioration, no loss of adhesion and no reduction of abrasion or craze resistance have been found after 100 cycles.

## 5.4 Salt spray

SULLINER coated samples have been tested according to MIL-STD-810D method 509-2, procedure J: temperature 35°C (95°F), duration 48 hours, NaCl concentration 5%.

No deterioration has resulted from this exposure.

## 5.5 Fungi

SULLINER coated samples have been tested according to MIL-STD-810D method 508-5-1, category 1: duration 28 days, temperature 30°C (86°F), relative humidity 95%, sowing by *aspergillus flavus*, *aspergillus niger*, *aspergillus versicolor*, *penicillium funiculosum* and *chaetomium globosum*.

No fungus development and no material deterioration have been observed.

## 5.6 Fluid contamination

Most of the common contaminants have no effect on SULLINER. Some more aggressive chemicals may produce slight superficial degradations, but the astonishing "self-healing" capability of SULLINER usually allows the material to spontaneously recover its original aspect after a limited period of time.

Actually, acrylic samples coated with SULLINER have been exposed to the following contaminants:

- mild soap and water
- 50% water + 50% alcohol
- kerosene
- carbon tetrachloride
- ethylen glycol
- oil F18, F34, F46, F54
- grease 0353, 0359, 0362, S720
- hydraulic liquid NATO 0150, 0156, C160

Each of these contaminants has been applied for 48 hours at 59°C (138°F). No permanent deterioration has resulted.

## 6. FLIGHT EVALUATIONS

Outer panes of passenger windows are ideal supports to evaluate an anti-crazing coating, since they usually work at a relatively high stress level and have therefore a greater tendency to craze than other acrylic windows. This is why the flight evaluations of SULLINER have been mainly concentrated on cabin windows of transport aircraft. Some parts have been flown incessantly since March 1987 and have now logged considerable numbers of flight hours and cycles.

- The coated passenger windows of a Lufthansa Boeing 747 did not show any trace of crazing after 23,800 flight hours and approximately 4,000 cycles.
- The coated passenger windows of an Airbus A300 of Air Inter (French domestic Airlines) did not show any trace of crazing after 9,555 flight hours and 10,153 cycles.

## 7. CONCLUSION

As established by laboratory and flight tests, SULLINER is a soft coating that totally prevents the acrylic materials from crazing since it fully protects them against all detrimental effects from the flight environment. A tremendous improvement of abrasion resistance is also provided with no modification of the basic material properties. At last, SULLINER can be applied over all cockpit and cabin windows, either new or properly repaired.



## P-STATIC CONTROL

E. Joy  
Flight Dynamics Directorate  
Wright Laboratory

J. Anderson  
Bell Helicopter Textron

N. Wild  
Jaycor

J. Short  
Texstar

## P-STATIC CONTROL

Lt. Erik Joy  
WL/FIVR  
Wright-Patterson AFB, OH

Joe Anderson  
Bell Helicopter Textron, Inc.  
Fort Worth, TX

Dr. Norb Wild  
Jaycor, Inc.  
San Diego, CA

John Short  
Texstar, Inc.  
Grand Prairie, TX

### Abstract

Electrostatic charge buildup occurs on aircraft transparencies during various operational and atmospheric conditions. One of the causes of the charge buildup comes from particles such as ice impinging on the transparency and leaving a net charge. This is called precipitation static (p-static) charging. This charging causes several problems for aircraft and personnel: electrostatic discharges (ESD), coating burn as a result of ESD, pilot and ground crew shock, dust and sand attraction and adhesion, and electromagnetic interference on radios and avionics. This project attempts to solve these problems by understanding the source, effects, and mitigation strategies of p-static charging on airborne transparencies by use of computer modeling and laboratory simulation to analyze and evaluate the static-charging susceptibility of different transparency configurations. The validated computer model will provide the necessary guidance in the design of the electrical properties of coating systems to find the best system to prevent or reduce the adverse effects of p-static charging on aircraft transparencies.

## 1. INTRODUCTION

### 1.1 Problem

Electrostatic charge buildup occurs on aircraft transparencies during various operational and atmospheric conditions. One of the causes of the charge buildup comes from particles such as ice or sand impinging on the transparency and leaving a net charge (usually negative) behind. This is called triboelectric charging. Even the friction of airflow over air vehicle surfaces leads to significant charging, leaving the whole aircraft at a high potential relative to earth. When excess charge arcs across the transparency to reach the equipotential airframe, the radio-frequency noise is called precipitation static (p-static).

This charging causes several problems for aircraft and personnel: visible electrostatic discharges (ESD), transparency metallic thin-film coating burns as a result of ESD, air crew and ground crew shock, dust and sand attraction and adhesion (a serious problem for helicopters), and electromagnetic interference on radios and avionics.

### 1.2 Approach

The problems associated with p-static charging have become increasingly troublesome with the growing airspeeds of modern aircraft and helicopters and the increased use of large-frontal-surface-area plastic (acrylic, polycarbonate) transparencies and canopies.

The goal of this study is to acquire an increased understanding of the processes associated with buildup of excess charge on plastic transparencies and the subsequent discharge to the

airframe "ground." As part of this effort, a computer model was developed to simulate the electrostatic charge buildup. This model can accept three-dimensional transparency geometries and includes the effects of air conductivity, pressure, and charging-particle angle of incidence. By using an estimated worst-case triboelectric charging environment for jet aircraft, the minimum conductivity required on the outer transparency surface to suppress ESD voltages can then be calculated.

New technology is now available to attack the two persistent problems of plastic transparencies: vulnerability to surface wear and triboelectric charging.

A solution to the abrasive wear problem is an exterior coating that is more durable than the plastic. Such coatings have been under development since the early 1980s.

It was realized that if these new antiabrasive coatings could be doped with a conductive component which did not impair any of their other properties, the p-static charging problem might be solved at the same time as the abrasion/scratch problem. Several companies which fabricate aerospace transparencies have developed such doped coatings which appear to have conductivities in the range needed to suppress ESD and its attendant effects.

### 1.3 Background

Triboelectric charging is a phenomenon whereby two electrically neutral material objects are placed in mechanical contact and then separated, each gaining equal and opposite charge upon separation. Materials are ranked qualitatively in a triboelectric series to denote their tendency to give up or attract electrons. In general, plastics tend to collect excess electrons. During flight conditions, this buildup of excess charge relative to the airframe ground can eventually lead to high current discharges to nearby ground points and result in damage to thin-film metallic coatings on the transparency. These discharges, together with the steady-state bleed-off of charge from the airframe, also lead to the electrical static noise referred to earlier as p-static.

During the last 40 years, a number of studies have been undertaken to understand and quantify the nature of the p-static noise problem (Refs. 1-6). This body of work contains numerous references to the magnitude of the charging term and its dependence on atmospheric conditions and airspeed. This information has been reviewed and utilized to provide estimates of worst-case charging environments. The highest reported charging term (Ref. 7) was  $440 \mu\text{A}/\text{m}^2$ . To maintain an adequate safety margin, we assume the worst case charging environment to be on the order of  $1,000 \mu\text{A}/\text{m}^2$ . Previous measurements of discharge-current waveforms have enabled calculations of the average energy released during a discharge and its effect on thin-film coatings. These will be presented in Section 2. Several of these past efforts have been associated with laboratory simulations of the charging environment and provided insight as to the types of discharges observed (flashover vs. punch through). This work was also reviewed and a small-scale charging simulator was constructed to measure discharging rates on coupon-size test samples.

Previous researchers realized that an electrically conductive outer layer would be capable of bleeding off the excess charge built up during flight and keeping induced voltages below discharge levels. However, conductive coatings such as gold, stannous oxide, or indium tin oxide (ITO) are not durable enough to be used as exterior coating materials on plastic substrates. The recent development of electrically conductive polymer materials which can withstand the rigors of high speed flight have the potential for solving the p-static charging problem by providing a low-resistance path to airframe ground for accumulated charge buildup.

## 2. DISCUSSION

### 2.1 Joint Services Organization

This study on the control of p-static charging of air vehicle transparencies is being supported by the U. S. Army and Air Force. The Army is especially interested in mitigating the static electricity effects on helicopter transparencies, while Air Force jet aircraft are experiencing higher voltage effects that can be hazardous to personnel and degrading to canopies. The cognizant Army office is the Army Research Laboratory in Watertown, MA, with Pete Dehmer being the point of contact (POC). For the Air Force, the Wright Laboratory at Wright-Patterson AFB, OH, is handling the analytical aspects, with Lt. Erik Joy as POC. For the Air Force hardware/test side of the house, Capt. Stephen Hargis and Stephen Wortman at McClellan AFB, CA, have been coordinating in these areas. All of these organizations have provided valuable inputs and support for this study.

### 2.2 Analytical Modeling of Proposed Canopy Configurations

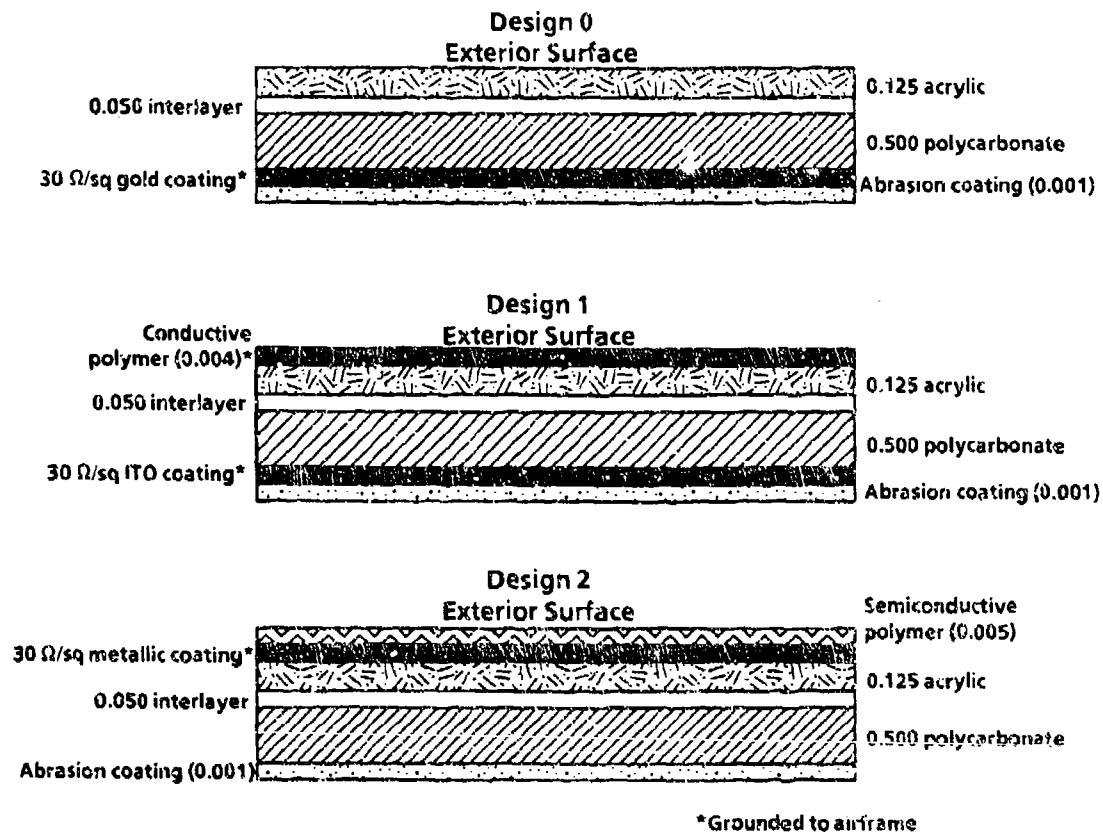
As mentioned earlier, excessive charge buildup can be controlled and maintained at nondischarging levels by giving the transparency an outer-surface coating with enough electrical conductivity to carry the collected charge to the airframe ground without requiring a large potential gradient. Developers of canopy substrate and coating materials are currently pursuing this approach in two ways. The first approach involves depositing an antiabrasive, semiconductive coating ( $10^6$ – $10^8$  ohms per square [ $\Omega/\text{sq}$ ]) over the outer surface of the dielectric transparency and grounding this coating to the aircraft through the transparency frame. Charge deposited on the transparency during flight then has a conductive path across the canopy surface to the aircraft structure thus avoiding the development of large differential potentials. The second approach is to utilize a thin metallic coating ( $30 \Omega/\text{sq}$  Au or ITO) on the outer transparency surface and then protect this film with a slightly conductive antiabrasion polymer coating. With this configuration, deposited charge flows normal to the surface to reach the conductive metallic layer and is regulated by the bulk resistivity of the conductive polymer. The metallic film is grounded to the fuselage via the canopy frame. The bulk resistivity of the conductive polymers used in both configurations must be low enough to prevent dielectric breakdown through the film (punch-through discharge), as well as surface flashover.

These two configurations, together with designs currently being flown, were analyzed assuming a steady-state charge injection rate. Figure 1 shows a cross-sectional view of a current F-16 transparency design together with the two proposed configurations. These will be referred to herein as Design 0, Design 1, and Design 2, respectively. In these analyses, a worst-case incident charging current density  $J_i$  of  $1 \text{ mA}/\text{m}^2$  was assumed. A circular slab geometry as illustrated in Figure 2 was used to calculate the electric field and potential profile as a function of radial distance to the grounded edge which simulates the canopy frame.

In Design 0, a metallic film is located on the inboard side of the transparency and grounded to the aircraft frame. The dielectric material has fairly high resistivity ( $> 10^{13} \Omega\cdot\text{m}$ ) and will quickly charge up to high potentials when exposed to an incident current source. As a capacitor, the voltage can be computed as

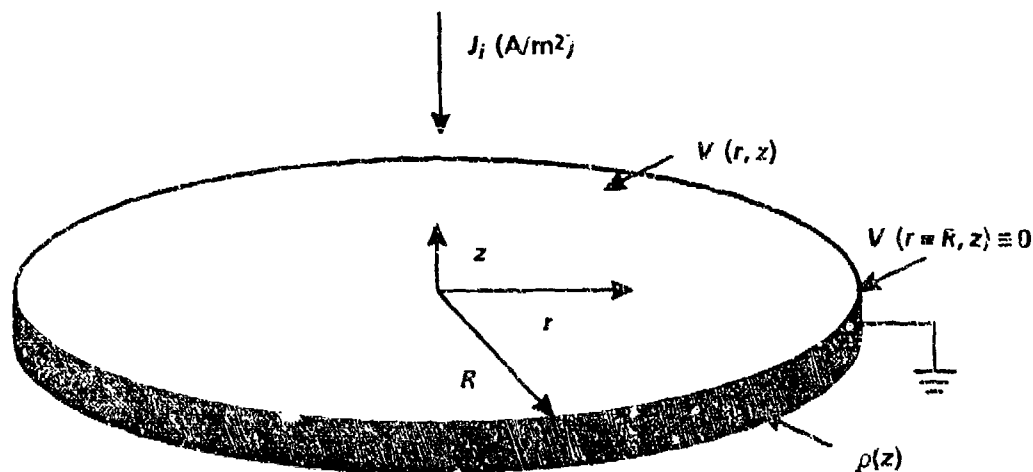
$$V = \frac{Q}{C} = \int \int \frac{J_i \cdot dA dt}{C} \quad (1)$$

where the integrals are over the area of the transparency and the time duration of the charging event. The capacitance  $C$  can be estimated as



31677

Fig. 1. Current F-16 canopy design (Design 0) and two proposed canopy configurations using conductive overcoats.



31678

Fig. 2. Cylindrical slab geometry used to analyze charging of different transparency material configurations.

$$C = \frac{\epsilon_r \epsilon_0 A}{d} \quad (2)$$

where  $d$  is the thickness of the dielectric. For a 1-m<sup>2</sup> area,  $d = 0.5$  inch, and a moderate charging term of 10<sup>-4</sup> A/m<sup>2</sup>, a charging rate of 70 kV/s is readily achievable. Unless a low impedance outlet for the charge buildup is provided, dielectric discharges (surface flashover or bulk punch through) will occur when the breakdown voltage threshold is reached. Typical breakdown threshold field values can range from 4×10<sup>5</sup> V/m (surface flashover) to 1×10<sup>6</sup> V/m (punch through).

It has been observed that, with regard to Design 0, gold films are more prone to show signs of discharge "tracking" than ITO coatings. The tracking appears to be oriented preferentially along the circumference of the canopy (perpendicular to the flight axis) but shows signs of random changes in direction, similar to a lightning bolt. The tracks are typically 1-2 mm in width, although gaps of up to 1 cm have been observed on severely damaged canopies. Using the thermophysical properties of gold and ITO, and measured discharge-current parameters ( $I = 1$  A,  $\tau = 0.33 \mu\text{s}$ ), the temperature rise produced by Joule heating in a thin film during a transient discharge can be calculated as

$$\Delta T = \frac{I^2 \rho_s \tau}{C \rho d x} = \frac{10^5}{C \rho d} \quad (3)$$

where  $d$  is the film thickness (Å),  $x$  is the track width,  $\rho$  is the mass density of the film material, and  $C$  is the specific heat (J/g·°C). The 10<sup>5</sup> multiplier assumes a channel width of 0.1 cm and that no significant thermal conduction takes place during the time scale of the discharge pulse (<1 μs). Table 1 summarizes these results, which show a much larger temperature excursion for gold than for ITO. This is due predominantly to the thinner coating of gold versus ITO needed to achieve the desired surface resistivity. A thicker layer of gold would be more robust, but would also suffer from a decrease in optical transmittance.

Table 1. Summary of gold and ITO thin film heating calculations assuming 1 A discharge current in 1-mm track for 0.33 μs duration.

Material Properties	Gold	ITO
30 Ω/sq thickness (Å)	10 <sup>4</sup>	300
Mass density (g/cm <sup>3</sup> )	19.3	7.1
Specific heat (J/g·°C)	0.333	0.067
Melting point (°C)	1,064	1,900
Temperature rise (°C)	15,700	540

\*Based on bulk resistivity of the materials. In actual practice, the films have to be 5 to 10 times thicker because the mass density is less than a perfect solid. However, the areal density ( $\rho d$ ) will be about the same for the actual thicknesses.

For Design 1, the incident charging current will flow radially to the edge creating a radial electric field given by

$$E_r = \rho_s \times J_s \quad (4)$$

where  $E_r$  is in V/m,  $\rho_s$  is the surface resistivity in  $\Omega/\text{sq}$ , and  $J_s$  is a surface current density in A/m. The field will increase as one nears the edge of the circular slab, since the current is increasing linearly with radius as

$$J_s(r) = J_i \left[ \frac{\pi r^2}{2\pi r} \right] = J_i \left( \frac{r}{2} \right) \quad (5)$$

Thus, the maximum electric field for Design 1 will be at the edge ( $r=R$ ) and is given by

$$E_{\max} = \rho_s \times J_i \times \left( \frac{R}{2} \right) \quad (6)$$

For a 0.2-m diameter slab, and  $\rho_s = 10^8 \Omega/\text{sq}$ , a field strength of  $5 \times 10^3$  V/m would be present at the edge of the transparency. The threshold for flashover discharges in air is about  $4 \times 10^5$  V/m, so that a safety margin of almost two orders of magnitude is available with Design 1. The size of the slab (0.2 m diameter) was chosen to correspond to the size of test articles which are being examined under this effort. From Equation (6), one can see that the maximum field will increase in a linear fashion as the radius increases. The maximum voltage on the slab occurs at the center, and can be obtained by integrating  $E_r$  along the radius. For the above conditions,  $V_{\max} = 250$  V.

For Design 2, a normal electric field is established which drives the incident current density through the semiconductive overcoat to the metallic film beneath and then to airframe ground. Using Ohm's law, the field strength is simply

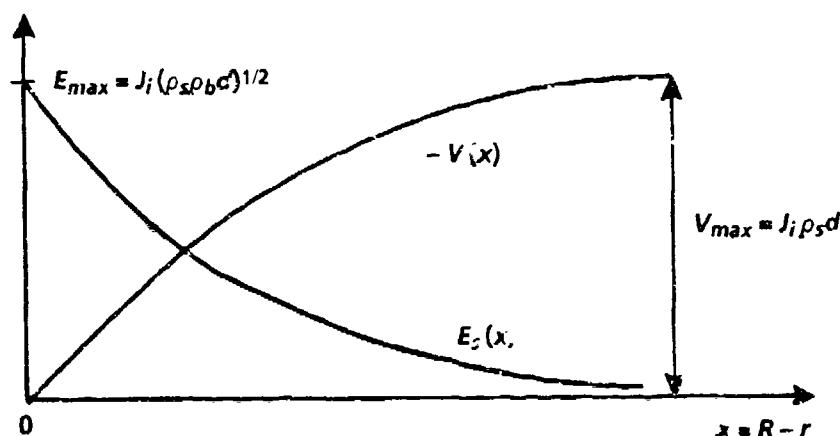
$$E_n = \rho_b J_i \quad (7)$$

where  $\rho_b$  is the bulk resistivity in  $\Omega \cdot \text{m}$  of the semiconductive overcoat,  $E_n$  is in V/m, and  $J_i$  is in A/m<sup>2</sup>. For  $\rho_b = 4 \times 10^{10} \Omega \cdot \text{m}$ , and assuming the worst case incident charging current density of  $10^{-3}$  A/m<sup>2</sup>, the normal electric field strength will be  $4 \times 10^7$  V/m. For this particular coating material, at a 5-mil thickness, the bulk dielectric breakdown field strength is on the order of  $1 \times 10^8$  V/m, i.e., voltages greater than 10 kV are needed to induce a breakdown. The calculation predicts a voltage level of about 5 kV, so a factor-of-two safety margin is present with Design 2 for the assumed conditions.

An additional consideration for Design 2 is the electric field strength in the region near the edge of the transparency. Due to the potential gradient between the grounded edge and the top surface of the semiconductive overcoat near the edge, an electric field will exist parallel to the overcoat surface which could initiate surface flashover discharges. From a steady-state analysis ( $\nabla \cdot \mathbf{J} = 0$ ) of this edge region, an expression for the tangential electric field can be derived as

$$E_t = J_i (\rho_s \rho_b d)^{1/2} \times \exp(-Kx) \quad (8)$$

where  $d$  is the coating thickness,  $x = R - r$  is the distance from the grounded edge frame and  $K$  is defined as  $K^2 = \rho_s / (\rho_b d)$ . Figure 3 plots the calculated electric field and potential profiles near the transparency edge. Note that the surface and bulk resistivities are treated independently. That is, if the surface resistivity  $\rho_s$  was just due to the bulk electrical conduction parallel to the surface of the overcoat throughout its thickness, then  $\rho_s = \rho_b / d$ . However, the surface resistivity is often influenced strongly by surface conditions, e.g., contaminants, moisture, or



31679

Fig. 3. Electric field and potential variation near grounded air frame for Design 2.

outgassed atoms. The result is that the surface resistivity is usually smaller than one would calculate from the bulk resistivity, at least for thin dielectrics.

The importance of the above expression for  $E_t$  with respect to Design 2 is that dielectric surface breakdown fields are much smaller than the fields required for breakdown through the bulk of a dielectric, especially under nonvacuum conditions. Assuming  $\rho_s = \rho_b/d$  (worst case), a maximum tangential field at  $x=0$  of  $E_t = J_i \rho_b = (10^{-3} \text{ A/m}^2)(4 \times 10^{10} \text{ } \Omega \cdot \text{m}) = 4 \times 10^7 \text{ V/m}$  is calculated. This is two orders of magnitude greater than typical surface breakdown field thresholds observed for dielectrics in air. It is envisioned that the susceptibility of Design 2 to surface flashover near the edge will be examined in more detail through the concurrent testing effort under the present program.

### 2.3 Computer Modeling of Proposed Canopy Configurations

Using a previously developed electrostatic computer code called EITACC (Equation Independent Time-Averaged Conformal Code), the two-dimensional cylindrical geometry was modeled in finer detail to compare with the above analytical results. The code modeling was also a test of the feasibility of performing a full three-dimensional computer analysis using a modified version of the EITACC code (BODY) developed by Jaycor, Inc. Both codes assume a steady state ( $\partial \rho / \partial t = \nabla \cdot \mathbf{J} = 0$ ) and Gauss's law ( $\nabla \cdot \mathbf{E} = \rho / \epsilon$ ), and that Ohm's law holds ( $\mathbf{E} = \rho_b \mathbf{J}$ ). The resistivity,  $\rho_b$ , is related to the charge density  $\rho$ , by the mobility,  $\mu$ , as

$$\rho_b = \frac{1}{\mu \epsilon} \quad (9)$$

Substituting for  $\mathbf{J}$  and  $\rho$  in the steady state relation yields the second-order equation

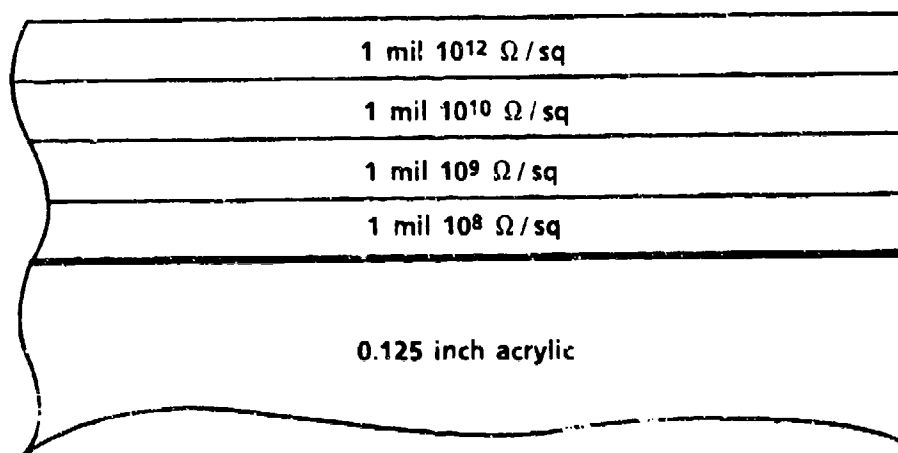
$$\nabla \cdot [\mathbf{E} (\nabla \cdot \mathbf{E})] = 0 \quad (10)$$

which assumes a constant mobility and permittivity. The codes solve this relation numerically to determine the vector electric field  $\mathbf{E}(r, z)$ . The potential profiles are calculated by integrating the electric field as



$$V(r, z) = - \int \mathbf{E} \cdot d\ell \quad (11)$$

with  $V=0$  at the grounded edges. As in the analytical approach, the two-dimensional problem was set up as a planar disc geometry with a uniform incident charging current density,  $J_i$ . To model the conductive polymer layer over a dielectric substrate, however, the coating was subdivided into four separate sublayers with different conductivities. This corresponds more closely to the actual nonuniform conductance profile in the coating material. Figure 4 shows the thickness and conductivity assumed for each of the four sublayers. Also, the finite conductivity of the surrounding air ( $\rho_b = 4 \times 10^{13} \Omega \cdot m$  at sea level) was included.



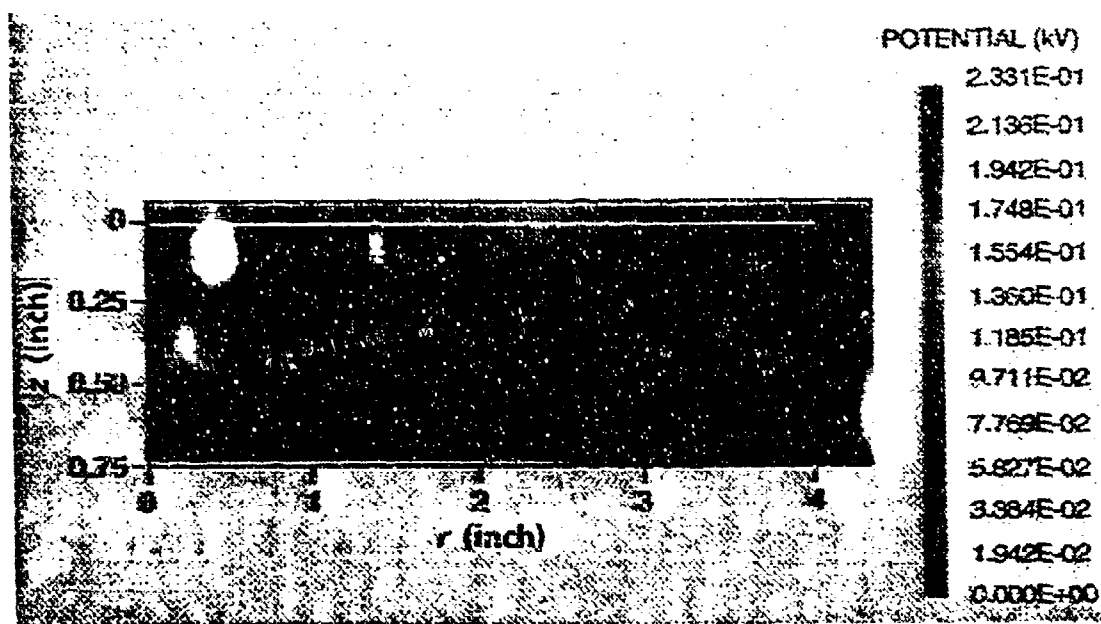
31680

Fig. 4. Configuration used to model 4-mil conductive polymer overcoat on Design 1.

For  $J_i = 10^{-3} A/m^2$  (assumed worst-case charging environment), Figure 5 shows the steady state solution of the potential profile for Design 1. A maximum voltage relative to the grounded edge of 233 V was computed compared with 250 V for the previous analysis. The lower value is due primarily to the air conductivity which acts as an additional drain for charging current. Figure 6 is a closeup of the vector electric field distribution near the edge of the coating where the largest field values exist. For this configuration, the maximum tangential electric field is  $2.4 \times 10^4 V/m$ . This is much higher (factor of 5) than the previous value calculated using the uniform conductance coating and is due predominantly to the higher value of surface resistivity in the outer two sublayers of the coating model.

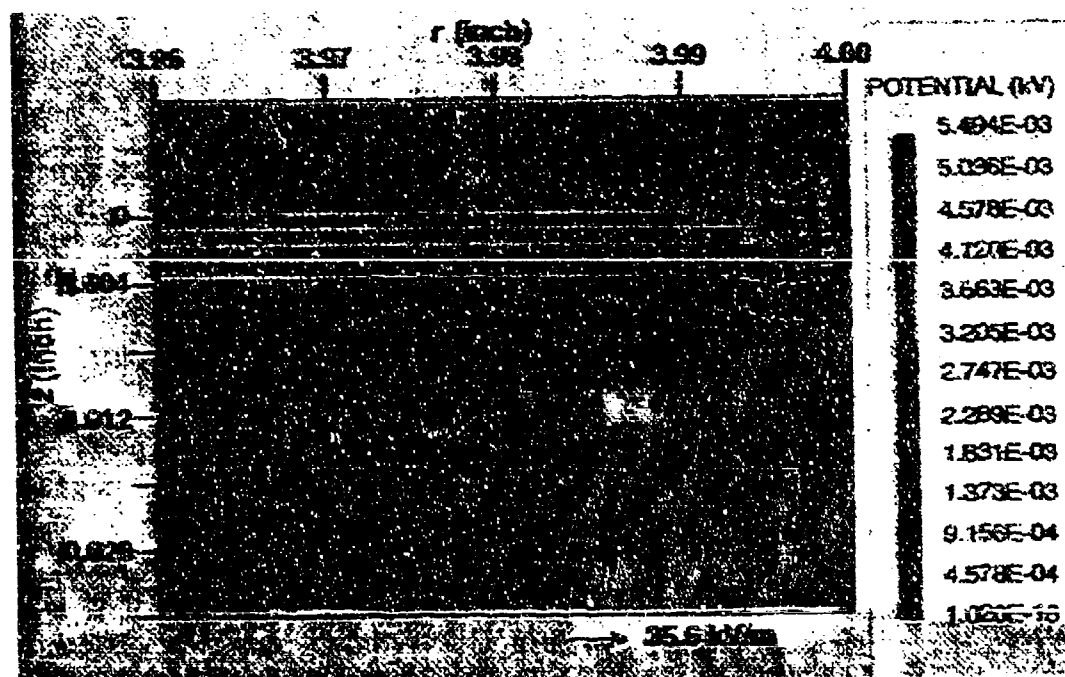
For Design 2, no additional changes to the coating model were needed since the conductivity is more uniform through the coating thickness than in Design 1. The computed maximum voltage of 5.08 kV is very close to what was calculated in the previous analysis. The maximum tangential electric field near the edge is  $4.8 \times 10^7 V/m$ , which is close to the analytical result of  $4 \times 10^7 V/m$ .

Using the BODY code and an engineering drawing of an F-16 canopy, a three-dimensional model of the worst-case charging potential profile of this canopy type was computed using the two different proposed transparency designs as input parameters. In addition to including the finite air conductivity, as was done in the two-dimensional case, the incident charging current density was made proportional to the angle of incidence relative to the flight vector (assumed to be parallel to the canopy axis for the initial computer runs). Thus, there are regions of the canopy, e.g., overhead and along the sides, which receive relatively low



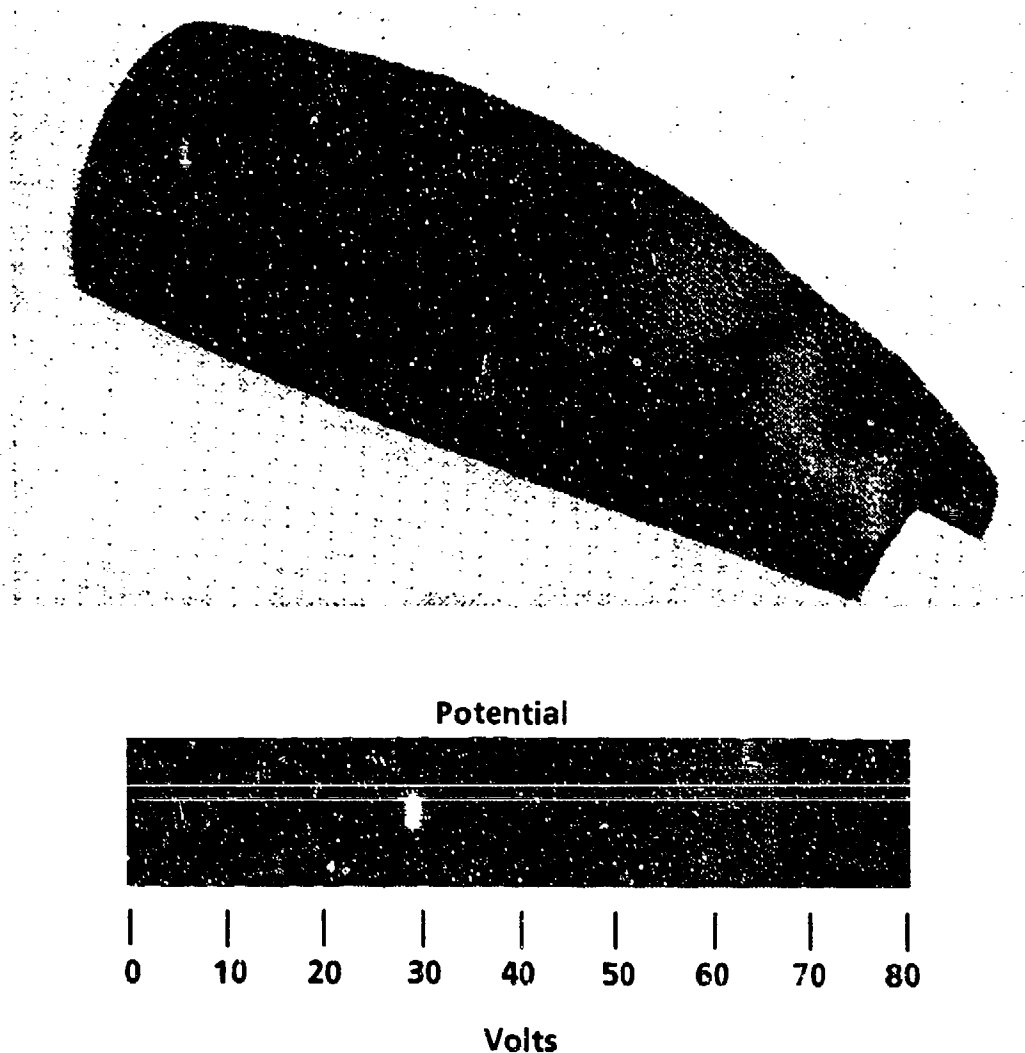
31681

Fig. 5. Steady-state electric potential contours for Design 1 with  $J_1 = 1 \text{ mA/m}^2$ .



31682

Fig. 6. Vector electric field  $E(r, z)$  near grounded edge for Design 1 with  $J_1 = 1 \text{ mA/m}^2$ .



31683

Fig. 7. Three-dimensional contour plot of the electrical potential profile for an F-16 canopy with  $J_i = 1 \text{ mA/m}^2$  parallel to the main body axis.

charging currents compared to the forward facing surfaces. Figure 7 shows the results of running this geometry for Design 1. The maximum potential is about 80 V. For Design 2, the maximum is about 1,970 V. Both maxima are located on the forward surface of the transparency, directly over where the heads up display (HUD) is located in the cockpit. For Design 0, voltages on the order of  $10^6 \text{ V}$  are predicted; however, discharge thresholds are reached well below this value. Also, air conductivity becomes a limiting factor in the computer model at these higher potential levels.

Future work will include modeling of different canopy types, e.g., an OH-58 helicopter transparency design. For helicopters, charging current densities are one to two orders of magnitude lower than for high speed jet aircraft; however, present designs typically have a high-resistance material on the outer surface and reports of static charging and dust attraction are common. As an extension of the present modeling techniques, a hydrodynamic airflow subroutine will be included in the BODY code to determine the pressure profile over the canopy during flight. From Paschen's law, as the pressure decreases from 1 atmosphere (atm) to levels

found at high altitude (30,000–50,000 ft), the breakdown voltage also decreases for gap spacings of 0.1–10 cm. For high-performance aircraft, local pressure minimums on the aft and sides of the canopy may be as prone to discharging as the forward-facing surfaces, due to the lower breakdown voltage threshold in these areas.

## 2.4 Test Program

As part of the current study, a laboratory examination of the material properties of commonly used transparency materials and of the newly proposed semiconducting polymer materials is being pursued. Test coupons of uncoated substrate materials (polycarbonate, acrylic, and stretched acrylic) and of various coating configurations were fabricated by Texstar.

The coupons are 10-inch squares approximately 0.25 inch thick. The polycarbonate substrate complies with MIL-P-83310, the cast acrylic meets MIL-P-5425, and the stretched acrylic is oriented-MIL-P-8184 meeting the requirements of MIL-P-25690.

The following coats were applied to the three different substrates, using the material types and thicknesses indicated:

- a. Soft coat (1–2 mil): aliphatic thermoset polyurethane.
- b. Soft coat (5 mil): aliphatic thermoset polyurethane.
- c. Soft liner (20–25 mil): aliphatic thermoplastic polyurethane.
- d. Hard coat (0.5 mil): methyl polysiloxane thermoset resin.
- e. Semiconductive coat (4 mil): inherently conductive polymer dispersed in the soft-coat formulation.

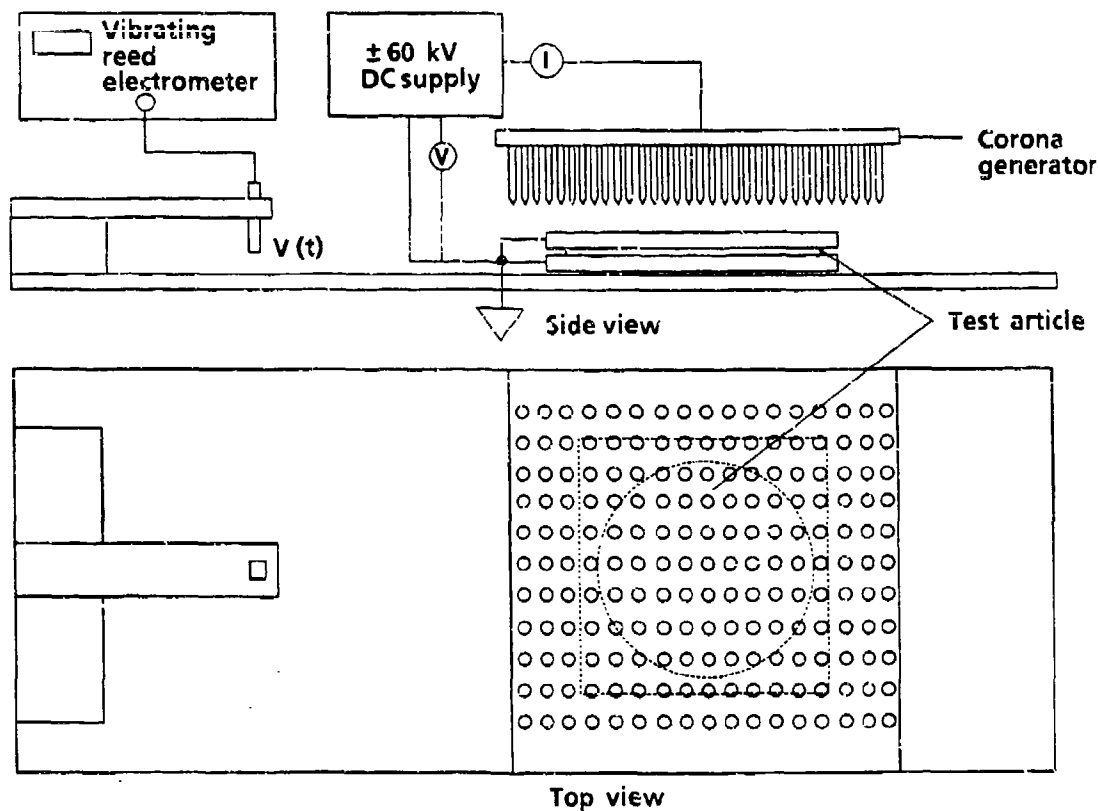
These coupons provided the samples from which the surface resistivities of the various coatings could be measured. In order to obtain a sample configuration from which the bulk resistivity of the coatings could be determined, the above coatings were also applied to substrates which had been given a sputtered gold film of 20  $\Omega/\text{sq}$ . The gold was treated to induce an oxide layer for enhanced optical transmission (enhanced gold). The gold film was left exposed around the border of the coupons so it could be accessed as an electrode.

As part of the testing procedures, all test coupons are measured for their bulk and surface resistivities following ASTM guidelines. A summary of those test samples measured to date is given in Table 2. These properties are used as input parameters in the analytical and numerical modeling to further refine the predicted performance for each transparency design in a given environment.

In addition to the static resistive properties of the materials, a measure of the material's ability to store and bleed off charge is made using a high-voltage-corona charging facility. The design of this facility was based on previous work (Ref. 1) and provides a simulation of the charging environments which might be encountered during actual flight. Figure 8 shows a schematic diagram of the apparatus used to deposit and measure the charge on a 10-inch square test sample. A high-voltage bias is applied to the array of nails and field emission from the nail tips (negative bias) results in electron flow toward the sample. A grounded plate is located beneath the test article to minimize the potential needed for corona discharge at the nail tip. Typical bias potentials of 30–40 kV are utilized to deliver up to 1 mA of charging current to the test sample.

Table 2 Summary of surface and bulk resistivity measurements made on test sample matrix.

Substrate	Coating	$\rho_s$ ( $\Omega/\text{sq}$ )	$\rho_b$ ( $\Omega\cdot\text{m}$ )
Polycarbonate	None	$3.6 \times 10^{17}$	$4.0 \times 10^{15}$
	Hard Coat (0.5 mil)	$2.5 \times 10^{17}$	
	Soft Coat (1-2 mil)	$2.0 \times 10^{14}$	
	Soft Liner (20-25 mil)	$1.8 \times 10^{14}$	
	Conductive Polymer (4 mil)	$10^{12}-10^{13}$	
Acrylic	None	$9.5 \times 10^{15}$	$1.3 \times 10^{16}$
	Hard Coat (0.5 mil)	$2.9 \times 10^{16}$	
	Soft Coat (1-2 mil)	$3.5 \times 10^{13}$	
	Soft Liner (20-25 mil)	$5.4 \times 10^{13}$	
	Conductive Polymer (4 mil)	$1.0 \times 10^{12}$	
Stretched Acrylic	None	$1.2 \times 10^{17}$	$3.5 \times 10^{16}$
	Hard Coat (0.5 mil)	$2.6 \times 10^{16}$	
	Soft Coat (1-2 mil)	$2.7 \times 10^{14}$	
	Soft Liner (20-25 mil)	$5.2 \times 10^{13}$	
	Conductive Polymer (4 mil)	$2.0 \times 10^{12}$	



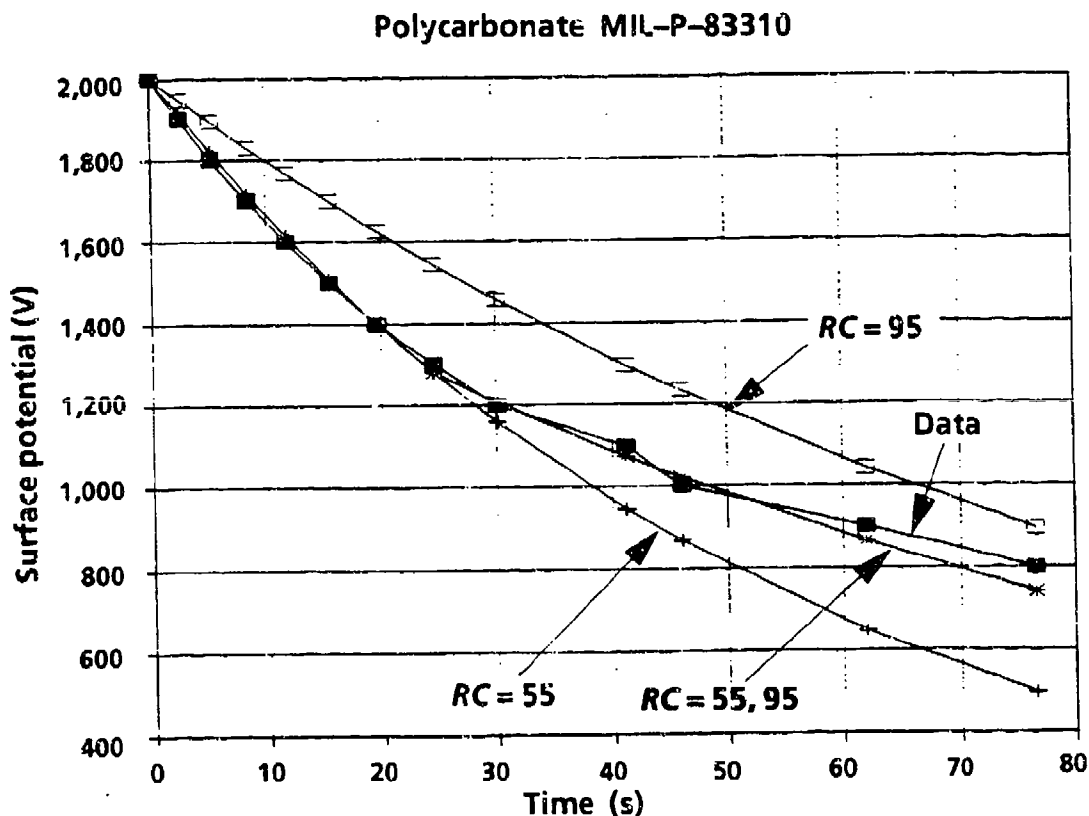
31684

Fig. 8. Diagram of high-voltage-corona charging source and potential profile diagnostics.

To determine the spatial charge distribution on the test article, a noncontacting high-voltage probe is moved in increments of 1 cm and the probe output is monitored on a strip chart recorder to determine the charge decay time constants. Figure 9 shows a typical decay curve for an uncoated polycarbonate substrate sample. From the measured capacitance of the test sample, the effective resistance is then calculated from the RC decay time and compared to that obtained from the measurements of bulk and surface resistivity and with the numerical modeling output, which includes air effects.

### 3. SUMMARY AND CONCLUSIONS

To summarize the results of the present effort to date, we have succeeded in modeling the charge up of two- and three-dimensional canopy geometries using realistic material properties and configurations. From past reports and field observations, an estimate has also been made that the worst case charging environment for high speed aircraft is on the order of  $10^{-3}$  A/m<sup>2</sup>. For present transparency designs, an understanding has also been reached as to the differences in performance of gold- and ITO-coated jet canopies, i.e., the thicker ITO coating is much less likely to reach melt/vaporization temperatures during discharge conditions than the thinner gold coating. From the analytical and numerical modeling, newly proposed semiconductive antiabrasion coating configurations appear capable of mitigating the effects of P-static charge buildup by providing relatively low impedance paths to airframe ground and thereby keeping impressed voltage levels below the thresholds for static discharge.



31685

Fig. 9. Typical voltage decay curve measured for polycarbonate (uncoated) compared with single and dual time-constant exponentials.

Further efforts in this study will include exposing the coupons that were tested for electrical properties by Jaycor to other environmental effects such as humidity, WeatherOmeter, UV, sand shake, and sand and dust. Then the electrical properties will be recharacterized. Of special interest will be any loss of conductivity in the doped antiabrasion coating.

When antistatic coated transparencies and canopies are deployed in the air vehicle fleets, it may be necessary to periodically check canopy surface electrical conditions and continuity between the surface and the airframe. A commercially available handheld surface-resistivity meter with decade resolution has been obtained and will be investigated for suitability for this purpose.

As a technology demonstration, a test transparency for an AH-1W SuperCobra helicopter will be fabricated with an antistatic abrasion-resistant coating. Several F-16 canopies with prototype conductively-doped coatings are presently being flown. They are being evaluated for their ability to suppress the effects of excessive p-static charging.

#### 4. REFERENCES

1. Twomey, R. C., "Effects of Laboratory Simulated Precipitation Static Electricity and Swept Stroke Lightning on Aircraft Windshield Subsystems," McDonnell Douglas Final Report to Air Force Flight Dynamics Lab, Wright-Patterson AFB, AFFDL-TR-76-75, July 1976.
2. Hanson, A. W., "Assessment of Aircraft Windscreen Static Electrification Problems," Lightning Test and Technology Centre, Culham Laboratory, UK, Report No. CLM/RR/T3/1, June 1976.
3. Tanner, R. L., and Nanevich, J. E., "Precipitation Charging and Corona-Generated Interference in Aircraft," Stanford Research Institute Final Report to Air Force Cambridge Research Laboratories, Bedford, MA, AFCRL-338-TR-73, April 1961.
4. Nanevich, J. E., "Studies of frictional electrification resulting from particle impact at supersonic speeds," Proc. of 3rd Conf. on Static Electrification, Paper 21, pp. 248-259, May 1971.
5. Illingworth, A. J., "A Laboratory Study of Aircraft Precipitation Static Charging," U. Manchester Inst. of Sci. and Tech. Final Report to Air Force Office of Scientific Research, AFOSR-TR-84-0540, May 1984.
6. Illingworth, A. J., and Marsh, S. J., "Static charging of aircraft by collisions with ice crystals (+)," *Revue de Phys. Appl.*, 21, 803-808 (1986).
7. Huang, G. C., Goldman, R., and Schulz, R. B., "Interference Characteristics of Streamer Discharges," IEEE Trans. on Electromagnetic Compatibility, Vol. EMC 12, No. 2, May 1970.



TRANSPARENCY REPAIR - TIME - TRAINING - QUALITY

J. Archer  
Micro-Surface Finishing Products, Inc.

## ABSTRACT

### TRANSPARENCY REPAIR TIME - TRAINING - QUALITY

by

John Archer

Micro-Surface Finishing Products, Inc.

Transparency repair and restoration methods are being scrutinized in an effort to develop more effective systems.

"Battle damage repair" during periods of conflict require methods that are not conducive to good repair but are expedient.

Day to day flightline or maintenance shop repair, while less pressured, still suffers from the need to get the aircraft flying again.

Logistic support centers, central repair stations, and contract repair stations doing off the aircraft repair, produce quality work using time effective methods.

This paper presents an overview of transparency repair situations, methods and personnel. The strengths and weaknesses of existing and experimental processes are examined.

Highlighted are the needs of aerospace, commercial and military aircraft in relation to transparency repair. Data collected over the past 25 years has been reviewed to determine if methods for more time effective transparency repair systems result in sacrifices in quality or safety.

The question is, can transparency users live with less quality as a trade off against speed of repair and the creation of expensive scrap? Is such a "trade off" necessary or only imagined?

TRANSPARENCY REPAIR  
TIME - TRAINING - QUALITY

John E. Archer  
MICRO-SURFACE FINISHING PRODUCTS, INC.

Aircraft transparency repair began shortly after the first plastic windscreen was installed on an aircraft.

The plastic was subject to natural and manmade crazing, bird strikes, rocks and other debris, and scratches of all kinds. Today the most commonly repaired transparencies are variations of stretched acrylic, polycarbonate or combinations of these materials. While much stronger, these transparencies are still subject to the same abuse. To repair or not to repair -- is not the question. Given a transparency price range of \$300 to \$30,000 or more, repair should always be considered.

Commercial airlines have repaired cabin and cockpit windows for twenty years with significant annual savings. A 1983 Navy study indicated that crazing removal on F-14 canopies at one base saved \$174,000/year(1). A later Airforce study on C-141 windows showed once again the cost of repairing was significantly less than the cost of new replacement material(2).

Given a transparency that is repairable that has a thickness above manufacturers minimum, the repair is a simple matter of removing the damage from the surface and restoring that surface to optical clarity - Or is it simple? The factors of time, training and quality are always involved in any transparency repair.

The urgent need to return an aircraft to service, during time of military conflict for example may dictate a radical departure from optimum repair procedures. Line of sight areas are the most critical for heads up display and weapon sighting. Other areas could get by with less than optimum optics.

- (1) Effectiveness Report on Acrylic Transparency Surface Restoration Utilizing MICRO-MESH Procedures, Harold G. Geasley, Value Engineering Administrator, Naval Air Rework Facility, Norfolk, VA 23511, February 1983
- (2) DCASMA Contract No. FO9603-87-C-1174, June 1987

However, other than battle damage repair, the urgency of transparency repair normally drops. The time factor is now more related to the economics of keeping the aircraft grounded long enough to replace the transparency or do an acceptable optically clear repair.

The key to producing an optically clear transparency is to have as simple a system as possible to use. The system must be one that produces the desired optical clearness with minimum amount of time. The system must be one that can be used by personnel whose training, skill and motivation may range from limited to highly skilled.

Because of this wide range of training, a system of transparency repair and surface restoration was developed about 25 years ago(3) that addresses all levels of operator skill and training. This system employs a two part approach whereby common coated abrasives were used to sand away the damage and cushioned abrasives were used to restore the optical clearness. This system is specified under Mil Spec MIL-M-58091A(4) and is incorporated into most aircraft manufacturers' specifications.

This system works because of its' use of cushioned abrasive products and because all the abrasive sanding was done by hand. While hand sanding was not time effective, everyone who used it arrived at the same result - optical clarity!

For those not familiar with normal transparency repair, it is first necessary to remove material from the surface to the level of the deepest damage. For example, on a scratch .015 deep, at least .015" of material must be removed. The removal can not be localized but must be spread over a wide area of the transparency or distortion will result. After the damage is removed the scratch marks from that sanding step must be removed with successive sanding or polishing steps to achieve optical clarity.

Under the pressure of time, the transparency users now call for machines rather than hand sanding as a transparency restoral method. For commercial airline cabin windows which are flat or nearly flat, the window can be brought to a milling or abrasive slurry machine and set on to it. The operator is only required to push a button.

- (3) Surface Restoration Techniques for the Repair of Acrylic Transparent Aircraft Enclosures, Robert J. Stillman, Micro-Surface Finishing Products, Inc.
- (4) MIL-M-58091A, 17 May 1971

However, with curved surfaces such as canopies, windscreens or cockpit windows the machine must be brought to the transparency due to the physical size configuration or location of the transparency.

The machine most commonly used by repair technicians is the random orbital sander usually with a 5" abrasive disc backed by a firm foam pad. Typically these machines move the abrasive disc in an elliptical orbit at 6000 - 10,000 rpm under no load. As compared to hand block sanding, this machine significantly increases productivity. However, now the operator has to do more than push a button. Without using a trained operator the use of a machine will result in significant problems.

The technician must hold this 3-4 pound machine, with abrasive disc attached, against a curved surface and move it up and down or back and forth across the surface at a uniform speed while applying uniform pressure. Holding the machine at the wrong angle, sanding too long in one area or not maintaining a sanding pattern, will result in distortion to a greater or lesser extent. There is great truth in the training axiom that putting distortion into a transparency is a heck of a lot easier than taking it out.

A quick word here to those advocates of robotic finishing where we replace the operator with a computer controlled robotic arm. One of the functions of the trained technician is to evaluate damage in all areas and remove only enough material in areas of different damage to get rid of damage.

Gages to accurately measure depth of damage in different areas such as crazing, scratches or gun gas clouding are available. However, to compute this and respond to different damage depths all across the transparency is not being done as far as I know. When all forms of damage are present on one transparency in different locations, the human technician can quickly adjust the removal rate to accommodate. However, when we attach the transparency to a robot, we set the robotic machine to remove material to a given depth or to dwell for a certain time. The benefit is time and labor saved. But often more material is removed in some areas than necessary. A well-trained technician can judge damage removal requirements and adjust as they work.

Whether human or robotic arm is used, we still must address the problems of a machine finish. The elliptical orbit of the random orbital sander produces a sanding pattern which appears as a series of "fishhooks" on the plastic. With common coated abrasive discs, the abrasive crystals are fixed in position. The abrasive crystals dig in like chisels and the fishhook pattern they generate is deep. Often even deeper random fishhooks are generated by the unevenness of the common abrasive cutting surface.

#### Page 4 - TRANSPARENCY REPAIR

It was observed in a 1988 paper on crazing of acrylic(5) "that crazing occurs more quickly in rough surfaces". Common coated abrasives, if used by themselves, will leave a potential craze producing scratch pattern. This scratch pattern is accentuated by the use of the random orbital sanding machine. The machine and operator together produce a heavier down pressure on the abrasive than a hand sanding block.

The key to produce the best surface finish on a transparency is to revert to the previously mentioned military specification method which starts with common abrasive to remove damage but uses cushioned abrasives to remove the deep scratches of the common abrasive and restore the optical clarity. Since cushioned abrasives can be used on a random orbital sander, the time element is improved significantly.

Cushioned abrasives are built with a thin resilient layer between the backing and the abrasive crystal. This allows the abrasive crystal to recede to a common level when applied to the transparency. This engineering produces a planing action rather than a chisel action on the transparency surface with the result of no deep scratches to propagate crazing.

Typical of industrial applications, using cushioned abrasive discs on the transparencies produce optical clarity in fewer steps than common coated abrasives discs. Fewer steps mean less total time the technician must spend on the transparency with abrasives and a random orbital sander. This shortened sanding time reduces the chances for a distorted surface.

The issue of time in transparency repair is unquestionably important. Taking the sanding materials from the technicians hand and putting those materials on a machine such as a random orbital sander will enable the technician to do more in less time.

Now the question becomes one of time, versus training, versus quality. Without adequate training, inadequate quality results. Inadequate quality means we must either A). rework the transparency which takes more time or B). scrap the expensive transparency and buy new at significantly greater expense.

- (5) UDR-TM-88-23 Crazing of Acrylic as Function of Surface Smoothness, Kevin L. Poorman & Blaine West, University of Dayton Research Institute, July 1988

To accomplish a quality repair the operators must be trained to use the tools, gages, and machines. The FAA requires an 18 month apprenticeship under FAA certified trainers to become a certified transparency repair person(6). This rule also allows a certified A & P mechanic to do this work with little specific training. Military training programs vary with the need of a particular base, aircraft type and frequency of repair normally done. The unfortunate cost of the inconsistency of these programs comes in the form of many scraped transparencies.

To accomplish a quality repair the correct machine techniques and materials must be used. Using the right machines and materials, such as cushioned abrasives that require less effort and less time spent in contact with the transparency, will reduce quality errors. The technicians must be trained to evaluate damage and how to use a grid board. They should have thickness measurement gages and minimum thickness specifications so they know how much material can be removed. The importance of quality repair is directly related to pilot safety. Keeping records of a repair and the history of the transparency also prevents serious quality errors.

The concerns of this conference center around providing a window through which a pilot or passenger can see with optimum clearness and adequate safety. I have addressed concerns that are directly related to these two issues.

If we are to maintain optical quality when repairing a damaged transparency, the time to do the work must relate to the level of training and skill of the worker and the tools and materials at his disposal. Anything else will result in safety concerns and scrap.

(6) FAR 65.101

EXTERIOR SURFACE COATING SYSTEM FOR ELECTROSTATIC DISCHARGE  
DAMAGE PREVENTION FOR THE F-16 CANOPY

S. Sandlin  
R. L. Fogarty  
M. V. Moncur  
Pilkington Aerospace Inc.





## **PILKINGTON AEROSPACE**

### **EXTERIOR SURFACE COATING SYSTEM FOR ELECTROSTATIC DISCHARGE DAMAGE PREVENTION FOR THE F-16 CANOPY**

S. L. Sandlin, R. L. Fogarty, M. V. Moncur

Pilkington Aerospace Inc.

#### **ABSTRACT**

Triboelectric charging on the outboard surface of F-16 forward transparencies is a major problem, especially for solar coated designs. The electrostatic charge build-up and associated discharging results in: shock hazards to pilots; damage to the transparency, especially to the solar coating system in the form of burn tracks; visual distractions in flight from "St. Elmo's fire"; and communication, navigation, and electrical subsystems interference and noise. Damage to the solar coating system often results in premature replacement of forward transparencies, sometimes after a single flight.

An exterior surface electrostatic discharge damage prevention coating system (EDS) has been developed by Pilkington Aerospace Inc. The EDS coating system consists of a polyurethane protective liner topcoat (SS-6831) and an Enhanced Gold conductive coating. The Enhanced Gold coating also functions as a solar coating.

This paper summarizes the results of a program sponsored by the Ogden Logistics Center, F-16 Structural & Systems Section (OO-ALC / LAAEA) to qualify the EDS coating system to the F-16 Transparency Critical Item Development Specification (16ZK002E) and to scale-up and manufacture prototype F-16 A/C forward transparencies for flight test evaluation (Contract No. F42600-89-D-0658, D.O. 0074). Three EDS-coated forward transparencies were manufactured and delivered to McConnell Air Force Base in February, 1993, where they are currently undergoing flight evaluation testing.

Performance data for the EDS coating system are presented. Qualification test results, including specimen-scale impact and full-scale p-static testing, are summarized. The EDS-coated forward transparencies are described and field performance results obtained to date are presented. Birdstrike test results for a new 550 knot, EDS-coated F-16 A/C forward transparency design are also discussed.

## INTRODUCTION

Pilkington Aerospace Inc. (PAI) has developed a family of transparent electrically conductive / protective liner coating systems for use on the exterior surface of plastic aircraft transparencies. The coatings may be applied to large compound curved shapes such as those currently used for military jet fighters.

One of the PAI coating systems, Enhanced Gold conductive coating with SS-6831 protective liner, was recently evaluated as a part of the MITS Advanced Canopy Coatings Program (ACCP). The coating system corresponds to samples coded "D-4" and "D-5" from the MITS Critical Design Review (REF 1). As a part of the ACCP Program, the coating system underwent extensive durability testing with impressive results. The Enhanced Gold / SS-6831 system emerged as the only conductive coating system to pass the MITS environmental, mechanical, erosion, and optical test requirements.

The F-16 solar-coated forward transparency has been plagued to date by substantial electrostatic charging problems. Based on the performance from the ACCP program, PAI proposed that its exterior surface coating system could be used on current F-16 forward transparencies to eliminate the static charging problems.

A contract was issued to evaluate the coating system thru the F-16 Structural & Systems Section (LAAEA), Ogden Logistics Center, Hill Air Force Base (OO-ALC). Mr. Reed Nelson served as the program engineer. The program was managed for OO-ALC by Lockheed Fort Worth Division (formerly General Dynamics Fort Worth Division) as a call contract (No. F42600-89-D-0658, D.O. 0074). Mr. Lynn Early was the engineer at Lockheed.

The program objective was to qualify the PAI coating system to the requirements contained in the F-16 Transparency Critical Item Development Specification (16ZK002E), to scale-up and manufacture prototype F-16 forward transparencies with the coating system, and to evaluate the prototype parts via flight testing. The program started in February, 1992; three prototype parts were delivered in February, 1993.

## TRANSPARENCIES AND ELECTROSTATIC CHARGING

Transparency electrostatic charging is caused by the impact of a transparency in flight with quantities of particles such as dust, ice, snow or rain droplets in a process known as triboelectric or frictional charging. Sometimes the phenomenon is also referred to as precipitation static (or p-static) charging since it is often associated with "static" noise detected over aircraft communication systems.

Electrostatic charging results from a charge transfer mechanism where initially neutral particles impact with a transparency surface, move away with a net charge, usually positive, acquired from the surface contact, and leave an opposite and equal charge, usually negative, on the transparency surface. The process may be regarded as a continuous current source event because the deposition of additional charge does not depend on the amount of charge previously transferred to the surface. Therefore, unless a charge dissipation mechanism is in place,

charge can continue to be transferred to the exterior surface, even when the surface is highly charged, such that hundreds of kilovolts of surface potential can be generated.

## F-16 ELECTROSTATIC CHARGING PROBLEMS

Solar coated F-16 forward transparencies currently have an electrically conductive coating located on the interior surface. The conductive coating is attached to system ground thru the transparency frame via grounding bushings. In general, location of a conductive coating on the interior surface (or within a laminate) increases the severity of electrostatic charging problems for transparencies. This has been the case for the F-16.

During an electrostatic charging event, charge deposited on the outside surface results in the generation of "mirror" charge of opposite polarity on the conductive coating on the inside surface. The mirror charge, in turn, holds the outside surface charge more efficiently thus allowing more charge to be bound to the outside surface. The resulting system may be thought of as a capacitor, consisting of the bound outside surface charge as one electrode, the conductive coating with mirror charge as the second electrode, and the structural cross-section as the dielectric.

For the F-16, in-flight electrostatic discharging has resulted in significant damage rates to the inside surface solar coating (REF 2). The damage often results in premature replacement of transparencies, including some after a single flight. The damage usually occurs in the form of burn tracks that typically extend hoop-wise across the transparency.

When enough charge is built-up on the outside surface in flight, the charge flashes over the surface to the frame or some other attachment point. When the flash-over occurs, mirror charge also flows thru the solar coating in a transient current pulse. The pulse may exceed the current carrying capability of the relatively thin and fragile solar coating. When this occurs, the coating can be evaporated and burn tracks formed. The tracks can then isolate different areas of the solar coating from each other and cause arcing between these isolated areas.

In-flight surface flash-over also results in additional problems for the F-16. "St. Elmo's fire" from the flash-over can temporarily blind or at least distract a pilot, especially at night. The flash-over also produces secondary current transients in electrical subsystems and may produce noise and interference in communication, navigation, and avionic equipment.

Shock hazards are also a problem. A pilot may be shocked in flight from the mirror charge and current transients that are generated on the inside solar coating surface, especially if he reaches toward the inside surface. It is also possible for ground crew to be shocked from residual charge stored on the outside transparency surface after the aircraft has landed. Just as a capacitor can store charge for a significant period of time, an F-16 transparency can, depending on humidity and atmospheric conditions, remain charged for hours after landing. Crew chiefs have been shocked so severely that their arms have been numbed for hours.

## EDS DESIGN

The Pilkington Aerospace Inc. EDS design utilizes a conductive coating on the exterior surface of the transparency to eliminate the F-16 electrostatic charging problems. The conductive coating provides a pathway to continuously drain charge deposited on the outside surface to system ground. By providing such a continuous path, all of the problems discussed in the previous section are eliminated. Surface voltages needed to create flash-over in-flight are never reached.

An exterior surface coating system was proposed for the F-16 as early as 1981 by General Dynamics (REF 3). However, until the recent development of the PAI Enhanced Gold / SS-6831 coating system, the technology for a durable exterior conductive coating system for plastic transparencies did not exist. For glass-faced windshields, however, anti-static coatings have been used for many years, including for the B-1B. Exterior glass anti-static coatings have been quite effective in eliminating electrostatic charging problems.

The EDS coating system is shown schematically in Figure 1. The exterior surface is coated with Enhanced Gold and SS-6831 liner. The Enhanced Gold also functions as the solar coating. SS-6831 is a durable polyurethane protective clear coat for the Enhanced Gold which is applied at a thickness of approximately 0.005 inch.

Because the Enhanced Gold coating on the outside surface also functions as the solar coating, the interior surface solar coating is not needed with the PAI EDS system. Therefore, the interior solar coating is removed from transparencies (where it exists) and replaced with SS-6590, a silica-filled polysiloxane hard abrasion resistant coating. SS-6590 protects the interior polycarbonate surface from scratches, marring, and environmental degradation. SS-6590 is currently used on B-1B and B-2 windshields.

To drain electrostatic charge to system ground, the Enhanced Gold coating must be grounded to the transparency frame around the circumference of the part. The prototype parts delivered under the EDS Program were grounded by a conductive paint that was placed over the outside surface of the edge of the transparency above the stop crack groove and on the top face of the bushings. An electrically conductive dry fairing seal contacted the paint and grounded the EDS coating directly to the canopy frame side fairings. Future configurations will ground the EDS coatings to the grounding bushings currently used on the F-16.

## EDS COATINGS

Enhanced Gold is a multiple layer coating in which a gold film is sandwiched between antireflective dielectric or semiconductor layers. The multi-layer gold stack has improved light transmittance and durability compared to conventional, single-layer gold. Although Enhanced Gold has somewhat lower light transmittance and more color than ITO, it has superior ductility and strain allowable compared to ITO and can withstand exterior surface thermal / pressure cyclic loading.

SS-6831 protective polyurethane liner is an extremely tough material optimized for exterior surface durability (REF 4). It has excellent tear strength, abrasion resistance, and erosion resistance (rain, sand, dust). SS-6831 is formulated with UV absorbers, antioxidants and heat stabilizers to further enhance its inherent environmental resistance and to protect the underlying Enhanced Gold film. SS-6831 also contains a proprietary treatment to efficiently drain electrostatic charge thru the coating to the Enhanced Gold film below.

The EDS coating system has undergone extensive durability testing at Pilkington Aerospace Inc. and at independent laboratories. It was the only conductive coating system on plastic to pass the MITS Program durability requirements from the ACCP program.

### **16ZK002E QUALIFICATION**

The performance, design, development, and test requirements for F-16 transparencies are documented in 16ZK002E, the Critical Item Development Specification. Along with the proposal for the EDS program, Pilkington Aerospace Inc. submitted a Qualification By Similarity Report (REF 5) to General Dynamics. The report contains data from previous testing of the EDS coating system that were applicable to the 16ZK002E requirements. General Dynamics responded with a test plan (REF 6) which qualified by similarity many of the performance requirements from 16ZK002E. Additional sub-scale tests were successfully completed for solvents/crazing and specimen scale impact requirements. A full-scale test was performed to demonstrate electrostatic charge drain capability.

Additional coupon scale high strain rate impact testing was performed on samples sectioned from an F-16 transparency. A set of control samples without EDS coatings was tested alongside the coated samples. The testing was conducted at the University of Dayton Research Institute in October, 1992. The tests were performed using three-point loaded beam specimens per ASTM F736, Type B. The strain rate was 70 - 100 in/in/sec and the samples were impacted on the EDS coated side (because the EDS coatings are on the exterior surface).

Test results are presented in Figure 2. The test demonstrated that there was no reduction in impact threshold energy density from application of the EDS coatings. Actually, the EDS coated samples had higher damage threshold energies than the uncoated control samples.

### **550 KNOT DESIGN BIRD STRIKE TEST**

In addition to the subscale impact tests, a full-scale F-16 part has been bird strike tested. An F-16 A/C forward transparency constructed from a two-ply polycarbonate laminate (polycarbonate exterior ply / interlayer / polycarbonate interior ply) with the EDS coating system, including SS-6590 abrasion resistant coating on the interior surface, was successfully bird strike tested at Lockheed Fort Worth Division on 10 March, 1993. The test was conducted with a Lantirn HUD. Bird velocity was measured at 548 knots. The new bird strike and EDS upgraded part configuration is identified as Pilkington Aerospace Inc. part number 93109-1.

The structural subassembly for the test part was designed and manufactured by Texstar, Inc.

## FULL SCALE ELECTROSTATIC TEST

### Method Selection

The F-16 Critical Item Development Specification states that precipitation static discharge "shall not degrade the solar coating". However, a test method and a current density (current per unit area) test level are not specified. To fulfill the full-scale electrostatic test requirement, a multiple point electrode charge spray head method was selected. The method was first developed at McDonnell Aircraft (REF 7,8) and has been extensively used for laboratory simulated triboelectric charging tests.

The multi-electrode charge spray method is ideal for evaluating external conductive coating systems. The method is a good laboratory simulation of true triboelectric charging because uniform current densities can be applied over large surface areas and to complex shapes. Voltages, currents and test area can be easily measured to determine the applied charging rate current densities.

Single electrode charging techniques, such as the Van deGraaff generator, are not as useful for exterior coating evaluations because they do not apply uniform current densities over large areas. Instead, they apply nonuniform, high charge densities to small, localized areas. This makes it difficult to determine an effective test area. The Van deGraaff generator is useful for creating and evaluating damage to interior surface coatings because the high (hundreds of kilovolts) exterior surface voltages needed to cause damage can be obtained.

### Test Description

Using the multi-electrode method, a full-scale test on an F-16 EDS coated transparency was conducted at the Northrop Aircraft Division (NAD) Lightning Laboratory Test Facility (REF 9,10). The test configuration is shown in Figure 3. The transparency was supported on non-conducting stands. A 40 KV DC power supply was connected to the multiple electrode assembly (MEA) thru a 15 ohm series resistance for isolation of the power supply. A fiber optic voltmeter was used to monitor the power supply output voltage. Negative voltage was applied to the MEA. Current was measured directly from the test part thru a 15 Kohm isolation resistor. Two current return leads were attached to the test part, one on each side, at the position where the frame side fairing would contact the conductive grounding paint. The test equipment set-up is shown in Figure 4.

The MEA (Figures 5 and 6) was shaped to the contour of the forward region of the transparency. The edge of the MEA was positioned approximately 2.5 inches from the inside edge of the part stop crack groove along the forward arch and longerons and extended back to bolt hole position number 23. The MEA consisted of 246 point electrodes equally spaced on 2 inch centers. A typical point electrode is shown in Figure 7. For testing, the electrode tips were positioned approximately 0.1 inch from the top surface of the liner coating. The MEA effective charging surface area was 7.2 square feet. For the transparency installation position on the

F-16, the air stream facing frontal area projected from the 7.2 square feet test surface area was 2.3 square feet (Figure 8).

### Current Density Test Level

As far as Pilkington Aerospace Inc. is aware, electrostatic charging levels have not been measured in-flight directly on the F-16 transparency. However, p-static current densities up to 50 microamps per square foot of frontal area have been published as extreme conditions (REF 2, 11). Frontal area refers to the transparency projected area normal to the flight path.

In addition, Hanson (REF 12) has also derived the following relationship which expresses charging current density as a function of aircraft velocity for flight thru cumulo nimbus ice crystal clouds (a severe charging condition):

$$J = 3 \times 10^{-6} v \quad (1)$$

v is velocity in meters per second.

J is current density in amps per square meter.

J refers to projected surface area of the windscreen normal to the line of flight or frontal area.

From the Hanson relationship, at a velocity of 700 knots, a frontal area current density of 1.1 milliamps per square meter or, after converting units, 102 microamps per square foot would occur. Using the frontal area to surface area ratio measured for the MEA test configuration described in the previous section for the F-16, the 102 microamps per square foot frontal current density level corresponds to 32.6 microamps per square foot of transparency surface area current density. Current densities at this level (and beyond) were applied during the full-scale electrostatic test.

### Test Results

Test results are summarized in Table 1. Frontal area current densities from 99.6 to 157.8 microamps per square foot were applied. Corresponding surface area current densities were 31.8 to 50.4 microamps per square foot, respectively. Exposure time at each level ranged from 1.5 to 4 minutes. The (negative) voltages needed to apply the current levels to the MEA ranged from 7.8 to 9.0 kilovolts. The relatively low voltages indicate the efficiency with which the EDS coating system was able to drain the current. As stated earlier, the current drain path is thru the liner to the Enhanced Gold and then to system ground.

No arcing or damage to the coatings was observed after testing at the 99.6 / 31.8 microamps per square foot test level (extreme flight conditions). At the highest test level (beyond conditions that could ever be reached in flight), at 157.8 microamps per square foot frontal area, a few isolated arcs were observed during the test. One of the discharge events was captured on film and is shown in Figure 9. The rows of lights are corona activity at the MEA electrode point tips. The single bright light right of center is the discharge event. Following the test, close inspection of the transparency revealed two pinholes in the liner coating, with diameters of 0.070 and 0.050 inches (Figure 10). The third arrow, at the bottom of

the photo in Figure 10, is an inclusion in the transparency interlayer and not a pinhole. The lack of burn tracks and the presence of only insignificant damage after the (beyond flight conditions) test level demonstrates the durability and current drain effectiveness of the EDS coating system.

Following each current density level test, after the MEA voltage was decreased to 0 volts, it was observed that the current decreased to 0 amps with a lag time of about 2 seconds. It was also observed that insignificant residual charge was left on the transparency (liner) surface. Shock hazards from residual stored surface charge are thus eliminated.

### **EDS F-16 PART CONFIGURATIONS**

For the prototype test parts manufactured during the program, the EDS system was applied to service used non-solar coated "clear" transparencies provided by OO-ALC (part number 16VK100001-813). The exterior acrylic ply surfaces were first refurbished and then coated with the EDS system, thus upgrading the parts to solar and EDS coated units.

The coating system may be applied to service used or new as well as to clear or previously solar coated parts. It may be applied to laminated acrylic exterior ply (type II) designs, to monolithic polycarbonate (type I) designs, or to the new laminated polycarbonate exterior ply (550 knot bird strike upgrade) designs.

### **FLIGHT HISTORY OF TEST PARTS**

Three prototype test parts were completed and shipped to McConnell Air Force Base, Wichita, Kansas, in February, 1993. The parts were installed on aircraft with the 184th Kansas Air National Guard and flew for the first time on 23 February 1993. Photographs of the aircraft are presented in Figures 11 thru 13.

As of July 28, 1993 the (three) parts have accumulated a total of 316 flight hours over five months of service. The aircraft have flown in heavy rain and have been used for a wide variety of mission profiles, including air to air and live bomb drops. Pilot comments for the test parts are being logged on special squawk sheets. Comments to date have been very favorable with many comments noting enhanced visibility.

There have been no reports of electrostatic discharge damage or shock occurrences to pilots or ground crew from the three EDS test transparencies. Other aircraft within the unit with conventional interior solar coated transparencies have experienced electrostatic charging damage and shocks to ground crew chiefs during this time period.

The exterior surface coating system is holding up well to regular squadron level maintenance functions. The crew chiefs have noticed that it is more difficult to clean bug splatter from the exterior surface, unless the surface is cleaned on the same day as the flight. However, even if the bug splatter has a chance to "bake" onto the surface, such as over a long weekend, it can still be cleaned with additional effort.



## ADDITIONAL BENEFITS FROM EDS SYSTEM

In addition to the elimination of electrostatic discharge problems, it is anticipated that the EDS coating system will improve service life for F-16 transparencies. By re-location to the exterior surface, damage to the solar coating from helmet scuffs, dings, etc., from the current inside surface location will be eliminated. Such damage is currently a significant "cause for removal" item. Also, the exterior surface coating system will provide additional environmental protection to the outboard acrylic ply (and to outboard polycarbonate plies for 550 knot upgrade designs). Star craze and sand erosion damage should be significantly reduced.

Enhanced Gold has improved light transmittance compared to conventional single-layer gold. The prototype parts have light transmittance values of 70%. The F-16 specification is 65%. The improved light transmittance allows conductive coatings with lower sheet resistance to be applied.

Near IR transmittance is also improved for Enhanced Gold with substantial transmittance improvements to 950 nanometer wavelengths. The EDS system is Night Vision Goggle (NVG) compatible.

## CONCLUSION

1. An exterior surface electrostatic discharge damage prevention coating system is now available for the F-16 forward transparency.
2. Preliminary field performance flight test results have been very encouraging.
3. The coating system can be applied to service used forward transparencies to refurbish and upgrade clear or solar coated transparencies to EDS and solar coated configurations.
4. The EDS coating system can also be applied to new 550 knot birdstrike protected F-16 designs, as well as to other advanced fighter canopy systems.
5. A full-scale, multiple electrode charge spray head electrostatic discharge test method was used to demonstrate the charge drain capability of the exterior surface EDS coating system. The method is ideal for evaluating exterior surface coating systems.

## ACKNOWLEDGEMENT

The authors would like to express appreciation to Reed Nelson at OO-ALC and Lynn Early at Lockheed Fort Worth for their support and technical assistance. The authors also would like to thank Daniel Bowman at UDRI for the coupon impact testing, Jeno Marczinko at Northrop Aircraft Division for the p-static testing, and Master Sargent Larry Freeman and the Egress Shop at the 184th Kansas ANG for the F-16 photographs.

## REFERENCES

1. MITS Critical Design Review, 12-16 August 1993.
2. Hinds, B. G., De Camp, H. "Electrostatic Discharge Damage To F-16 Canopy Solar Coatings," 15th Conference on Aerospace Transparent Materials and Enclosures Sponsored by the Air Force Wright Research and Development Center, WRDC-TR-89-4044, April 1989, pp. 898 - 916.
3. Zeitler, R. T., "F-16 Canopy Static Charge Test Report," GD 16PR1687, General Dynamics Fort Worth Division, 27 Jan 1981.
4. Lewis, W. L., Andrechak, J. A., "Versatile Applications Of Polyurethanes In Aircraft Transparencies," 15th Conference on Aerospace Transparent Materials and Enclosures Sponsored by the Air Force Wright Research and Development Center, WRDC-TR-89-4044, April 1989, pp. 212 - 226.
5. Moncur, M. V., "Qualification By Similarity Report, Swedlow Electrostatic Discharge Coating System For F-16 Transparencies," PAI ER#1554, Pilkington Aerospace Inc., 9 August 1991.
6. Early, W. L., Webster, C. A., "Test Plan For Qualification Of Swedlow Inc Coating System," GD 16PP1995, General Dynamics Fort Worth Division, 13 December, 1991.
7. Twomey, R. C., "Effects Of Laboratory Simulated Precipitation Static Electricity And Swept Stroke Lightning On Aircraft Windshield Subsystems," AFFDL-TR-76-75, Douglas Aircraft Co., July 1976.
8. Twomey, R. C., "Precipitation Static Electricity And Swept Stroke Lightning And Their Effects On Windshield Subsystems," 12th Conference on Aerospace Transparent Materials and Enclosures Sponsored by the Air Force Wright Aeronautical Laboratories, AFFDL-TR-78-168, December 1978, pp. 219 - 233.
9. Marczinko, J. N., "Precipitation Static And Qualification Test Report On The Pilkington Aerospace Inc. Anti-static SS-6831 Liner For F-16 A/C Forward Transparency," NAD 8010-93-075, Northrop Aircraft Division, Hawthorne, Ca., 25 January 1993.
10. Sandlin, S. L., "Qualification Test Report, F-16 EDS Full Scale P-static Testing," PAI ER#1574, Pilkington Aerospace Inc., 30 June 1993.
11. Nanevich, J. "Advanced Materials Aspects And Concepts For Development Of Antistatic Coatings For Aircraft Transparencies," Contract F33615-72-C-2113, Project 2393, Stanford Research Institute, Menlo Park, Ca., 22 February 1973.
12. Hanson, A. W., "Assessment of Aircraft Windscreen Static Electrification Problems," CLM-RR-T3-1, Lightning Test and Technology, AEA Technology, Culham Laboratory, Abingdon, Oxfordshire, United Kingdom, June 1976.

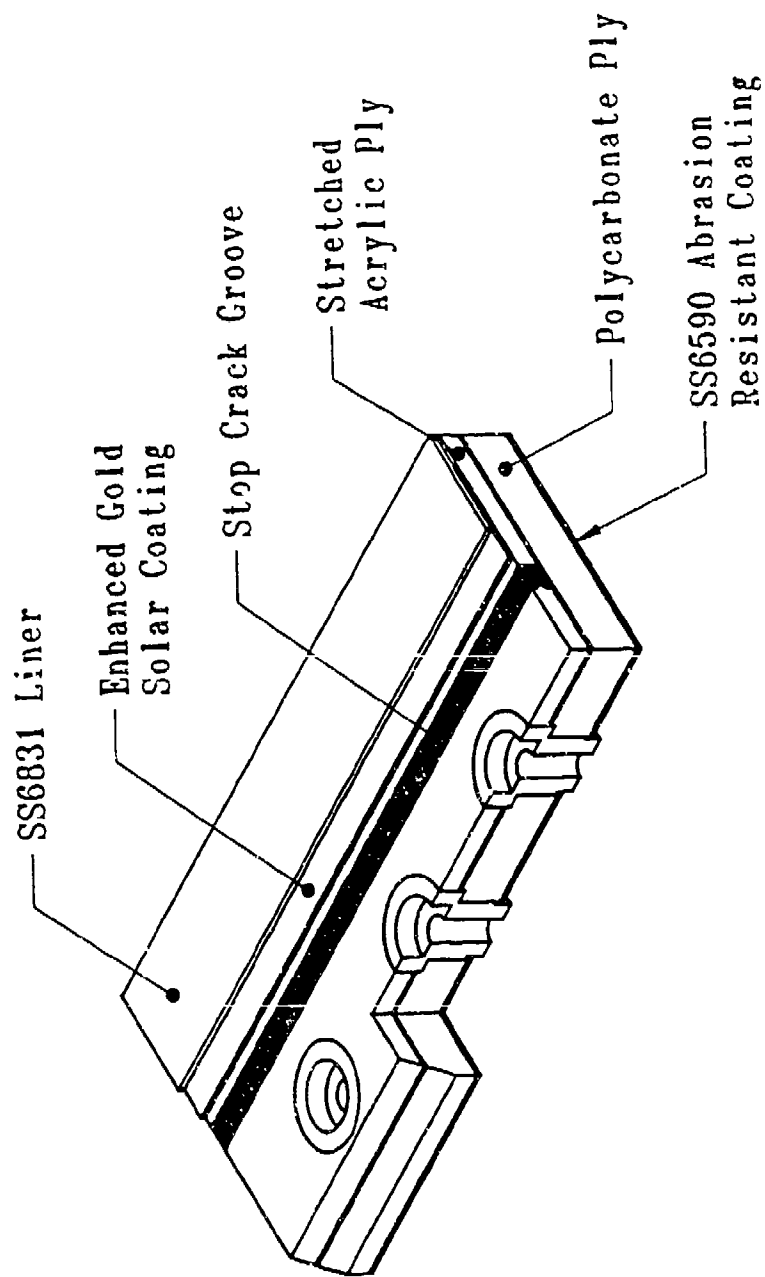


FIGURE 1 - EDS COATING SYSTEM

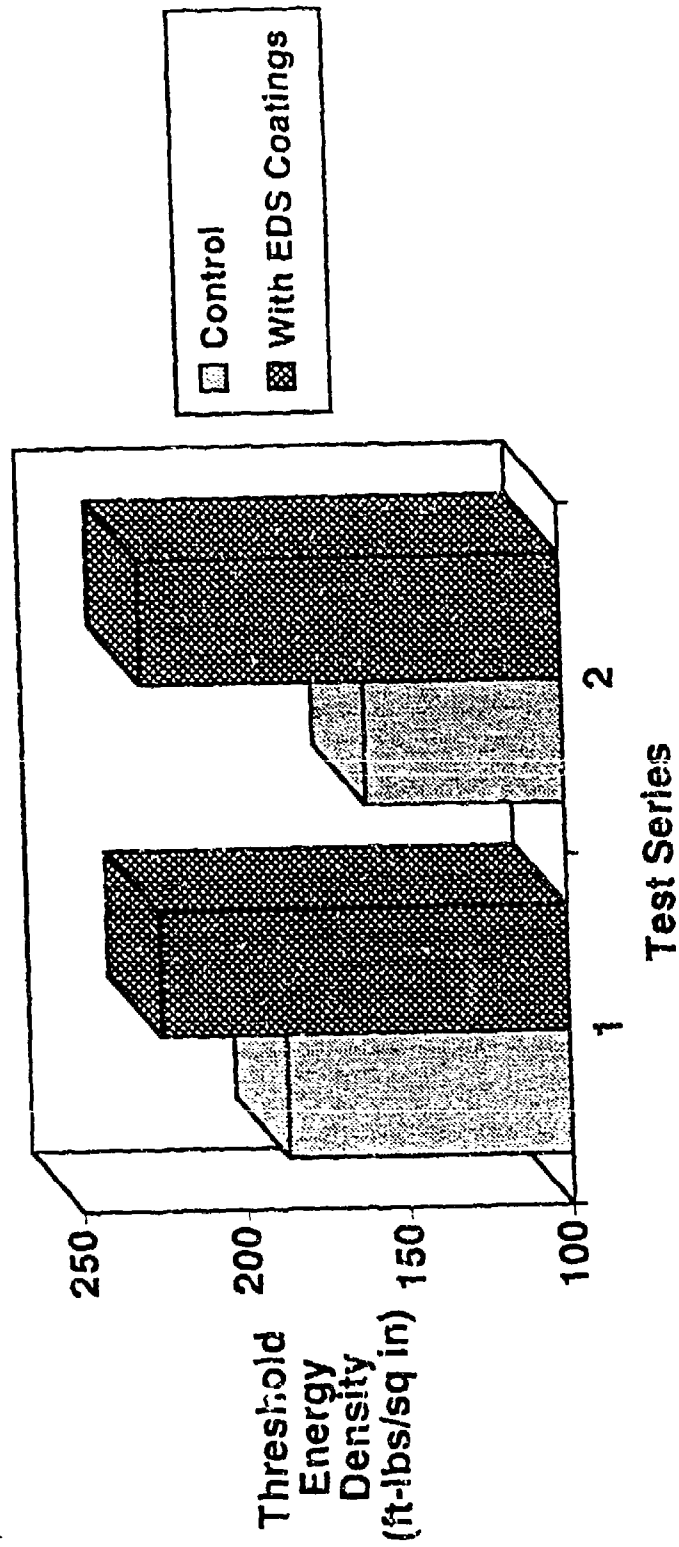


FIGURE 2 - SPECIMEN SCALE IMPACT RESULTS

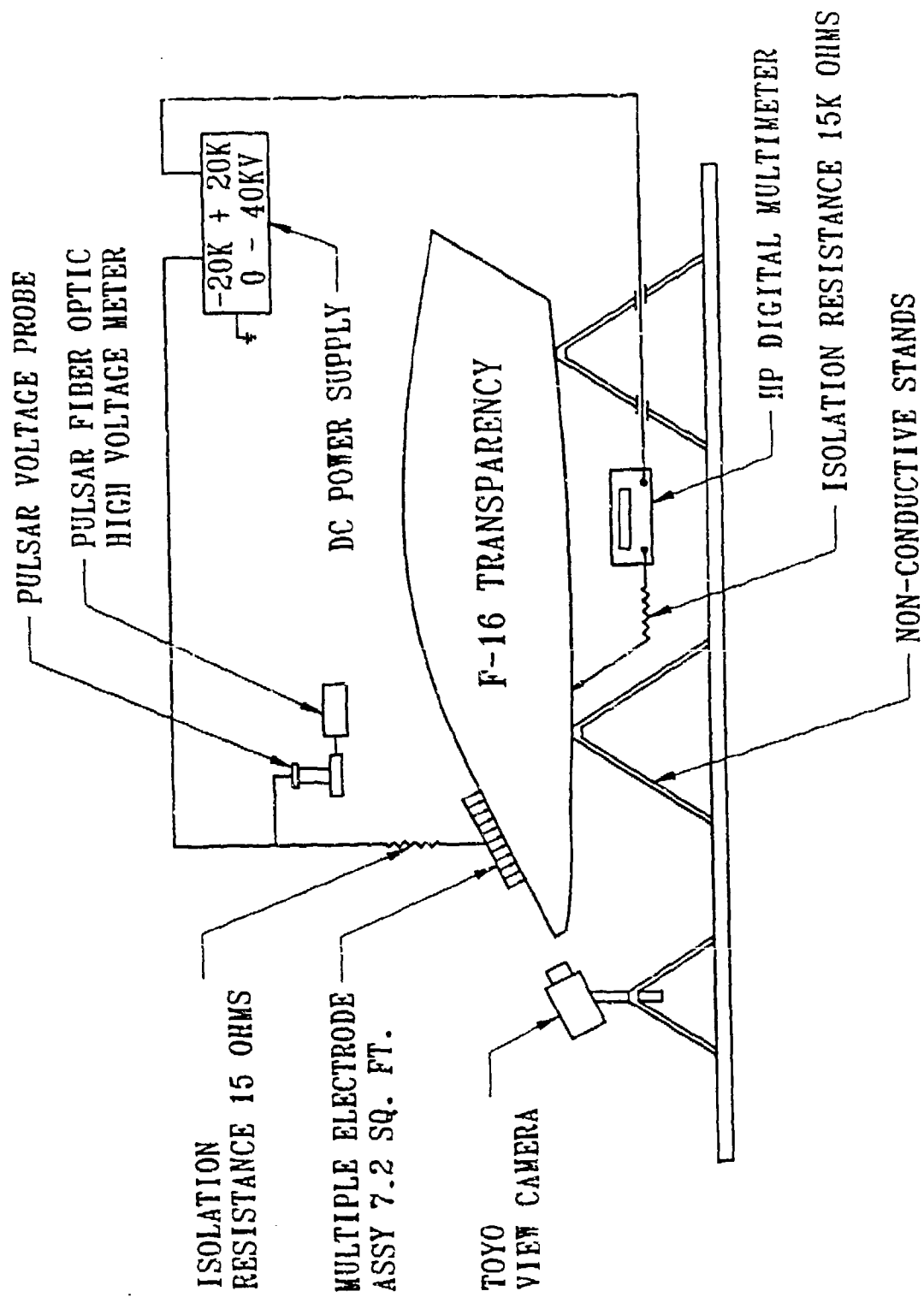
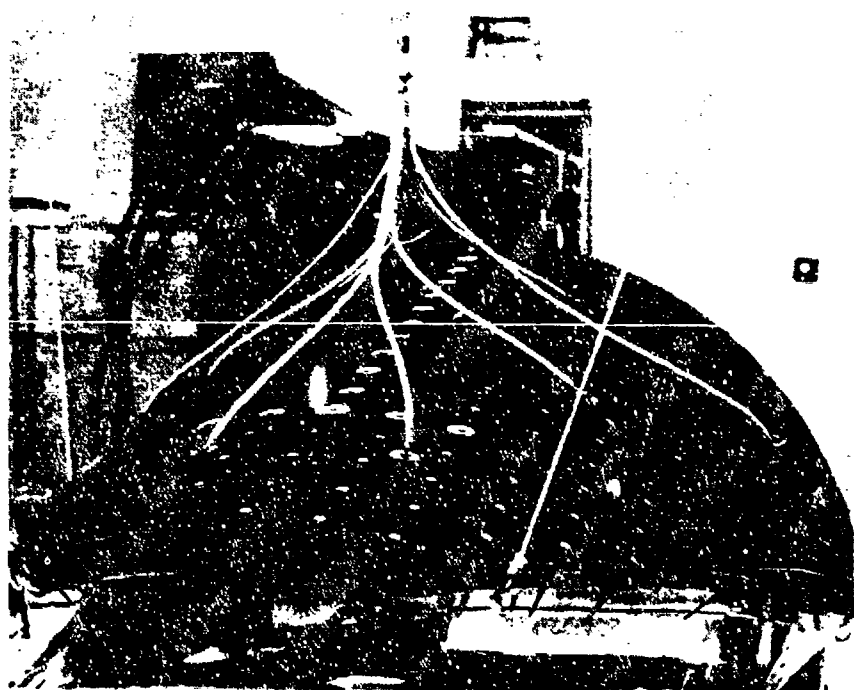


FIGURE 3 - ELECTROSTATIC TEST CONFIGURATION



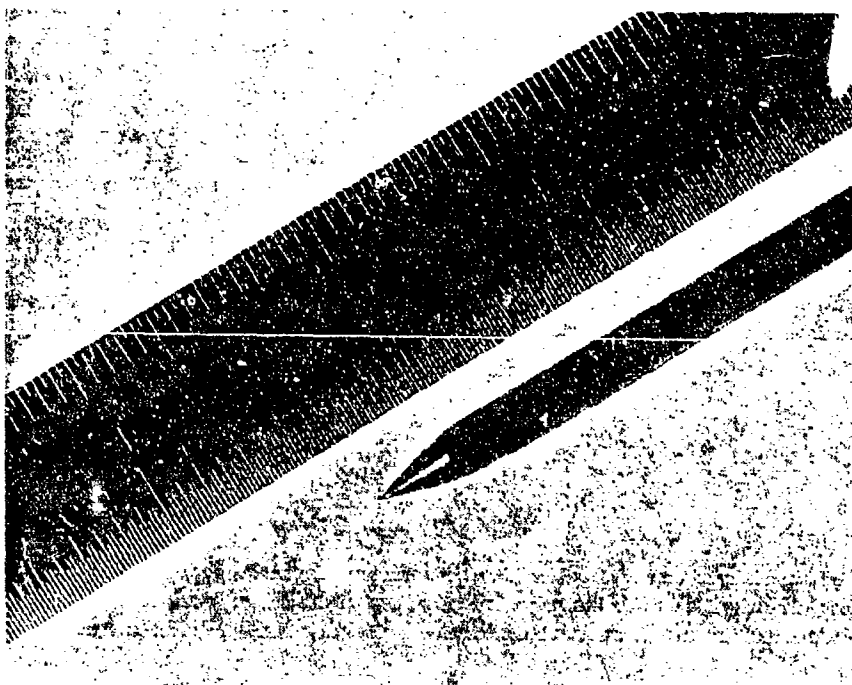
**FIGURE 4 - ELECTROSTATIC TEST EQUIPMENT SET-UP**



**FIGURE 5 - MULTIPLE ELECTRODE ASSEMBLY**

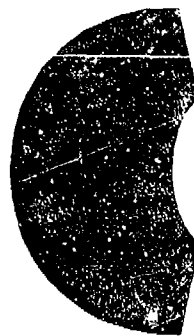


**FIGURE 6 - MULTIPLE ELECTRODE ASSEMBLY**



**FIGURE 7 - POINT ELECTRODE CLOSE-UP**

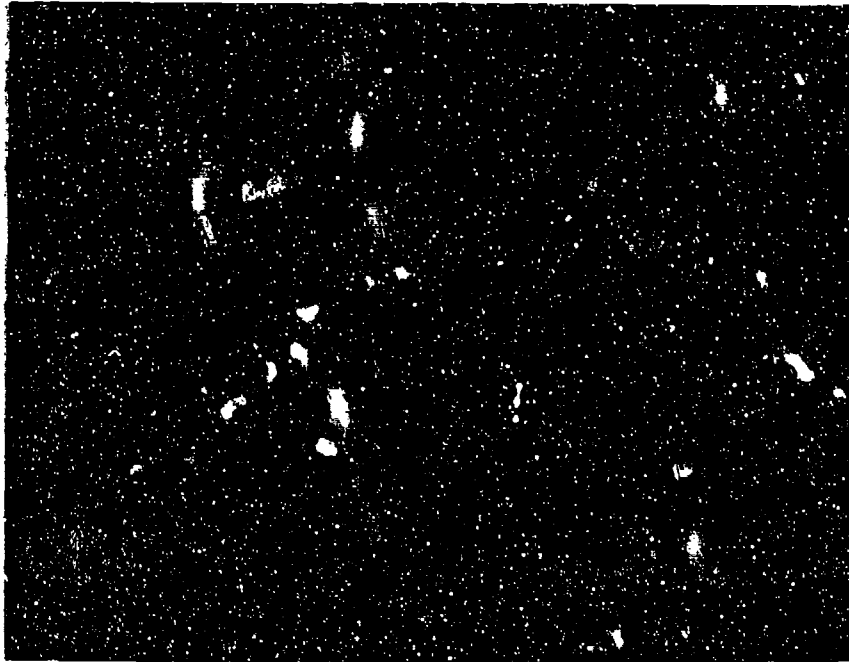
Frontal Area  
2.3 Sq.Ft.



Surface Area  
7.2 Sq.Ft.

FIGURE 8  
ELECTROSTATIC TEST  
PART SURFACE AREA vs. AIR STREAM FRONTAL AREA





**FIGURE 9 - ELECTROSTATIC DISCHARGE EVENT**



**FIGURE 10 - PINHOLE LOCATIONS ON TEST PART**

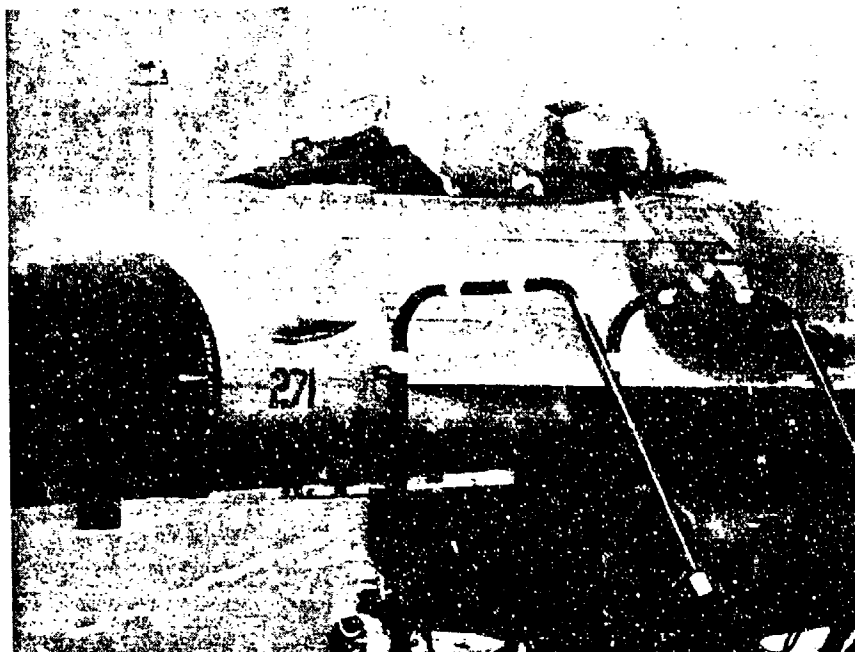


FIGURE 11 - EDS TEST AIRCRAFT

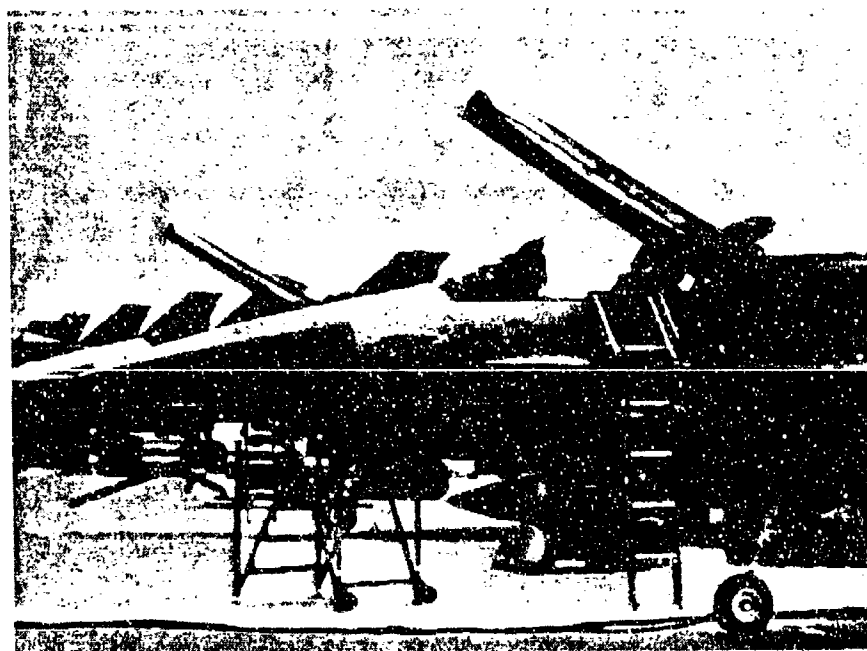
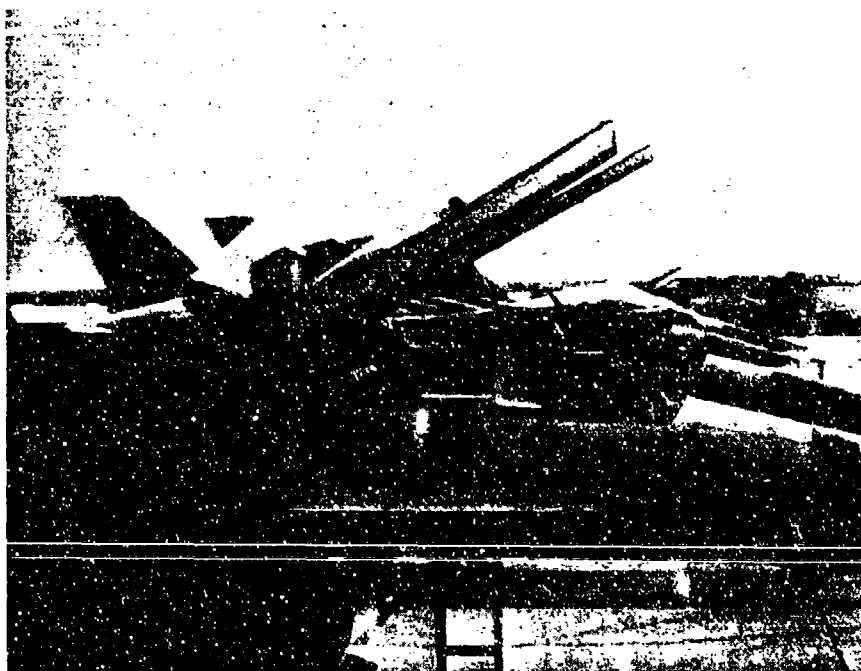


FIGURE 12 - EDS TEST AIRCRAFT



**FIGURE 13 - EDS TEST AIRCRAFT**

**TABLE 1**  
**FULL SCALE ELECTROSTATIC TEST RESULTS**

<b>Current (<math>\mu</math>amps)</b>	<b>Voltage (kV)</b>	<b>Surface Current Density (<math>\mu</math>A/sq.ft.)</b>	<b>Frontal Current Density (<math>\mu</math>A/sq.ft.)</b>	<b>Comments</b>
229	7.8	31.8	99.6	Corona audible
292	8.4	40.6	127.0	Corona visible
363	9.0	50.4	157.8	(2) pinholes in liner 0.070 in dia.

SESSION VIII

COMPUTER AIDED ANALYSIS- PART A

Chairman: R. McCarty  
Flight Dynamics Directorate  
Wright Laboratory

Co-Chairman: M. Gran  
Flight Dynamics Directorate  
Wright Laboratory

Coordinator: M. Bouchard  
University of Dayton

## TRANSPARENCY IMPACT SIMULATION: STATUS AND RESEARCH ISSUES

R. A. Brockman  
T. W. Held  
University of Dayton

# TRANSPARENCY IMPACT SIMULATION: STATUS AND RESEARCH ISSUES

R. A. Brockman & T. W. Held  
University of Dayton Research Institute  
Dayton, OH 45469-0110 USA

---

## INTRODUCTION

Computer simulation of transparency birdstrikes has reached an exciting state: computer technology and mathematical modeling techniques both are powerful enough that very large, detailed impact calculations can be made on a routine basis even on desktop computer systems. This improved analytical capability opens up new opportunities for exploring new designs, materials, and manufacturing methods for transparency system components. At the same time, many limitations exist in the current state of the art in transparency impact analysis, which call for careful and critical thinking by the engineering analyst.

In this paper, we review the current technology for performing analytical simulations of soft-body impact events. While the methods employed at various organizations differ in detail, a number of basic trends are quite clear; in what follows we will attempt to provide a realistic summary. In some technical areas, significant research issues exist which affect the reliability of these simulations in a fundamental way. For these subjects, we take this opportunity not only to identify the shortcomings of existing technology, but to emphasize the need for sensitivity experiments and parametric study in current applications.

## IMPACT SOLUTION TECHNOLOGY: CURRENT STATUS

This section reviews the primary ingredients of current impact simulation techniques, including physical models, approximation techniques, and solution technology. We confine our discussion to detailed analysis models, typified by finite element techniques, as opposed to many simpler techniques used for more preliminary design work.<sup>1</sup>

### *Solution Methodology*

Discretization techniques such as finite elements, finite differences, or assumed mode techniques lead to systems of algebraic equations, usually quite large in size, which must be integrated in time to determine the impact response. The choice of a solution method is crucial because it affects one's choice of physical models and discretization techniques rather dramatically.

In the past several years, *explicit solution methods* have emerged as the most effective choice for birdstrike simulation. Explicit techniques are markedly different from the more familiar *implicit* (matrix-oriented) solution procedures embedded in popular finite element packages such as NASTRAN, ANSYS, and MARC. The explicit approach employs no large matrices, advances in time by extremely small (sub-microsecond) time steps, and works best with very simple finite element approximations. To the analyst familiar with more conventional finite element methods,

the number of elements, degrees-of-freedom, and time steps used in an explicit solution all seem an order of magnitude too large.

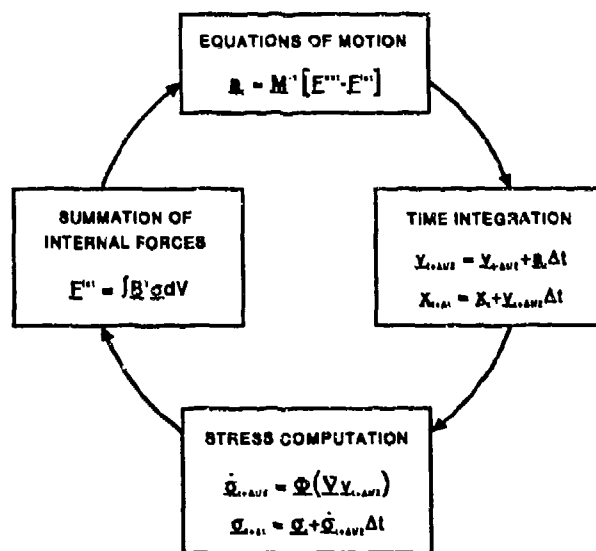


Figure 1. Explicit Solution Procedure.

The advantages of explicit techniques for soft-body impact analysis include the ability to employ more detailed material models, to consider complicated nonlinearities (contact and sliding, material failure) without numerical misbehavior, and to recover time history data in much more detail than is possible with conventional solution methods. Due to the absence of large matrix operations, the explicit solution data normally resides entirely in high-speed memory, with disk access limited to initial input and output dumps. Conventional, matrix-oriented solutions quickly become I/O-bound for larger models, making less efficient use of computer resources.

One factor limiting the rate of growth of explicit solution techniques has been lack of quality software. This class of methods originated in the high-energy physics community, with software being generated in-house by DOE<sup>2,3,4</sup> and Army<sup>5</sup> laboratories and their contractors. Other explicit codes<sup>6,7</sup> have originated in university environments, functioning primarily as research tools. In most cases, the software has been designed and written by engineers and physicists; the lack of a commercial market has, until recently, made user support a minor issue.

Commercial explicit finite element packages are beginning to appear, mainly in the form of modified versions of the earlier codes mentioned above. MSC/DYTRAN<sup>8</sup>, for instance, combines the explicit DYNA3D<sup>3</sup> code and the Eulerian continuum mechanics program PISCES<sup>9</sup>; HKS' ABAQUS/Explicit<sup>10</sup> appears to draw heavily from the methods and algorithms in the earlier PRONTO<sup>4</sup> code. LS/DYNA<sup>11</sup> is a commercial version of the Lawrence Livermore National Laboratory's original DYNA3D.



## *Finite Element Technology*

While it is possible to model the transparency impact problem using fully three-dimensional elements, this strategy is impractical in general. Several solid elements per layer are needed to match the stress accuracy of plate or shell elements, which in turn produces extremely thin elements and unacceptable time step limitations.

Researchers have made steady progress in improving the state of shell element technology<sup>12,13</sup>. In particular, the causes of fundamental problems such as shear and membrane locking are known, and several effective approaches have been identified for avoiding such pathological behavior. A basic deficiency of low-order, selectively integrated and hybrid elements, in the form of excessive twisting flexibility,<sup>14</sup> has been removed<sup>13</sup> to permit good behavior in both bending and twisting modes. Most shear-flexible shell elements still restrict attention to moderate transverse shear strains, but this assumption normally is reasonable in transparency applications.

Most of the remaining critical problem areas in plate and shell elements are related either to material modeling, or to the representation of laminated constructions. Each of these items is discussed separately in what follows.

Some strategies for bird impact modeling involve detailed finite element modeling of the impacting body with three-dimensional solid elements. A number of open questions exist, as discussed in the section on impact loading below.

### *Structural Modeling*

Some interesting problems persist in the representation of structural characteristics which do not appear explicitly in the nodal geometry of a finite element model. Examples include shell laminate stiffness properties, cross sectional properties of beam/arch elements, and discrete connections (fasteners) between components.

Perhaps the most difficult structural modeling problems arise in connection with laminated transparency sections. The extremely small stiffness of most interlayer materials permits relatively large transverse shear deformations in the interlayers, even when the overall rotation of the shell cross-section is quite small. The most dramatic effect is the resulting bending flexibility, which allows the shell to absorb impact energy more readily. Unfortunately, the kinematic assumptions embedded in virtually all common plate and shell elements assume a linear displacement variation through the thickness, resulting in excessive bending stiffness.

One solution to the laminate problem which has been used with some success is based on shear flexibility corrections<sup>15</sup>. This method captures the gross bending and twisting properties of the laminated section, and permits the estimation of transverse shear stresses layer by layer. For more complicated material models (specifically, those which include viscous effects), certain theoretical problems exist with the shear correction model. More general laminate models are needed to describe the transverse shear behavior of laminates with viscoelastic and inelastic layers.

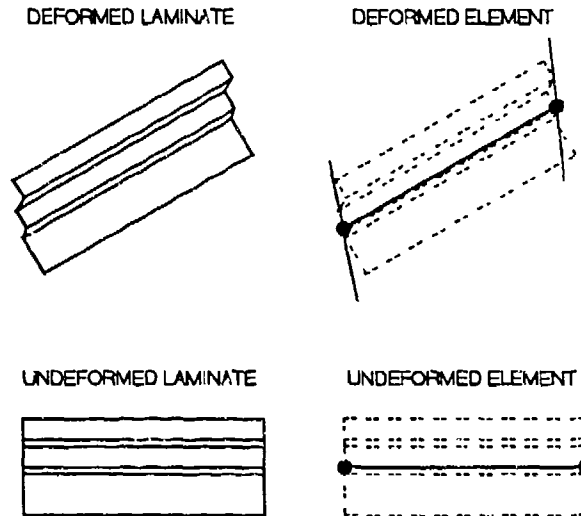


Figure 2. Deformation of a Laminate with Soft Interlayers.

Conventional beam elements are adequate for representing closed-section, metal arch designs. Composite arch designs, which may have significant off-axis stiffness, exhibit coupling effects which cannot be modeled correctly using traditional beam elements. A suitable theoretical basis for composite beam elements, which strikes an appropriate balance between beam- and plate-like response modes, is needed. An additional gap in existing element technology is open-section beam models (including cross sectional warping). Open-section formulations exist (and are available in a few general purpose codes) but have not been implemented in a general-purpose, explicit finite element code.

#### *Material Characterization and Failure Models*

The lack of adequate material models and data is the most serious weakness in our ability to simulate transparency impact response. Structural materials for transparency applications exhibit viscoelastic response, rate-dependent yielding and plastic flow, and failure characteristics which are poorly understood. Interlayer materials typically are nearly incompressible and nonlinear, and exhibit viscoelastic behavior which can become an important feature of the impact response.

The material models present in the current generation of impact analysis codes were developed with *metals* in mind, and cannot capture the complex behavior of high polymers under rapid loading. Figure 3 shows an example of a typical rate-dependent plasticity model with failure criterion based on von Mises stress. The yield point increases with strain rate, according to a power law formula. The strain hardening characteristics are reduced to a single parameter, the post-yield slope of the stress-strain curve, and the onset of failure is determined by the value of the von Mises stress.

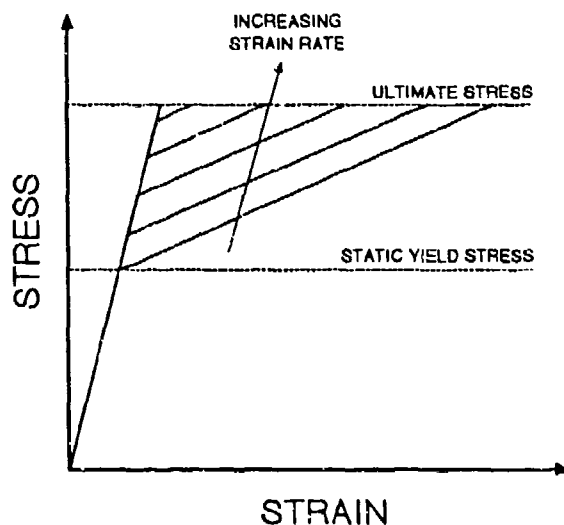


Figure 3. Rate-dependent Elastic-plastic Material Model.

Clearly such a model is inadequate to describe the time-dependent response of a viscoelastic, viscoplastic polymer under rapid loading. Figure 4 shows a common side effect of using such an oversimplified material model. As a single integration point (or element) reaches failure, the internal forces are redistributed throughout the section, which tends to increase the strain rate (and the strain) in the remaining material. With increasing rate, however, the failure strain in this remaining material decreases. The result is that the complete section "unzips" far too readily when isolated material points approach failure. This particular problem is a direct result of the failure criterion, which is sensitive to von Mises stress but not to mean stress or strain rate. If the material model parameters are defined in a way which reproduces the rate dependence of the *yield* stress, failure occurs at strains which are much too small.

For interlayer materials, the situation is equally poor. Many finite element impact codes contain models for incompressible materials, and models for viscoelastic materials, but not for viscoelastic materials which are incompressible (or nearly so). Furthermore, some viscoelastic models are restricted to a single viscous term, which implies a single characteristic relaxation time; such a model is incapable of capturing the damping effect of the interlayer during impact, which involves a wide variety of frequency components.

### *Impact Loading Models*

Description of the loading which occurs during a transparency birdstrike is a difficult question. The bird behavior is fluid-like, although the presence of material strength effects is evident in high-speed films of full-scale tests. A number of approaches have been attempted, each with some success: Lagrangian<sup>7,16</sup> (solid) and Eulerian<sup>8</sup> (pure fluid) finite element models of the bird; specialized numerical models based on potential flow solutions<sup>17</sup>; *ad hoc* loading models based

on overall momentum transfer<sup>18</sup>; and "free Lagrangian" techniques with variable mesh connections.<sup>19</sup>

One problem area common to all methods which model the bird explicitly is the issue of material modeling. Both real and artificial birds are used in transparency development tests, and our knowledge of the mechanical behavior of both types is rather poor. The range of velocities of interest for transparency birdstrikes encompasses both solid-like and fluid-like behavior, for both real and artificial birds, so that the choice of a basic material model is not always clear. Furthermore, little effort has been devoted to the experimental determination of mechanical properties for either real or artificial birds.

Lagrangian finite element bird models are attractive since they take advantage of existing element and modeling technology, including the contact algorithms needed to handle the interface conditions. Potential problems exist with Lagrangian methods when excessive mesh distortions occur, since the mesh (which is updated continuously) can become tangled. As a result, the simplest elements tend to work best. We routinely perform applications with tetrahedral Lagrangian elements in which the failure strains are on the order of 500 percent.

Eulerian finite element models of the bird, which employ a mesh fixed in space, remove the mesh distortion problem entirely. The most challenging aspect of the solution is in locating and tracking the boundaries of the body, which consist of both free surfaces and moving contact interfaces. An additional burden of the Eulerian solution is the need to solve the continuity equation, since mass is not conserved automatically in an Eulerian mesh. At present, there are few codes with the capability to address the birdstrike problem using Eulerian bird models, and most Eulerian models are limited to fluid-like behavior. MSC/DYTRAN has been used with success to model turbine blade birdstrikes, with the bird replaced by water. For transparency birdstrikes, which often involve much lower velocities, it may be necessary to introduce fluid viscosity and/or strength effects with this approach.

The "fluid element" technique originated by Martin<sup>19</sup> is quite interesting, since it has a finite element flavor, but without predetermined mesh connections. Internal forces are developed in response to changes in the mean radial distance to an element's nearest neighbors. Thus far this method has been used only for higher-speed (turbine blade) problems, but appears promising for use in transparency impact problems if a suitable material model can be introduced.

### *Visualization*

Ten years ago, engineers performing transparency impact simulations viewed color-coded plots and animated results sequences as luxury items, usually reserved for dog-and-pony show use. As our ability to perform more simulations, using more refined models, increases, we find that tools like animation are essential to a thorough understanding of our numerical solutions. With explicit solutions in particular, an impact simulation using a mesh fine enough for reasonable stress accuracy produces far too much data to be assimilated any other way.

From our perspective, the ability to animate analysis results within a short period of time has changed our basic approach to birdstrike simulation. Viewing an animated results sequence very

often reveals response which, with a small change in physical data, might change in character rather dramatically. Considering the uncertainties in the submodels for material behavior, laminate response, impact loading, and other details of the solution, some numerical experimentation is usually a wise idea. As such, the typical transparency impact study often involves several individual simulations even for a single impact condition. The results of a successful study consist not of precise numerical data for a single computed solution, but of information about the *response regime* for a particular impact situation.

Although the visualization tools needed to support high-quality animation have existed for quite some time, the task of animating engineering data in a highly automated fashion still is not well supported by the mainstream modeling and graphics packages. At present, we produce animations using a sequence of half a dozen software packages, moving data between two or three computer systems in the process. The work required to integrate these rather tedious steps into a seamless, automated process which deals properly with the finite element data and provides useful engineering data (as opposed to colorful images) is straightforward, but remains to be accomplished in full.

## RESEARCH IN PROGRESS

Having enumerated some of the shortcomings and problem areas in current impact simulation methods, we wish to mention some current work which addresses the most serious of these issues. The list presented below is not exhaustive, but provides a brief summary of the kinds of research efforts currently directed toward improving the state of transparency impact simulation techniques.

An effort is underway to combine nonlinear viscoelastic material models based on the free volume concept<sup>20</sup> with rate-dependent viscoplastic models<sup>21</sup> to represent the nonlinear behavior of structural plastics like acrylic and polycarbonate. In connection with this work, material tests (some conventional, some rather unusual) are being performed to collect data for several materials of current interest. A description of the approach, with some preliminary results, is available elsewhere in this proceedings.<sup>22</sup>

Definition of the impact loading, another major concern in most simulations, is addressed in a current effort at the University of Dayton.<sup>23</sup> In this work, emphasis is placed on separating the issues of "bird material modeling" and "structural material modeling." Most experimental soft body impact data involves structural plastics as the target which, for purposes of simulation, introduces the additional question of accuracy in the target material model. Our current attempts to isolate a suitable soft body model focus on reproducing rigid-target force data<sup>24</sup> and response data for metal targets<sup>25</sup> for which relatively accurate material modeling is possible.

In the area of transparency design software, a major effort is underway involving the U. S. Air Force, the University of Dayton, and PDA Engineering to integrate existing computational tools into a common software environment called ADP2.<sup>26</sup> This work encompasses both impact simulation software and graphics/animation tools, in addition to other major transparency design codes. A related effort is directed toward the management and manipulation of materials-related data, both for impact simulation and other transparency design tasks.<sup>27</sup>

## SUMMARY AND CONCLUSIONS

This paper provides a brief review of current capabilities for transparency impact simulation. Emphasis has been given to technology gaps, things that can go wrong, and open research issues.

The good news is that the state of the art in impact analysis has advanced tremendously during the past several years; very large, detailed models may be analyzed in a timely fashion, providing much more information to the analyst. On the other hand, modeling and sub-model uncertainties are such that numerical experimentation is needed routinely, and some improvement is called for in results presentation and graphics to assist the engineer in assimilating such a large volume of information.

We describe several current research efforts intended to address the problem areas identified with theoretical models and software tools. More detailed descriptions of this work may be found elsewhere in the proceedings.<sup>22,23,26,27</sup>

## REFERENCES

1. J. H. Lawrence, Jr., *Guidelines for the Design of Windshield/Canopy Systems*, AWFAL-TR-80-3003, Air Force Wright Aeronautical Laboratories, Wright-Patterson Air Force Base, Ohio, February 1980.
2. S. W. Key, *HONDO - A Finite Element Computer Program for the Large Deformation Dynamic Response of Axisymmetric Solids*, SLA-74-0039, Sandia National Laboratories, New Mexico, 1974.
3. J. O. Hallquist, *DYNA3D User's Manual*, Report UCID-19592 Rev. 4, Lawrence Livermore National Laboratory, California, 1988.
4. L. M. Taylor and D. P. Flanagan, *PRONTO 2D: A Two-dimensional Transient Solid Dynamics Program*, SAND86-0594, Sandia National Laboratories, New Mexico, 1987.
5. G. R. Johnson, D. D. Colby, and D. J. Vavrick, Three Dimensional Computer Code for Dynamic Response of Solids to Intense Impulsive Loads, *Int. J. Numer. Meth. Engng.* 14, 1865-1871, 1979.
6. T. B. Belytschko, R. L. Chiapetta, and H. D. Bartel, Efficient Large-scale Nonlinear Transient Analysis by Finite Elements, *Int. J. Numer. Meth. Engng.* 10, 579-596, 1976.
7. R. A. Brockman and T. W. Held, *X3D User's Manual*, UDR-TR-92-59, University of Dayton Research Institute, Ohio, April 1992.
8. H. Lenselink, *Introduction to MSC/DYTRAN*, MacNeal-Schwendler Company B.V., Gouda, 1992.
9. \_\_\_\_\_, *PISCES-3DELK*, Physics International, San Leandro, California.
10. \_\_\_\_\_, *ABAQUS/Explicit User's Manual*, Version 5.2, Hibbitt, Karlsson, and Sorensen, Inc., Pawtucket, Rhode Island, 1992.
11. *LS/DYNA*, Livermore Software, Inc., Livermore, California.
12. T. Belytschko, A Review of Recent Developments in Plate and Shell Elements, in A. K. Noor (ed.), *Computational Mechanics - Advances and Trends*, AMD Vol. 75, ASME, New York, 1986.
13. T. Belytschko, B. L. Wong, and H. Y. Chiang, Improvements in Low-Order Shell Elements for Explicit Transient Analysis, in A. K. Noor, T. Belytschko, and J. C. Simo

- (eds.) *Analytical and Computational Models of Shells*, CED Vol. 3, ASME, New York, 1989.
14. R. H. MacNeal and R. L. Harder, A Proposed Standard Set of Problems to Test Finite Element Accuracy, *Finite Elements in Analysis and Design* 11, 3-20, 1985.
  15. R. A. Brockman, *Simple Finite Elements for Layered Plates and Shells*, UDR-TR-87-111, University of Dayton Research Institute, Ohio, 1987.
  16. M. P. Bouchard and J. C. Davisson, Advanced Transparency Development for USAF Aircraft, *Proceedings of the AIAA/ASME/ASCE/AHS 34<sup>th</sup> Structures, Structural Dynamics, and Materials Conference*, La Jolla, California, 19-21 April, 1993.
  17. A. F. Storace, *Foreign Object Impact Design Criteria*, AFAPL-TR-78-81, Volume IV, Wright-Patterson Air Force Base, Ohio, 1985.
  18. R. E. McCarty, Three Dimensional Nonlinear Dynamic Finite Element Analysis for the Response of a Thick Laminated Shell to Impact Loads, *Proceedings of the AIAA/ASME/ASCE/AHS 26<sup>th</sup> Structures, Structural Dynamics, and Materials Conference*, Orlando, Florida, 1985.
  19. N. F. Martin, Jr., Nonlinear Finite Element Analysis to Predict Fan Blade Damage Due to Soft Body Impact, *J. Propulsion* 6(4), 445-450, 1990.
  20. W. G. Knauss and I. Emri, Nonlinear Viscoelasticity Based on Free Volume Considerations, *Computers and Structures* 13:123, 1981.
  21. S. R. Bodner and Y. Partom, Constitutive Equations for Elastic-viscoplastic Strain Hardening Materials, *J. Appl. Mech.* 42:385, 1975.
  22. G. J. Frank and R. A. Brockman, Constitutive Models for Rate-sensitive Transparency Materials, *Proc. Conf. on Aerospace Transparent Materials and Enclosures*, San Diego, California, August 1993.
  23. F. Stoll and R. A. Brockman, Assessment of Mathematical Bird Models for Bird Impact Analysis with an Explicit Finite Element Code, *Proc. Conf. on Aerospace Transparent Materials and Enclosures*, San Diego, California, August 1993.
  24. J. R. Barber, H. R. Taylor, and J. M. Wilbeck, *Bird Impact Forces and Pressures on Rigid and Compliant Targets*, AFFDL-TR-77-60, Wright-Patterson Air Force Base, Ohio, 1978.
  25. B. S. West and R. A. Brockman, *Evaluation of Bird Load Models for Dynamic Analysis of Aircraft Transparencies*, AFWAL-TR-80-3092, Wright-Patterson Air Force Base, 1980.
  26. J. Wuerer, M. Gran, and T. Held, Analytical Design Package, ADP2: A Computer Aided Engineering Tool for Aircraft Transparency Design, *Proc. Conf. on Aerospace Transparent Materials and Enclosures*, San Diego, California, August 1993.
  27. T. E. Mack, T. E. Kipp, T. J. Whitney, and M. Gran, The Use of Computerized Materials Data in ADP2, *Proc. Conf. on Aerospace Transparent Materials and Enclosures*, San Diego, California, August 1993.

CONSTITUTIVE MODELS FOR RATE-SENSITIVE TRANSPARENCY MATERIALS

G. J. Frank  
R. A. Brockman  
University of Dayton



# CONSTITUTIVE MODELS FOR RATE-SENSITIVE TRANSPARENCY MATERIALS

G. J. Frank and R. A. Brockman  
University of Dayton Research Institute  
Dayton, Ohio 45469-0110 USA

## Abstract

One major impediment to computer aided design and simulation for transparency systems is the lack of appropriate mathematical models for the most commonly used structural materials. Acrylic and polycarbonate compounds exhibit both viscoelastic (rate-sensitive modulus) and viscoplastic (rate-sensitive flow stress) behavior. Typically, such materials are analyzed using elastic-plastic or linear viscoelastic models, which capture only selected features of the material response. A related problem area is the uncertainty associated with the material test results for moderate strain rates ( $10^2$ - $10^3$  in/in/sec), at which uniform rates are not achievable in conventional tests.

This paper describes our recent efforts to construct mathematical material models for transparent structural materials. The objective of this work is to capture the essential features of the nonlinear viscoelastic-viscoplastic material response in a model compatible with existing finite element analysis methods. The paper outlines the theoretical basis of a general material model formulated for use in transparency impact simulation, where nonlinear and rate-dependent material behavior plays a central role in determining the structural response. Issues related to test data reduction and experimental evaluation of the model parameters are discussed as well.

## Introduction

Due to their high impact resistance glassy thermoplastics such as polycarbonate and acrylic constitute the most commonly used materials for aircraft transparencies. The primary reasons for their high impact resistance are high ductility, which allows structures made from these materials to undergo large deformation before failure, and nonlinear viscoelastic/viscoplastic response, which allows the materials to transform a great deal of impact energy into heat or internal energy.

The same nonlinear viscoelastic/viscoplastic behavior which gives these plastics good impact resistance also makes prediction of their response very difficult. In general, the state of stress and strain at any point in a structure is dependent on the temperature, pressure, and time history of loading. The types of equations developed to model the stress-strain relations are usually highly nonlinear and, hence, difficult to use for analyzing structures of non-simple shape.

The possibility of analyzing complex structures using constitutive theories which include all of the key features observed in tests have been made possible by recent order of magnitude

increases in computational speed and by the development of explicit finite element analysis (FEA) techniques. In explicit FEA, which is best suited for short duration dynamic or impact problems, a stress wave is propagated across a mesh of discrete regions, or elements, which represent the structure being analyzed. The time increment by which the solution can be propagated is limited by the minimum time for a stress wave to traverse the smallest element in the mesh. Thus, many thousands of time steps may be required to complete the problem. Because the time increments are very short, stress and strain states change by only small amounts within an individual increment. Fairly simple schemes may be employed to integrate nonlinear constitutive relations over each time increment, and one can use sophisticated constitutive models without the computational cost becoming prohibitively large.

Currently, nonlinear viscoelastic and viscoplastic model exist which, based on results presented in the literature, appear to encompass the types of material behavior observed in short time duration events. However, very little research has been done in combining these theories in a consistent manner to arrive at mathematical models which describe all of the phenomena of interest. Also, due to the complexity of the material response, those performing mechanical property tests on plastics have generally taken a rather narrow view of constitutive models (such as examining just viscoelasticity or just plasticity) and have not examined critically all of the phenomena which occur simultaneously.

The objective of the research outlined in this paper is to combine recent theoretical developments in viscoelasticity and viscoplasticity with information collected from a variety of mechanical tests to produce a correct mathematical model of the time dependent behavior of some common plastics. Accomplishment of this objective requires efforts in four areas. First, existing specialized theories must be adapted to form a complete model capable of characterizing the materials in both the elastic and plastic regimes. Second, mechanical tests sufficient for characterizing the response of the materials over the range of conditions typical of bird impact must be performed. Third, methods for identifying material model parameters from experimental data using numerical optimization procedures must be developed. Finally, the ability of the mathematical theory to represent the behavior of the specific polymers should be demonstrated for impact problems with practical applications. Accomplishments to date and planned efforts are described below.

### Material Model Development

For developing nonlinear viscoelastic/viscoplastic constitutive relations we are following a methodology similar to that of Kitagawa, Mori, and Matsutani<sup>1</sup>. This approach is to use an existing elastic/viscoplastic law which does not use a yield criteria and replace the linear elastic portion with a nonlinear viscoelastic relation. This approach was chosen for two reasons. First, it appears to be much simpler for implementation and experimental validation than viscoelastic/plastic constitutive relations which include a yield surface<sup>2,3</sup>. Second, and perhaps more importantly, this approach appeared to provide good agreement with experimental data for glassy polymers.

In this development we want to expand Kitagawa, Mori, and Matsutani's work in three areas. The goals for expanding this theory are: (1) include multiaxial deformation, (2) use a theory which is suitable for reversed loading, and (3) use a general nonlinear viscoelasticity theory which can model most of the pressure, rate, and strain effects observed in tests. Although properties of the materials are also a strong function of temperature, the constitutive relations are only being developed for isothermal conditions. One set of constitutive equations which should meet these goals can be obtained using the viscoplasticity theory developed by Bodner and Partom<sup>4,5</sup> and replacing the elastic portion with the nonlinear viscoelastic relations developed by Knauss and Emri<sup>6-8</sup>.

Numerical simulations will be used to determine whether these equations meet the three goals. If they do not, it may be necessary to use similar but more general viscoelasticity relations, such as those developed by Shay and Caruthers<sup>9</sup>, or more general viscoplasticity relations, such as those developed by Stouffer and Bodner<sup>10</sup> or Bodner<sup>11</sup>.

Regardless of which sets of viscoelasticity and viscoplasticity equations are used, we characterize the Cauchy (true) stress  $\sigma_{ij}$  and the strain  $\epsilon_{ij}$  as separable deviatoric (shear) and dilatational (bulk) components.

$$\sigma_{ij} = \bar{\sigma}_{ij} + p\delta_{ij} \quad (1)$$

$$\epsilon_{ij} = \bar{\epsilon}_{ij} + e\delta_{ij} \quad (2)$$

Furthermore, we assume that the deviatoric portion of the strain rate can be divided into viscoelastic and viscoplastic components:

$$\bar{\epsilon}_{ij} = \bar{\epsilon}_{ij}^{ve} + \bar{\epsilon}_{ij}^p \quad (3)$$

and that the dilatational portion is defined only by viscoelastic relations. With these assumptions, we can evaluate the viscoelastic and viscoplastic contributions to the total stress and strain rate.

### Emri-Knauss Viscoelastic Model based on Free Volume

The following equations identify the key relations used in defining the viscoelastic stress-strain relations. The dilatational and deviatoric stresses are related to their respective strain components by through relations similar to the integral relations of linear viscoelasticity:

$$p = \int_0^t K[t'(t)-t'(\xi)] \frac{\partial e(\xi)}{\partial \xi} d\xi \quad (4)$$

$$\bar{\sigma}_{ij} = \int_0^t G[t'(t)-t'(\xi)] \frac{\partial \bar{\epsilon}_{ij}^{ve}}{\partial \xi} d\xi \quad (5)$$

The bulk and shear relaxation moduli used in these relations are those typically used for linear viscoelasticity:

$$K(t) = K_0 + \sum_{n=1}^N K_n e^{-t/\tau_n} \quad (6)$$

$$G(t) = G_0 + \sum_{n=1}^N G_n e^{-t/\tau_n} \quad (7)$$

Nonlinearity is introduced into the relations through a reduced time relation which couples the dilatational and deviatoric stresses. The reduced time is computed as:

$$t' = \int_0^t \frac{d\tau}{\phi(e(\tau))} \quad (8)$$

where the shift function is related to the free volume through Doolittle's relation:

$$\log \phi = \frac{b}{2.3} \left( \frac{1}{f(t)} - \frac{1}{f_0} \right) \quad (9)$$

Finally, the free volume is linearly related to the dilatation:

$$f(t) = f_0 + C_v \epsilon(t) \quad (10)$$

This model, or a similar procedure developed by Schapery<sup>12</sup>, have been shown to provide most of the characteristics observed for glassy polymers undergoing monotonic loading<sup>7,13,14</sup>. The ability of these relations to model reversed loading conditions remains to be verified.

In these viscoelasticity equations, the stress components are derived from hereditary integrals. That is, the computation of stresses at time  $t$  requires the strain history for the entire interval  $[0, t]$ . It is possible, however, to recast these equations in a rate form<sup>15</sup>. This form eliminates the need for storing strain components at each time increment of an analysis and makes the relations suitable for use in an explicit finite element code.

For the preceding relations, the parameters which must be experimentally identified are:

Shear moduli	$G_n$ ( $n = 0, 1, 2, \dots, N$ )
Bulk moduli	$K_n$ ( $n = 0, 1, 2, \dots, N$ )
Relaxation times	$\tau_n$ ( $n = 1, 2, \dots, N$ )
Initial free volume	$f_0$
Doolittle constant	$b$
Free volume coefficient	$C_v$

## Bodner-Partom Viscoplasticity Model

The following equations identify the key relations used in defining the viscoplastic stress-strain relations. In these equations, as in many plasticity relations, it is assumed that the plastic portion of the deviatoric strain rate is proportional to the deviatoric stress:

$$\dot{\epsilon}_{ij}^p = \lambda \bar{\sigma}_{ij} \quad (11)$$

The factor of proportionality is defined in terms of the second invariant of the deviatoric stress,  $J_2$  and the "flow resistance,"  $z$ :

$$\lambda = \frac{D_0}{\sqrt{J_2}} e^{-\frac{1}{2} \left( \frac{z^2}{J_2} \right)^n} \quad (12)$$

where  $J_2$  is:

$$J_2 = \frac{1}{2} \bar{\sigma}_{ij} \bar{\sigma}_{ij} \quad (13)$$

The flow resistance is defined in terms of the first order evolution equation

$$\dot{z}(t) = m(Z_1 - Z(t)) \dot{W}_p \quad (14)$$

where the rate of plastic work is given by:

$$\dot{W}_p = \sigma_{ij} \dot{\epsilon}_{ij}^p \quad (15)$$

It should be noted that in Equations 11 and 15 the total and deviatoric plastic strain rates are the same since the dilatational component of plastic strain is assumed to be zero.

For the preceding viscoplasticity relations, the parameters which must be experimentally identified are:  $D_0$ ,  $n$ ,  $m$ ,  $Z_0$ , and  $Z_1$ .  $Z_0$  is the initial value for the flow resistance  $z$ .

## Mechanical Properties Testing

In order to develop appropriate material constants for any constitutive models, good data from mechanical properties tests are needed. Although a large amount of data from mechanical properties tests on glassy polymers is available in the literature, most of this data deals with only a single indicator of behavior, such as yield or failure, from a single type of test, such as tension or shear. In order to obtain complete descriptions of the behavior of a select group of polymers, a variety of tests are being performed on coupons from a single formulation of each polymer.

For this effort, tests are being performed on three materials which are representative of those used for aircraft transparencies. These are: Rhom & Hass Tuffak (MIL-P-83310)

polycarbonate, Polycast P-84 (MIL-P-8184) cast acrylic, and Swedlow (MIL-P-25690) stretched acrylic. All three materials were formed as 1/4-inch thick sheets. For purposes of describing the characteristics that we wish to capture, only results of tests on the stretched acrylic are shown in this paper. Results for the other materials follow similar trends, except cast acrylic has less ductility and polycarbonate has less rate sensitivity.

In general, a majority of constitutive models attempt to represent the response observed in a tensile test. Figure 1 illustrates some of the effects observed from nominal stress and strain data (that is, loads and deformations normalized by initial dimensions) for tensile tests on glassy polymers. As is the case with most materials, both the initial slope of the stress strain curve and the stress at yield (which we can take for this discussion as the location of an initial maximum of the nominal stress-strain curve) decrease with increasing temperature. These curves also illustrate the effect called strain softening, which is the decrease in nominal stress which occurs after yield for most glassy polymers.

Strain softening is generally accompanied by the formation of a "neck," or region of reduced cross section, which travels along the length of the specimen. The formation of this traveling neck can be predicted from the Considere' construction<sup>16</sup>, which is shown in Figure 2. If the true stress (that is, load normalized by the instantaneous cross section of the specimen as the tests progresses) versus nominal strain curve has only one tangent point, as shown in Figure 2a, then a traveling neck will not occur. However, if the curve has two tangent points, Figure 2b, then a traveling neck can occur. Although Figure 2b shows a decrease in true stress with increasing strain, only the two tangent points are required to initiate a neck, and the true stress may be monotonically increasing<sup>17-19</sup>. The presence of necking makes the determination of true stress and strain significantly more complicated since, even for test as simple as uniaxial tension, the stress and strain states are not constant over the length of a test specimen once necking commences.

Figure 3 shows true stress and strain data for both tensile and compression tests at two rates. This figure shows that, at a given temperature, the slope of the stress-strain curve is a function of strain rate, strain, and loading direction. Other measurements have shown that a tensile stress-strain curve for glassy polymers can also be strongly affected by application of a hydrostatic pressure<sup>20</sup>.

All of the preceding describe characteristics observed in monotonic loading tests. Reversed loading tests show other types of nonlinear behavior. Figure 4 shows stress versus time data from a series of tensile tests in which deformation was applied under strain control up to a preset strain level, unloaded back to zero and held at zero strain to allow relaxation to occur. The curves show that, for tests in which the peak stress does not exceed the initial peak in the nominal stress-strain curve, the stress relaxes to zero. This indicates that all of the deformation for strains in this range can be characterized as nonlinearly viscoelastic with no plastic deformation. For tests in which the stress does exceed the peak in the curve the stress does not relax to zero, indicating that plastic deformation begins near this apparent yield point.

In Figure 5 the stresses and strains shown in Figure 4 are plotted against one another. The hysteresis curves show highly nonlinear recovery. Cyclic tests at strain levels above yield

also show extremely nonlinear recovery<sup>21</sup>. The hysteresis shown in these curves indicates that large amounts of energy are being converted to heat or internal energy by the material. This energy conversion tends to rapidly damp out free vibrations of structures made with these materials, such as the free vibration of a transparency after bird impact. Accurate modeling of this nonlinear recovery is necessary for appropriately representing the response of transparencies subject to impacts which do not cause plastic deformation.

Figure 6 shows isochronous curves based on the initial loading portion of the data shown in Figure 4. Each curve is created by taking corresponding values of stress and strain at a specific time from a series of tests at different rates. A straight line on this plot indicates that the material follows the relations of linear viscoelasticity. It can be seen from Figure 6 (and has been observed from tests on a wide variety of glassy polymers<sup>22</sup>) that, for strains less than about 1%, the stress-strain trace can be approximated well by the relations of linear viscoelasticity. However, cyclic loading tests with peak strains between 1% and yield deviate from linear viscoelasticity rather rapidly.

In order to define parameters for material models which adequately include all of the effects described in the preceding paragraphs, it will be necessary to perform a fairly wide variety of tests. These types of tests can be classified in two general categories: "traditional" tests, which have simple, well-defined stress states (at least, up to yield) and are commonly used to identify properties of material, and "non-traditional" tests, which have less-well defined stress states or load histories but which are necessary to fully define the response of materials under complex load situations. The "non-traditional" tests are required because "traditional" types of tests often do not provide accurate representation of strain rate effects, and, in many cases, do not provide predictable strain rates at all.

The "traditional" tests will include standard tensile and compression load-to-failure tests, such as those for which data is shown in Figures 1 and 3, at strain rates up to 200/second. Unfortunately, some of the data measured by experimental stress-strain trace may not accurately represent the properties of the materials. The onset of plastic deformation may not always coincide with the peak in the nominal stress-strain curve. Also, the measured changes in initial slope of the stress-strain curve may be due to both changes in viscous response and elastic stiffness.

In order to define the yield and post-yield behavior, cyclic load and unload tensile tests, such as those shown in Figure 4, will be performed. Tensile specimens will be loaded to pre-set strain levels and subsequently unloaded. The strain levels will be increased until permanent deformation is measured at zero load (after sufficient time for creep to occur), indicating the onset of plasticity.

In order to distinguish changes in viscous response from changes in elastic stiffness, tensile tests with an oscillating strain will be performed. Specimens will be stretched or compressed at a low rate to a nominal strain level and a small oscillating load will be applied. The time lag between the applied load and the measured displacement will allow the determination of the viscous response and the amplitude of the stress-strain trace will allow a determination of the elastic stiffness. The tests will be performed at a variety of strain rates and

strains in the range preceding the onset of plasticity. The properties measured in the oscillating tests should validate those measured in the initial portion of the standard load-to-failure tests.

Since impacts of polymers usually generate strain rates on the order of  $10^2$  or  $10^3$  per-second, tensile property data at strain rates up to 1000 per-second will be generated using a split Hopkinson bar test. In this test a specimen is attached between two steel bars. The input bar is impacted, sending a compressive wave through the input bar, specimen, and output bar. The wave reflects off the end of the output bar, travels back through the output bar as a tensile wave and into the specimen. The strains in the input and output bars are measured throughout the test and used to compute the time history of deformation of the specimen.

The "traditional" tests described above have (up to the onset of plasticity) reasonably simple load histories and stress states which can be analyzed to provide direct estimation of some of the parameters required for any constitutive models. Since the goal of this research is to establish constitutive relations which predict the response of materials under multiaxial stress states, it will be necessary to perform some "non-traditional" tests (i.e. those which aren't performed in any standard set of material characterization experiments). The non-traditional tests will not be used to directly determine properties of the materials, but will form part of the database from which "optimized" material model parameters are developed. Two types of tests will fall into this category: tension-torsion and flatwise tension/compression.

Tension-torsion tests will be performed on thin-walled cylinders of material. The cylinders will be simultaneously stretched and twisted to produce a bi-axial state of stress. Different combinations of stretching and twisting will allow a series of stress states to be applied to the materials.

Flatwise tension/compression tests will be performed on coupons which are much larger in the two lateral dimensions than they are thick. The coupons will be bonded between steel plates and stretched or compressed. Mechanical response in these tests, which approximates a state of plane strain, is dominated by the dilatational components of stress and strain. These tests contrast with the standard tension and compression tests, where the response is dominated by the deviatoric components of stress and strain.

### Optimum Parameter Estimation

For selection of optimum parameters, test simulation models will be developed for each of the types of tests described in the preceding section. Parameter estimation will be performed in two steps. First, trial-and-error will be used to define parameters which reasonably approximate the results of the "traditional tests." Subsequently, a least squares error minimization procedure will be used to minimize the total error between the predicted and measured responses for both the "traditional" and "non-traditional" tests.

The least square error minimization process is outlined in Figure 7. Code for implementing this process is currently being developed using the ADS optimization software<sup>23</sup>.



In this procedure each of the test simulation models is run sequentially, based on the initial estimates of the material model parameters. Experimentally determined strains (or displacements) as a function of time are used as inputs to the models. The predicted stresses (or loads) are used to form an objective function which is defined as the weighted sum of the squares of the differences between the predicted and measured stresses (loads) at a given time and strain. Function minimization routines are used to minimize the objective function by modifying some or all of the material model parameters.

Although the approach described above appears relatively straightforward, there are some key difficulties which must be overcome to make the procedure feasible. The nonlinear equations make the possibility of multiple local minima of the error function highly likely. In fact, attempts by this author to use least squares error minimization on the linear viscoelastic series representations for moduli given in Equations 6 and 7 have shown that these functions alone produce an objective function with multiple local minima. In order to overcome these difficulties, it is anticipated that some of the parameters, such as the terms in the linear viscoelastic representations, will be determined directly from the test data and held fixed during the optimization process. The remaining parameters will serve as variables for optimization. The methods used in this research to resolve these problems should provide guidelines for obtaining parameters for materials other than those evaluated here or for other nonlinear constitutive relations.

### Material Model Validation

Of course, developing new material models is only useful if the models do a better job of representing structural response than currently-available models do. The ability of the constitutive relations and parameters selected to model short duration events will be evaluated using tests which have more complex stress states and/or loading histories than those used in developing the parameters for the models. The constitutive relations will be implemented in the explicit FE code X3D<sup>24</sup>. Impact-type tests will be performed and compared to predictions made with the FE code. Two tests suitable for this purpose at a coupon level are the three-point bend test and the free-falling dart impact test.

Three-point bending tests will be performed at cross-head rates up to 12,000 inch/minute. Both monotonic and cyclic loading tests will be performed. Loads and displacements will be measured throughout the tests. Good agreement between predicted and experimentally observed responses should provide confidence in the material model to match the modulus of the material at various loading rates and strain levels.

The free-falling dart test is a standardized test used for determining the impact resistance of plastic sheeting<sup>25</sup>. The test uses a metal impactor with a hemispherical tip which is dropped onto a flat sheet of plastic. Typically, this test is run as a pass-no pass test at a series of increasing velocities for determining the energy required to fracture a particular material. However, for ductile plastics impacted below the velocity which induces failure, a permanent

indentation forms. Good agreement between the predicted and experimentally observed post-test shapes for a range of tests velocities should provide confidence in the material model to predict yield and plastic deformation of the polymers evaluated for impact loading.

### Conclusions

Currently, nonlinear viscoelastic and viscoplastic models exist which, based on results presented in the literature, appear to encompass the types of material behavior observed in short time duration events. However, very little research has been done in combining these theories in a consistent manner to arrive at mathematical models which describe all of the phenomena of interest. The efforts currently underway will provide a general mathematical model of the nonlinear time-history dependent stress-strain relations for thermoplastics in the glassy state. In addition to advancing present analysis capabilities, this work will form a broad foundation for further investigation of the response of thermoplastics at moderate and large strains. Many related areas of analysis, such as long-term creep and stress relaxation, exist for which the results of this work may serve as a suitable starting point.

A second important result of this work will be the development of guidelines for, and the performance of, a set of tests for determining appropriate parameters for modeling the high-rate response of specific polymers. Numerical experiments will be made to determine the capabilities of nonlinear optimization procedures for defining "optimum" parameters for the model based on the test data. Although tests are being performed only on a few selected polymers, the guidelines will be general enough that the same strategy can be applied to other materials.

## References

1. Kitagawa, M., T. Mori, and T. Matsutani, "Rate-dependent Nonlinear Constitutive Equation of Polypropylene," *J. Poly. Sci.: Part B: Poly. Phys.*, 1989, 27: p. 85.
2. Naghdi, P.M. and S.A. Murch, "On the Mechanical Behavior of Viscoelastic/Plastic Solids," *J. Appl. Mech.*, 1963, 30: p. 321.
3. Ghoneim, H. and Y. Chen, "A Viscoelastic-Viscoplastic Constitutive Equation and its Finite Element Implementation," *Computers and Structures*, 1983, 17: p. 499.
4. Bodner, S.R. and Y. Partom, "A Large Deformation Elastic Viscoplastic Analysis of a Thick-Walled Spherical Shell," *J. Appl. Mech.*, 1972, 39: p. 751.
5. Bodner, S.R. and Y. Partom, "Constitutive Equations for Elastic-Viscoplastic Strain Hardening Materials," *J. Appl. Mech.*, 1975, 42: p. 385.
6. Knauss, W.G. and I. Emri, "Non-Linear Viscoelasticity Based on Free Volume Considerations," *Computers and Structures*, 1981, 13: p. 123.
7. Emri, I. and W.G. Knauss, "Pressure Induced Ageing of Polymers," in *Nonlinear Constitutive Relations for High Temperature Applications*, Vol. Conference Publication 10010, 1986, Akron, Ohio: NASA.
8. Knauss, W.G. and I. Emri, "Volume Change and the Nonlinearly Thermo-Viscoelastic Constitution of Polymers," *Poly. Eng. Sci.*, 1987, 27: p. 86.
9. Shay, R.M.J. and J.M. Caruthers, "A Nonlinear Viscoelastic Constitutive Equation: Yield Predictions in Multiaxial Deformations," in *Developments in Mechanics, Proceedings of the 20th Midwestern Mechanics Conference*, Vol. 14(b), 1987, West Lafayette, Indiana: Purdue University.
10. Stouffer, D.C. and S.R. Bodner, "A Constitutive Model For the Deformation Induced Anisotropic Plastic Flow of Metals," *Int. J. Engrg. Sci.*, 1979, 27: p. 757.
11. Bodner, S.R., "Further Developments of a Viscoplastic Constitutive Model for High Temperature Applications," in *High Temperature Constitutive Modeling - Theory and Application (presented at Winter Annual Meeting of the American Society of Mechanical Engineers)*, Vol. MD - 26, 1991, Atlanta, Georgia: ASME, Materials Div.
12. Schapery, R.A., "An Engineering Theory of Nonlinear Viscoelasticity with Applications," *Int. J. Solids Structures*, 1966, 2: p. 407.
13. Schapery, R.A., "On the Characterization of Nonlinear Viscoelastic Materials," *Poly. Engrg. Sci.*, 1969, 9: p. 295.
14. Caplan, E.S. and H.F. Brinson, *Nonlinear Viscoelastic Characterization of Polycarbonate*, NASA-CR-166351, March, 1982, NASA Ames.
15. Brockman, R.A., *A Nonlinear Viscoelastic Material Model with Pressure Ageing*, UDR-TM-90-12, April, 1992, University of Dayton Research Institute.
16. Young, R.J. and P.A. Lovell, *Introduction to Polymers*, 2 ed., London: Chapman & Hall, 1991.
17. Tugcu, P. and K.W. Neale, "Necking and Neck Propagation in Polymeric Materials under Plane Strain Tension," *Int. J. Solids and Structures*, 1987, 23: p. 1063.
18. Hutchinson, J.W. and K.W. Neale, "Neck Propagation," *J. Mech. Phys. Solids*, 1983, 31: p. 405.

19. Nimmer, R.P. and L.C. Miller, "Neck Propagation in Tensile Tests: A Study Using Rate-Independent, Strain Hardening Plasticity," *J. App. Mech.*, 1984, 51: p. 759.
20. Inoue, N., T. Nakayama, and M. Shimono, "Pressure and Strain-rate Dependence of Yield Behavior of Some Polymers," in *The 21st Japan Congress on Materials Research - Non Metallic Materials*, 1978.
21. Bordonaro, C.M. and E. Kremple, "The Effects of Strain Rate on the Deformation and Relaxation Behavior of 6/6 Nylon at Room Temperature," in *Winter Annual Meeting of the American Society of Mechanical Engineers*, Vol. 29, 1991, Atlanta, Georgia: ASME, Materials Division.
22. Orgorkiewicz, R., ed. *Engineering Properties of Thermoplastics*, 1970, Wiley-Interscience: New York, 318.
23. Van der Plaats, G. N., "ADS - A Fortran Program for Automated Design Synthesis (Version 1.10)," Engineering Design Optimization, Inc., Santa Barbara, CA, May, 1985.
24. Brockman, R.A. and T.W. Held, *X3D User's Manual*, UDR-TR-92-59, December, 1992, University of Dayton Research Institute.
25. ASTM, "Standard D-3029: Impact Resistance of Rigid Plastic Sheeting or Parts by Means of a Tup (Falling Weight)", in *Annual Book of ASTM Standards*, Vol. 8.02, 1985, American Society for Testing and Materials: Philadelphia.

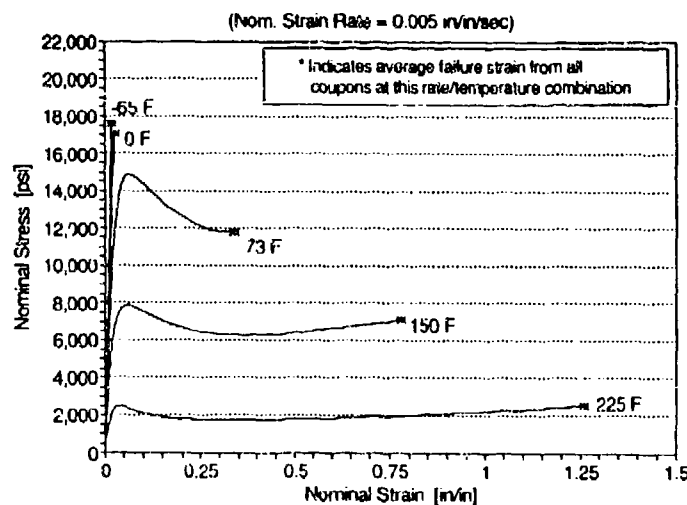


Figure 1 Effect of Temperature on Tensile Response of Stretched Acrylic

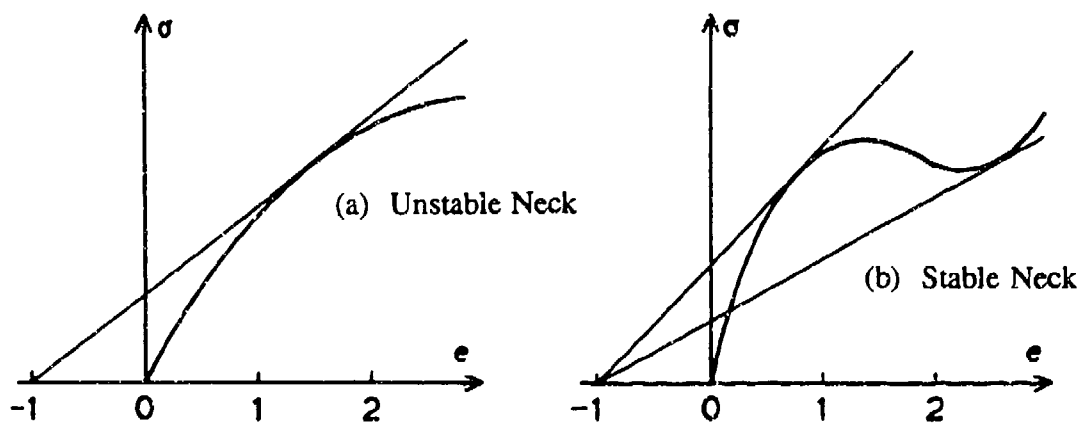


Figure 2 True Stress versus Nominal Strain Showing Considere's Construction

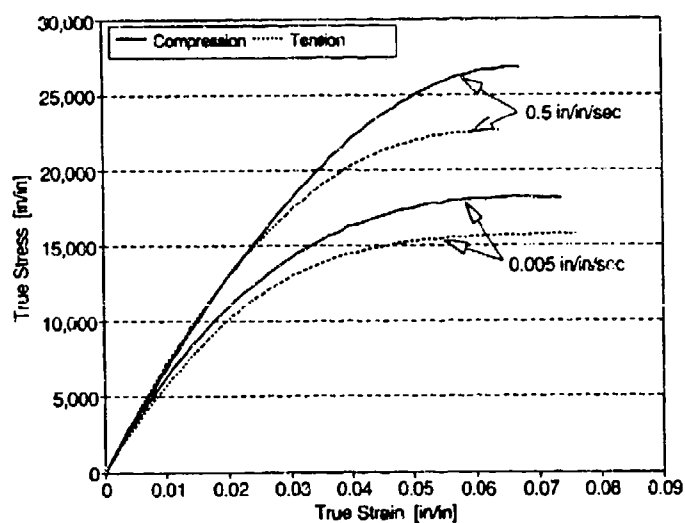


Figure 3 Effect of Rate and Loading Type on Response of Stretched Acrylic

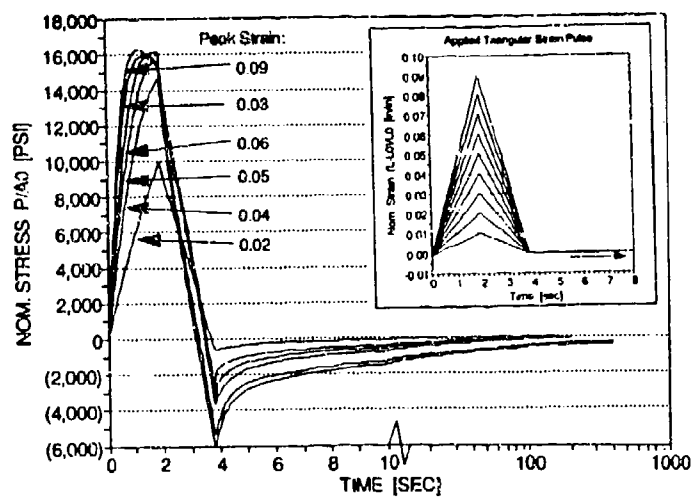


Figure 4 Response of Stretched Acrylic for Single Load-Unload Cycle

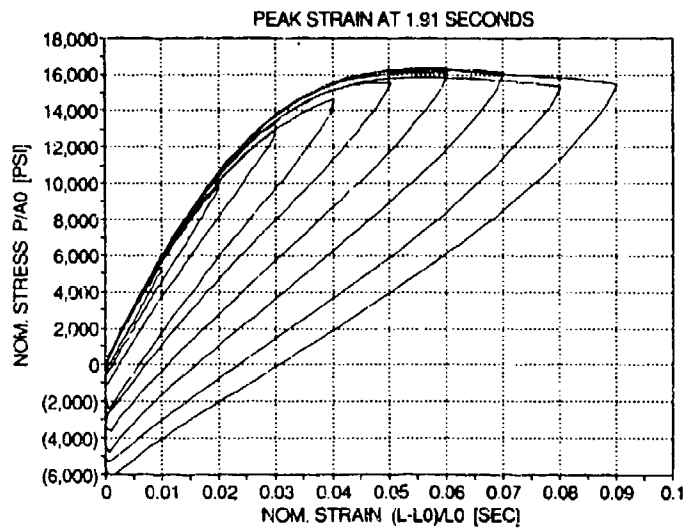


Figure 5 Hysteresis of Stretched Acrylic for Various Strain Amplitudes

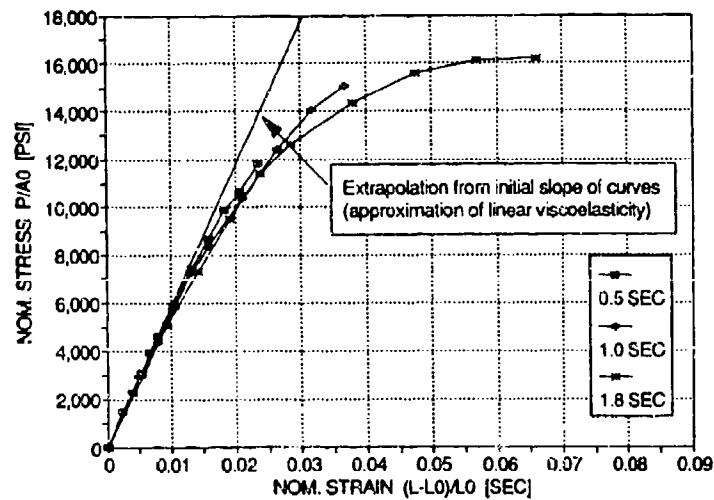


Figure 6 Isochronous Curves Showing Deviation from Linear Viscoelastic Resonse

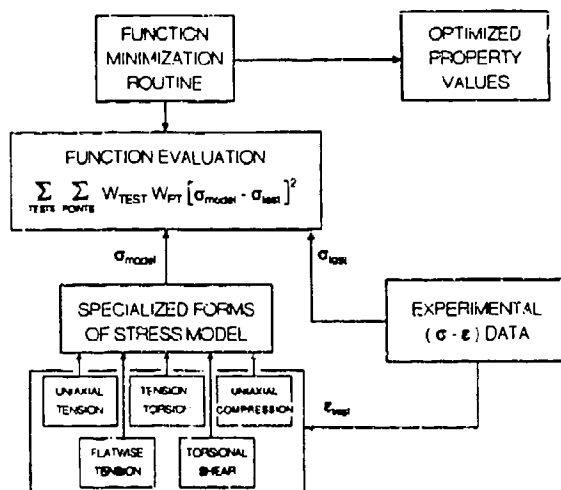


Figure 7 Constitutive Model Parameter Estimation by Least Squares Error Minimization

**ANALYTICAL SIMULATION OF LOW PRESSURE, THICK WALLED INJECTION  
MOLDING FOR AIRCRAFT TRANSPARENCIES**

**W. R. Pinnell  
Flight Dynamics Directorate  
Wright Laboratory**

**Analytical Simulation  
of  
Low Pressure, Thick Walled Injection Molding  
for  
Aircraft Transparencies**

William R. Pinnell  
WL/FIVR, WPAFB OH

for  
*Conference on Aerospace Transparent Materials and Enclosures*  
12 August 1993

**Abstract**

The Wright Laboratories effort to develop technology for direct forming of aircraft transparencies has demonstrated that thick walled optical quality transparencies can be injection molded utilizing low pressure, long cycle processes. Complexity and cost of molds dictate that the molding process and inputs to the mold design be generated analytically. Molded transparencies and molds should not be built by trial and error.

Commercial-Off-The-Shelf (COTS) computer software is available for simulating typical injection molding processes for thin walled parts. Major differences exist between the direct forming process for transparencies and typical injection molding. This paper addresses the application of one COTS simulation package to direct forming of aircraft transparencies. Typical injection molding is contrasted to expected cycles for molding aircraft transparencies. Modifications to simulating software which may be necessary for simulating transparency molding are highlighted. Utilization of molding simulation software as an integrated module of the aircraft transparency Analytical Design Package (ADP) developed by Wright Laboratories is also discussed.

**Introduction**

Under the current Air Force effort to develop technology which permits forming aircraft transparencies directly from molten bulk resin, injection molding has been demonstrated as a direct forming process. This capability generates potential improvements in life cycle cost and performance which is unprecedented in the history of transparency design and manufacturing. A discussion addressing these potentials and progress in demonstrating the new technology is included in reference 1. Identifying and simulating major differences in the demonstrated injection molding process and "normal" injection molding are critical to the success of this direct forming method.

The purpose of this paper is to introduce the analytical simulation of injection molding, to illustrate how these simulations are being confirmed as a part of the direct forming and frameless transparency technology development, and to discuss known disparities in existing simulation and the specialized process needed to produce aircraft transparencies.



Since transparency design for high performance aircraft must consider flight loads, impact resistance, and thermal environment, efficiency of design and manufacture demands that analytical structural and thermal simulations be utilized to perform design iterations prior to investing in tooling and prototype fabrication. Finite element analysis is common to analytical simulations for static loading, impact loading, thermal exposure, and injection molding. Because a common geometrical model can be shared by these simulations and because design iterations are coupled, the development of an Analytical Design Package (ADP) which integrates software packages has been added to the technologies currently being demonstrated. The major goal of the effort to develop technology for directly formed and frameless aircraft transparencies is the development and confirmation of the ADP represented in Figure 1. C-mold, a Commercial-Off-The-Shelf Software (COTS) package for simulation of injection molding is currently being integrated into the ADP.

The approach to confirming the ADP includes exercising the ADP to produce a directly formed frameless transparency design and the injection molding parameters which dictate the design of an injection mold, fabricating the mold, molding transparencies, testing these transparencies, and comparing test results to transparency design objectives. When the ADP objectives and test results are in agreement, the ADP can be applied to specific transparency requirements to produce directly formed transparencies for use in the field.

The transparency currently being utilized for ADP confirmation is generic in nature as opposed to a configuration for a specific flight vehicle. This transparency is referred to as the Confirmation Frameless Transparency (CFT) and is described in reference 1. The CFT configuration (Figures 2 and 3) will be utilized in illustrations which accompany the text of this paper.

#### Description of Injection Molding Simulators

Software for simulation of injection molding may be obtained in a package for this purpose alone or integrated with Computer Aided Design (CAD) packages or Computer Aided Engineering (CAE) packages which may include capabilities for geometric design, structural design, and numeric machine control typical of Computer Aided Manufacturing (CAM).

Injection molding software normally includes the capability for modeling geometry of the molded part, a capability for creating a finite element mesh for this geometry (see example in Figure 4) and routines for numeric solution of governing equations for fluid flow and heat transfer from resin as it fills the mold cavity, cools, and solidifies. Forms of finite element and finite difference methods are used to obtain solutions for generalized flow of viscous, compressible molten resin under non-isothermal conditions with asymmetric thermal boundary conditions. Calculations should be performed across the full thickness of the molded part for generalized thermal conditions and generalized flow. Various simplifying assumptions can be made when desired results are limited, or when molded parts or process can be simplified. One approach is to conduct a series of simulations with increasing analysis complexity and model refinement.

Successful simulation of injection molding is highly dependent on properties of the material to be molded. Further the methods for obtaining material properties

must be orchestrated with simulation modeling and analysis. A typical approach for simulation vendors is to offer testing of resin to the users of their software. Variations of thermal and rheological properties with temperature must be known for successful molding simulation. Handbook material property values are not generally considered adequate for rigorous simulation.

### Typical Process and Cycle

Injection molding includes forcing molten resin into a relatively cool cavity, holding the resin under pressure as it solidifies, and additional cooling to a condition compatible with removal of the molded part. The mold is then closed and the cycle repeated. Equipment required includes a method for melting and injecting resin, a mold enclosing a cavity and a resin delivery path, and a method for removing heat. Figure 5 is a schematic representation of a typical molding system. Additionally, a clamping method for holding the mold together during injection and permitting molded part removal is required.

Simplistically, the cycle can be characterized as having three stages: Filling, post filling, and mold open. Figure 6 shows these sequential stages.

#### Filling:

Filling is initiated when the mold is closed. A hydraulically driven displacement controlled ram (generally, the screw for masticating resin as it is melted also serves as the ram) forces resin injection. The filling stage is complete when the cavity is filled and ram motion has essentially stopped. Often, stopping the ram just before the cavity is completely filled is necessary to offset the effects of inertia and to prevent a very high momentary pressure which would result as the cavity is completely filled.

#### Post Filling:

After the cavity is filled, pressure (typically less than the maximum injection pressure) is maintained on the molten resin by the ram. As polymeric resin cools to solidification, resin volume decreases generating the need for entry of additional resin into the cavity. This phase in the post filling stage is referred to as packing.

When all of the resin in the cavity has solidified, the ram can be retracted, relieving pressure. During the remainder of the post filling stage, heat is removed until the temperature of the molded part has dropped to a level which insures stability of the molded part after removal from the mold.

#### Mold Open:

During this stage the mold is prepared for the next cycle. In simple cycles this may reflect the only time required for the mold clamping hardware to effect closing of the mold. When inserts are required in the molded part, they are placed in the mold at this time. In typical injection molding, part removal temperature is essentially equal to the mold temperature during filling so heating or cooling of the mold is not required during this stage.

### Macroscopic Flow and Cooling Considerations

As the molten resin fills the mold cavity, a flow front with meniscus like cross sectional shape is formed (see Figure 7). When the resin contacts the cool (relative to melt temperatures) cavity wall a thin solidified skin is immediately formed. As the flow front progresses, the thickness of solidified resin previously formed thickens at a rate which depends on the rate of removal of heat from the resin and the volumetric flow of the new melt. This concept points out several very important situations:

As frozen resin at the walls thickens, flow cross section area decreases, and higher pressure is required to maintain flow. This effect is prominent in molding of thin walled parts. At some pressure level the clamp holding the mold together will be defeated and the part will flash with resin extruding outside the cavity and compromising process control.

Ram displacement control must be programmed to maintain volumetric flow to adequately fill the cavity while preventing excessive friction heating which will occur if the flow area is excessively reduced due to the thickness of frozen resin at mold walls. At some temperature level the resin will be degraded.

After filling, resin volume decreases as the resin cools, , requiring more resin to enter the cavity. This resin must flow through cavity walls near the gate where frozen skin has been building in thickness since the beginning of the filling process. If the demand for additional resin due to cooling cannot be met, the frozen skin will pull away from the mold wall to offset volume decreases. A surface defect in the molded part known as "sink" will result.

Remedies for these concerns can be applied. Design of the molded part and the mold can prevent the need for filling large volumes through smaller volumes, multiple gating arrangements can shorten the length of injection paths, or the mold could be differentially heated. Predicting these situations and application of effective remedies can be part of the design stages if simulation is used.

#### C-Mold, an Injection Molding Simulation Package

The software currently being considered by WL/FIVR in the development of direct forming technology and specifically for ADP integration is a COTS package available from AC Technology, Inc., Ithaca New York (reference 3). This package is well developed for conventional injection molding of thin walled parts. C-Mold contains three simulation programs: C-Flow, C-Pack, and C-Cool.

#### C-Flow

C-Flow addresses only the mold filling. This analysis considers generalized incompressible flow of a viscous polymeric melt under non-isothermal conditions. Thermal boundaries are assumed to be symmetrical. The analysis seeks numerical solution for pressure and temperature fields and tracks moving melt fronts.

Potential problems related to filling the mold can be studied with minimal input from the user. Short shots, weld lines, and air traps can be discovered.

Optimum process conditions including melt temperature and filling time can be developed. A WL/FIVR study comparing shapes of intentional short shots and predicted flow front shape and position confirmed the validity of this type of modeling and analysis for predicting flow front junctures (weld lines) and air traps in sub scale panels with thickened edges. Figure 8 illustrates C-Flow indication of an air trap near the center of the CFT aft arch when latch inserts are not modeled. This air trap is not indicated (Figure 9) in C-Flow simulations of the CFT when latch inserts are included in the thickened sills. Flow front contours in Figure 9 also indicate the effects of inserts on flow front velocity in thickened sills.

A simplified version of filling simulation is included in C-Mold as C-Flow EZ. This simulation requires minimal user input and computer time. The geometric model and finite element mesh can be checked out and a profile for controlling ram speed is suggested.

### C-Pack

C-Pack simulates the entire molding process including fluid flow and heat transfer within the polymer as it fills the cavity, solidifies during the packing process, and cools to a temperature suitable for part removal from the mold. Mold wall temperature is not varied during the C-Pack analysis. If a C-Cool analysis has preceded the C-Pack simulation, a temperature distribution over the mold is used. If no C-Cool distribution is available, C-Pack uses an average mold wall temperature value based on temperatures in cooling channels if channels are included in the finite element model. If channels are not modeled, an average temperature value based on coolant manifolds is used.

C-Pack can be utilized to improve the current mold design, optimize packing pressure profile and duration, determine overall part weight, and verify flow orientation.

As an example of C-Pack output, Figure 10 shows temperature variation through the thickness of CFT nodes at 1040 seconds into the cycle time. A much higher temperature exists at the center of the 2 inch thick aft arch than at nodes in the optical area where the thickness is .75 inches. Also it is obvious that the pack/hold pressure should not be removed at this time since the aft arch has not cooled significantly.

### C-Cool

Based on a cooling channel network which can be geometrically modeled utilizing C-Mold software and techniques, a program for obtaining flow rate and pressure drop in each cooling channel element runs as a part of C-Cool. Using the flow rates, C-Cool calculates the heat transfer coefficients for heat exchange between the mold and the coolant. In addition to this heat transfer, heat transfer within the polymer melt and heat transfer within the mold material is considered. The analysis matches the temperature and heat flux at the mold/melt interface. Direct output includes mold wall temperature and heat flux distributions, polymer bulk temperature, and heat load from the molded part. Heat removed by each channel is predicted and can be used to size pumps and temperature controllers. Uneven cooling when comparing cavity and core walls can be identified.

When C-Cool is run prior to C-Pack, a file is generated which permits C-Pack to utilize a more realistic temperature distribution at mold walls. Without the C-Cool result, C-Pack will reflect the same average temperature on cavity and core walls. With this improvement in thermal boundary condition, improved C-Pack simulation can be expected.

Figure 11 shows the CFT C-Mold model including cooling channels and a distribution of mold wall temperature during the filling.

### CFT Molding

Efforts are currently underway to develop a molding process for directly formed frameless transparencies at Envirotech Molded Products, Salt Lake City UT. A more detailed discussion of this effort is included in reference 1. For this development a unique mold and Heating-Cooling (H-C) system have been prepared and installed at the Envirotech facility. Some of the mold and H-C features which may impact the simulation of injection molding for aircraft transparencies will be discussed here.

The CFT is a large molded part, but is not unprecedented in size. Envirotech has extensive experience in molding items which are much larger (reference 2). Relative to many large injection molded parts the CFT is very simple, requiring no complicated ribs, bosses, sharp corners or flanged openings. Figures 12 and 13 are photographs of the CFT mold cavity and core. The combination of requirements for transparency, impact resistance and wall thickness which varies from thick (.75 inches) to very thick (2.25 inches) makes molding the CFT a unique challenge. A collapsing core has been incorporated into the mold for demonstrating the capability to mold large objects which would "wrap around" or trap a one piece core.

The first 80 shots at Envirotech will be made to develop molding process. The starting point for these shots will reflect the process developed during the molding of about 500 flat and conical panels which were sub scale, but incorporated most of the CFT features and requirements. Based on this experience, expected successful process parameters for CFT molding are as follows:

Melt temperature	560 deg F (normal for polycarbonate)
Mold temp during fill	300 deg F (avg for 8 zones, unusually high)
Injection pressure	1000 psi (low for simulating software)
Total time for resin at melt temp	45 minutes (unusually long)
Filling time	60 seconds (long for simulating software)
Pack/hold pressure & cooling	50 minutes (long for simulating software)
Mold open time	10 minutes (long for simulating software)

The H-C system developed for the CFT (and anticipated subsequent transparency molding) has the capability for independently heating and cooling eight mold zones. This is accomplished by maintaining two constantly flowing oil

circuits. The hot oil circuit can be maintained at a maximum of 500 deg F and the cold oil circuit can be kept at a temperature as low as 37 deg F. Set temperatures and temperature ramps are achieved for each mold zone by a feed back control system which, based on temperatures sensed in input lines to each zone, cycles a controller which controls flow rate and alternates flow from the hot or cold circuit to achieve the desired temperature set values at programmed times. As many as eight temperature ramps can be programmed for each of the eight mold zones during the molding cycle.

As a simulation system C-Mold has the capability to model independent zones (manifolded coolant channels) in the mold, but the temperature and flow rate of coolant is constant for the cycle and the temperature is not normally greater than the temperature for opening the mold. Normally simulated systems are for cooling (removing the heat brought to the mold by the molten resin).

Low injection pressure anticipated for the CFT molding cycle is representative of the 750 psi pressure used to mold the sub scale panels. Pressures ten to twenty times these values are utilized in most injection molding and the simulation routines are written for that magnitude. In C-mold, 1,000 psi and the resulting filling times are considered beyond "reasonable" limits. Low injection pressure results in several advantages for transparency molding. It is suspected that long time intervals at melt temperatures can be better tolerated by the resin if the resin is not subjected to shear and friction associated with being forced through small gates and between thinly spaced mold walls at high velocity. Transparencies are thick walled and are relatively simple shapes with a minimum of corners or other restrictions to the flow of resin. A major driver for conventional injection molding is high production rate which dictates high pressure and short cycles. At present, the motivation to make more than one transparency per hour is not great.

Because the wall thickness of the typical aircraft transparency is thick compared to typical injection molded parts, the effect of the thickness of frozen resin at the mold wall has minimal effect on the resin passing through during the mold filling when these velocities are highest. Mold zoning and the capability for programmed changes in heating and cooling during the molding cycle are expected to permit filling of thick sections at the end of long injection paths and to enhance resin flow to these areas during packing thereby minimizing sink. Also, to promote filling and surface quality, zones near the gate may need to be heated to temperatures greater than the mold open temperature which is normal for simulated injection molding. The H-C system developed for transparency molding will be utilized to accomplish this during the mold open phases of each cycle.

The current simulation of flow front and associated benefits is expected to be applicable to the injection molding of transparencies. Utilizing present programs for simulations strongly related to low injection pressures and changes in the temperature of coolant during the molding cycle will probably require changes to the software or changes in the methods for modeling the molded parts, molds, and systems for thermal control.

The CFT mold has been fitted with 33 thermocouples and 8 pressure transducers which are monitored continuously through each molding cycle. Molding personnel may scan current values or view time histories of these data during the molding cycle. Data from these sensors can be utilized singly or in arrays to adjust subsequent cycles or to assess causes for molded transparency defects and the

effects of cycle changes on the quality and performance of molded parts. The effectiveness of simulation will also be assessed utilizing this data.

### Conclusions

1. Simulation of injection molding as the direct forming process for aircraft transparencies permits identification and correction of problems related to transparency design, mold design and process parameters during transparency design. This prevents the need for costly post fabrication modification of molds and other molding hardware. Simulation capability is critical to the success of injection molding of aircraft transparencies.
2. Commercial-Off-the-Shelf simulation packages are currently capable of simulating the filling phase of anticipated aircraft transparency injection molding cycles.
3. Successful simulation of packing and cooling phases of anticipated aircraft transparency injection molding cycles have not been demonstrated. Modifications to existing software to obtain useful simulation of these phases is believed to be necessary.

### Recommendations

1. Utilize currently available mold, heating-cooling system, and instrumentation to get experience in molding CFT full scale frameless transparency (this molding is currently being conducted).
2. Augment current molding efforts with simulations and study simulation and actual molding results to identify disparities between simulation and molding.
3. Involve vendors of simulation software packages in the resolution of mismatches in current simulation programs and the process which is being developed for directly formed aircraft transparencies.
4. Customize, if necessary, at least one simulating software package for maximum effectiveness in simulating injection molding of aircraft transparencies. This customization should reflect molding experience gained during current molding efforts to develop molding process.

### References

1. Pinnell, W. R., "Development of Directly Formed and Frameless Aircraft Transparency Technology, an Overview," to be published with the proceedings form A Conference on Aerospace Transparent Materials and Enclosures, San Diego CA, 9 - 13 August 1993.
2. Mills, C., and Pinnell, W. R., "Injection Molding as a Direct Forming Method for Aircraft Transparencies," to be published with the proceedings form A Conference on Aerospace Transparent Materials and Enclosures, San Diego CA, 9 - 13 August 1993.
3. ———, "C-Mold v3.2 Reference Manual and Users Guides," Advanced CAE Technology, Inc., January 1993

DIRECTLY FORMED  
FRAMELESS AIRCRAFT TRANSPARENCY  
TECHNOLOGY DEVELOPMENT

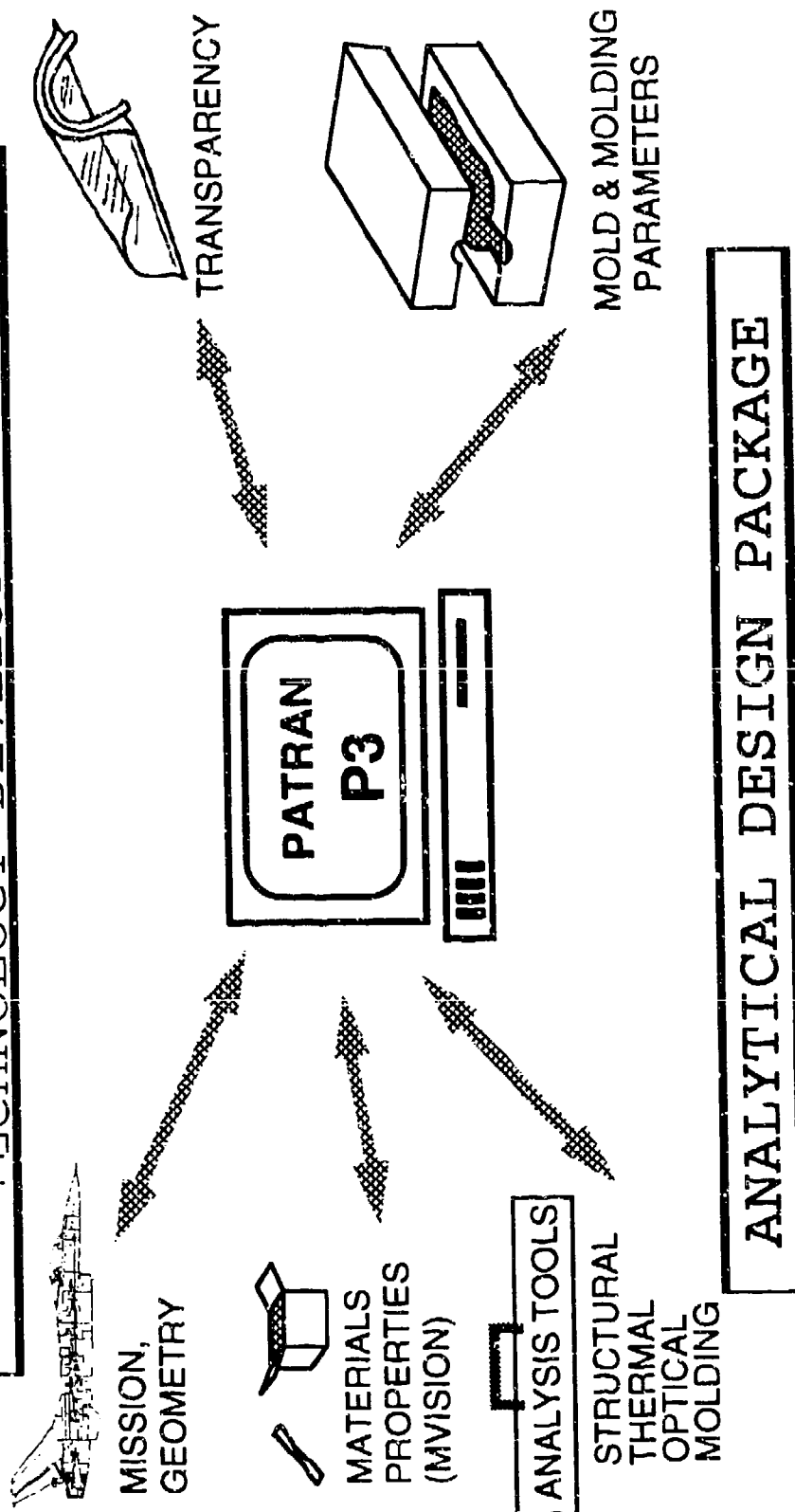


FIGURE 1



# CONFIRMATION FRAMELESS TRANSPARENCY

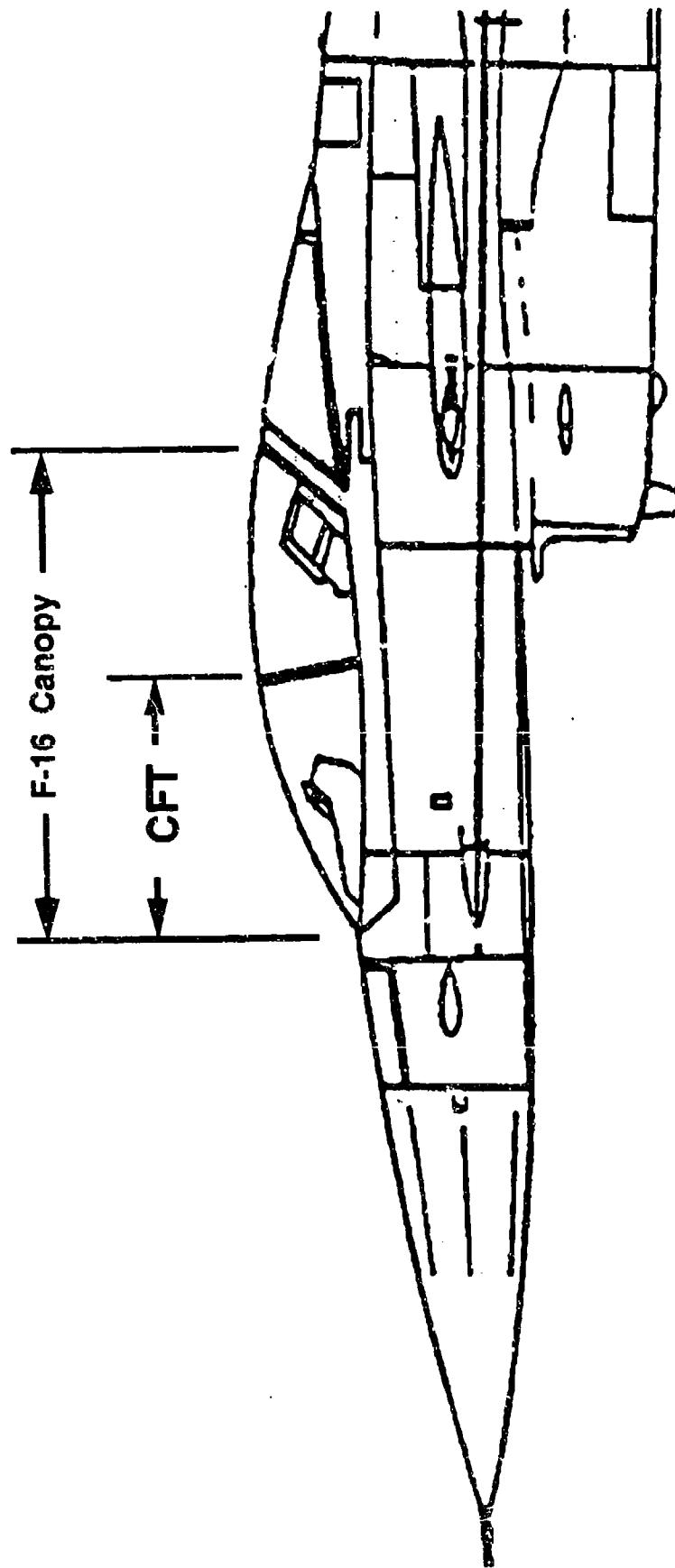


FIGURE 2

# CONFIRMATION FRAMELESS TRANSPARENCY (CFT)

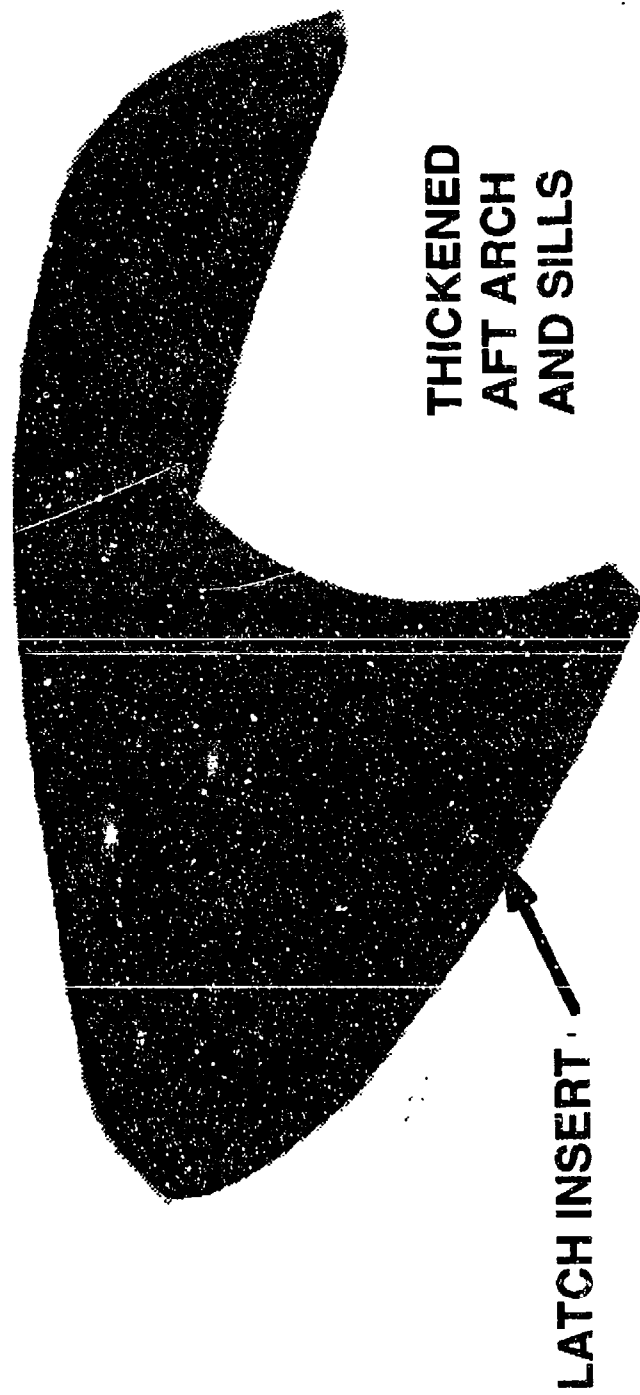


FIGURE 3

# CFT MOLDING SIMULATION MODEL FINITE ELEMENT MESH

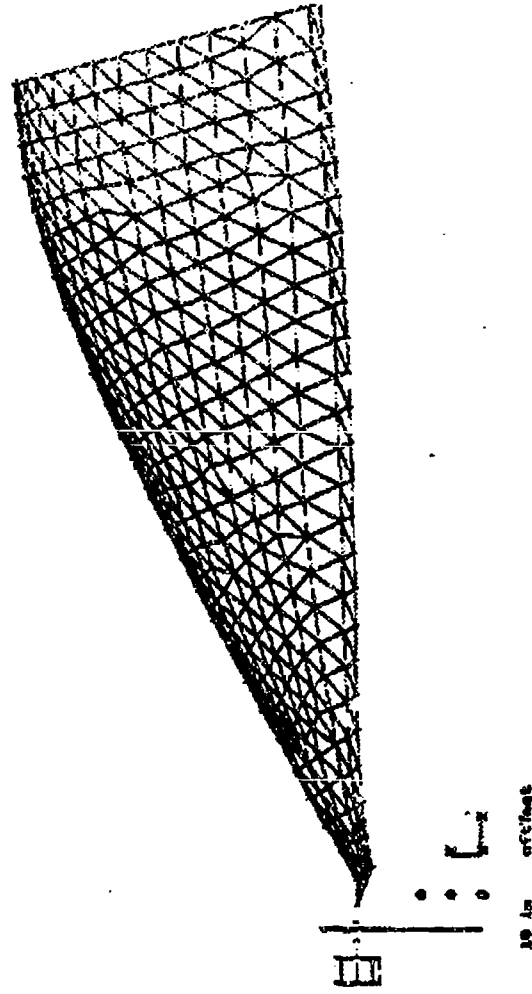


FIGURE 4

# TYPICAL INJECTION MOLDING SCHEMATIC

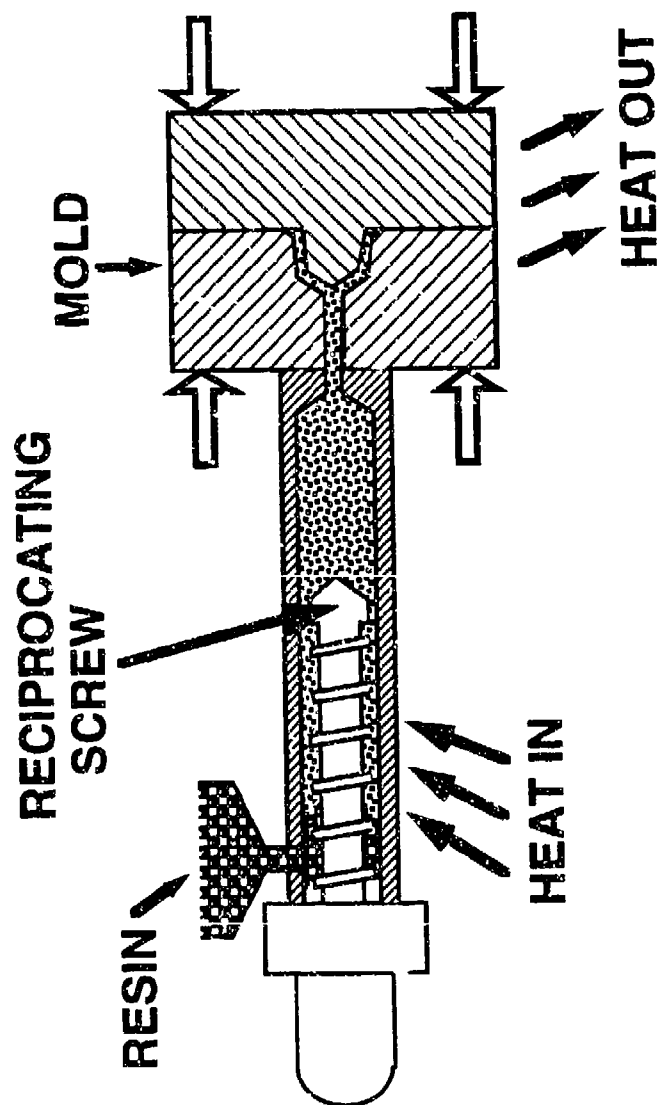


FIGURE 5

# TYPICAL INJECTION MOLDING CYCLE

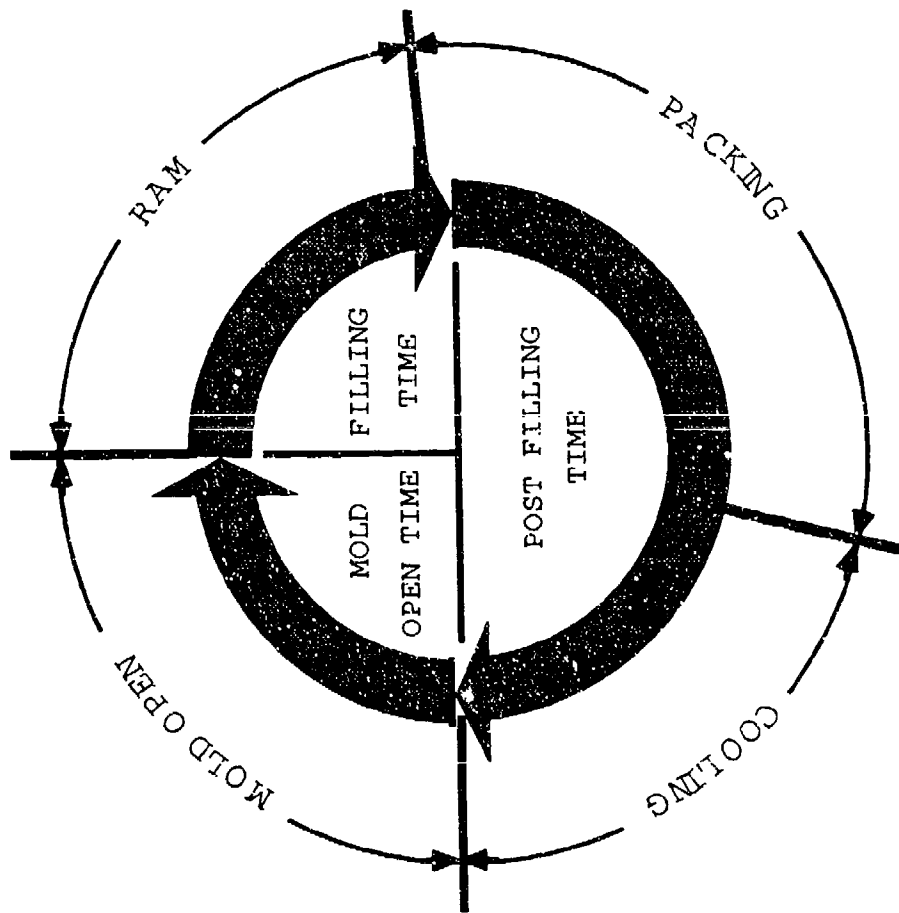


FIGURE 6

## Macroscopic View of Mold Filling

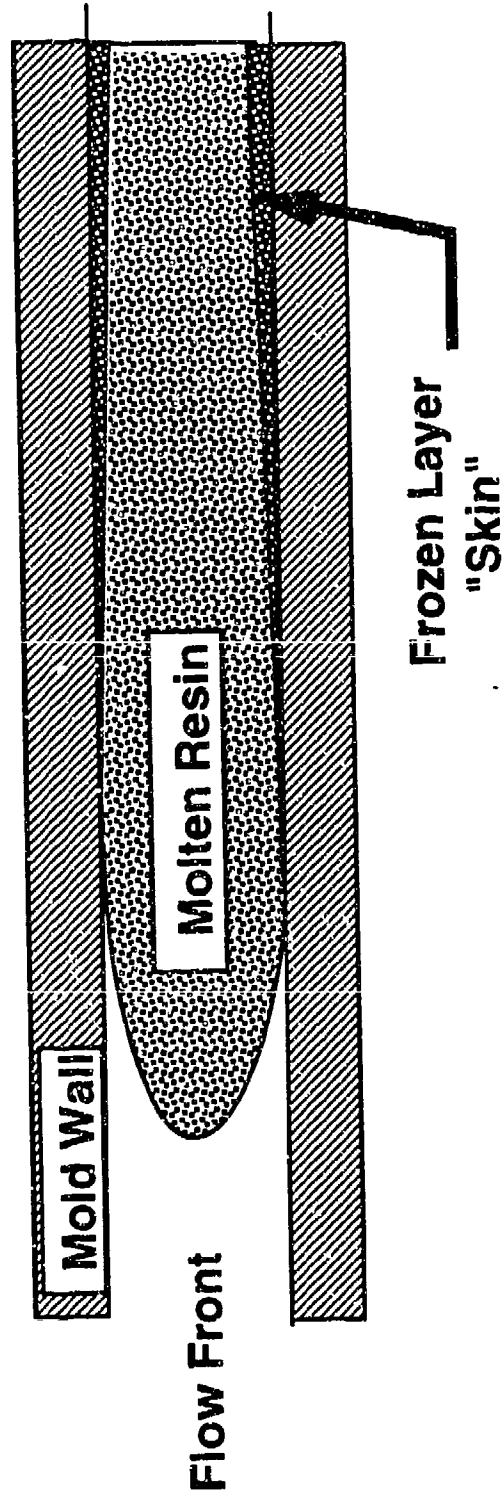
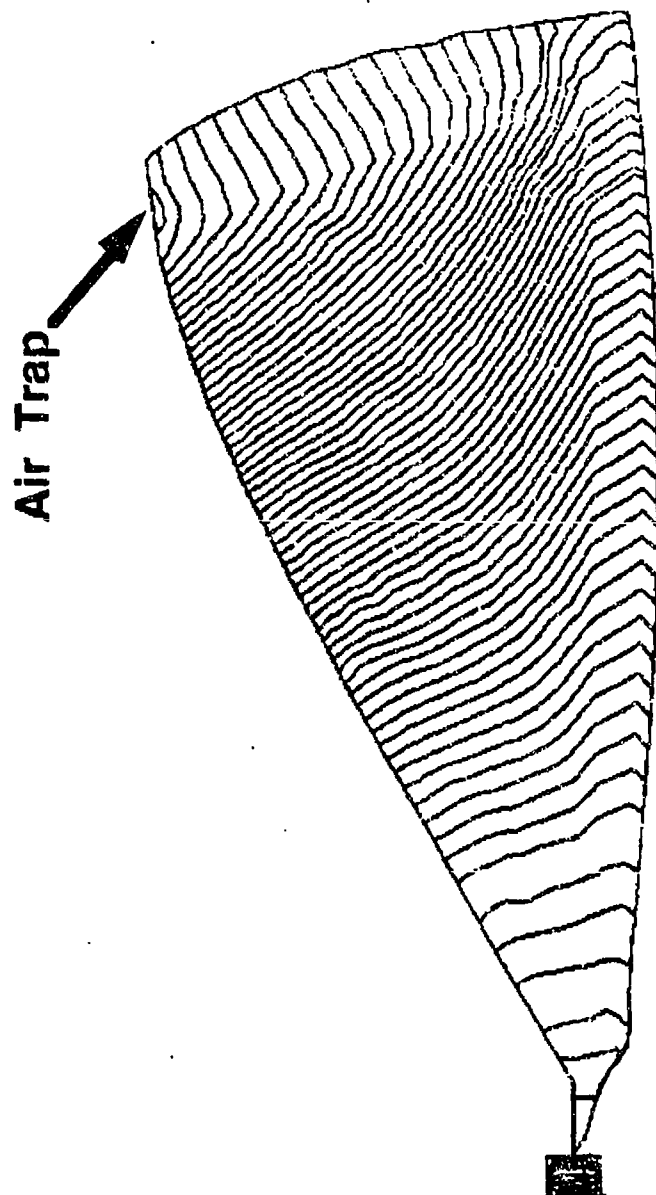


FIGURE 7



No Latch Inserts in Sills

100 mm C-Flow : cft10gt

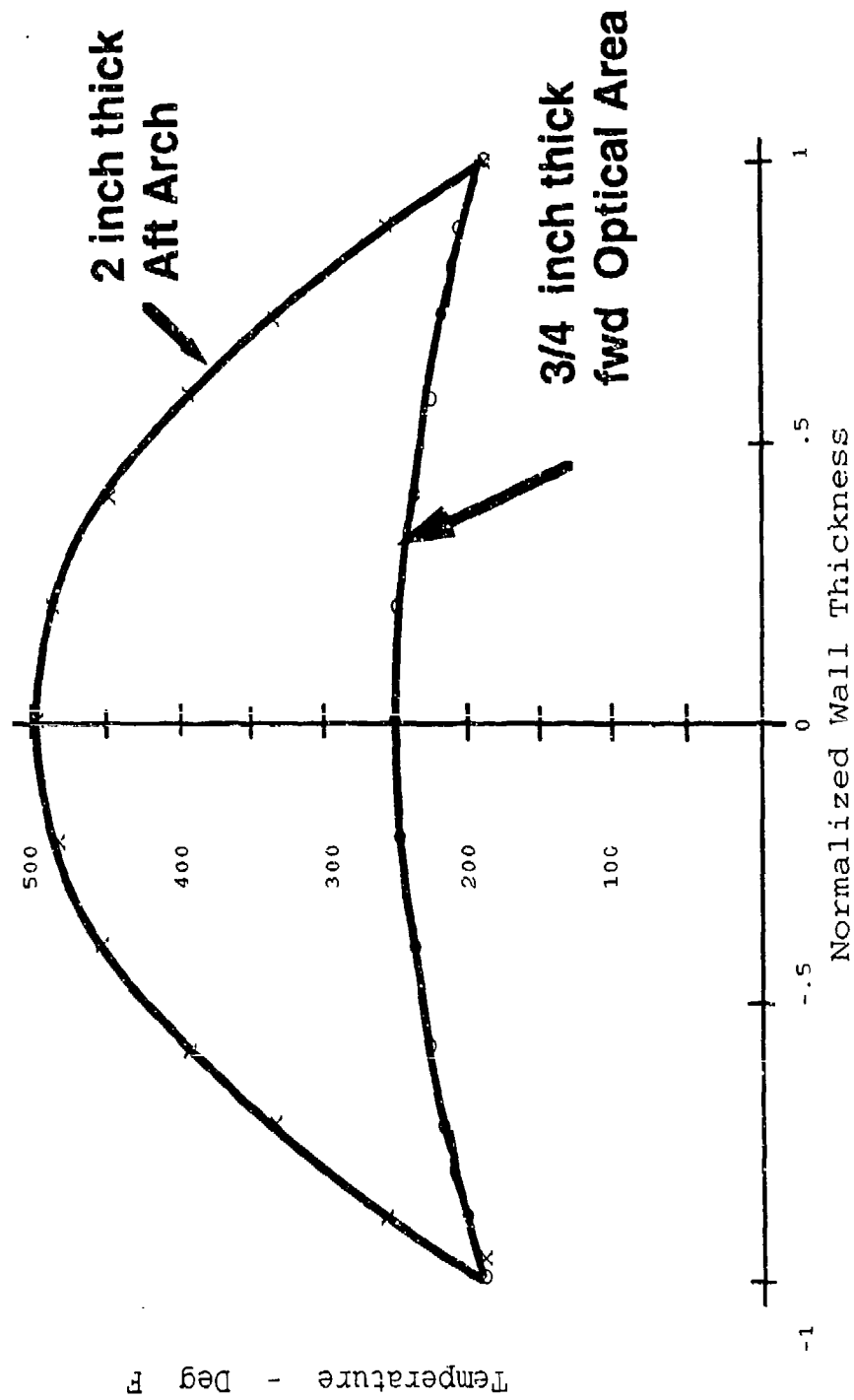
Figure 8 Flow Front Advancement Without Inserts



**Figure 9 Flow Front Advancement With Inserts**



Figure 10 - Temperature thru Thickness  
Frameless Transparency - 1040 seconds



# CONFIRMATION FRAMELESS TRANSPARENCY MOLD COOLING CHANNELS

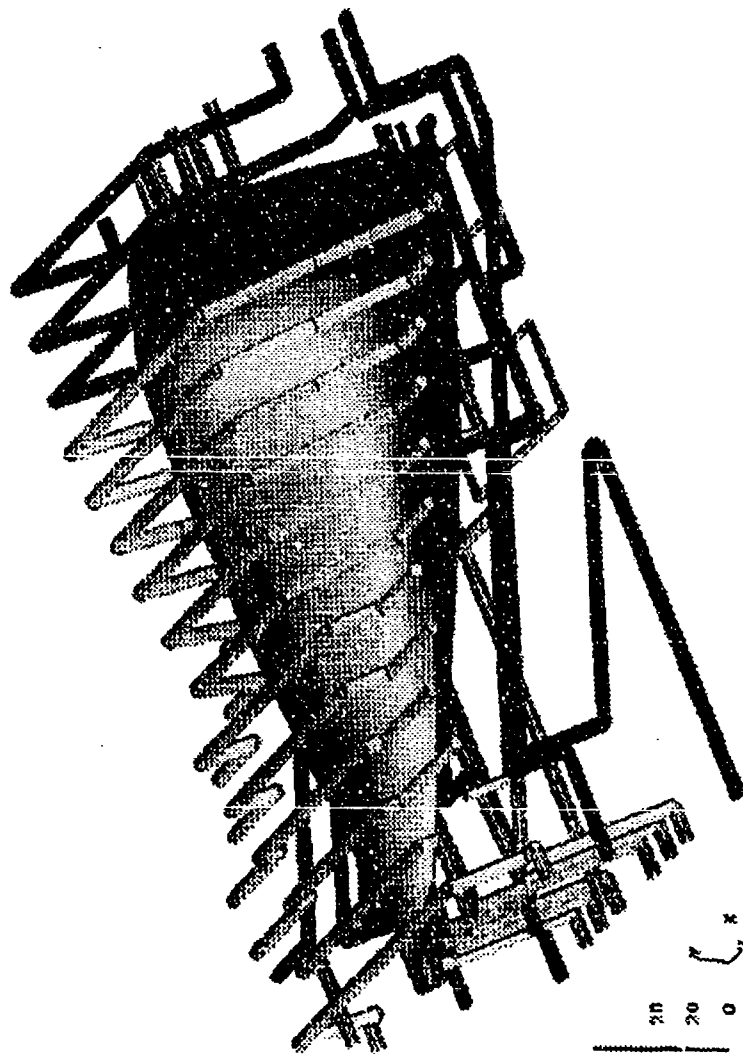


Figure 11

# CONFIRMATION FRAMELESS TRANSPARENCY MOLD



Figure 12 CAVITY

# CONFIRMATION FRAMELESS TRANSPARENCY MOLD



**Figure 13 CORE**

SESSION VIII

COMPUTER AIDED ANALYSIS - PART B

Chairman: M. Gran  
Flight Dynamics Directorate  
Wright Laboratory

Co-Chairman: R. McCarty  
Flight Dynamics Directorate  
Wright Laboratory

Coordinator: M. Bouchard  
University of Dayton

**ANALYTICAL DESIGN PACKAGE - ADP2 A COMPUTER AIDED ENGINEERING  
TOOL FOR AIRCRAFT TRANSPARENCY DESIGN**

**J. Wuerer  
PDA Engineering**

**M. Gran  
Flight Dynamics Directorate  
Wright Laboratory**

**T. W. Held  
University of Dayton**

# **ANALYTICAL DESIGN PACKAGE - ADP2 A COMPUTER AIDED ENGINEERING TOOL FOR AIRCRAFT TRANSPARENCY DESIGN**

J.E. Wuerer, PDA Engineering  
M. Gran, Wright Laboratory  
T.W. Held, University of Dayton

## **ABSTRACT**

The Analytical Design Package (ADP2) is being developed as a part of the Air Force Frameless Transparency Program (FTP). ADP2 is an integrated design tool consisting of existing analysis codes and Computer Aided Engineering (CAE) software. The objective of the ADP2 is to develop and confirm an integrated design methodology for frameless transparencies, related aircraft interfaces, and their corresponding tooling. The application of this methodology will generate high confidence for achieving a qualified part prior to mold fabrication.

ADP2 is a customized integration of analysis codes, CAE software and material databases. The primary CAE integration tool for the ADP2 is P3/PATRAN, a commercial-off-the-shelf (COTS) software tool. The open architecture of P3/PATRAN allows customized installations with different application modules for specific site requirements. Integration of material databases allows the engineer to select a material and those material properties are automatically called into the relevant analysis code. The ADP2 materials database will be composed of four independent schemas: CAE Design, Processing, Testing and Logistics Support.

The design of ADP2 places major emphasis on the seamless integration of CAE and analysis modules with a single intuitive graphical interface. This tool is being designed to serve and be used by an entire project team, i.e., analysts, designers, materials experts and managers. The final version of the software will be delivered to the Air Force in January, 1994. The Analytical Design Package (ADP2) will then be ready for transfer to industry. The package will be capable of a wide range of design and manufacturing applications.

# 1 INTRODUCTION

ADP2 is an integrated design tool consisting of existing analysis codes and Computer Aided Engineering (CAE) software. The objective of the ADP2 effort is to develop and confirm an integrated design methodology for frameless aircraft transparencies. ADP2 analysis capabilities include: aerodynamic heating, transient thermal response, static and dynamic structure response, optical ray trace, injection molding process simulation, and an aircraft transparency related material properties modeling and databank system. The design process is to be iterative and capable of producing frameless transparency designs, information needed for the design of integral aircraft interfaces, and information needed to support the design of injection molding tooling and the specification of molding process parameters for specific materials.

ADP2 is a second generation analysis system. The initial ADP development was initiated in 1989, References 1, 2 and 3. Since the inception of the original ADP, significant developments in both CAE and design support software relevant to aircraft transparency design have evolved. In addition, certain current design requirements, e.g., optics analysis and material properties modeling, were not addressed in the original ADP. Finally, significant advances in computing hardware have occurred making it possible to perform the required computations on workstation systems as opposed to mainframe platforms.

Recent developments in CAE design tools have introduced the ability to integrate special purpose and commercial-off-the-shelf (COTS) software in a user friendly (intuitive/interactive) environment. That is, to have a single user interface serve the primary analysis functions, specifically:

## 1. Modeling

- Geometric Modeling (construction and modification)
- CAD and IGES File Import
- Graphics Manipulation
- Meshing
- Loads and Boundary Conditions Specification

## 2. Materials Data Management

- Analysis Code Properties Input
- Test Data Processing and Reduction

## 3. Analysis Module and Module Parameter Specification



#### 4. Results Evaluation

The design of ADP2 places major emphasis on the seamless integration of CAE and analysis modules with a single intuitive graphical user interface.

## 2 ADP2 SCOPE

The principal objective of the ADP2 end product is to provide an integrated CAE tool to support the design of frameless (injection molded) aircraft transparencies. This tool is being designed to serve and be used by the entire project team, i.e., analysts, designers, materials experts, and managers. Emphasis is being placed on ease of use with the need for the user to learn only one common graphical user interface.

The ADP2 design places emphasis on the use of standardized methods for electronic communication of data to support the CAE process. Specific examples include: (1) the ability to import CAD and/or IGES files to simplify geometry model development, (2) the ability to store, process and import materials property data to support the design process, and (3) to allow users (including users at different sites) to share analysis results.

Finally, the ADP2 design addresses the issue of cost effectiveness. Where possible, commercial off-the-shelf (COTS) software is specified. This approach alleviates the need for the software owner to support and upgrade the software system as relevant new developments and improvements emerge. In addition, COTS software portability is generally maintained for common engineering work station platforms. Cost effectiveness is also addressed through ease of use and enhanced design team communication. For example, the design team will have the ability to review analysis results from the perspective of their individual needs. Ease of use will allow all members of the design team to communicate through direct use of the ADP2 to support their individual roles.

The specified analysis module requirements for the ADP2 are listed in Table 1, (note the ADP2 column). A comparison of the original ADP and ADP2 analysis module set is shown. It can be seen that the specified upgrades are extensive. In fact, none of the original ADP modules are planned for the ADP2 end product. This is the result of several major developments since the original ADP was defined some four years ago. It is planned that ADP2 will be configured so as to eventually allow the evolution of an ADP based on commercial-off-the-shelf (COTS) software. This potential evolution is indicated as ADP/COTS in Table 1. Although ADP/COTS is not a development target for the present program, it is, however, an important planning issue for ADP supportability and has a direct impact on the ADP2 architecture.

Table 1 ADP Development Phases

MODULE FUNCTION	ADP	ADP2	ADP/COTS
Design Process Manager, Graphical User Interface, and Project Manager	IRIS 4-SIGHT	P3/PATRAN	P3/PATRAN
Modeling/Post-Processing	PATRAN 2.4	P3/PATRAN	P3/PATRAN
CAD Interface	IGES File	P3/UNIGRAPHICS P3/IGES	P3/UNIGRAPHICS P3/IGES
Aeroheating Environment	STAHET	STAHET II	P3/CFD
Thermal Response	TAP	TAP II	P3/THERMAL
Structural Analysis	MAGNA	P3/FEA	P3/FEA
Birdstrike Analysis	MAGNA	X3D	ABAQUS EXPLICIT
Optical Raytrace	NONE	OPTRAN	CODE V
Injection Molding	C-MOLD 1.5	C-MOLD 3.2	C-MOLD 3.2
Materials Properties and Process Data Management Sys.	FIPMAT	M/VISION P3/MATL. SELECTOR	M/VISION P3/MATL. SELECTOR
Results Animation	NONE	P3/ANIMATION	P3/ANIMATION

The primary CAE integration tool for ADP2 and ADP/COTS is P3/PATRAN. The open architecture of P3/PATRAN provides the option to use several solver modules other than the baseline modules indicated in Table 1. A listing of alternative solvers which are commercially integrated with P3/PATRAN are listed in Table 2. This flexibility of P3/PATRAN will expand the opportunity for ADP2 and or ADP/COTS users to use their favorite solvers.

Table 2 Application Modules Commercially Integrated With P3/PATRAN

MODULE FUNCTION	MODULE TRADE NAME
CAD INTERFACE	UNIGRAPHICS CADD5 CATIA Pro/ENGINEER EUCLID-IS IGES PDES/STEP
THERMAL RESPONSE	P3/THERMAL SINDA P3/ADVANCED FEA ABAQUS
STRUCTURAL ANALYSIS	ABAQUS ANSYS MARC MSC/NASTRAN P3/FEA P3/ADVANCED FEA

ADP2 is initially being developed for the Silicon Graphics (SGI) Iris workstation which has a UNIX (IRIX 4.0.5) operating system. A development goal is to have the end product portable to common UNIX based engineering workstations. The specific development work station is an SGI IRIS CRIMSON / ELAN with 64 megabyte main memory, a 50 megahertz (MIPS R4000) processor, and a 3.8 gigabyte capacity system disk.

The overall architecture of the planned ADP2 end product is shown in Figure 1. The primary CAE integration element of ADP2, P3/PATRAN, provides the basic framework for the executive control to implement application module integration, preprocessing (modeling) capability and post-processing (results display) capability. The basic capability of P3/PATRAN is extended by the ADP2 customization, indicated by the shaded area in Figure 1.

### 3 ADP2 INTEGRATION

What does the ADP2 Customization consist of? This is a question that many ADP2 users have asked. Comments have been made to the effect that one is not able to determine where P3/PATRAN ends and ADP2 begins. The reason for this is actually one of the advantages of using the customization features of the all new P3/PATRAN as the core of ADP2. Enhancements made to P3/PATRAN via the use of the COTS supported PATRAN Command Language (PCL) tool kit makes all added functionality seamless. In other words, the enhancements actually appear to be a part of P3/PATRAN.

#### 3.1 ADP2 System

The ADP2 system includes several specified commercial and non-commercial software application modules which support the design and manufacturing process. These software products are then integrated with custom software to simplify the work of the engineering analyst.

Specifically, the software modules specified for ADP2 were listed in Table 1. ADP2 System functionally consists of two major parts: the Project Manager and the Application Interfaces. The Project Manager manages all data which the engineer creates and accesses. It also manages the process flow between P3/PATRAN and the various simulation tools. The Application Interfaces integrate the specific simulation tools with P3/PATRAN. The overall architecture of the system was shown in Figure 1.

### 3.2 Project Manager

The Project Manager is responsible for all items that relate to Project Management and Process Flow. Under most instances, the user will no longer need to keep track of his files. All data within ADP2 is referenced with respect to a specific project or task. The user simply selects the task or project that he is interested in and begins modeling or analyzing. ADP2 will even keep track of where the user was during his last visit to ADP2 and place him at the same task the next time he visits ADP2.

The Project Manager also ensures that the analysis tool requested by the user will be used on the model associated with the specified task. The Project Manager actually informs P3/PATRAN of which analysis tool is to be used with a specific model. So, when the engineer specifies that he would like to perform an analysis, P3/PATRAN will know exactly which analysis to perform.

Another feature of ADP2 is the ability for engineers to share data. An engineer can easily copy data from one project to another. He can also copy data from the outside world (data existing outside of the ADP2 system) into the ADP2 Project Management System.

### 3.3 Application Interface

The Application Interface consists of all analysis tools as well as their forward and reverse translators to P3/PATRAN. It also consists of the graphical forms interface with which the user interacts with to specify what it is that he would like to do with a specific analysis tool.

For instance, take the case of the application interface for the birdstrike analysis module, X3D. Once the Project Manager has handed the model to P3/PATRAN, the user can use P3/PATRAN to improve upon the model. When the user is ready for analysis, he selects "Analysis" on the menu bar and the X3D graphical forms are displayed to assist the user in specifying the parameters for the type of simulation he would like X3D to perform. These forms are part of the custom code developed for the Application Interface of ADP2. When the user is satisfied with the model and parameters that he has specified, he will "Apply" these parameters and begin the simulation task. In the case of X3D, The model and parameters are automatically input into the forward translator. This translator converts the data into the format required by X3D. This translator is also a part of the custom code developed for the Application Interface of ADP2. After the model and parameters have been translated, X3D is automatically submitted as a background job. Once the X3D job has completed, the results can be imported back

into the PATRAN 3 model by use of the reverse translator, another piece of the custom code developed for the Application Interface of ADP2.

## 4 ADP2 APPLICATION MODULES

There are a total of nine primary modules integrated into the ADP2 analysis tool. An overview of the functionality embedded in each of these modules follows.

### 4.1 P3/PATRAN

P3/PATRAN is an advanced computer aided engineering (CAE) integration tool introduced by PDA Engineering, Costa Mesa, CA, in June of 1992, Reference 4. P3/PATRAN tool has an open architecture which provides several important capabilities. These include:

1. direct software links to leading CAD systems,
2. direct software links to analysis software programs, both leading commercial and user developed programs,
3. pre- and post-processing capabilities to allow geometry and FEM development, as well as analysis results display,
4. an integrated subset of the materials selection capability from PDA's M/VISION family of products, and
5. a fully integrated set of P3/PATRAN analysis modules for performing structural, thermal, computational fluid dynamic, fatigue, and other types of mechanical analyses.

P3/PATRAN has a user friendly "mouse activated" window environment graphical user interface (GUI) which provides execution of the analysis system without the need to remember a particular command syntax. The open system architecture and GUI provide the basic capability to build a user friendly executive control capability for ADP2.

P3/PATRAN has been specified for ADP2 primarily for its capability as a CAE system integration tool. However, there are several analysis modules that are fully developed and completely integrated with P3/PATRAN. These analysis modules include:

1. P3/FEA for comprehensive finite element analysis,

2. P3/ADVANCED FEA which is a non-linear module developed jointly with HKS based on ABAQUS analysis technology,
3. P3/FATIGUE for durability analysis,
4. P3/CFD is a state-of-the-art computation fluid dynamics module for workstations,
5. P3/THERMAL is a state-of-the-art finite element based thermal analysis, and
6. P3/ANIMATION is an advanced, state-of-the-art animation capability co-developed with Intelligent Light.

All of the above modules have specific relevance to the requirements of the ADP. However, the initial development plan includes only two modules. These are P3/FEA which is reviewed in Section 4.5 and P3/ANIMATION which is reviewed in Section 4.7.

## 4.2 M/VISION

M/VISION is a PDA Engineering materials software system which provides for data visualization, selection and integration, Reference 5. M/VISION uses centralized relational databases organized to reflect the classes of material's information needed in the design-to-manufacturing process:

1. Material: Material source and designations, as well as extension to account for the multiple source associated with composite materials.
2. Specimen: Detailed information about the specimens including composition and processing specifics
3. Environment: Specific information about the experimental conditions including temperature and humidity as well as statistics and quality.
4. Properties: Mechanical, physical, thermal, and electrical properties of materials including extension to account for anisotropy. Curves and rasterized images are represented as well.

Data stored in M/VISION may be directly accessed by P3/PATRAN via the P3/MATERIALS SELECTOR.

M/VISION provides a very significant upgrade for ADP2's materials database management functionality, compared to that in the original ALP. Details of the role of M/VISION in the ADP2 design methodology are presented in Reference 6. The following partial list summarizes several pertinent features provided by the M/VISION COTS product:

1. Complete graphical user interface (GUI) that provides visualization of all materials database functions.
2. Customization of database schema; i.e., attribute list, relationships, etc. Easy to expand database to include more properties and more property types.
3. Units easily changed to SI or any user defined system.
4. Metadata and footnotes provided with data values that enable inclusion of material source, specimen conditions, test environment, test anomalies, etc.
5. Data can be stored and manipulated using an extensive spreadsheet functionality.
6. Database queries using engineering terminology to define search conditions.
7. Full-featured manipulation and storage of tables, graphics, and CAT scan images.
8. Strict adherence to government and industry standards.
9. Provides data importing and exporting features using the following exchange protocols:
  - IGES
  - PDES/STEP
  - PATRAN Neutral File
  - ASCII Text Spreadsheet Files
10. M/VISION databases can be accessed directly or queried using the new P3 "materials selector" functionality (via GUI form driven features).

As a powerful stand-alone product, M/VISION can be utilized in a variety of ways, within the design-to-manufacturing process. Generally, throughout the design process, engineers do not have a central on-line source and electronic access to high quality materials information required for analytical design assessment simulations. Often the materials information that is available is missing critical property values requiring further testing or analytical material synthesis. Therefore, M/VISION's role could be two-fold. As a central source for database management, M/VISION could serve to create, update, and store all the available materials information pertinent to the transparency design community. In this role, M/VISION would be executed and maintained by a Materials and Processes group(s) for the overall design-to-manufacturing process. Materials data, needed by design

simulation modules, would be accessed using one of the various transfer protocols listed above.

### 4.3 STAHET II

STAHET II performs the computations which predict the aerodynamic heating history to the transparency system for a specific aircraft configuration and mission profile. The results of these computations are then used as input boundary conditions to the transient heating analysis (TAP II) for the detailed transparency model, as discussed in Section 4.4.

The STAHET II and TAP II codes are embedded in the STAPAT II (Specific Thermal Analyzer Code for Aircraft Transparencies) development. STAPAT II, rather than a single computer program, is actually an analysis methodology incorporating a set of computer codes. There are 5 major elements of this methodology, specifically:

1. develop the forebody model,
2. compute the aeroheating over the transparency surface using the STAHET computer code and these models (STAHET),
3. develop the transparency finite element model (STABLD),
4. compute the transient, three dimensional transparency system temperatures using the TAP computer code and the finite element model (TAP), and
5. display the models and results using the STAPLT computer code (STAPLT).

Details of the above methodology are reported in References 7, 8, and 9.

The above methodology has several inconsistencies with the ADP2 architecture, specifically with respect to Item 1, forebody model; Item 2, transparency finite element model; and Item 5, display models and results. In ADP2, all of these tasks are handled by P3/PATRAN. In addition STAPAT II was specifically developed for the DEC VAX/VMS computer systems. For ADP2, both STAHET II and TAP II have been ported to UNIX based platforms.

STAHET I represents a significant upgrade to the STAHET code which is embedded in the first generation of ADP (Reference 3). The ground rules for developing the code were that STAHET II must: (1) be user friendly and non-proprietary, (2) provide accurate transparency temperatures without excessive computing resources; (3) use existing methodologies to predict heating rates and



temperatures; and (4) retain or improve all original STAHET capabilities, Reference 7.

The general capabilities of the STAHET II code are summarized in Table 3. Details of the indicated capabilities, their assumptions and limitations, and their implementation are presented in References 8 and 9.

Table 3 General Capabilities of STAHET and STAHET II

STAHET	STAHET II IMPROVEMENTS
<ul style="list-style-type: none"> <li>• Two Streamline Tracing Methods</li> <li>• Modified Newtonian Pressure Calculation</li> <li>• Laminar and Turbulent Heating Correlations</li> <li>• Boundary Layer Transition Options</li> <li>• Wall Temperature Effect Modeling</li> <li>• Mission Profile (Mach and Altitude) Input for 3-D Geometries</li> <li>• 2-D Wind Tunnel Modeling</li> <li>• Standard Day, Hot Day, Cold Day Atmospheres</li> <li>• Ideal Gas Air Model</li> </ul>	<ul style="list-style-type: none"> <li>• Simplified Streamline Tracing Techniques Selected as Default</li> <li>• User Input of Streamline Starting Angles Added</li> <li>• Four Shadow Region Pressure Prediction Techniques Added</li> <li>• Wall Temperature Effect Modeling Improved</li> <li>• 3-D Wind Tunnel Model Capability Added</li> <li>• Extension to Hypersonic Flow</li> </ul>

The integration of STAHET II into the ADP2 product is limited to those capabilities relevant to current tactical and strategic aircraft. Capabilities relevant to hypersonic vehicle applications, i.e., Mach Number greater than about 4 and altitude greater than 100,000 feet, exist in the basic STAHET II code. The implementation of this capability would require an extension of the ADP2/STAHET II application interface.

An important feature of the STAHET II integration into ADP2 is the inclusion of (and ready availability of) aircraft forebody geometries. The complete file of 16 STAHET II geometries has been included. Geometries relevant to conventional military aircraft include F-16, F-15, F-4, F-18, and B-1B. Low RCS aircraft, missile, and several hypersonic forebodies also exist in the library. The example of the F-16 forebody configuration is shown in Figure 2.

An example of an ADP2/STAHET II result is provided in Figure 3. Shown is a fringe plot of aerodynamic heating rate over the portion of the forebody relevant to the transparency. The relevant aerodynamic heating parameters are then transferred to TAP II where the predictions of the transient thermal response for the transparency are conducted.

#### 4.4 TAP II

The TAP (Transparency Thermal Analysis) application module performs the transient thermal response analysis for the transparency structure. The primary end result of the analysis is the temperature field as a function of time for the detailed 3-dimensional finite element model. These data may then be queried to examine for critical temperatures and/or be directly handed off to the thermal stress finite element model via the P3/PATRAN FEM Field Interpolator.

The general capabilities of the TAP application module are summarized in Table 4. Details of the above capabilities and their implementation are discussed in References 8 and 9.

An example geometry used to build the TAP finite element model (FEM) is shown in Figure 4. The specific geometry is for the designated "Confirmation Frameless Transparency" (CFT7A) as specified by Wright Laboratories. Example TAP II results are shown in Figure 5. Shown is the temperature field, at a specific mission time point, displayed in the TAP II FEM via the P3/PATRAN post-processing capability.

Table 4 General Capabilities of TAP and TAP II

TAP	TAP II IMPROVEMENTS
<ul style="list-style-type: none"><li>• 3-D Finite Element Solution</li><li>• Material Property Data Base</li><li>• Aeroheating Imposed on External Surface</li><li>• Thermal Boundary Conditions<ul style="list-style-type: none"><li>- Generalized Convection</li><li>- Defog</li><li>- Anti-Ice (Hot Air Blast)</li><li>- Electrical Anti-Ice</li><li>- Generalized Heat Flux</li><li>- Radiation-to-Sky</li><li>- Element-to-Element Radiation</li></ul></li><li>• Standard Day, Hot Day, Cold Day Atmospheres</li><li>• Mission Profile (Mach, Altitude and Time) Input</li></ul>	<ul style="list-style-type: none"><li>• Defog Modeling Improved</li><li>• Cabin Cooling Air Velocity Default Added</li><li>• Fluid Gap Modeling Improved</li><li>• External Anti-Icing Improved</li><li>• Line Source Capability for Convection Added</li><li>• Earth Radiation Sink Temperature Added</li><li>• Expanded Material Property Data Base</li><li>• Viscosity and Molecular Weight Added to Material Property Data Base</li><li>• Gap Fluids Added to Material Property Data Base</li><li>• Extension to Hypersonic Flow</li></ul>

#### 4.5 P3/FEA

P3/FEA is a finite element based structural analysis solver that is fully integrated with the P3/PATRAN family of COTS products. P3/FEA has a wide variety of analysis capabilities, solution sequences, element types, and material

models, including temperature dependent laminated composite and nonlinear material properties, Reference 10. P3/FEA makes full use of the graphical user interface (GUI) forms system provided by P3/PATRAN. P3/FEA analysis jobs are assembled, submitted, queried, or aborted from within the P3/PATRAN environment. Results evaluations are completely menu driven and fully integrated with the P3/FEA results database.

P3/FEA solves a wide variety of structural problems. An extensive finite element library and set of solution procedures, which can handle very large matrix equations are available in P3/FEA. No translators are needed to transfer model data from P3/PATRAN to P3/FEA or to transfer results back to P3/PATRAN for post-processing. The close coupling of P3/PATRAN and P3/FEA provides the user with all the efficiencies related to integrated software.

P3/FEA can handle extremely large problems. Models of over one-hundred thousand degrees-of-freedom have been analyzed. A restart capability is provided for large problems that require efficient re-analyses as new cases are defined for existing models.

P3/FEA will provide two basic analytical simulations needed to support the ADP2 transparency design assessments. These are:

1. static analysis (linear and nonlinear) and
2. dynamic normal modes.

The static analysis will include mechanical load environments (pressures) and/or thermal load environments (in-depth thermal gradients). The load/temperature values defined for these analyses are provided by the TAP II aerothermal simulation module solution results. Automated procedures to interpolate the TAP II results onto and into the P3/FEA model are included in the P3/PATRAN FEM field interpolation function. The transparency FEM can include "contact only" nonlinear elements in the regions of attachment to simulate joint details. The nonlinear iterative procedures to establish the discontinuous contact elements' unique combination of contact and gapping is provided as one of the P3/FEA solution procedures. The transparency material properties used in these static analysis simulations can be temperature dependent and/or nonlinear in their defined constitutive relationships. P3/FEA provides the static solution procedures to accommodate temperature dependent element material property evaluations.

The dynamic environments to be simulated by P3/FEA for the transparency design assessments will include normal modes evaluations and possibly subsequent frequency response and random vibration solutions. P3/FEA provides enhanced dynamics analysis capability sufficient to simulate any foreseen transparency dynamic load environment or modal content survey. P3/FEA can solve these problems in either a time or frequency domain.

An example P3/FEA result is shown in Figure 6. Shown is a fringe plot of Von Mises stress on the transparency surface displayed on the P3/FEA finite element model. The illustrated stress is the result of the combined effects of pressure and thermal loading.

#### 4.6 X3D

X3D is an explicit FEA code, used to simulate soft body impact problems, including the birdstrike of aircraft transparencies. It provides substantial improvements over the MAGNA analytical functionality of the original ADP.

The analytical simulation of transparency non-linear transient dynamic response to birdstrike represents a distinctive class of impact structural behavior. The University of Dayton Research Institute (UDRI) has developed and is continuing to enhance a new explicit non-linear dynamic response FEA code, X3D (References 11, 12 and 13). X3D utilizes an explicit solution approach similar to other well-known FEA codes; e.g., DYNA3D, WHAMS, and ABAQUS Explicit. These solution methods and codes have been widely used for the numerical simulation of a variety of shock and wave propagation problems. Impact problems in general can be dominated by complicated contact surface conditions which can require very small numerical integration time steps which in turn remove the solution advantages of an implicit solution approach.

X3D provides functionality to idealize both the bird (impactor) and the transparency (target) and to allow them to come into transient contact with the physics of momentum transfer defined by the non-linear explicit solution algorithm solution results. That is, no analysis assumptions regarding contact pressure time histories or spatial distributions are required.

X3D has been evaluated through executions and correlations with benchmark test cases; i.e., impacting Taylor cylinder, exploding cylindrical shell, and F-16 centerline transparency impact. Although documented validation problems are limited, those completed to-date show promising correlations and demonstrate the improved simulations possible with the use of X3D code.

The X3D impact dynamics code provides a significant numerical tool kit to simulate the complex soft body impact environment of transparency birdstrike:

1. FEA Elements

- Both 3D solid (HEX and TET) and 2D layered shell elements are provided. The 2D layered shell element accommodates soft interlayers (plane selections do not remain plane over the overall layered shell thickness)

2. Material Models (2D)

- Elastic-Plastic, Rate Sensitive, Isotropic
  - Linear Elastic, Orthotropic, Brittle Failure
  - Viscoelastic with failure
3. Material Models (3D)
- Elastic-Plastic, Rate Sensitive, Isotropic
  - Same as above with Discontinuous P-V
  - Newtonian Viscous Fluid
4. Automated Contact Surface Evaluation Procedures
- Slave and Master node sets that are nonlinearly evaluated for contact
5. Simple "Rigid Wall" designation procedures
6. Linked element lists for failure assessments
7. Element and integration stabilization features

An example X3D result is shown in Figure 7. The deformed transparency and bird finite element models are displayed, for the specified time point. A fringe plot of Von Mises stress is displayed on the model.

#### 4.7 OPTRAN

OPTRAN is a raytrace code which evaluates the optical quality of aircraft transparencies subjected to operational load conditions. The code was developed by the University of Dayton Research Institute, References 14 and 15.

The raytrace optical code is interfaced to finite element thermal and stress analysis codes to permit the effects of operational loads to be modeled. Thermal, displacement, and stress field definition data computed by the finite element codes are input to the optics module. This information is required to compute the orthotropic indices of refraction throughout the material volume of the aircraft transparency. This computation is performed at each step along the propagation path of each ray.

The optics code tracks rays of various wavelengths through the transparency. The deformed geometry generated by the stress analysis is used to determine angles of reflection and refraction at transparency layer boundaries. Birefringent indices of refraction are computed as a function of material, temperature and stress state at the refracting surfaces and within the transparency material.

Key results include angular deviation, transmittance, and polarization effects over specified regions of the transparency. Displacement vectors and deformed grids can also be generated.

#### 4.8 C-MOLD

The C-MOLD product is a family of computer codes designed to support the design of tooling and specification of process parameters for fabrication by injection molding, Reference 16. The modular product supports both the processing of thermoplastic and reactive materials. C-MOLD is a commercial-off-the-shelf (COTS) product developed and marketed by AC Technology, Ithaca, NY. AC Technology also provides materials characterization services and maintains a materials database relevant to the injection molding of plastics.

The frameless transparency development is concerned with the use of thermoplastic materials. Therefore, there are three primary processes requiring simulation. These are:

1. the process of the initial filling of the mold (C-FLOW),
2. the post-filling process where shrinkage occurs (C-PACK), and
3. the transient cooling of the part prior to mold separation (C-COOL).

The product modules which address these processes are defined in parentheses above.

The C-FLOW analysis models the mold filling process as a generalized Hele-Shaw (very slow motion) flow (Reference 16). The flow conditions are for an incompressible viscous polymeric melt under non-isothermal conditions and symmetric thermal boundary conditions. The numerical solution is based on a hybrid finite-element/finite-difference method to solve pressure and temperature fields, and a control-volume method to track moving melt fronts. Details of the analysis methodology are presented in References 17 and 18.

The C-PACK analysis module extends the above analyses module to include the effects of asymmetric thermal boundary conditions. A set of unified governing equations for the flowfield is used throughout the filling and post-filling stages. The analyses can model a three-dimensional, thin cavity with a melt-delivery system that may contain cold or hot, circular or non-circular runners. The influence of shrinkage is also included. Details relevant to the C-PACK analysis are presented in References 19, 20, and 21.

C-COOL is a three-dimensional mold cooling simulation to assist in designing the cooling channel system for plastics injection molding processes. The capability exists to model a homogeneous, three-dimensional mold with a thin

cavity and with a cooling system that contains circular or non-circular channels, baffles and bubble. A channel network analysis within the program within C-COOL predicts flow rates in different cooling lines.

The C-COOL module uses a strategy which minimizes input data requirements, user time and computer memory requirements. Heat transfer within the polymer melt is treated as transient, local, one-dimensional heat conduction with static solidification. Heat transfer within the mold is treated as transient, three-dimensional conduction. Heat exchange between the channel surfaces and the cooling fluid is treated as steady and is accounted for using correlations for the convective heat transfer coefficient. To solve the relevant governing equations simultaneously, C-COOL uses a hybrid scheme consisting of a modified, three-dimensional boundary element for the mold region and a finite difference method with a variable mesh for the melt region. These two analyses are coupled iteratively to match the temperature and heat flux at the mold/melt interface. A special algorithm has been developed which reduces the computational memory requirements by a factor of 100, compared to the requirements for a traditional approach.

An example C-MOLD result is shown in Figure 8. Shown is a result from the C-FLOW module, which shows the melt front as a function of time during the mold filling process. The example modeled the Configuration Frameless Transparency, using a representative polycarbonate resin.

#### 4.9 P3/ANIMATION

P3/ANIMATION is a powerful tool that offers interactive visualization, animation, photo-realistic rendering and video tape output of geometry and results data, Reference 22. It is designed to assist engineers in the investigation and presentation of data which are normally very difficult to visualize. With P3/ANIMATION, information can be displayed in a number of different ways including: Wireframe, Hidden Line, Solid Shaded and Fringed models. Display can be further enhanced with the use of motion to view the data from a variety of angles and a host of other variables such as transparency, surface coloring and shading characteristics.

P3/ANIMATION uses on-screen animation to show geometry and results as dynamic moving pictures. After completing an analysis in P3/PATRAN, static, modal and transient data sets are read directly into P3/ANIMATION. The user then has complete control over visualization in both space and time. Models may be positioned or rotated to gain a better view and any single time step or range of time may be examined. Fringe plots and arrow fields are used to display scalar and vector data, respectively, and model deformations may also be displayed. Sophisticated timing controls can be used to zoom in on portions of the analysis that are particularly interesting, while skipping over portions of less interest.

The Animator Tool can be used to create simple or key frame animations. In simple animations, models cycle through the results data while rotating about a single axis. In key frame animations, different groups can be posed with various rotations, scales and rendering transforms applied. Posing allows for much more creative and illustrative animations, in which many attributes and transforms can be set or varied over time.

Once an animation is defined, the Flipbook Tool can be used to compute sequences of frames or flipbooks for subsequent playback on any X Windows device in the network. Flipbook images are created and displayed using available graphics hardware to increase performance.

## 5 CONCLUDING REMARKS

ADP2 has been designed specifically to support the Air Force Frameless Transparency Program. The completion of the planned work will provide an important suite of tools to aid in the design and performance evaluation of injection molded transparency systems. The validation of these tools will be a critical aspect of the ADP2 development process.

ADP2 provides a fully integrated methodology relevant to the general problem of aircraft transparency design. A key aspect of ADP2 is the seamless integration of the analysis modules with P3/PATRAN, an advanced commercially supported CAE integration tool. This integration provides a single form driven user interface which serves to manage the analysis process and the analysis module input and output (results) data. The user remains in an intuitive environment and is freed of the complexities and/or peculiarities of the computer operating system throughout the entire design process. The support provided by the employment of a commercial CAE integration tool and the selection of state-of-the-art application modules will provide Air Force and its contractors with a cost effective tool with a significant life potential.

## 6 REFERENCES

1. Turner, D.L., "Interim Report Draft III: Development Plan for Frameless Transparency Analytical Design Package," Contract No. F33657-84-C-0247, CDRL No. 34002, Report No. FZM-719-001, General Dynamics Corp., Ft. Worth, TX; 28 June 1990.



2. Hunten, K.A., "Analytical Design Package Development Report," Contract No. F33657-84-C-0147, CDRL No. 34002, Report No. FZM-719-009, General Dynamics Corp., Ft. Worth, TX; 21 November 1991.
3. Hunten, K.A., Analytical Design Package Version 1.2c Operation Manual, Contract No. F33657-84-C-0247, CDRL No. 34002, Report No. FZM-719-010, General Dynamics Corp., Ft. Worth, TX; 22 November 1991.
4. P3/PATRAN User Manual, Vols. 1, 2, 3, 4, Publication No. 903000, PDA Engineering, Costa Mesa, CA; September 1992.
5. M/VISION, Materials Visualization, Selection and Data Integration, User Manual, Publication No. 2190011, PDA Engineering, Costa Mesa, CA; September 1990.
6. Mack, T.E., Kipp, T.E., Whitney, T.J., and Gran, M., "The Use of Computerized Materials Data in ADP2," Conference on Aerospace Transparent Materials and Enclosures. (Sixteenth), U.S. Air Force Wright Laboratories; 9-13 August 1993.
7. Varner, M.O., et al, "Specific Thermal Analyzer Program for High Temperature Resistant Transparencies for High-Speed Aircraft (STAPAT)," Report No. AFWAL-OTR-84-3086, Volumes I, II and III, AD B089 497, AD B1090 894L, and AD B090 896L, Wright Research and Development Center, Wright-Patterson AFB, OH; October 1984.
8. Bowman, B.L., "Hypersonic Thermal Analysis for Aircraft Transparencies, Vol. I: STAPAT II Description," Report No. WRDC-TR-90-3053, Wright Research and Development Center, Wright-Patterson AFB, OH; September 1990.
9. Bowman, B.L., "Hypersonic Thermal Analysis for Aircraft Transparencies, Vol. II: STAPAT II User's Manual," Report No. WRDC-TR-90-3053, Wright Research and Development Center, Wright-Patterson AFB, OH; September 1990.
10. P3/FEA Application Module User Manual, Publication No. 903006, PDA Engineering, Costa Mesa, CA; September 1992.
11. Brockman, R.A. and Held, T.W., "Explicit Finite Element Method for Transparency Impact Analysis," Report No. WL-TR-91-3006, Wright Laboratory, Wright-Patterson AFB, OH; June 1991.
12. Brockman, R.A. and Held, T.W., "X3D--3D Explicit Finite Element Analysis--Tutorial," University of Dayton Research Institute, Dayton, OH; July 1991.

13. Brockman, R.A. and Held, T.W., "X3D Users' Manual, Updated for X3D Version 3.04," Report No. UDR-TR-92-59, University of Dayton Research Institute, Dayton, OH; April 1992.
14. Fielman, J.W. and Loomis, J.S., "Optical Analysis of Aircraft Transparencies (OPTRAN), Volume II: Theoretical Manual," Report No. WRDC-TR-90-3058, Volume I, Wright-Research and Development Center, Wright-Patterson AFB, OH; October 1990.
15. Fielman, J.W. and Loomis, J.S., "Optical Analysis of Aircraft Transparencies (OPTRAN), Volume I: OPTRAN User's Manual," Report No. WRDC-TR-90-3058, Volume I, Wright-Research and Development Center, Wright-Patterson AFB, OH; June 1990.
16. CMOLD Reference Manual, AC Technology, Ithaca, NY; 1992.
17. Hieber, C.A. and Shen, S.F., "A Finite Element/Finite-Difference Simulation of the Injection Molding Filling Process, *Journal of Non-Newtonian Fluid Mechanics*, Vol. 7; 1980.
18. Wang, V.W., Hieber, C.A., and Wang, K.K., "Dynamics Simulation and Graphics for the Injection Molding of Three-Dimensional Thin Parts," *Journal of Polymer Engineering*, Vol. 7, No. 1; 1986.
19. Chiang, H.H., et al, "Integrated Simulation of Fluid Flow and Heat Transfer in Injection Molding for the Prediction of Shrinkage and Warpage," Vol. ASME-HTD-175/MD-25, pp. 133-146; 1991.
20. Chiang, H.H., Hieber, C.A., and Wang, K.K., "A Unified Simulation of the Filling and Postfilling Stages in Injection Molding. Part 1: Formulation and Part 2: Experimental Verification," *Polym. Eng. Sci.*, Vol. 31, pp 116-139; 1991.
21. Hieber, C.A., Chapter 1 in *Injection and Compression Molding Fundamentals*, A.I. Isayev, Ed., Marcel Dekker, New York; 1987.
22. P3/ANIMATION Application Module User Manual, Publication No. 903003, PDA Engineering, Costa Mesa, CA, February 1993.

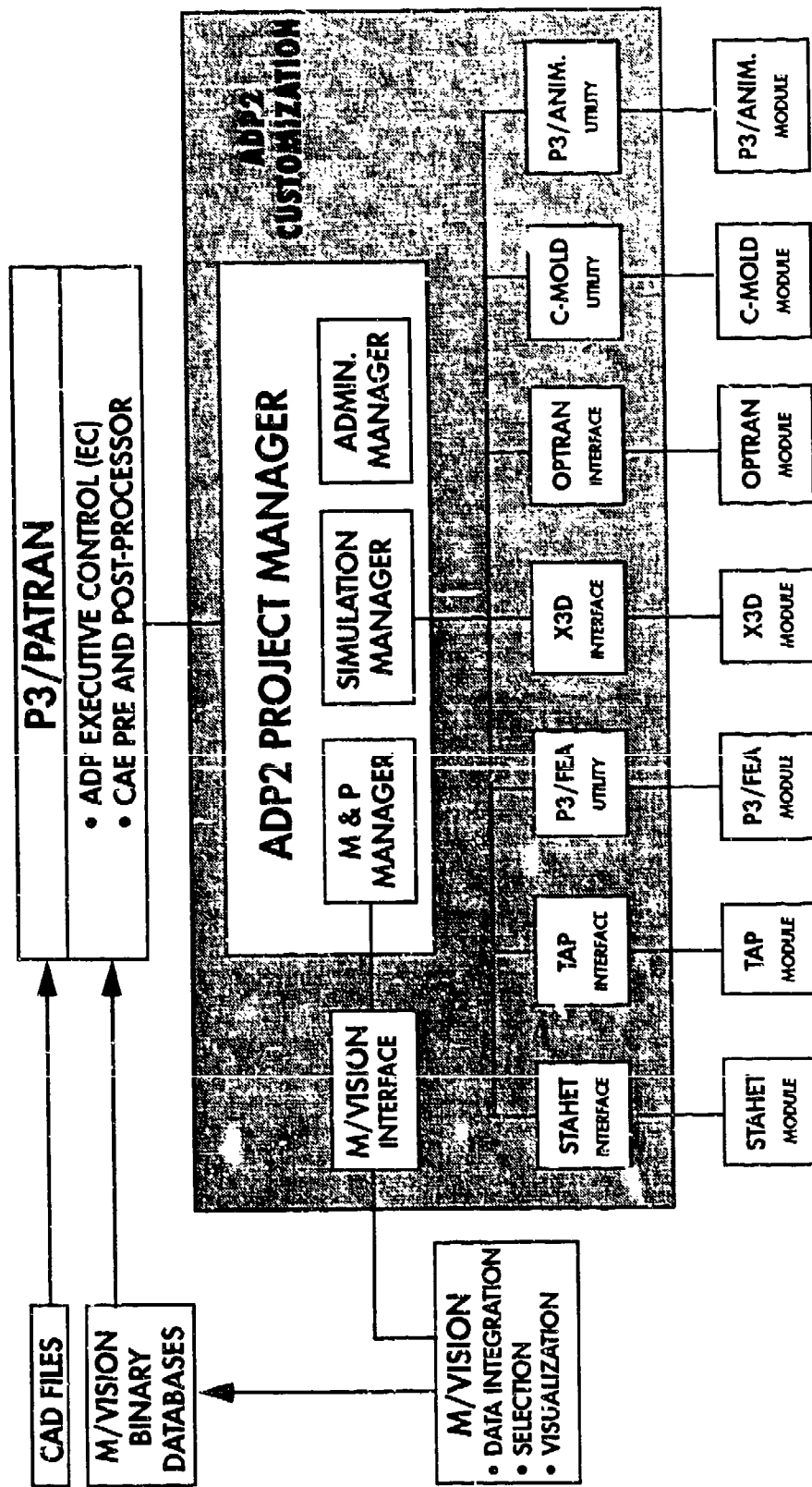
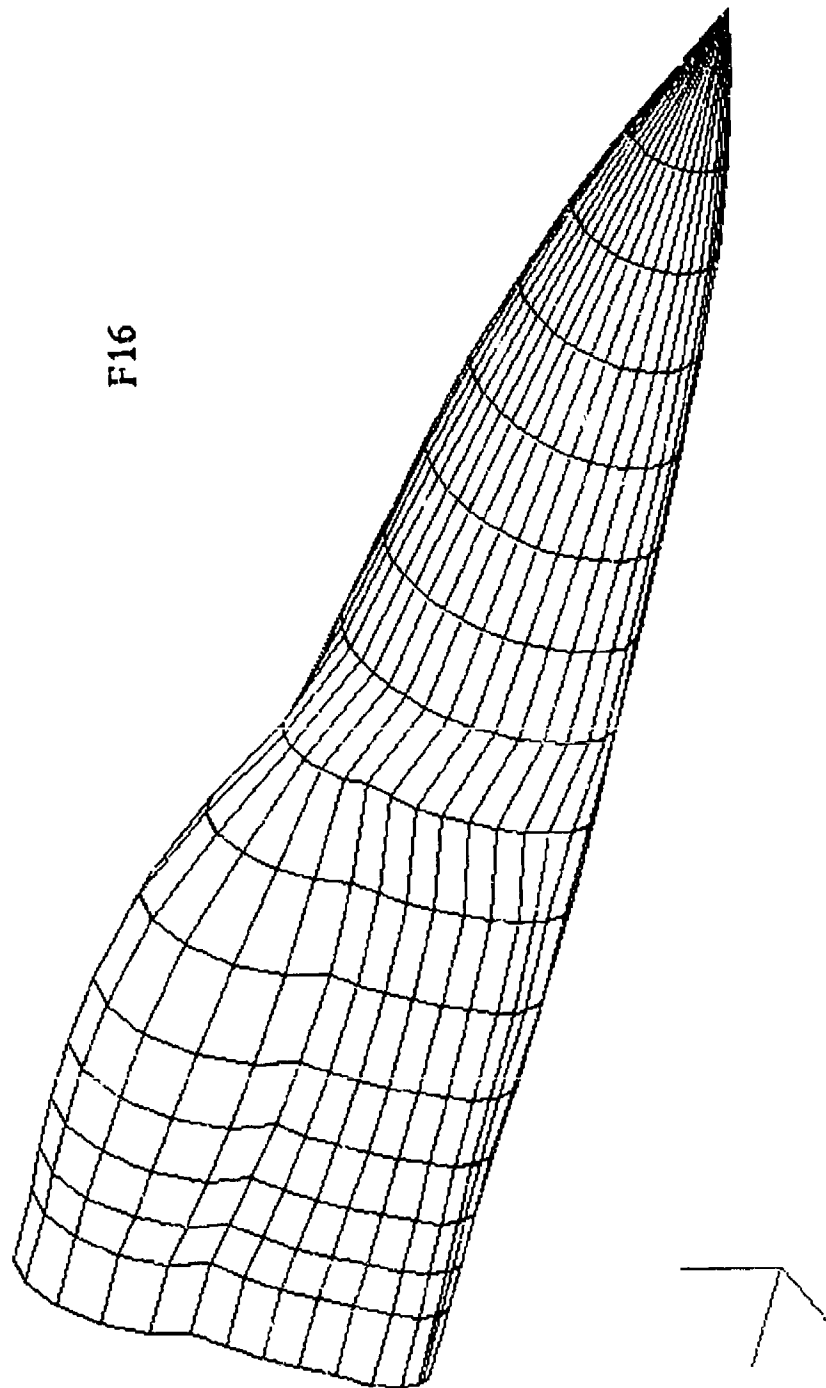


Figure 1 ADP2 Architecture



**Figure 2 F-16 Aircraft Forebody Model, S-10 Library**

Time: 16:05:18  
Date: 07/29/93

Contour  
Node Scalar1

Color Index

8 0.299E+02  
9 0.278E+02  
0 0.258E+02  
9 0.238E+02  
8 0.218E+02  
7 0.197E+02  
6 0.177E+02  
5 0.157E+02  
4 0.136E+02  
3 0.116E+02  
2 0.958E+01  
1 0.756E+01

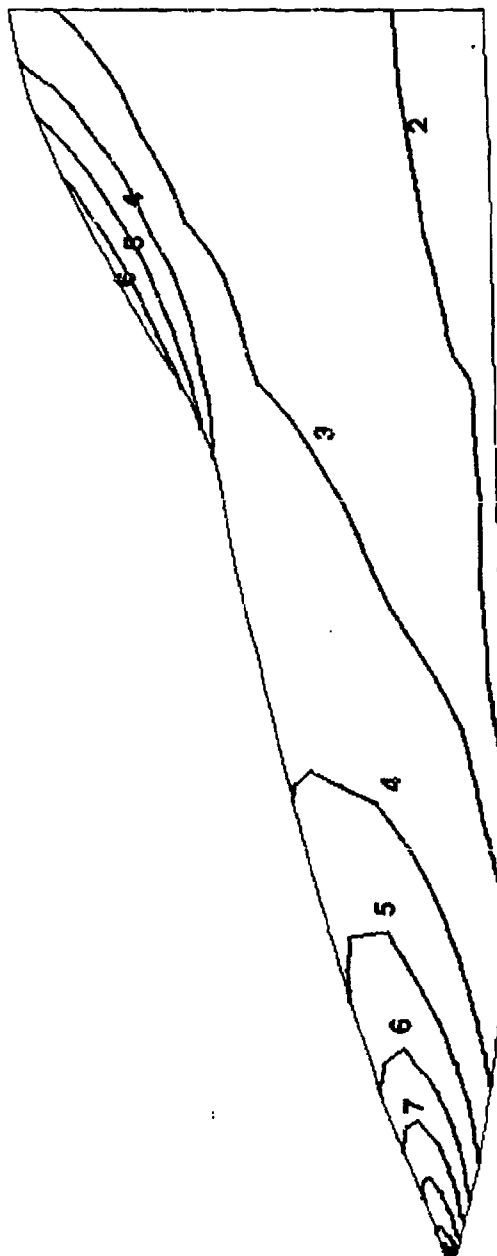
Min= 0.7557E+01  
Max= 0.3189E+02  
Min ID= 101850  
Max ID= 100025

Contour1:

Nodal

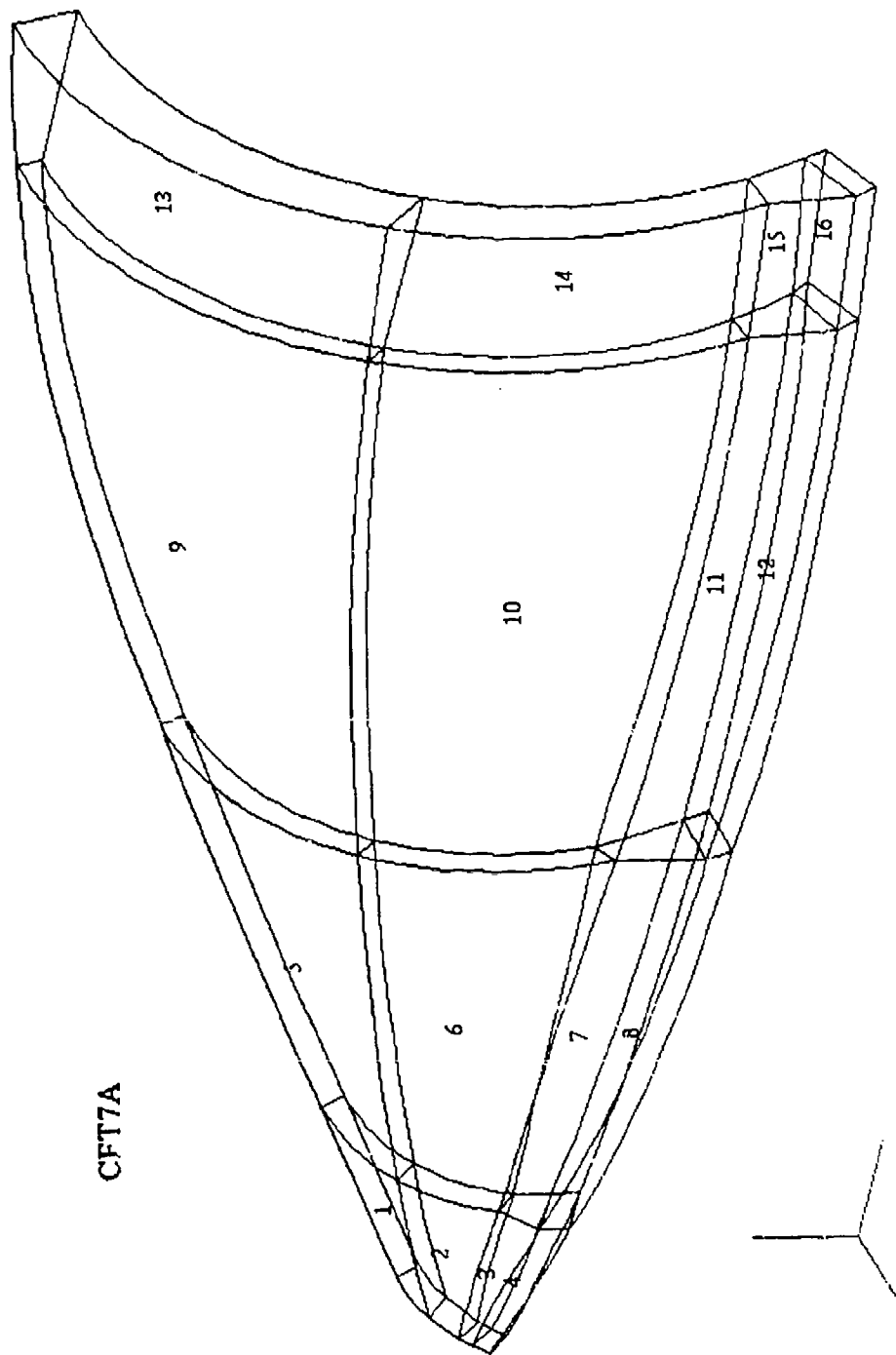
Surface Heat Transfe  
Scalar  
(NON-LAYERED)

Job One -- Results  
Flight Condition Num



Y  
X

Figure 3 STAHET II Result, Aerodynamic Heating Rate (Btu/ft<sup>2</sup> sec)



**Figure 4 CFT7A Transparency Geometry Model**

Fringe: LC=2.5-RES=1.1-P3/PATRAN R1.2-Nodal-TAP-26-Jul-93 16:31:30

TAP Thermal Results for CFT7A

Mission point at 1519 seconds

Mach 2.05, 35089 ft.

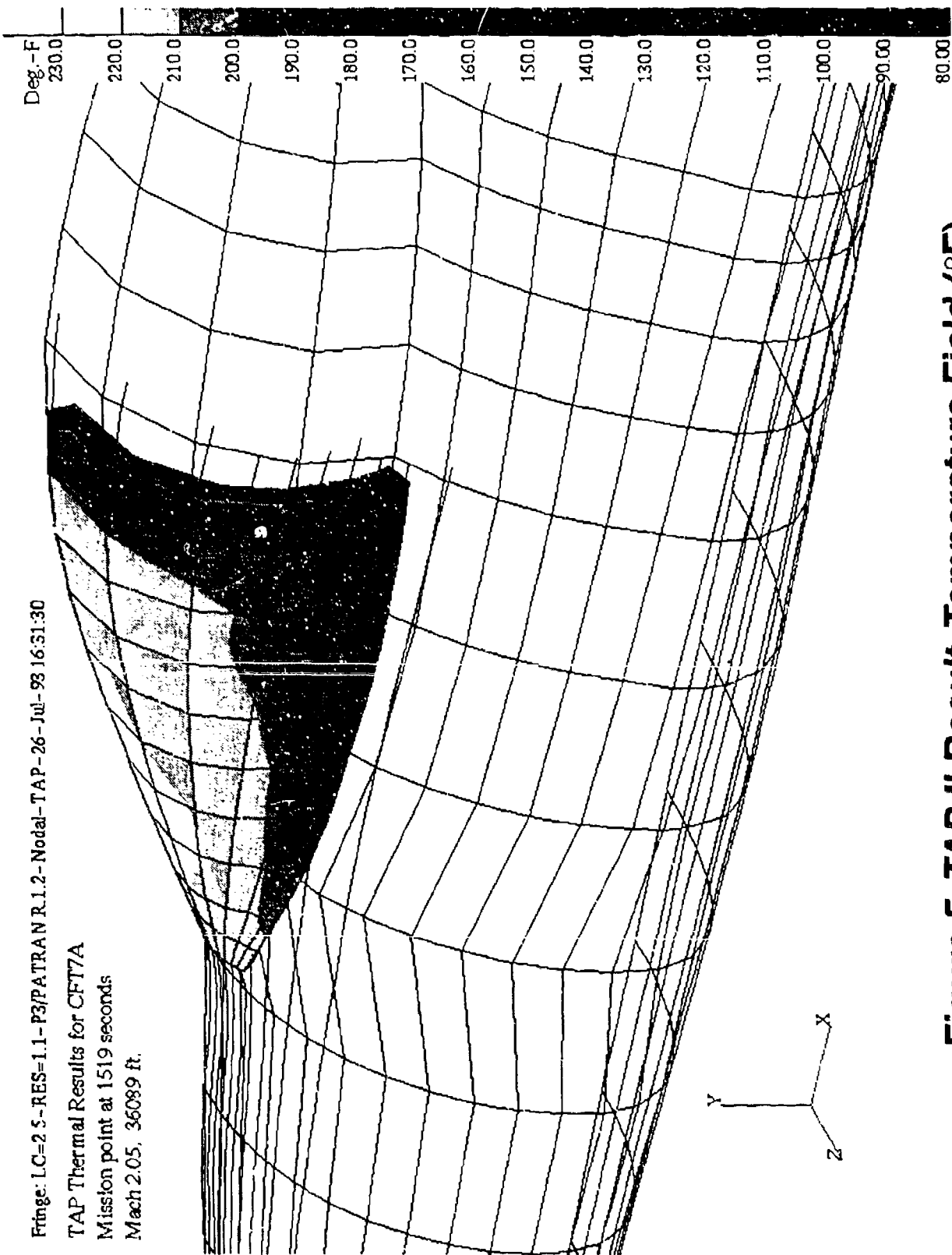
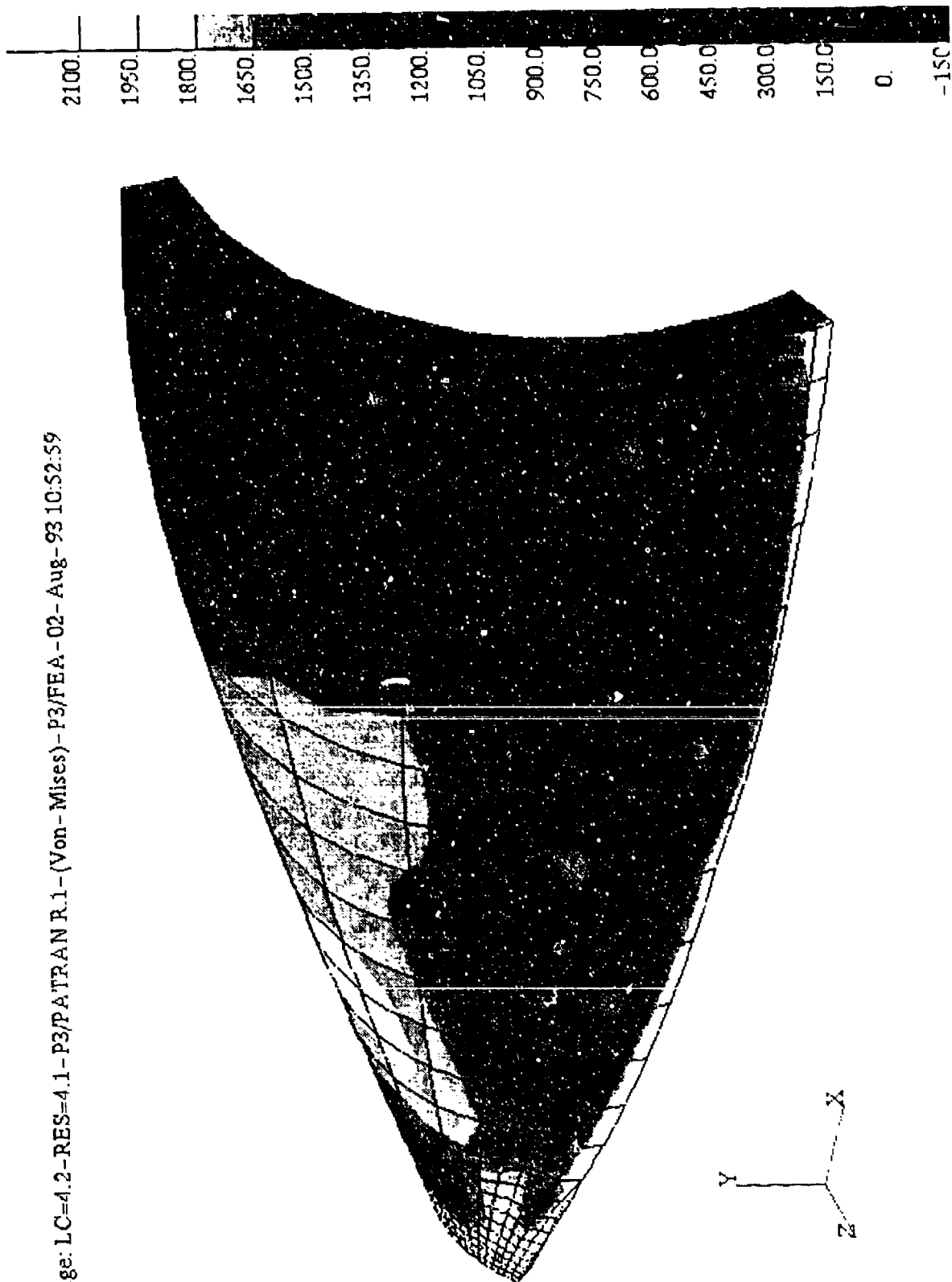


Figure 5 TAP II Result, Temperature Field (°F)

Fringe: LC=4.2-RES=4.1-P3/PATRAN R.1-(Von-Mises)-P3/FEA-02-Aug-93 10:52:59



**Figure 6 P3/FEA Result, Von Mises Stress, Static Case (psi)**



8 0.960E+04  
 7 0.883E+04  
 6 0.805E+04  
 5 0.728E+04  
 4 0.651E+04  
 3 0.573E+04  
 2 0.496E+04  
 1 0.418E+04  
 0 0.341E+04  
 -1 0.263E+04  
 -2 0.186E+04  
 -3 0.109E+04

Min ID= 42  
 Max ID= 49

Contour1:  
 Centroidal  
 Von Mises Stress  
 Scalar  
 0-(NON-LAYERED)

First Run  
 Time 0.003  
 Max. Deformation =  
 2.046820E+01  
 @Node 292

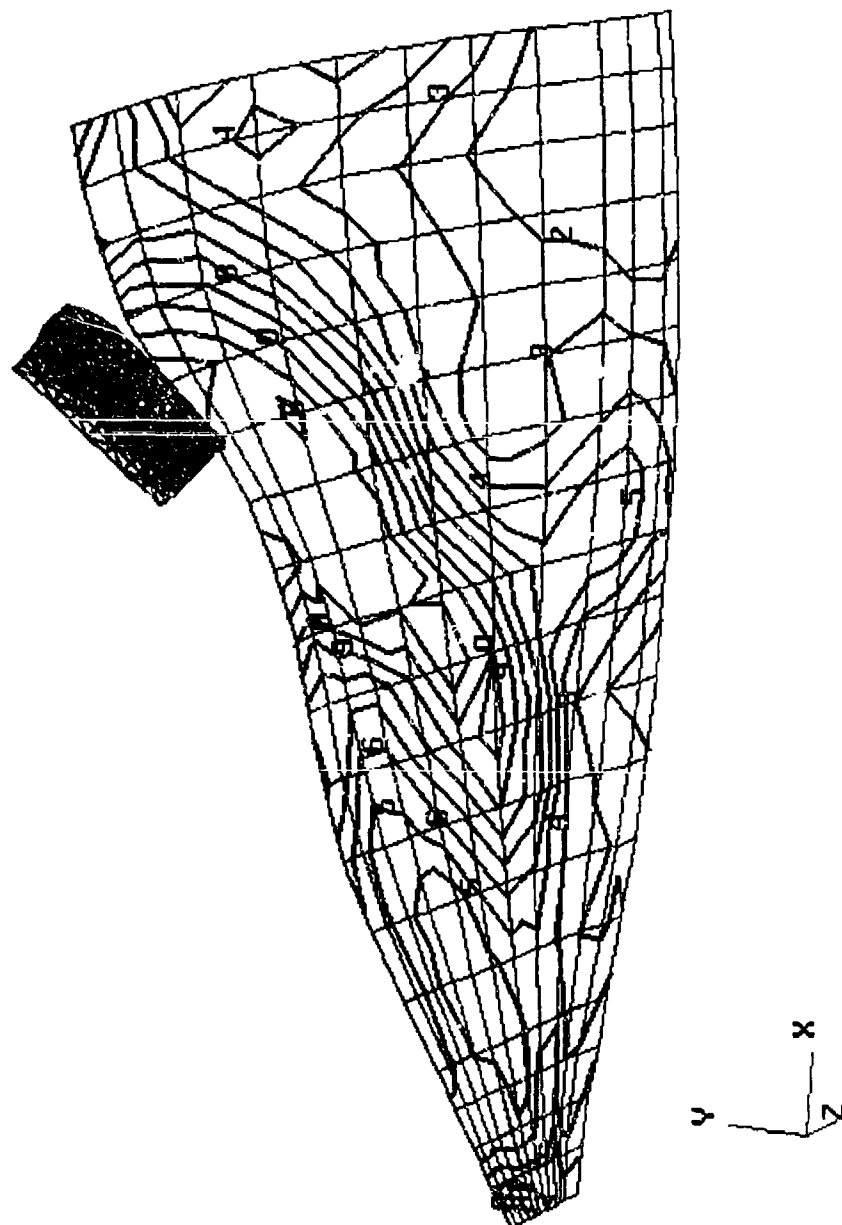
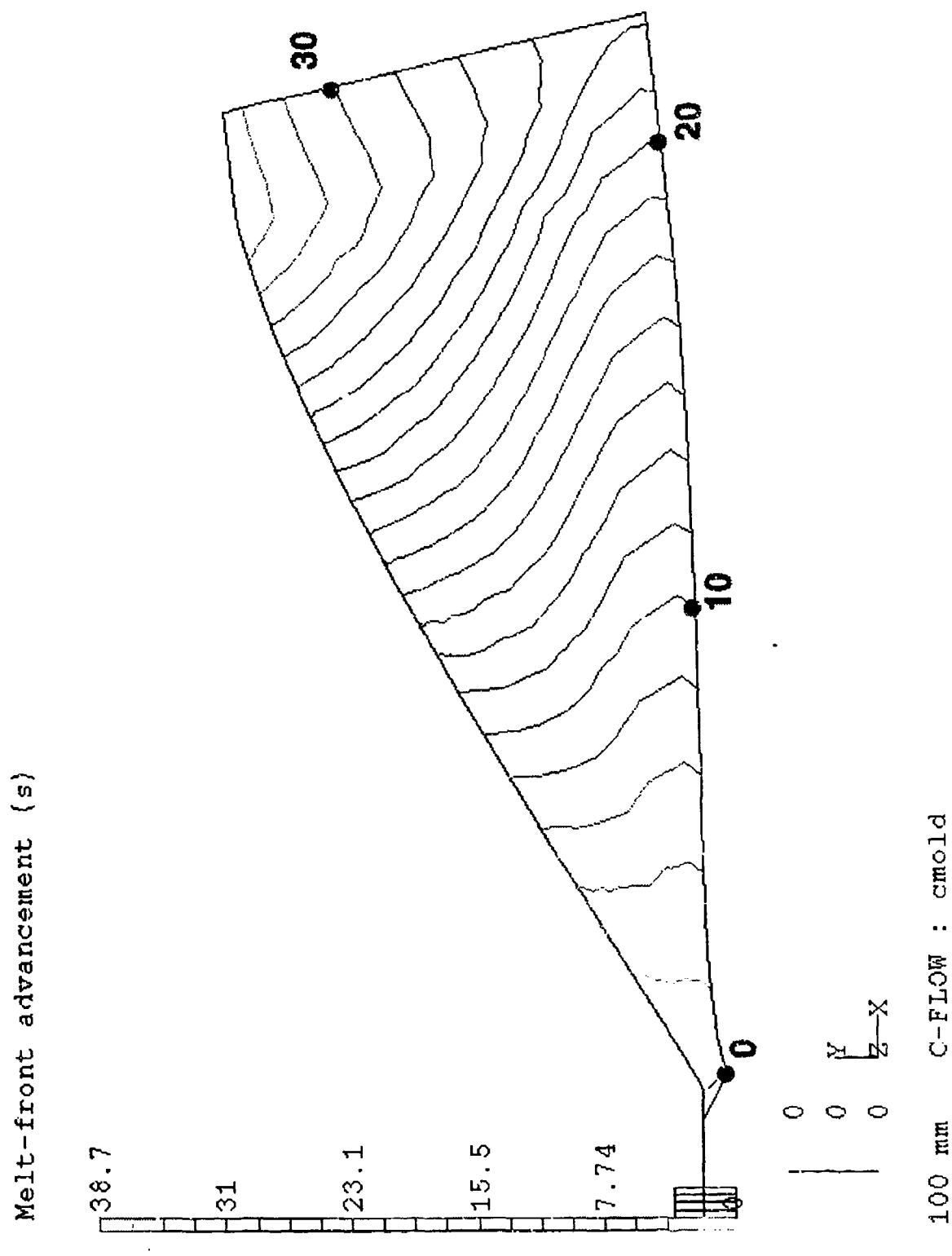


Figure 7 X3D Result, Time Resolved Von Mises Stress (psi)



**Figure 8 C-MOLD Result, Melt Front Advancement (sec)**

## THE USE OF COMPUTERIZED MATERIALS DATA IN ADP2

T. E. Mack  
T. E. Kipp  
PDA Engineering

T. J. Whitney  
University of Dayton

M. Gran  
Flight Dynamics Directorate  
Wright Laboratory

## THE USE OF COMPUTERIZED MATERIALS DATA IN ADP2

Thomas E. Mack and Thomas E. Kipp, Jr.  
PDA Engineering, Inc.  
2975 Redhill Avenue  
Costa Mesa, CA 92626

Thomas J. Whitney  
University of Dayton Research Institute  
JPC 317/MS-0110  
300 College Park Avenue  
Dayton, Ohio

Michael G. Gran  
WL/FIVR Bldg. 255  
2079 Tenth Street  
WPAFB, Ohio 45433-7502

---

### ABSTRACT

An Air Force program for creating an engineering workstation devoted to the design of aircraft transparencies, ADP2 (Analytical Design Package), was structured around a materials data server (M/VISION coupled with PATRAN), [1]. The material data server is at the core of the system and is used to integrate a number of applications and databanks, both commercial off-the-shelf (COTS) and special purpose items developed by the Air Force and the University of Dayton Research Institute (UDRI). It provides the focal point for loading, processing, cataloging and automated transferring of materials data between the various applications.

The ADP is being developed as a part of the Frameless Transparency Program (FTP). It is a design tool consisting of existing analysis codes and Computer Aided Engineering (CAE) software. Within the FTP, the objective of ADP2 is to develop an integrated design methodology for frameless transparencies, aircraft interfaces, and their corresponding tooling. The scope goes all the way from materials testing through design and analysis to manufacturing. Several categories of materials data are handled, including raw test data, manufacturer's raw test data, manufacturer's product data, evaluated property and specification data (such as from Military Handbooks), and synthesized or simulated properties data. The functional environment requires multiple iterations or cycles through the design process, with evolving material properties, processing parameters, as well as various testing, manufacturing, and analysis environments.

### INTRODUCTION

Modern transparency system design drivers, and their associated information database requirements, are both diverse and complex, as illustrated in Figure 1, [2]. This, combined with the transition from a "build and bust" to a "design and analytically simulate" philosophy for transparency system development, has led to an ongoing need to organize and subsequently computerize the vast amounts of new and existing information. With new transparency materials, new design and manufacturing concepts, and improved analytical simulation tools continually emerging, the need for computerized access to concurrent, consistent and controlled (quality standards) materials and manufacturing process data has become an important, but difficult, problem within the transparency design community. Recent ADP2 software system development efforts have addressed the technical information database access requirement and, more specifically, have provided direct computerized access to materials and manufacturing process data within the ADP2 integrated design/simulation module software system environment. It is this integrated functionality which is addressed in this paper.

### WHY MATERIALS AND MANUFACTURING PROCESS DATA HAVE BEEN COMPUTERIZED WITHIN ADP2

A concurrent "Design/Analysis/Manufacturing" engineering process requires concurrent access to concurrent, consistent and controlled (quality standards) materials and process information. Computerization can provide a method for the systematic organization of large amounts of diverse and complex information (i.e., relational databases), while simultaneously providing for rapid electronic access (i.e., standard SQL database queries) by designers, analysts and process/test engineers within the product development cycles. Once

computerized, materials information can be more easily integrated into the CAD/CAE simulation process, and then updated, if needed, during product development cycles where materials and/or manufacturing processes are evolving.

Standard M&P data control and quality procedures are more easily maintained and enforced across all disciplines in the transparency design/simulation process. Accurate and up-to-date material properties for multiple complex analytical simulations can be provided from one source (i.e., thermal, structural, injection molding, optics, etc.). Automated materials data production can be supported to reduce cost and time to input, synthesize, store, generate, and access material properties. Reliable units' conversions can be ensured through user (or developer) definable and selectable "soft" templates, provided within the computer software being utilized. Both tabular and graphical data can be provided (displayed) simultaneously in a spreadsheet environment that accommodates data modification/generation and subsequent database storage. Consistent material and manufacturing process designations (attributes) can be defined across all information databases (CAE, Processing, Testing, Logistics, etc.), which provides a method to eliminate a well documented product development problem; that being non-conforming materials and processes. The provision for consistent material and process designations is of particular importance for plastics and composites, which often evolve as part of the product development cycle.

### **HOW MATERIALS AND MANUFACTURING PROCESS DATA HAVE BEEN COMPUTERIZED WITHIN ADP2**

The Analytical Design Package (ADP2) is being developed as part of the Air Force Frameless Transparency Program (FTP). ADP2 is a software design tool that has a single graphical user interface (GUI) and executive control system (ECS) provided by a PATRAN Command Language (PCL) customization of P3/PATRAN, [3]. The ADP2 Project manager, as illustrated in Figure 2, provides a fully integrated transparency design software system environment with the following features:

- Computer Aided Design (CAD) import
- Computer Aided Engineering (CAE) functionality
  - Geometric and finite element modeling (FEM)
  - Analytical simulation code (FEA) solutions
    - Structural (MAGNA, X3D, P3/FEA)
    - Thermal (TAP)
    - Aeroheating (STAHET)
    - Optic (OPTRAN)
    - Injection Molding (C-Mold)
    - Animation (P3/Animation)
  - Analytical results post-processing
- Materials and Processes (M&P) database access and modification (CALS compliant)

The objective of the ADP2 effort, as part of the FTP, is to develop and validate an integrated design methodology for frameless transparencies and their associated aircraft interface and tooling requirements.

The overall design process must be iterative, and capable of producing frameless transparency and associated aircraft interface designs, high confidence transparency injection mold designs, and analytically defined molding process parameters and complex high strain rate material property relationships. This will help ensure accurate simulations of actual full-scale transparency processing and test (i.e., birdstrike) results. The computerization of materials and manufacturing process database information, and its subsequent implementation within the ADP2 software system architecture (Figure 2), is critical to the overall design process, and the subject of discussion for the remainder of this paper.

### **ADP2 Materials Software Tools' Functionality and Role Within the ADP2 System**

As shown in Figure 2, two (2) commercial off-the-shelf (COTS) software products are at the core of the ADP2 materials and manufacturing process data server:

- M/VISION Materials System Builder (MMSB) [4]

Figure 3 summarizes the key materials environment functionality that this COTS product provides the integrated ADP2 system. MMSB serves as the central electronic databank source for all ADP2 materials and manufacturing process test data and CAE analytical simulation module material property data. Each material property can have its own units, precision and footnotes. Materials behavior, best described by figures (i.e.,  $\sigma$ - $\epsilon$  curves, S-N curves, etc.), are storable directly in MMSB databanks as curve, scatter and runout points with error bars, axis labels, units, and footnotes. Property tables, figures and images (i.e., micro-photographs, CT images, ultrasound scans, etc.) are related with the complete pedigree of material, processing and test conditions.

Databanks, spreadsheets and other MMSB component building blocks can be customized and assembled to meet specific company, project and/or user needs; fulfills critical requirement of the ADP2 software system integration solution. Requirements for company, project or user MMSB databanks are easily defined and constructed into new user-defined databases. Extension of the database schema, including the addition of new attributes and extension of relations, can be implemented at any time, even after partial loading of the database. Customized spreadsheets can be seamlessly integrated to input, synthesize and store data, to visualize trends (full graphics functionality of spreadsheet data), to model material responses, and to build entire databanks. The MMSB's spreadsheet environment is the gateway to electronic manufacturer's or test data sources, other spreadsheets, and other databases. Standardized Remote Procedure Call (RPC) [5] access to C or FORTRAN programs is provided from within the spreadsheet environment. The RPC spreadsheet interface is a feature of particular importance to the ADP2 system integration solution.

MMSB adheres to current and emerging standards for materials data exchange [6,7]. MMSB supports data transfer in PATRAN® neutral file and IGES standard formats. MMSB reflects a continued participation, by its developers, in the emerging product data exchange standard using ISO/STEP (PDES). This has produced an MMSB which supports both EXPRESS import and export Physical file data.

- P3/MATERIALS SELECTOR (P3MS) [3]

PATRAN 3 module that provides a direct, auditable link between MMSB material databanks and the PATRAN 3 CAE simulation modeling environment (core COTS product of the ADP2 system solution). As shown in Figure 4, P3MS provides a form driven graphical user interface environment, within the PATRAN 3 "Materials" Application, to select material property information directly from MMSB binary databanks (i.e., Standards (MIL-HDBK-5 and 17, PMC90), Producers (Plastics, Metals, Ceramics, Composites), and ADP2 Defined (CAE, Processing, Testing, Logistics)).

As shown in Figure 5a, a simple mouse pick selects the particular MMSB materials databank to be accessed for consistent, concurrent and controlled material properties to be assigned to a particular simulation module's analytical material property model. The entire selected databank, including footnotes, is displayable within the "Material Selector (MS)" form, as illustrated in Figure 5b. A full feature spreadsheet environment, with database query functionality, is provided to reduce the desired database set for review. Once selected, a particular material's database properties are automatically transferred from the MMSB binary database to the P3/PATRAN model database, as illustrated in Figure 6a, including the time and date, the source MMSB databank identification, the pedigree of the property set, and a record of any data that was modified from its original database value or supplied by the analyst (if data value is non-existent within the MMSB databank).

Invoking the "Query" button in the MS form (shown in Figure 5b), opens the MS Query panel, shown in Figure 6b. The query is "constructed" (operator panel assistance) to describe the design criteria that identifies acceptable material conditions. The query form lists all available types of materials information, and requires no knowledge of database terminology or programming. The user can select the desired units system to represent the material property data, as shown in Figure 7a (soft template units file provided for customized units definitions). P3MS is not restricted to special databanks with specific property (attribute) names, but rather works on any MMSB databank. The key to this flexibility is the properties mapping form, Figure 7b, where each P3/PATRAN material property is associated with its MMSB counterpart. The mappings can be modified, saved and recalled. The mappings work in combination with all ADP2 simulation module preferences, and all other P3/PATRAN supported solvers.

## ADP2 Database Requirements and Implementation

Although serving the transparency design community well for many years, MIL-HDBK-17A, Part II, [8] was last updated in 1977, to reflect major changes in material utilization required by evolving birdstrike design requirements [2]. Today's transparency systems are not only faced with the evolving design requirements shown in Figure 1, but with evolving design and manufacturing concepts, as well as vastly improving analytical simulation tools. A key to successfully meeting all these evolving design, manufacturing, analysis, testing and supportability requirements is the development of expanded materials and processes information databases, fully integrated into a design-to-manufacture software environment, such as that provided by the ADP2 system.

Figure 8 summarizes the specific databases defined for the ADP2 system, to meet all of the aforementioned transparency system evolving requirements. Critical database design/support issues for the CAE design database are summarized below:

- Must support multiple material types (i.e., plastics, composites, metals, ceramics, elastomers, etc.)
- Must support multiple CAE user requirements (i.e., mechanical, thermal, optical, electrical, etc.)
- Must support automated, electronic input, synthesis, and storage of raw test data (i.e., load-time, strain-time, etc.)
- Must support standard property data (i.e., D3039 tensile test, etc.)
- Must provide access to a variety of data sources (i.e., Military handbooks, Producers data sheets, ADP2 test/computed, etc.)
- Must provide for modeled material properties (i.e., Rule-of-Mixtures, Lamination Theory, synthesized elastoplastic/rate sensitive relationships, etc.)
- Must provide a database schema that supports relations for typing, designating, describing, the testing of, and the definition of material properties and material responses.

The CAE Design database schema, shown in Figure 9, has been implemented and lightly populated for the ADP2 System's rapid prototyping code development effort. Figures 10 and 11 show examples of MMSB GUI displays of CAE Design database information which was instantiated. The "Report Window" (right-most vertical form) presents a continuous update of all higher level relations' picks.

The Transparency Processing database must provide information (knowledge base) for frameless transparency design and development that includes process (injection molding) optimization, material property identification/classification, and processing data archiving. The Transparency Processing database schema must address the following ADP2 issues:

- Promote information transfer from processing site (data, metadata, footnotes)
- Bridge information to the CAE Design database
- Allow for expansion (i.e., relations, attributes, etc.)

The Transparency Processing database schema, shown in Figure 12, has been defined and lightly populated for the ADP2 System's rapid prototyping code development effort. Figure 13 shows examples of MMSB GUI displays of Transparency Processing database information which was instantiated. The "Report Window" (right-most vertical form) presents a continuous update of all higher level relations' picks.

The Transparency Test and Logistics Support database schemas (i.e., relations and associated attribute lists) are under review at the present time, and will be implemented within the ADP2 System's rapid prototype code development effort. The highest relation level for both of these additional databases might be more appropriately defined using transparency designation information, such as canopy type (FI6A), construction (injection molded), etc., where specific material designations are defined in lower relations. Again, consistent attribute naming for material designations will accommodate a conforming materials "finger print" throughout all ADP2 database information.

The Transparency Test database must support the following information requirements:

- Access to data to validate simulation module(s) analytical predictions
- Access to data that provides design guideline information for new design concept definitions
- Access to data to verify or define supportability/maintainability requirements and/or limits

The Logistics Support database should be configured to support the decision making process (i.e., maintain, repair or replace) for each individual aircraft transparency. Each transparency should have its own service-life record stored in this database, that contains on-going inspection data (i.e., NDE images, aging surveillance reports, etc.), environmental exposure data, repair history data, etc. This type of logistics information can provide qualitative data needed to complete "in-service" transparency system analytical evaluations. As logistic support criteria are defined for transparency replacement, the particular inspection data requirements, test procedures (i.e., modal surveys, etc.), analysis margin prediction levels, fatigue life estimates, etc., can be stored, accessed and updated periodically. Once a transparency is replaced, it could be used for further testing and analysis correlations (i.e., birdstrike), with the test results stored in the Transparency Test database and used to establish service-life reductions in transparency design allowable bird impact velocities. The retired transparency tests could also include "aged" material property characterization testing (stored in CAE Design database with "AGE" attribute defined), local attachment detail subelement tests and full-scale durability testing (stored in Transparency Test database).

#### **Automated Spreadsheet Procedures to Input, Reduce and Store Test or Processing Data**

Figure 14 summarizes the hierarchy of structural property characterization test parameters typically considered in support of birdstrike analytical assessments. Fundamental test data quantities (force, displacement, strain, etc.) are measured as a function of time, as well as geometric data. The data is acquired digitally and stored as columns of ASCII text data. From these data, derived quantities, such as stress-strain or pressure-volume curves are constructible for each specimen.

A customized MMSB spreadsheet was designed and developed for ADP2 to support the automated, electronic data input, reduction and storage requirements, outlined in Figure 14, for the abridged and reduced fundamental test data (i.e., force versus time, strain versus time, etc.). The procedures followed by this example illustrate a computerized data exchange paradigm that will be utilized for other ADP2 system requirements (i.e., injection molding processing data import, synthesis and storage procedures for the Transparency processing database).

Figure 15a shows a simplified spreadsheet layout schematic of this customized MMSB spreadsheet, and Figure 15b shows the specific reduction parameters provided for input to cells B6 through B10. The piecewise linear curves shown in Figure 15b typify the type of fundamental test data to be input, reduced and stored. Figures 16 and 17 show selected portions of this customized spreadsheet with instantiated example values input. This spreadsheet provides the following specific functionality:

- Cells B2:L2 — ASCII input file name designations that contain the text descriptions (test\_info\_specific.dat) and data points (i.e., specimen1\_e.dat) acquired digitally during testing.
- Cells A4:B12 — Input quantities (user typed) that define the specific "Master Curve" type (i.e., strain versus time, EPS11VS1) the number of specimens (3) to be input reduced and the reduction parameter values, shown in Figure 15b (3,1e-6,0.01,300,0,2e-6,5,100).
- Cells A20:B64 — Attribute designations and instantiated values (i.e., Type of Material = Plastic) for the test series being input, as input automatically from the text description file, whose name is input in Cell A2.



- Cells C20:V"max"  
(max = maximum number of data pairs encountered for any specimen) — Piecewise linear test data pairs (i.e.,  $(\epsilon, t)$ ) for "n" specimens ( $n = 1$  to 10 for this demonstration spreadsheet). Unlimited number of unabridged data points accommodated. This data is automatically loaded into the spreadsheet when the associated test specimen text data file is designated in one of the Cells C2:L2 (i.e., specimen\_e.dat in Cell C2). At this time a curve representation is generated automatically and defined as a "polyline" entity (Cell C18) for the data points input (Cell C21:D"a", where a = number of input pairs encountered in the input read function).
- Cells W20:BK"a"  
(a = Cell B12 Value + 20) — Cell locations associated with the Remote Procedure Call (RPC) that accesses the specific FORTRAN code(s) to perform the shift, clip, and regression fits of all input and abridged test specimen data pair sets (Cells 20:V "max")
- Cells AQ20:AZ31 — Second order regression fit equation coefficients for all input specimens.
- Cells BA20:BK"a" — Fitted test data at Cell B11 increments up to Cell B12 upper limit value.
- Cells CA20:CG"a" — Averaged data set from all specimen sets input, and standard deviation data set.
- Cells C5:D14 — Database "put" function directives that automatically instantiate the opened database with the data contained by its argument list designations. Up to ten (10) specimens possible, including specimen average and standard deviation sets, also.

In summary, the spreadsheet user first inputs the ASCII data file names (B2:L2) and then the nine (9) input quantities in Cells B4:B12. He then selects and invokes the RPC function in Cell W20, and lastly selects and invokes the database "put" directives in Cells D5:D14, to load all abridged data sets (Cells W20:AP"a") and fitted data sets (BA20:BK"a", CA20:CG"a") into the database. The user may cycle through the shift/clip/fit process as many times as he desires (changing the values in Cells B6 through B12), before invoking the "put" function commands, based on his visual inspection of the spreadsheet "polyline" sets illustrated in Figure 18a. Once the user has obtained the desired data reductions, and the data is then stored in the database, it can be called up and displayed, as shown in Figure 18b, with its full "Report Window" pedigree shown.

Further customized spreadsheet development is planned for ADP2 to support property synthesis procedures, as summarized pictorially in Figure 19. Master curves from selected material/temperature combinations and from available nominal strain rates will be loaded into the customized spreadsheet, from the CAE Design database. Finite element analysis results can be imported into the spreadsheet from an ADP2 simulation module (X3D) configuration if necessary. RPC access to material property synthesis FORTRAN codes will be accomplished from within the spreadsheet. The RPC function will return an updated set of X3D analysis properties to be stored, by the spreadsheet ("put" commands), in the CAE Design database. These synthesized analysis properties will be selected (P3MS) by the X3D simulation module user to complete the FEA birdstrike analyses. Figure 20 illustrates the basic scheme for the RPC synthesis routines. It is essentially a function minimization procedure, in which the function is an error quantity arrived at by comparing analytically generated stress-strain curves to stress-strain test data. The analysis consists of calculating stresses (using the new material model) from strains recorded in the material test, or generating stress-strain curves from a full X3D analysis of the material test. An initial guess at the material properties is input to the routine. Strain rate (or displacement rate) data from the master curves is used to run an analysis of the material tests and compute a stress strain curve. This curve is compared to the stress-strain test data from the master curves. If the error between the two is acceptably small, the properties input to the analysis are correct, and are stored. If not, new trial properties are computed, and the cycle repeated until correct properties are obtained.

### Computerized Materials and Manufacturing Process Needs

The computerization of materials data clearly requires careful attention to standards to control (quality issue) and communicate materials and manufacturing process data. ASTM and other standards organizations, such as the International Standards Organization (ISO), are continuing to promote and develop new data exchange standards, like the Standard for the Exchange of product Data (STEP). STEP provides a mechanism

for sharing product data, including data specific to materials and manufacturing process information needs. The transparency design-to-manufacture community needs to be aware of STEP, and plan for its acceptance and use. This means supporting and promoting the definition and implementation of application protocols (AP) that explicitly deal with the problem of representing and exchanging product data within the transparency design community and between software systems (tools) that use them. Also, it means becoming familiar with the information modeling language, EXPRESS, which is used for all STEP standards.

Without a common data exchange format, specialized translation programs must be continually written to meet the format requirements of all programs that must share the data. Consequently, if a materials database must be interfaced with several COTS software packages (or systems) a considerable effort must be extended. If, however, one common neutral format, such as the STEP/EXPRESS standard, is used, then only one translation program would be necessary to translate the data into and out of the neutral format. Other software can then access the data through their own specific translation codes. It should be the goal of the transparency community to support and promote standards for data exchange. The benefits to be gained are enormous and lasting.

## CONCLUSIONS

Computerized materials and manufacturing process data requirements have been defined and implemented within the ADP2 transparency design software system. Commercial off-the-shelf (COTS) software tools have been used exclusively, to define, construct, and load the necessary database schemas, to support complete automated, electronic data exchange (customized spreadsheets, materials information selector module, ADP2 executive control utilities (PCL based), etc.), and to support material property data modifications and databank updates. The updates are based on improved correlations with actual test results (RPC FORTRAN code access from within a customized spreadsheet environment). Continued instantiation of the defined databanks and continued implementation of PDES/STEP standards for data exchange are the primary tasks still ahead for the evolving ADP2 system.

## REFERENCES

- [1] Wuerer, J. E. (PDA Engineering), M. Gran (Wright Laboratory) and T. W. Held (University of Dayton), Analytical Design Package-ADP2 A Computer Aided Engineering Tool for Aircraft Transparency Design, Conference on Aerospace Transparent Materials and Enclosures (Sixteenth), U. S. Air Force, Wright Laboratory, Dayton, OH, 9-13 August 1993.
- [2] Smith, Richard A., Blaine S. West and Robert A. Brockman, Aircraft Transparent Materials Characterization, Conference on Aerospace Transparent Materials and Enclosures, U. S. Air Force, Wright Laboratory, Dayton, OH, 16-20 January 1989.
- [3] PATRAN 3 Users Manual, P/N 9033000-1, PDA Engineering, Costa Mesa, CA, March 1993.
- [4] M/VISION Materials System Builder Manual 1.1B, P/N 2190086, PDA Engineering, Costa Mesa, CA, March 1992.
- [5] Bloomer, John, Power Programming with RPC, O'Reilly & Associates, Inc., Sebastopol, CA, February 1992.
- [6] IGES/PDES Organization, Reference Manual, National Computer Graphics Association, Fairfax, VA, June 1993.
- [7] ASM International, *Advanced Materials & Processes*, Chicago, IL, November 1992.

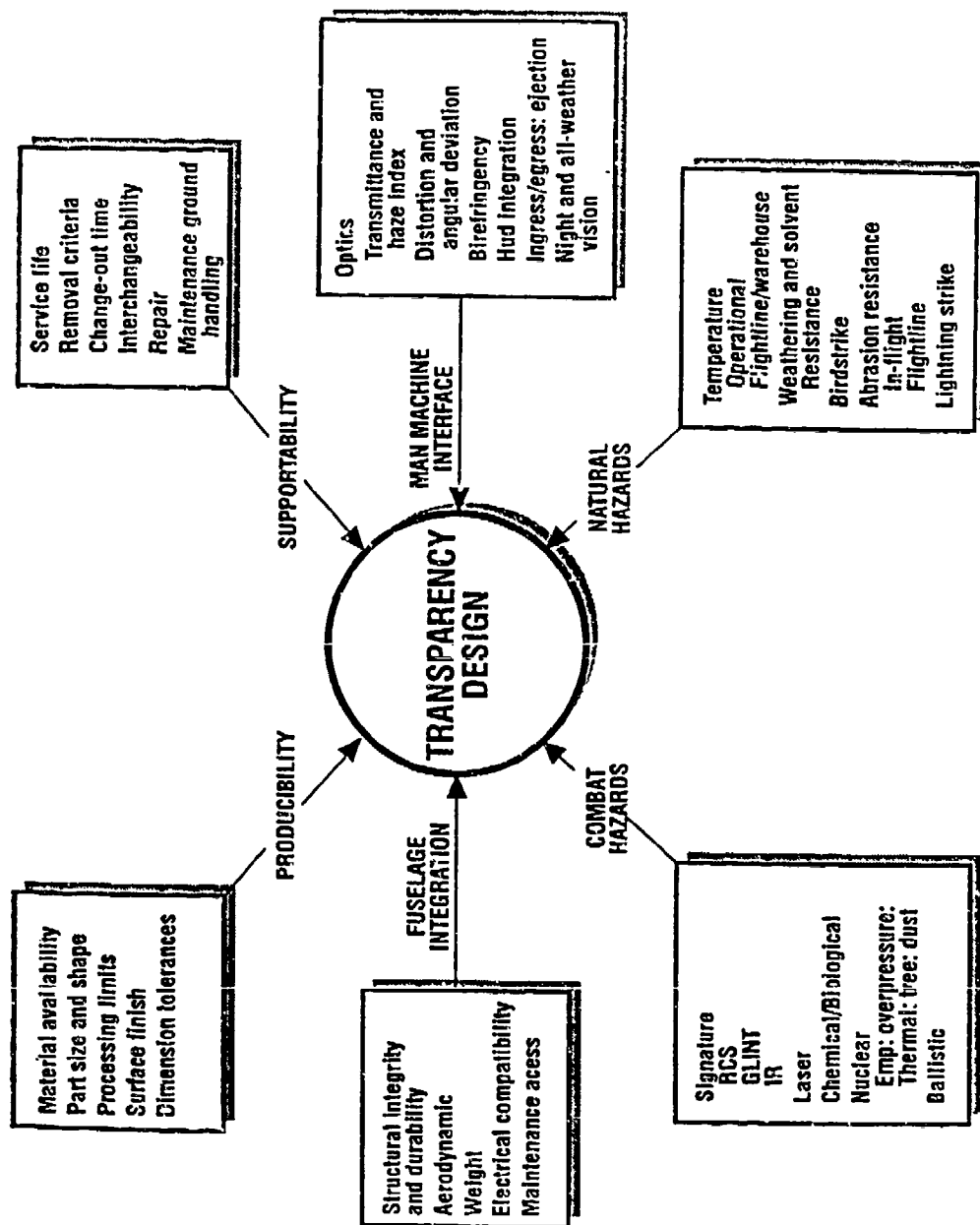


Figure 1. Transparency System Design Drivers [2]

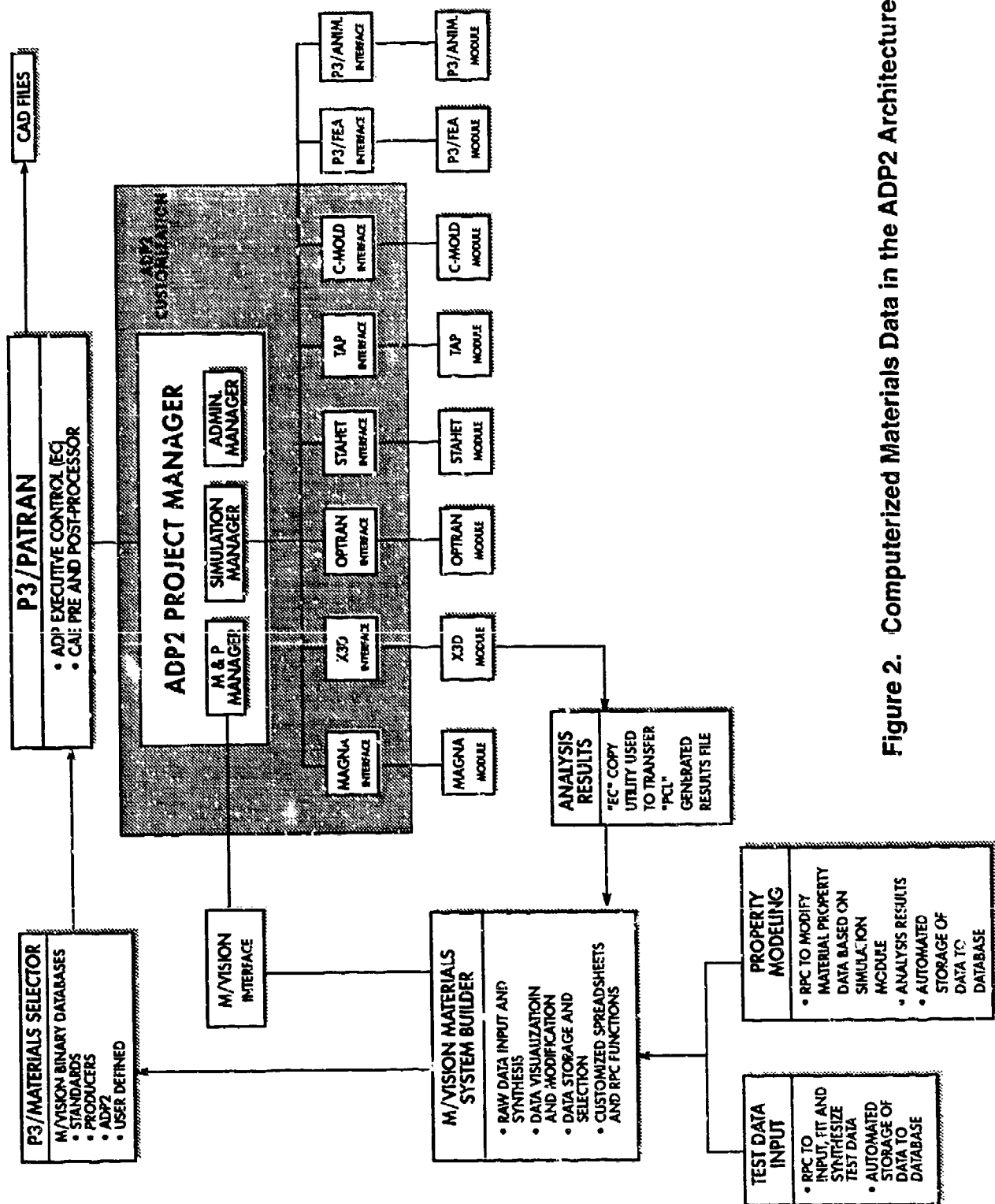


Figure 2. Computerized Materials Data in the ADP2 Architecture

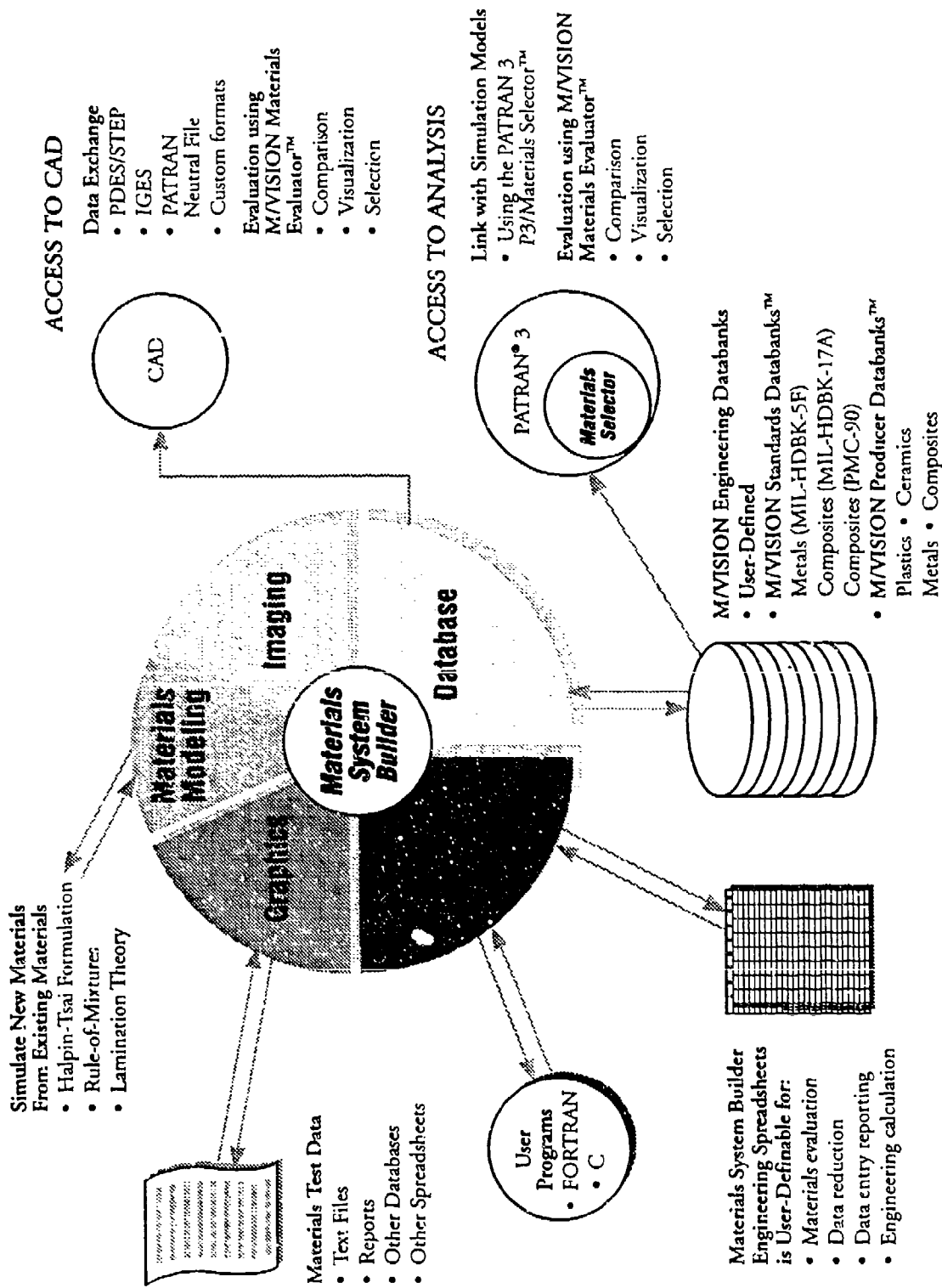
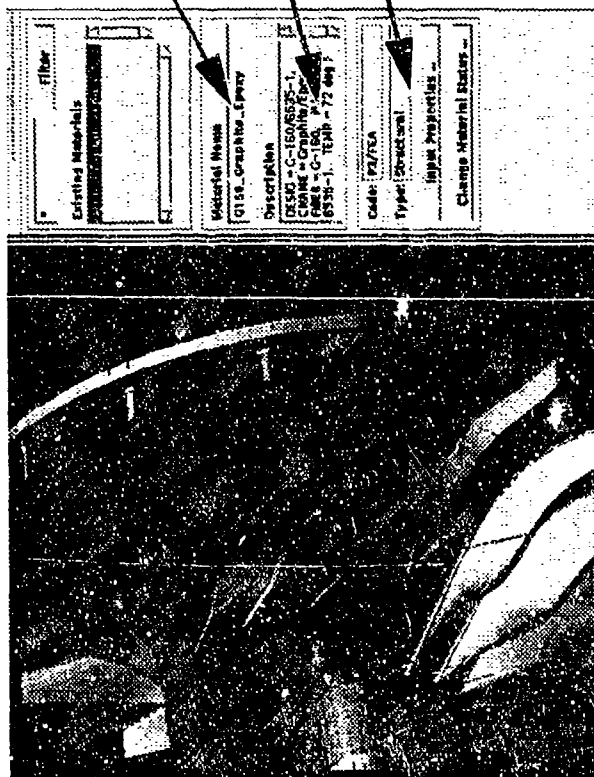


Figure 3. M/VISION Materials System Builder Functionality







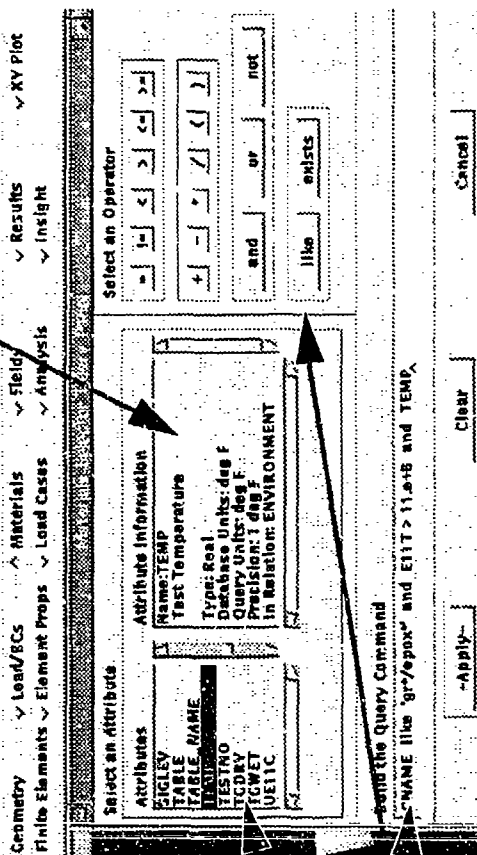
MATERIAL NAME ASSIGNED  
TO SELECTED MATERIAL

SELECTED MATERIAL  
INFORMATION WINDOW

ACTIVE SIMULATION  
MODULE

ATTRIBUTES  
DESCRIPTION

A) DIRECT PROPERTY DATA TRANSFER TO  
SPECIFIC SIMULATION MODULE MATERIAL  
PROPERTY MODEL



ATTRIBUTES  
LIST

OPERATOR PANEL USED TO  
CONSTRUCT QUERY

B) P3MS QUERY PANEL FEATURE

Figure 6. P3MS Database Query and Material Transfer Features



**Select Attributes...**

**Apply** **Clear**

UNIT	TEMP
	deg C
	-55
	22.2
	82.2
	121.1
	-55
	22.2
	176.7

Action: **Create**

Object: **3d Orthotropic**

Method: **Material Selector**

Database: **SI** PATRAN

Units: **SI**

**Properties Mapping...**

Material Name: **C-160-6535-1**

Material Properties: **P3/PATRAN PROPERTY DA1**

AVAILABLE  
UNITS SOFT  
TEMPLATES

A) P3MS UNITS SELECTION FEATURE

**Materials Selector Database**

**Mapping Templates...**

P3/Patran Label	Database Attribute
Reference Temperature =	TEMP
Elastic Modulus =	E11T
Elastic Modulus 22 =	E22T
Elastic Modulus 33 =	E22T
Poisson Ratio =	NU12

ADP2  
SIMULATION  
MODULE  
MATERIAL  
MODEL  
NAME

MMSB  
DATABASE  
ATTRIBUTE  
NAME

C) P3MS DATABASE TO SIMULATION MODULE  
MAPPING TEMPLATE FEATURE

Figure 7. P3MS Database Units and Attribute Mapping Template Functionality

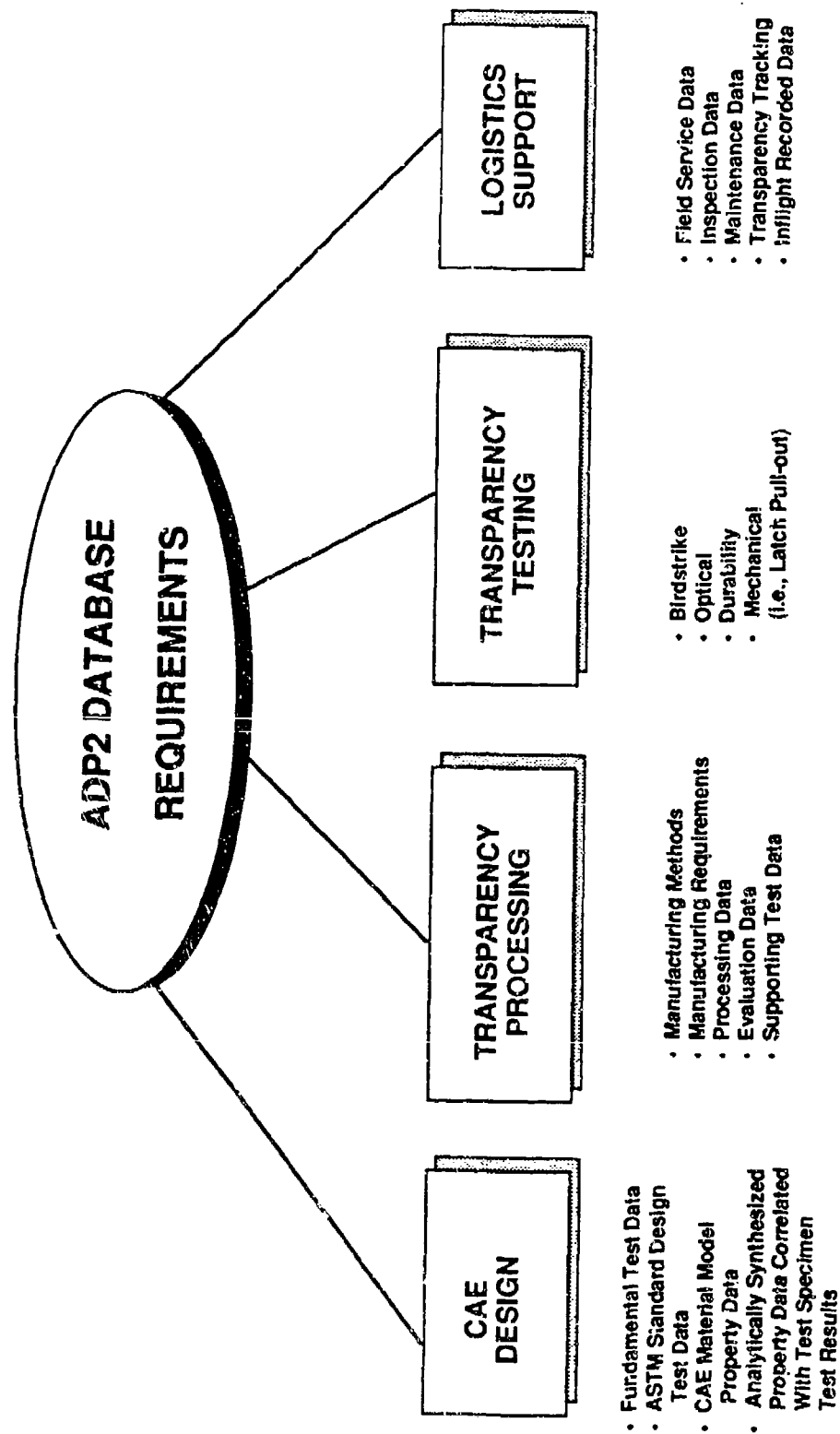


Figure 8. ADP2 Database Requirements

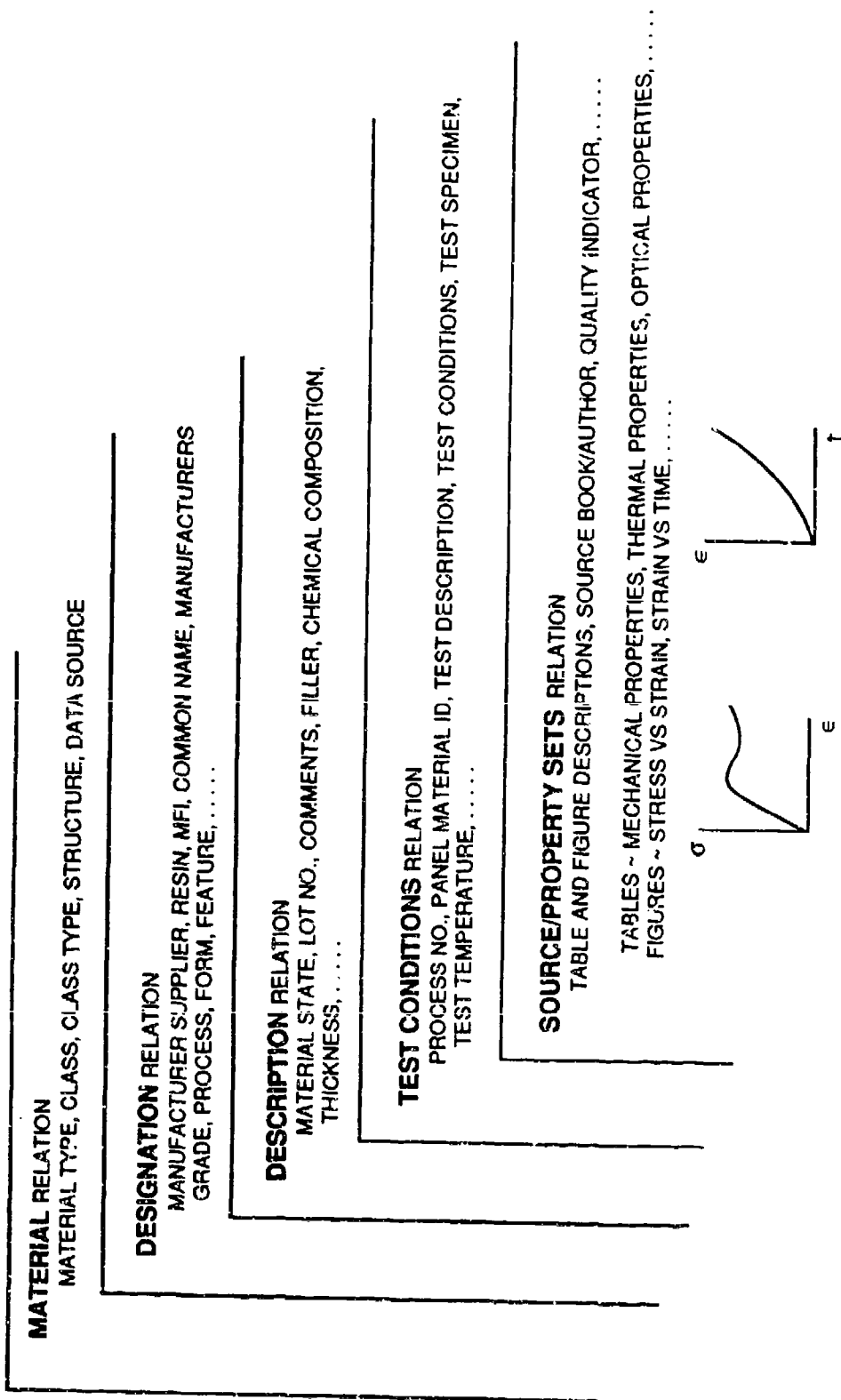
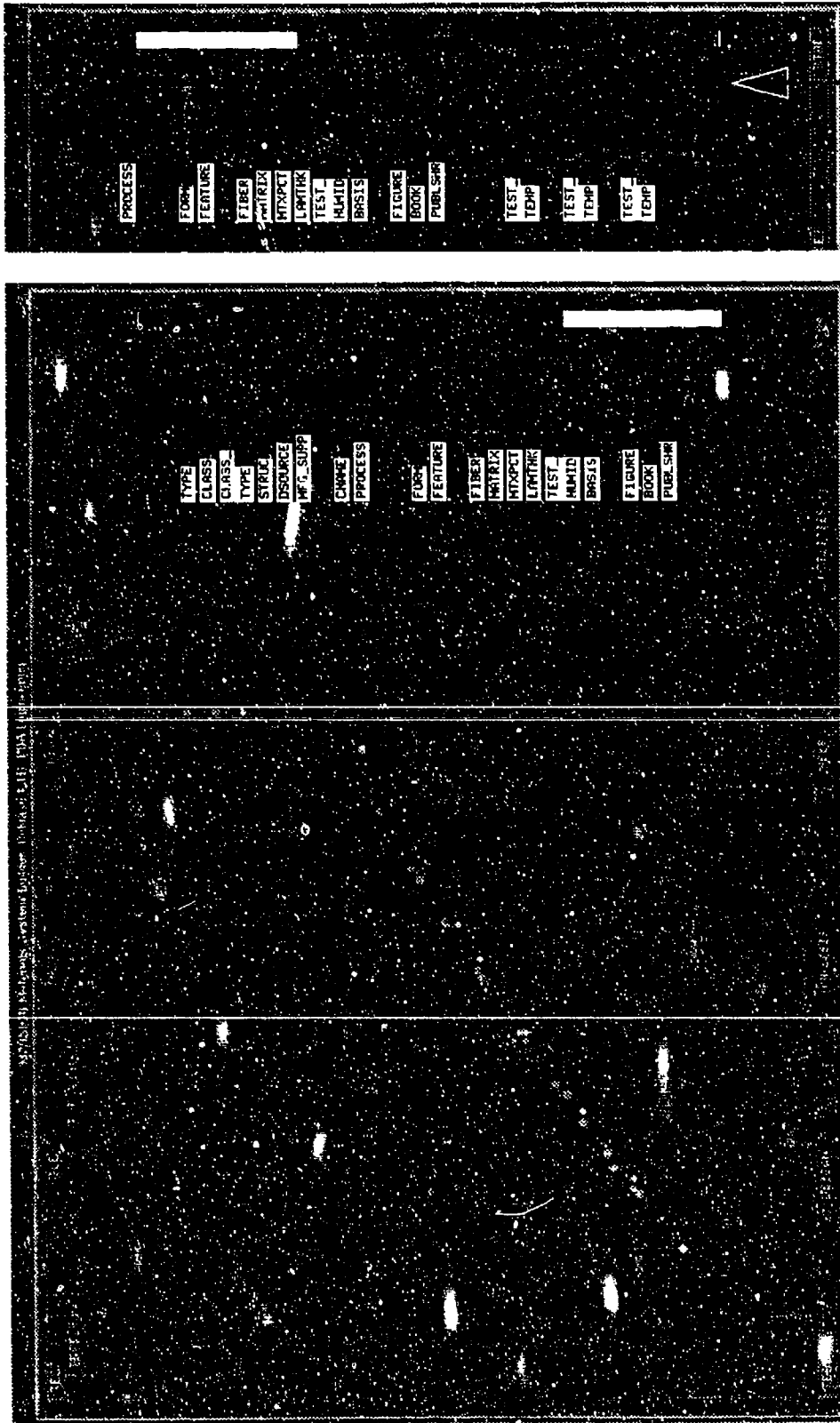


Figure 9. CAE Design Database Schema Relations And Attribute Examples

## REPORT WINDOW



1058



REPORT WINDOW SUMMARIZES  
ALL HIGHER LEVEL PICKS

Figure 11. MMSB CAE Design Database Curve Data Example Display

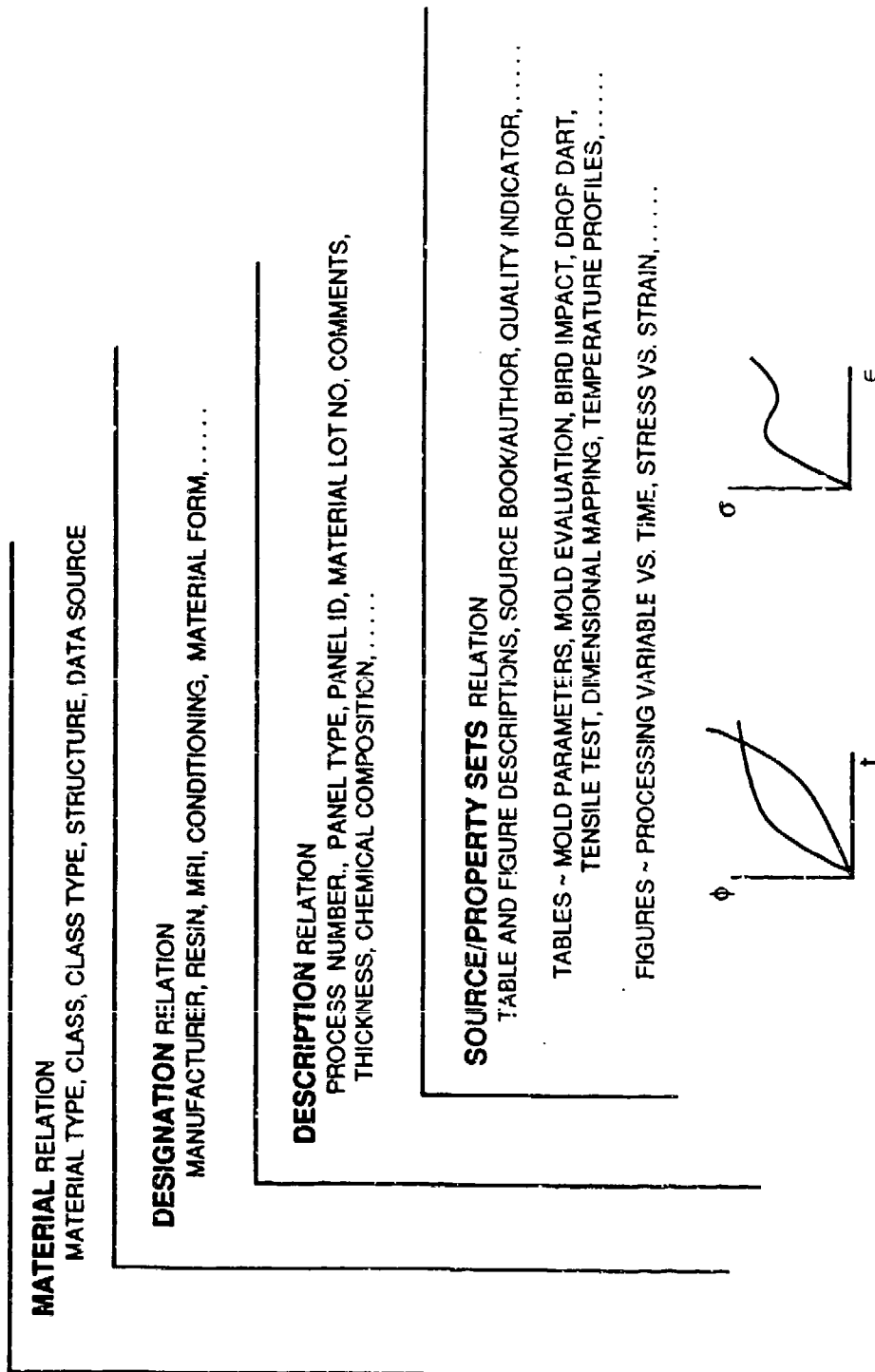


Figure 12. Transparency Processing Database Schema Relations And Attribute Examples

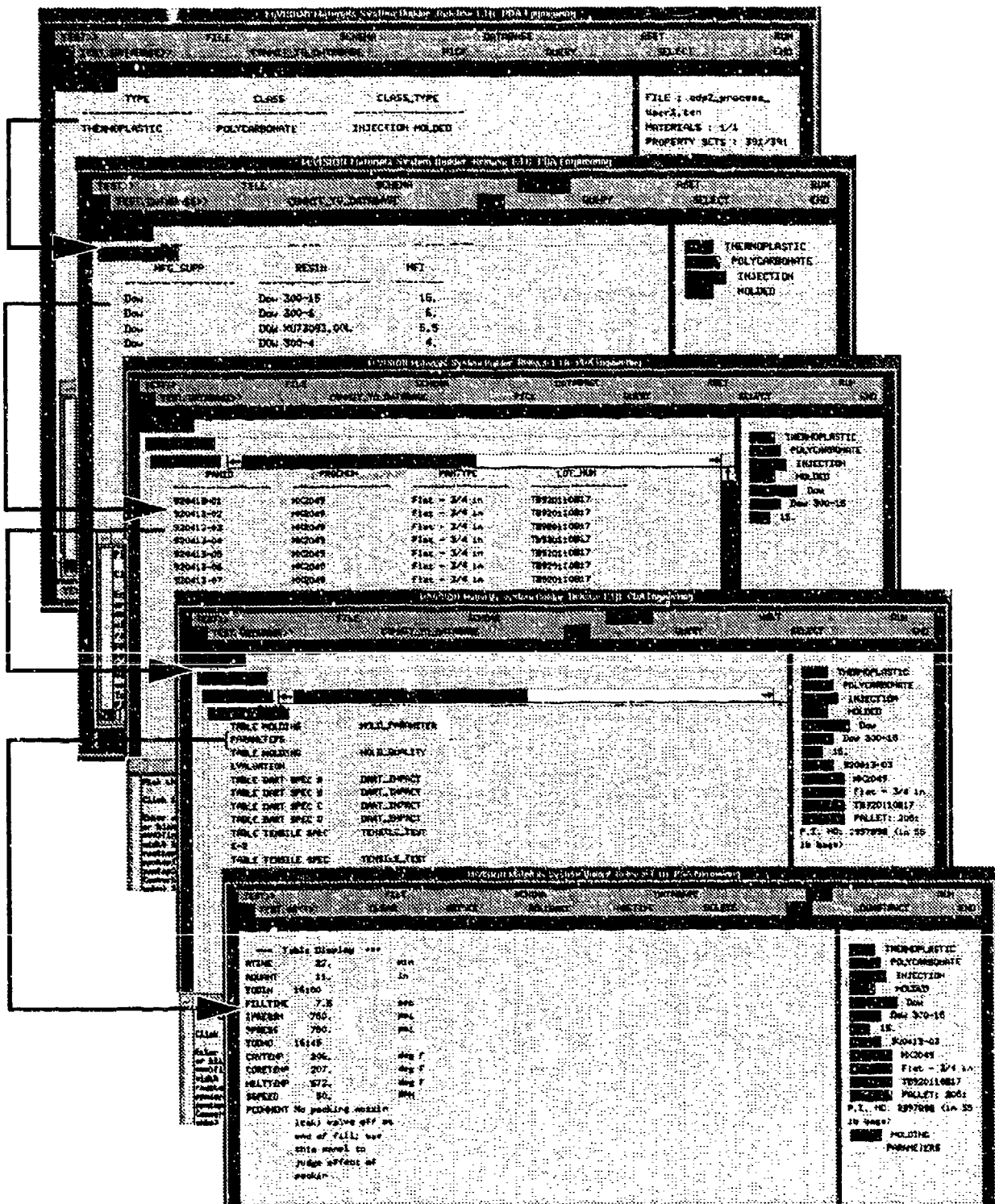


Figure 13. MMSB Transparency Processing Database Relations, Attributes and Tabular Data Example Display

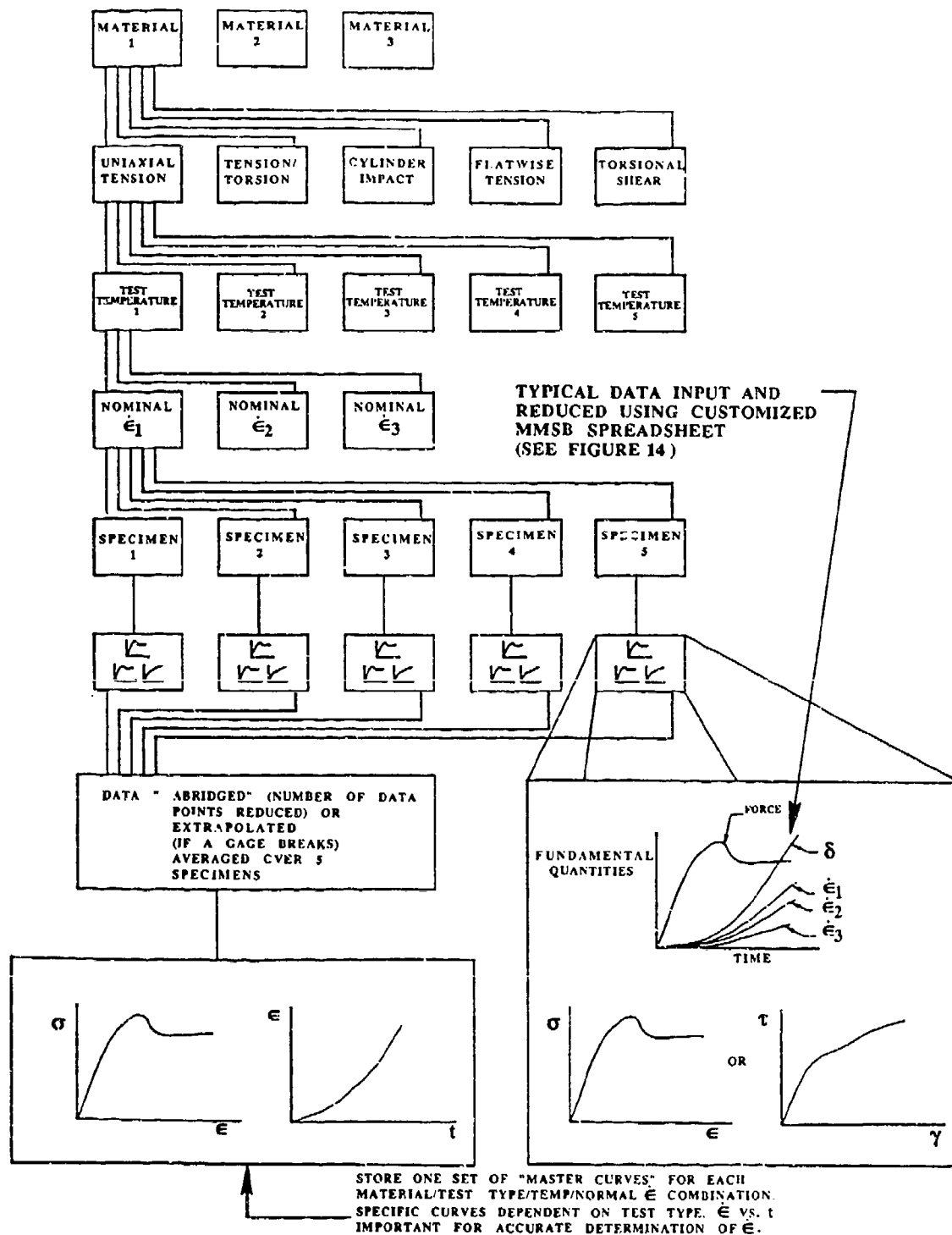
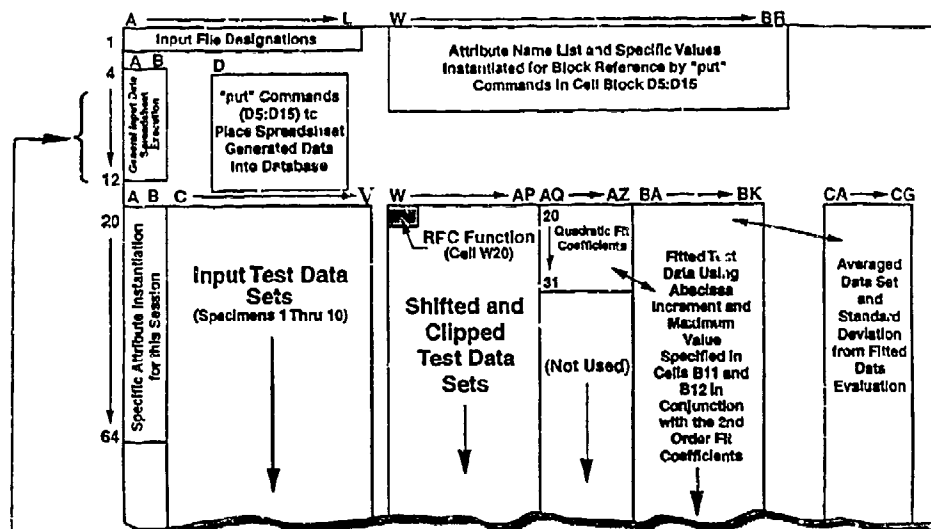
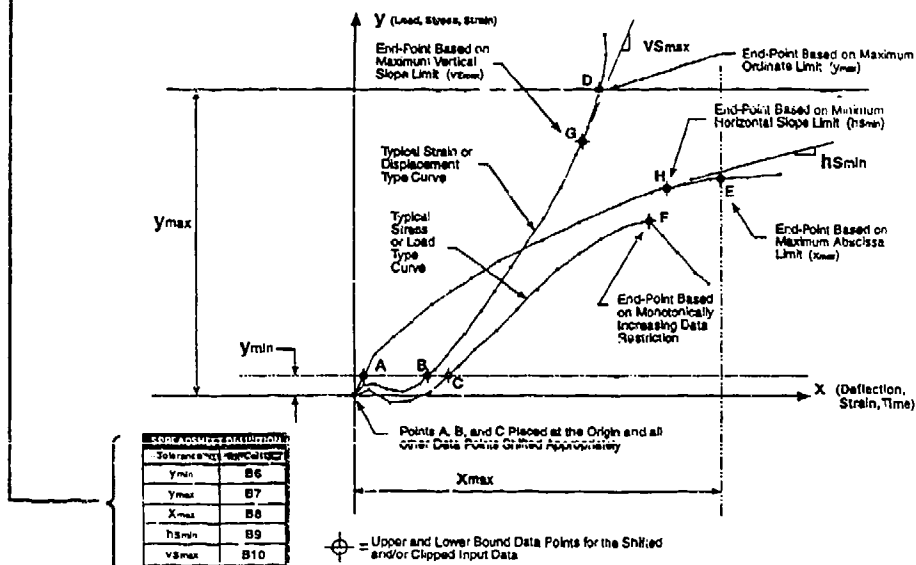


Figure 14. Typical Hierarchy Of Structural Property Characterization Tests Required To Support Birdstrike Analytical Assessments





a) Customized Spreadsheet Layout



b) Customized Spreadsheet Input Reduction Parameters

Figure 15. Customized MMSB Spreadsheet Used To Input, Reduce, And Store Fundamental Test Data

PROBLEM SPECIFIC  
INPUT DATA CELLS

File Edit Function Database Format Help				
	A	B	C	D
1	Directory Path:	/	Specimen #1	Specimen #3
2	File Name:	test_infra_specific.dat	specimen2_e.dat	specimen3_e.dat
3	Input Directive:	./test_infra_specific 10 40	./specimen2_e.dat	./specimen3_e.dat
4	Master Curve Attributes:	[PSI]St		
5	No. of Specimens =	15-06	Specimen #1 Into Data	spec("test", sheet1:BR1, 342:4BR2)
6	Min Limit Value =	0.01	Specimen #2 Into Data	spec("test", sheet1:BR1, 343:4BR3)
7	Max Limit Value =	300	Specimen #3 Into Data	spec("test", sheet1:BR1, 344:4BR4)
8	Min Slope Limit Value:	0	Specimen #4 Into Data	spec("test", sheet1:BR1, 345:4BR5)
9	Max Slope Limit Value:	24-06	Specimen #5 Into Data	spec("test", sheet1:BR1, 346:4BR6)
10	Ver. Slope Limit Value:	5	Specimen #6 Into Data	spec("test", sheet1:BR1, 347:4BR7)
11	Abscissa Increment =	100	Specimen #7 Into Data	spec("test", sheet1:BR1, 348:4BR8)
12	Maximum Abscissa Value:		Specimen #8 Into Data	spec("test", sheet1:BR1, 349:4BR9)
13			Specimen #9 Into Data	spec("test", sheet1:BR1, 350:4BR10)
14			Specimen #10 Into Data	spec("test", sheet1:BR1, 351:4BR11)
15			Average Specimen Data	spec("test", sheet1:BR1, 352:4BR12)
16			TEST_HIM	TEST_HIM
17			Specimen#1-10.1	Specimen#1-10.2
18			(Polylite)	(Polylite)
19	Master Attribute Designations		Specimen #1 Input Data	Specimen #3 Input Data
20	Type of Material =	Plastic	40	48
21	Class of Material =	Polycarbonate	2.6	10
22	Type of Material Class:	Amorphous	7.5	50
23	Structure of Material =	Liquid Crystal	10	70
24	Source of Data =	Dr. Brockman (IBRI)	15	75
25	Manufacturer or Supplier:	Wunderland	24	80
26	Manufacturer Grade =	Hytelal	35	90
27	Material Common Name =	Looking Glass	45	97.5
28			55	

CELLS  
THAT  
PLACE  
SPREAD-  
SHEET  
DATA INTO  
DATABASE

Figure 16. Customized MMSB Spreadsheet Region Used to Input Data

DATA PASSED TO  
FORTRAN CODES

REMOTE PROCEDURE CALL  
INVOKED FROM CELL W20

File Edit Function Database Format Display

N2C

c:\types\m\part", "ENHANCED", "FILE", "CLIP", "FILE", "620", "N2C", "N

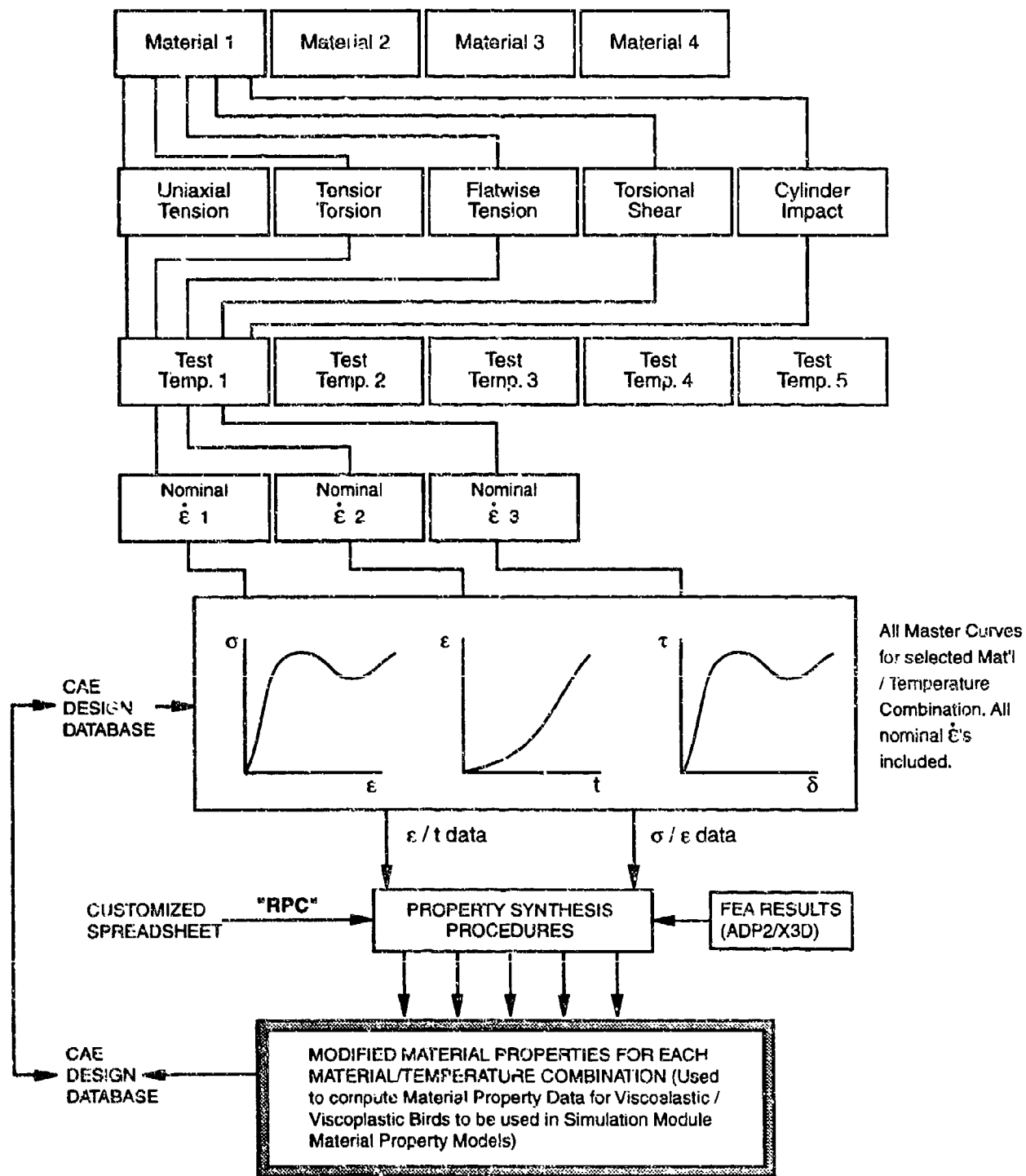
"POLYLINE"  
CURVES OF  
SHIFTED,  
CLIPPED,  
AND FIT  
DATA SETS  
(See Figure  
18A)

Figure 17. Customized MMSB Spreadsheet Region Used to Invoke RPC Function

B) MMSB GRAPHICAL  
DISPLAY OF CURVE  
ATTRIBUTES  
INSTANTIATED BY  
SPREADSHEET "PUT"  
COMMAND

B) MMSB GRAPHICAL  
DISPLAY OF CURVE  
ATTRIBUTES  
INSTANTIATED BY  
SPREADSHEET "PUT"  
COMMAND

**Figure 18.**



**FIGURE 19. Schematic Showing Further Customized Spreadsheet Functionality Requirements to Modify Input Test Data Sets.**

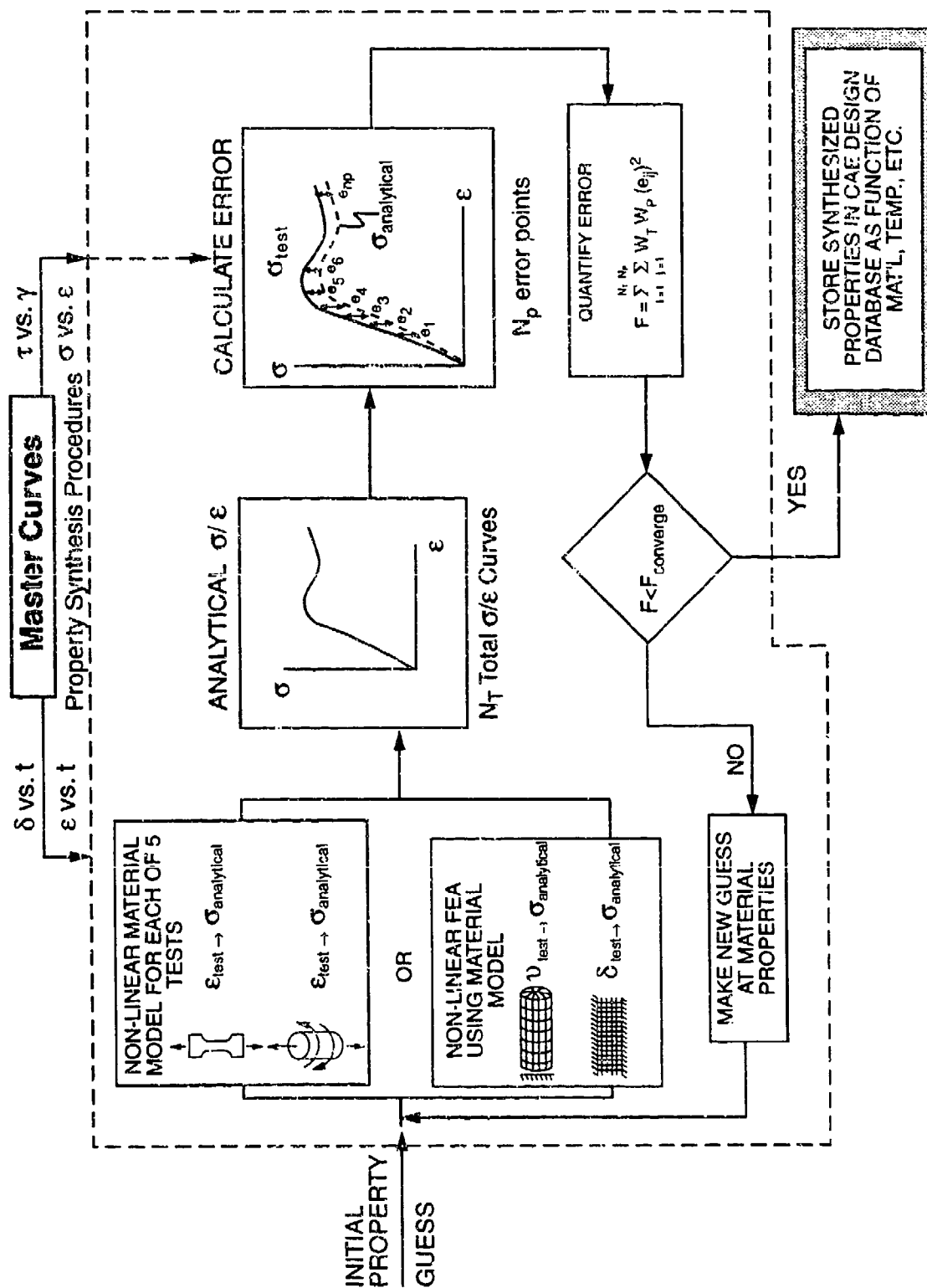


Figure 20. Scheme For the Property Synthesis Procedures Accessed By the Customized Spreadsheet "RPC" Function Noted in Figure 19

**VALIDATION OF BIRD IMPACT DESIGN TOOLS FOR THE F-22 CANOPY SYSTEM**

M. P. Bouchard  
University of Dayton

J. C. Davisson  
Flight Dynamics Directorate  
Wright Laboratory

# VALIDATION OF BIRD IMPACT DESIGN TOOLS FOR THE F-22 CANOPY SYSTEM

---

Michael P. Bouchard  
University of Dayton Research Institute  
Dayton, Ohio

Lt. Joseph C. Davisson  
USAF/WL/FIER  
Wright-Patterson AFB, Ohio

## ABSTRACT

A combined experimental and analytical program to validate analytical tools and procedures used for bird impact-resistant design of the F-22 canopy system is described. The program utilizes the prototype YF-22 canopy system as the baseline for validation of FEA (finite element analysis) models used for "bird-proof" design of the production F-22 canopy system. MAGNA and X3D analysis of the YF-22 canopy system are described and compared. Test setup and plan for bird impact testing of the prototype canopy system are then presented. The results of the analyses, including deflection, plastic strain, and reaction loads, will be compared with the test results. The finite element models will be tuned, if necessary, to better reproduce the test behavior. The lessons learned in tuning the YF-22 models will be incorporated into the models utilized in the design and analysis of the production F-22 canopy system.

## INTRODUCTION

The YF-22 aircraft (Figure 1) brings together many advanced technologies in providing the USAF with a prototype of the next generation of air superiority fighter aircraft. The aircraft features state-of-the-art technologies including "supercruise" (supersonic flight without afterburner), vectoring thrust for greater maneuverability, and reduced radar signature. The YF-22 canopy's single piece elongated bubble shape is similar in concept to, but larger than, the F-16 canopy. The canopy is monolithic polycarbonate of nominal (prior to forming) 0.75 inch thickness.

As the aircraft design nears its final configuration, canopy design refinements to incorporate the very latest technologies are anticipated. Prior to incorporation of design refinements, however, validation of analytical tools to be used in the redesign must be accomplished. The objective of the effort described herein is to validate the FEA (finite element analysis) tools and procedures used for bird impact design and analysis of the F-22 production canopy system. The approach to meeting this objective involves both analysis and test of the prototype YF-22 prototype canopy system. The approach is to perform FEA of the YF-22 canopy using the MAGNA and X3D FEA programs, perform bird impact testing of the prototype canopies, correlate analytical and experimental results, and tune the finite element models, if



necessary, to better reproduce the test behavior. The lessons learned for the prototype canopy can then be applied to the design and analysis of the production canopy system.

## BIRD IMPACT ANALYSIS

Both MAGNA<sup>1</sup> and X3D<sup>2</sup> FEA programs were used for the analysis. MAGNA utilizes traditional isoparametric element technology, requires assembly and solution of global stiffness and mass matrices, utilizes Newmark time integration (resulting in unconditional solution stability), and includes piece-wise linear uniaxial plastic stress-strain behavior. X3D uses "simple" elements (linear displacement, constant stress elements), employs single-point integration stabilized with anti-hourglassing forces, utilizes explicit central difference time integration (which results in conditional stability but forgoes assembly of global stiffness and mass matrices), provides a number of advanced material models including strain rate sensitive plasticity and viscoelasticity, allows for direct modeling of the bird, and provides for element and ply failure.

Figure 2 shows the MAGNA finite element model. The MAGNA model consisted of 545 20-node solid elements representing the canopy and aft cockpit bulkhead and 65 3-node beam elements representing the perimeter frame, resulting in 4106 nodes and 12,826 degrees of freedom. Boundary conditions were applied along the centerline to enforce symmetry and at five locations along the sill to represent the canopy assembly latch-down hooks. Additional beam elements linked the nodal rotations of the perimeter beam elements to the nodal translations of the solid elements. Table 1 presents the elastic-(piecewise-linear) plastic material properties which were used to describe the polycarbonate. Bird loads were estimated prior to FEA based on rigid target pressure data and applied via user subroutines.<sup>3</sup> The loading was conservative in that no lateral spreading of the bird was allowed, thereby concentrating the loads over the projected area of the bird onto the canopy. The peak pressure point was assumed to remain fixed at the point of initial bird-canopy contact (the pressure dropped linearly from this point to the farthest point away in the bird footprint). A correction to the load was made in the user subroutines to account for the change in impact angle due to deformation of the canopy. Figure 3 presents the bird load (before impact angle correction) and loaded area. The combined Newton-Raphson iteration scheme (two full Newton iterations followed by constant-stiffness iterations) was used, with iteration being performed at every fifth time step.

The X3D model shown in Figure 4 consisted of 1520 4-node plate elements, resulting in 1620 nodes and 9203 degrees of freedom. The bird was represented by a 4.2 in DIA x 8.4 in long cylinder consisting of 1920 tetrahedral elements, 561 nodes, and approximately 1500 degrees of freedom. Boundary conditions enforced symmetry along the centerline of the canopy and bird. The frame was simulated by boundary conditions, either all fixed or all pinned, around the canopy perimeter. The polycarbonate was represented by a bilinear elastic-plastic stress-strain curve, with the yield point stress being a function of the strain rate. The bird was represented by an elastic-plastic material with discontinuous pressure-volume behavior. The material models and properties are given in Table 2 and 3.

To date, analyses have been performed to investigate the following parameters: 1) X3D

bird strength; 2) X3D perimeter boundary conditions; and 3) bird impact location. The analyses and results are discussed below.

### X3D Boundary Conditions

A simple approach for modeling of the perimeter frames was tried for the X3D analyses. Rather than extensively model the frame with finite elements, boundary conditions were tried. Two cases were run: all fixed or all pinned around the perimeter. The results are shown in Figure 5 using a "semi-strong" bird (see next section for discussion of bird strength) impacting a one inch thick canopy. Virtually identical peak deflections and plastic strains (4% fixed, 3.9% pinned) were obtained. Thus the perimeter boundary conditions in the X3D model are a sufficiently accurate representation of the frame for capturing the canopy centerline behavior. (On the other hand, obtaining accurate support reactions will require a more realistic simulation of the edge support.) Pinned conditions were chosen for all subsequent analyses.

### X3D Bird Strength

The X3D bird material model describes both the bulk and shear behavior of the bird material. The shear strength has been found to have a major influence on bird behavior and canopy response, necessitating a parametric study of this value.<sup>5</sup> "Weak," "semi-strong," and "strong" birds (Table 3) were analyzed. Figures 6 and 7 present a series of deformed geometry plots for "weak" and "semi-strong" birds. The "weak" bird elements failed early in the impact event, while most of the "semi-strong" bird elements remained intact. Note that though elements fail and their stiffness is dropped from the solution, the nodes (dots in Figures 6 and 7) and their mass were free to move and contact the canopy, transferring momentum. Figure 8 shows the effects of the "weak" and "semi-strong" birds on peak canopy deflection. Table 4 summarizes the peak deflection values and includes peak plastic strain values (see Figure 9 for a typical plastic strain plot). Also included in Figure 8 and Table 4 are the results for the MAGNA analysis. Both the MAGNA peak deflection and peak strain values are bounded by the X3D results for the "weak" and "semi-strong" birds. The shift in peak deflection times for the MAGNA and X3D runs was due to the difference in bird loading models: the X3D model permitted sliding of the bird along the canopy, so that peak deflection occurred farther aft and therefore later in time for X3D compared to MAGNA. The use of the "semi-strong" bird was conservative compared to the MAGNA bird loads.

### Bird Impact Location

This effort was performed to ascertain the "worst-case" centerline bird impact location. Six different locations were chosen for analysis, as shown in Figure 10. Output data of interest were peak deflection, deflection at the HUD location, peak plastic strain, and plastic strain at the HUD at the instant of initial canopy-HUD contact. Results are summarized in Table 5. The results indicate that impact at Site E maximized the deflection and strain at the HUD. The high deflection at the HUD location indicates that high canopy-HUD contact forces will be encountered. Impact Site E was therefore chosen as the impact site for future bird impact testing of the YF-22 canopy system. Additional analyses are being considered to include the HUD model and therefore the interaction between the canopy and HUD. Such complex contact analysis has proven difficult in the past using MAGNA (time steps become too small for efficient solution), but has been performed successfully using X3D.<sup>5</sup>

### Computer Resources

The MAGNA analysis was conducted on the ASD/WPAFB CRAY X-MP/28 (two processors, 8 megawords = 64 MB memory). To speed throughput, the analysis was split into four medium-sized jobs, thereby permitting use of a higher priority queue. The X3D runs were performed on the ASD/WPAFB EASE SS2 SUN SPARCstation 10 workstation. Usage of the Sun Server was much heavier than the CRAY. Run times and storage requirements are summarized in Table 6. MAGNA run mag02c was run to 6.8 msec. Time step size for mag02c started at 50  $\mu$ sec, switching to 100  $\mu$ sec after the bird load was gone. All X3D analyses were run to 10 msec. In contrast to MAGNA, the average X3D time step size was 2.7  $\mu$ sec, characteristic of the need to maintain stability of the explicit time solution. Printed MAGNA output was obtained for every other time step. Printed output and restart file for X3D were obtained at 0.5 msec steps (approximately every 185 time steps). Disk storage space requirements for MAGNA were high primarily because the results file was in ASCII format and also because a separate restart file was generated. X3D combines results and restart information into a single binary file. Note that without a judicious choice of output frequency, X3D could easily generate an order of magnitude more output than MAGNA simply because so many time steps are required for a solution.

Considering the differences in computer workload, solution time, and computer charges (the CRAY required payment for use while the workstation did not), and considering the need to divide the MAGNA job into medium-sized jobs (with attendant need for file management and job resubmittal), the bird impact simulation using the X3D program on a UNIX workstation provided a competitive alternative to performing this task using an implicit-formulation program on supercomputers.

### **BIRD IMPACT TESTING**

Preparations are in progress for performing the bird impact tests. A rigid stand was constructed to which the canopy/frame assembly will be attached. Attachment is via the canopy system latching hooks and pivot hinge, thereby simulating the actual installation on a fuselage. Triangulation of points marked on the canopy and recorded by high speed (5000 frames/sec) movie cameras during the bird impact tests will provide canopy deflection data. Strain gages will be applied in back-to-back pairs along the inside and outside of the perimeter fairing to monitor the load being transmitted by the canopy into the frame. Strain gages will also be applied to the canopy hinge structure and HUD to determine the hinge and HUD reactions. The first shot will be conducted without a HUD to provide the simplest case for collecting canopy deflections, while the second will be conducted with a HUD to determine the canopy-HUD interaction. The deflection and reaction results will be correlated with the finite element results to provide a check on FEA parameters such as bird strength.

### **SUMMARY**

A program to validate the FEA tools and procedures to be used for design of the production F-22 canopy system has been initiated. The program utilizes the prototype YF-22

canopy as the test bed for the validation. MAGNA and X3D FEA models have been constructed. To date, the models have been analyzed for bird strength, boundary conditions, and bird impact location. Additional X3D analyses which incorporate the HUD and account for thinning of the canopy due to forming are being considered.

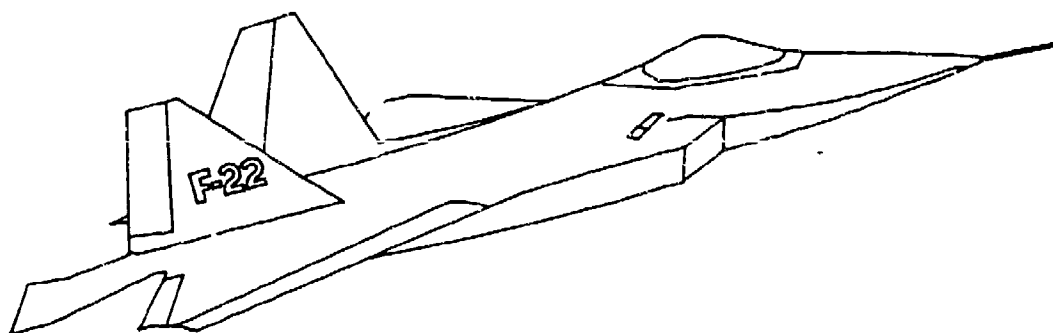
The test program to validate the FEA results is underway. A rigid stand to support the canopy assembly has been designed and constructed. Bird impact tests will be performed with and without the HUD. The FEA will be correlated with the test results and the models tuned (e.g., adjust boundary conditions or bird strength) as necessary to better simulate the tests. The lessons learned will be applied to the use of FEA in the design of the production F-22 canopy.

### ACKNOWLEDGEMENTS

The effort reported herein represented the team effort of the University of Dayton Research Institute, Wright Laboratory, F-22 SPO, Lockheed Aerospace Corp., PPG Industries, Inc., and Sierracin/Sylmar Corp.

### REFERENCES

1. Brockman, R. A., MAGNA: Materially and Geometrically Nonlinear Analysis Volume I: Finite Element Analysis Manual, AFWAL-TR-82-3098, Part I, Air Force Wright Aeronautical Laboratories, Wright-Patterson AFB, OH, December 1982.
2. Brockman, R. A., and T. W. Held, "X3D User's Manual," UDR-TR-92-59, University of Dayton Research Institute, Dayton, OH, April 1992.
3. Brockman, R. A. and B. S. West, "Bell-Boeing V-22 Birdstrike Loads Estimation," UDR-TR-86-12, University of Dayton Research Institute, Dayton, OH, July 1986.
4. McCarty, R. E., report to be published documenting finite element analysis of T-46A windshield system.
5. Bouchard, M. P. and J. C. Davisson, Advanced Transparency Development for USAF Aircraft, AIAA Paper 93-1391, Proceedings of 34th AIAA/ASME/ASCE/AHS/ASC Structures, Structural Dynamics, and Materials Conference, La Jolla, CA, 19-22 April 1993.



**Figure 1. YF-22 Aircraft.**

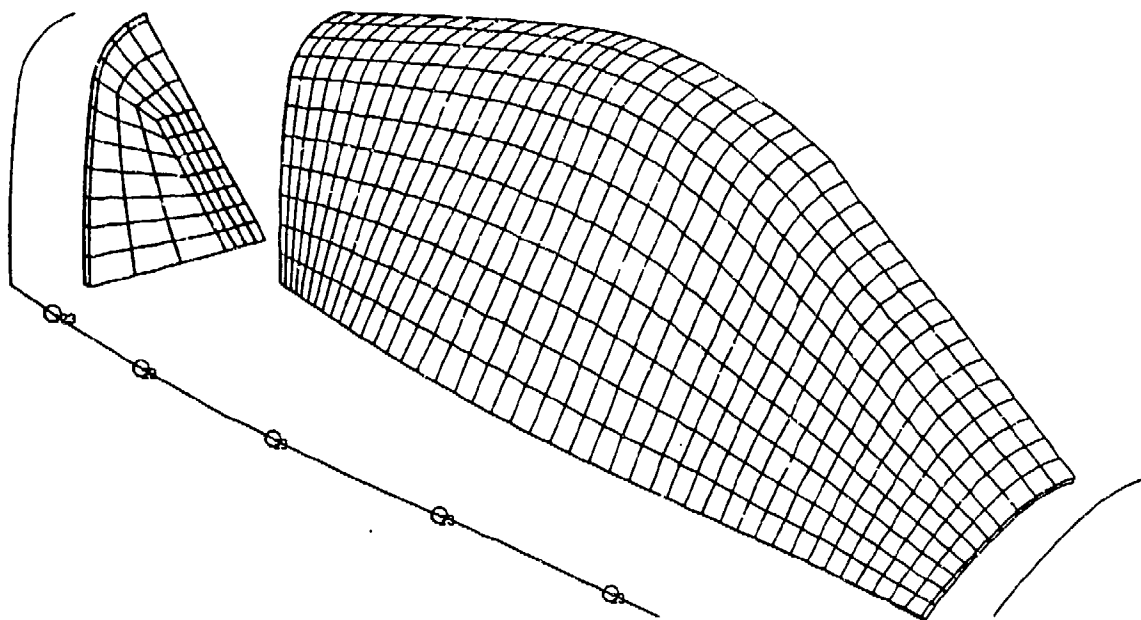


Figure 2. MAGNA Finite Element Model (Exploded View).

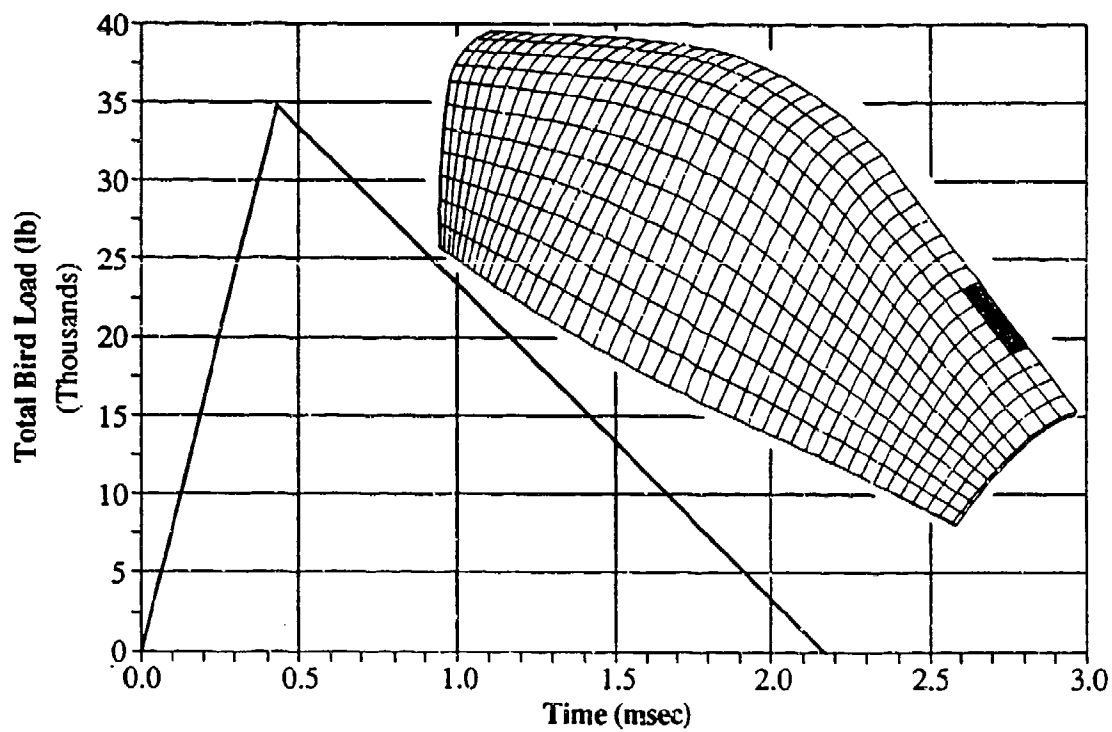


Figure 3. MAGNA Bird Load History and Distribution.

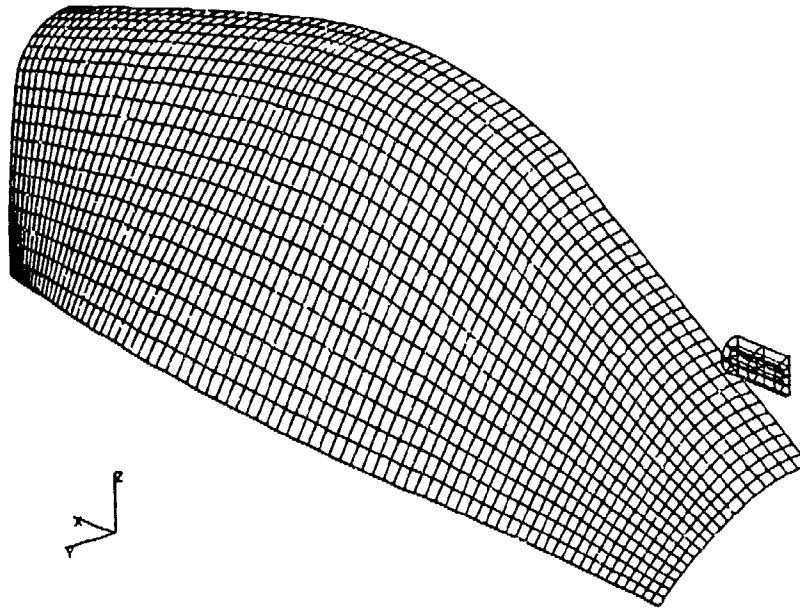


Figure 4. X3D Finite Element Model (Bird Elements Not Shown for Clarity).

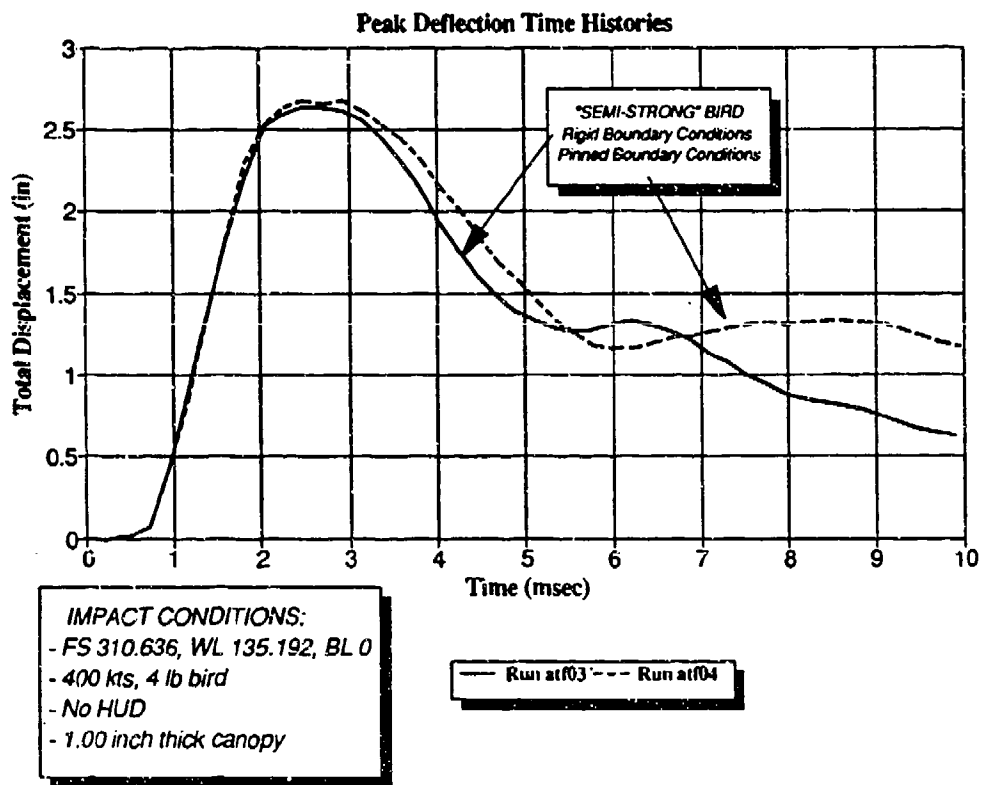
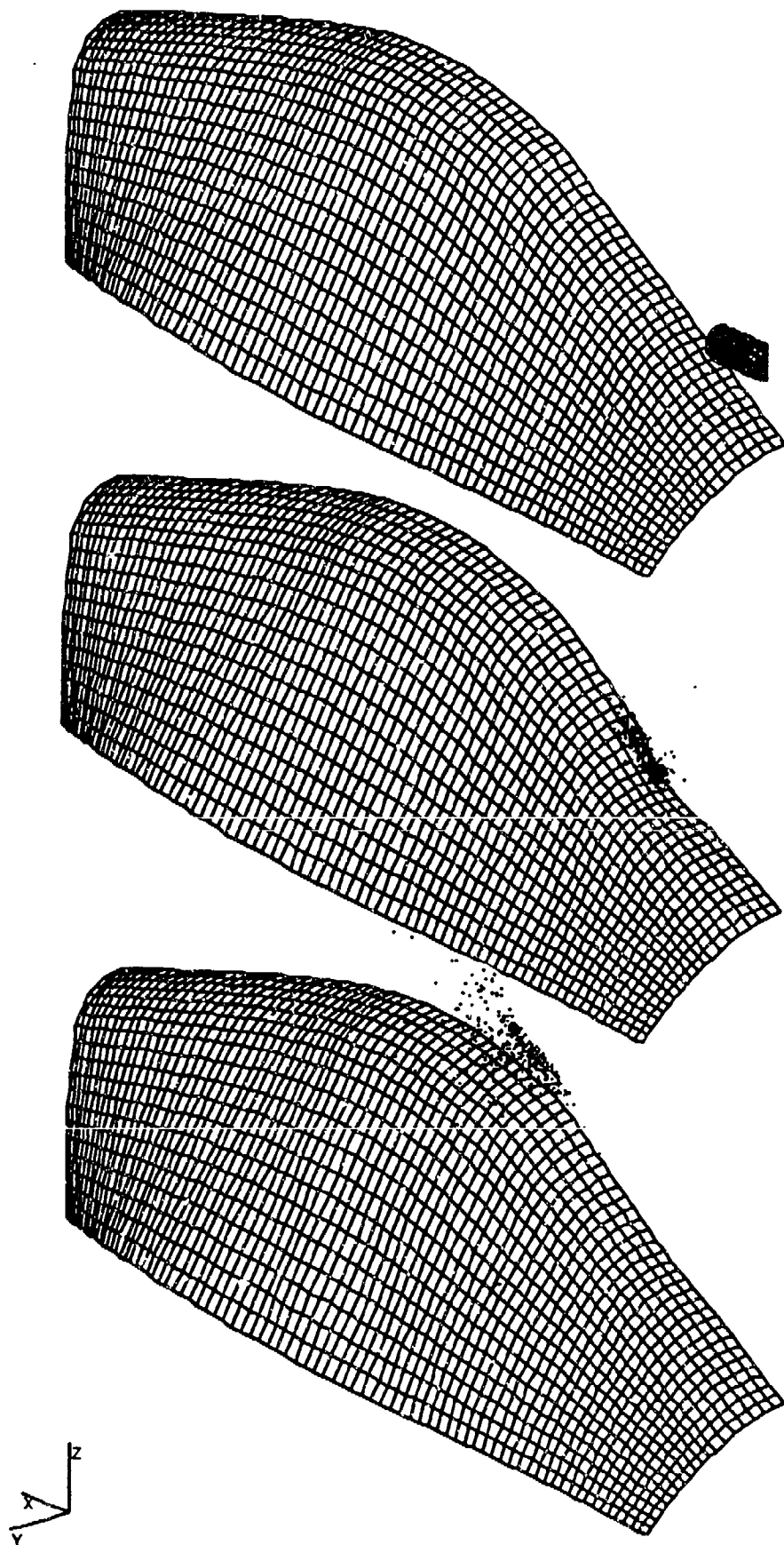


Figure 5. Effect of Boundary Conditions on X3D Peak Deflections (1 in Thick Canopy).



**Figure 6.** Deformation Sequence Showing Behavior of "Weak" Bird (X3D Run atf05).



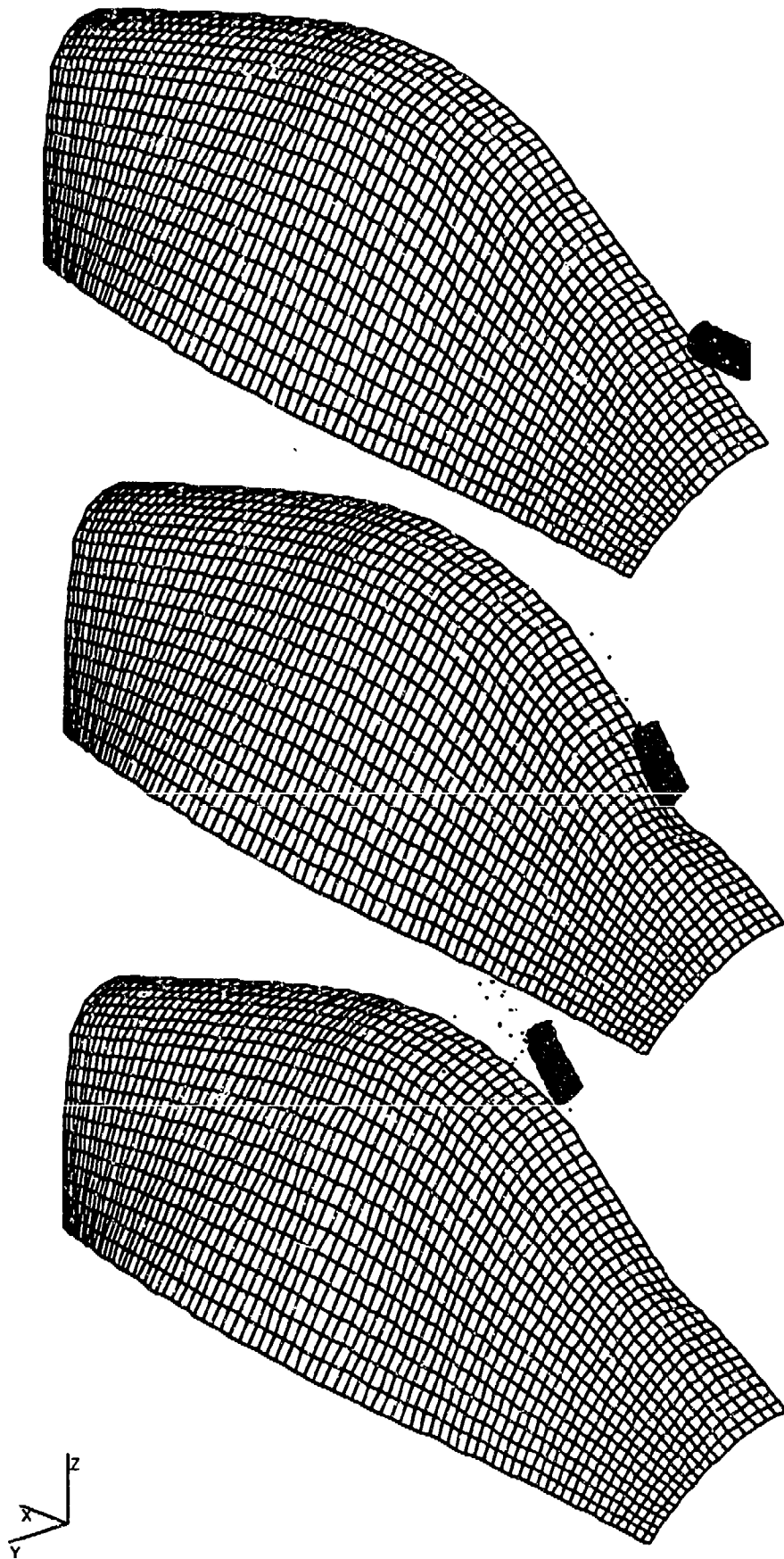
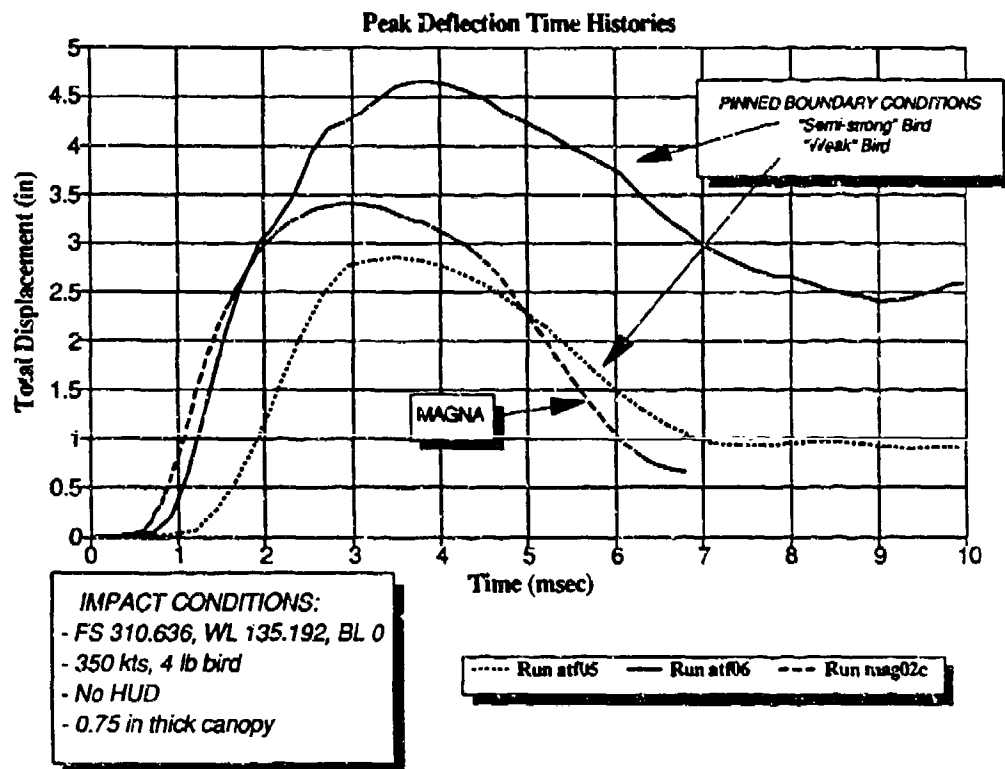
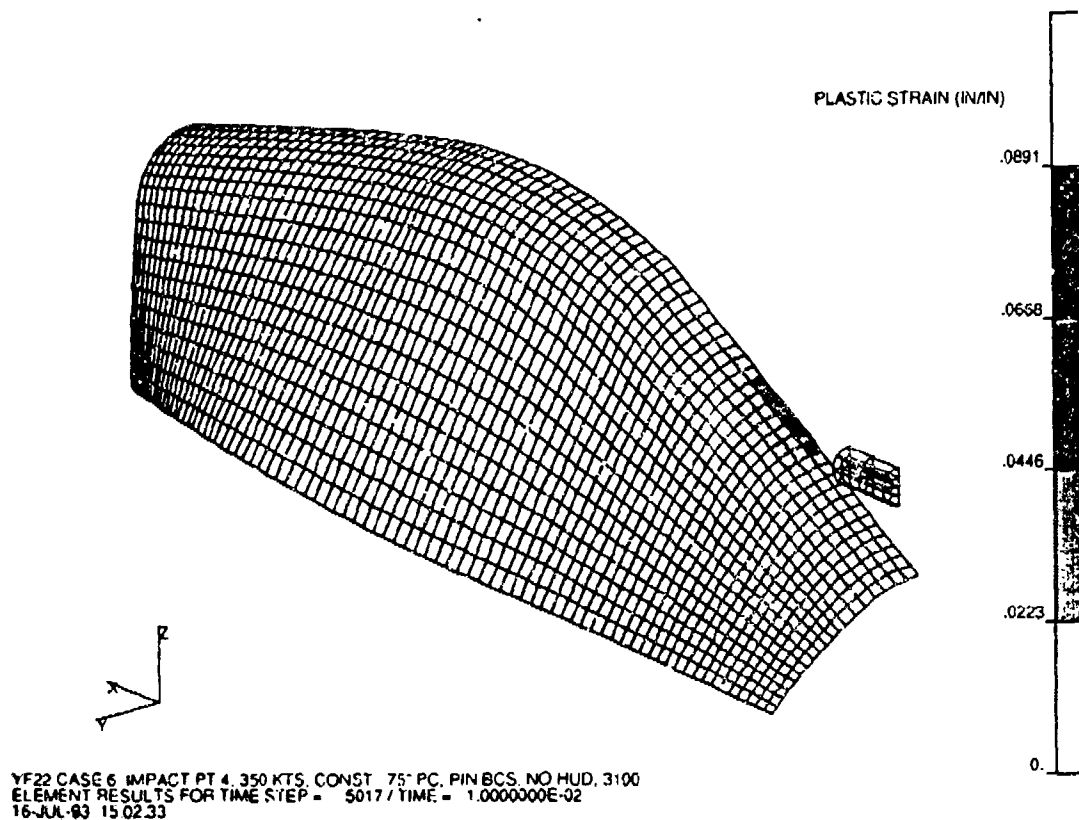


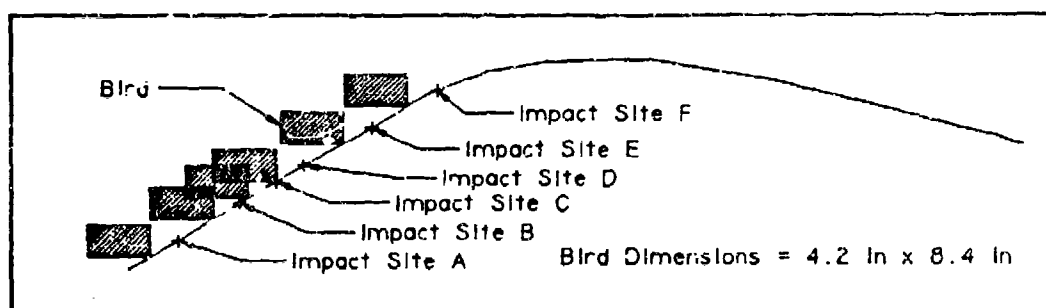
Figure 7. Deformation Sequence Showing Effect of "Semi-Strong" Bird (X3D Run atf06).



**Figure 8. Effect of X3D Bird Strength on Peak Canopy Deflection.**



**Figure 9.** Typical Plastic Strain Plot (X3D Run atf06).



**Figure 10.** Centerline Impact Sites for X3D Bird Impact Location Study.

**Table I. MAGNA Model Polycarbonate Mechanical Properties.**

$E$  = Young's tensile modulus = 324,000 psi

$\nu$  = Poisson's ratio = 0.38

$\rho$  = Density = 0.043 lb/in<sup>3</sup>

Plastic stress-strain curve:

Stress (psi)	Strain (in/in)	Plastic Strain (in/in)	Comments
6,353	0.0195	0.0000	Yield Point
8,061	0.0262	0.0066	
9,392	0.0450	0.0254	
9,700	0.2696	0.2500	
10,043	0.5196	0.5000	Break Point (50% Strain)
10,728	1.0196	1.0000	Extra point so MAGNA will not "fall off" end of curve

Note: These properties from Reference 4.

**Table II. X3D Model Polycarbonate Mechanical Properties.**

**Material Model:** Elastic-Plastic, Rate-Sensitive Isotropic

$E$  = Young's tensile modulus = 325,000 psi

$\nu$  = Poisson's ratio = 0.39

$\rho$  = Density = 0.043 lb/in<sup>3</sup>

$\sigma_y^0$  = quasi-static yield = 7140 psi

$H$  = hardening slope = 36,100 psi

$D$  = inverse of rate sensitivity scale factor = 196,500

$p$  = inverse of rate sensitivity exponent = 12

$\sigma_{ult}$  = ultimate stress = 13,000 psi

where  $\sigma_y = \sigma_y^0 [1 + (d/D)^{(1/p)}]$

**Table III. X3D Bird Material Model.**

**Material Model:** Elastic-Plastic with Discontinuous Pressure-Volume Behavior

$\rho_0$  = initial density = 0.0343 lb/in<sup>3</sup>  
 $K_1$  = linear bulk coefficient = 337,000 psi  
 $K_2$  = quadratic bulk coefficient = 729,000 psi  
 $K_3$  = cubic bulk coefficient = 2,020,000 psi  
 $G$  = shear modulus = 30,000 psi  
 $\sigma_y$  = yield strength = 3000 psi  
 $H$  = hardening slope = 300 psi  
 $\sigma_{ult}$  = ultimate strength = 3000, 3100, or 3500 psi  
 (corresponding to "weak," "semi-strong," "strong")

where  $p = \Sigma K_i \eta^i$ ,  $i = 1, 2, 3$ ,  $p$  = pressure,  $\eta = \rho/\rho_0 - 1$

**Table IV. Effect of X3D Bird Strength on Canopy Response.**

Canopy = 0.75 in thick YF-22  
 Boundary Conditions = pinned  
 Impact Location = WL 135.192, BL 0  
 Bird Mass = 4 pounds  
 Bird Velocity = 350 knots

Bird Strength (psi)	Run I.D.	Peak Deflection (in)	Peak Plastic Strain (percent)
3000 (Weak)	atf05	2.9	3.0
3100 (Semi-Strong)	atf06	4.6	8.9
MAGNA	mag02c	3.8	3.3

**Table V. Effect of Impact Location on Canopy Response.**

Canopy = 0.75 in thick YF-22  
Boundary Conditions = pinned  
Bird Mass = 4 pounds  
Bird Velocity = 350 knots  
Bird Strength = 3100 psi

Impact Site	Run I.D.	Peak Deflection (in)	Peak Plastic Strain (percent)	Deflection at HUD (in)	Plastic Strain at HUD* (percent)
A	atf07	4.1	10.3	0.2	NC
B	atf08	4.6	10.2	0.6	NC
C	atf09	4.2	6.9	1.2	NC
D	atf10	3.8	6.0	2.3	2.3
E	atf11	5.0	6.8	5.0	3.9
F	atf12	2.6	3.9	1.5	NC
C**	mag04b	3.8	3.4	TBD	TBD

\* At instant when canopy/HUD contact would first occur.

\*\* MAGNA analysis.

NC = No Contact between HUD and canopy.

TBD = To Be Determined.

**Table VI. Typical Computer Resources Required for MAGNA and X3D.**

Run ID	No. Time Steps	Total Run Time (msec)	CPU Time (sec)	Wall Clock Time (hrs)	Memory (MB)	Disk* (MB)
MAGNA (mag02c)	90	6.8	386	3	11.4	235
X3D (atf01)	3678	10.0	N/A	9	N/A	20

\*Disk space required to store all output

N/A = Not Available

MAGNA run on CRAY, X3D on SUN workstation; see text for description of computers.

ESTIMATING LIFE-CYCLE COSTS OF HAZARDOUS MATERIALS

J. J. Short  
Flight Dynamics Directorate  
Wright Laboratory

## ESTIMATING LIFE-CYCLE COSTS OF HAZARDOUS MATERIALS

Lt Col Jeffrey J. Short, USAFR  
WL/FIVR  
Wright-Patterson AFB, Ohio

### Abstract

In its 1986 report, Selection and Use of Hazardous and Toxic Materials in the Weapons System Development and Acquisition Process, the United States Air Force Scientific Advisory Board noted that the extensive use of hazardous materials during the development and maintenance of weapons systems must be curtailed to reduce costs associated with the generation of hazardous wastes and improve workforce health and safety. With the Department of Defense Directive 4210.15, Hazardous Material Pollution Prevention (July, 1989), the concept was extended to consider the entire life-cycle of systems through avoiding or reducing the use of hazardous materials during the acquisition process.

The Air Force has developed a Hazardous Materials Life Cycle Cost Estimator (HM LCCE) that could be used for estimating the costs of using hazardous materials during the lifetime of a weapons system, from concept to disposal. The estimator is based on validated hazardous materials and hazardous waste costs from the deployment of three weapons systems. The HM LCCE is designed for use by the systems program offices to compare hazardous material alternatives during system acquisitions. The HM LCCE is programmed in Ada and designed for use on an IBM-compatible microcomputer using an MS-DOS operating system.

The transparency design community should become aware and utilize, where appropriate, the existing life cycle cost estimation tools and expertise to reduce the costs of ownership that are related to hazardous materials during the design, production, maintenance and disposal of aircraft transparencies. Inputs are needed to refine the HM LCCE regarding transparency systems.



## INTRODUCTION

Annually, the Air Force spends about \$30 million to dispose of over 20,000 tons of hazardous wastes from over 200 installations and facilities. Sixty percent of the total volume comes from depot level maintenance at the Air Logistics Centers (ALCs). The majority of Air Force hazardous waste results from maintenance operations involving: (1) cleaning and degreasing; (2) protective coating application and removal; (3) electroplating and finishing; and, (4) vehicle maintenance. These requirements for specific maintenance processes that result in hazardous wastes are called for during the system acquisition and procurement procedures; they are "built in" during the acquisition process.

By 1992, the Air Force had reduced its generation of hazardous waste by 56 percent from 1987 levels (Figure 1), thereby exceeding the Department of Defense goal. Much of this reduction was due to improved waste minimization and management initiatives. However, this strategy often resulted in shifts of pollution from one media to another (e.g.; wastewater to landfill). Continued progress in reducing waste must rely more on preventing pollution than merely managing pollutants. To accomplish this, systems must rely less on the hazardous materials and supporting processes must be developed and evaluated that generate less hazardous waste.

In recent years, hazardous waste minimization initiatives have focused on industrial plant end-of-pipe controls and associated hazardous waste minimization research, development and acquisition programs. But end-of-pipe controls merely serve to contain hazardous waste which eventually find its way into the environment through further treatment and disposal. Additionally, ever more stringent environmental criteria continually drive up the costs of compliance. The Air Force has realized that to prevent the generation of hazardous waste, it must focus on the source of the waste which is conceived at the earliest phases of acquisition. Source reduction (sometimes called pollution prevention) is more desirable than simply managing the waste because it reduces cost and liability.

## PURPOSE

The purpose of this paper is to discuss the development of a tool that can be used to compare the life-cycle costs of using hazardous materials in the development and production of transparency materials and enclosures. Reducing the use of hazardous materials will ultimately reduce the cost of ownership of transparency systems and will minimize associated environmental, occupational health and safety concerns for both the manufacturer/vendor and the Air Force.

## POLICIES AND GUIDANCE

A 1986 Air Force Scientific Advisory Board (SAB) report entitled, "Selection and Use of Hazardous and Toxic Materials in the Weapons System Development and Acquisition Process", concluded that many hazardous processes or substances are built

into weapons systems early in the concept and design stages. The SAB report noted that the acquisition process lacks the technical expertise to adequately address hazardous materials issues at the Systems Program Offices (SPOs). Basically, the Air Force needed a comprehensive program to identify, evaluate and prevent pollution throughout the life of a weapon system--from production to disposal.

In July 1989, the Deputy Secretary for Production and Logistics approved DoD Directive 4210.15, Hazardous Material Pollution Prevention (HMPP). Under this Directive, Defense Components are required to develop HMPP Plans to consider the total life-cycle costs associated with our weapons systems. The Directive emphasized less use of hazardous materials rather than simply managing hazardous waste. The Directive provides for the selection of hazardous materials based on the lowest life cycle cost by considering environmental, safety and occupational health costs associated with manufacturing, operation, maintenance and disposal. Subsequent changes to the DoD 5000-series of acquisition directives in 1991 have ensured further that environmental concerns are considered on par with safety and health issues presented by the requirements for hazardous materials.

Department of Defense Instruction 5000.2, Defense Acquisition Management Policies and Procedures, ensures that system designs incorporate safety, health and environmental considerations into the systems engineering process. System safety hazards resulting from either the operation or support activities must be eliminated or mitigated before Milestone III, Production Approval. The environmental, safety and occupational health concerns associated with the selection and use of hazardous materials in the system must be evaluated as to the impacts associated with the manufacturing, operation, maintenance and disposal of the system.

The Air Force is committed to maintaining environmental quality as an integral part of supporting the overall mission to fly, fight and win. Compliance with environmental mandates is an issue of paramount importance; failure to comply may not only subject the Air Force, its commanders and employees to civil and criminal liabilities, but may also prevent timely accomplishment of some important aspect of the mission.

A joint Air Force Chief of Staff and Secretary of the Air Force memorandum (dated 7 January 1993) proposed an action plan to meet an Air Force goal of reducing hazardous waste generation to as near zero as feasible. The first objective of that plan focused on reducing the reliance on hazardous materials during the development and fielding of new weapons systems. Other objectives were to improve inventory control and identify opportunities to replace hazardous materials and processes with non-hazardous ones. Achieving these objectives will eventually save the Air Force operations and maintenance resources through integrated planning, programming and budgeting of improvements to the system acquisition and support process. The Air Force's strategies, policies and regulations reinforce its commitment to

national environmental values and will conserve resources.

In 1989, the Air Force conducted a preliminary study of the aircraft systems acquisition process and to identify tasks to reduce the use and generation of hazardous materials. A series of issues and tools was defined that will improve the incorporation of hazardous materials concerns into the decision-making process. Integral to this process is the application of a tool to calculate the contribution of costs over the expected system lifetime for a specific hazardous material alternative.

#### HAZARDOUS MATERIALS LIFE CYCLE COST ESTIMATOR (HM LCCE)

Developing the tool for estimating the life-cycle costs of using hazardous materials for new as well as existing systems is a complex matter. A life cycle cost estimating methodology is under development by the Human Systems Center Pollution Prevention Office at Brooks AFB, Texas. The HM LCCE focuses on the direct and indirect costs of using hazardous materials during the design, production, operation, support, and disposal of weapons systems. The HM LCCE was developed by studying cost and usage data for the B-1 bomber, F15 and F-16 fighters and aircraft engines. Other data on the acquisition of the U.S. Army M1-A1 (Abrams) Tank and the H-60 (Blackhawk) Helicopter and the U.S. Navy M-50 Torpedo. Data was collected from maintenance depots, operating locations and prime contractors. West, Long and King (1993) note that seven out of twelve cost elements (asterisked below) account for over ninety-five percent of weapon's life-cycle cost:

\* 1. Procurement - the actual purchase price of the hazardous materials including the cost of transportation to the contractor, base or depot site;

2. Transportation - the cost to transport material from one location to another at the point of use;

\* 3. Handling - the cost of subdividing, labeling, and distributing the materials as well as any productivity that is lost due to restrictions and controls;

\* 4. Management - the cost of those functions necessary to maintain oversight of the hazardous materials where used;

5. Training - the cost of training personnel in the proper handling, storage, and use of hazardous materials plus the cost of training personnel in the proper use of protective equipment;

\* 6. Personal Protection - the cost of personal protection equipment including its maintenance and support, the cost of worker inefficiency from wearing equipment and the costs of dispensing the equipment;

\* 7. Potential legal/environmental liability - the potential costs of toxic torts, correspondence with regulators, damage to real property or natural resources and treatment of contaminated water;

\* 8. Medical - the costs for occupational physical examinations (including lost time while they are being administered, medical surveillance and industrial hygiene surveys, and worker lost time due to illness/injury as a result of exposure to hazardous materials;

9. Facilities - The cost of facility cost and maintenance required for the use of hazardous materials;

10. Support equipment - the cost of special equipment needed to handle hazardous materials and hazardous wastes;

11. Emergency response - the costs of personnel and equipment to respond to an emergency related to hazardous materials including lost time from work stoppage;

\*12. Disposal - the cost of operating an industrial wastewater treatment plant, when applicable, the labor costs for waste collection and handling, the cost of contractor disposal of hazardous waste (including permit and licenses), costs of hazardous waste analyses and classification.

#### HM LCCE and DEPOT CANOPY REPAIR

The HM LCCE can be used to evaluate the total environmental, safety and occupational health costs of employing hazardous materials during depot canopy repair. The HM LCCE contains a section that can calculate the expenses accordable the hazardous materials used in removing, refurbishing and replacing canopies at the depot level.

Inputs to the HM LCCE are provided by knowledgeable systems engineers or occupational health professionals. The HM LCCE provides a variety of outputs that will support the decision-making process at each milestone. Hazardous materials tradeoffs are most cost-effective when made prior to decisions to actually produce and field a system. The use of a standardized HM LCCE will help remove institutional impediments to decisions regarding the tradeoffs involved with hazardous materials during the systems acquisition process.

The HM LCCE was used to estimate the environmental and occupational health concerns relating to hazardous materials used during depot-level canopy repair activities. The estimation parameters are summarized on Table 1. Those substances required by military specifications were highlighted for the analysis. The estimated canopy repair costs, by cost element in discounted 1991 dollars, show that personal protection and medical cost drivers are nominal and relatively reasonable (Table 2). A breakout of the specific hazardous substances and related personal protection equipment required for their use indicates that opportunities still exist to reduce associated personal

protection and medical costs during depot canopy repair activities (Table 3).

The HM LCCE can be used to consider the economic tradeoffs involved with design, acquisition and operation of replacing hazardous substances for inclusion in the supportability cost. A good application of the HM LCCE would be to reduce the use of ozone depleting chemicals during the design, testing, production and support of aircraft canopy systems. Certain chlorofluorocarbon (CFC) and halon chemicals are believed to contribute to the depletion of stratospheric ozone. The production and use of the most environmentally harmful (Class I) of these potentially ozone depleting chemicals (ODCs) will be phased out by 1995. For other CFC chemicals that are not being phased out, financial disincentives may drive up the expenses of using CFC chemicals to where their continued use may not be economically practicable. One solution may be to substitute alternate chemicals and processes for those now requiring CFCs.

As of June 1, 1993, the Air Force requires waivers prior to the award of any contract that requires the use of Class I ODCs. Waivers are evaluated by representatives from the acquisition, logistics and maintenance and civil engineering functional areas. Waivers are also required for the purchase of Class I ODCs or for their withdrawal from stockpiles for replacing diminished stock.

#### CONCLUSION

The Air Force is moving from strictly an industrial plant pollution prevention strategy to one encompassing all phases of the Air Force way of life. Considerable progress already has been made in the reduction of hazardous waste by replacing hazardous processes of cleaning and protecting aircraft parts. The Air Force is successfully integrating environmental considerations and assessment techniques into the basic design of new systems. Integral to this process is the full inclusion of environmental, safety and occupational health costs of operation with other supportability costs.

Contractors involved in the design and production of weapons systems can have the most effect by choosing materials and processes that will not require the use of hazardous materials or generate hazardous wastes. Inputs into the HM LCCE by the transparency design community can improve life cycle cost estimation to reduce the costs of transparency ownership that are related to hazardous materials.

#### LITERATURE CITED

West, B.S., J.A. King and E.W. Long. The real cost of using hazardous materials. Proceedings of the 86th Air and Waste Management Association; Denver, Colorado, June 13-18, 1993: working paper # 93-WP-83B.07



Figure 1.  
**DOD HAZARDOUS WASTE GOAL**

**DOD GOAL: 50% REDUCTION: AF ACHIEVED 56%**

**TONS**

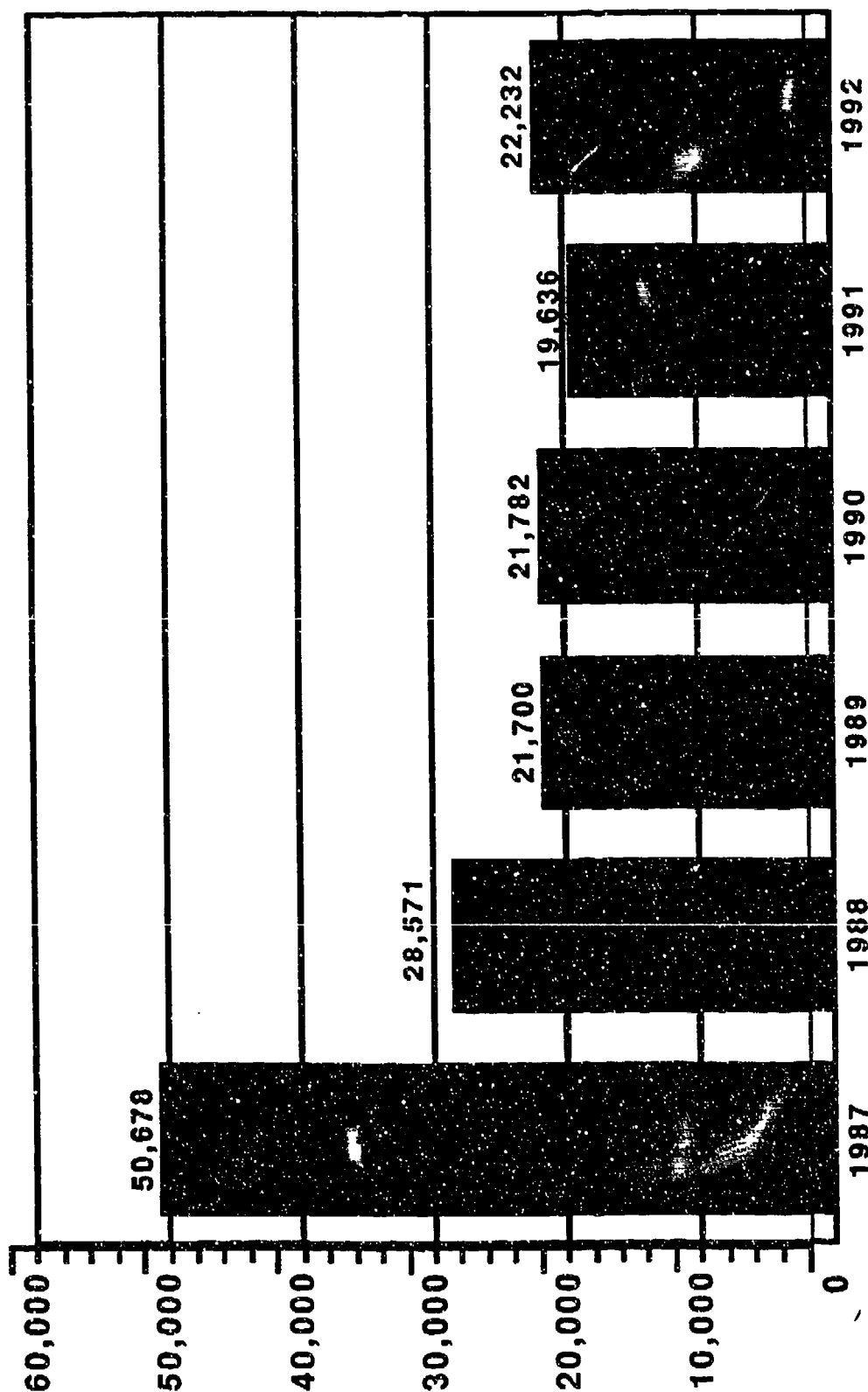


Table 1.

HAZMAT ESTIMATE PARAMETER INFORMATION REPORT

ESTIMATE TITLE: TRANSPARENCY CONFERENCE EXAMPLE  
ESTIMATE DATE : 08- 11-93

DISCOUNT RATE: .100  
INPUT BASE YEAR: 1991  
ESTIMATE BASE YEAR: 1991

SERVICE.....: AIR FORCE  
SYSTEM NAME...: AIRCRAFT  
SYSTEM TYPE...: FIGHTER  
SUBSYSTEM NAME: AIRFRAME

NUMBER OF SUBSYSTEMS: 1  
SYSTEM ECONOMIC LIFE: 5  
NUMBER OF OPERATING UNITS: 48  
NUMBER OF TYPE PER UNIT: 1  
NUMBER OF OPERATING LOCATIONS: 18  
OPERATING & SUPPORT QUANTITY: 864

SURFACE AREA OF SUBSYSTEM: 24  
COMPOSITE SURFACE AREA OF SUBSYSTEM: -----  
TITANIUM SURFACE AREA OF SUBSYSTEM: -----

ESTIMATE MEMO:

Table 2.

TRANSPARENCY CONFERENCE EXAMPLE  
 Costs by Cost Element in DISCOUNTED Dollars  
 as of 08-11-93  
 THOUSANDS of FY 1991

	1997	1998	1999	2000	2001	2002	2003	Running Total
	----	----	----	----	----	----	----	
DISPOSAL	.00	.00	.00	.00	.00	.00	.00	.00
EMERGENCY RESPONSE	.00	.00	.00	.00	.00	.00	.00	.00
FACILITIES	.00	.00	.00	.00	.00	.00	.00	.00
HANDLING	.01	.01	.01	.01	.02	.02	.02	.10
POTENTIAL LIABILITY	.08	.07	.06	.06	.11	.09	.08	.55
MEDICAL	18.50	16.82	15.29	13.90	25.28	22.98	20.89	133.66
MANAGEMENT	.00	.00	.00	.00	.00	.00	.00	.00
PERSONAL PROTECTION	104.95	95.41	86.73	78.85	143.36	130.33	118.48	758.11
PROCUREMENT	.37	.33	.30	.28	.51	.46	.42	2.67
SUPPORT EQUIPMENT	.00	.00	.00	.00	.00	.00	.00	.00
TRAINING	.00	.00	.00	.00	.00	.00	.00	.00
TRANSPORTATION	.00	.00	.00	.00	.00	.00	.00	.00
TOTALS	123.94	112.67	102.43	93.12	169.30	153.90	139.91	895.27
	2004	----	----	----	----	----	----	
	----							
DISPOSAL	.00	-----	-----	-----	-----	-----	-----	.00
EMERGENCY RESPONSE	.00	-----	-----	-----	-----	-----	-----	.00
FACILITIES	.00	-----	-----	-----	-----	-----	-----	.00
HANDLING	.01	-----	-----	-----	-----	-----	-----	.11
POTENTIAL LIABILITY	.07	-----	-----	-----	-----	-----	-----	.62
MEDICAL	18.99	-----	-----	-----	-----	-----	-----	152.65
MANAGEMENT	.00	-----	-----	-----	-----	-----	-----	.00
PERSONAL PROTECTION	107.71	-----	-----	-----	-----	-----	-----	865.82
PROCUREMENT	.38	-----	-----	-----	-----	-----	-----	3.05
SUPPORT EQUIPMENT	.00	-----	-----	-----	-----	-----	-----	.00
TRAINING	.00	-----	-----	-----	-----	-----	-----	.00
TRANSPORTATION	.00	-----	-----	-----	-----	-----	-----	.00
TOTALS	127.19	-----	-----	-----	-----	-----	-----	1022.46



Table 3.

PHASE/PROCESS: OPERATING &amp; SUPPORT /AFA DEPOT CANOPY REPAIR

SUBST ID	SUBSTANCE NAME	MSUR	PROQTY	QTY USED	EQUIPMENT NAME
000822450	EPOXY PRIMER COATING	KIT	1	.0896	
001178310	ADHESIVE	KIT	1	.0299	
001429193	ADHESIVE	BOX	1	.0040	CHEM-RESISTANT SAFETY GOGGLES COMB FACE-SHIELD KIT W/SAFE CP AIR RESPIRATOR SCBA (15MIN) RESPIR ORGANIC VAPOR ACID GAS
001450020	ADHESIVE	OZ	3	.0075	CHEM-RESISTANT SAFETY GOGGLES COMB FACE-SHIELD KIT W/SAFE CP
001658614	ADHESIVE	QT	1	.0896	CHEM-RESISTANT SAFETY GOGGLES PCB RESISTANT GLOVES
001711509	LACQUER	GAL	1	.0001	
002232737	DICHLOROMETHANE	PINT	1	.0224	
002254548	ADHESIVE	KIT	1	.0096	CHEM-RESISTANT SAFETY GOGGLES COTTON INSPECTOR'S GLOVES RESPIR ORGANIC VAPOR ACID GAS
002348378	SODIUM SULFIDE, MONOHYDRATE, A	GRAM	500	.0224	COMB FACE-SHIELD KIT W/SAFE CP CHEMICAL COVERALL AIR RESPIRATOR SCBA (15MIN)
002300926	PETROLEUM	LB	1	.0003	FACE SHIELD PCB RESISTANT GLOVES
002648983	METHYL ETHYL KETONE	OZ	3	.0000	VISITOR'S SAFETY CHEM-RESISTANT SAFETY GOGGLES COMB FACE-SHIELD KIT W/SAFE CP
002650664	NAPTHA	GAL	5	.0090	CHEM-RESISTANT SAFETY GOGGLES AIR RESPIRATOR SCBA (15MIN)
002867748	ENAMEL, ALKYD-GLOSS	GAL	5	4.7761	FUTURA GOGGLES PCB RESISTANT GLOVES ORGANIC VAPOR RESPIRATOR
003190834	CLEANING COMPOUND	LB	11	.0038	COMB FACE-SHIELD KIT W/SAFE CP RESPIR ORGANIC VAPOR ACID GAS
003577386	DETERGENT	OZ	22	.0038	
004222169	CALCIUM CHLORIDE	LB	80	.7463	CHEM-RESISTANT SAFETY GOGGLES CHEMICAL COVERALL RESPIR ORGANIC VAPOR ACID GAS
005152211	PRIMER COATING	GAL	5	.0299	SPLASH GUARD CHEM SPLASH GOGG TYVEK DISP ELASTIC TOP BOOTS NEOPRENE GLOVES CHEMICAL COVERALL RESPIR ORGANIC VAPOR ACID GAS
005270216	ENAMEL	GAL	1	.0010	CHEM-RESISTANT SAFETY GOGGLES
005511487	1,1,1-TRICHLOROETHANE	GAL	55	.0000	CHEM-RESISTANT SAFETY GOGGLES COMB FACE-SHIELD KIT W/SAFE CP POLY-COATED GLOVES AIR RESPIRATOR SCBA (15MIN)
006446910	GLASS CLEANER	BOX	1	.0014	
007019546	ADHESIVE	KIT	1	.0036	WILLSON GALAXY SAFETY GLASSES SEAMLESS NATURAL RUBBER GLOVES
007770631	EPOXY PATCH	KIT	1	.0009	CHEM-RESISTANT SAFETY GOGGLES SEAMLESS NATURAL RUBBER GLOVES
003234039	ALODINE COATING	GAL	1	.0002	GENERAL PURPOSE FACE SHIELD

PHASE/PROCESS: OPERATING & SUPPORT /AFA DEPOT CANOPY REPAIR

SUBST ID	SUBSTANCE NAME	MSUR	PROQTY	QTY USED	EQUIPMENT NAME
					DISPOSABLE BOOTS
					SEAMLESS NATURAL RUBBER GLOVES
					NEOPRENE APRON
					RESPIRATORS DUST & MIST
008430802	ADHESIVE SEALANT	KIT	1	.0023	WILLSON GALAXY SAFETY GLASSES
					COTTON INSPECTOR'S GLOVES
008510211	ADHESIVE	KIT	1	.0033	COMB FACE-SHIELD KIT W/SAFE CP
					COTTON INSPECTOR'S GLOVES
008556160	ISOPROYL ALCOHOL	GAL	5	.0075	CHEM-RESISTANT SAFETY GOGGLES
					CHEMICAL COVERALL
					RESPIR ORGANIC VAPOR ACID GAS
008700877	PRIMER ADHESIVE	QT	1	.0075	COMB FACE-SHIELD KIT W/SAFE CP
					RESPIR ORGANIC VAPOR ACID GAS
008807616	SILICONE COMPOUND	OZ	8	.0224	CHEM-RESISTANT SAFETY GOGGLES
					COMB FACE-SHIELD KIT W/SAFE CP
					COTTON INSPECTOR'S GLOVES
					RESPIR ORGANIC VAPOR ACID GAS
009023871	ADHESIVE	KIT	1	.0007	WILLSON GALAXY SAFETY GLASSES
					SEAMLESS NATURAL RUBBER GLOVES
009353794	PLASTIC POLISH	BOX	1	.1194	WILLSON GALAXY SAFETY GLASSES
					SEAMLESS NATURAL RUBBER GLOVES
009923154	RESIN COATING	GAL	1	.0149	FUTURA GOGGLES
					SEAMLESS NATURAL RUBBER GLOVES
					RESPIRATORS DUST & MIST
011200408	METHYL ETHYL KETONE	LB	5	.0089	
011840329	SEALING COMPOUND	OZ	6	.8420	COMB FACE-SHIELD KIT W/SAFE CP
012602534	LUBRICANT	OZ	16	.0075	

SESSION IX  
INJECTION MOLDING - PART A

Chairman: K. Roach  
University of Dayton

Co-Chairman: W. R. Pinnell  
Flight Dynamics Directorate  
Wright Laboratory

Coordinator: R. Wagner  
Flight Dynamics Directorate  
Wright Laboratory

DEVELOPMENT OF DIRECTLY FORMED AND FRAMELESS AIRCRAFT  
TRANSPARENCY TECHNOLOGY

W. R. Pinnell  
Flight Dynamics Directorate  
Wright Laboratory

**Development  
of  
Directly Formed and Frameless  
Aircraft Transparency Technology**

William R. Pinnell  
WL/FIVR, WPAFB OH

for  
*Conference on Aerospace Transparent Materials and Enclosures*  
*13 August 1993*

Abstract

Based on a direct forming method demonstrated under a Wright Laboratories contracted effort completed in 1988, a major effort to develop technology for directly forming aircraft transparencies is nearing completion. Since direct forming affords designers the capability to tailor thickness and to form the transparency with integral attachment hardware, thickened edges can be utilized to eliminate the necessity for peripheral metal or composite frames. This class of transparency is referred to as "Frameless". Elimination of the frame also eliminates the necessity for bonding or bolting and sealing a conventional "bent-from-sheet" transparent panel to a frame. Since directly formed transparencies have (except for sprue removal) their final shape when they are removed from the mold, the requirement for post forming machining is also eliminated.

Direct forming can be utilized to manufacture transparencies as replacements for bent-from-sheet panels attached to frames with conventional methods. The directly formed transparent panel can feature thickness tailoring to save weight, gain bird impact resistance, or to achieve improved optics. Because direct forming (injection molding) is not labor intensive and produces consistent and repeatable parts in a very short time (one hour molding cycle), transparencies can be produced at very low cost.

Introduction

The evolution of windshields and canopies for high performance fighter and trainer type aircraft has been heavily influenced by the need to provide resistance to in flight impact with birds. Another influence has been the requirement for maximum and unobstructed field of view for pilots and aircrew members. Often modern designs sacrifice optical quality and weight to attain these goals. Because unobstructed field of view demands minimal opaque structure and compound curvature, transparent panels must be formed from very tough and formable plastic materials. Currently, impact resistance in transparencies is provided by extruded flat polycarbonate sheet.

## Current Transparency Design and Manufacturing

The extruding process for sheets of molten polycarbonate resin produces surfaces which must be heated and pressed between high quality surfaces to gain optical quality. Flight and impact loads require thicknesses of three quarters to one inch in forward facing transparencies. Extruded sheet stock does not have dependable impact resistance in thicknesses over about three eighths of an inch. To obtain the necessary structure, transparent panels must be laminated from two or more sheets. Further, to prevent migration of cracks from one ply to another, the laminations must be separated by an elastomeric inner layer. The lamination process must be closely controlled to minimize optical distortions which can result from unparallel surfaces and dissimilar materials. Laminating is labor intensive, expensive, and can produce rejects for imperfect bonding or optical quality.

Flat constant thickness laminates must be heated to a state which permits bending to the final transparent panel shape. Bending is accomplished by wrapping around a mandrel for simple shapes or forcing the laminated sheet into a cavity for shapes with compound curvature. This bending process requires stretching which also thins the laminate in an uncontrolled manner. The integrity of the lamination is threatened by the thermal cycle and stresses associated with bending and stretching. Variations in design shape and thickness as large as two tenths of an inch are not uncommon. Optical distortion is difficult to control during the heating and bending process and residual stresses are difficult to prevent and detect.

After forming, the transparent panel must be trimmed to final shape by machining the peripheral edges. When the panel is to be bolted to a frame, holes for the fasteners are drilled along the edges. Polycarbonate is notch sensitive and even very fine machine marks can become the origin for cracks as the material ages or is loaded. Machined edges are more susceptible to moisture and chemical absorption than surfaces formed during the polymer cooling process. Cracks often originate at holes for fasteners. Delaminations usually start at or near fastener holes or machined surfaces.

In transparencies with laminated panels, the juncture with the frame may loosen due to thinning of the soft inner layer material. Inner layer thinning can be caused by fastener compression or the clamping action of frame edge members or fairings. A loose joint is subject to penetration of moisture and chemicals which can be absorbed by the machined polycarbonate edges causing crazing, cracking, material degradation, delamination, and shortened service life. This juncture may be the source of cockpit pressure leaks.

Major discontinuities in load paths exist at the juncture between frames and transparent panels where fasteners or bonding immobilizes plastic material. Bird impact failures in forward facing windshields often originate at the aft arch where this discontinuity exists. Although elastomeric bushings are often used in oversized fastener holes, differences in thermal elongation in the frame material and in polycarbonate can result in stresses in the panel material. Bonding panels to frames, if the bond is successful, immobilizes the polycarbonate with respect to the frame material and stress in the plastic is highly concentrated along this line. Utilizing the structural benefits inherent in polycarbonate toughness depends on permitting elastic deformation of the material. Large permanent plastic

deformations should be permitted for absorbing dynamic loading associated with bird impact.

The need for frame attachment along the edges of transparent panels leads to the necessity for greater thickness in the panel to obtain strength where sections are reduced by holes or where the plastic is immobilized by a bond to very stiff frame material. Since extruded sheets or laminations of sheets are of constant thickness before forming this added thickness may be carried in areas of the transparency where thinner sections would withstand applied loads.

### Concepts for Technology Development

Technology is being developed for two related concepts; *Direct Forming* and *Frameless Aircraft Transparencies*. Direct forming technology can be applied to eliminate undesirable attributes associated with the current bend-from-sheet manufacturing method while reducing cost, extending service life, and improving performance. Direct forming advantages can be applied to existing and new aircraft. The frameless concept can be utilized to eliminate undesirable traits associated with the current necessity for attaching transparent panels to peripheral frames. Since frameless transparencies are directly formed, all of the direct forming advantages are also included. Potentials associated with the frameless concept may be limited in retrofits to existing aircraft, but offer major advantages to the designers of new aircraft.

### Direct Forming

Direct forming entails manufacture of an aircraft transparency directly from molten thermoplastic resin in one thermal process. This technology can be utilized to produce replacements for bent-from-sheet transparent panels or as a method for producing frameless aircraft transparencies. Low pressure, long cycle injection molding (Reference 1) is the direct forming method which is the basis for current technology development.

Injection molding produces transparencies by filling a mold cavity with molten resin, packing additional resin into the mold as the resin solidifies, cooling, and removing the molded transparency from the mold. The thermal condition of the mold and enclosed resin/polymer is closely controlled to insure optimum material properties, transparency quality, and dimensional repeatability. The forming cycle takes only about one hour and can be repeated immediately. Post forming machining is limited to removal of gating sprue for frameless transparencies. Drilling of fastener holes in the molded transparent panel which must be mounted into a frame is necessary only if molding the panel with holes is impractical.

Because direct forming is not labor intensive, major manufacturing cost reductions relative to bent-from-sheet methods can be realized.

Injection molding is a repeatable process which can be simulated (Reference 2) in computer aided engineering software, eliminating the need for trial and error development of most process parameters. Control and programming of temperature and pressure conditions during injection and polymer cooling produces material with consistent and repeatable properties in thicknesses required for reacting both static and dynamic loading conditions. Based on testing (Reference 3) of directly

formed sub scale panels, monolithic cross sections are expected to provide bird impact resistance in full scale transparencies.

Forming in a cavity which controls all surfaces and produces the final transparency shape affords the capability for tailoring and closely controlling thickness. Thickness tailoring can provide optimized structure while reducing overall weight (Reference 4). Weight reduction can be accomplished by thickening the forward facing areas for bird impact resistance and gradually decreasing thickness as impact incidence decreases to aft facing area where only flight loads must be reacted.

For given outside mold lines, optical characteristics can be optimized by distribution of thickness and inboard shape to achieve the best optical relationship between inside and outside surfaces. Precision control of thickness and shape, and the distribution of thickness and shape may afford the capability for designing transparencies to optical requirements. Thickness and shape distribution must consider both structure (impact and static) and optics. Repeatability of thickness in sub scale panel molding where simplified molds and thermal control were utilized, has been demonstrated within plus or minus .002 inches. Utilizing dimensional mapping (Reference 5) of molds and molded parts, a method for predicting shrinkage distribution (Reference 6) has been developed. Thickness control and repeatability in full scale transparencies is expected within .005 inches of design thickness in optical areas. This precision, which is unrelated to complexity of shape and curvature, may be more than an order of magnitude better than uncontrolled thickness variations associated with bend-from-sheet forming methods.

### Frameless

Contrasted to conventional aircraft transparencies which are assemblies of transparent panel(s) and a frame of dissimilar material, the frameless transparency requires no peripheral frame, has thickened sill edges of the same material as the optical areas, includes minimal molded in hardware for attachment to aircraft, and is formed in a single thermal process. The frameless concept is dependent on direct forming technology and offers all of the advantages of direct forming in addition to advantages associated with elimination of the requirement for a peripheral frame.

Elimination of the frame can substantially reduce transparency acquisition and life cycle cost. Although frames are typically (for bolted panels) reused, the initial cost is great, and the cost of inspection and refurbishment each time the transparent panel is replaced must be considered. Logistics for supplying the frame, fasteners, bushings, and seal (panel to frame) sets must also be considered. Because the panel to frame seal, attachment fasteners, and fairings are eliminated, changing the frameless transparencies in the field requires less aircraft down time.

Residual stresses in transparent panels which result from deformations of the panel to fit the frame, compression of plastic by fasteners, and continuous attachment of the panel to a thermally dissimilar material can be eliminated. Considering the eliminated installation stresses, minimal residual stress due to forming with the long molding cycle, elimination of machined edges and fastener



holes, and elimination of the panel to frame seal, significant increases in service life are expected.

Loads as great as 11,000 pounds have been required to pull a single latching insert from a molded panel thickened edge. Testing of insert pull out loads after hot and cold mission cycling has indicated that the inserts can be expected to react mission loads successfully in a frameless transparency. A seal required between transparency frames and aircraft cockpit sills will be required for frameless transparencies and will require that the thickened edge be structurally designed to prevent deflections between latching inserts which would break this seal. This stiffness has been analytically predicted for the design of the first frameless transparency which is presently being molded.

Elimination of the need for dissimilar (frame) materials and attachment at arches and sills precludes major structural discontinuities. Designers can utilize thickness and shape tailoring to transition static and impact loads to aircraft structure through tough plastic materials without the effects of fastener holes and materials that have greatly different response characteristics. This capability is specifically important during bird impact on forward facing surfaces which include an arch. Balanced design at the arch juncture is critical to preventing bird penetration and controlling deflections. Cross sections (Figure 1) and shapes which utilize the toughness inherent in impact resistant plastic can be chosen to dissipate energy and transmit loads efficiently. These all plastic designs without fasteners or dissimilar materials are simple to model for structural analysis tools. Predictions of deflection and failure conditions can be made analytically with good confidence. Bird impact testing of molded sub scale panels with thickened and shaped edges have demonstrated the capability for large elastic deformations which have been indicated by analytical prediction methods (Reference 4).

### Technology Development

#### Approach

Technology for directly formed and frameless aircraft transparencies is being developed in three phases:

First, a contracted study identified low pressure, long cycle injection molding as a candidate for forming thick walled and impact resistant transparent parts. This contract also included molding and testing sub scale panels to demonstrate the feasibility of this method. This effort (Reference 5) was completed in June 1988.

Second, development of technology required to design and fabricate directly formed and frameless transparencies utilizing the direct forming method previously demonstrated is currently being completed. The product of this phase has been defined as the Analytical Design Package (ADP) for aircraft transparencies. This phase includes design of a Confirmation Frameless Transparency (CFT), design and fabrication of a mold, molding of this transparency, testing, and utilizing test data to confirm the ADP.

The Third phase includes production of a prototype frameless transparency for field use utilizing the ADP for design and methods

developed during the confirmation of the ADP (second phase) for fabricating this transparency and the required mold. This phase will terminate with the delivery of the mold, process, and prototype test data to the acquisition organization for the aircraft which will use the transparency in the field.

## Progress

### Technology Based on Sub Scale Molded Panels

Table 1 summarizes demonstrated facets of the overall technology based on molded sub scale flat and conical panels (Figure 2). The effort to accomplish these demonstrations has been conducted in parallel with, and in support of major contracted efforts to design and fabricate the CFT mold, molding hardware, and support equipment. Contracted support in the form of molding and testing has been essential to these demonstrations which have been conducted by WL/FIVR as In-House projects.

Table 1

#### Technology Demonstrations Based on Injection Molded Panels

##### Direct Forming Process

Two Molding Sources  
Five Resin Types  
Thick Monoliths  
Mold Temperature Zoning  
Molding with Inserts  
Melt Flow Index Effects

##### Structural (UDRI Test Support)

Dart Impact  
Bird Impact  
Static Material Properties  
Insert Loads  
Thermal Cycling  
Thermal Cycling Loads

##### Dimensional Design/Control

Dimensional Mapping Methods  
Mold Design Methods

## ADP Development

An early form of the ADP was developed and delivered as a part of the Frameless Technology Program (FTP) conducted by Lockheed Fort Worth Company (LFWC), then General Dynamics, Fort Worth Division.

The ADP as delivered by LFWC is being further developed by PDA Engineering and the University of Dayton Research Institute (UDRI) as a part of a WL/FIVR contract. ADP development is proceeding in accordance with an ASTM method for software development which includes two Beta evaluation cycles. The Beta 1 evaluation was conducted in February 1993. This evaluation included on site participation of potential users at PDA Engineering in Costa Mesa, California.

Figure 3 is a graphical representation of the ADP. The ADP utilizes P3/Patran, a Computer Aided Engineering (CAE) code to generate a common model which can be utilized by structural, thermal, optical, and molding simulation codes

to iteratively develop transparency designs from aircraft geometry and mission requirements. As the common CAE software, P3/Patran accesses material properties from an M/Vision data base and maintains pre and post processing files for each of the analytical tools. Reference 8 includes a detailed discussion of the ADP and progress in ADP development.

### ADP Confirmation Frameless Transparency

The design of the Confirmation Frameless Transparency (CFT) has been completed. The CFT geometry is based on the forward half of the F-16 canopy as shown in Figure 4. Design input includes F-16 mission and 350 knot, four pound bird impact requirements. Thickened sills and an aft arch were added to generate a forward windshield sized frameless transparency. Thickened sills enclose latch inserts and an aft threaded insert for attachment to a modified F-16 frame for ground testing. The CFT design represents the mission of a high performance fighter with complex optical shape and frameless forward windshield features. No attempt to optimize optics by thickness tailoring was made. The design goal includes a constant three quarter inch thickness in the optical area. Figure 5 is a graphic representation of the CFT showing thickened edges and latch inserts.

### CFT Mold

A single cavity collapsing core mold was designed and fabricated. Figures 6 and 7 are photographs of the mold cavity and core respectively. A 2.75 inch diameter sprue bushing is transitioned to the shape of the most forward CFT cross section by a single fan gate. This resin delivery system reflects the low pressure, thick wall, long injection molding cycle demonstrated in previous molding of sub scale panels.

Based on experience in molding sub scale conical panels, the mold cavity thickness was tapered to correct for the effects of shrinkage (Reference 6). Sizing of the mold cavity also included thermal expansion effects. The objective of mold cavity sizing is to produce a constant thickness optical area and CFT design dimensions. The mold has been thoroughly dimensionally mapped utilizing a coordinate measurement machine with methods developed by WL/FIVR for obtaining an accurate cavity thickness distribution.

Because the CFT interior surface "wraps around" (larger cross sections exist inside the peripheral edges) the mold core, the CFT could not be removed from a single piece mold core. Two opposed areas of the core surface were replaced by sliding blocks which will be retracted by a hydraulically driven internal mechanism before the mold can be opened. These slides produce the "collapsing core" mold feature and permit CFT removal. A witness line in the form of a small ridge extending from the surface will be formed at the edges of the sliding blocks. The shape and location of these blocks was chosen to keep witness lines away from the prime optical area.

The CFT mold was cut from solid billets of P20 steel. The cavity surface was polished to a 1200 diamond paste "mirror" finish. Cavity surfaces were hardened by ion nitriding for durability.

Blocks for retention of latch and threaded inserts are fitted into the mold core billet. These blocks secure inserts during injection and are removed from the

mold with the CFT, then separated and replaced in the mold with an insert set for the next injection. A system for initial motion of the retention blocks at mold opening is provided.

Thirty seven channels were drilled for heating/cooling oil to control the temperature of the mold. A total of 32 thermocouples and 8 pressure transducers are located in cavity, core, slide, and slide mechanism billets.

Design, fabrication, polish, surface hardening, and mechanical confirmation checks have been completed. The CFT mold has been installed in an Envirotech molding station and prepared for process development molding trials.

#### CFT Removal System

To preclude manual handling of molded CFTs, a mechanism for CFT removal from the mold has been designed and fabricated. This removal system is attached to the aft face of the mold cavity and includes a carriage which travels along rails to position cradling fixtures at the sprue and CFT aft corners when the mold is open. The cradling fixtures are hydraulically actuated to lift the CFT off mold stripping blocks and the carriage is removed from the mold bearing the CFT. Molded CFTs will be lifted from the removal system and placed on wooden pallets which are also the bases for storage and shipping containers.

Fabrication and installation of the removal system is complete. An opaque CFT casting which was formed inside the mold was used for functional checks of the mold and removal system.

#### Mold Heating/Cooling (H-C) System

The H-C system developed for the CFT (and anticipated subsequent transparency molding) has the capability for independently heating and cooling eight mold zones. This is accomplished by maintaining two constantly flowing oil circuits. A hot oil circuit can be maintained at a maximum of 500 deg F and a cold oil circuit can be kept at a temperature as low as 37 deg F. Set temperatures and temperature ramps are achieved for each mold zone by a feed back control system which, based on temperatures sensed in input lines to each zone, cycles a controller which controls flow rate and alternates flow from the hot or cold circuit to achieve the desired temperature set values at programmed times. As many as eight temperature ramps can be programmed for each of the eight mold zones during the molding cycle.

Figure 8 is a schematic of the H-C system as it is presently installed at the Envirotech plant. The system is on four modular skids designed for mobility. A gas fired burner on one skid supplies heat for oil in the hot oil circuit, a chiller skid removes heat from the cold oil circuit, oil supply and reservoir tanks are contained on a tank skid, and a secondary loop skid includes a pumping and control circuit for each of the eight mold zones. Skids are installed exterior to the molding facility building and oil piping connects the skids to inside manifolds where oil flow in each zone is divided to specific channels in the mold.

The H-C system represents a major investment in an asset which can be utilized for development of additional technology related to direct forming of

aircraft transparencies. It is also anticipated that the H-C system will be utilized in production molding of directly formed and frameless transparencies in the future.

Programming, control, and monitoring the H-C system will be accomplished by a series of virtual instruments within LabView software utilizing a Macintosh computer. The LabView system will also continuously record output from each of the mold thermocouples and pressure sensors. LabView software has been configured to record data in files on a hard disk with the capability for observing current values, recent data history, and down loading time segments of data as the molding cycle progresses.

The H-C system and the LabView based control and recording system are complete and installed at the Envirotech plant. Testing to establish performance limits are currently being conducted prior to initial CFT molding trials.

#### Current Effort

##### CFT Molding

A three phase program for molding the CFT as the first directly formed aircraft frameless transparency is currently being conducted. All molding will utilize Dow 300-6 Calibre polycarbonate resin. It is expected that CFT molding will be completed by 30 September 1993.

##### Process Development Molding

Eighty injection molding "shots" will be devoted to the development of an optimum process for forming the CFT. During this molding phase process parameters will be varied and resulting molded CFTs tested at the molding site to assess effects.

##### Process Development Testing

During process development molding, each molded CFT will be tested to assess the effects of process changes and to evaluate CFT quality, repeatability, and performance. The results of this testing will be utilized by the molding team to direct the evolution of the CFT molding process. Control coupons from unbent polycarbonate extruded sheet and coupons cut from bent-from-sheet F-16 canopies will also be tested. Testing at the molding site will include:

*Inspection and Evaluation* of CFTs for molding defects and overall quality will result in a grading value for each CFT. All CFTs will be subjected to this inspection and evaluation.

*Measurement of Overall Dimensions* to establish conformance to design and repeatability. This data will also be used to evaluate methods for sizing the CFT mold cavity.

*Micrometer Measurement of Thickness* at the edges of dart test coupons removed from CFTs. This data will be indicative of actual thickness distribution in the CFT optical area. Data will be compared to mold cavity thickness distribution based on dimensional mapping of the mold cavity

and core. The effectiveness of the WL/FIVR method for shrinkage distribution in cavity design will be assessed for process parameter sets.

*Drop Dart Impact* testing to establish the impact resistance of molded material will be conducted after each CFT has reached ambient temperature. Six inch square coupons will be cut from four CFT locations, held in apparatus which matches the local curvature of each coupon, and subjected to the impact of a 60 pound dart dropped from heights up to 23 feet. The dart has a 1.5 inch hemispherical nose. Process parameters will be varied to attain maximum impact resistance within the dart testing capability. Coupons will be subjected to impact on both inside and outside CFT surfaces.

*Optical Distortion Mapping* for each CFT will be conducted utilizing an on site Optical Test Fixture (Reference 9). Angular deviations in azimuth and elevation will be measured over the CFT optical surface from the design eye point. Effects of process parameter changes will be assessed.

*Light Transmittance and Haze* will be measured for dart coupons before impact. Effects of process changes will be assessed.

#### Effectiveness of Injection Molding Simulation

During process development molding, consultants from AC Technology, the vendor for the C-Mold software package, will join WL/FIVR and UDRI personnel at the molding site for assessing the effectiveness of this simulation package. An on site Silicon Graphics Indigo work station will be utilized with a CFT model previously generated by LFWC and WL/FIVR to simulate molding and generate process parameters. Process parameters generated by the simulation will be compared to the actual process. Because C-Mold is intended for typical (see Reference 2) injection molding cycles, it is expected that major disagreements will be evident. AC Technology consultants will be expected to provide changes to modeling methods, C-Mold run procedures, and minor changes to C-Mold default restrictions which will improve the accuracy of simulation for the low pressure, thick wall, long cycle CFT molding process. Additionally the simulation effectiveness effort is expected to result in recommendations for customizing the C-Mold package as necessary for effective simulation of the direct forming process for aircraft transparencies.

#### CFT Test Item Molding

The process which evolves from process development molding will be utilized to produced 55 identical CFT items to be utilized for ADP confirmation testing subsequent to the molding trials. As a check on process stability and to establish repeatability limits, every tenth CFT will be subjected to the on site testing utilized for process development. Depending on the magnitude of observed variation, optical distortion mapping may be conducted for all CFTs. All CFTs will be subjected to inspection and evaluation. Gating sprues will be removed from these CFTs by the molding contractor.

### CFT Molding for Coating Trials

Fifteen CFTs will be molded utilizing the process which evolves from process development molding for subsequent application of abrasion resistant coating. These items will then be tested for effectiveness of the coating relative to material properties, coating adhesion, and bird impact resistance. The seventh of these CFTs will be subjected to on site testing to check for continuity in molding process. All CFTs will be subjected to inspection and evaluation. Gating sprues will be removed from these CFTs by the molding contractor.

### ADP Development

Efforts to complete the development of the ADP are currently concentrated on refinement of thermal and structural code integration, incorporation of an optical code, and limited application of the ADP to current design tasks. Preparations for the Beta 2 evaluation are under way.

### Planned Effort

#### CFT Testing

Testing for generating data to be used to confirm the ADP, methods utilized in mold design, and the effectiveness of abrasion resistant coating will include dimensional mapping, establishment of material properties, static structural testing, and bird impact testing. This testing will begin at the end of test item molding with dimensional mapping. After mapping, some CFTs will be cut into coupons for materials property testing, and some will be shipped to coating facilities for application of abrasion resistant coating. Both coated and uncoated CFTs will be subjected to bird impact testing to obtain deflection time data and to determine failure conditions. CFT testing is expected to be complete by the end of calendar year 1993.

#### ADP Development and Confirmation

ADP development will continue with the integration of an optical code and the Beta 2 evaluation. After incorporating feedback from potential users during the Beta 2 evaluation, PDA Engineering, the development contractor will prepare the ADP for delivery early in calendar year 1994.

#### ADP Confirmation

The ADP configuration delivered at the end of the development contract will be utilized to redesign the CFT based on the same mission requirements and geometry input set which was used in the original CFT design. Materials properties used as ADP input will include those resulting from CFT testing.

If the resulting CFT design is substantially different in thickness, aft arch cross section, or thickness distribution, then the ADP structural, thermal, and optical analytical modules will be utilized to assess the CFT configuration as molded and tested for insert latch load limits, bird impact failure condition (including origin of failure), deflection histories for selected CFT surface points (including points on the aft arch) during the bird impact event, and distribution of optical

distortion. The customized (if appropriate) version of the molding simulation software will be exercised to obtain process parameters and mold design input.

Actual test results are to be compared with the CFT design goals or with the assessed performance in areas mentioned in the preceding paragraph. Where differences exist, changes to modeling methods, application of analysis tools, methods of design iterations, or interpretation of material properties will be identified to improve this agreement. After making appropriate changes, and after reasonable agreement between ADP results and actual test data has been reached, the ADP will be considered confirmed. Documentation of these efforts and limitations of the ADP, including molding simulation, will be generated and distributed. This documentation is expected to be available in mid calendar year 1994.

### Technology Transition

Transition of developed technology to users was started in the second technology development phase by actively involving potential users in the ADP Beta 1 evaluation. This will continue with the Beta 2 evaluation. In parallel with WL/FIVR testing to confirm the ADP, users will be offered an opportunity to become operational with the ADP and to apply the ADP to design tasks which may or may not involve direct forming or frameless transparencies. After ADP confirmation molding and testing, SM-ALC/TIEC will initiate a program to apply the ADP and direct forming technology to the development of a directly formed (but not frameless) replacement for the current F-16 canopy. WL/FIVR will support this program by providing technical consultation and assistance.

Frameless aircraft transparency technology can also be transitioned to users when the ADP has been confirmed since the transparency configuration for ADP confirmation is frameless. The frameless flight demonstration to be conducted as a part of the third phase will complete the technology development.

### Contractors

Conduct of this technology development program has been the responsibility of WL/FIVR. Additionally WL/FIVR has assumed a major role in the technical achievements and technical direction of the program. Some aspects of the program are beyond the scope of WL/FIVR capabilities and could not be accomplished without substantial contracted effort. The following list identifies contractors which have been or are now involved in this program:

*Loral* (formerly Goodyear Aerospace) - Direct forming process

Subcontractors:

*Envirotech* (formerly Einco) - sub scale panel molding

*UDRI* - sub scale panel testing

*Lockheed Fort Worth Company* (formerly General Dynamics) - Prime contractor for initial ADP development, Optical test fixture, CFT design, CFT mold, H-C system, and CFT molding.



**Subcontractors:**

*Envirotech* (formerly Eimco) - CFT molding and sub scale panel molding

*Delta Tooling* - Design and fabrication, CFT mold and removal fixture

*Budzar* (sub to Delta) - H-C system design and fabrication

*UDRI*, (under WL/FIVR Transparency Technology Support Contracts) - Prime contractor for sub scale panel molding testing and evaluation, fabrication of CFT and panel test apparatus, CFT insert fabrication, CFT molding (coating evaluation), ADP development, ADP confirmation testing, and ADP confirmation.

**Subcontractors:**

*Envirotech* (formerly Eimco) - CFT molding and sub scale panel molding

*ALCOA* - Thermoplastic insert molding, sub scale panel molding

*Hettinga Molding Equipment Co.* - sub scale panel molding

*PDA Engineering* - ADP development

*Giddings and Lewis* - Dimensional mapping of sub scale panels

**Funding**

Funding for this effort has been shared by WL/FIVR (30%) and the Reliability And Maintainability Technology Insertion Program (RAMTIP), managed by the U. S. Air Force Material Command, CSTI/PIPR.

**Conclusions**

1. A low pressure, long cycle injection molding process has been demonstrated for forming thick walled, impact resistant, and transparent panels from polycarbonate resins.
2. Tailoring thickness in injection molded thick-walled panels without loss in material properties including impact resistance has been demonstrated.
3. Forces required to pull latch inserts from thickened edges of molded panels before and after hot and cold thermal cycling indicate the feasibility of utilizing latch inserts to resist transparency attachment loads.
4. Thickness distribution in sub scale molded panels with directly formed frameless aircraft transparency features can be controlled with better precision than thickness in transparencies formed using bent-from-sheet methods.

5. Fabrication of injection molds for frameless transparencies with collapsing core segments to permit removal of molded transparencies is feasible.

### Recommendations

1. Planned efforts for completing ADP development and confirmation, including CFT molding and testing, should be completed.
2. Actions to proceed with the development and subsequent production of a directly formed (but not frameless) F-16 canopy should be launched when CFT bird impact testing has indicated that injection molded monolithic sections are suitable for impact resistance in aircraft transparencies.
3. WL/FIVR efforts to produce a frameless forward wind shield prototype should proceed when CFT bird impact testing has indicated that injection molded monolithic sections are suitable for impact resistance in aircraft transparencies.
4. The capability for designing directly formed aircraft transparencies to optical requirements should be pursued. This capability should be added to the ADP.
5. An investigation to determine the feasibility of removing witness lines which result from segmented molds should be conducted.
6. The CFT mold and the H-C system should be utilized for demonstrating technologies related to direct forming for aircraft transparencies. CFT molding with abrasion resistant film in the mold before injection should be considered.
7. CFT molding for refining process beyond the 80 shot process development molding of the current program should be considered.
8. Formulation of resins specifically for the low pressure, thick wall, long cycle process should be considered. These formulation efforts should strive for improvements in impact resistance in monolithic sections, higher temperature resistance for molded transparencies, and increased abrasion resistance.
9. The CFT mold and H-C system should be utilized for qualifying resins formulated specifically for the direct forming of aircraft transparencies.
10. A study to develop methods for and the effectiveness of molding transparency panels with holes for fasteners should be conducted.
11. The H-C system developed for CFT molding should be considered for production molding of transparencies for field use.

### References

1. Mills, C., and Pinnell, W. R., "Injection Molding as a Direct Forming Method for Aircraft Transparencies," to be published with the proceedings form A

Conference on Aerospace Transparent Materials and Enclosures, San Diego CA, 9 - 13 August 1993.

2. Pinnell, W. R., "Analytical Simulation of Low Pressure, Thick Walled Injection Molding for Aircraft Transparencies," to be published with the proceedings form A Conference on Aerospace Transparent Materials and Enclosures, San Diego CA, 9 - 13 August 1993.

3. Frank, G. J., and Pinnell, W. R., "Mechanical Properties Evaluation of Frameless Transparency Materials," to be published with the proceedings form A Conference on Aerospace Transparent Materials and Enclosures, San Diego CA, 9 - 13 August 1993.

4. Braisted, W. R., Huelsman, M. A., and Pinnell, W. R., "Bird Impact Resistance Evaluation of Frameless Transparency Materials," to be published with the proceedings form A Conference on Aerospace Transparent Materials and Enclosures, San Diego CA, 9 - 13 August 1993.

5. Roach, K. P., and Chow, J. G., Ph.D., "Dimensional Mapping and Shrinkage Characterization of Large, Thick-Walled, Directly-Formed, Transparent Panels," to be published with the proceedings form A Conference on Aerospace Transparent Materials and Enclosures, San Diego CA, 9 - 13 August 1993.

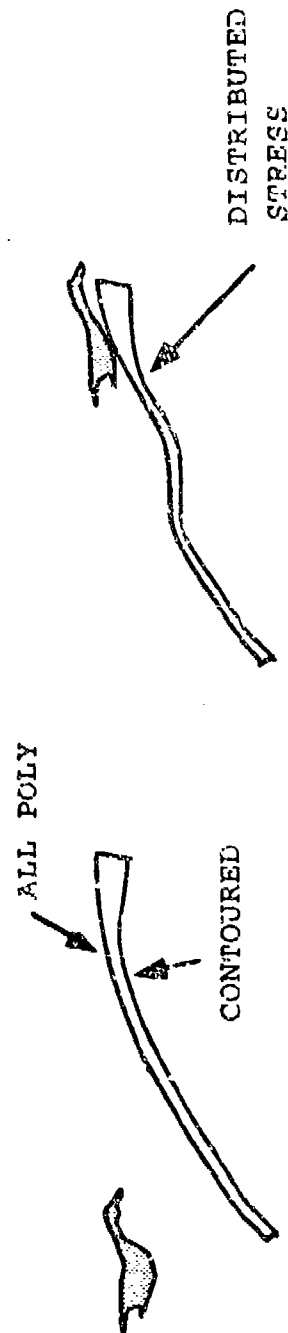
6. Chow, J. G., Ph.D., and Roach, K. P., "Analysis of Transparency Panel Shrinkage Characterization and their Application to Transparency Mold Design," to be published with the proceedings form A Conference on Aerospace Transparent Materials and Enclosures, San Diego CA, 9 - 13 August 1993.

7. Fuller, D. B., Perunuri, B. L., and Taylor, T. A., "Development of Forming Process for Frameless Aircraft Transparencies," AFWAL-TR-88-3071, Air Force Wright Aeronautical Laboratories, Wright-Patterson Air Force Base, OH, October 1988

8. Wuerer, J., Gran, M., and Held, T. W., "Analytical Design Package - ADP2 A Computer Aided Engineering Tool for Aircraft Transparency Design," to be published with the proceedings form A Conference on Aerospace Transparent Materials and Enclosures, San Diego CA, 9 - 13 August 1993.

8. Robson, T. L., and Pinnell, W. R., "Optical Evaluation of Transparencies Utilizing New Test Apparatus," to be published with the proceedings form A Conference on Aerospace Transparent Materials and Enclosures, San Diego CA, 9 - 13 August 1993.

# FRAMELESS AFT ARCH VS FRAMED TRANSPARENCY ARCH DURING BIRD IMPACT



## FRAMELESS AFT ARCH

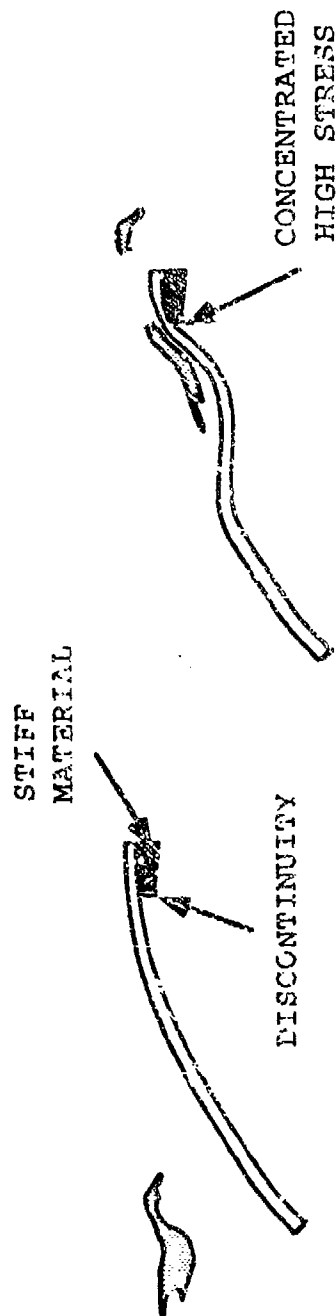


FIGURE 1

## FRAMED ARCH

# **DIRECTLY FORMED FRAMELESS AIRCRAFT TRANSPARENCIES**

## **SUB SCALE DEVELOPMENT PANELS**



**Conical Panel**

**1/2 in thick**

**2 in thickened edges**

**basis for shrinkage tech.**



**Flat Panel**

**1/2 and 3/4 in thick**

**2 in thickened edges**

**Simulated Junction**

**FIGURE 2.**

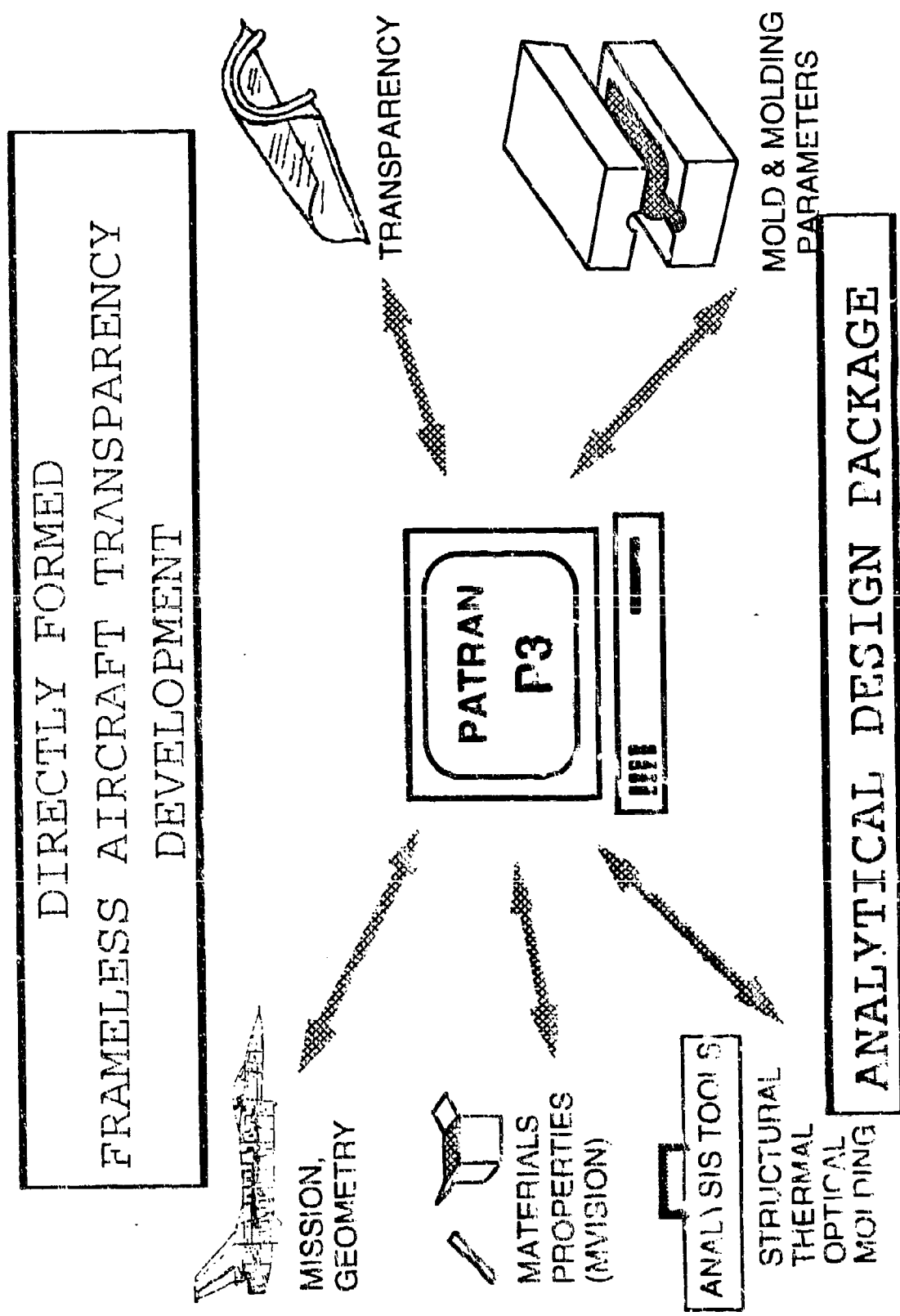


FIGURE 3

# CONFIRMATION FRAMELESS TRANSPARENCY

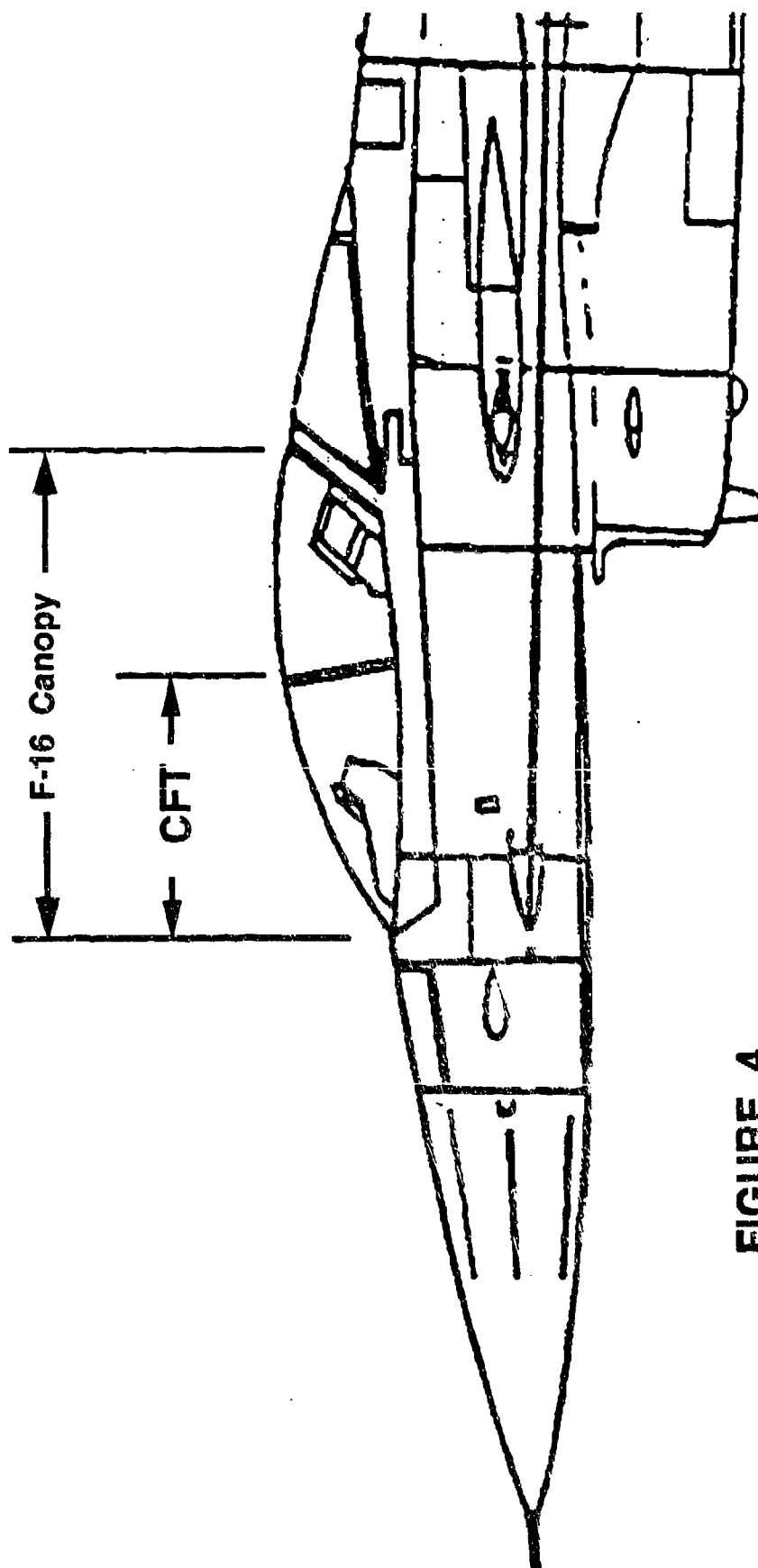


FIGURE 4

# CONFIRMATION FRAMELESS TRANSPARENCY (CFT)

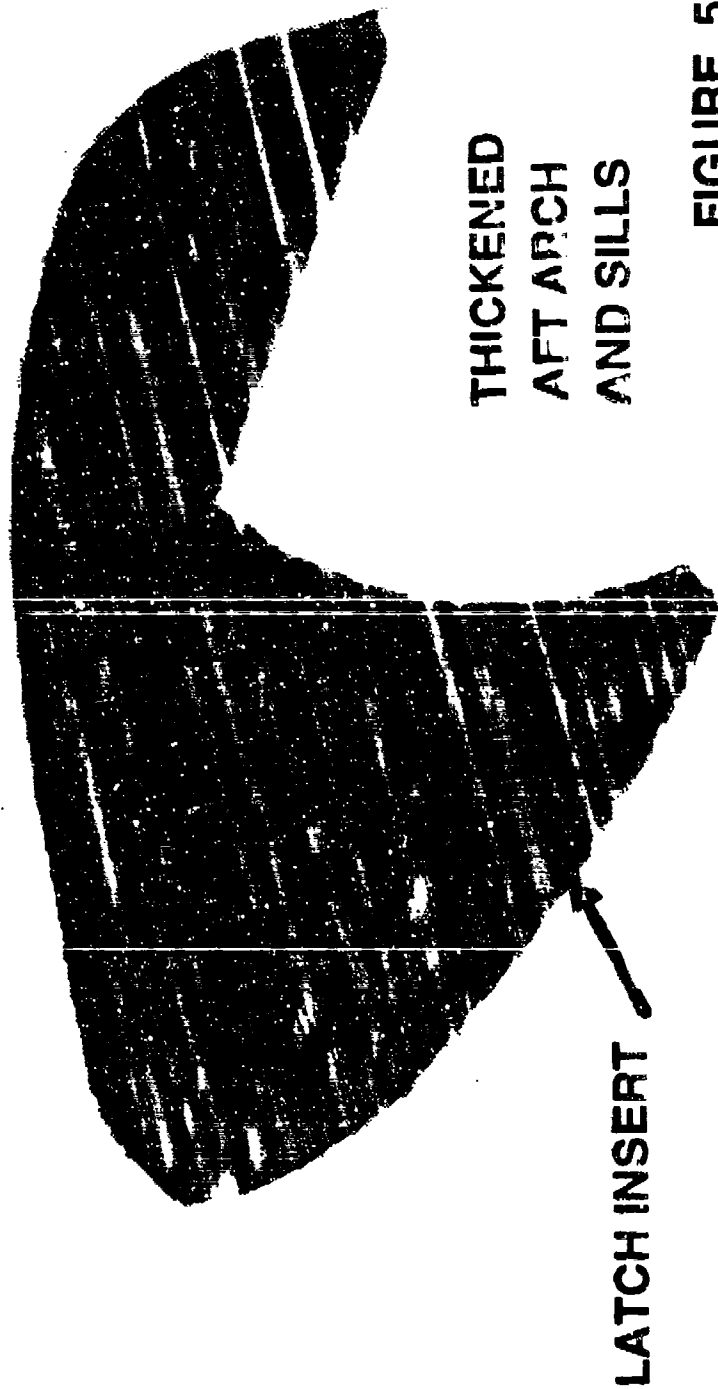


FIGURE 5



# CONFIRMATION FRAMELESS TRANSPARENCY MOLD



CAVITY

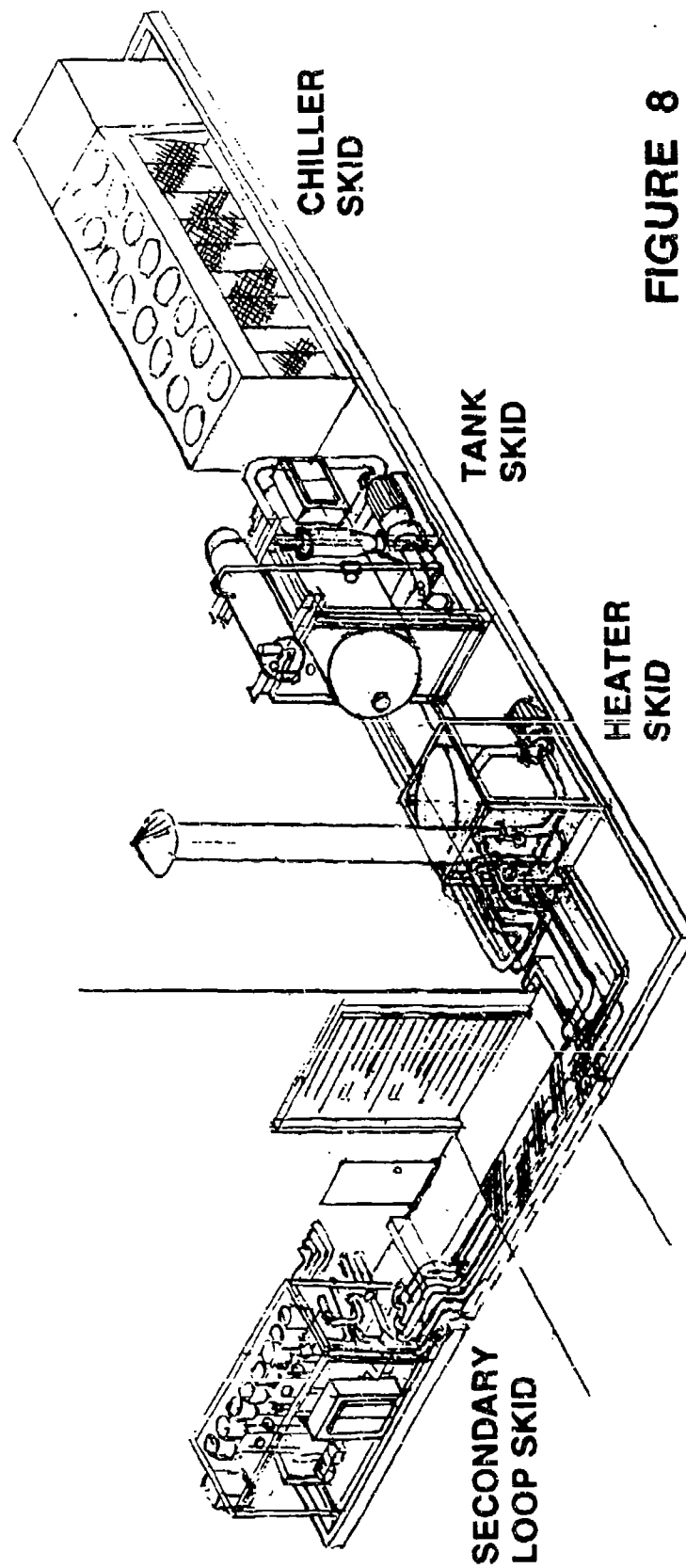
FIGURE 6



CORE

FIGURE 7

**INJECTION MOLD  
HEATING AND COOLING SYSTEM  
FOR DIRECT FORMING OF  
AIRCRAFT TRANSPARENCIES**



**FIGURE 8**

INJECTION MOLDING AS A DIRECT FORMING METHOD FOR AIRCRAFT  
TRANSPARENCIES

C. Mills  
Envirotech Molded Products

W. R. Pinnell  
Flight Dynamics Directorate  
Wright Laboratory

**Injection Molding  
as a  
Direct Forming Method  
for  
Aircraft Transparencies**

Calvin Mills  
Envirotech Molded Products  
Salt Lake City UT  
and  
William R. Pinnell  
WL/FIVR, WPAFB OH

for  
*Conference on Aerospace Transparent Materials and Enclosures*  
*12 August 1993*

**Abstract**

Envirotech has been instrumental in molding thick walled transparent panels under projects funded by the Air Force Wright Laboratories since 1986. More than 350 flat and conical test panels have been molded. Envirotech is presently conducting a molding program for developing the process for the first full scale directly formed frameless transparency.

This paper addresses injection molding practices applicable to forming thick walled large transparent parts. Low pressure, long process injection molding is compared to standard molding processes. How low pressure processes can produce required dimensional control, impact strength, and optical quality will be explained. Transparency design features which can simplify molding and enhance molding quality will be suggested.

**Introduction**

Envirotech has unique and extensive experience in injection molding of very large parts. Shot sizes as large as 460 pounds and dimensions as large as 60x80x4 inches have been molded from a variety of resins. The majority of items molded by Envirotech are industrial and municipal products including staged mining filters (Figure 1) and fittings for large, heavy walled plastic piping (Figure 2). Envirotech's products are generally opaque. Filled and unfilled resins are used. Polypropylene, PVDF and nylon are the most commonly molded resins. Envirotech routinely works with innovative molds and the development of processes which economically produce large parts is a specialty. Envirotech has been involved in the Air Force effort to develop direct forming technology since 1986 and is currently conducting frameless transparency molding programs for the Air Force as a subcontractor to Lockheed Fort Worth Company (LFWC) and the University of Dayton Research Institute (UDRI). Sub scale panels (Figure 3) molded for the Air

Force were subjected to extensive testing including simulated in flight impacts with birds.

Based on the successful molded panels, the Air Force has funded design and fabrication of a full scale mold for the first frameless transparency, a heating and cooling system for the mold, and handling fixtures for the molded transparency. These items are currently installed at the Envirotech plant where functional checks are being conducted. Molding will consist of three phases: The first 80 shots will be dedicated to developing the optimum process to produce impact resistance, optical clarity, minimal optical distortion, and dimensional consistency. A second molding phase will produce 55 transparencies using the developed process to be tested off site by the Air Force to obtain data for confirmation of an Analytical Design Package (ADP) for directly formed transparencies which includes injection molding simulation. The third molding phase will produce 15 frameless transparencies which will be used to demonstrate the effectiveness of abrasion resistant coatings. An in-depth discussion of this testing and the technology development program is included in Reference 1.

The purpose of this paper is to contrast Envirotech's bulk molding process with standard molding processes and to discuss advantages offered by the bulk process to molding of transparencies.

#### Standard Injection Molding

The main advantage of standard injection molding over other thermoplastic processes is high production rates at low cost. To do this, parts are designed with thin walls to decrease cycle time. The limiting factor for cycle time is how fast the part can be cooled to a temperature low enough to eject the part from the mold. Non uniform walls increase the cycle time as the thicker sections are the controlling feature. The experience of most molders is that thick sections have sink marks and/or voids especially where the flow is from thin to thick sections. Proper gating is a must to avoid this problem.

Injection molding is essentially flowing a fluid (molten plastic) between parallel walls. The pressure required to force fluid flow is inversely proportional to the distance between the walls to the third power. The viscosity of most plastics is high and flowing through small areas requires pressures from 5,000 psi to 20,000 psi. Some molding machines are designed for pressures up to 30,000 psi. for injecting very high viscosity engineering plastics.

During the injection cycle, the mold must be held closed by a clamp. The force necessary is equal to the injection pressure times the part projected area in the direction normal to the mold parting plane. For 10,000 psi injection pressure, the clamp force is 5 tons per square inch.

The use of chillers to keep the mold temperature low is common practice in injection molding. Plastics are natural thermal insulators and the higher the temperature differential between the molten material (typically 400 - 600 deg F) and the mold, the greater will be the removal of heat from the part. Chillers are used to lower the temperature of the mold to as low as 40 deg F.

Standard injection molding machines are usually fully automated. Robots are used to install inserts and to remove and handle the parts as they come out of the

mold. Hydraulic rams and mechanical cams are used to actuate side draw cores and mold sections if needed. The molding cycle is fully automated with all of the different portions of the cycle actuated by timers. Operators are present to monitor the process, check parts, and usually do some part finishing.

Standard injection molding machines are very efficient when the parts are properly designed for the process and the maximum automation and optimum processing conditions are used. This results in the maximum production rate and the lowest unit costs.

#### Standard Injection Molding Summary:

Molded parts with thin, nearly uniform wall sections.

High injection pressures (10,000 to 20,000 psi), high injection rates

2.5 to 15 tons per sq. in. clamp forces

Chilled molds

Highly automated tooling and molded part handling

Short molding cycles, maximum part production rate

Standard molding is a well developed practice which is at its best for small or thin walled parts which must be produced at high rates. Existing simulation software packages have been developed for this type of molding. Many of the characteristics which make the standard molding optimum for small thin walled parts are not appropriate for large parts with thick walls. The high injection pressure related to production rate and fast injection would necessitate very large clamping capacities for large items.

#### Bulk Injection Molding

Early in the 1960's a need was seen for thick-walled, heavy plastic industrial parts to be used as replacements for stainless steel and other exotic alloys used in the chemical process industries. Equipment was designed and process parameters were determined that allowed plastics, mostly polypropylene at the start, to be molded in sections from 3/8 to 5 inches with sinks and the other problems associated with thick sections. The molding equipment was not automated because none of the parts required high volume production and manual operation was less costly overall. This process, which concentrated on molding very large parts with thick walls and with limited production rates, was termed bulk injection molding.

Several benefits associated with bulk injection molding have been discovered. Material flowed readily and filled molds at 1,000 psi or less. This means that clamping pressure could be 1/2 ton per square inch. For a given clamp capacity, much larger parts could be molded. Low injection pressure requires that molds be heated to produce a smooth surface finish. Even for industrial parts, an acceptable surface could not be produced unless the mold was heated. This resulted in very long cycle times required to cool the part and to pack in additional material as the part shrank. With long cooling time, the hot mold is a natural annealing fixture, therefore, bulk molded parts have low molded-in-stress. Since stress

reduces impact strength in polycarbonate, transparencies must be molded with minimal residual stress. High injection pressure and cold mold surfaces are known to induce stress in molded parts.

The equipment designed for the bulk injection molding process allows greater freedom in gating most parts. This equipment permits gating into the thickest sections and permits part designs with large differences in wall thickness. Material can be readily packed into thick sections reducing sinks and voids.

#### Bulk Injection Molding Summary:

Thick cross sections 3/8 in. minimum

Injection pressures 1,000 psi or less

1/2 tons per sq. in. or less clamp force

Wide variations in cross section thickness can be molded

Long pack times, reduction of voids and sinks

Heated molds for good surface finish

Manual operation for most molding

#### Conclusion

Bulk injection molding offers the following advantages to molding aircraft transparencies:

1. Thick monolithic parts can be molded with minimal residual stress.
2. Thickened edges, relative to the optical area, can be molded.  
This permits elimination of a bolted or bonded frame.
3. Thickness can be tailored over the entire part to match local structural or optical needs.
4. Production of one transparency per hour is possible.
5. Materials can be molded which are not normally available in sheet form.

#### References

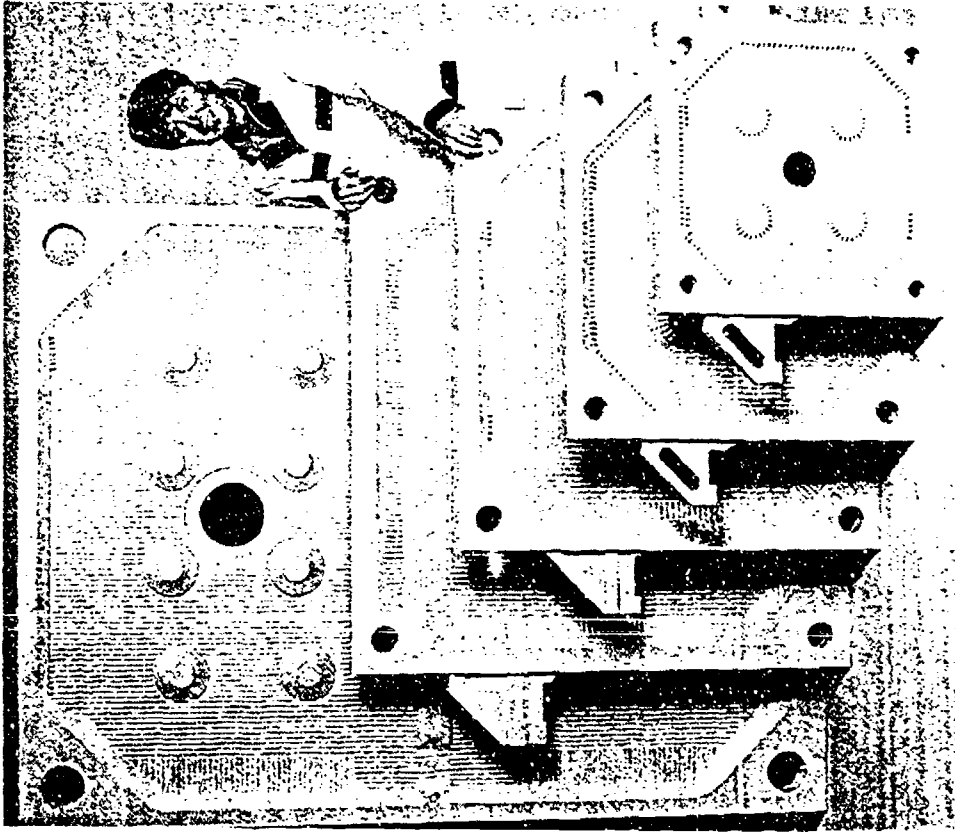
1. Pinnell, W. R., "Development of Directly Formed and Frameless Aircraft Transparency Technology, an Overview," to be published with the proceedings form A Conference on Aerospace Transparent Materials and Enclosures, San Diego CA, 9 - 13 August 1993.

**ENVIROTECH  
BULK INJECTION  
MOLDING**

**FILTER PLATES**

**PART WEIGHT:  
35 to 350 pounds**

**WALL THICKNESS:  
3/4 to 3 - 3/4 inches**



**Figure 1**



**ENVIROTECH  
BULK INJECTION  
MOLDING**

**INDUSTRIAL PIPE  
FITTINGS**

**PART WEIGHT:**  
3 to 165 pounds

**WALL THICKNESS:**  
1 to 4 inches

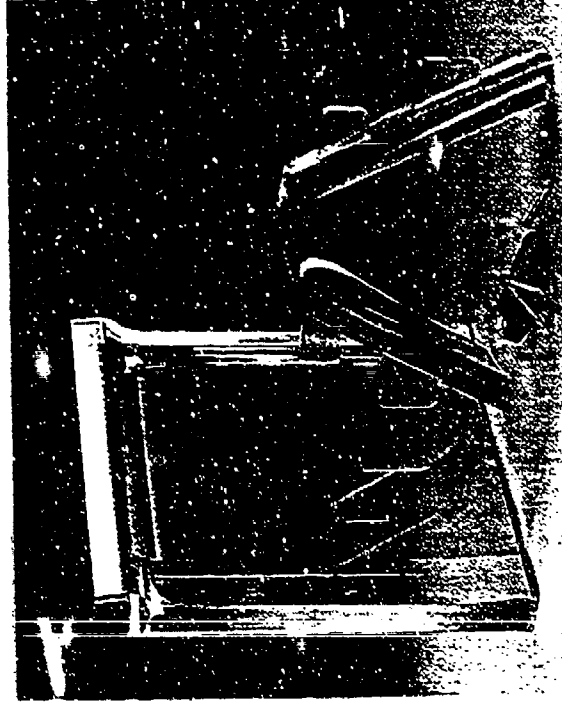


**Figure 2**

**ENVIROTECH  
BULK INJECTION  
MOLDING  
POLYCARBONATE  
TEST PANELS**

**PART WEIGHT:  
22 to 27 pounds**

**WALL THICKNESS:  
1/2 to 2 - 1/2 inches**



**Figure 3**

OPTICAL EVALUATION OF TRANSPARENCIES UTILIZING NEW TEST APPARATUS

T. L. Robson  
W. R. Pinnell  
Flight Dynamics Directorate  
Wright Laboratory

## Optical Evaluation of Transparencies Utilizing New Test Apparatus

Teri L. Robson  
WL/FIVR, WPAFB OH  
and

William R. Pinnell  
WL/FIVR, WPAFB OH  
for

*Conference on Aerospace Transparent Materials and Enclosures  
13 August 1993*

### Abstract

An Optical Test Fixture (OTF) developed for WL/FIVR for evaluating directly formed and frameless transparencies at molding sites has been evaluated and will be utilized to determine optical quality of injection molded transparencies. The OTF features an external collimated light source directed through a rotating test transparency. A computerized system synchronizes rotational position with televised screen images of the light source which has passed through the canopy. The light image position in captured screens is compared to an image without the transparency. Changes in the image position due to the transparency are utilized to calculate angular deviation in azimuth and elevation. Distribution of angular deviation can be obtained and displayed over large azimuth and elevation sweeps.

This paper includes a discussion of unique OTF features, mounting of transparencies, and conduct of evaluation runs. Optical evaluation results for a control transparency is presented. OTF data are compared to results obtained utilizing another apparatus. The plan for using the OTF as an on site facility to optimize transparency direct forming processes is discussed.

### Introduction

Under a current US Air Force effort, technology which permits fabrication of aircraft transparencies directly from bulk resin is being developed (ref 1). As opposed to traditional transparency forming by bending previously extruded sheets to transparency shapes, direct forming permits closely controlled tailoring of thickness over the transparency. In addition to permitting fabrication of transparencies optimized for structural and impact loading, and elimination of peripheral frames ("frameless"), the potential for varying thickness in optical areas to obtain optimum optical quality for a given external geometry is afforded.

Low pressure injection molding is the direct forming process currently being demonstrated by the Air Force effort. It has been shown that the precision with which thickness can be controlled is as much as an order of magnitude better than can be achieved in bent sheet forming when curvature and depth are extreme. Further, it is known that precise control of the relationship of the inside to outside transparency surfaces is dependent on injection molding process parameters including zoned temperature control of the mold.

Initial molding of a transparency configuration includes optimizing the molding process. A series of molded transparencies will be necessary to establish the molding process. Testing at the molding site to insure that design objectives are being met are essential. In addition to coupon impact, dimensional accuracy and consistency, and molded quality inspection, confirmation of optical quality and consistency will be necessary to assure that the process produces the desired optical design. Direct forming implies a transparency production rate of about one per hour.

The OTF was developed for the Air Force program by Lockheed Fort Worth Company (LFWC, formerly General Dynamics, Fort Worth Division). Requirements for this apparatus included:

- Portability to permit relocation at molding sites.
- Automated data acquisition and processing to permit on-line feedback.
- Data sampling over a wide azimuth and elevation range
- Emphasis on geometry related optics (angular deviation)
- Quick and accurate mounting of test transparency
- Eliminate need for reflective screens, target boards and photographs
- Eliminate the need for personnel with special interpretative skills

#### Geometry Related Optics

Optical performance in aircraft transparencies can be expressed in quantifications or characterizations of distortion, binocular disparity, angular deviation, displacement, haze, transmission loss, multiple imaging, and birefringence. Angular deviation (Figure 1) is caused by relatively local areas of nonparallelism as well as overall nonparallelism of transparency surfaces. Lateral displacement (also Figure 1) is a small constant effect which is normally neglected as small relative to the image distance. Angular deviation can be measured by comparing the displacement of some form of "line of sight" like a, laser, or theodolite when the "line of sight" passes through the transparency. Distortion is often defined as the rate of change of angular deviation. The OTF is an apparatus for determining angular deviation. Light transmission and haze will also be evaluated at molding sites utilizing a haze meter under standard conditions. Other optical anomalies may become important, but are not presently being considered for on line feedback at molding sites. The OTF can be utilized to evaluate binocular disparity by gathering and combining angular deviations with the transparency positioned for right and left eye positions.

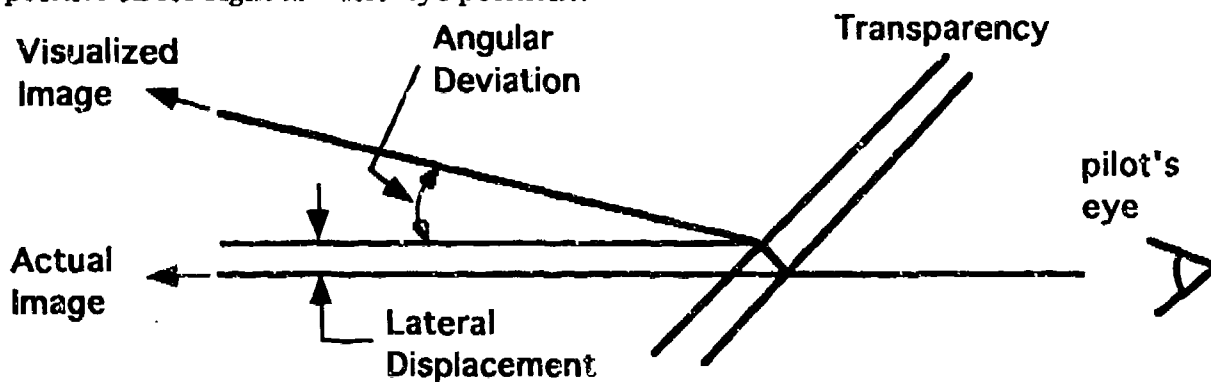


Figure 1 Graphical Representation of Angular Deviation (ref 3)

### OTF Description

The OTF consists of a transparency mounting platform which rotates about a vertical axis and an arm which rotates about a horizontal axis while holding a collimated light source and a video camera so that the collimated light is coincident with the camera optical axis. Test transparencies are mounted so that the eye point is located at the intersections of the platform and arm rotation axes. For given arm positions (elevation), the mounting platform is rotated (azimuth sweep) at a controlled speed. During the azimuth sweeps at each elevation setting, video screen grabbing software captures the collimated light source image. The combination of image capture frequency and mounting platform rotational speed determines the

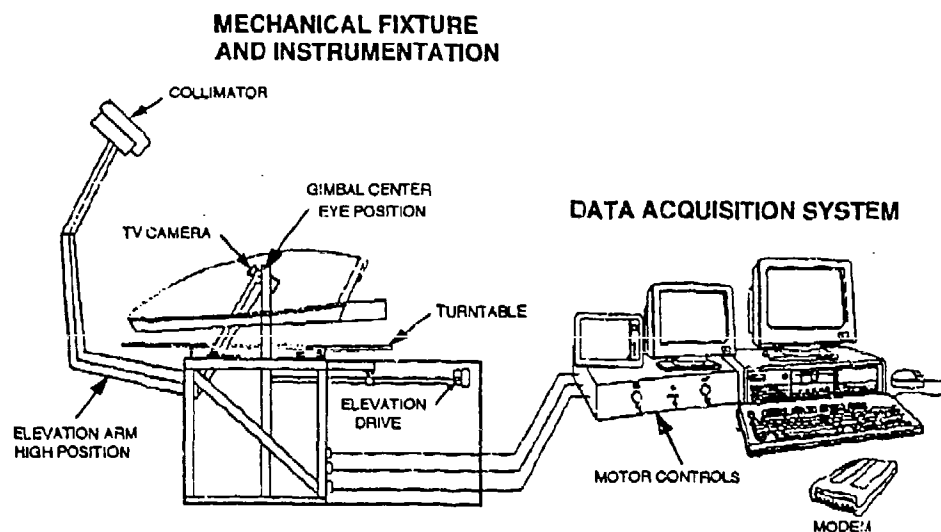


Figure 2 Optical Test Fixture, Schematic

azimuth position at the time of image capture. The mounting platform moves continuously between azimuth extremes. The video camera focal plane is inside the transparency (located at the design eye point) and fixed with respect to the elevation arm at the arm rotational axis. An in depth description of the OTF is included in reference 2. The OTF mechanical arrangement is shown in Figures 2 and 3.

Variable speed permanent magnet motors are utilized for the mounting platform and elevation arm chain drives. A position potentiometer is also driven by each chain. Output from the potentiometers is fed back to control circuits within the PC for precise control of the mounting platform speed and position and for position of the elevation arm.

The OTF is configured to cover maximum elevation and azimuth ranges of -14 to 34 and -80 to 80 degrees respectively. Default angle increments are two degrees. Ranges less than maximum and the angle increment can be chosen by the operator.

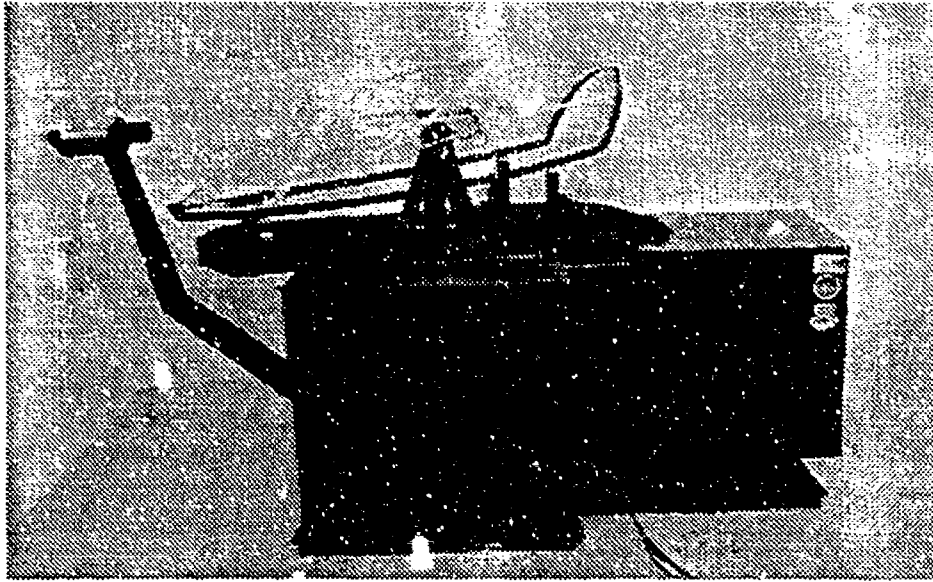


Figure 3 Optical Test Fixture

Captured video screens are 262 by 144 pixtels (about 10 by 7 inches). Prior to initiation of azimuth sweeps, PC software prompts the OTF operator to set a threshold which ignores illuminated pixtels outside the circular (10 pixtel diameter) collimated light image. A two stage search of each video screen is conducted to locate the light image centroid. The first search covers the entire screen and results in a rough location. An area (approximately 2 inches square) is then searched which results in a more precise centroid location. Angular deviation in azimuth and elevation directions are computed by comparing the light image centroid position to the reference (transparency not mounted) image position.

#### OTF Operation

The entire OTF operation routine is controlled by PC software which prompts the operator for a sequence of actions. The OTF routine includes the following actions.

- Enter data file header information.
- Set azimuth and elevation ranges and limits
- Adjust pixel illumination threshold
- Establish reference screen and light image position
- Mount test transparency
- Set platform and elevation arm zero positions
- Conduct rotational speed check runs and return to zero positions
- Initiate azimuth sweeps and data gathering routines
- Close data files
- Check data validity utilizing PC software for reading and plotting files
- Remove transparency

After five tear down, move, and set up cycles for the CFT, portability can be said to require three persons for four hours for each tear down and pack or for each unpack and set up. The entire OTF including PC, all control equipment, and

tools for operating and assembly can be packed in a crate approximately 6 x 10 x 7 feet.

Approximately 45 minutes was required to complete 25 azimuth scans required to cover the maximum OTF range at 2 degree increments. A 60 minute total evaluation time would including time for pre and post run operations.

#### Typical Test Results

Data files saved to the PC hard disk contain angular deviations for azimuth and elevation, intermediate centroid calculation values, and speed and timing information. Menu driven software is provided to convert these files from binary to text format. Data manipulation and plotting software is provided which can be used to produce data listings, histograms, statistical representations, contour or shaded angular deviation maps, distortion grid plots, and data comparisons for different transparencies.

Figures 4 and 5 are representative of angular deviation contour maps and histograms for azimuth and elevation respectively. Contour maps are generally printed in color. Figure 6 shows combined azimuth and elevation angular deviations in distortion plots employing gain levels of 1, 5, and 10 to amplify areas (bands for this canopy) of relatively high distortion.

#### Repeatability

The demonstrated OTF repeatability for repeatedly measuring angular deviations at the same point is .07 milliradians.

A flight worthy (acceptable angular deviations less than 10 milliradians) laminated F-16 canopy was adopted for repetitive OTF evaluations. Considering two evaluations by LFWC at the original set up site, one evaluation after a LFWC relocation, and two evaluations after moving the OTF to WL/FIVR, repeatability within .2 milliradians was observed for given data points.

A second control transparency was a very old monolithic F-16 canopy which has several scuffs and scratches in the outside surface. Only the forward portion of this canopy (removed by cutting at approximately the maximum cross section) was evaluated. Opaque tape two inches wide was added to the outside surface of this canopy surface simulating an aft arch. This configuration roughly simulates the geometry of a fighter/trainer forward windshield. Repeated OTF evaluations before and after moving the OTF at WL/FIVR also indicate repeatability within .2 milliradians.

#### Qualification

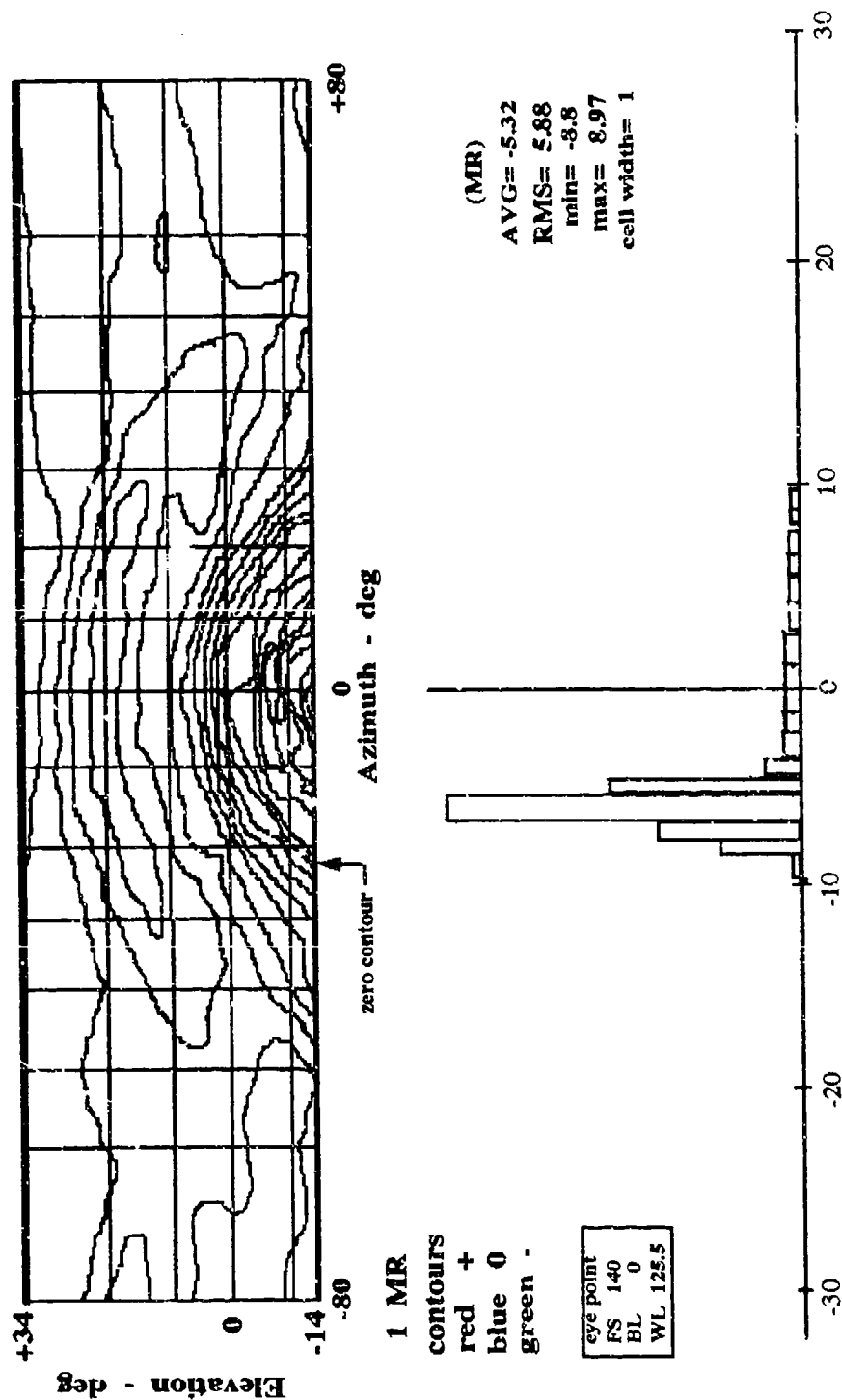
In order to confirm OTF capability, OTF evaluations were compared to angular deviation evaluations conducted by Armstrong Laboratory (AL), Human System Division at Wright Patterson AFB. The flight worthy F-16 canopy utilized as an OTF control transparency was evaluated by AL utilizing a fixture developed by them. A second F-16 canopy retained and evaluated by AL was evaluated by WL/FIVR utilizing the OTF. The transparency areas evaluated were limited to the area (-2 through -12 degrees elevation, -10 through 10 degrees azimuth, at 2 degree increments) usually covered by AL for F-16 canopies.



# WL/FIVR Optical Evaluation

18 Feb 93

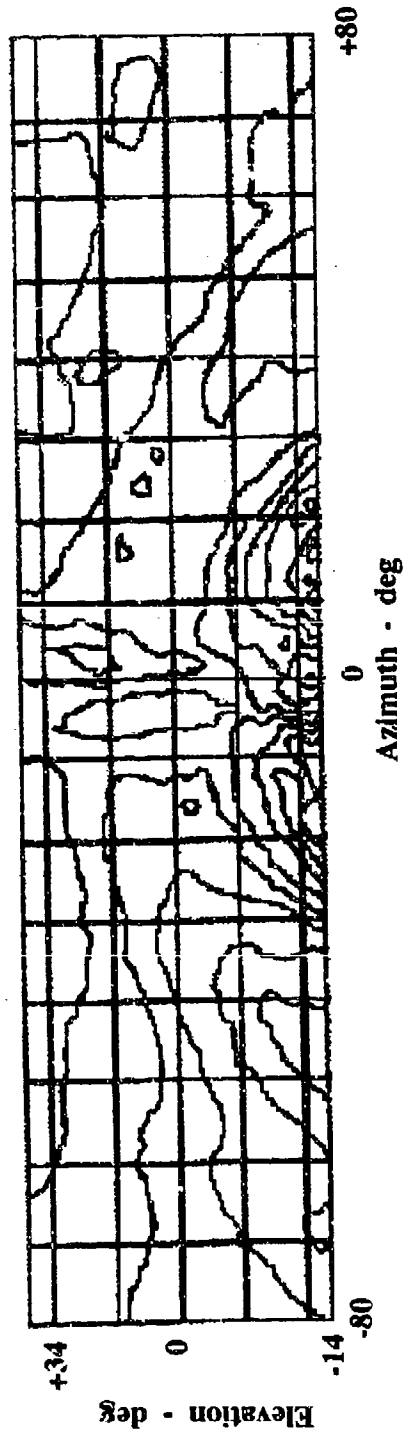
F-16 Canopy P/N 183100-01 S/N 492



# WL/FIVR Optical Evaluation

18 Feb 93

F-16 Canopy P/N 183100-01 S/N 492



(MR)  
AVG= -5.32  
RMS= 5.88  
min= -8.8  
max= 8.97  
cell width= 1

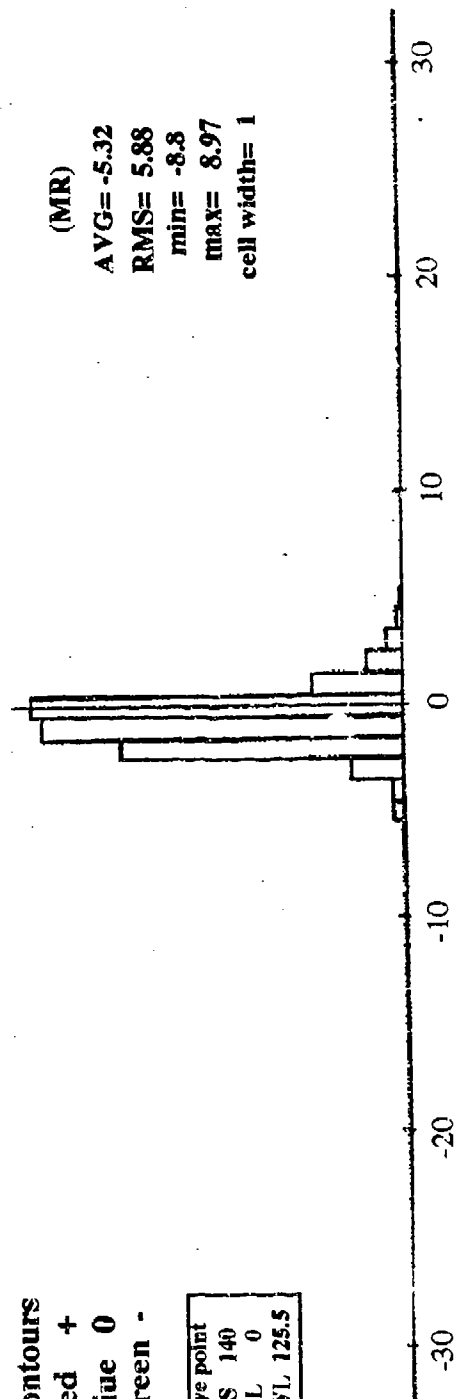


Figure 5 Histogram - Azimuth Deviation - milliradians

eye point
FS 140
BL 0
WL 125.5

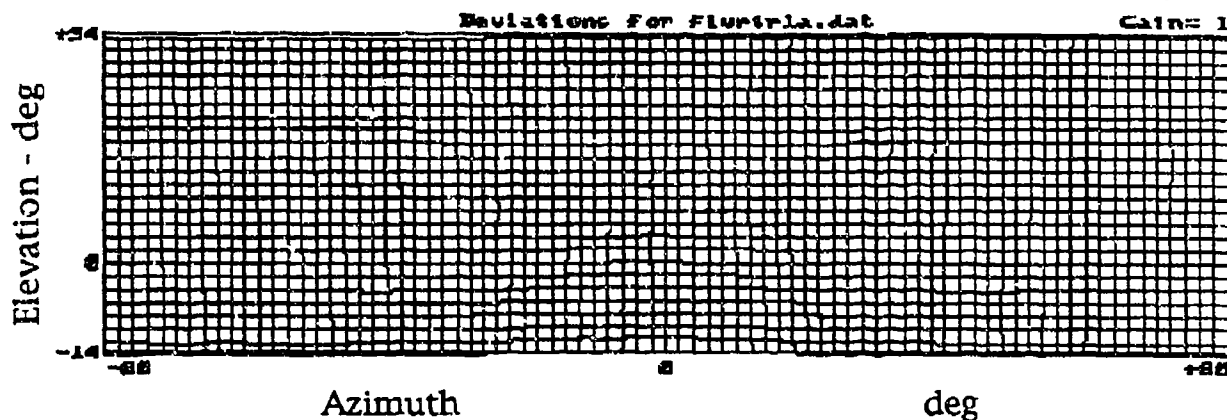
# Figure 6 WL/FIVR Optical Evaluation

18 Feb 93

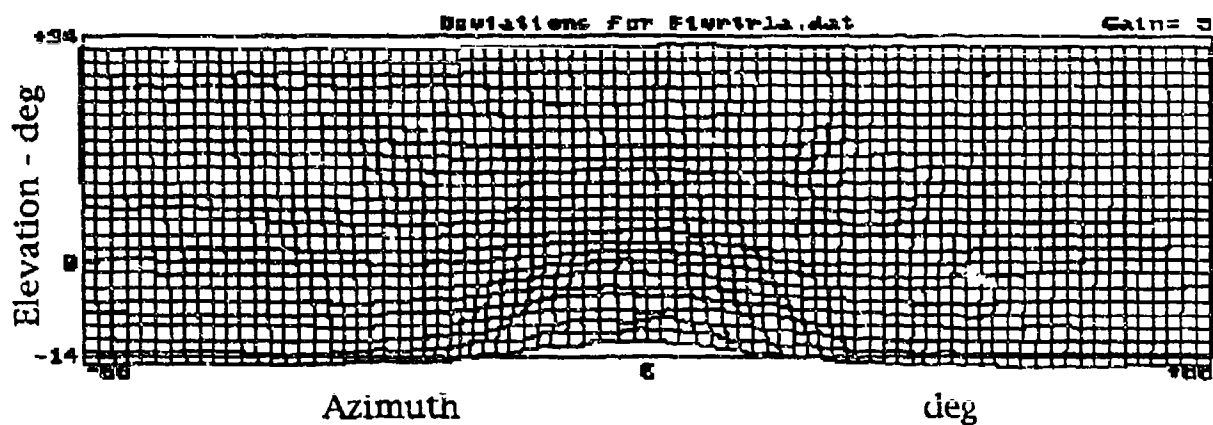
F-16 Canopy P/N 183100-01 S/N 492

eye point
FS 140
BL 0
WL 125.5

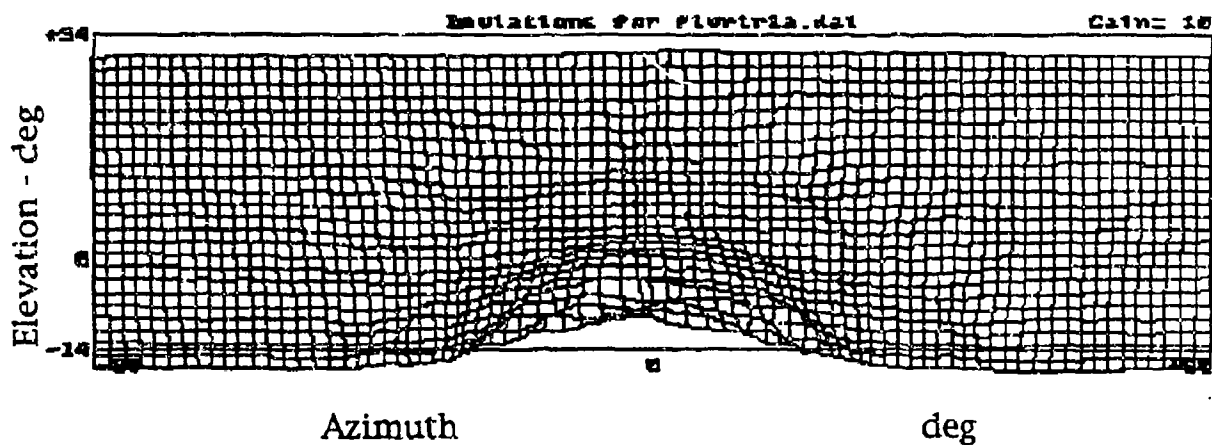
## Deviations - Gain 1



## Deviations - Gain 5



## Deviations - Gain 10



The AL evaluations were conducted utilizing the Windscreen Angular Deviation Measuring Device (WADMD). The WADMD is a fixed location device based on a collimated light source internal to the transparency and an external receiving unit. A function of the light source is to project an L shaped beam through the transparency. The receiving unit splits the L shaped beam into separate legs for azimuth and elevation. Each of these beams is projected on a charge coupled linear array which (with associated electronics) quantifies beam position. Comparing beam positions with "no transparency" beam positions yields angular deviations for azimuth and elevations. A more rigorous description of the WADMD is included in reference 3.

Figure 7 is a histogram showing a distribution of the absolute value of the angular deviation difference for one evaluation of the same transparency on the OTF and on the WADMD. Results are within 1.4 milliradians for 75% of the data and within 3.5 milliradians for 96% of the data. A few (8 of 264) wild points are believed to have resulted from local damage or contamination on the transparency surface. These differences also include unknown effects of transparency mounting and relative accuracy of angular positioning. Reference 4 includes data lists and more information on this comparison.

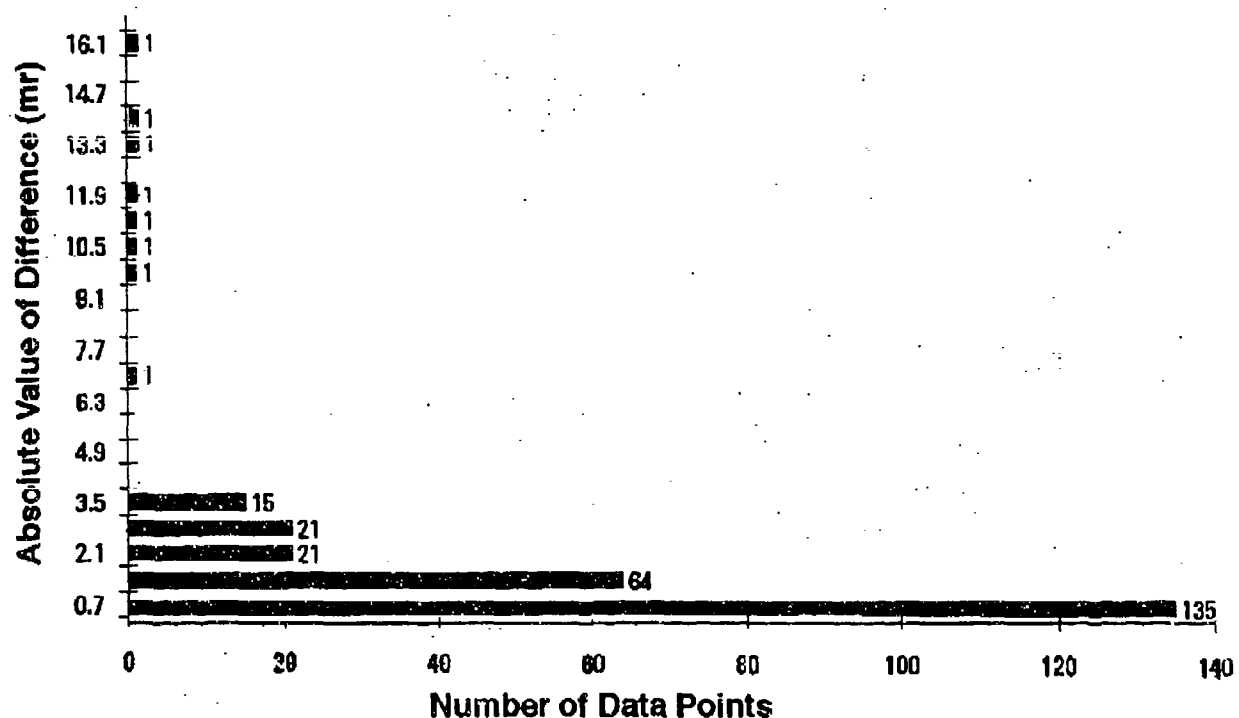


Figure 7 Histogram - Absolute Difference Between OTF and WADMD

### Conclusions

1. The OTF can be utilized to measure angular deviation over a large transparency area.
2. The OTF is portable to the extent that relocation at potential transparency molding sites is feasible.
3. A 60 minute OTF evaluation cycle time is compatible with anticipated production rates for directly formed (injection molded) transparencies.
4. Based on evaluation of the same transparency, and a limited transparency area, the OTF results are in good agreement with those produced utilizing the WADMD.

### Recommendations

1. The effectiveness and applicability of OTF evaluations to evolution of direct forming processes (injection molding) should be established as a part of the first molding program.
2. Although the OTF was developed to support the development of technology for directly formed and frameless transparencies, this device should be considered for angular deviation evaluations for transparencies in general.

### References

1. Pinnell, W. R., "Development of Directly Formed and Frameless Aircraft Transparency Technology, an Overview," to be published with the proceedings from A Conference on Aerospace Transparent Materials and Enclosures, San Diego CA, 9 - 13 August 1993.
2. FMZ-719-014-007, Revision B, 3 April 1992, "Design-Development of the Optical Test Fixture for the Frameless Transparency Program," generated by Lockheed Fort Worth Company (formerly General Dynamics Fort Worth Division), copy available from W. R. Pinnell WL/FIVR, WPAFB OH, phone 513 255 2516.
3. Genco, Louis V., O.D., Lt Colonel and Task, Harry L., Phd., "Aircraft Transparency Optical Quality: New Methods of Measurement," AFAMRL-TR-81-21, AFAMRL, Aerospace Medical Division, WPAFB OH, February 1981.
4. Robson, Teri L., "Comparison of Two Methods for Optical Evaluation of Aircraft Transparencies," WL/FIVR, WPAFB OH, 17 May 1993

EFFECTS OF THICKNESS TAILORING ON THE IMPACT RESISTANCE OF  
DIRECTLY FORMED TRANSPARENCIES

W. R. Braisted  
M. A. Huelisman  
University of Dayton

W. R. Pinnell  
Flight Dynamics Directorate  
Wright Laboratory

## **EFFECTS OF THICKNESS TAILORING ON THE IMPACT RESISTANCE OF DIRECTLY FORMED TRANSPARENCIES**

William R. Braisted  
Marc A. Huelsman  
University of Dayton Research Institute  
Dayton, OH 45469

William R. Pinnell  
WL/FIVR  
Wright-Patterson Air Force Base, OH 45433

### **ABSTRACT**

Technology for directly forming aircraft transparencies is currently being developed under a US Air Force program. As part of this effort, sub-scale flat panels have been injection molded from various polycarbonate resins. One of the capabilities of the new technology is precisely controlled thickness tailoring. A series of bird impact tests has been conducted to demonstrate the relative suitability of the resins for designing and molding full-scale frameless transparencies. Deflection shapes during the impact event were derived from high-speed photographic data utilizing an Air Force developed triangulation technique. An explicit finite element analysis was qualified by comparing predicted deflection shapes with the experimental data. Once qualified, the analytical technique was utilized to conduct a limited study illustrating the effectiveness of thickness tailoring for weight reduction while maintaining bird impact resistance and acceptable deflection.



## **EFFECTS OF THICKNESS TAILORING ON THE IMPACT RESISTANCE OF DIRECTLY FORMED TRANSPARENCIES**



William R. Braisted and Marc A. Huelsman (UDRI)  
William R. Pinnell (WL/FIVR)

---

### **INTRODUCTION**

Recent advances in manufacturing technology permit the fabrication of large, thick-walled, transparent, impact resistant plastic components by injection molding. This method of manufacturing eliminates the necessity of a constant-thickness transparency, removing the need for a separate frame and its associated fasteners. The techniques required to manufacture transparencies by injection molding are being developed as part of the Air Force effort to develop technology for directly formed and frameless aircraft transparencies. This effort has been referred to as the Frameless Transparency Program (FTP). As part of this program, candidate materials, injection molding parameters, and different configurations for attaching frameless transparencies to aircraft are being evaluated. During the next phase of the FTP, a windshield-size transparency having a mold-line shape based on the forward half of the current F-16 aircraft canopy will be molded. This Confirmation Frameless Transparency (CFT) will not be a flight item, but will become the subject of extensive optical and structural testing. CFT test results will form the basis for confirming an Analytical Design Package (ADP), which is currently under development, for the directly formed and frameless transparency concept.

Structural integrity of the injection molded transparency systems must be maintained during a bird impact. This paper describes bird impact testing and triangulation analyses conducted to evaluate structural performance of several candidate CFT resins. Birdstrike results were used to confirm the explicit finite element analysis code, X3D, which is being integrated into the ADP. Finally, a series of X3D analyses was performed to demonstrate how the ADP can be used to design a canopy with a tailored thickness to provide a lightweight transparency with the required birdstrike protection. This thickness tailoring capability with the associated weight savings is a primary advantage of a directly formed transparency design.

### **BIRDSTRIKE TESTING**

The ability to injection mold transparency materials which maintain structural integrity during a bird impact is one of the primary objectives of the FTP. A birdstrike test program was conducted at the University of Dayton



Research Institute (UDRI) to evaluate the birdstrike resistance of panels molded utilizing an Envirotech molding machine and several candidate CFT resins [1]. The test article was a relatively flat injection molded polycarbonate panel, depicted in Figure 1. The thickened edge sections of the panel represent a potential method for eliminating the frame used in current transparency designs. Inserts can be molded into the thickened edge regions to attach the transparency directly to the aircraft. The panel also contains a coupling region which represents a coupling between two panels as might occur between a windshield and a canopy.

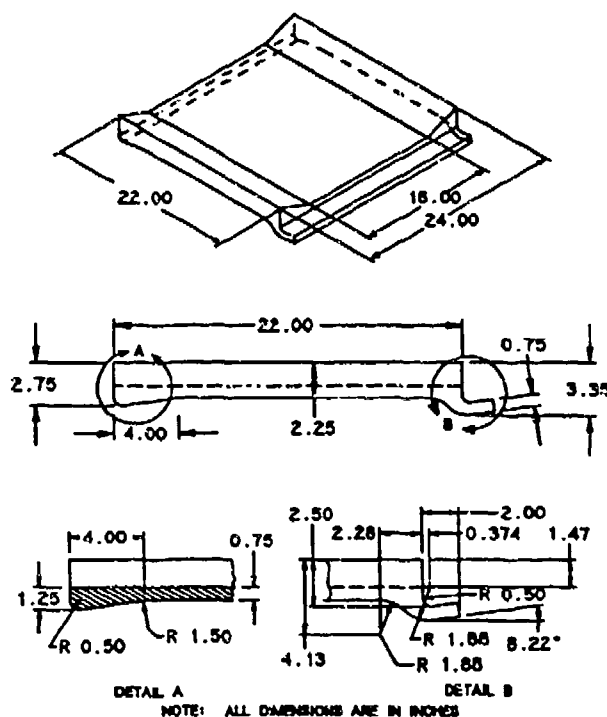


Figure 1. Injection Molded Panel Geometry.

The polycarbonate panels that were tested were molded from four different Dow resins, namely, XU-5.5, 300-15, 300-6, and 300-4. The testing objective was to identify the birdstrike threshold of each resin to determine if one resin was preferable based upon the birdstrike resistance.

Birdstrike testing to support the FTP was performed in the UDRI Impact Physics Laboratory with a seven inch internal diameter gun. Plastic sabots were used to deliver the 2.0 lb artificial birds to the target. The Air Force test fixture allowed for adjustments so that the panel could be positioned at the appropriate height for the gun barrel while maintaining a 30 degree impact angle. Laser timing equipment was used to compute impact velocity and synchronized high-speed cameras were used to record each shot.

During testing the panels were clamped to the fixture on three sides, leaving the aft edge (coupling region) unrestrained. Rubber pads were placed between the test fixture and the panel along the clamped edges to prevent the panel from being in direct contact with the steel fixture. The support clamps were tightened until compression of the rubber pads was visible.

Each impact test was performed in the same manner, except that the bird velocity was varied. The impact location was a point on the panel centerline, 9" forward of the aft edge, as indicated in Figure 2. Projectiles used in the test program were 2.0 lb artificial birds molded from gelatin [2]. The bird geometry was a right circular cylinder with a 3.5" diameter and a 6.0" nominal length. Minor adjustments were made to the bird length to obtain the 2.0 lb weight specification.

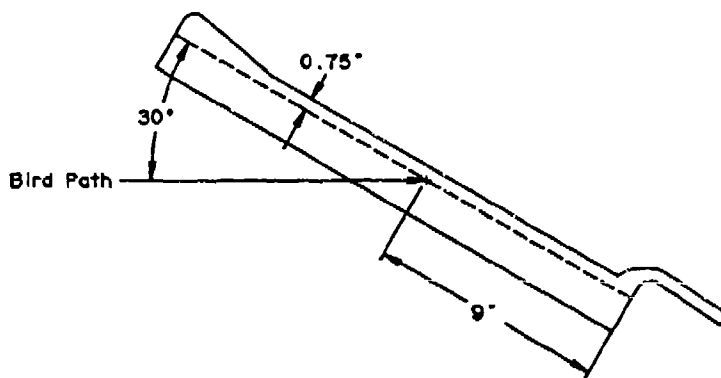


Figure 2. Impact Location.

### TRIANGULATION ANALYSIS

A method for obtaining deflection-time-history data for points on a transparency during a bird impact event has been developed by the Air Force [3]. This triangulation method determines point locations as functions of time from two simultaneous high-speed film images, known pre-test point locations, and known camera positions. Appropriate camera positions, which were selected based upon light requirements, lens combinations, camera mounting sites, and camera shielding requirements, are depicted in Figure 3.

A coordinate system (triangulation space) was defined at the test site to define the relative positions of the triangulation cameras and the initial location of the points on the panel. Acrylic paint, which does not degrade the polycarbonate, was used to mark the points on the panel with a template having a known grid spacing as indicated in Figure 4.

Calibration data was obtained for each camera/lens/shield/projection combination to account for the magnification of the cameras, lenses, protective

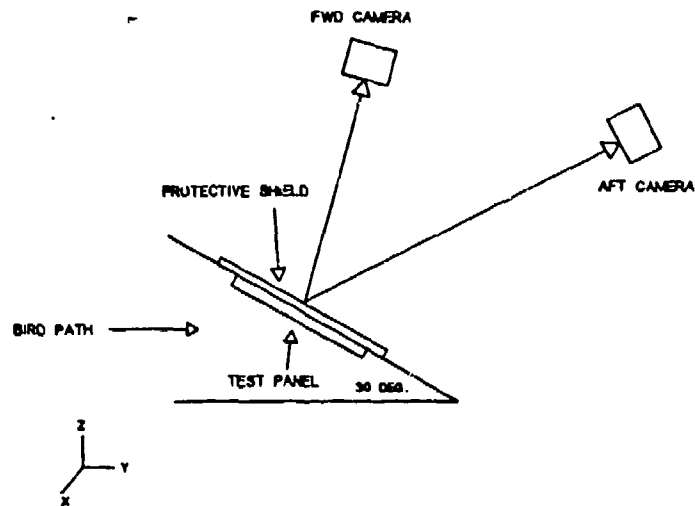
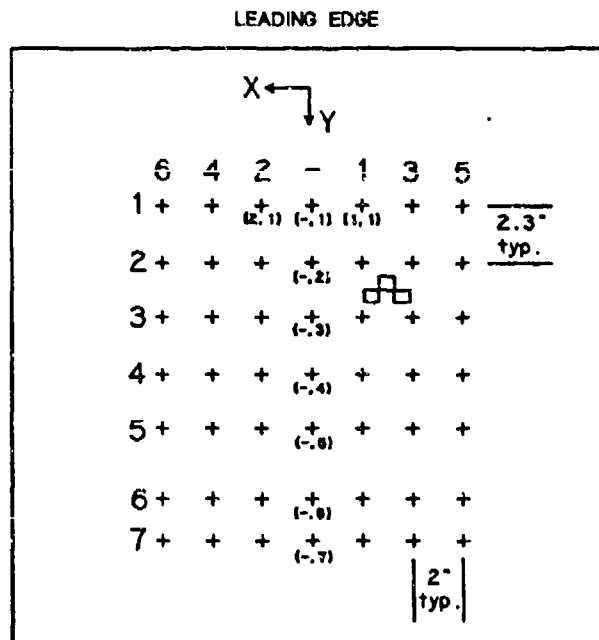


Figure 3. Triangulation Space Definition.



Grid View From Camera Side of Panel

Impact Point on Opposite Side of Panel from (-.4)

Figure 4. Panel Grid Definition.

shielding, and projection equipment used in the birdstrike testing. A calibration film was generated by exposing several film frames with the camera positioned at various distances away from a uniform grid board. During calibration the distance between the camera and grid board was varied over a range of distances which encompassed all likely point-to-camera distances to occur during the birdstrike.

To insure results validity, a single projector and projection size (15" x 11.125") was maintained for all triangulation data reduction. A calibration film was loaded into the projector and measurements were made from behind a transparent screen to determine the length of three 2" grid spaces at several different locations and orientations on the image. A magnification factor was computed by dividing the known actual length by the measured projected image length from the calibration film. Results from the measurements made at several different locations and orientations on the projection were averaged to determine an effective magnification factor at each grid distance. Linear regression was used to determine a relationship between magnification factor and distance for each camera.

After the test the triangulation films were examined to identify the film frame at or just prior to impact (frame 0) in order to sequence the cameras. Using the same projection size that was used in the calibration effort, the film from one of the cameras was loaded into the projector and advanced to frame 0. The data reduction procedure entailed placing a piece of tracing paper behind a transparent screen and recording the positions of each grid point at every frame of interest over the impact event. Several points which remained stationary during the impact event, such as a portion of the support frame, were also traced to align each frame image properly prior to data collection.

At the end of the tracing procedure, there was a tracing sheet for each camera which indicated the change in position of the grid points during the impact event. For each grid point of interest, data files consisting of azimuth (AZI) and elevation (ELE) data from each triangulation camera were generated. The positive ELE direction is defined on the tracing sheet as the direction opposite of the bird path. For a rear projection tracing the positive AZI direction is defined such that the resultant of AZI crossed with ELE is in the direction away from the origin of the projected image. The AZI/ELE data was generated using a digitizing tablet to extract the coordinates and to record them in a file.

A common pulsating timing light signal on the films was used to calculate the frame rate of each camera. For the triangulation algorithm to function properly, both cameras must provide information about the motion of a particular point at the same instant in time. When the frame rates of the two cameras vary significantly, the effects of simultaneity can be lost. The Air Force triangulation program contains modules to normalize the faster camera data to the frame rate of the slower camera.

With the normalized AZI/ELE data files for each camera, the camera frame rates, the calibration films, and the coordinate data for the cameras and panel grids, the triangulation code was executed. The triangulation code runs on an IBM compatible PC under GW BASIC. Output from a triangulation analysis was a single file which indicated the deflection-time-history of a single grid point during the birdstrike. To evaluate the deflection response of other points on the

transparency the triangulation program was rerun. Once the deflection of several points was evaluated, the results were combined to determine the deflected shape of the transparency at various times during the impact event.

### X3D FINITE ELEMENT ANALYSIS

An impact analysis was performed using the X3D finite element analysis code [4]. The objective of the impact analysis was to determine analytical deflection-time-history data which could be correlated with triangulation results. The X3D analyses simulated a 2.0 lb artificial bird impacting a panel at 256 knots. The 30 degree angle between the surface of the panel and the bird path, as well as the impact point, matched the configuration of the test program.

Figure 5 shows the model constructed within the ADP for the bird impact simulation. The panel was assumed to be rigidly constrained along the forward edge and along the panel edge opposite the centerline. Symmetry conditions were enforced along the panel centerline. The model contained 1200 shell elements in the panel and 960 tetrahedral elements in the bird, and potential contact surfaces on both the panel and bird. Note that X3D permits modelling of both the target panel and the impacting bird. Algorithms in X3D automatically account for the contact conditions so that no ad hoc loading condition or estimation of the impact zone was necessary.

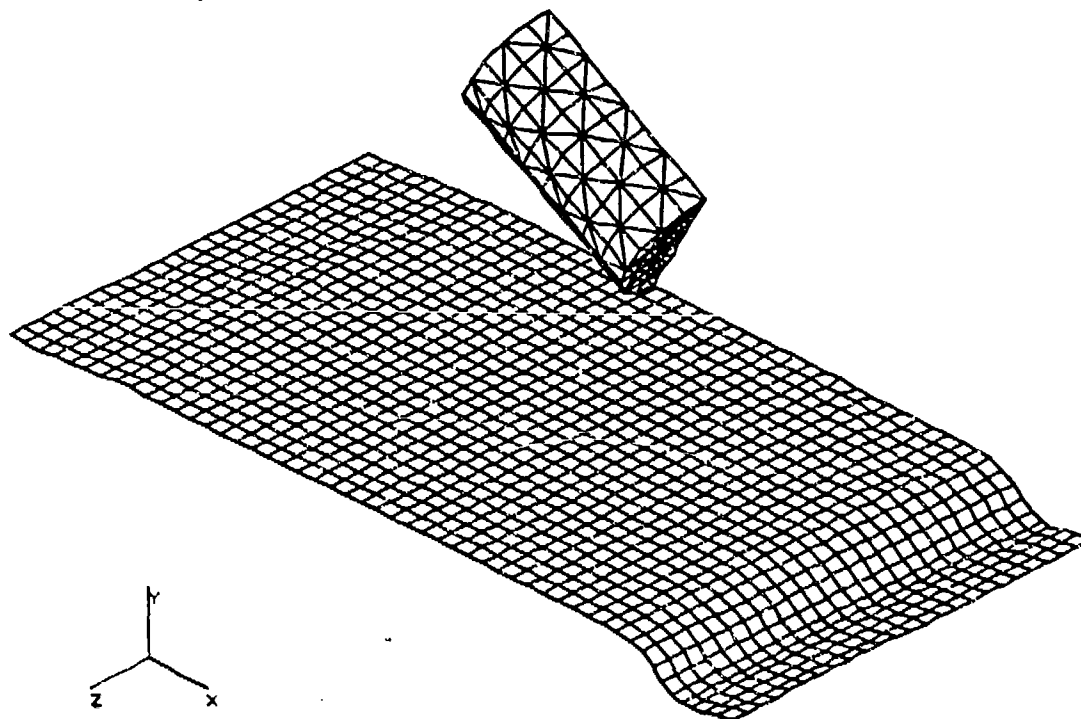


Figure 5. X3D Impact Analysis Model.

The polycarbonate material was modelled using the following material property data obtained from 1991 CFT materials characterization testing [5]:

$E = 300,000 \text{ psi}$	$H = 7,000 \text{ psi}$	$\nu = 0.39$	$D = 1.E+07 \text{ sec}^{-1}$
$\rho = 0.000111 \text{ lb}_f\text{-sec}^2/\text{in}^4$	$p = 14$	$\sigma_y = 7,970 \text{ psi}$	$\sigma_u = 16,400 \text{ psi}$

Note that the polycarbonate material model in X3D is a bilinear stress-strain curve with strain rate dependence and ultimate failure. The artificial bird material was represented by the following material properties [4]:

$\rho = 0.0000888 \text{ lb}_f\text{-sec}^2/\text{in}^4$	$G = 30,000 \text{ psi}$	$H = 300 \text{ psi}$	$\sigma_y = \sigma_u = 3,000 \text{ psi}$
$K_1 = 337,000 \text{ psi}$	$K_2 = 729,000 \text{ psi}$	$K_3 = 2,020,000 \text{ psi}$	$K_4 = 1,000 \text{ psi}$

This represents what is referred to in the X3D manual as a low strength bird model. A high strength bird model with  $\sigma_u = 4,500 \text{ psi}$  ( $\approx 500\%$  plastic strain to failure) was considered, but these bird properties resulted in deflections considerably larger than the experimental results indicated.

The X3D solution was performed for 10.0 milliseconds with displacement and stress results being generated every 0.5 milliseconds. The X3D trace option was used to determine the deflection-time-history response of nodes which corresponded to the panel grid points on the centerline. Thus, trace results were compared directly to triangulation data to evaluate the analysis tool and material properties.

## RESULTS AND DISCUSSION

Results of the 0.75" polycarbonate panel birdstrike testing are summarized in Table 1. The 0.75" thick panels were studied in great detail because the CFT will be that thickness, and the birdstrike threshold of each resin was desired to help determine the optimal CFT material. [1, 6, 7]

The impact thresholds of the three candidate CFT materials for the 0.75" panels are summarized in Table 2. Note that the XU-5.5 was evaluated in the test program, but the resin was experimental, not as well characterized as the other resins, and not available in sufficient quantities for use in the CFT. Results show a slight decrease in birdstrike resistance with an increase in melt flow index (dashed number in the resin name) for the Dow 300 resins, but the effect does not appear to be significant based on the limited test data. For the purposes of CFT materials selection any of the Dow 300 resins should provide adequate birdstrike protection.

A pattern in the failures became evident when the test films were reviewed. A majority of the panels that failed had failure initiation along the sides of the panel near the aft edge of the clamp. It appeared that the boundary conditions

Table 1. Birdstrike Test Summary of 0.75" Polycarbonate Panels

Panel	Resin	Velocity (kts)	Result	Triangulation $\delta_{max}$ (in)
920415-05 MX2050	Dow XU-5.5	450	Fail	-
920415-06 MX2050	Dow XU-5.5	355	Fail	-
920415-07 MX2050	Dow XU-5.5	297	Pass	-
920413-07 MX2049	Dow 300-15	201	Pass	-
920413-09 MX2049	Dow 300-15	302	Fail	-
920413-10 MX2049	Dow 300-15	256	Pass	1.0
920414-05 MX2048	Dow 300-6	302	Fail	1.4
920414-07 MX2048	Dow 300-6	252	Pass	1.2
920414-08 MX2048	Dow 300-6	277	Pass	-
920413-05 MX2047	Dow 300-4	302	Pass	1.4
920416-07 MX2047	Dow 300-4	357	Fail	-
920416-08 MX2047	Dow 300-4	327	Fail	-

Table 2. Birdstrike Threshold for 0.75" Polycarbonate Panels

Resin	Impact Threshold (kts)
Dow 300-15	250-300
Dow 300-6	275-300
Dow 300-4	300-325

were inducing failure such that the birdstrike threshold became a system property, not a material property. Changing the test fixture may be required should additional testing be warranted.

Four 0.75" thick panels were selected for triangulation analysis; three panels that passed the birdstrike test, and one panel that failed. One panel that failed was selected to determine if the deflection-time-history response prior to failure was similar to that of panels which passed the birdstrike test. It was determined that no considerable differences existed between the panel responses. Maximum deflections from the triangulation analyses were presented in Table 1. Deflection-time-history results for the different Dow resins were very similar.

An X3D analysis simulating the 256 knot birdstrike test of panel 920413-10 MX2049 (Dow 300-15) was performed to correlate the finite element analysis and

triangulation results. Figure 6 shows the deformed geometry at one millisecond intervals during the X3D impact simulation. Note that the low strength bird model used in the X3D analysis resulted in a large number of bird element failures.

Figure 7 compares the X3D and triangulation results from impact test on panel 920413-10 MX2049 at centerline panel locations near the leading edge, (-,1), at the impact point, (-,4) and near the aft edge, (-,7). The X3D results showed good agreement with the experimental data up to the point of maximum deflection. However, during the rebound the X3D solution diverged from the triangulation results, particularly in the aft portion of the panel. Potential reasons for the solution divergence include different boundary conditions between the testing and analysis, possible slippage of the test article during impact, and uncertainty in material properties of the polycarbonate and the bird. It appears that the X3D model does not have sufficient damping built into the material model, which may be another cause for the solution divergence.

The analysis results indicated that X3D is a useful tool in the study of bird impact response. The X3D solutions were able to capture the fundamental behavior of the bird impact event up to the point of maximum deflection. More work is required to refine the analysis tool, but X3D shows promise for transparency design within the ADP.

### THICKNESS TAILORING STUDY

To demonstrate the use of X3D within the ADP, a preliminary design study was performed to determine if the thickness of a transparency could be tailored to produce a lighter-weight design that maintained sufficient birdstrike protection. Traditional transparency construction results in a nominally uniform thickness over the part. Thus, a traditional canopy has a thickness based upon the birdstrike requirement at the worst impact location. The remaining portion of the transparency is thicker than required to resist a birdstrike because the impact angle diminishes as a result of the transparency curvature.

With the processes now available in direct forming of transparencies developed under the FTP, it is possible to vary the transparency thickness continuously over the part. To study the effectiveness of the thickness tailoring concept, a series of X3D analyses was performed to assess the difference in birdstrike performance resulting from thickness changes on F-16 canopies. Only one impact location was considered, namely F.S. 113.5, which is the design eye location and a critical location for the birdstrike requirement. The F-16 canopy model is shown in Figure 8.

A baseline analysis was performed to determine the capability/response of a 0.75" monolithic polycarbonate canopy to a 4.0 lb bird impact at 350 knots. The



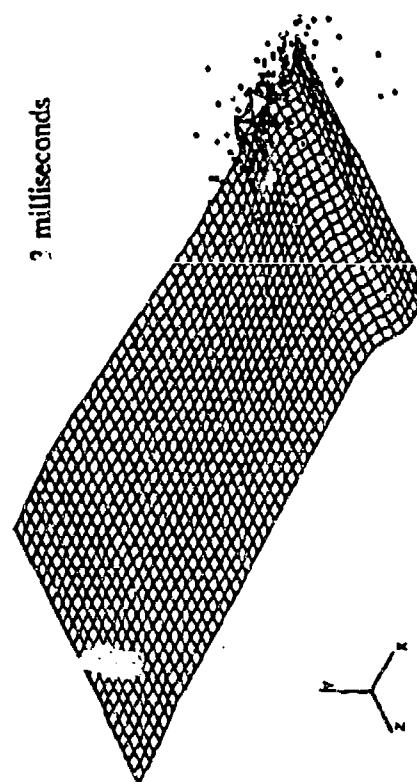
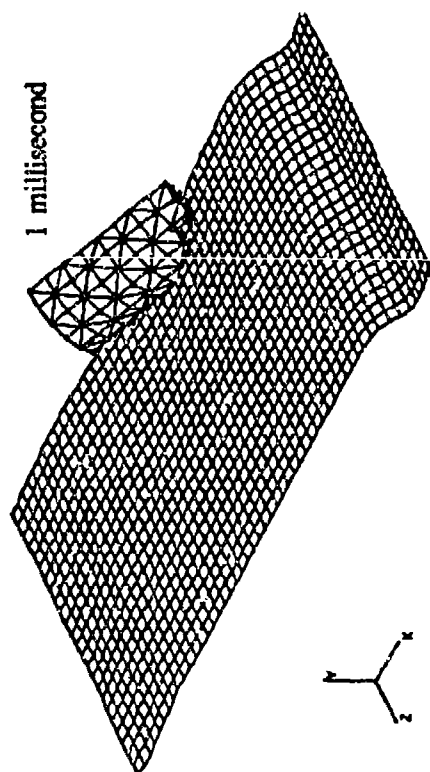
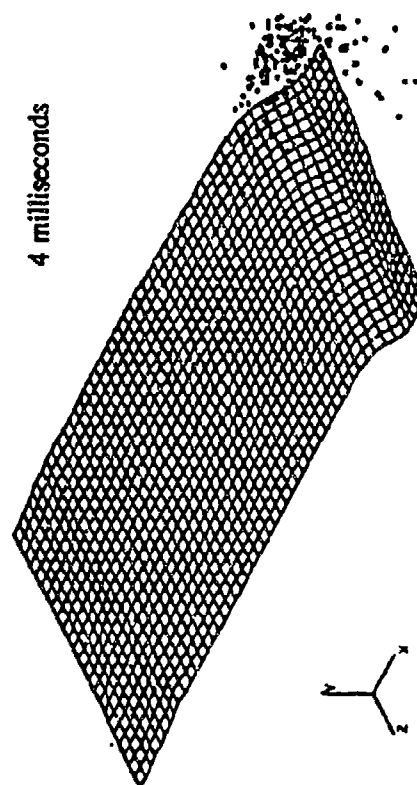
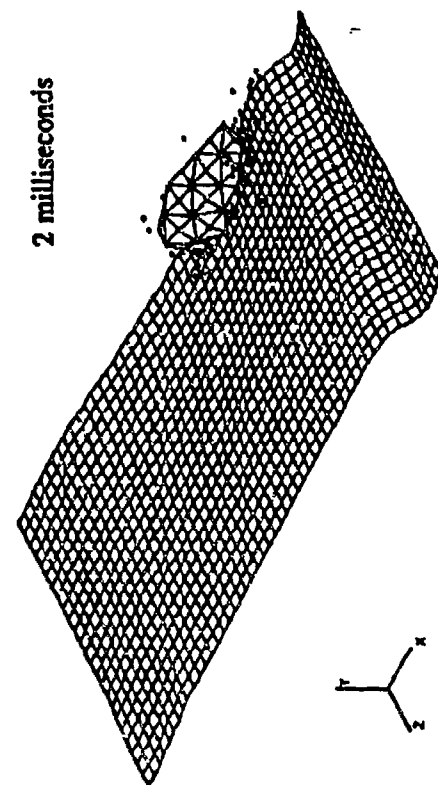


Figure 6. Deformed Geometry Plots.

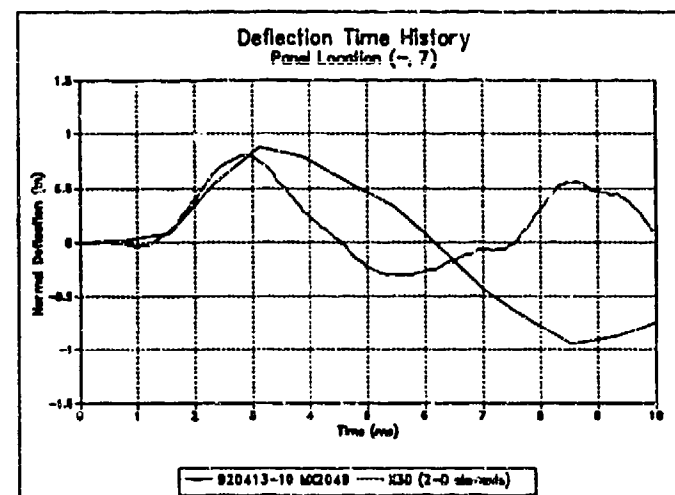
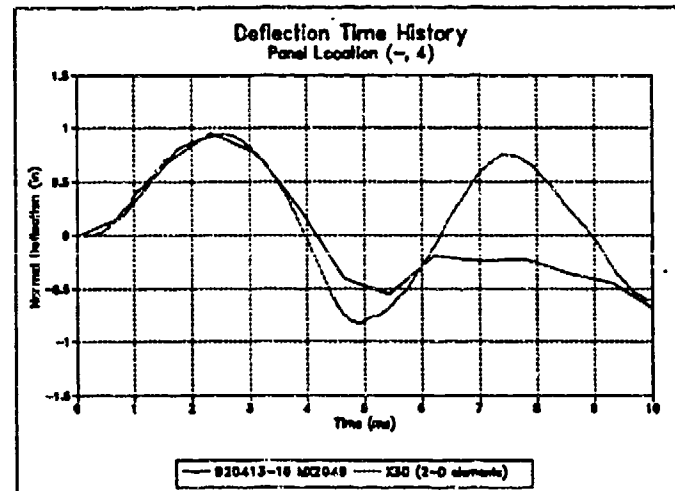
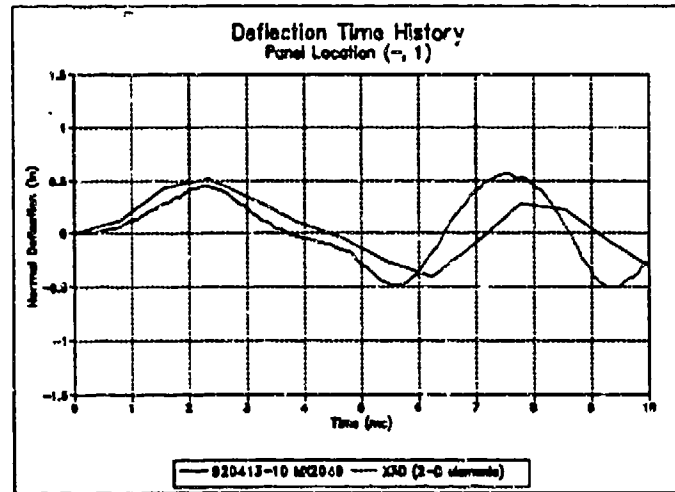


Figure 7. Deflection Comparison of Triangulation and X3D Analyses.

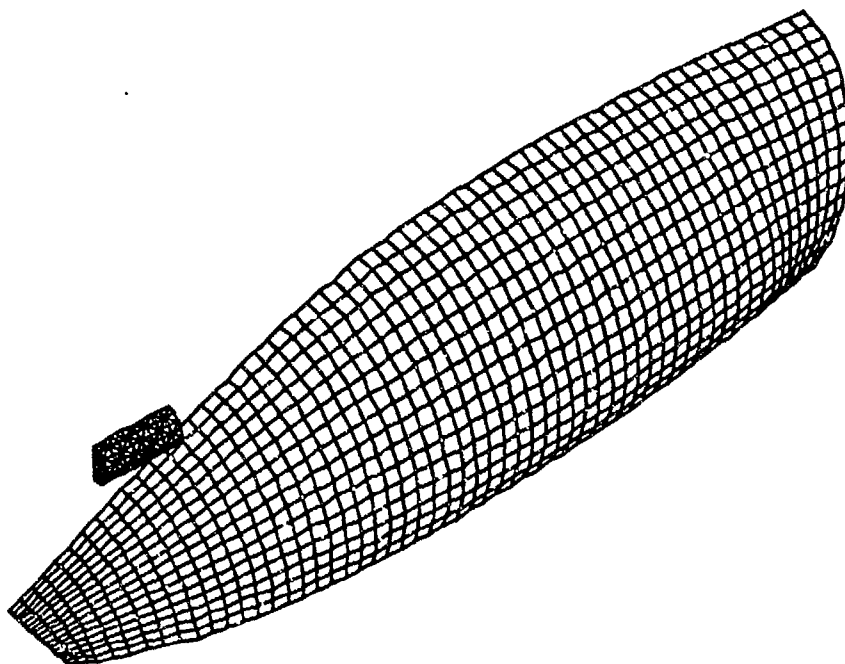
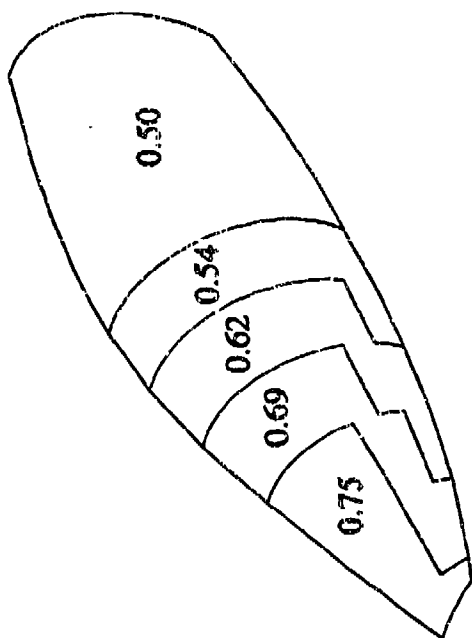


Figure 8. F-16 X3D Analysis Model.

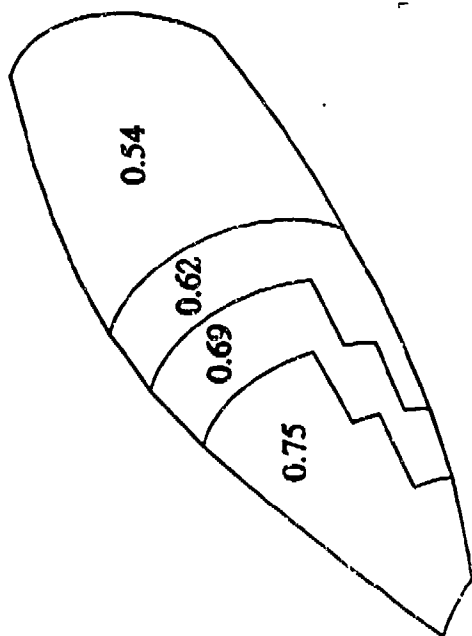
baseline model did not represent thinning which might occur in the extremely stretched crown area. Next, a series of tapered canopy models were evaluated at the same 350 knot, F.S. 113.5 condition. The tapered configurations are depicted in Figure 9. These hypothetical canopies are directly formed but not frameless. A molded canopy of this configuration could be utilized as a replacement for the current canopy and be attached to the current F-16 frame.

The initial approach was to optimize the thickness so that the birdstrike capability was the same over the frontal projection area of the canopy. This resulted in models 1 and 2. Concern about maintaining optics and sufficient thickness along the sill led to additional models 3 and 4. Table 3 shows the weight savings for each of the tailored models of the uniform thickness canopy. Note the potential for a 5-15% weight reduction is achievable through directly formed processing. For this preliminary study, only one impact location and one impact velocity were used, but the X3D results were encouraging. Figure 10 shows the deflection-time-history for the baseline and each tapered model at F.S.130. Table 3 lists the maximum centerline deflections at F.S. 130, F.S. 113.5 (design eye location), and F.S. 140 (pilot's head).

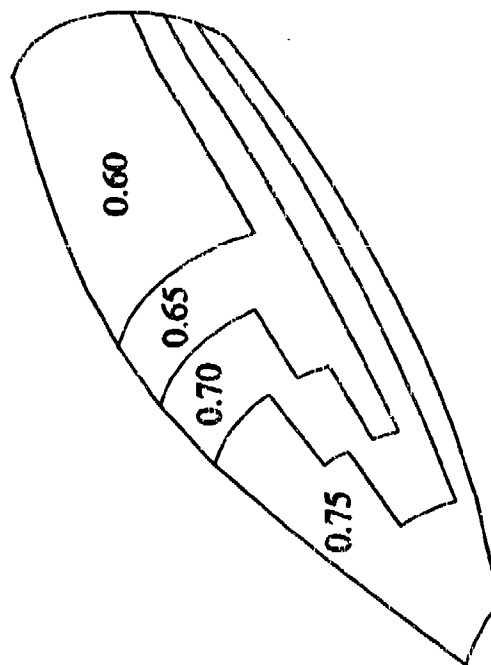
The capabilities developed under the FTP have made transparency thickness tailoring a realistic possibility which warrants much more study by the transparency community. With the exception of the most severely tapered case which has unacceptably large deflections (see Table 3 and Figure 10), the tapered



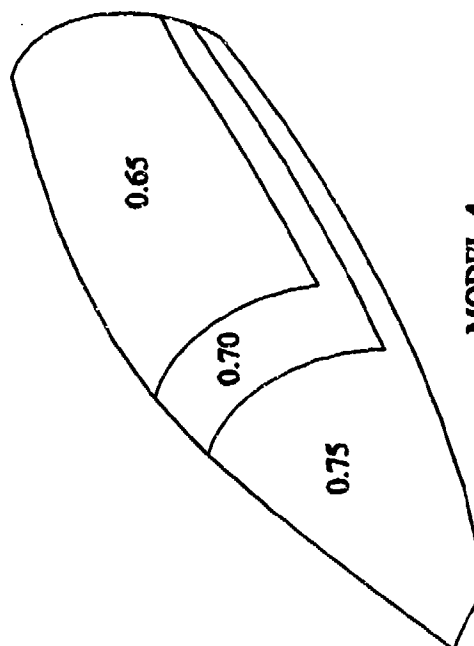
MODEL 1



MODEL 2



MODEL 3



MODEL 4

Figure 9. Thickness Tailoring Canopy Models.

Table 3. Thickness Tailoring Summary

Model	Max. Centerline Deflection (in)			Canopy Weight (lb)	Weight Reduction (lb)	% Weight Reduction	Acceptable?
	FS 113.5	FS 130.0	FS 140.0				
Baseline	2.62	1.30	0.71	145.3	--	--	yes
Model 1	2.80	3.18	1.17	110.7	34.6	23.8	no
Model 2	2.64	1.52	0.90	119.4	25.9	17.8	yes
Model 3	2.68	1.55	0.86	130.0	15.3	10.5	yes
Model 4	2.63	1.47	0.81	134.3	11.0	7.6	yes

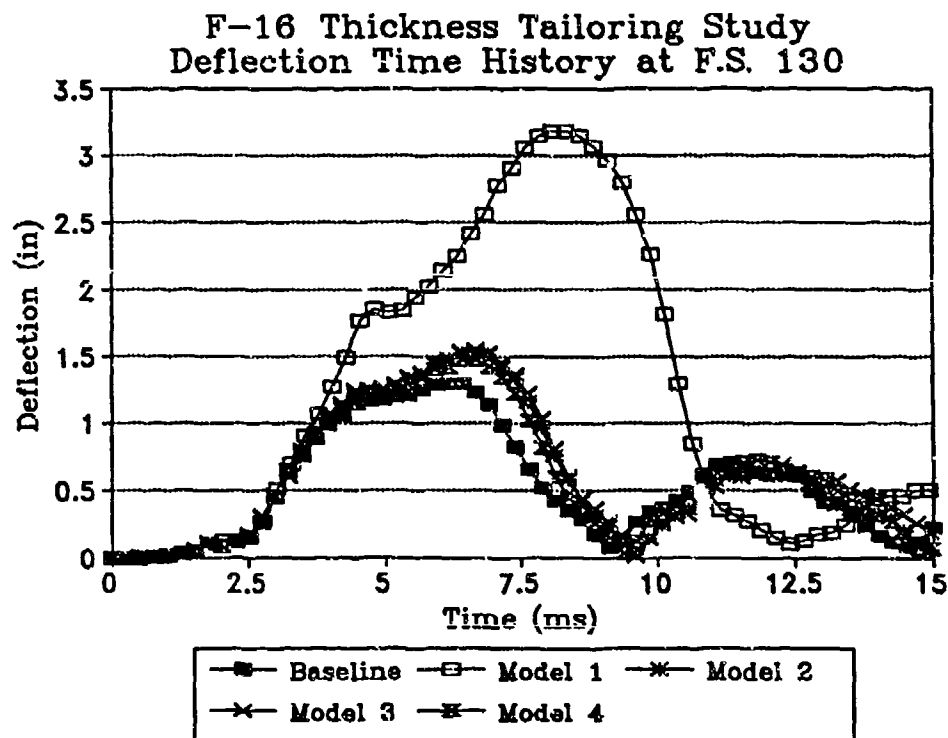


Figure 10. Deflection Time Histories of Tailored Analyses.

model deflections were not much greater than the uniform thickness model. Much more work is necessary to investigate other impact locations, optical integrity, and direct forming limitations, but the preliminary study has demonstrated an enormous potential for thickness tailored transparency designs which have significant weight savings over conventional transparencies.

## CONCLUSIONS

As a result of the birdstrike test program, triangulation/X3D analyses, and thickness tailoring study, the following conclusions were reached regarding the birdstrike resistance of candidate materials for the Confirmation Frameless Transparency (CFT):

- Twelve polycarbonate panels were successfully birdstrike tested at UDRI. Each panel was impacted by a 2.0 lb artificial bird at a 30° impact angle with an unrestrained aft edge. Approximate thresholds of the three candidate CFT resins were 250-300 knots for Dow 300-15, 275-300 knots for Dow 300-6, and 300-325 knots for Dow 300-4.
- Triangulation data was successfully obtained using the Air Force triangulation program. Of the twelve 0.75" thick panels tested, triangulation was performed on three of the panels that passed and one of the panels that failed. Triangulation results indicated that maximum panel deflections ranged from 1.0 to 1.4 inches approximately 3-5 milliseconds after impact, depending upon the resin and impact velocity. Note deflection-time-history response of the panel that failed was similar to that of the panels which survived the birdstrike.
- The explicit finite element analysis program, X3D, was successfully employed to simulate 256 knot impact by a 2.0 lb artificial bird on an FTP polycarbonate panel. Results from the X3D analysis compared well with triangulation results up to the point of maximum deflection. Divergence in the X3D and triangulation results after maximum deflection was thought to be the result of differences in boundary conditions and material properties between the test and analysis. Continuing development is necessary, but the results from this program indicate that X3D is a viable tool for impact simulation in support of the ADP of the Frameless Transparency Program.
- Repeated failure occurrences along the right side of the panel near the aft edge indicate that the materials have become strong enough to withstand a sufficient birdstrike, such that a change in the test fixture may become an issue of concern in the future.
- X3D analyses performed to demonstrate the usefulness of the ADP indicated potential significant weight savings could be achieved by tailoring the thickness of the canopy. Thickness tailoring is now a realistic possibility due to the advances under the FTP. Preliminary studies showed good promise, but many issues such as optics, producibility, and latching (for frameless configurations) must be addressed along with considering additional impact locations.

## **- RECOMMENDATIONS**

As a result of the birdstrike testing and analysis conducted under this program, the following recommendations are made regarding the birdstrike resistance of candidate materials for the Confirmation Frameless Transparency (CFT):

- X3D results compared favorably with triangulation data from a Dow panel up to the time of maximum deflection at which point the solutions diverge. Results from this program indicate that X3D is a viable tool for impact simulations, but that more effort is recommended to determine the cause for the solution divergence and to implement appropriate modifications.
- To perform comparative impact analyses, it is critical that high strain rate material property data be available for each candidate material, and that updated material models be incorporated into X3D. More effort is recommended to refine the material modelling techniques in X3D and to define appropriate parameters for the material models used for the CFT.
- Bird impact analyses of thickness tailored transparencies indicated a potential for weight savings over traditional transparency designs. The preliminary efforts conducted to date are promising, but different impact locations need to be considered as well as optical, latching, and producibility issues.
- Thickness tailoring for structural and weight benefits must be compatible with optical quality. An optical code which is planned for the ADP is a necessity for a viable thickness tailored transparency design evaluation.

## REFERENCES

1. Huelsman, M. A., G. J. Frank, W. M. Braisted, and G. J. Stenger, "Birdstrike Resistance Evaluation of Injection Molded Transparent Panels," UDR-TR-93-25, University of Dayton Research Institute, Dayton, Ohio, 1993.
2. Barber, J. P., H. R. Taylor, and J. S. Wilbeck, "Bird Impact Forces and Pressures on Rigid and Compliant Targets," AFFDL-TR-77-60, University of Dayton Research Institute, Dayton, Ohio, May, 1978
3. \_\_\_\_\_, "The Triangulation Program Z-248 GW BASIC User's Guide," SofTech, Inc., Fairborn, Ohio, 1987.
4. Brockman, R.A. and T. W. Held, "Explicit Finite Element Method for Transparency Impact Analysis," UDR-TR-90-114, University of Dayton Research Institute, Dayton, Ohio, 1990.
5. Frank, G. J. and G. J. Stenger, "Frameless Transparency System Material Property Evaluation," UDR-TR-92-51, University of Dayton Research Institute, Dayton, Ohio, July, 1992.
6. Braisted, W. R., G. J. Stenger, and P. G. Szalek, "Birdstrike Resistance Evaluation of Flawed Injection Molded Transparent Panels," UDR-TR-92-44, University of Dayton Research Institute, Dayton, Ohio, March, 1992.
7. Fuller, D. B., B. L. Penunuri, and T.A. Taylor, "Development of Forming Process for Frameless Aircraft Transparencies," AFWAL-TR-88-3071, Wright-Patterson Air Force Base, Ohio, 1988.



SESSION IX

INJECTION MOLDING - PART B

Chairman: W. R. Pinnell  
Flight Dynamics Directorate  
Wright Laboratory

Co-Chairman: K. Roach  
University of Dayton

Coordinator: R. Wagner  
Flight Dynamics Directorate  
Wright Laboratory

MECHANICAL PROPERTIES EVALUATION OF DIRECTLY FORMED  
TRANSPARENCY MATERIALS

G. J. Frank  
University of Dayton

W. R. Pinnell  
Flight Dynamics Directorate  
Wright Laboratory

# **Mechanical Properties Evaluation of Directly Formed Transparency Materials**

Geoffrey J. Frank  
University of Dayton Research Institute, Dayton, Ohio

William R. Pinnell  
WL/FTVR, Wright-Patterson Air Force Base, Ohio

## **Abstract**

Techniques required to manufacture aircraft transparencies by injection molding are currently being developed as part of a US Air Force program for developing the technologies required for directly formed and frameless aircraft transparencies. Components have been molded from several candidate materials under a variety of molding process conditions. Several types of coupon-level tests have been performed to identify the best combinations of materials and process conditions, to measure the mechanical properties of the materials, and to validate the capability of directly-formed components to perform like components fabricated with current processes. Strength, stiffness, and elongation to failure have been evaluated using tensile tests at several rates. Impact resistance has been evaluated using falling dart tests. Integrity of latch inserts, which could be used to attach a frameless transparency to an aircraft fuselage, has been evaluated through static pullout after thermal and load cycling. Results and conclusions from the tests will be presented.

## **Introduction**

The primary manufacturing technique for the current generation of high performance aircraft transparencies consists of extruding flat sheets of plastic, laminating these sheets with interlayers, and bending the laminated assembly into the desired shape. Fasteners at the edges of the assemblies are used to mount the transparencies into metal or composite frames. The holes near the edge which are required for installing the fasteners, the stresses due to differential thermal expansion between the frame and plastic, the multiple thermal cycles required to form the panel, and the necessity of constant panel thickness all tend to degrade the performance of the transparency during a bird impact<sup>1</sup>.

Utilizing the toughness inherent in impact resistant transparent plastics and methods for direct forming provides many potential improvements over current design and manufacturing practices. Elimination of frames from transparency assemblies and single process direct forming permits both an improvement in performance and a reduction in costs. Previous investigations have indicated that injection molding is currently the most viable method for direct forming transparencies from bulk polymers<sup>2,3</sup>. Techniques required to manufacture aircraft transparencies

by injection molding are currently being developed as part of a US Air Force program for developing the technologies required for directly formed and frameless aircraft transparencies. As part of this program methods for attaching frameless transparencies to the aircraft are also being evaluated<sup>4</sup>.

This paper describes tensile, falling-dart impact, and latch insert pullout tests performed on coupons cut from injection molded polycarbonate panels. The tests described in this paper represent a portion of the tests performed as part of a study<sup>5,6</sup> whose objectives were to characterize the mechanical properties of injection molded materials being evaluated for use in directly formed and frameless transparencies and to validate the capability of directly-formed components to perform like components fabricated with current processes. Results of these and other tests<sup>5-8</sup> were used to select materials for developing the Confirmation Frameless Transparency (CFT), a test item for confirming the developed technology.

Three formulations of polycarbonate were used for molding the panels evaluated: Mobay APEC 9350, Dow Calibre 302-5, and GE Lexan 4701. Additionally, extruded GE Lexan 9034-112 was used as a baseline for comparison with the results for the molded materials. This extruded material had not been subjected to any of the thermal or mechanical forming processes which are required to form a transparency and which may alter the properties of the polymer.

### Tensile Tests

Tensile tests were performed on injection molded materials at two strain rates using the two types of coupons shown in Figure 1. Comparison of the data from the coupons<sup>5</sup> showed that the moduli and yield strengths were consistent between the two geometries within the experimental variation observed for the individual specimen geometries. Differences between the two coupons were noted in the elongation at failure, where the failure point had a higher value for the mini-tensile rod than for the ASTM coupons. This difference can be attributed both to the much larger volume and surface area of the ASTM coupons, which allows for more failure initiation sites, and to the sharp corners on the ASTM coupons, which are the most common location for failure initiation.

The results presented here are from the tensile tests on the mini-tensile rods only. These coupons, which are planned for use in quality control tests on future directly-formed transparencies, are preferred over standard ASTM coupons because: they require less material; they can be machined from irregularly shaped material, and they can be used for high-rate tests on machines with limited load capacities. However, this testing showed higher scatter in the results from the mini tensile rod coupons than from the ASTM coupons. Thus, to achieve a specific confidence level requires more mini-tensile rod coupons than ASTM coupons.

Results of the tests on three molded and one extruded formulations of polycarbonate are summarized in Table 1. The values listed in this table, identified as "engineering" properties, are based on the dimensions of the samples in an undeformed state. Trends indicated by the data in this table are presented in graphic form in Figures 2 through 5.

Figure 2 shows the tangent modulus as a function of strain at a nominal 0.5 in/in/sec strain rate. The decrease in slope of the stress-strain curve is typical of glassy polymers. It can be observed that the molded GE material has an initial modulus which is 10-15% lower than that of the other materials. The low initial modulus occurred for several, but not all, of the molded GE panels, and may have been caused by poor packing of the material during molding. Figure 3 shows the change with strain rate of the tangent modulus at 1% strain. These two figures illustrate that the modulus of the molded materials, with the exception of the molded GE material, is very similar to that of the extruded polycarbonate.

Figure 4 shows the ultimate elongation of the four materials as a function of strain rate. It can be seen that, on average, the molded Dow material had an elongation at failure nearly equal to that of the extruded material. Figure 5 shows the increase in yield point with increasing strain rate. The yield stress shown in this figure is the "true" stress which is based on the cross section of the coupon as the test progresses rather than the initial cross sectional area. True stress is used in this figure in order to facilitate identification of a "critical" strain rate, at which the yield stress equal the stress at rupture. True stress at rupture was determined for the coupons by dividing the load just before failure by the measured the cross sectional area after failure and compensating for elastic recovery. The yield stress versus strain rate curves were then extrapolated out to determine the point at which the yield stress would equal the true stress at failure. It can be seen that the molded GE and Mobay materials have critical strain rates on the order of  $10^3$  in/in/sec while the molded Dow and extruded GE materials have critical strain rates on the order of  $10^6$  in/in/sec. This indicates that the molded Mobay and molded GE materials were more brittle than the molded Dow and extruded GE materials for the processing conditions chosen.

The tensile test show that the molded Dow polycarbonate has properties which are very similar to those of extruded material, while the molded Mobay and GE materials appear to be more brittle. This embrittlement may reflect formulation modifications necessary to allow higher temperature uses for the Mobay and GE resins or may have been caused by the higher temperatures used in molding these materials.

It should be noted that the data indicates that there is a correlation between the degree to which the mold is packed (i.e. how well the material is compressed in the mold) and the tensile properties of the material. Thus, when using properties such as those presented here for predicting the response of directly formed transparencies to impact, the particular molding process as well as the type of resin must be considered.

#### Falling Dart Impact Test

Falling dart impact tests were performed on 6-inch square samples of material with a nominal thickness of 0.5-inch. The coupons were mounted in a holder which had a 5.5-inch square opening and were impacted by a dart with a 1.5-inch diameter hemispherical nose. The fixture is illustrated in Figure 6. For all of the tests, the dart was dropped from a height of 20 feet, providing an impact velocity of approximately 35.9 ft/sec. Weight of the dart was varied to provide a range of impact energies.

Results of the tests are summarized in Table 2. For each of the four materials tested, the table indicates the percentage of coupons at a specific impact energy which deformed in a ductile manner or shattered in a glassy manner. Also, a few coupons, identified under the heading "pass with cracks," showed large ductile deformation with small cracks near the tip of the indentation, which indicated that the coupons were on the verge of failing.

Results of the tests show a few key trends for the molded materials. The molded Dow material showed ductile response up to an impact energy of 1200 ft-lbs, where testing was halted due to machine limitations. Small cracks in the some coupons indicated that 1200 ft-lbs was near the fracture threshold for the Dow material. The molded GE material showed ductile behavior for an 800 ft-lb impact, but failed in a brittle manner under a 1200 ft-lb impact, indicating that the energy required to fracture the molded GE coupons was in between these two levels. A lack of samples prevented a more refined definition of the energy which would cause this material to fracture. The molded Mobay coupons showed rather erratic results. All of the coupons taken from one panel which was molded improperly fractured under impacts as low as 400 ft-lbs. Coupons from other panels indicated that the threshold for fracture of properly molded materials was on the order of 1100 ft-lbs. The extruded GE polycarbonate used as a baseline material behaved in a manner similar to the molded Dow material. A 1200 ft-lb impact was sufficient to cause small cracks in some coupons, indicating that 1200 ft-lbs was near the threshold beyond which the baseline material coupons would fracture.

Deformed shapes formed by the convex surface of coupons from the molded Dow and the extruded GE polycarbonates are compared in Figure 7 at three different impact energies. When normalized by thickness (all coupons were between 0.46 and 0.53-inch thick), the deformations of coupons from the two materials are very similar at the two higher rates, thus illustrating the similarity in yield and plastic flow behavior of the two materials.

The dart impact tests indicate that the molded Dow polycarbonate had properties similar to those of extruded polycarbonate. For the molding process conditions used, the molded GE and Mobay materials had lower impact resistance than the extruded polycarbonate or molded Dow.

#### Latch Insert Evaluation

An important feature of any frameless transparency is the hardware used to connect the transparency to the aircraft fuselage. One promising configuration is a hollow shell which can be overmolded by the frameless transparency material and which contains a pin with which a hook mounted in the fuselage can hold the transparency in place. This type of hardware, referred to as latch inserts, must be capable of reacting cabin pressure loads, thermal stresses, and birdstrike forces. Structural integrity must be maintained throughout the life of the transparency.

Latch inserts were molded from aluminum and GE Ultem 2300 (a glass-reinforced polyetherimide) and were subsequently overmolded with polycarbonate. The latch insert/molded polycarbonate coupons were then subjected to thermal/load cycles and room-temperature pull-to-failure.

The setup used for the tests is shown in Figure 8. The 14-inch long coupon was placed in a yoke and supported by pads 10-inches on center. A hook engaged a pin in the latch insert and applied load to the coupon. The entire assembly was placed in the environmental chamber of an Instron machine, allowing both temperature and load to be varied simultaneously. Tests were also performed on coupons cut from production F-16 canopies in which the standard F-16 edge attachment was simulated over a span of 4 bolt holes.

Thermal/load cycles were designed to simulate a typical F-16 mission of 68-minute duration on a hot or cold day<sup>9</sup>. Temperature profiles in the environmental chamber were based on computed outer-surface temperatures of the CFT and loads applied to the coupons were based on the difference between internal and external cabin pressure plus an allowance for compression of the sill seal. Figure 9 shows the loads and temperatures used to represent a cold day mission. The duration of the test cycle exceeds the 68-minute duration of the mission due to limitations on heating and cooling rates for the environmental chamber, which lessens the severity of thermal shock during the test but increases the stresses due to thermal mismatch between the insert and polycarbonate. Figure 10 shows the load and thermal cycle initially used to represent the hot day mission. After initial tests showed extreme softening and deformation of both latch insert coupons and production F-16 coupons, the peak temperature for the hot day mission was reduced from 340 °F to 265 °F, which is the maximum temperature required by F-16 canopy specifications<sup>10</sup>. Figure 11 shows the loads and temperatures used to represent the hot day simulation cycle with a 265 °F peak temperature.

Results of the tests are summarized in Table 3. Results are grouped by molded material and latch insert type. Coupons molded from Dow Calibre 202-5 and 302-5 resins with aluminum latch inserts soften during the hot day mission 340 °F cycle, but showed no visually observable degradation after up to seven cycles of the cold day mission or hot day mission 265 °F simulations. Static pullout tests showed that failure loads after the cold day mission cycles were the same as for coupons which had not undergone any cyclic testing. Failure loads for coupons which had undergone the hot day mission 265 °F cycles were somewhat lower than those of the other coupons in this category, but were nearly a factor of 2 higher than the 3,200 pounds peak burst pressure plus seal loads which could occur for the CFT.

Coupons molded from Dow Calibre 202-5 and 302-5 resins with Ultem inserts also showed no degradation after three cycles of the cold day mission cycle or the hot day mission 265 °F cycle. Static pullout tests showed that failure loads after thermal/load cycles were the same as for coupons which had not undergone any cyclic testing. In all cases, failure of these coupons was caused by brittle fracture of the Ultem (as opposed to the fracture of the polycarbonate which occurred for those coupons which had aluminum inserts). Failure loads for the coupons with Ultem inserts were significantly lower than those for the coupons with aluminum inserts.

Coupons molded from Mobay APEC 9350 with aluminum latch inserts showed potential for better high temperature capability than coupons manufactured from Dow materials but were also more brittle. The Mobay coupon tested using the hot day mission 340 °F cycle did not show any softening, but cracked at room temperature at the end of the cycle. Also, two of three Mobay coupons tested at with a cold day cycle cracked at the extreme cold temperatures. The

cracking appears to be caused by a combination of residual stresses and brittleness of this material, both of which result from the relatively high temperature used in molding. Thermal and mechanical stresses during the cyclic tests were sufficient to fracture the coupons.

Although the number of coupons evaluated in each category was relatively small, the testing indicates that CFT's formed from Dow Calibre 202 or 302 class materials with aluminum inserts meet current pressure loading and temperature requirements for F-16 transparencies. Ability of the latch inserts to withstand bird impact forces must still be evaluated. The Ultem inserts offer the potential of reducing stress due to thermal mismatch, and the Mobay material offers the potential of higher temperature performance. However, additional effort will be required to permit the use of either of these materials.

### Conclusions

Coupon-level tests indicate that some molded polycarbonate formulations have mechanical properties and impact resistance similar to an unprocessed extruded polycarbonate sheet. Thus, transparencies molded from these formulations can be expected to have bird impact resistance similar to transparencies of similar design fabricated from extruded materials. Also, tests indicate that latch inserts can be overmolded with polycarbonate to provide a means of attaching a frameless transparency to an aircraft fuselage. Coupon-level tests indicate that structural integrity requirements can be met for all expected thermal and flight load conditions.

### References

1. Pinnell, W. R., "Frameless Aircraft Transparency Technology Development," published proceedings from the Conference on Aerospace Transparent Materials and Enclosures, WRDC-TR-89-4044, Volume I, Wright-Patterson AFB, OH, April 1989, pp. 508-521.
2. Fuller, D. B., B. L. Penunuri, and T. A. Taylor, "Development of Forming Process for Frameless Aircraft Transparencies," AFWAL-TR-88-3071, Air Force Wright Aeronautical Laboratories, Wright-Patterson AFB, OH, October 1988.
3. Fuller, D. B., "Direct Forming Processes for Aircraft Transparencies," published proceedings from the Conference on Aerospace Transparent Materials and Enclosures, WRDC-TR-89-4044, Volume I, Wright-Patterson Air Force Base, OH, April 1989, pp. 522-554.
4. Wade, L. A., "Transparency Insert and Molding Program," Report No. 53-91-04, Alcoa Technical Center, Alcoa, PA, November 18, 1991.



5. Frank, G. J. and G. J. Stenger, "Frameless Transparency System Material Property Evaluation," UDR-TR-92-51, University of Dayton Research Institute, Dayton, OH, July 1992.
6. Frank, G. J. and G. J. Stenger, "Frameless Transparency System Latch Insert Evaluation," UDR-TR-92-21, University of Dayton Research Institute, Dayton, OH, March 1992.
7. Braisted, W. R., G. J. Stenger, and P. G. Szalek, "Frameless Transparency System Birdstrike Resistance Evaluation," UDR-TR-92-44, University of Dayton Research Institute, Dayton, OH, March 1992.
8. Huelsman, M. A., et. al., "Birdstrike Resistance Evaluation of Injection Molded Transparent Panels," UDR-TR-93-85, University of Dayton Research Institute, Dayton, OH, March 1993.
9. Babish, C. A. III and M. G. Gran, "Thermal and Pressure Environments for the Confirmation Frameless Transparency (CFT) of the F-16 Aircraft and Procedures for Testing the CFT Latch Insert," WL/FIVR Memorandum, Wright-Patterson Air Force Base, OH, January 1991.
10. \_\_\_\_\_, "Critical Item Development Specifications for F-16A/B/C/D Transparencies," Specification No. 16ZK002E, Revision A, 26 December 1985.

Table 1 Room Temperature Engineering Properties  
From Mini-Tensile Rod Tests

MATERIAL	STRAIN* RATE (1/SEC)	TANGENT MODULUS (0% STRAIN) (KSI)	TANGENT MODULUS (1% STRAIN) (KSI)	TANGENT MODULUS (2% STRAIN) (KSI)	TENSILE STRENGTH AT YIELD (FSI)	PERCENT ELONGATION AT YIELD	AVERAGE ELONGATION AT BREAK
MOLDED	0.005	370	302	234	9,440	6.2%	173%
DOW	0.5	361	299	236	10,440	6.5%	140%
CALIBRE 302-S	100 **	402	338	273	11,456	7.2%	140%
MOLDED	0.005	375	305	236	10,480	6.5%	115%
MOBAY	0.5	371	299	227	11,430	7.0%	100%
APEC 9350	100 **	386	343	299	12,290	7.6%	70%
MOLDED	0.005	347	288	228	11,002	7.7%	145%
GE	0.5	316	280	245	12,190	8.2%	70%
LEXAN 4701	100 **	413	360	306	13,255	9.2%	110%
EXTRUDED	0.005	395	311	226	9,984	6.4%	180%
GE LEXAN	0.5	373	313	254	11,058	6.9%	190%
9034-112	100 **	420	357	302	11,999	7.3%	170%

- \* - Strain rates measured during elastic portion of test.  
Strain rates during plastic portion of test are approximately 3 times as large.
- \*\* - Strain rates vary during elastic portion of high rate tests.  
Strain rate of 100/sec is approximate value when specimen yields.

Table 2 Results of Falling Dart Impact Tests

Material	Impact Result	Impact Energy (ft-lbs)								
		500	500	500	700	800	800	1000	1100	1200
Molded Dow Calibre 202-4/302-5	Pass					100%		100%		80%
	Pass w/ cracks					0%		0%		20%
	Shatter					0%		0%		0%
Molded GE Lexan 4701	Pass					100%				0%
	Pass w/ cracks					0%				0%
	Shatter					0%				100%
Molded Mobay APEC 9350	Pass	33%		0%		50%		100%	0%	0%
	Pass w/ cracks	0%		0%		0%		0%	100%	0%
	Shatter	67%		100%		50%		0%	0%	100%
Extruded GE 9034-112 Lexan	Pass					100%		100%		50%
	Pass w/ cracks					0%		0%		50%
	Shatter					0%		0%		9%

NOTE: Impacts at nominal velocity of 36 ft/sec  
Coupons are nominally 1/2-inch thick

Table 3 Latch Insert Evaluation Test Summary

PANEL I.D.	COUPON POSITION	LOAD/THERMAL CYCLE TEST DESCRIPTION	STATIC PULLOUT FAILURE LOAD
Dow 202/302 polycarbonate with #6 aluminum insert:			
900108 #1	port	n/a	7500
900108 #1	stbd	n/a	11025
900108 #2	stbd	7 HOT DAY 265 F CYCLES	5950
D910109 #16	port	3 COLD DAY CYCLES	9120
D910109 #16	stbd	7 COLD DAY CYCLES	10500
D910109 #19	port	SOFTENED DURING HOT DAY 340 F CYCLE	n/a
D910109 #19	stbd	3 HOT DAY 265 F CYCLES	7920
Dow 202/302 polycarbonate with Ultram insert:			
D910109 #17	port	OVERLOAD DURING HOT DAY 265 F CYCLE	n/a
D910109 #17	stbd	3 HOT DAY 265 F CYCLES	4640
D910110 #06	port	3 COLD DAY CYCLES	4800
D910110 #06	stbd	n/a	4100
D910110 #06	port	SOFTENED DURING HOT DAY 340 F CYCLE	n/a
D910110 #06	stbd	n/a	4480
Mobay APEC DP9 9350 polycarbonate with #6 aluminum insert:			
900116 #2	stbd	n/a	6975
900116 #3	port	n/a	3900
900116 #1	port	3 HOT DAY 265 F CYCLES	4080
900116 #1	stbd	CRACKED DURING HOT DAY 340 F CYCLE	n/a
900116 #2	port	n/a	7200
M910111 #12	port	3 COLD DAY CYCLES	5130
M910111 #12	stbd	CRACKED DURING COLD DAY CYCLE	n/a
M910111 #13	stbd	CRACKED DURING COLD DAY CYCLE	n/a
F-16 production transparency with load plate bolted to edge			
0433-1	n/a	SOFTENED DURING HOT DAY 340 F CYCLE	n/a
0433-2	n/a	3 HOT DAY 265 F CYCLES	5950
0433-3	n/a	3 COLD DAY CYCLES	9700
0433-4	n/a	n/a	8740

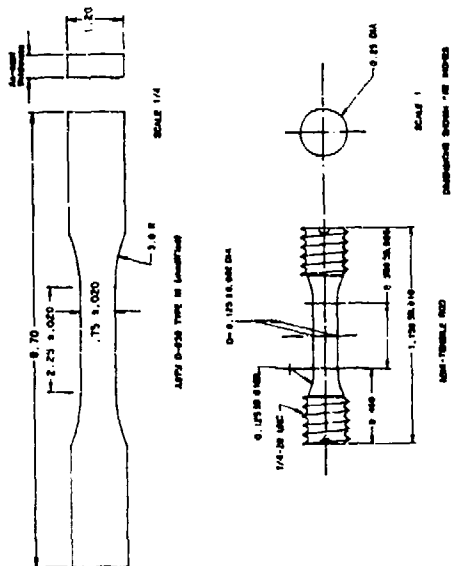


Fig. 1 Tensile Test Coupon Geometry

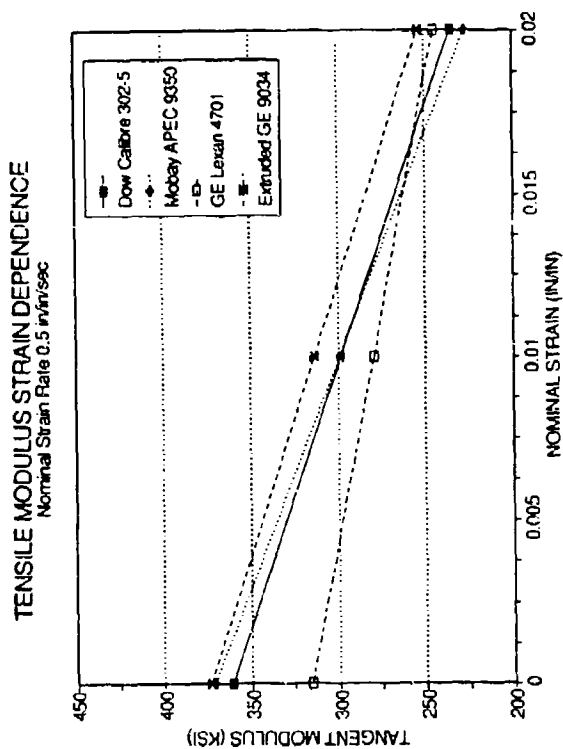


Fig. 2 Strain Dependence of Tensile Modulus at 0.5 inch/inch/sec.

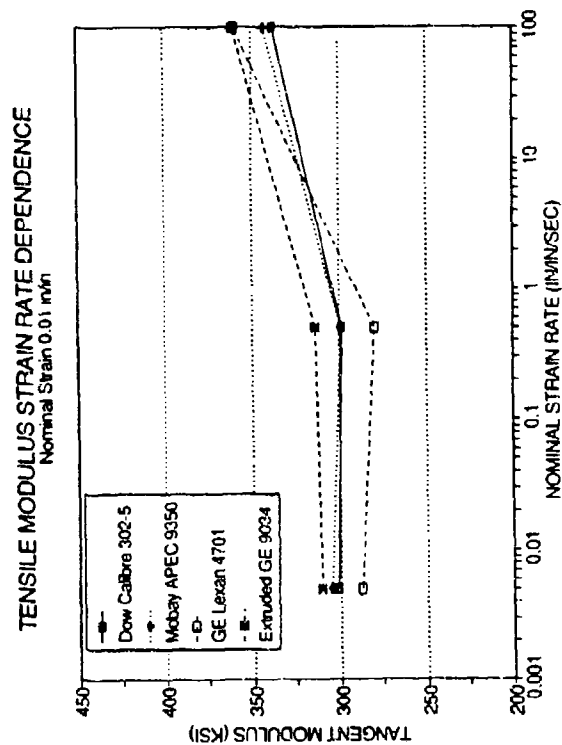


Fig. 3 Strain Rate Dependence of Tangent Modulus at 1% Strain

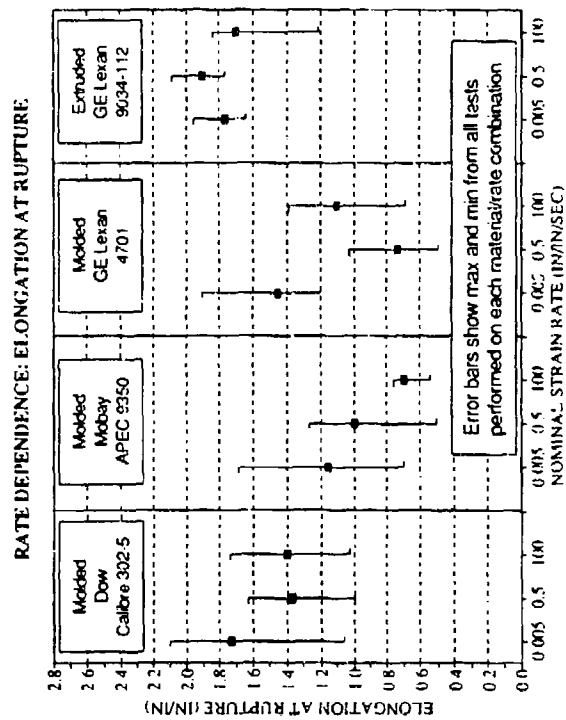


Fig. 4 Ultimate Elongation of Mini-Tensile Rod Coupons

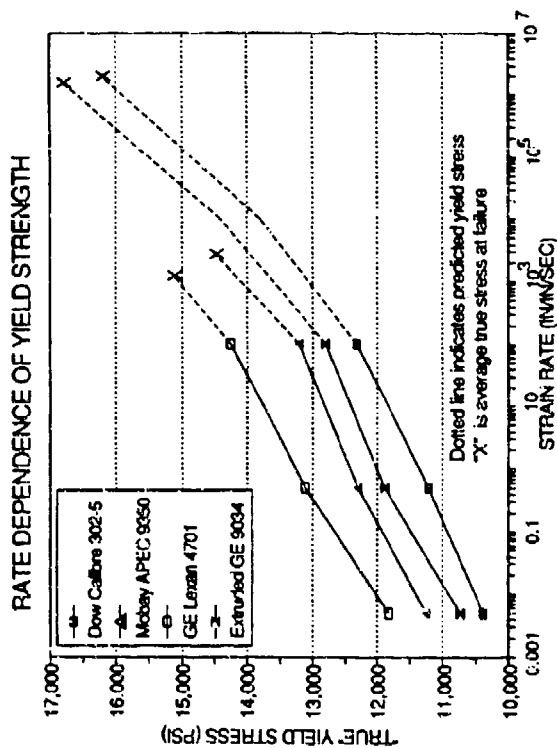


Fig. 5 Strain Rate Dependence of Yield Stress

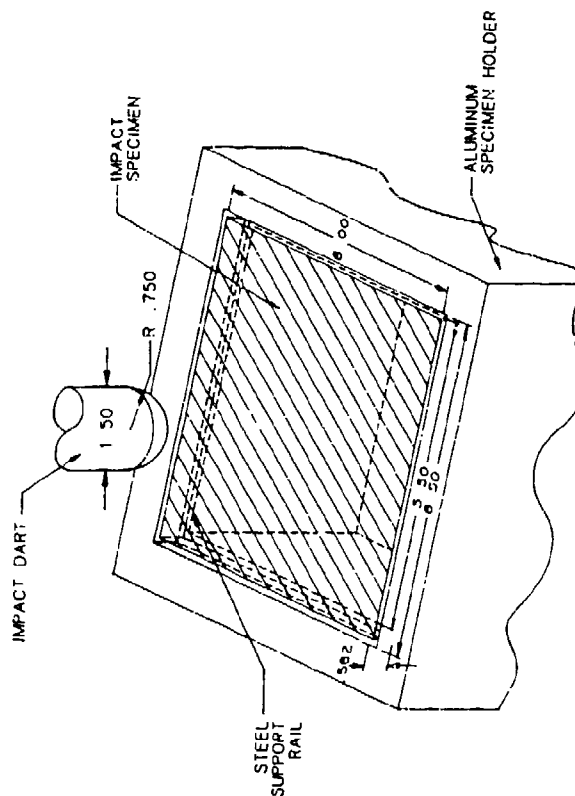


Fig. 6 Falling Part Impact Test Setup

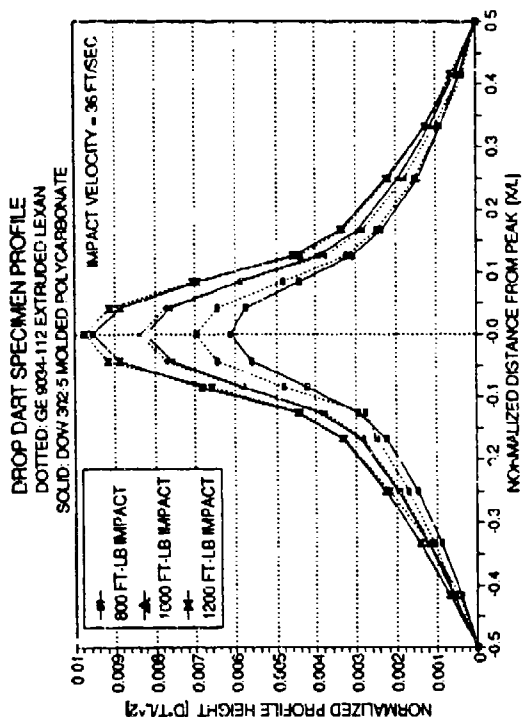


Fig. 7 Comparison of Deformed Shapes After Part Impact

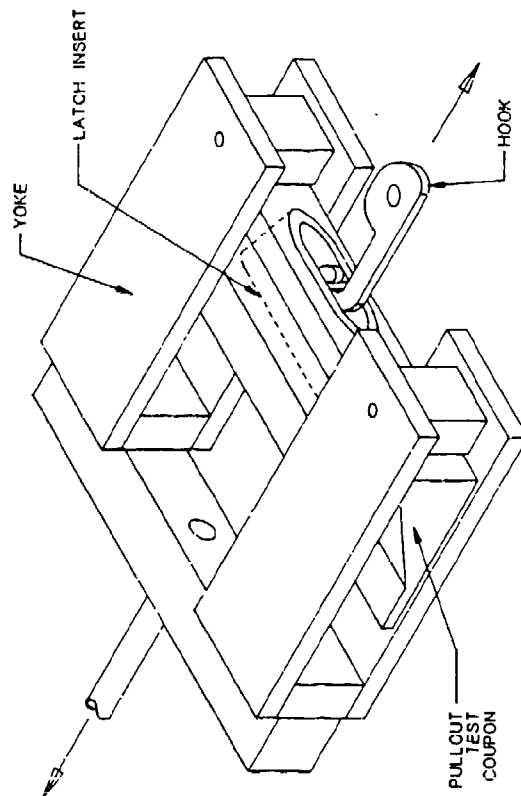


Fig. 8 Latch Insert Evaluation Test Setup

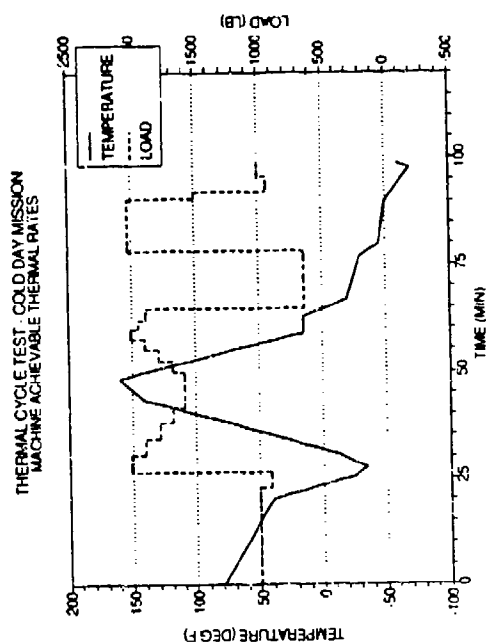


Fig. 9 Loads and Temperatures Used for cold Day Mission Simulation Cycle

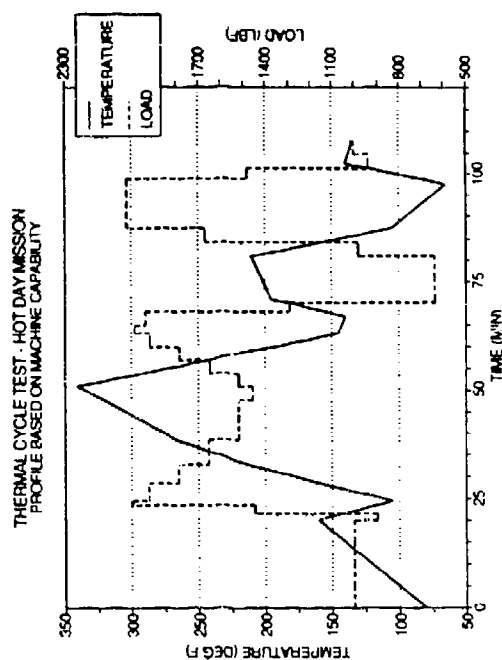


Fig. 10 Loads and Temperatures Used for Hot Day Mission Simulation 340 Degree F. Cycle

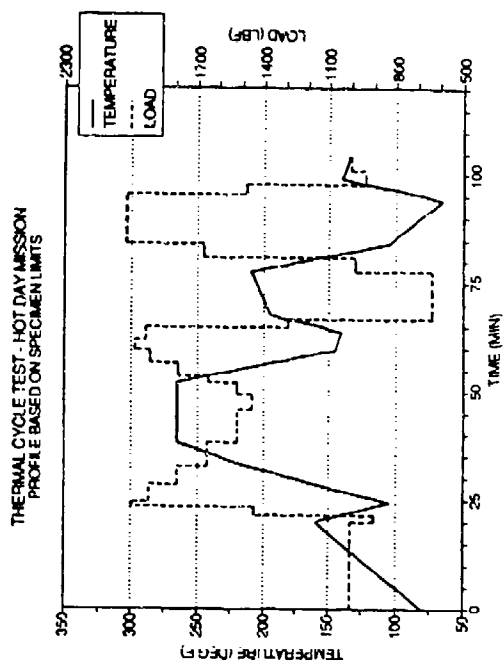


Fig. 11 Loads and Temperatures Used for Hot Day Mission Simulation 265 Degree F. Cycle

**DIMENSIONAL MAPPING AND SHRINKAGE CHARACTERIZATION OF LARGE,  
THICK-WALLED, DIRECTLY-FORMED TRANSPARENT PANELS**

K. Roach  
University of Dayton

J. G. Chow  
Florida International University

**Dimensional Mapping And Shrinkage  
Characterization Of Large, Thick-Walled,  
Directly-Formed, Transparent Panels**

Mr Kevin Roach, University of Dayton  
Dr Joe Chow, Florida International University

for  
**Conference On Aerospace Transparent Materials And Enclosures  
9-13 August 1993**

**Abstract**

A significant advantage of directly forming transparencies is the potential capability to closely control the dimensions of the finished part, and to repeat this control from part to part. This control can result in better fitting transparencies, improved optical quality, "designed in" thickness variation, and optical tailoring. However, it is well known in the molding industry that finished plastic parts have a slightly different size and shape than the mold from which they were made because the part shrinks as the molten plastic cools and solidifies.

A dimensional mapping effort was initiated to investigate the shrinkage characteristics (i.e. the differences between final panel dimensions and mold dimensions) of large, thick-walled, directly formed, transparent panels. The term "dimensional mapping" refers to the acquisition of coordinates of points on the surfaces of a molded part and/or it's mold, using a coordinate measuring machine (CMM). Thickness and overall dimensions are then calculated from the point coordinates. A CMM was used to take advantage of it's high accuracy, repeatability, and automation capabilities.

The paper will discuss the CMM procedures used, and the difference between dimensional mapping and other measurement techniques. Results of the investigation include confirmation of standard shrinkage factors used in the molding industry, and a description of the variable shrinkage found in the subject panels.

**Introduction**

The Aircrew Enclosures Section of the US Air Force - Wright Laboratories (WL/FIVR) at Wright-Patterson AFB, OH currently manages and directs the

Directly Formed Frameless Aircraft Transparency Program (i.e., the Frameless program). The objective of the program is to demonstrate the feasibility of directly forming (ie. injection molding), frameless aircraft transparencies, and to confirm the analytical tools used to design a directly formed transparency. An overview of the potentials and progress of the Frameless program are discussed in Reference 1. Included in that discussion are potentials for cost savings in manufacture, life-cycle cost savings, and improved performance, as well as other potential benefits. This paper addresses efforts undertaken by WL/FIVR to quantify the potential for improved dimensional control by directly forming transparencies.

Preceding the Frameless program, WL/FIVR funded Loral Defense Systems in a program (October 1985 - September 1988) to identify and demonstrate an optimum forming process for large, thick-walled, transparent parts. The process Loral and WL/FIVR selected was a low pressure, long cycle, injection molding process. The molding took place at Envirotech (formerly EIMCO) Molded Products, Salt Lake City, Utah. Hundreds of flat and conical panels (Fig 1) were molded during the program, using several different materials, and a wide variety of processing parameters (temperatures, pressures, shot size, cycle times, etc.) Panels with desirable characteristics were typically molded from clear polycarbonate, at approximately 750 psi, with a cycle time of approximately 30 minutes.

After the Loral effort was completed, WL/FIVR participated in three more molding trials. In January 1990, 68 half-inch flat panels were molded from four different materials at Envirotech Molded Products, Salt Lake City, Utah. In October 1990 and January 1991, 105 half-inch flat panels were molded at Hettinga Equipment Company, Des Moines, Iowa. During this molding, four materials were used for molding. In April 1992, WL/FIVR went back to Envirotech and molded 27 half-inch conical panels, 32 half-inch flat panels, and 35 three-quarter inch flat panels. The April 1992 molding was done with resins having four different melt flow indices. All of the above molding trials used a low-pressure, long cycle molding process; one not used for typical injection molded parts.

### **Why WL/FIVR Dimensionally Mapped Panels**

Under the frameless program in February 1991, the design of the CFT was nearing completion, and conceptual designs of the CFT mold were underway. One of the many points for consideration in the CFT mold design was how much the molded CFT would shrink after molding. Because the molding process to be used for the CFT is much different from typical injection molding processes, a concern was that standard shrinkage factors provided by resin vendors may not apply to the CFT molding.

Also at the time, preliminary work was underway to outline the CFT testing that would take place after CFT molding. One of the efforts envisioned for testing was an extensive dimensional check of the molded CFTs. The flat and conical panels molded under the Loral and subsequent efforts were measured, but not



extensively, and the values available were not sufficient to make an assessment of how different the panels were from their molds. It was evident that a more complete dimensional check of the CFT and CFT mold was going to be required.

With these future CFT related tasks in mind in February 1991, WL/FIVR initiated an effort to do a rigorous dimensional check of a number of suitable flat and conical panels that had been previously molded, and had not been cut up for testing. There were 4 conical panels and 15 flat panels available at the time. The flat and conical molds were also included in this effort. The objectives of this effort were to; measure the panels and molds, compare the dimensions of like panels, and to compare panel dimensions to mold dimensions. If applicable, information obtained would be applied to the CFT and to the CFT mold.

The checking of panels and their molds came to be known as "dimensional mapping" (DM), and the February 1991 effort was the first of two dimensional mappings of the flat and conical panels and their molds. The second DM effort was planned for panels molded in April 1992. One of the objectives of that molding was to mold panels from the same family of Calibre polycarbonate, but to include resins having four different melt flow indices. Based on this molding trial and subsequent testing, a resin would be selected for CFT molding in 1993. One of the tasks in the testing was dimensionally mapping the panels, and again, the molds. Typically, the molds would not have had to be mapped again, but both molds had been altered slightly. The cone mold's optical surface had been scratched during shipment the year before, and the scratch had to be polished out before molding in April. The polishing had changed the mold cavity thickness an unknown amount. Also, the flat plate mold was changed slightly in that it now incorporated a removable shim, which allowed the molding of both 1/2" and 3/4" panels.

The DM effort for the April 1992 molded panels began in July 1992. In the 1991 DM effort, we could only choose from panels left over from previous molding and testing, and this limited our selection. Since mapping was planned for the April 1992 panels, a better selection could be made. Essentially 12 groups of panels were molded; 1/2" cones from each of 4 resins, 1/2" panels from each of 4 resins, and 3/4" panels from each of 4 resins. We selected at least 3 panels from each of the 12 groups for dimensional mapping.

### **What is Dimensional Mapping**

The term "dimensional mapping" was coined by WL/FIVR because a description, or mapping, of the thickness distribution of panels and their molds was required, as well as the overall dimensions. "Dimensional Mapping" (DM) seemed to describe the whole exercise nicely. On the flat panels, the DM effort required obtaining thickness values at target point locations described by a one inch by one inch grid on the 2' x 2' surfaces (Fig 2). Also, the length and width of the flat panels was required at several locations. The same grid was used for the target points on the flat panel mold. On the conical panels, thickness values were required at target point locations described by a one inch by five degree grid on the

optical surfaces of the panel, and a one inch by one inch grid on the sill edges (Fig 3). Again, the same grid of target point locations was used for the cone mold.

A couple of approaches were considered to perform the DM effort. One approach briefly considered was measuring the items with hand held instruments; either traditional measurement tools such as calipers and micrometers, and/or surface positioned devices which can measure normal thickness using either light or sound. These approaches were not pursued because of the problems involved in repeating the measurement locations from panel to panel, accessing desired locations without destroying the panels, and/or the inherent possibility of human error degrading the measurement process. Also, measuring the thickness of the molds presented special problems since the mold halves had to be measured separately, and then the data combined to yield cavity thickness.

The approach chosen to perform the DM effort was to use a coordinate measuring machine (CMM). A CMM (Fig 4) is a measurement device that incorporates a precision probe with a spherical ruby tip, electronics, and part measuring routines to contact surface points on a part.

**Fig 4 Ring-Bridge Coordinate Measuring Machine**

The CMM keeps track of the probe's X, Y, Z position in the measurement space, and records the coordinates of the contact point. There were several advantages to the use of a CMM, including; accuracy, repeatability, automation, and minimal operator interface in data acquisition. Additionally, the manufacturer of a line of high precision CMMs happened to be located locally. Sheffield Instruments Company (now known as Giddings and Lewis Measurement Systems) manufactures CMMs and other measurement devices in Dayton, OH.

The type of CMM used in the dimensional mapping efforts was an Apollo Cordax "ring-bridge" model. The details of the specifications for the CMM are quite complex, involving considerations for specifications relative to gauge surfaces, unknown surfaces, and flat or curved surfaces. To summarize though, the accuracy of the CMM used in the DM effort, on the panels and molds, is on the order of  $\pm 0.0001$ ". The accuracy can be viewed as the confidence one has in the actual spatial location of the probe's position. The repeatability of the CMM is defined as the capability to repeatably obtain the same coordinates for the same physical point on a surface. To record the repeatability of the CMM as used on our parts, a test procedure was run where the probe contacted a series of 24 widely spaced points on the surfaces of a flat panel, and the series was repeated 20 times. The variance in the data was on the order of  $\pm 0.0002$ ". Data acquisition by CMM can be highly automated. For our purposes, a part measurement program was developed for each type of panel, and the program was run to acquire the

coordinates of the points of interest. This approach allowed the CMM to obtain data on each panel in the same fashion, with no operator intervention.

### **The Dimensional Mapping Procedure**

As mentioned above, grids of target point locations were defined by WL/FIVR for the panels and molds. The task of the CMM operator was to locate these target points and to obtain the actual point coordinates in the same manner for each panel and its mold. It was essential that the same point location was contacted on each part. In only this way could comparisons between panels, and between panels and molds, be made. The procedure of staging (mounting) a part, locating the part in the measurement volume of the CMM, locating the target points, and approaching and contacting the points on the part is described in this section.

The electronics and software routines resident on the CMM eliminated the need for a precision mounting of the parts. The CMM can orient a frame of reference relative to a part, instead of having the part fixtured precisely in a certain place and orientation relative to the CMM's default frame of reference. The chance for error in fixturing was thus not present in the dimensional mapping of the panels and molds. A consideration in mapping the molds was that we had no choice but to map the mold halves separately. This presented a challenge in bringing the 2 sets of data together (1 for the mold core, 1 for the mold cavity), in an accurate manner. The trials and errors of this will be discussed later. In contrast to the molds however, we could stage the panels in such a manner that all target point coordinates could be obtained in one staging. This eliminated the need for bringing 2 sets of data together; all data acquired on the panels was relative to a single frame of reference.

### **Flat Panels**

The flat panels were staged on the CMM as shown in Fig 5. The panel was set upright, on one thickened sill edge. Blocks were placed under the lower sill edge so the target points on the lower edge could be contacted. The panel was held in place by a simple C-clamp and angle iron jig. Although the flat panel data acquisition program would automatically establish the reference frame and acquire the data, the operator had to initialize the program by letting the CMM know where the panel was. This was accomplished by the operator manipulating the probe to contact several points on the panel. The operator touched 3 points on one of the optical surfaces, 2 points on the upper sill edge, and 1 point on the flat surface adjacent to the curved "arch" of the flat panel (the arch-plate surface). The part program already had the nominal dimensions of the panel, so with these operator-supplied points as input, the part program could then take over the mapping procedure.

**Reference Frame Establishment:** The CMM first established a primary plane by touching seven widely spaced points on the core side optical surface (Fig

6). A best-fit plane was then calculated through the seven points, and this was defined as the  $X = 0$  plane. Next, five points were touched on the arch-plate surface, at  $X = -0.25$ ". A best-fit line was calculated through the five points, translated to  $X = 0$ , and was defined as the Z axis. This fixed the  $X = 0$  plane in rotation, and defined  $Y = 0$  location on the  $X = 0$  plane. The  $Z = 0$  point on the Z axis was found by calculating the mid-line between two lines best-fit through five points on each of the sill edges, at  $X = 0$ . This procedure produced a flat panel reference frame that had its origin midway between the sill edges, at the intersection of the core side optical surface and the arch-plate surface. This procedure for reference frame establishment was used on all flat panels, and a slightly modified version was used on the flat plate mold.

**Data Acquisition:** With the reference frame established, the CMM proceeded to acquire the coordinates of the target points. During data acquisition, the part program directed the probe to move in a systematic order across the panel's optical surfaces. With the probe positioned approximately  $1/4$ " off (in either the + or - X direction) of the intended surface, the CMM moved and positioned the probe to the desired Y and Z coordinates. Once in position, the probe then approached the surface in the desired X direction until contact was made. Upon contact, the CMM first recorded the actual X, Y, Z coordinates of the probe tip's center. Because the location of the target points for the flat panel were all on flat surfaces, the CMM could easily approach the points in a normal direction. This simple surface shape allowed for a simple "**ball radius compensation**" to be calculated (Fig 7) by the CMM which translated the X, Y, Z coordinates of the probe tip center, in the approach direction, to the surface of the probe tip. This resulted in the X, Y, Z of the actual contact point. In a like manner, the CMM obtained the coordinates of all target points on all the intended surfaces of the flat panels.

### Flat Panel Mold

**Reference Frame Establishment:** As mentioned above, we had no choice but to dimensionally map the mold halves separately. Although the mold surfaces are mirror images of the part surfaces, features found on the cavity half of the mold may not be present on the core half. For this reason, reference frame establishment on the flat panel mold halves was modified from that on the flat panels. The core of the mold happened to have all the surfaces required to establish the frame of reference in the same manner as the panel, using the optical surface, arch-plate surface, and sill edge surfaces. The cavity, on the other hand, has no arch-plate surface and it only had a couple of very small surfaces at the sill edges. The cavity does have an optical surface, although it is offset from the core side optical surface by either  $1/2$ " or  $3/4$ ". To establish the "same" frame of reference then on the cavity half, we had to make use of other features of the mold.

During operation, the mold halves are aligned by tapered guide pins on one half, and tapered sockets on the other half (Fig 8). When establishing the frame of

reference on the core half, the intersections of the axes of the guide pin sockets with the parting plane were found. The positions of these intersection points were then recorded relative to the established frame of reference. In this manner, the distance from the mid-line and the arch-plate surface to the intersection points was found. On the cavity half, the primary plane and mid-line were found using the optical surface and the small sill edge surfaces, respectively. A temporary arch-plate location was assumed, in order to establish a temporary frame of reference. The intersections of the axes of the guide pins with the parting plane were then found. Based on these intersection point locations, appropriate translations were performed to bring the cavity half's frame of reference into alignment with the core half's.

During the 1991 DM effort, in order to have more confidence in bringing the data for the core together with the data for the cavity, 12 additional target points (six on the core, six on the cavity) were identified for the mold. Six widely spaced parting plane points on the core would be acquired, as would six similarly located parting plane points on the cavity. When the data halves were brought together, the two sets of six points should have been coincident. In practice, this did not happen. Although the 1991 DM data was usable, lessons learned during that effort resulted in external tooling spheres being used in mold mapping in the 1992 effort. The reasons why, and the adjustments made will be discussed in detail later.

**Data Acquisition:** After reference frame establishment, the dimensional mapping of the flat panel mold halves proceeded much in the same manner as on the panels. The probe was positioned over a target point in Y and Z, and then approached in the X direction until contact was made. The same ball radius compensation was performed, and the contact point coordinates were recorded.

### Conical Panels

The conical panels were staged on the CMM as shown in Fig 9. The cone was placed nose down on the CMM table, so that all desired target points were accessible by the probe. The cone was held in place with a simple clamping arrangement that applied a slight pressure to the aft faces of the two aft tabs (however, Fig 9 shows the clamps on the forwrd tabs). As with the flat panels, the CMM operator needed to manipulate the probe to contact several points on the cone so the CMM knew where the cone was in its measuring volume. The operator touched three points on the flat, semi-circular aft edge surface, two points on each of the flat sill edges, and three points on the outer optical surface. The part program already had the nominal dimensions of the cone, so with these operator-supplied points as input, the part program could then take over the mapping procedure.

**Reference Frame Establishment:** The CMM first established a primary plane by touching seven widely spaced points on the flat, semi-circular aft edge (Fig 10). A best-fit plane was then calculated through the seven points, and this

was defined as the  $Y = 0$  plane. Next, three points were touched on each of the flat sill edges. A best-fit plane was calculated through the six points, and the intersection of this plane with the primary  $Y = 0$  plane was defined as the X axis. This fixed the  $Y = 0$  plane in rotation, and defined the  $Z = 0$  location on the  $Y = 0$  plane. Next, the probe touched seven equally spaced points on the outer optical surface, at  $Y = -0.25$ ". A best fit circle was generated through the seven points, and the center point of the circle calculated and translated in Y and Z to the X axis. This procedure produced a conical panel reference frame that had its origin at the intersection of the aft edge plane and the axis of the cone described by the outer conical surface. This procedure for reference frame establishment was used on all conical panels, and a slightly modified version was used on the cone mold.

**Data Acquisition:** With the reference frame established, the CMM proceeded to acquire the coordinates of the target points. During data acquisition, the part program directed the probe to move in a systematic order around the cone's surfaces. A short discussion of the target point grid for the cone is in order here (ref Fig 3).

**Sill Edge Target Points:** The sill edge target points were arranged in a one inch by one inch grid. The grid was defined by the intersections of two sets of section cuts. One set of sections were parallel to the aft edge surface, spaced one inch apart, starting at 0.25" forward of the aft edge. The other set of sections were parallel to the flat sill edge surface, spaced one inch apart, starting at 0.25" from the sill edge surface. This grid defined four stations (or rows) of target points on each of the four curved sill edge surfaces, with each station having 13 points in the aft to forward direction.

**Optical Surface Target Points:** The optical surface target points were arranged in a one inch by five degree grid. The grid was defined by the intersections of two sets of section cuts. As on the sill edges, one set of sections were parallel to the aft edge surface, spaced one inch apart, starting at 0.25" forward of the aft edge. The other set were radial sections originating on the cone's axis. These included a centerline section, and sections from +65 degrees from centerline to -65 degrees from centerline, at 5 degree increments. This grid defined 27 stations of target points, with a varying number of points in each station, counting from aft to forward. The centerline station had 13 points, while the  $\pm 65$  degree stations only had 3 points each.

At the sill edges, the CMM acquired data by positioning the probe at the desired Y and Z coordinates. Once in position, the probe then approached the surface in the desired X direction (either inboard or outboard) until contact was made. At the optical surfaces, the CMM positioned the probe at the desired Y coordinate, and then approached the surface along the radial direction, toward (or away from) the cone axis. Upon contact, the CMM first recorded the actual X, Y, Z coordinates of the probe tip's center. As with the flat panels, the simple "ball

**radius compensation**" (ref Fig 7) was calculated by the CMM which translated, in the approach direction, the X, Y, Z coordinates of the probe tip center to the surface of the probe tip. In a like manner, the CMM obtained the coordinates of all target points on all the intended surfaces of the conical panels. However, unlike the flat panels, where approach by the probe was normal to the surface, the actual contact on the cone surfaces was not completely normal to the approach direction. This effect is called "**ball tangency error**" and was compensated for during the reduction of the conical data. This will be discussed later in this paper.

## **Cone Mold**

**Reference Frame Establishment:** As with the flat panel mold, the cone mold halves had to be mapped separately. Also like the flat panel mold, the parting plane and tapered pins and sockets were used to align the two reference frames with each other. The core half of the cone mold had all features necessary to establish its reference frame in the same manner as the conical panel (Fig 11). Intersection points of the socket axes and the parting plane were also found so that these locations could be used to assist in reference frame establishment on the cavity half. The features used on the cavity half were the conical surface, parting plane, and the tapered pin axes. Through translations of feature locations, the cavity reference frame was brought into alignment with the core halves.

Again as with the flat panel mold, 12 additional parting plane target points (six on the core, six on the cavity) were identified for the cone mold, to assist in bringing the two halves of data together during data reduction. Also as with the flat panel mold, external tooling spheres were used in the 1992 DM effort to do a better job of bringing the data halves together.

**Data Acquisition:** After reference frame establishment, the dimensional mapping of the cone mold halves proceeded much in the same manner as on the panels. At the sill edges, the probe was positioned over a target point in Y and Z, and then approached in the X direction until contact was made. The ball radius compensation was performed, and the X, Y, Z coordinates were recorded. At the optical surfaces, the CMM positioned the probe at the desired Z coordinate, and then approached the surface along the radial direction, toward (or away from) the cone axis until contact was made. The ball radius compensation was performed, and the X, Y, Z coordinates were recorded. In a like manner, the CMM obtained the coordinates of all target points on all the intended surfaces of the cone mold halves. As with the conical panels, the ball tangency error encountered was compensated for during data reduction.

## **Data Reduction and Post-Processing**

The data for each of the panels and mold halves was delivered to WL/FIVR as ASCII text files on computer diskette. The data was transferred to a workstation and converted to a format readable by PATRAN, a computer aided

engineering (CAE) software package marketed by PDA Engineering, Inc. Once read into PATRAN, the data could be processed in a 3D environment, making the task of data reduction and post-processing easier to visualize (Fig 12-14). The data reduction procedure essentially consisted of calculating thickness values and overall dimensions from the point coordinates. The panel thickness values were subtracted from the mold thickness values to yield through-the-thickness shrinkage values. Panel overall dimensions were subtracted from mold overall dimensions to yield overall shrinkage. The post-processing basically entailed creating contour plots and X-Y plots of thickness and shrinkage results (Fig 15-16).

**Flat Panels and Mold:** Since the CMM probe had approached the flat panel and mold surfaces in a normal direction, the data delivered was coordinates of actual contact points. Furthermore, the grid of target points was constructed such that the points on the core side of the mold had the same Y and Z coordinates as the points on the cavity side (ref Fig 6). Thickness calculations were performed by finding the X displacement between the core points and the cavity points. The length measurements were determined by finding the difference in Y between the points on the arch end of the panel and the points on the gate end of the panel. Likewise, width measurements were determined by finding the difference in Z between points on opposite sill edges. Typical results for the flat panels are shown in Fig 16.

**Conical Panels and Mold:** The thickness and overall dimension calculations for the cones and the mold required additional calculations because of the ball tangency error noted above. Fig 17 shows an exaggerated blow-up of the probe tip contacting a small portion of the center line section on a cone. The probe approaches the target point T at a constant Z value, and toward the cone axis. Instead of contacting point T however, actual contact is made at point A. The CMM is keeping track of the probe tip center O, and upon contact performs the ball radius compensation that results in the coordinates of point C being recorded. The point recorded is short from the target point T by the distance "d". If not corrected, the result would be panel data that showed a thickness greater than actual, and mold data that showed thickness less than normal. The correction applied was to further translate the coordinates the additional distance "d". There were several reasons this correction was carried out during the data reduction instead of internally to the CMM including: programming difficulties, CMM scheduling, and the fact that the correction seemed simple enough to take care of in the data reduction.

Once the cone and cone mold data were in PATRAN on the workstation at WL/FIVR, the ball tangency error was corrected. The correction entailed generating lines through the "C" data points, finding the local angles required at the "C" data points, calculating the distance "d" required, and generating the new coordinates of the intended target points "T" (ref Fig 17). Once this was done, lines were generated through the new data points on the outer surface, and the normal thicknesses from the inside surface points to these lines were calculated.



Appropriate care was taken to account for the reversed direction of approach to mold surfaces as compared to panel surfaces. For the probe to approach the outer surface of the panel, it travelled toward the cone axis; while to approach the outer surface of the mold, it travelled away from the cone axis.

The overall dimensions of the cone and cone mold were found in much the same manner as in the flat panels and mold. Width measurements were calculated from the difference in X of corresponding points on opposite sills. Length measurements were calculated from Z differences between points on the aft edge surface and points on the forward faces of the forward tabs. The nose face of the cone was not used because it was not a molded surface, but a machined or sawed off surface. Additionally, the cone mold did not have a corresponding nose surface. Typical results for the cones are shown in Fig 18.

**Data From Separate Mold Halves:** Care was taken to establish reference frames on the mold halves such that the data obtained from one half was correctly orientated with data obtained from the other half. In theory, this was a sound approach, but in practice slight adjustments had to be made. When the mold data was reviewed, we found that the parting plane points from the core half of each mold were located internal to the plane defined by the cavity half parting plane points. In essence, that the mold halves were compressed together further than physically possible. This was attributed to the fact that the primary planes are best fit to points on a machined surface, and the best fit was different for the two halves. On a panel, only one primary plane was defined, and all data from the panel was taken relative to the one reference frame. On the molds, a primary plane is found for each half, and hence two separate reference frames are generated. An adjustment was in order, and the approach taken in 1991 was to translate all data points from one half until the parting plane points became as coincident as possible, without the parting planes penetrating one another.

The same approach was used during the initial stages of the 1992 DM effort. However, another complication arose. We knew that the cone mold had been scratched and then polished between the two DM efforts. We therefore expected to see slightly thicker cones and a slightly thicker cone mold cavity. We mapped the cones first, and did indeed see the increased thickness where the polishing took place. However, when we applied the same parting plane point adjustment to the cone mold data, we observed reduced thickness in the cone mold cavity as compared to the 1991 data. After checking the data and adjustments made for both efforts, it was decided to re-map the cone mold with external tooling spheres attached.

Three tooling spheres were attached to the external surfaces of each mold half (Fig 19, only two spheres are seen here, the third is hidden from view). The tooling spheres were calibration balls precision ground to within 0.000005" of perfect roundness. The mold halves were mapped as before, except that the CMM also calculated the three centers of the core tooling spheres relative to the core frame of reference, and the three centers of the cavity tooling spheres relative to

the cavity frame of reference. Then the mold was put together (Fig 20, two of the spheres are hidden from the view), as it would be just prior to molding, and the six centers of the tooling spheres were calculated relative to a single reference frame. When the mold data was brought up on the workstation, an adjustment in mold half positions could be made using the tooling sphere centers. When the adjustment was made, it was found that the parting plane points did not "pierce-through" each other. In fact, there was a slight gap (0.001" - 0.005") between five of the six sets of parting plane points. The gaps can be attributed to imperfections, such as unobserved high spots, in the parting plane. The lesson learned here was that in combining two separate halves of data, precise external surfaces need to be used as references.

Although the imperfect parting plane adjustment brought into question the validity of the 1991 DM data, results of the 1992 DM effort showed the same trends and magnitudes of shrinkage. This indicates that the errors in the values of the 1991 data are slight, and that the general approach used in applying the 1991 data to the CFT and CFT mold design was still sound.

### **Results Summary Of The '91 And '92 Dimensional Mapping Efforts**

It was found that staging a part only once for data acquisition is highly preferable to multiple stagings. If a part must be staged more than once, extreme care must be taken to ensure that the multiple sets of data can be accurately combined.

An attempt was made to confirm the thickness values calculated from CMM data by cutting up one of the dimensionally mapped cones, and using a micrometer to measure the thickness at a group of target points. The micrometer thickness readings were consistently within 0.001" of the dimensional mapping thickness values. However, the repeatability of the micrometer readings also varied by approximately  $\pm 0.001$ ", presumably from human factors and/or positioning the micrometer accurately in the same place.

The results of both efforts showed that the overall shrinkage (length, width) observed in the flat and conical panels was very close to the shrinkage quoted by resin manufacturers, even though the panels were molded using an atypical low pressure, long cycle process. The shrinkage observed for panels molded from plain vanilla polycarbonate was on the order of 0.007 inch/inch, essentially the same as the quoted 0.006 inch/inch.

Shrinkage through the thickness of the panels was not only much higher than quoted values (ie. 0.020 - 0.035 inch/inch), it also varied with location on the panels. The details of shrinkage observed and possible reasons for the shrinkage are described in Reference 2.

## **Conclusions**

Based on the same trends and magnitudes shown in both DM efforts, the use of a CMM to acquire data points for part measurement is determined to be a very reliable method.

The accuracy, repeatability, and automation capabilities of a CMM are very desirable in part measurement. When compared to techniques involving human manipulation of hand held instruments, the CMM is at least an order of magnitude more accurate and reliable.

The use of a CMM however, is orders of magnitude more complex and expensive than using hand held instruments. The automation capabilities can't be realized without a potential lengthy program development period. Additionally, CMM's are definitely not portable, they require installation in a controlled environment in order to realize the accuracy and repeatability benefits.

Extensive communication is required between the party wanting the part measured, and the party using the CMM to measure the part. Both parties in these efforts learned a great deal from each other.

## **Recommendations**

The data for these efforts has been acquired and processed over the last two years. Most recently, the flat plate mold data was processed in June 1993. Although the data has been processed and analyzed, a complete and final study and analysis of all the data should be accomplished.

The CFT mold fabrication was recently completed in June 1993, and the mold was dimensionally mapped as a final step in that fabrication. The CFT mold DM data should be analyzed and thickness values produced prior to CFT molding in August 1993.

Once molded, the CFTs should be dimensionally mapped using the same target point grid as the CFT mold.

The CFTs should also be thoroughly measured by hand, and a determination should be made as to whether or not dimensionally mapping transparencies by CMM is required.

Optical evaluation data for the CFTs should be correlated with the CFT dimensional mapping data. This correlation may prove valuable in possible future efforts to design transparencies to specific optical requirements.

## **References**

1. Pinnell, W. R., "Development of Directly Formed and Frameless Aircraft Transparency Technology, an Overview", to be published with the proceedings from A Conference on Aerospace Transparent Materials and Enclosures, San Diego, CA, 09-13 August 1993.
2. Chow, Dr Joe, "Analysis of Transparency Panel Shrinkage Characteristics and Their Application to Transparency Mold Design", to be published with the proceedings from A Conference on Aerospace Transparent Materials and Enclosures, San Diego, CA, 09-13 August 1993.

# **DIRECTLY FORMED FRAMELESS AIRCRAFT TRANSPARENCIES**

## **SUB SCALE DEVELOPMENT PANELS**

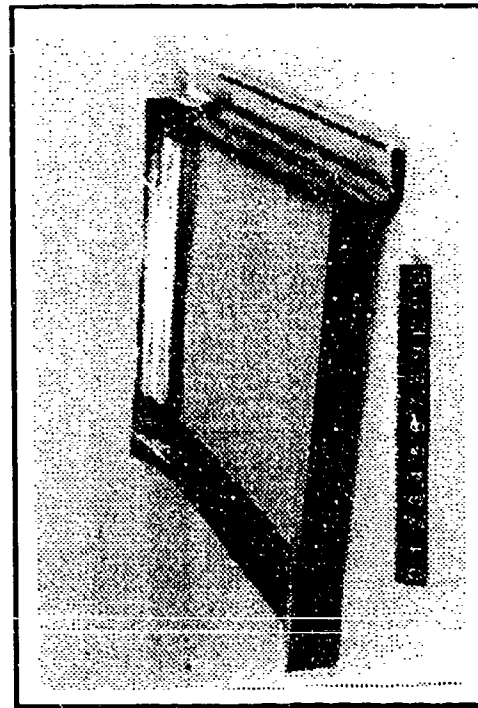


**Conical Panel**

**1/2 in thick**

**2 in thickened edges**

**basis for shrinkage tech.**



**Flat Panel**

**1/2 and 3/4 in thick**

**2 in thickened edges**

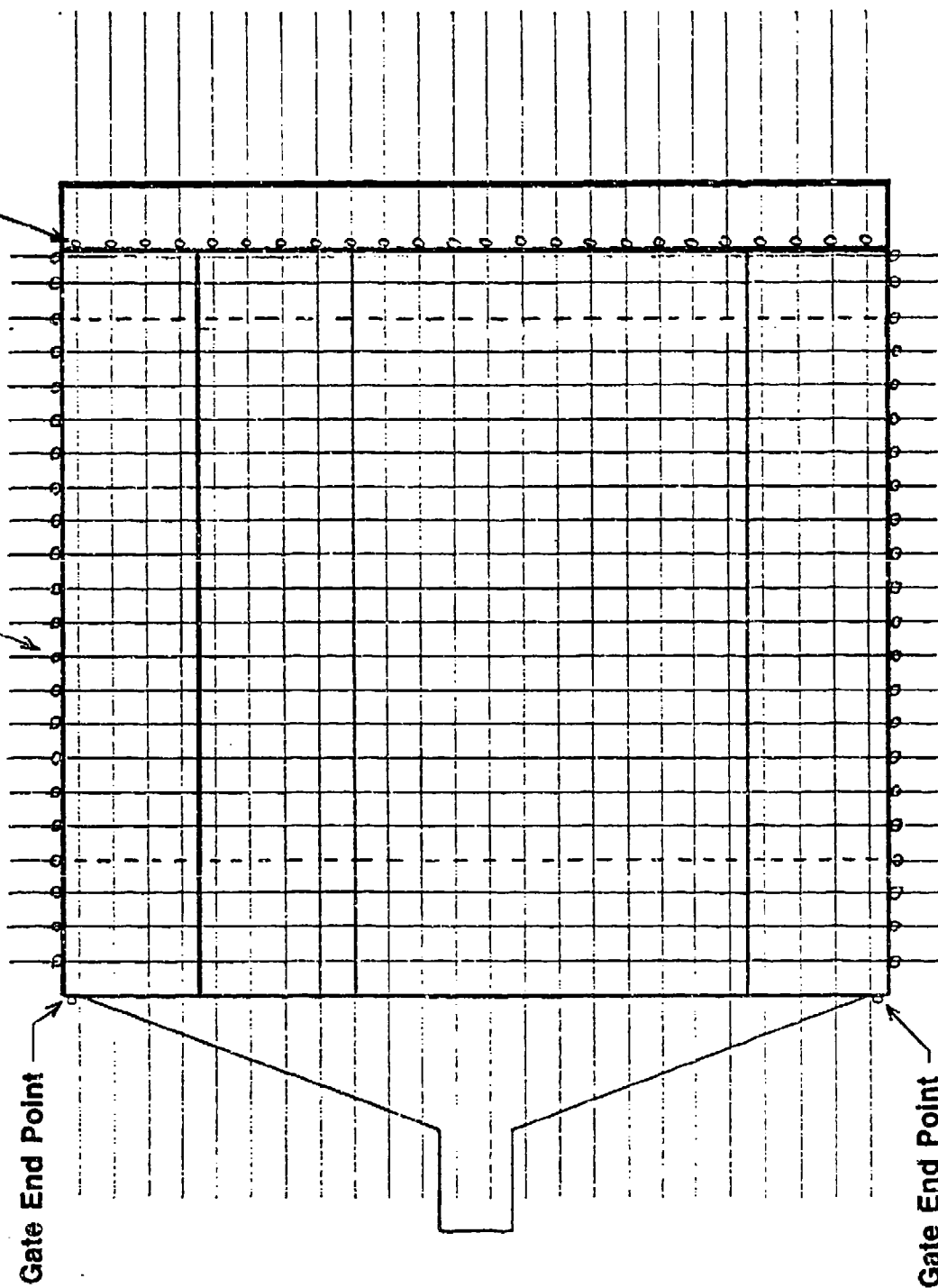
**Simulated Juncture**

**FIG 1**

Arch-Plate Surface  
Points (24 Typ)

Sill Edge Points (44 Typ)

Gate End Point



Gate End Point

FIG 2 - FLAT PANEL GRID LAYOUT

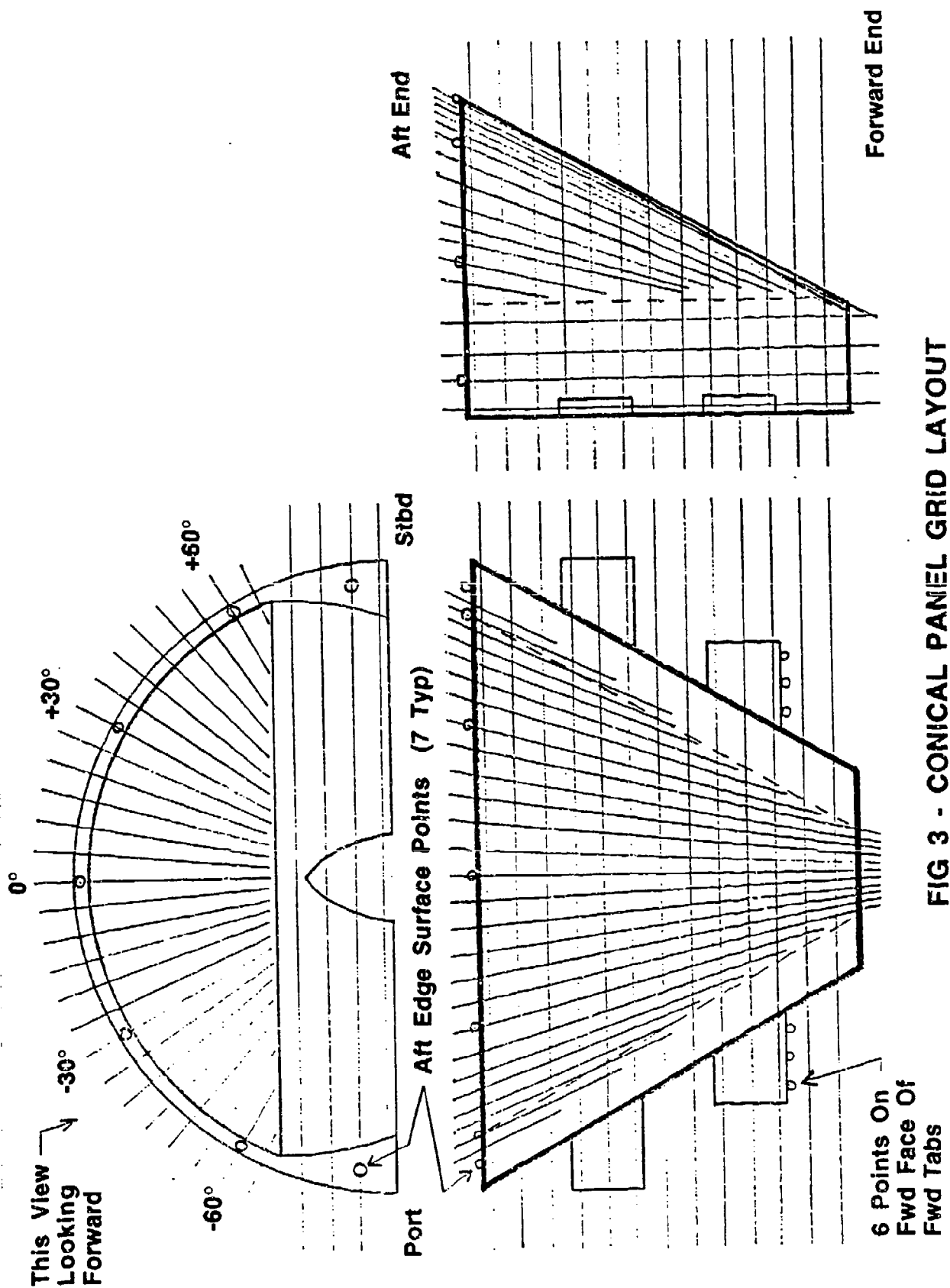


FIG 3 - CONICAL PANEL GRID LAYOUT

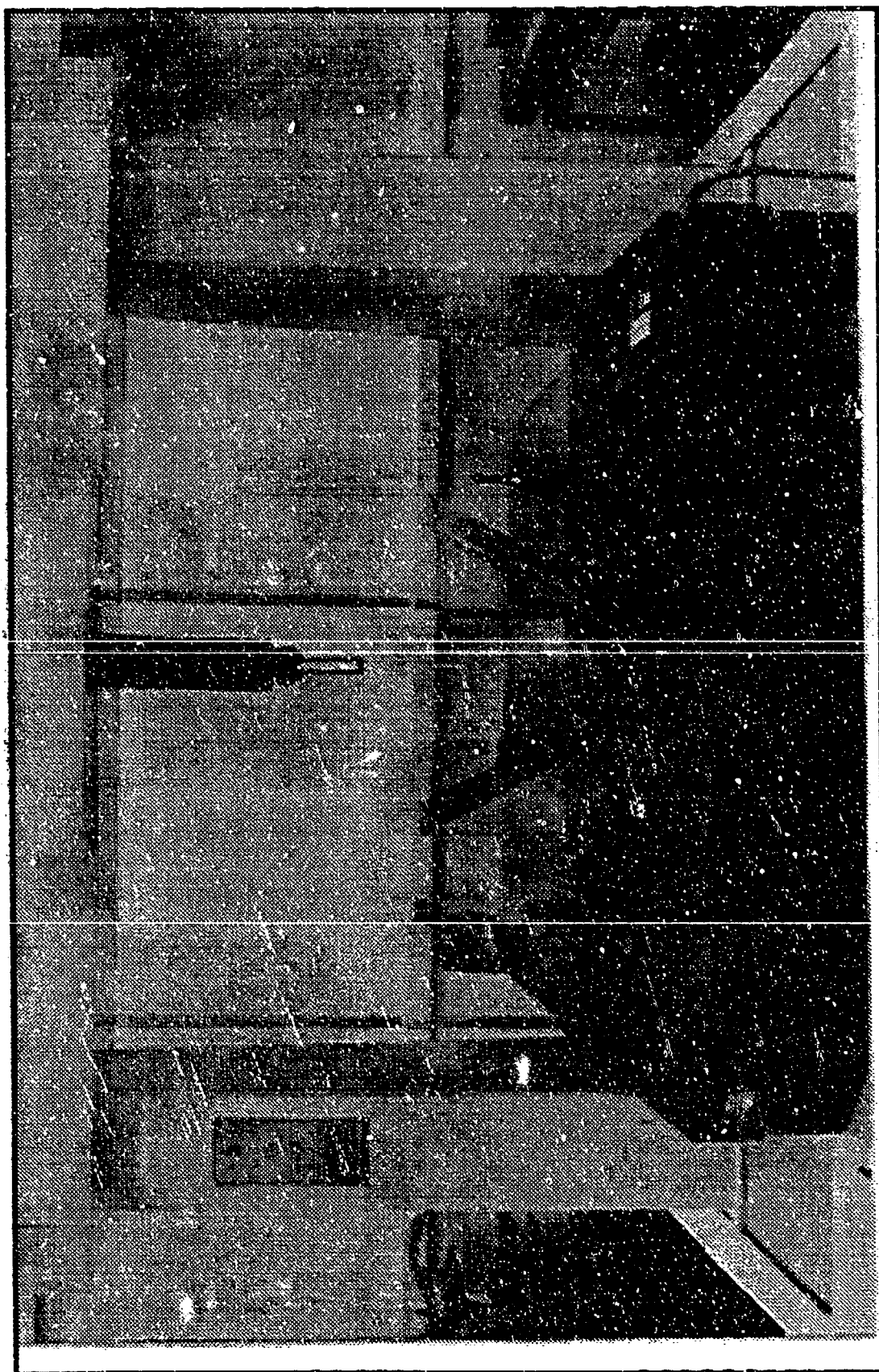


FIG 4 RING-BRIDGE COORDINATE MEASURING MACHINE



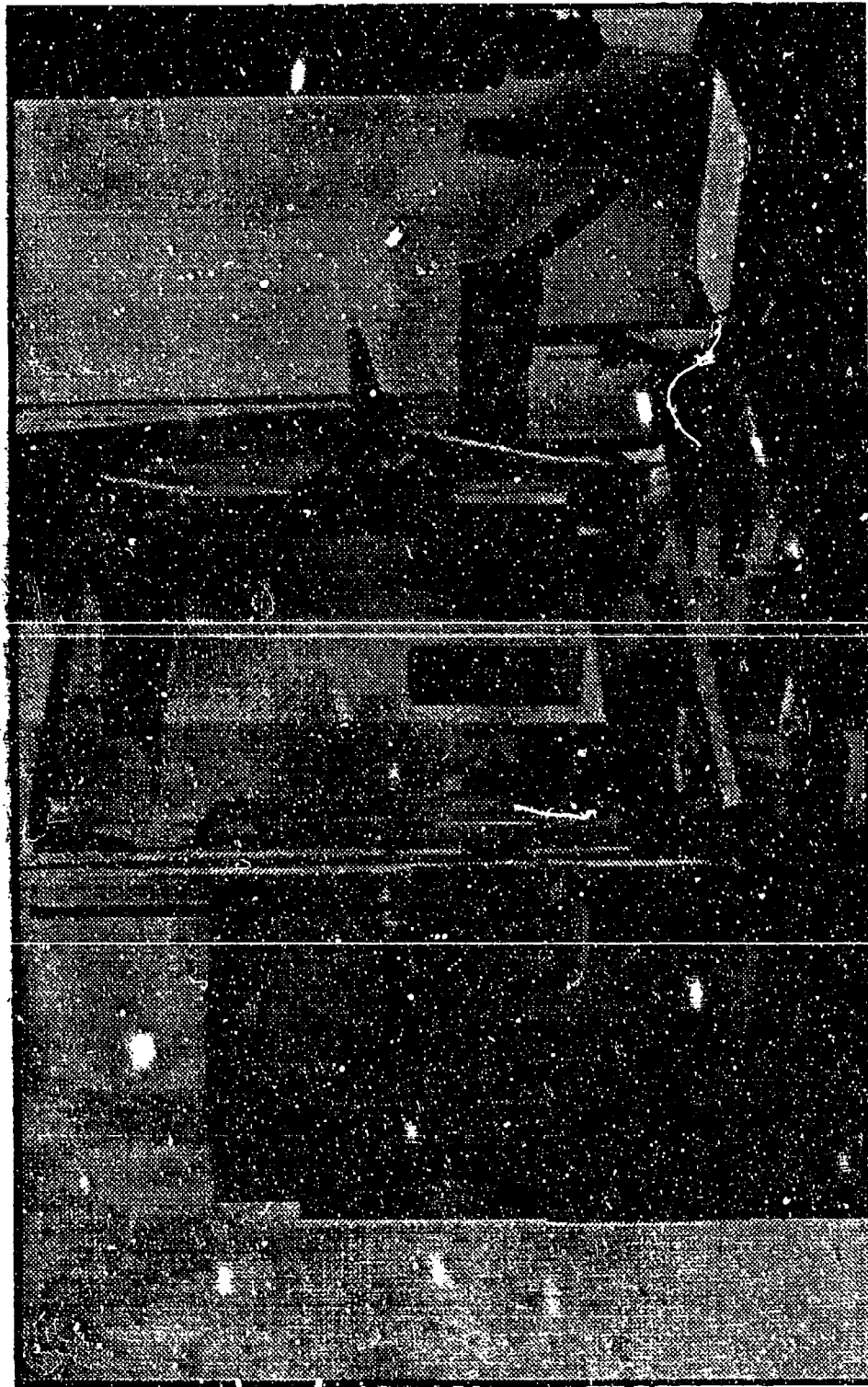


FIG 5 FLAT PANEL STAGING

Points Shown Used  
To Establish Frame  
Of Reference

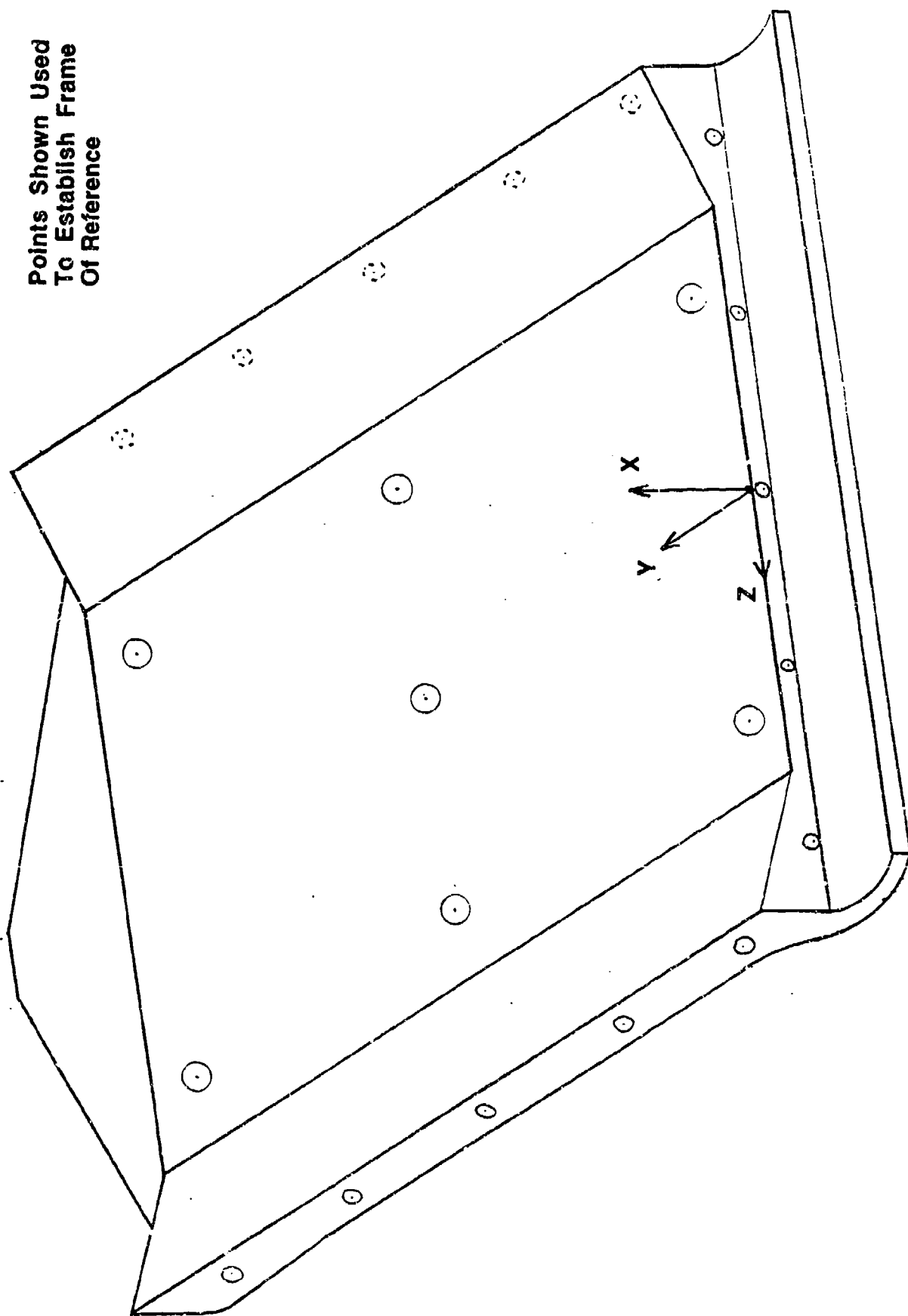
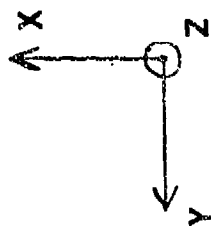
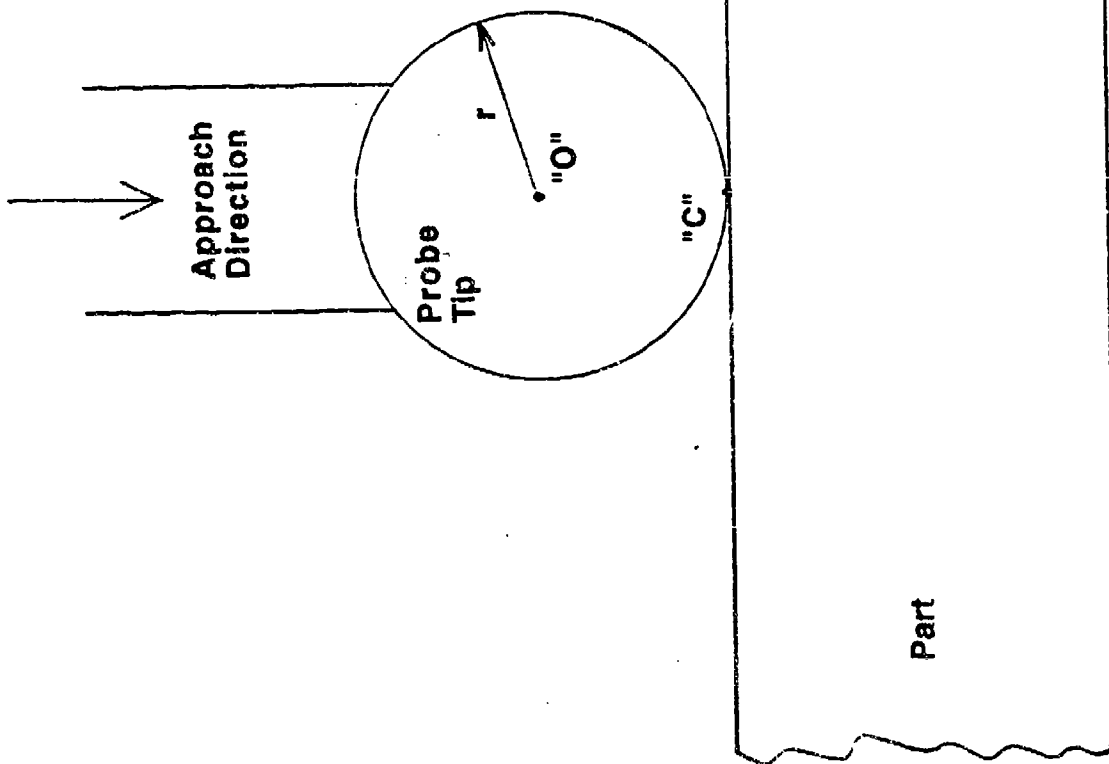


FIG 6 - FLAT PANEL REFERENCE SYSTEM



Not To Scale



The CMM keeps track of the probe tip center, "O". Upon contact with the part surface, the coordinates of "O" are translated in the approach direction a distance  $r$ .

The new coordinates are those of contact point "C". The coordinates of "C" are then recorded.

Here:  $X_c = X_o - r$

FIG 7 - BALL RADIUS COMPENSATION



FIG 8 FLAT PANEL MOLD - TAPERED SOCKET ON PARTING PLANE



FIG 9 CONICAL PANEL STAGING

Points shown used  
to establish frame  
of reference

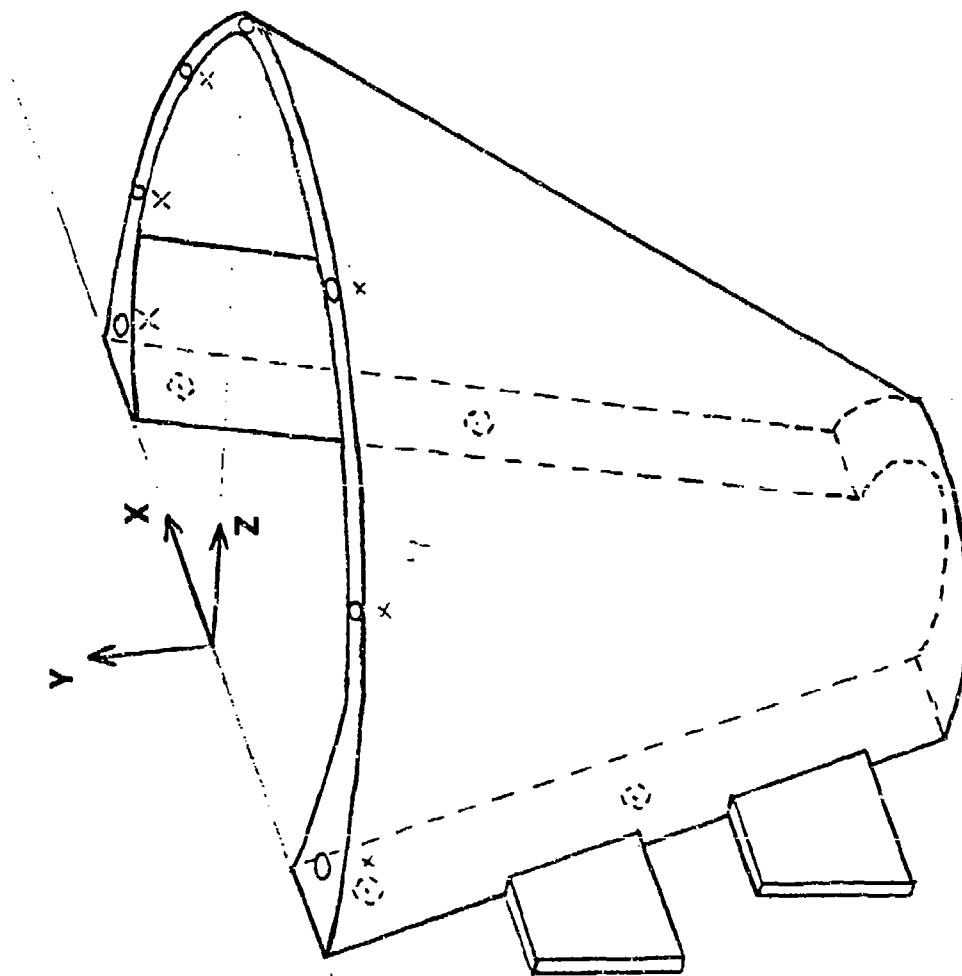


FIG 10 - CONICAL PANEL REFERENCE SYSTEM



FIG 11 CONICAL PANEL MOLD

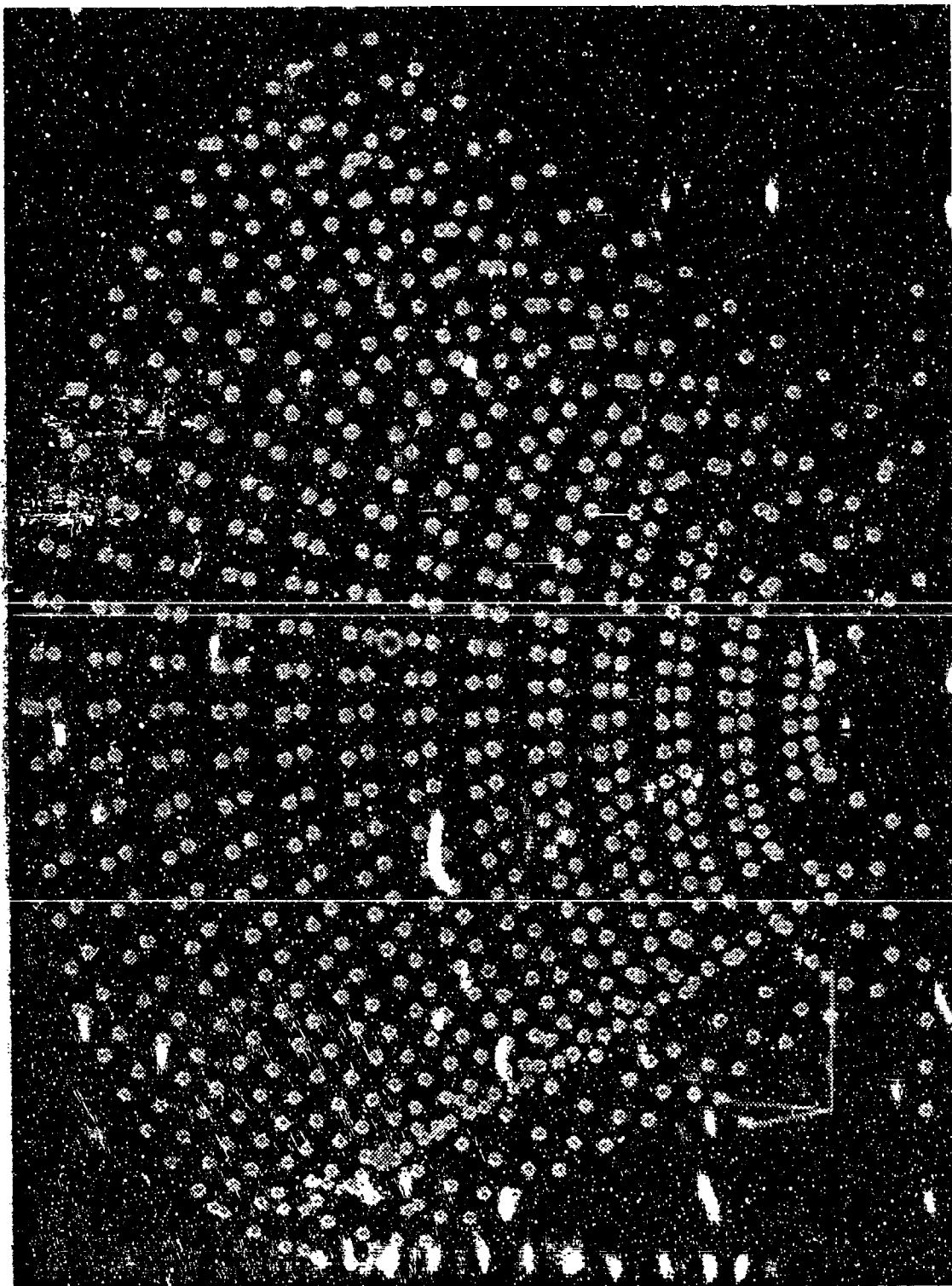


FIG 12 CMM DATA POINTS TRANSFERRED TO WORKSTATION



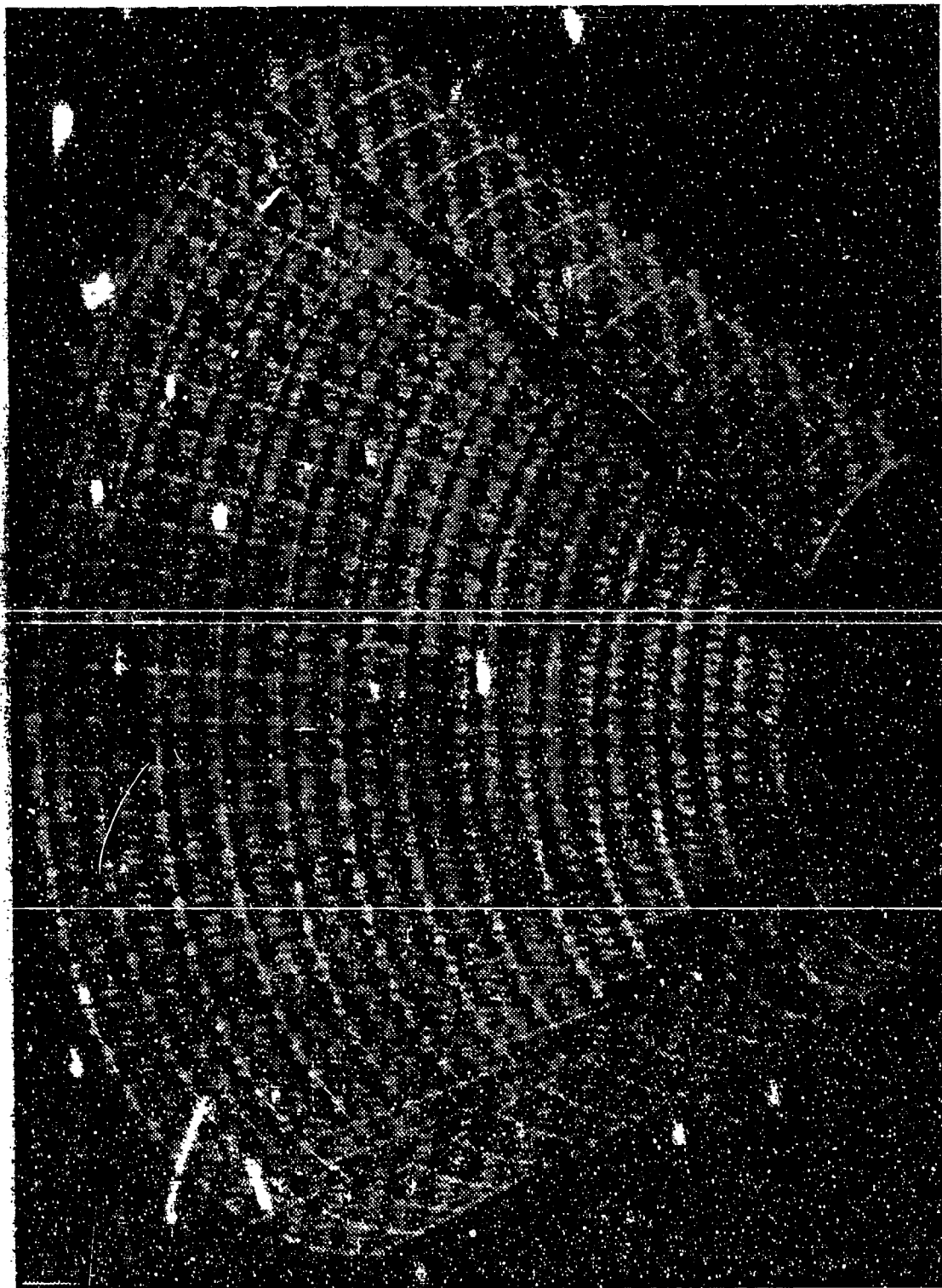


FIG 13 SURFACES CONTAINING CMM DATA POINTS

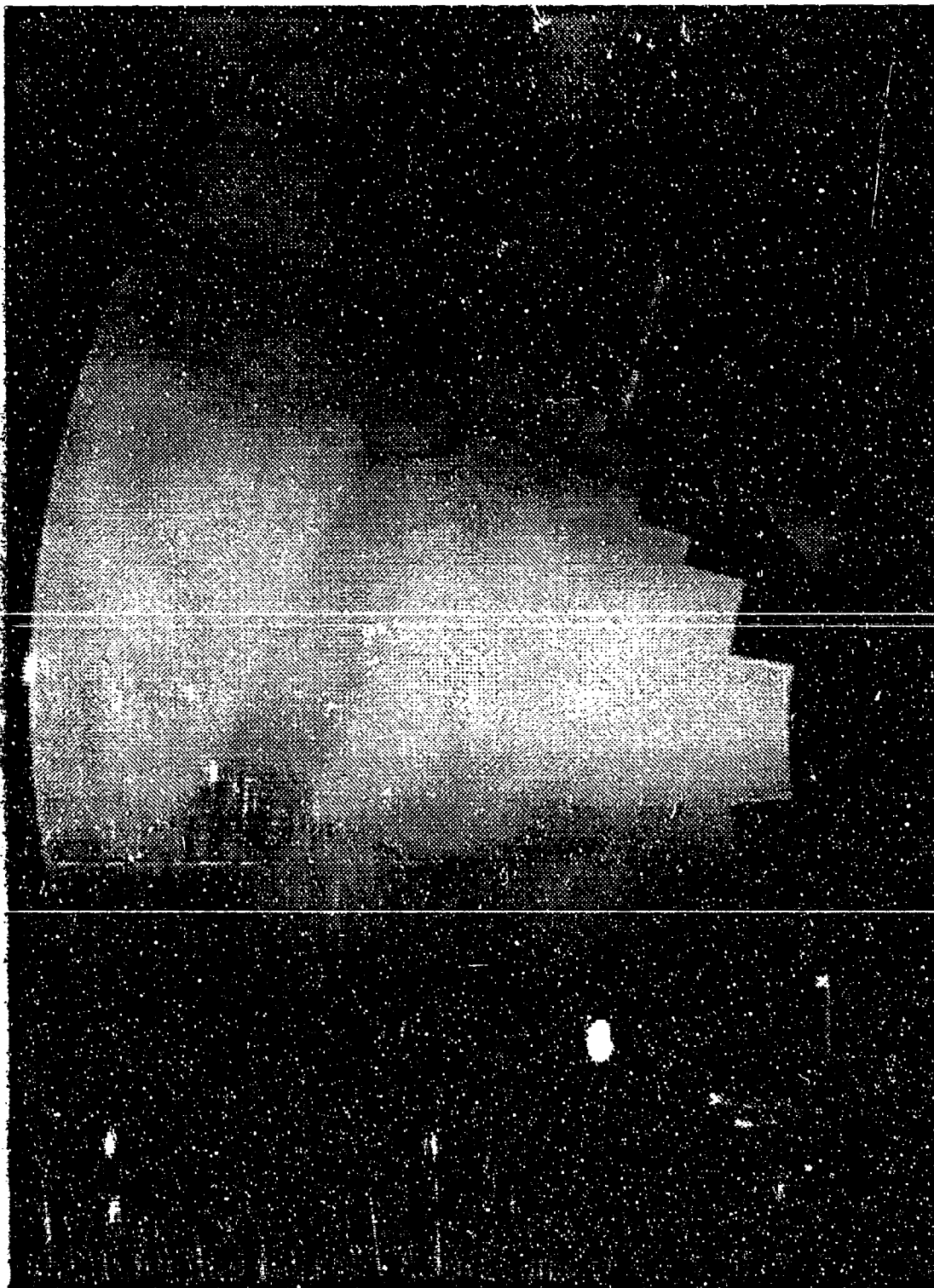


FIG 14 SOLID SHADING OF SURFACES CONTAINING CMM DATA POINTS

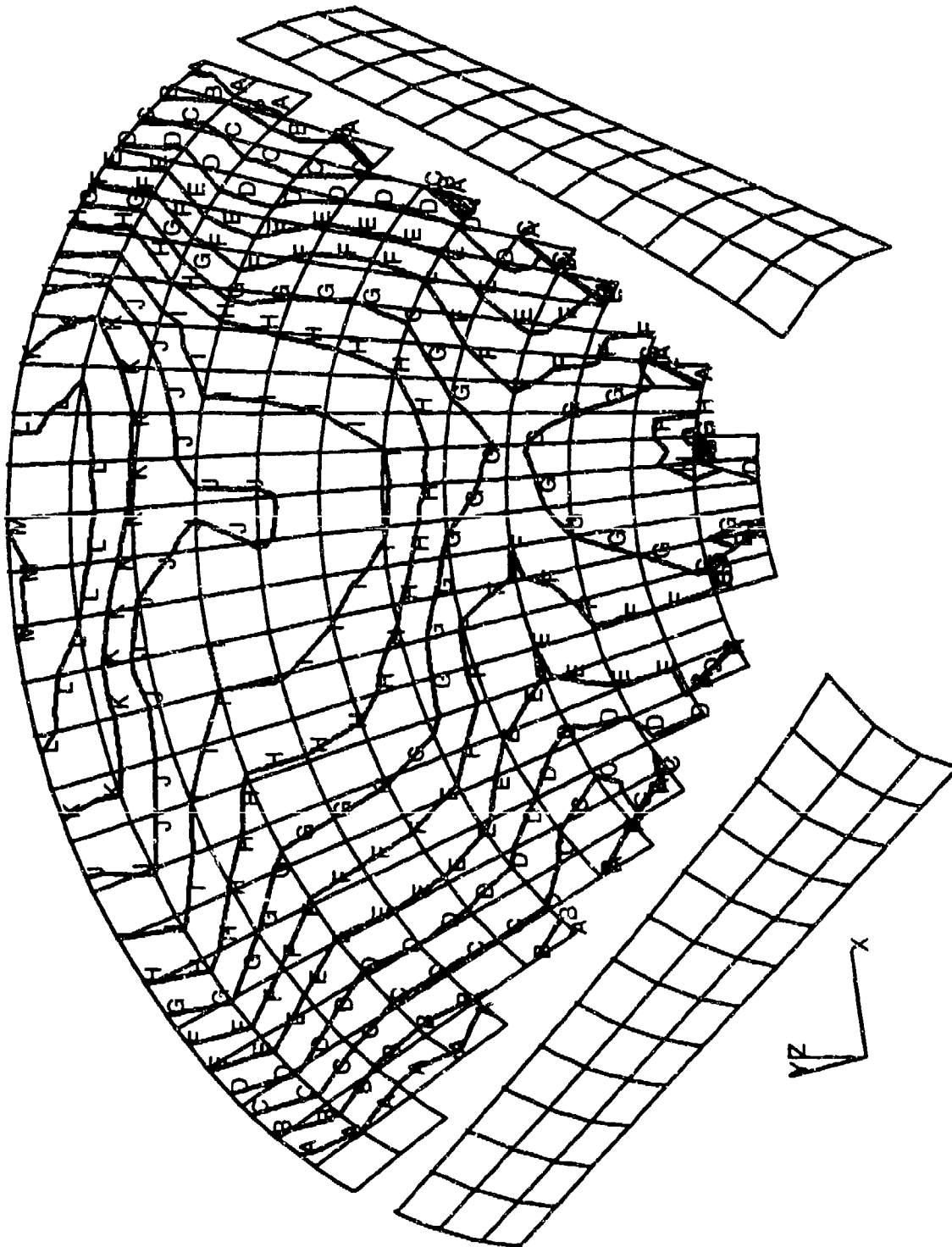
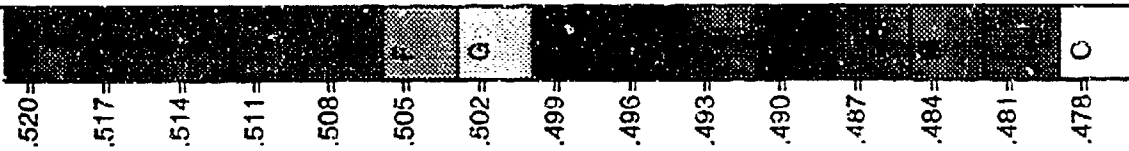


FIG 15 - CONTOUR PLOT OF CONE THICKNESS DATA

# 3/4" Flat Plates, Centerline

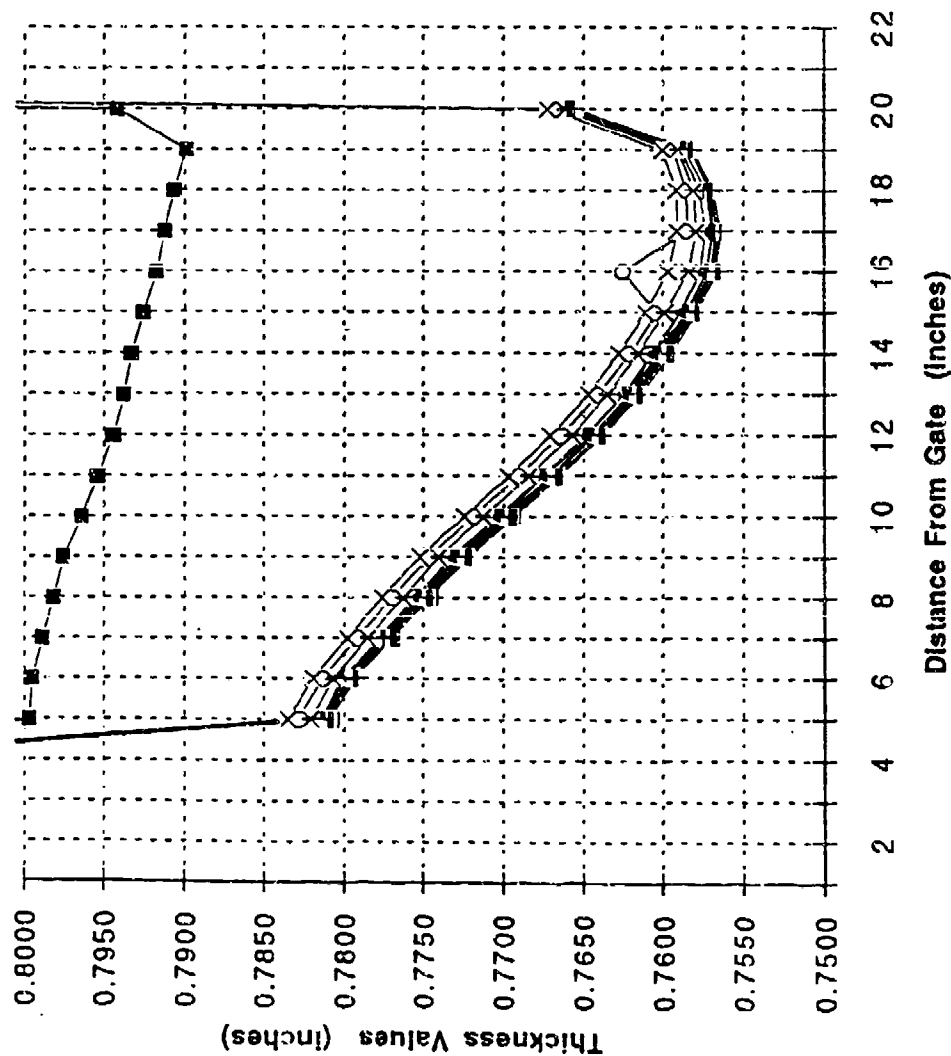


FIG 16 - X - Y PLOT OF FLAT PLATE THICKNESS DATA



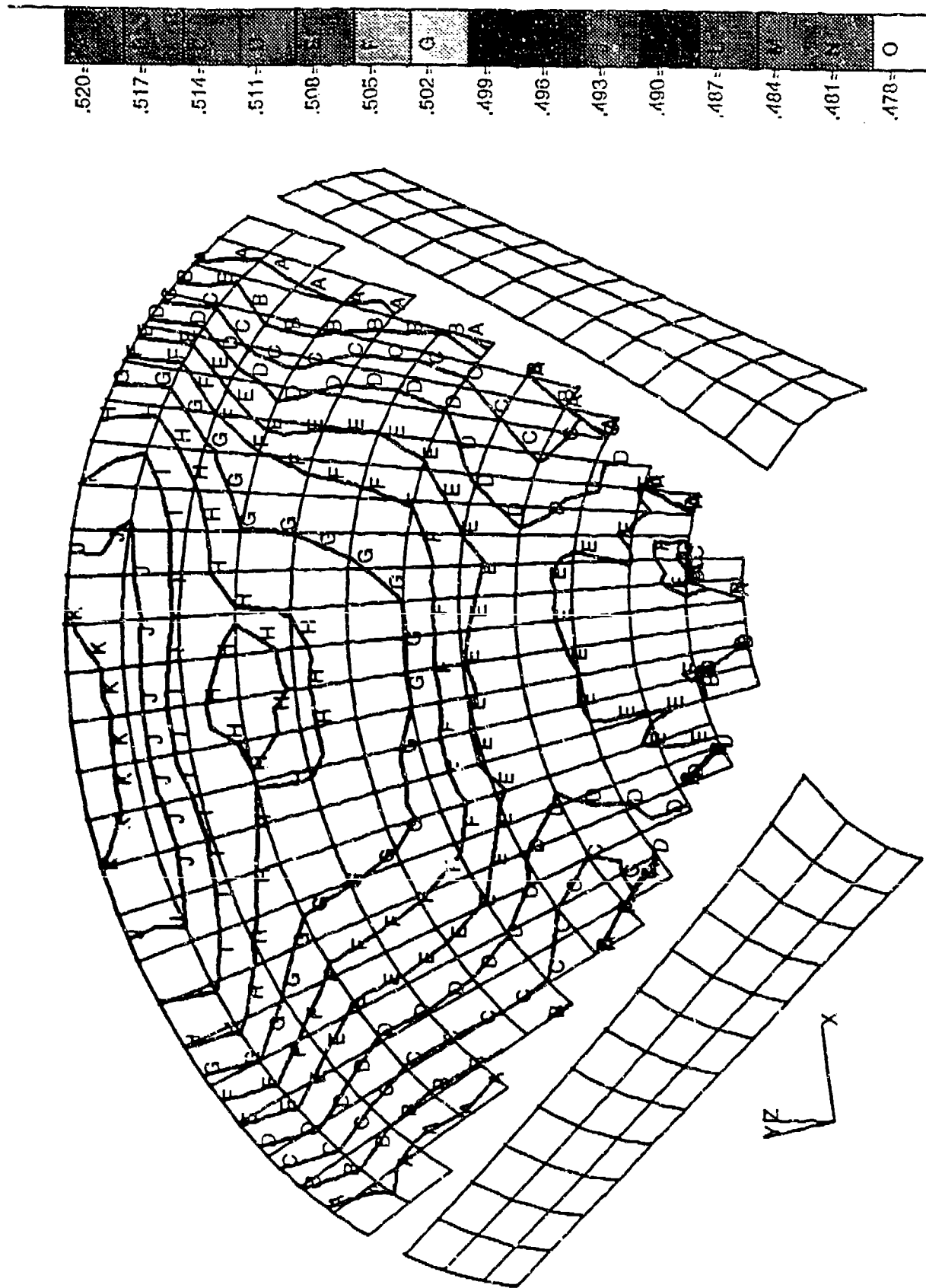


FIG 18 - TYPICAL TREND OF CONE THICKNESS RESULTS



FIG 19 CORE HALF OF CONE MOLD, WITH TOOLING SPHERES



FIG 20 CLOSED CONE MOLD, WITH TOOLING SPHERES



ANALYSIS OF TRANSPARENCY PANEL SHRINKAGE CHARACTERISTICS  
AND THEIR APPLICATION TO TRANSPARENCY MOLD DESIGN

J. G. Chow  
Florida International University

K. Roach  
University of Dayton

**ANALYSIS OF TRANSPARENCY PANEL SHRINKAGE CHARACTERISTICS  
AND THEIR APPLICATION TO TRANSPARENCY MOLD DESIGN**

Joe Chow  
Department of Industrial and System Engineering  
Florida International University  
Miami, FL 33199

Kevin Roach  
Aerospace Mechanics Division  
University of Dayton Research Institute  
Dayton, OH 45469

Conference on Aerospace Transparent Materials and Enclosures  
9-13 August, 1993 San Diego, CA

**ABSTRACT**

One of the objectives of the WL/FIVR frameless program is to mold the Confirmation Frameless Transparency (CFT), a research and verification windshield. Although the CFT was not designed as an actual flight item, it has a size and shape representative of a typical aircraft windshield. One of the many tasks involved in designing the CFT and the CFT mold was to attempt to compensate for the variable shrinkage found in large, thick-walled, directly formed transparency panels. Excessive thickness variation in the optical area would result in distortion of scenes viewed through the transparency. In order to produce closely toleranced, directly formed transparencies, it is essential to understand the relationships between molding process parameters and part shrinkage, and to apply that understanding to the design of the mold.

This paper includes an analysis of the shrinkage characteristics of large, thick-walled, directly formed transparency panels, and a review of the molding parameters used for each panel. The optimum molding conditions, based on overall molded quality are discussed. The potential causes of variable shrinkage were investigated, and correlations between shrinkage and process parameters are included. Additionally the application of shrinkage compensation to the CFT mold and to future transparency molds is presented.

## INTRODUCTION

The increasing demand for more efficient transparency design, low cost manufacturing, and longer service life has led to the concept of the directly formed frameless transparency program. The goal of the frameless transparency program is to eliminate the metal frame and all components necessary for attachment of the transparency panel to the frame. This can be achieved by forming the transparency directly from the molten plastic resin in a mold which permits thickness control to provide structural stiffness at transparency edges. The hardware facilitating a direct interface between the transparency and the aircraft can also be molded in place when the transparency is formed.

The direct forming method offers many potential advantages for aircraft transparency fabrication. It is capable of producing transparencies in large quantities at a low cost with practically no finishing operations. The surfaces of injection molded parts are usually as smooth as the surfaces of the mold cavity in which they are formed. Furthermore, the process allows tailoring of transparency thickness in the optical area to achieve optical quality and structurally adequate sills to accommodate transparency to aircraft interfacing. Compared to current forming techniques which are labor intensive and difficult to control, injection molding is primarily a one process technique in which part quality can be closely controlled and repeated.

To produce closely toleranced transparencies using a direct forming (i.e. injection molding) process, it is essential to be able to characterize part shrinkage after forming. This shrinkage data will then be used to compensate future molds to obtain parts of desired shape and size. To incorporate part shrinkage into the mold design, the current practice is to scale up the mold cavity dimensions uniformly by a constant shrinkage allowance factor, which in theory indicates how much the part will contract after it cools down. But except for simple shapes, some critical dimensions of the part will generally deviate from the compensated values as the shrinkage tends to vary with location.

The thickness distribution in the optical area is critical to optical quality of a transparency. Excessive thickness variation would result in distortion of scenes viewed through the transparency. Dimension control objectives for the Confirmation Frameless Transparency (CFT) included achieving design thickness in the optical area within plus or minus .008 inches and thickness gradients of less than .004 inches in 4.0 inches in any direction from any point in the optical area. This stringent requirement for dimensional accuracy has made compensation for variable shrinkage one of the most critical tasks during the mold design.

## OBJECTIVES

The goal of this research was to characterize shrinkage which occurred in thermoplastic injection molded panels in support of the directly formed frameless transparency program. The effects of molding process parameters on part shrinkage were examined and the causes of variable shrinkage in the part were investigated. Specifically, this study aimed to achieve the following objectives:

- (1) Correlate part shrinkage to molding parameters used.
- (2) Apply a shrinkage compensation to the CFT mold.

## LITERATURE REVIEW

The increasing use of injection molding in the plastics industry during the past few decades has spawned a great deal of research on part shrinkage after molding. Many studies have been carried out to understand and predict shrinkage for the purpose of sizing the mold. Part shrinkage for molding with different types of plastic resins, geometries, and process conditions have been documented in References 1 and 2. The results pertinent to this work are summarized here.

1. Part shrinkage is a local phenomenon, instead of a global one. Therefore, shrinkage values in a part would vary from location to location. For simple parts, the variation is minimal. But for large, thick-walled components, the variation can be quite significant. Since shrinkage is not uniform in all directions, this may often lead to many modifications of the mold and occasionally to a complete retooling.

2. Part shrinkage is a function of molding process conditions and possibly of geometric factors. It depends on the parameters such as packing pressure, melt temperature, injection pressure, packing time, screw speed, melt flow index, part thickness, and flow length. To completely characterize part shrinkage, the dominant process variables must be identified and the correlations between those variables and shrinkage established.

Typically, previous studies have been limited to molding of relatively small plastic parts. Shot sizes of only a few ounces in weight are common. Consequently, the findings from previous work may not be directly applicable to the mold design for large thick-walled parts, which is the main interest of this study.

## PROCESS CONDITIONS AND PART SHRINKAGE FOR PANELS

To further develop process conditions and study the shrinkage characteristics for large, thick-walled panels, WL/FIVRB has molded hundreds of process evaluation test panels during a number of injection molding trials. The process evaluation panels fabricated consist of two shapes: flat and conical panels, as shown in Figure 1. Both geometries possess key features of a frameless transparency: a constant-thickness optical area and thickened edge sections. The thickened edge sections simulate the potential to eliminate the frame currently used on aircraft transparencies. In addition, mechanical inserts could be molded into this region to facilitate direct attachment of the transparency to the aircraft. The development of the process conditions and the characteristics of part shrinkage are discussed as follows.

### Molding conditions:

- Injection pressure : 750 psi
- Packing pressure : 750 psi
- Melt temperature: 572 deg F
- Screw speed : 50 rpm
- Filling time : 7.5 - 11 sec.
- Cycle time : ~30 minutes
- Mold temperature: 200 deg F

The molding process for large, thick-walled parts is characterized by a low injection pressure and a long cycle time. The low injection pressure was selected to reduce residual stress in the part and a lower machine clamping force during molding. As a result, the filling and cycle times for large thick-walled panels are substantially larger than those for traditional molding processes. Molding with these parameters has produced panels with acceptable overall molded quality. Extensive coupon testing has also shown that impact resistance and other material properties of injection molded panels meet or exceed properties measured for extruded sheets of the same material.

To characterize through-the-thickness shrinkage after the part cooled to room temperature, a dimensional mapping study of molds and molded parts was undertaken at Sheffield Measurements Inc. of Dayton, OH. Dimensional mapping is simply a recording of the X,Y,Z coordinates of selected points on the surface of the parts and the molds, using a coordinate measuring machine (CMM). The raw CMM data was processed on a Silicon Graphics Iris workstation by Patran/PCL routines to produce part and mold cavity thickness data and contours. The shrinkage pattern of the part was then calculated by subtracting the part thickness from the mold cavity thickness. A typical tabular listing of shrinkage in thickness and shrinkage contours for a conical panel are shown in Figures 2 and 3, respectively. The details of dimensional mapping of flat and conical panels are described in Reference 3.

The general characteristics of part shrinkage from the dimensional mapping studies are summarized below.

- The thickness dimensional data revealed some unusual values and trends. Along the flow direction, the molded panels are generally thicker near the gate and become progressively thinner away from the gate, toward the aft plane. Along the transverse direction, variable shrinkage is also observed. Shrinkage is largest along the centerline and decreases gradually toward the thickened edges on each side.

- The overall dimensions of the panels also shrink after molding. The dimensional differences between a conical panel and the mold at five locations are shown in Figure 4. In general, the overall dimensional data revealed no extraordinary results. Values and trends shown in the data support the magnitude of a standard shrinkage factor that would typically be considered for clear polycarbonate.

- Part dimensions from panel to panel are fairly consistent. For both flat and conical panels, the variation in thickness is between 0.001" - 0.003" for the same location and similar molding conditions. This result illustrates one of the advantages in using injection molding to fabricate aircraft transparencies.

- The material on the thickened edges actually expanded, making the thickened edges thicker than the mold cavity itself. This is an unusual phenomenon but is not a major concern as the thickness of the thickened edges, used mainly for structural purposes, is not critical for the transparency's optical performance.

#### EFFECTS OF MOLDING PARAMETERS ON THE SHRINKAGE PATTERN

During the injection molding trials of transparent panels, several molding parameters had been varied. The effects of these varied parameters on part shrinkage are presented here.

Molding Machine Two different types of molding machines at two molding facilities have been used to mold flat panels; Hettinga and Envirotech (formerly Eimco) molding machines. One of the main differences between these two machines was the size of the nozzle/gate in the mold. The nozzle on the Hettinga machine was 0.525" in diameter, as opposed to the 2.25" diameter nozzle on the Envirotech machine. A smaller gate promotes shrinkage because it can freeze off prematurely and thus terminate part packing too soon. As a result, the shrinkage in the thickness direction showed two different patterns. The ones molded using the Envirotech machine showed larger shrinkage away from the gate,

with maximum shrinkage along the centerline being approximately 0.024". The flat panels molded at Hettinga showed less shrinkage variation in the optical area, with as much shrinkage near the gate as shrinkage away from the gate. The higher shrinkage near the gate was possibly caused by premature freezing of the gate as a result of smaller nozzle.

Resin material Several polycarbonate resins by different manufacturers have been used in the molding trials: Dow Calibre 200-4 and 300-6, and General Electric Lexan 4701. The shrinkage patterns for different resins are generally similar, except for slight differences in values. The Lexan 4701 exhibited more shrinkage than the Dow materials.

Packing Different degrees of mold packing has also been studied: fully packed and unpacked. Fully packed panels exhibited much lower shrinkage than those not packed (approximately 0.024" less) in the optical area.

Melt flow index (MFI) Dow Calibre 300 polycarbonate resin with three different indices: 4, 6 and 15, and an experimental resin with an MFI of 5.5 were molded. The larger the melt flow index is, the easier for the resin to flow in the mold. Thus the resin with larger index tends to fill the mold easier and shrink less. The melt flow index vs. shrinkage obtained for flat and conical panels show different results. For flat plates, the results in Figure 5 indicate that the larger the index, the lower the shrinkage. For conical panels, larger index did not cause lower shrinkage. This discrepancy may be caused by the interaction between MFI and the geometry. However, the effect of melt flow index on shrinkage is small and resins with different MFI show the same shrinkage trends in the optical section.

Geometry Two geometries have been tested: flat and conical panels. Even though the flow pattern during filling for both panels are quite different, the shrinkage patterns in the thickness are fairly similar: shrinkage is lower near the gate, and higher away from the gate. However, the shrinkage along the transverse direction are much more pronounced in the case of conical panels, probably due to higher pressure drop in that direction.

Part thickness There were two different thicknesses used in this experiment for flat panels: 0.5" and 0.75". Figure 6 shows that the shrinkage values along the centerline for 0.75" thick plates are slightly larger, but the difference is negligible. The higher shrinkage associated with thicker plates can be attributed to the fact that the cooling rate is reduced for larger thickness and consequently shrinkage increases.

This study indicates that, among different parameters investigated, cavity pressure (pressure inside the mold cavity) seems to be the most dominant molding parameter responsible for

the variable shrinkage in the thickness direction. Other parameters may also affect shrinkage, but their effects are either negligible or can be compensated easily. The mechanism for cavity pressure causing variable shrinkage is offered as follows:

As the molten resin flows through the gate and enters the mold cavity, the material that comes into contact with the mold wall will solidify immediately since the wall temperature is maintained around 200 deg F. The temperature and pressure of the resin will drop as it enters the gate and flows toward the aft portion of the part. The incoming new material will keep the solidified material thin and close to the wall near the gate. For the region far away from the gate, the molten material is cooler and pressure lower, the solidified plastic is thicker and can shrink. It is harder to push it against the wall. Therefore, the part away from the gate is less compact and exhibits more shrinkage.

The shrinkage variation due to pressure drop during packing is inherent in the process, especially for the geometry with long flow length. To reduce thickness variation, the best way is to understand the process, come up with a best estimate for variable shrinkage, and then try to correct it by design the mold cavity slightly differently from the intended part.

#### APPLICATION OF PANEL RESULTS TO CFT MOLD DESIGN

The shrinkage pattern for conical molds have been used to attempt to account for expected variable shrinkage in the CFT. The Confirmation Frameless Transparency, a research and verification windshield, has been designed to demonstrate the viability of injection molding in fabricating an aircraft transparency. The molding trials for the CFT are currently under way at Envirotech Molded Products at Salt Lake City, UT. The compensation is accomplished by adding the "thickness correction" to the target CFT optical area and then base the mold cavity surface on the thickness corrected CFT's outer mold line surface. The thickness correction factor used can be represented graphically by a 3-D curved surface, shown in Figure 7.

In that figure, the X-axis represents the normalized distance from centerline to sill. The Y-axis represents the normalized distance from the gate to the aft arch, along the centerline. The Z-axis represents the "expected" shrinkage, and therefore, the value to add to the design thickness at that location. The tapers in Figure 7 are to account for the shrinkage in the longitudinal and transverse direction, respectively. The detailed description for including thickness correction data in the optical area of the confirmation frameless transparency is given in Reference 4.

#### CONCLUSIONS AND RECOMMENDATIONS



- Based on the experimental results for process evaluation panels, it can be concluded that injection molding is a viable technique for fabricating aircraft transparencies.

- Two types of shrinkage were examined in this study: shrinkage in overall dimension and shrinkage through the thickness. While the shrinkage in overall dimensions can be compensated for by a constant shrinkage factor, the shrinkage compensation in part thickness can only be made by proper mold design.

- The relationships between process parameters and shrinkage for large thick-walled parts, in general, are similar to those for the traditional thin-walled parts. However, the long flow length typically encountered in large, thick-walled parts, such as aircraft transparencies, makes variable shrinkage a very pronounced phenomenon.

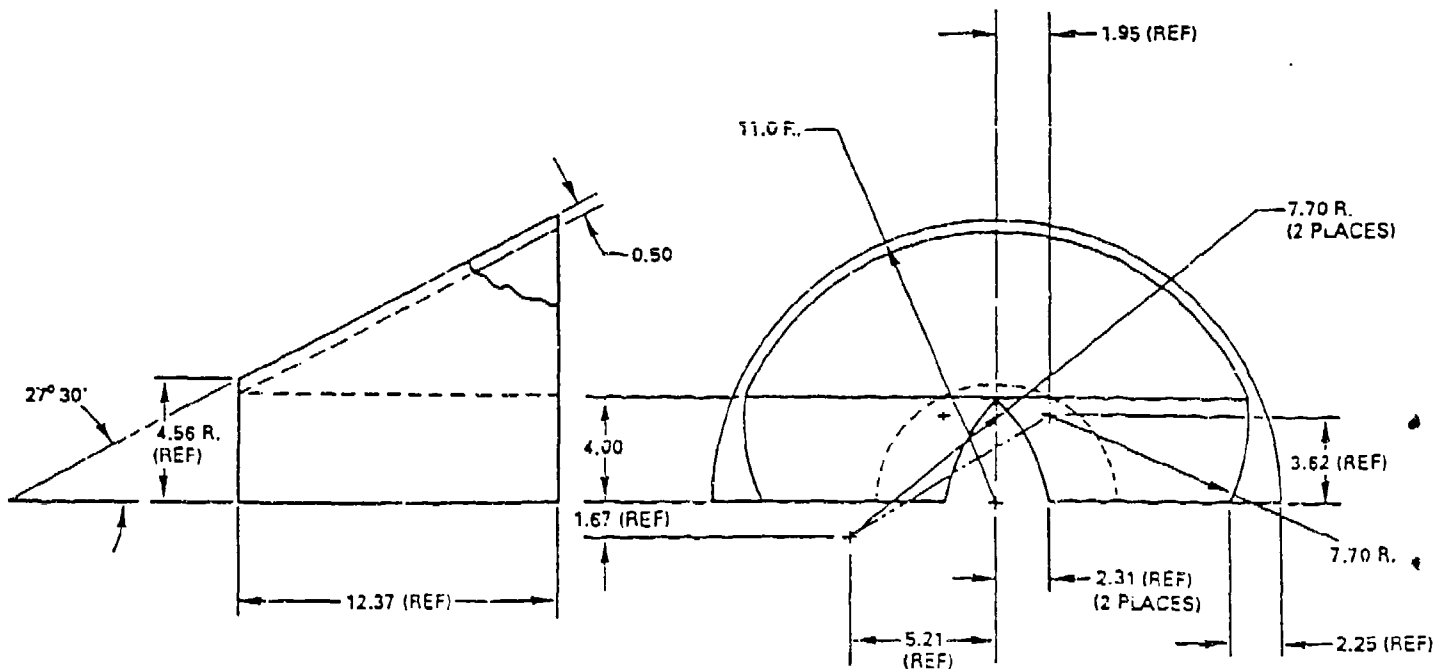
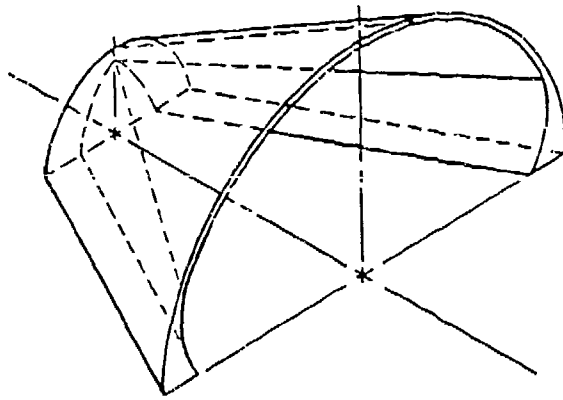
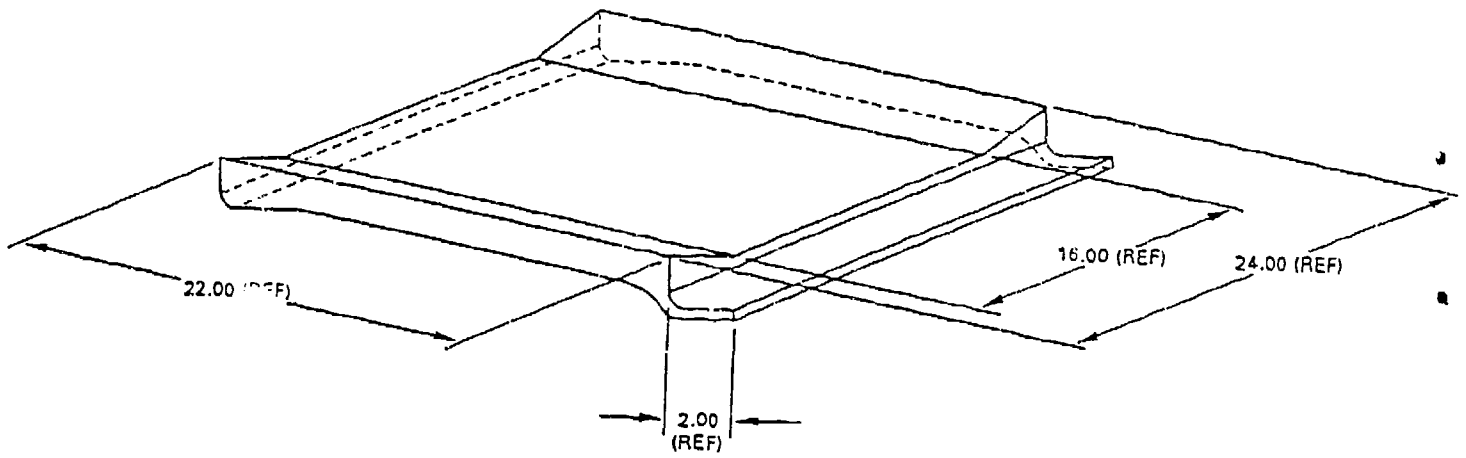
- Cavity pressure is the most dominant molding parameter for part shrinkage. Another parameter that may also influence shrinkage strongly is cavity temperature. To study its effect, a mold with variable temperature capabilities should be used. An ideal mold should have different temperature zones that can be controlled independently.

- An instrumented mold with the capability of measuring cavity pressure and temperature should be used to monitor pressure and temperature in the mold cavity and to correlate those parameters with variable shrinkage.

- The predictive procedure developed in this study will be refined after dimensional mapping results are obtained for the CFT's. In particular, magnitude of shrinkage correction for mold cavity will be determined for future frameless transparencies.

#### REFERENCES

- 1.D. Pierick, and R. Noller, "The Effect of Processing Conditions on Shrinkage" ANTEC '91, pp 252-258.
2. B. Miller, "Predicting Part Shrinkage is a Three-Way Street", *Plastics World*, December 1989, pp 47-52.
3. K. Roach, and J. Chow, "Dimensional Mapping and Shrinkage Characterization of Large Thick-Walled, Directly-Formed, Transparent Panels", 1993 Conference on Aerospace Transparent Enclosures and Materials, August 8-13 San Diego, CA.
4. M. Winfrey, "Method for Including Thickness Correction Data in the Optical Area of the Confirmation Frameless Transparency", General Dynamics Report FZM-719-014-010, January 31, 1992.



NOTE: ALL DIMENSIONS ARE IN INCHES

Figure 1. Flat and conical process evaluation panels

INCHES FROM AFT EDGE----		1.25"	2.25"	3.25"	4.25"	5.25"	6.25"	7.15"	8.25"	9.25"	10.25"	11.25"	12.25"
<==== PORT SILL =====>													
AFT	-26.1	-23.4	-22.9	-23.0	-22.7	-21.6	-19.8	-17.4	-15.1	-11.7	-7.0	-1.4	-6.1 FWD
PORT	-20.1	-16.4	-15.3	-14.4	-13.8	-13.1	-10.6	-8.4	-6.8	-3.5	0.3	8.9	-18.0 PORT
	-16.3	-15.7	-13.5	-13.7	-12.8	-12.3	-11.7	-10.5	-9.6	-8.3	-8.5	-7.9	-70.7
	-27.4	-23.7	-20.4	-17.6	-13.2	-9.2	-8.1	-7.5	-7.3	-7.0	-7.7	-11.6	-107.7
	-6.0	-4.2	-9.4										
	-2.1	-0.9	-0.8	-0.0	-0.2	1.3	1.3		-18.3				
	2.4	4.0	3.8	2.8	3.0	4.7	3.7	2.8					
	6.2	8.4	7.7	6.2	5.3	7.2	6.2	5.1	3.7	-15.4			
	9.5	11.6	10.7	9.2	8.4	9.8	8.6	6.8	5.9	4.2			
	12.0	14.6	13.0	11.6	10.8	11.9	10.9	9.0	7.6	5.6			
	15.7	17.0	15.5	13.9	12.9	13.8	12.5	11.0	9.5	7.4	5.2		
	18.2	19.0	17.5	15.5	14.9	15.3	13.9	12.4	10.8	8.9	6.1	6.1	
	20.2	20.8	19.0	17.4	16.5	15.3	13.9	12.4	12.0	10.0	7.9	6.6	
	21.6	22.3	20.6	18.8	17.9	16.7	15.2	13.5	12.0	10.8	7.8	6.8	-195.0
	22.2	23.3	21.6	20.2	19.1	17.7	16.2	14.3	12.8				-17.6
	21.7	23.8	22.5	20.8	19.8	18.5	17.0	14.5	13.4	11.4	8.7	5.9	2.5 CENTER
	21.4	24.2	23.2	21.6	20.4	19.0	17.4	15.7	13.9	11.8	9.0	5.8	2.8 (-----
	21.0	24.7	23.7	22.3	20.9	19.4	17.8	16.0	14.2	12.0	9.2	6.2	2.4 LINE
	17.9	21.8	20.5	21.7	20.8	19.2	17.6	15.9	13.9	11.9	9.3	6.7	-21.5
	21.4	24.5	23.8	22.3	21.1	19.5	17.9	16.1	14.1	12.2	9.6	6.6	-195.5
	22.5	24.6	23.0	21.5	20.5	19.1	17.5	15.3	13.7	11.6	8.1	6.6	
	22.6	24.1	22.4	20.7	19.6	18.1	16.4	14.2	12.9	10.7	7.1	5.7	
	22.2	23.1	21.3	19.5	18.5	17.0	15.1	13.3	11.6	9.1	6.1	5.7	
	20.9	21.8	19.8	17.7	17.0	15.4	13.8	12.0	9.9	7.4	4.7	-37.2	
	19.0	19.9	18.0	16.3	15.1	13.7	12.2	9.9	8.0	5.9	4.4		
	16.7	17.8	15.8	14.2	13.1	11.6	9.8	7.7	6.0	4.6			
	13.8	14.0	13.2	11.7	10.5	9.1	7.4	5.7	3.5	-6.7			
	10.4	11.7	10.2	8.8	7.5	6.3	4.9	3.3	-17.3				
	6.6	7.8	6.7	5.2	4.5	3.2	2.3						
	2.9	3.5	2.7	1.8	1.1								
	-0.9	-0.3	-6.3										
	-6.1	-6.3	-6.4	-6.5	-6.4	-6.8	-7.1	-7.5	-7.6	-7.8	-10.8	-13.9	-107.6
	-11.2	-11.2	-11.0	-10.6	-10.5	-11.0	-10.7	-10.5	-10.1	-9.5	-11.8	-11.4	-73.8
	-10.4	-15.1	-15.0	-15.7	-15.2	-14.8	-11.1	-10.4	-9.1	-6.4	-2.3	4.0	-20.8 FWD
AFT	-23.6	-21.5	-21.8	-23.5	-20.5	-23.1	-22.5	-20.8	-18.8	-15.8	-12.0	-6.7	-11.2 STBD
STBD													
<==== STBD SILL =====>													

Figure 2. Shrinkage data for conical panel (in thousandth of an inch)

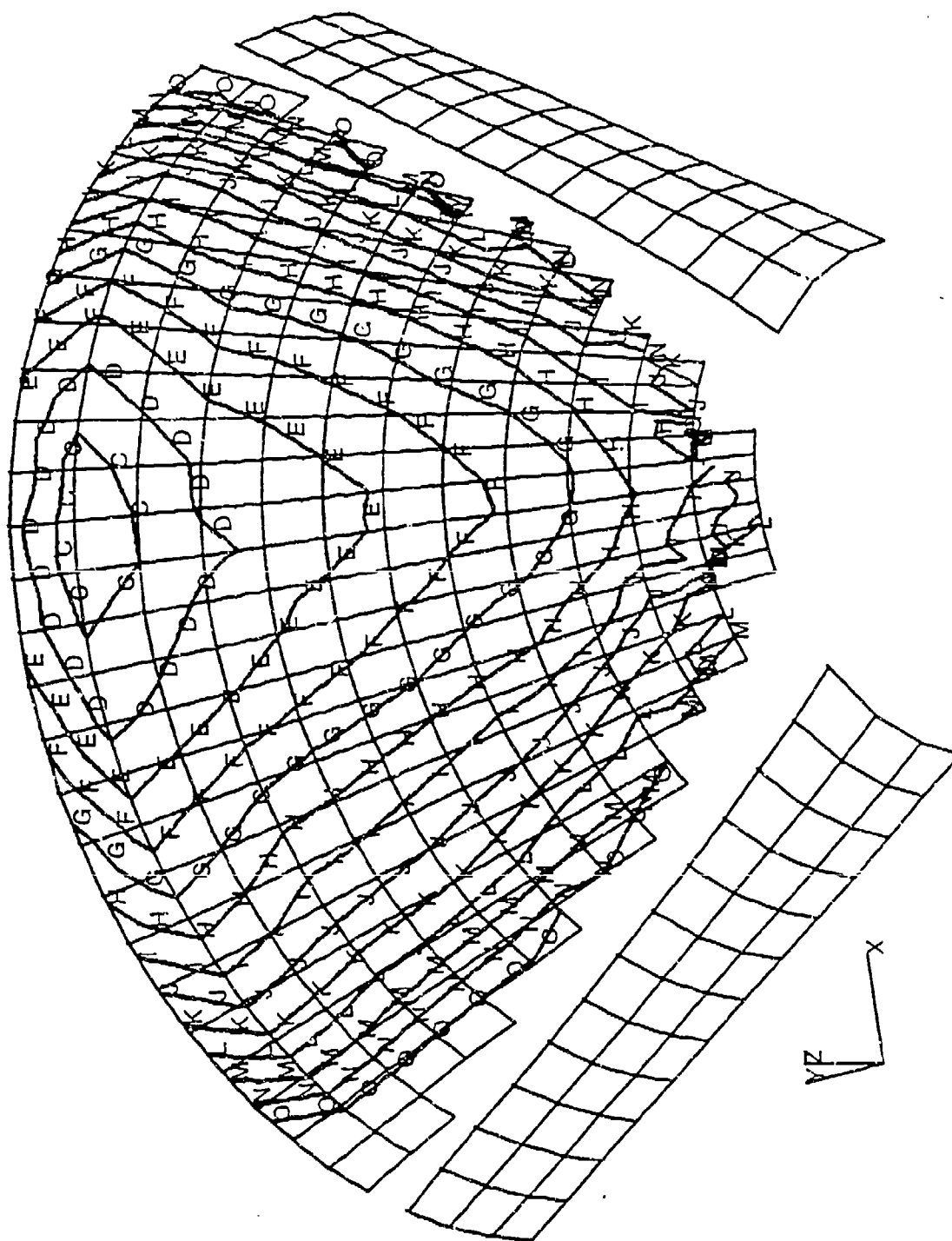
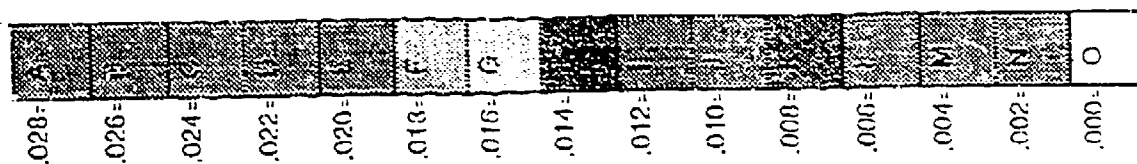


Figure 3. Shrinkage contours for conical panel.

Figure 4. Overall Dimensions at five locations (A-E)

<u>PART</u>	<u>A</u>	<u>B</u>	<u>C</u>	<u>D</u>	<u>E</u>
MOLD	21.891	9.3095	12.005	12.006	10.9440
D880614_09	21.852	9.2380	11.961	11.963	10.8720
D880614_12	21.757	9.1556	11.953	11.941	10.8595
D880614_13	21.926	9.2439	11.946	11.955	10.8500
D880615_01	21.760	9.1695	11.956	11.955	10.8725

A - Aft end

B - Forward end

C - Port, measurement from aft plane to forward face of forward tab

D - Starboard, measurement from aft plane to forward face of forward tab

E - Distance from sill edge base to aft-most, center-line grid point.

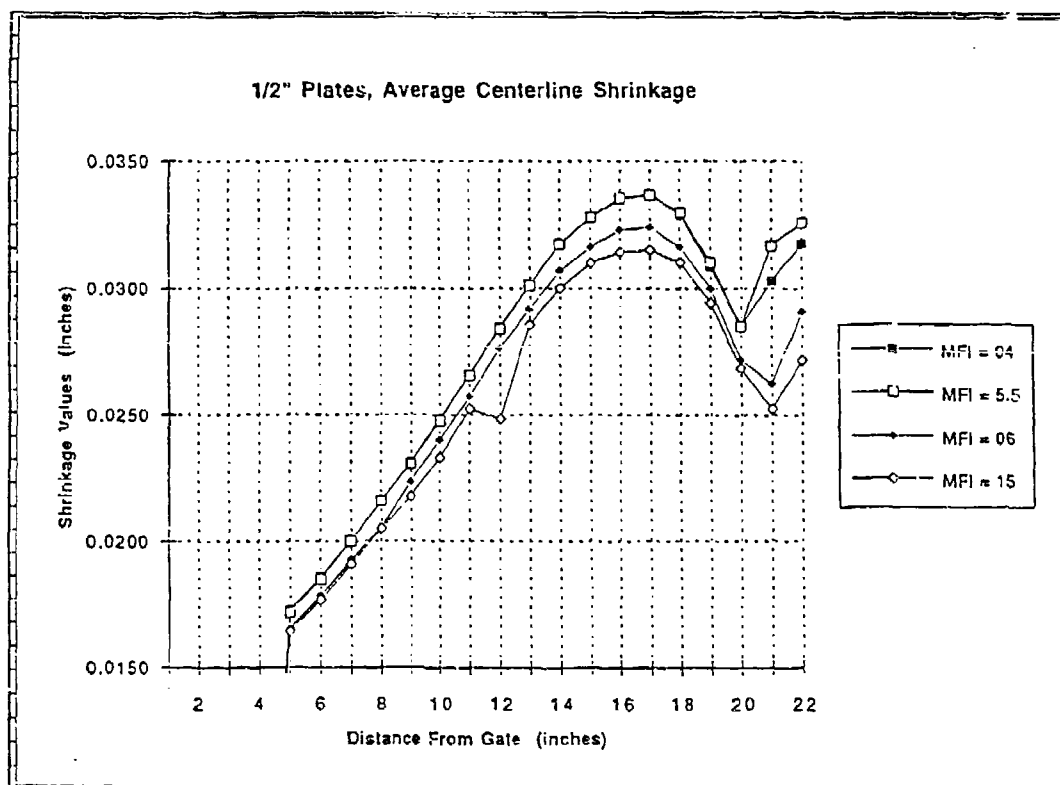
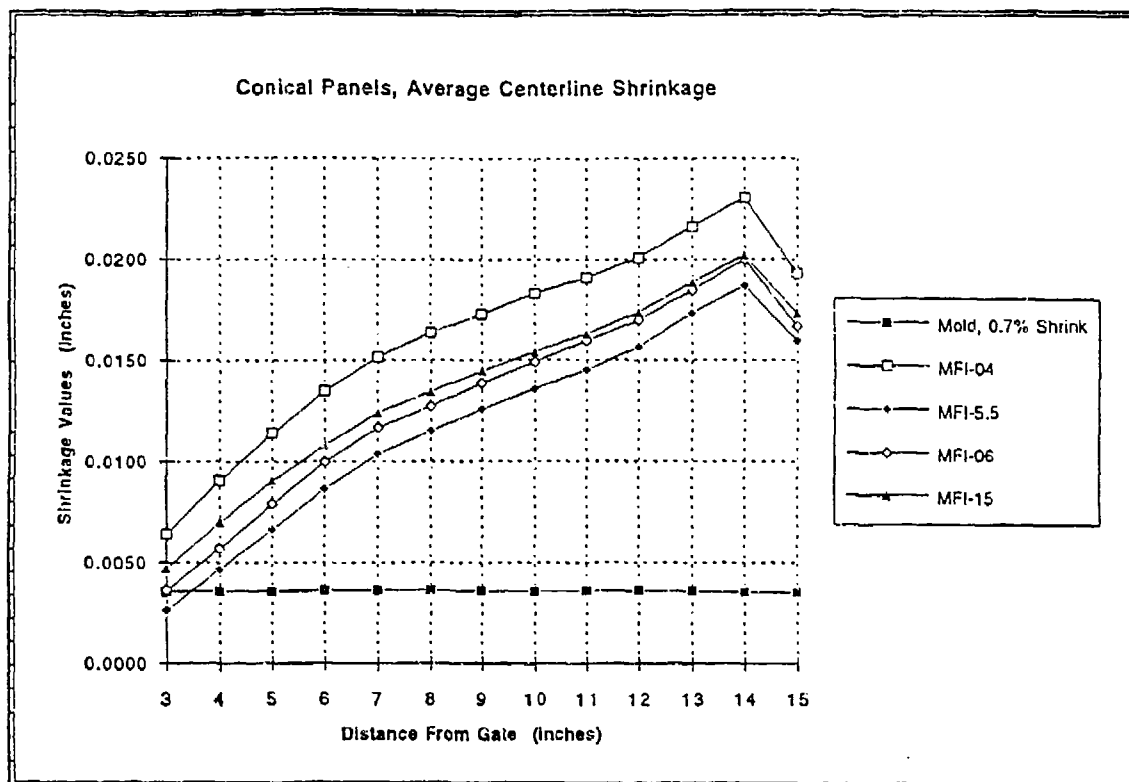


Figure 5. Melt flow index vs shrinkage

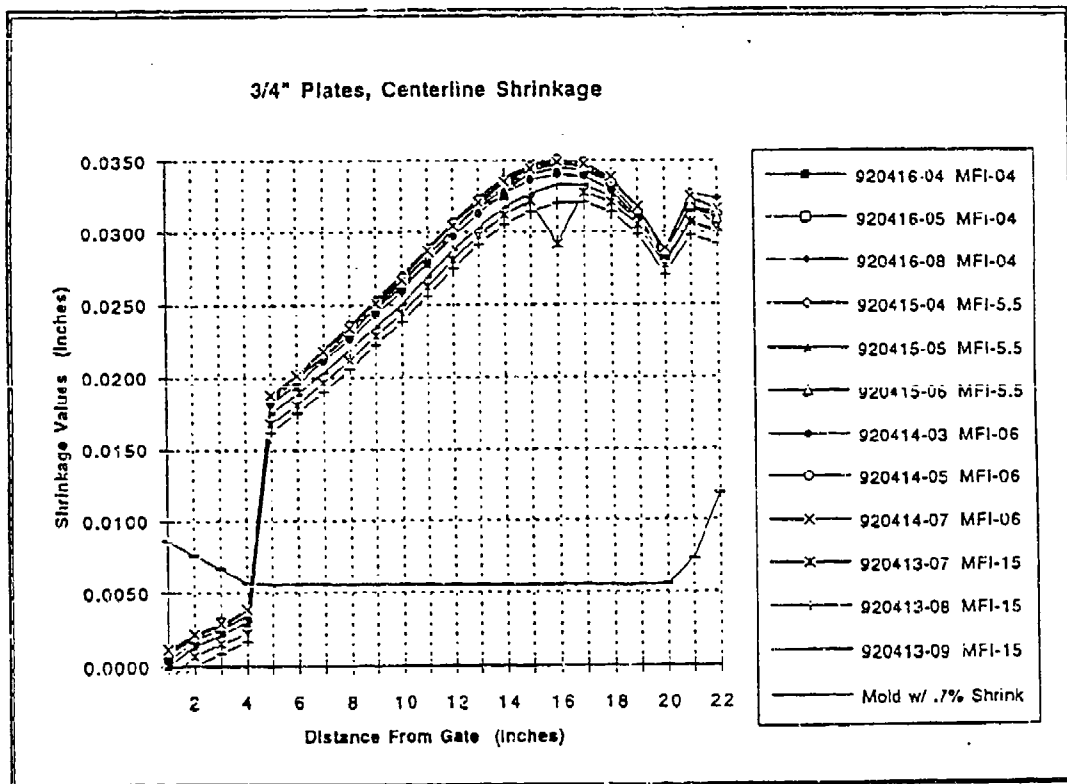
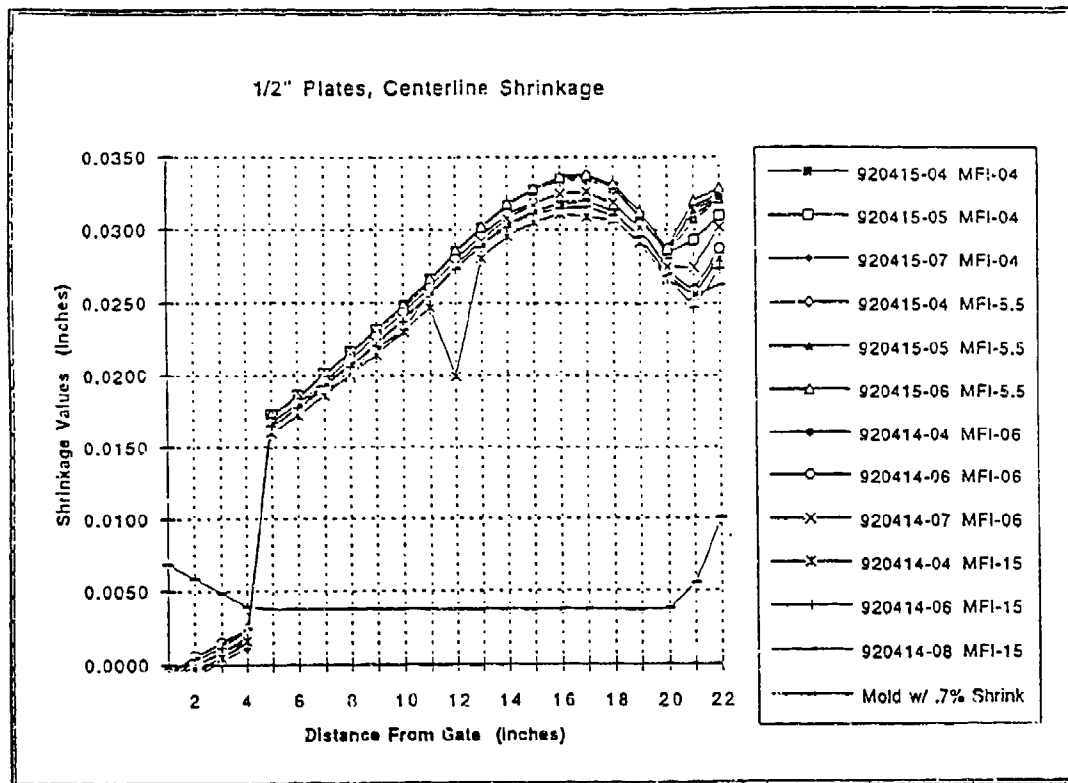


Figure 6. Part thickness vs shrinkage

# 3-D Shrinkage Compensation Surface

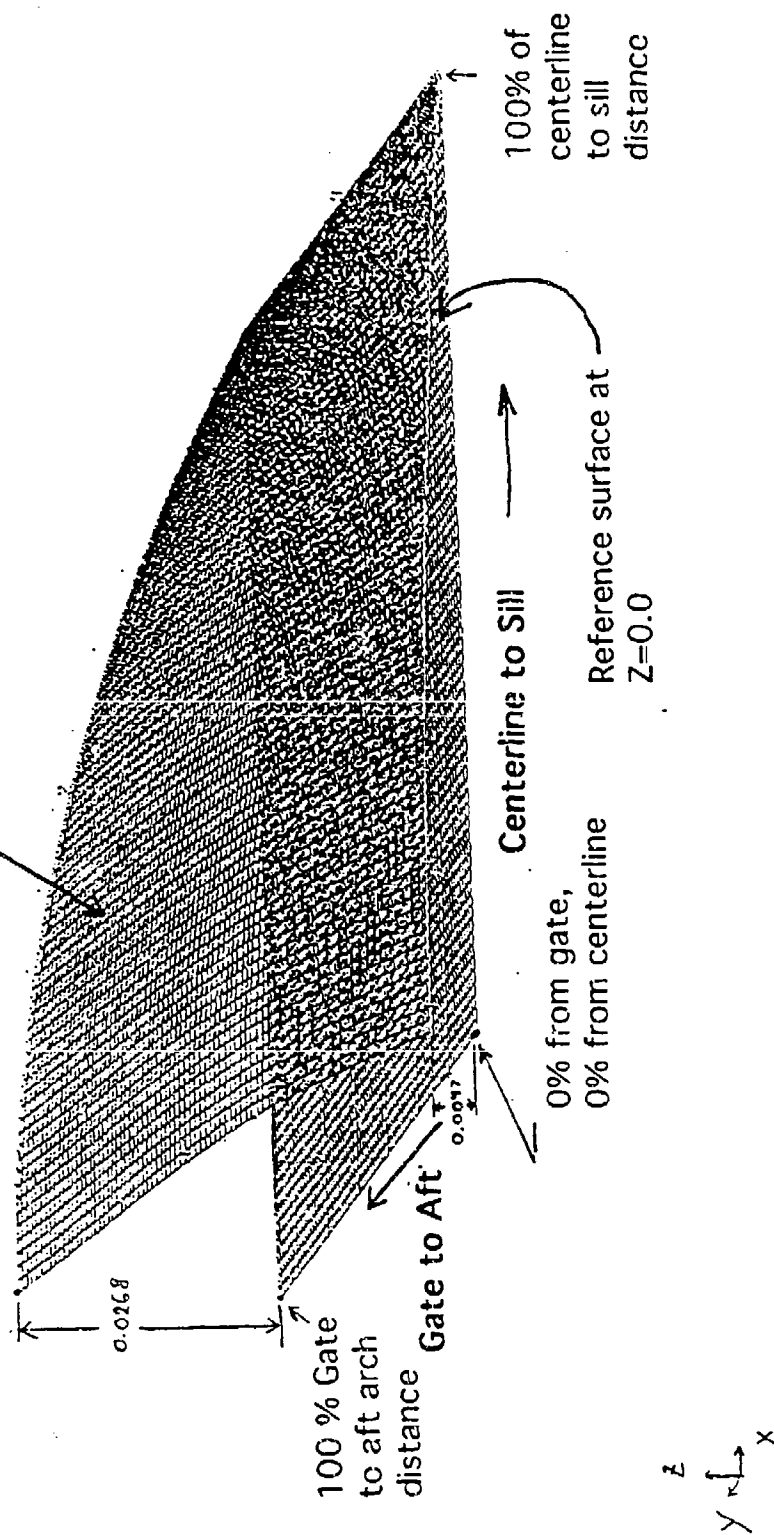


Figure 7. Shrinkage compensation for CFT mold cavity geometry